Magnetospheric Multiscale Mission (MMS): Extended Mission

B. L. Giles, MMS Project Scientist • J. L. Burch, MMS Science PI

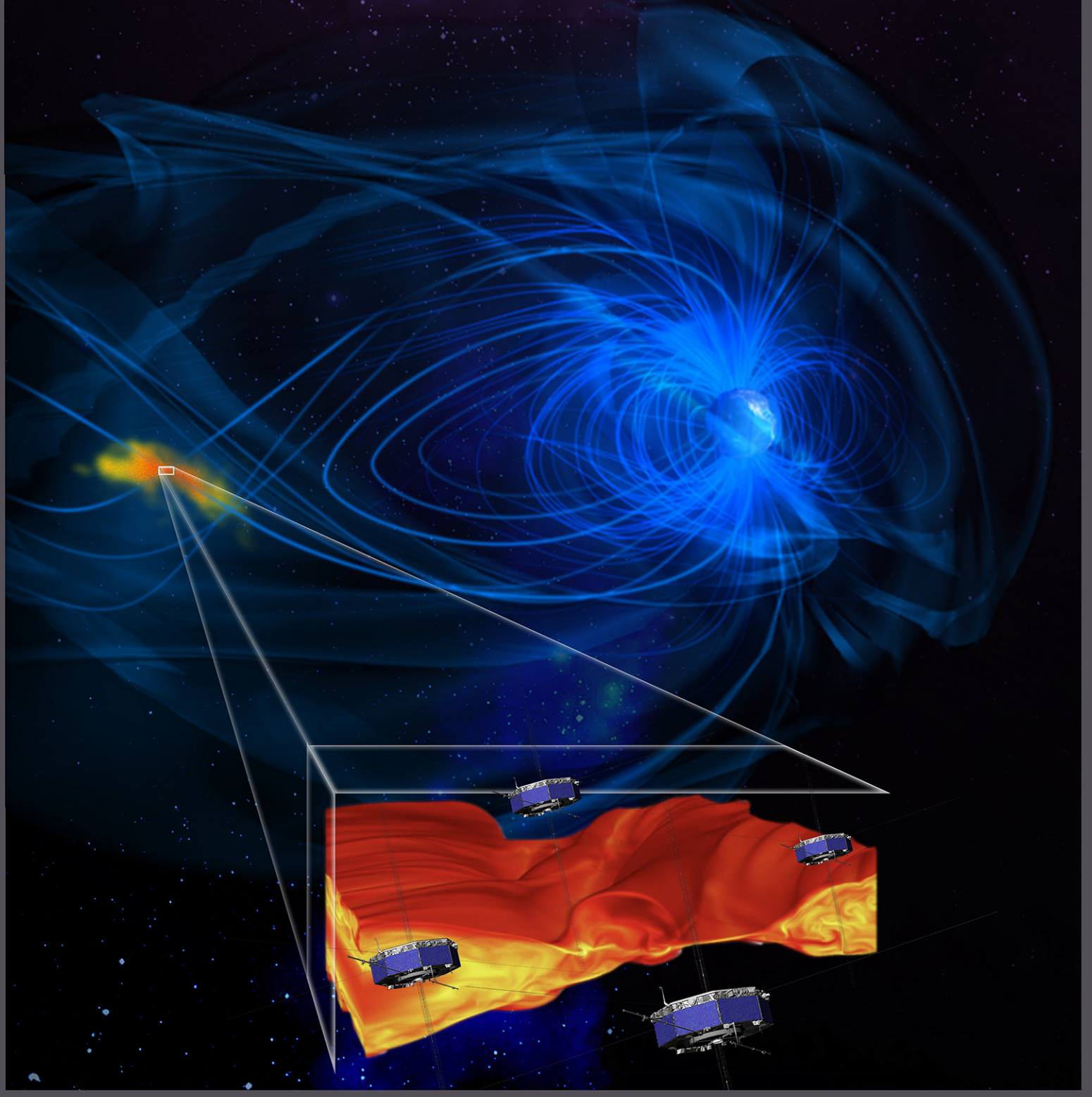

Submitted to the 2023 Heliophysics Division Senior Review of the Mission Operations and Data Analysis Program for Heliophysics Operating Missions
November 22, 2022

Table of Contents

Executive Summary

MMS has the overall objective of solving magnetic reconnection in the boundary regions of the Earth's magnetosphere. During the most recent extended mission, MMS discovered (1) an accurate way to measure the reconnection rate based on electron inflow velocity, (2) highly dynamic electron diffusion regions with alternating loads and generators, (3) the separatrix layers being the site of significant electron heating and thermalization, (4) a dominant mechanism for suprathermal electron acceleration in exhausts, (5) a new formation mechanism for flux transfer events from interlinked reconnection, (6) turbulent structures in Kelvin-Helmholtz vortices leading to entangled field lines and reconnection, (7) the prevalence of electron-only reconnection in turbulent structures throughout the near-Earth space, (8) a new stochastic shock drift acceleration mechanism, and (9) the nature of kinetic-scale turbulence and its role in reconnection and particle acceleration. These results and many others are reported in the over 1100 MMS papers that have been published over the mission lifetime.

Results to date were obtained during the declining phase of solar cycle 24 through the 2020 minimum and the start of cycle 25. This extension will occur during rising solar activity through the solar maximum in 2025. We expect more active conditions in the boundary regions where magnetic reconnection occurs, as well as in interplanetary space where interplanetary shocks should become more numerous.

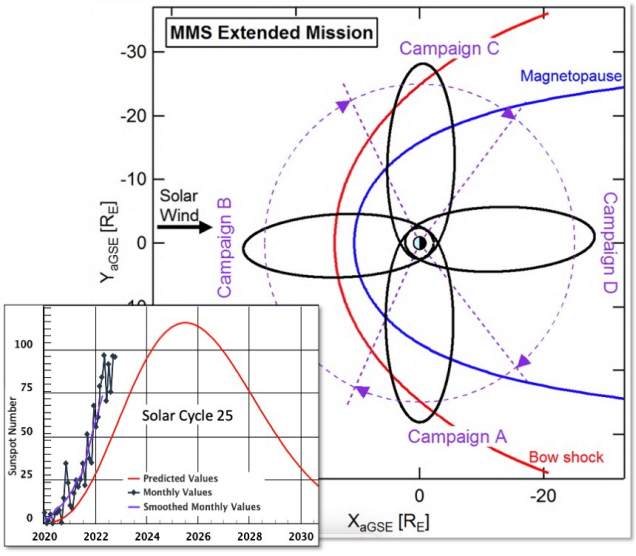

MMS orbits are divided into four campaigns (A-D) with specific objectives defined for each region.

Objectives for FY24-FY26 Extended Mission:

SO1: Understand the role of kinetic physics in the strongly driven magnetosphere during intense space weather events near solar max

SO2: Discover how the electron-kinetic dynamics that enable magnetic reconnection couple to the larger-scale geospace environment

SO3: Understand particle acceleration processes in the magnetotail and their relationship to magnetic reconnection

SO4: Understand the fundamental nature of kinetic-scale turbulence, including its coupling to larger scales

SO5: Understand the role of kinetic physics in the bow shock and interplanetary shocks

These more active conditions – and a new multiscale spacecraft separation strategy – allows us to refine our scientific goals in order to determine how electron-kinetic physics contributes to the large-scale dynamics of our geospace environment.

MMS is uniquely suited to accomplish its FY24-FY26 objectives with its 4-point measurements of particle and fields at the highest time resolution and accuracy ever achieved in space. During this extended mission, MMS science continues its yearly observing campaigns (A–D) with emphasis on certain regions of space: A, duskside flank; B, dayside; C, dawnside flank; and D, magnetotail (see figure). The MMS spacecraft remains in the electron-scale tetrahedron configuration through calendar year 2023, after which we propose changes to the spacecraft configuration. Examples of new configurations include a multi-scale tetrahedron, allowing for simultaneous sampling of adjacent plasma regimes and a logarithmic string-of-pearls formation with separations approximating a geometric series, e.g., 30 km, 650 km, 15,000 km in order to sample electron, ion and MHD scales simultaneously.

Both in-guide and over-guide cost estimates are provided. With the over-guide, all objectives can be accomplished. The in-guide budget requires staff reductions, prioritization of the objectives, and the potential that the cross-scale constellation reconfigurations cannot be afforded. As a result, at the in-guide level only the primary objective of electron-scale reconnection physics can be addressed while the work on turbulence, shocks, particle acceleration, multi-scale coupling, and other important phenomena may be curtailed.

1. Completion of Previous Objectives

In the 2.5 years since the last Senior Review proposal, more than 540 papers have been added to the MMS publication list. Important discoveries and advances have been made in the understanding of the microphysics of magnetic reconnection, shocks, turbulence, and their inter-relationships. Equally important, MMS has played a central role in numerous large-scale studies of magnetospheric processes in conjunction with other missions. This section highlights the key discoveries; many more related contributions are cited within the representative references provided here.

In 2020, as required, MMS proposed a five-year science plan for FY2021-FY2025. All objectives proposed for the period FY2021-FY2023 – labeled "prioritized science goals" at that time – have been substantially completed, with further closure being in progress through FY23, the third year of the present mission extension. Previous plans for FY24-FY25, when MMS would incorporate one or more ion-scale or multi-scale string-of-pearls formations have been refined in Section 2 for the new FY24-FY28 five-year plan. Table 1.1 maps the previous objectives to the accomplishments review in this proposal, which lists just a few key results in each category.

1.1. Understand how reconnection works in all boundary regions in Geospace

1.1.1. Accurate reconnection rate determination from electron inflow velocity. The all-important reconnection rate is notoriously difficult to measure experimentally. Historically, the rate is determined using the ion inflow velocity and the out-of-plane reconnection electric field. Because these quantities are exceedingly small compared to other velocity and electric field components, any small uncertainty in the knowledge of the current sheet and X-line frames and motions can affect the accuracy of the reconnection rate estimation. Burch et al. (2020, 2022) have pioneered a more accurate way to measure the rate using the electron inflow velocity, based on the fact that electron inflow velocity at the edges of the electron diffusion region scales with the electron Alfvén speed, and therefore is much faster than the current

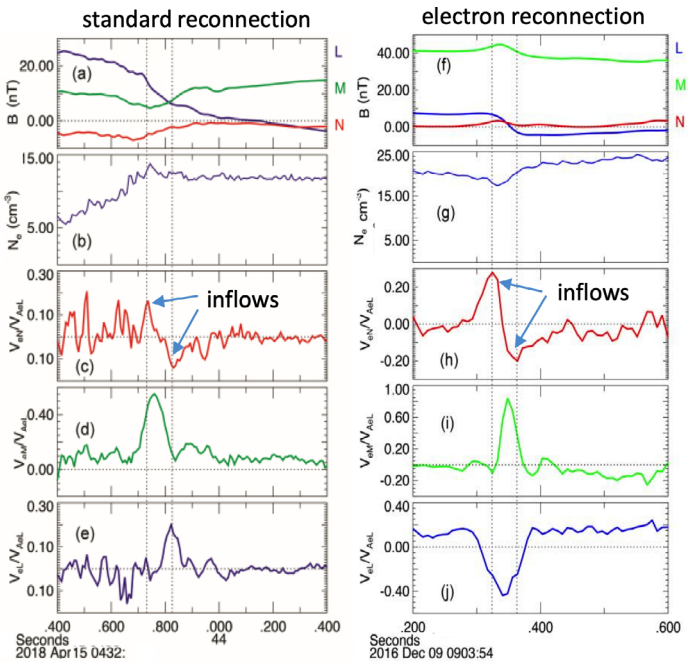

Figure 1.1. Reconnection rate obtained from electron inflow velocity for standard and electron-only reconnection (Burch et al., 2020).

sheet and X-line motions. This method revealed a dimensionless rate of 0.05-0.25 for magnetopause and magnetotail events, with the rate for electron-only reconnection (Figure 1.1) being larger than those of standard ion-coupled reconnection.

1.1.2. Dynamic electron diffusion region (EDR). Research on EDR physics in the last 2-3 years was marked by numerous discoveries not anticipated by theory. One such discovery is the highly patchy but coherent energy conversion inside EDRs (Genestreti et al. 2022), often with alternating load and generator signatures (Payne et al., 2021). While variable inflow plasma and field conditions could contribute to the patchiness of energy conversion (Genestreti et al., 2022), kinetic simulations suggest that the generators (i.e., particle to field energy conversion) form where the outflowing super-Alfvénic electrons locally lose bulk kinetic energy to the fields as they become re-magnetized (Payne et al., 2021). In another surprising discovery, MMS observed evidence for magnetic annihilation, rather than magnetic reconnection, in a magnetotail current sheet (Hasegawa et al., 2022). Magnetic en-

Table 1.1: Mapping of 2020 SR Goals/Objectives to the Accomplishment Review in this Proposal	
Understand how reconnection works in all boundary regions in Geospace	1.1.1-1.1.6, 1.1.8- 1.1.10
Understand particle acceleration processes in the outer magnetosphere and bow shock and their possible relationship to magnetic reconnection	1.1.7, 1.2
Determine the nature of kinetic-scale turbulence and its role in reconnection and particle acceleration.	1.3, 1.2
Heliophysics System Observatory Science	1.4

ergy dissipation occurred in an elongated EDR with embedded electron-scale islands, in contrast to the standard EDR where the energy is mostly converted to electron flow energy via magnetic topology change.

1.1.3. Transition from EDR to ion diffusion region (IDR). Fortuitous ion-scale MMS spacecraft separations during orbit adjustment periods provided the first observations of the transition between EDR and IDR at the magnetopause. Simultaneous MMS observations detected the transition from super Alfvénic electron outflow near the EDR to the emergence of sub-Alfvénic ion outflow in the IDR. Unique to MMS, these observations revealed the conversion of electron kinetic energy to magnetic energy in the region where the inflowing electrons braked and turned into the outflow direction (Genestreti et al., 2020). MMS also discovered, surprisingly, that the bifurcation of the reconnected current sheet, often seen extending far downstream of the X-line, originates already in the IDR (Øieroset et al., 2021). These "serendipitous" spacecraft formations show the promise of the proposed reconfigurations for the coming extended mission.

1.1.4. 3-D magnetic field reconstruction. An important polynomial magnetic field reconstruction method has been developed by the MMS team to place in-situ measurements into reconnection context (Torbert et al., 2020). This new method provides 3D and time-varying reconstruction of the field lines around the four MMS spacecraft and was successfully used in EDR events to visualize the spatial and temporal evolution of reconnection X-lines and O-lines (Figure 1.2).

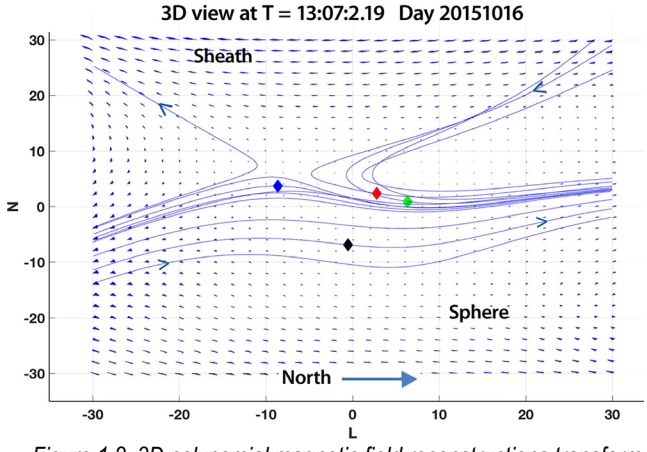

Figure 1.2. 3D polynomial magnetic field reconstructions transform MMS point measurements into time-varying 3D visualizations of reconnection topology. Pictured is one frame of the 2015-10-16 magnetopause EDR reconstruction (Torbert et al., 2020).

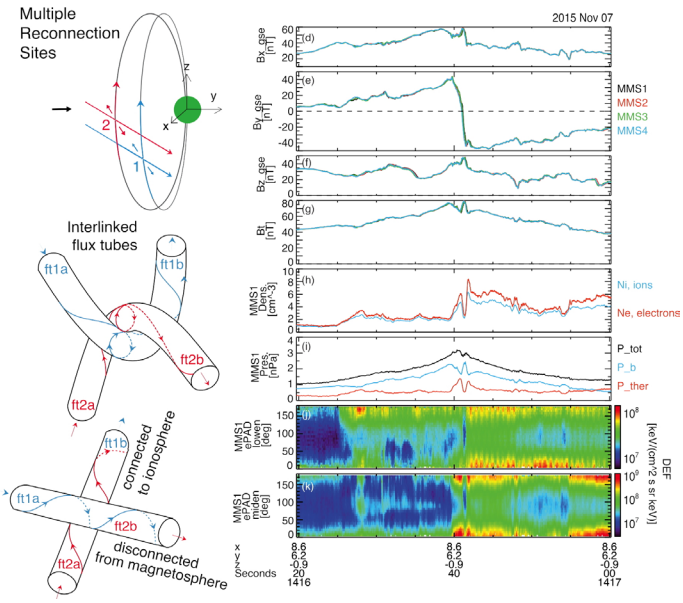

Figure 1.3. Formation of FTE via interlinked reconnection (Russell and Qi, 2020).

1.1.5. Formation of flux transfer events (FTEs) from interlinked reconnection. MMS revealed that reconnection between interlinked flux tubes originating from multiple X-lines leads to the formation of flux ropes at the magnetopause (Russell and Qi, 2020; Hwang et al., 2021; Jia et al., 2021) (Figure 1.3). This 3D FTE formation process occurs predominantly when the interplanetary magnetic field has a strong east-west component, a condition that leads to guide field reconnection at the magnetopause, where field lines from multiple X-lines get tangled up and reconnect (Fargette et al., 2020).

1.1.6. Kinetic structure of Kelvin-Helmholtz (K-H) vortices. MMS detected the generation of turbulence in K-H vortices (Hasegawa et al., 2020), including large amplitude ion acoustic waves, as well as time domain structures such as double layers and electrostatic solitary waves (Wilder et al., 2021). The K-H waves further amplify electromagnetic fluctuations in the magnetopause boundary layer and induce entangled field lines. Subsequent reconnection between entangled field lines can cause efficient plasma transport across the magnetopause (Kieokaew et al., 2020).

1.1.7. Super-thermal particle acceleration processes. One of the most spectacular and difficult to explain consequences of reconnection is the observed efficient acceleration of particles to high energies. MMS's small-scale multiple-point measurements have made it possible to quantitatively evaluate the various acceleration mechanisms. Eriksson et al.

(2020) compared the power density converted via the Fermi, betatron, and parallel electric field acceleration in magnetotail reconnection, and found that the dominant electron acceleration mechanism was Fermi acceleration around the current sheet center.

1.1.8. Kinetic structures in separatrix layer. MMS has revealed that significant energization occurs in the separatrix layers in the magnetotail (Norgren et al., 2020; Holmes et al., 2021). Cold electron inflow populations are accelerated toward the X line, forming beams with energies up to a few keV. The accelerated electron populations are unstable to the formation of electrostatic waves, which develop into nonlinear electrostatic solitary waves. The waves interact efficiently with a large part of the electron population and gradually thermalize the beams, transforming directed drift energy into thermal energy.

1.1.9. Role of waves in reconnection. MMS made important contributions to the understanding of wave-particle interactions and the role of waves in reconnection. For the first time, anomalous resistivity and diffusion from lower hybrid waves were calculated directly (Graham et al., 2022). MMS showed that while anomalous resistivity was unlikely to contribute significantly to reconnection, the anomalous diffusion was sufficiently large to broaden the current layer and lead to particle transport. Electromagnetic lower hybrid waves associated with the electron diffusion region were found to cause kinking of current sheets (Cozzani et al., 2021), and lead to agyrotropic electron distributions and heating (Chen et al., 2020).

1.1.10. Prevalence of electron-only reconnection. MMS continues to discover electron reconnection (without ion coupling) in kinetic-scale turbulent structures. These included substructures inside foreshock transients (Liu et al., 2020), flux ropes (Man et al., 2020), and dipolarization fronts (Marshall et al., 2020). Such structures are highly 3D, with enhanced reconnection rates (Pyakurel et al., 2021). These findings suggest that electron reconnection plays an important role in the dynamics of shocks and turbulence.

1.2. Determine the nature of kinetic-scale turbulence and its role in reconnection and particle acceleration

MMS is the best tool to study kinetic-scale physics of plasma turbulence. Afshari et al. (2021) examined correlations between particles and electric fields in velocity space and quantified the extent to which Landau damping contributes to turbulent dissipation. Stawarz et al. (2021) used multipoint MMS observations to directly probe the terms in generalized Ohm's law and assess how the turbulent electric fields dynamically arise from MHD to electron scales (see Figure 1.4). Stawarz et al. (2022) systematically identified reconnection events in the turbulent magnetosheath, finding that the presence of electron-only reconnection is linked to the correlation length of the turbulence. Along with complimentary studies quantifying how current sheets and reconnection in the bow shock act as a driver for magnetosheath turbulence (Schwartz et al. 2021; Gingell et al. 2020; Yordanova et al. 2020; Bessho 2022), MMS is bringing together three fundamental areas of plasma physics research – turbulence, shocks, and reconnection. Meanwhile, MMS observations in the magnetotail have shed light on how turbulence generated within large-scale reconnection outflows contributes to superthermal energetic particle acceleration (Ergun et al. 2020a,b).

1.3. Understand particle acceleration processes at bow shock and their possible relationship to magnetic reconnection and turbulence

MMS provides a unique opportunity to study shocks at all kinetic scales. At electron-scales, the discovery of whistler turbulence and associated acceleration of electrons has led to a new stochastic shock drift acceleration theory (Amano et al., 2020) (Figure 1.5). At ion-scales, MMS demonstrated the role of gyro-resonance in producing solitary magnetic structures that may be important for the acceleration of ions to very high energies (Chen et al., 2021a). At the Debye-scale, MMS revealed that

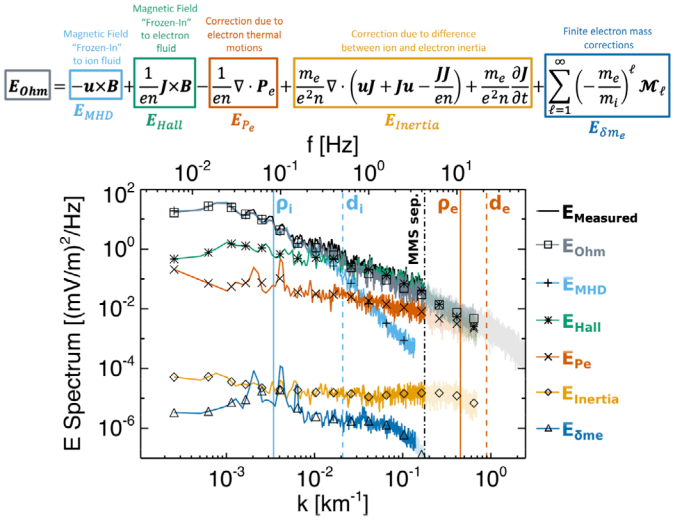

Figure 1.4. MMS reveals how the different contributions to generalized Ohm's law govern the turbulence dynamics in the magnetosheath from MHD through kinetic scales (Stawarz et al., 2021).

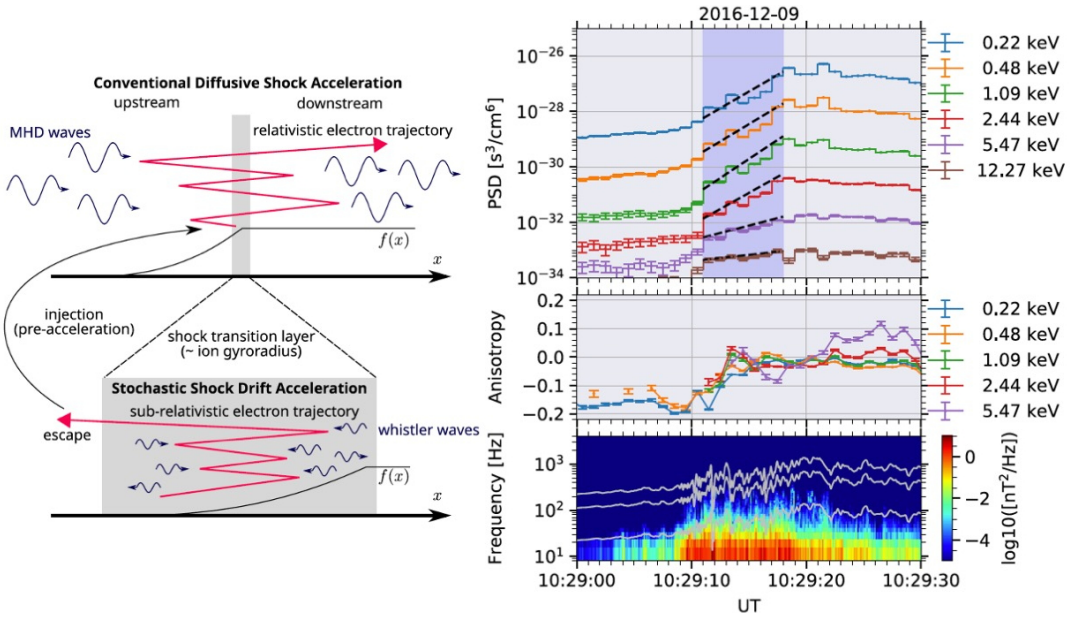

Figure 1.5. A new picture of electron acceleration (left) that emerged from MMS measurements of both particles and electromagnetic turbulence at Earth's bow shock (right) (Amano et al., 2020)

electrostatic solitary waves are predominantly ion phase space holes produced by ion steaming instabilities (Vasko et al., 2020; Wang et al., 2020; Wang et al., 2021). MMS also revealed evidence that magnetic pumping in spatially varying flux tubes can lead to effective power law particle energization via magnetic trapping of superthermal particles (Lichko and Egedal, 2020).

1.4. Heliophysics System Observatory Science

MMS provides valuable microscopic, multipoint observations that contributed to the greater network of NASA's HSO. Some of the latest results include the magnetospheric response to solar wind driving, magnetotail sources and magnetopause losses of Earth's radiation belt electrons, the complexity of Earth's bow shock, and the nature of dipolarization in Earth's magnetotail. Highlighted results include: the combination of remote sensing, using IBEX energetic neutral atoms (ENAs), and MMS in-situ observations revealed (a) a measure of the curvature and asymmetric geometry of Earth's bow shock (Starkey et al., 2022) and (b) the distribution of cold magnetospheric plasma along the magnetopause and how exospheric neutral density may exhibit a solar cycle dependence along the dayside magnetopause (Fuselier et al., 2020). To better understand the extreme variability of Earth's outer radiation belt electrons, MMS was used in combination with Van Allen Probes, THEMIS, and GOES to (1) establish the role of electron acceleration in the magnetotail as a possible source of outer belt electrons (Turner et al., 2021) and (2) quantify the role of losses of radiation belt electrons through Earth's dayside magnetopause (Cohen et al., 2021; Staples et al., 2022). MMS also proved critical in the HSO alongside observations from TWINS, Van Allen Probes, Cluster, and THEMIS to refine understanding of the magnetotail current sheet (Artemyev et al., 2021), as well as the nature of magnetotail dipolarization, including associated injections and ring current enhancements (Goldstein et al., 2020) (Figure 1.6).

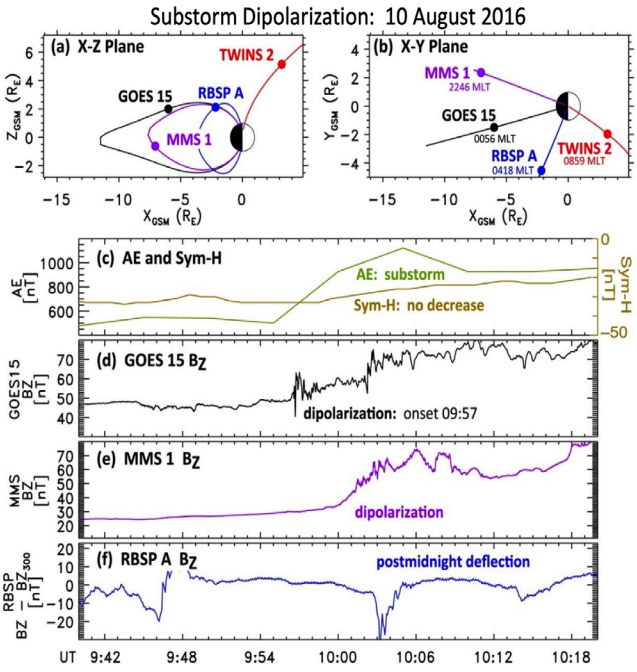

Figure 1.6. HSO observations of magnetotail dipolarization associated with auroral substorm (Goldstein et al., 2020).

2. Scientific Goals and Objectives for New Funding Period

MMS targets the fundamental physics that drives magnetic reconnection, energy conversion, particle acceleration, mass/energy transport, and turbulence and proposes to continue its unique role within NASA's Heliophysics System Observatory as the fleet's and world's sole geospace microscope. MMS prioritized science goals (SG) are well aligned with NASA's goals for Heliophysics research. The science objectives (SO) for this extended mission are chosen to target the most pressing scientific questions within those overarching goals, emphasizing microphysics in a variety of contexts and increasingly targeting connections to larger spatial scales. New observing opportunities are afforded by the upcoming extended mission, which provides the first electron-scale measurements (a) in the high-latitude magnetosphere and (b) during the rising and solar maximum phases.

2.1 SO1: Understand the role of kinetic physics in the strongly driven magnetosphere during intense space weather events near solar maximum.

Reconnection remains one of the main foci of MMS, as is fitting given its unique capabilities. Objectives for the extended mission advance our understanding of reconnection in three key ways:

(1) By answering remaining open questions on the electron diffusion region (EDR), including testing of our understanding,

(2) By understanding how processes at multiple scales couple and regulate energy conversion, the reconnection rate, and particle acceleration, and

(3) By understanding how reconnection ceases to operate.

The impacts of the proposed research plan test and substantially advance our understanding of the fundamental microphysical processes that enable reconnection. By understanding how these microphysical processes couple to the larger-scale geospace environment, we provide a new level of understanding of magnetospheric dynamics, and of the dynamics of a cross-scale coupled plasma system.

2.1.1. How does turbulence modify reconnection in the active plasma sheet? The pressure in the storm-time equatorial magnetotail is often dominated by the magnetic field as reconnection ejects high-beta plasma-sheet field lines and replaces them with low-beta lobe field lines. In an active plasma sheet, signatures of multiple reconnection sites were observed with large-amplitude and persistent (10's min) kinetic plasma turbulence (Ergun et al. 2018, 2020a, 2020b). This observation showed an association between magnetotail reconnection and turbulence and revealed the role of kinetic turbulence in accelerating ions and electrons to non-thermal energies. One observation of an EDR embedded in turbulence shows a near-laminar process (Ergun et al., 2022) albeit with a temporary disturbance. Understanding of the behavior of the EDR in turbulent magnetotail reconnection is elusive because magnetotail EDR encounters can be elusive. Another mystery is that,

SMD Heliophysics Goals:

G1: Explore the physical processes at work in the space environment from the sun to Earth and throughout the solar system

G2: Advance our understanding of the connections between the sun, Earth, the planetary space environments, and the outer reaches of our solar system

G3: Develop the knowledge and capability to detect and predict extreme conditions in space to protect life and society and to safeguard exploration beyond Earth

MMS Goals, since and including Prime Mission:

SG1: Understand how reconnection works in the boundary regions of Geospace for a wide range of plasma conditions (G1, G2, G3)

SG2: Understand the processes that heat plasma populations and accelerate particles to large energies, especially their relationship to magnetic reconnection (G2, G1, G3)

SG3: Determine the nature of kinetic-scale turbulence and its role in reconnection and particle acceleration (G1, G2)

SG4: Investigate the microphysics of collisionless shocks (G2, G1, G3)

Objectives for FY24-FY26 Extended Mission:

SO1: Understand the role of kinetic physics in the strongly driven magnetosphere during intense space weather events near solar max (SG1)

SO2: Discover how the electron-kinetic dynamics that enable magnetic reconnection couple to the larger-scale geospace environment (SG1, SG2)

SO3: Understand particle acceleration processes in the magnetotail and their relationship to magnetic reconnection (SG2, SG1)

SO4: Understand the fundamental nature of kinetic-scale turbulence, including its coupling to larger scales (SG3)

SO5: Understand the role of kinetic physics in the bow shock structure and interplanetary shocks (SG4)

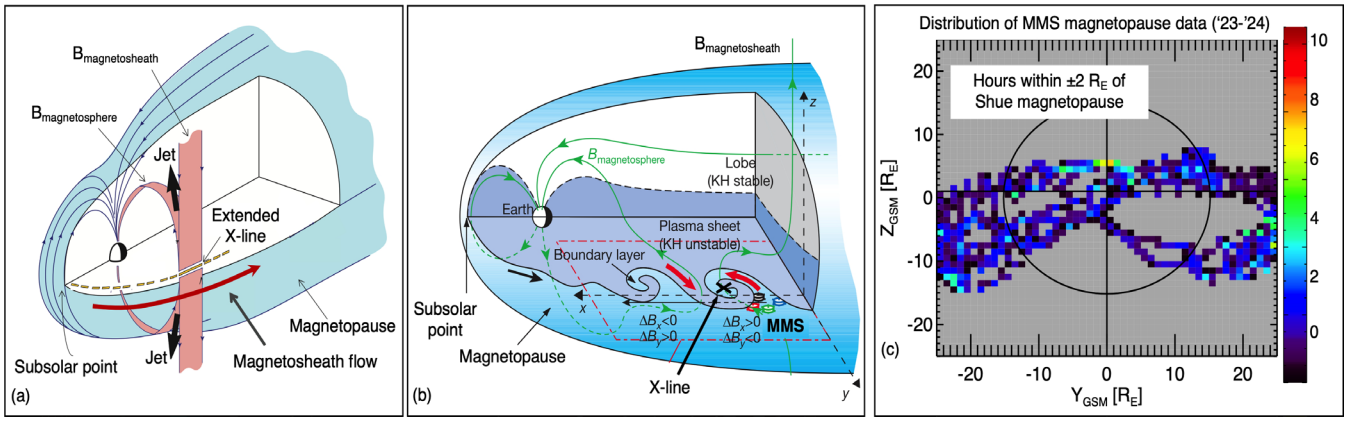

Figure 2.1: During the early extended mission, MMS encounters the dayside and flank low- and high-latitude magnetopause (c), enabling studies of magnetopause reconnection in the presence of strong flow shears. MMS observations distinguish between extended X-line and Kelvin-Helmholtz scenarios at the magnetopause flanks, as illustrated in (a) and (b), respectively.

in some events, the observed ion jet reverses only once and persists for many ion cyclotron periods, indicating a single EDR dominating the reconnection process, while other turbulent events show several jet reversals suggesting multiple EDR formation. This line of research is critical to understanding how magnetic reconnection operates in turbulent and strongly driven conditions and is pursued during the proposed extended mission.

2.1.2. How is magnetic reconnection enabled at current sheets with large velocity shears? Flow shear across the magnetopause is common and may affect key aspects of reconnection, e.g., the reconnection rate (Cassak and Otto, 2011), the stability and motion of a reconnection site (Wilder et al., 2014), the efficiency of and mechanism for electron dissipation and demagnetization (Eriksson et al., 2016), and the structure of the EDR (Liu et al., 2018). Under strong solar driving, it remains unknown as to how flow shear in asymmetric magnetopause reconnection affects reconnection at the kinetic level and beyond. For southward IMF, important open questions include (i) whether stable low-latitude reconnection, of the type depicted in Fig 2.1a, persists in the presence of a super-Alfvénic flow shear or whether reconnection in Kelvin-Helmholtz vortices (KHVs) dominate in this regime, (ii) whether the reconnection rate is reduced or suppressed by flow shear in the outflow direction larger than twice the Alfvén speed, and (iii) whether the electron inertia-based demagnetization model is generally valid for a wide range of upstream conditions in the presence of a super-Alfvénic out-of-the-reconnection-plane flow shear.

2.1.3. Researching these topics with MMS. The apogee and inclination of the extended MMS mission orbit are ideal for studying the effects of flow shear on magnetopause reconnection at both low- and high-latitudes. MMS typically encounters the dayside magnetopause above and below the subsolar point, where reconnection occurs with flow shears approximately parallel to Earth's dipole (Figure 2.1c), and the nightside flank magnetopause where reconnection is observed for large flow shears perpendicular to Earth's dipole field (Figure 2.1a,b). High spatiotemporal resolution measurements, unique to the mission, of electron distribution functions, current densities J, and electric fields E, characterize the reconnection rate, the energy conversion rate (J·E), the diffusion region structure, and the electron nongyrotropy (or lack thereof). The mission's multi-spacecraft capability identifies the presence (or lack thereof) of KHVs and characterizes the strength and orientation of flow shear by taking upstream measurements before and after the magnetopause moves across the spacecraft.

The MMS extended mission is ideal for studying the strongly-driven, low-beta plasma sheet as the orbital plane becomes near-equatorial for the 2024 and later tail seasons, coinciding with the rising solar phase toward the maximum. The occurrence rates of geomagnetic storms and magnetotail diffusion regions are expected to be higher during the extended mission than for past MMS magnetotail observing seasons (which began in 2017), which all occurred during the deep minimum of solar cycle 24 (Genestreti, 2014).

2.1.4. Extensions via the Heliophysics System Observatory. The HSO plays an important role in putting MMS observations into a global context. Specifically, the HSO provides information related to

solar-wind driving (L1 monitor), larger-scale evolution in the magnetotail (THEMIS), and cusp magnetosheath (Cluster), as well as connections with the ITM region (ICON, GOLD). Observations by these and other assets are used to assess the macro-scale impacts of the microscale dynamics observed directly by MMS, providing a powerful research tool to the scientific community.

2.2 SO2: Discover how the electron-kinetic dynamics that enable magnetic reconnection couple to the larger-scale geospace environment.

2.2.1. What controls the effectiveness of magnetic reconnection? The effectiveness of magnetic reconnection depends critically on its duration, rate, and spatial dimensions. Candidate mechanisms to reduce the reconnection rate or shut off reconnection altogether are accessible to MMS measurements. An overview of candidate mechanisms is shown in Figure 2.2. MMS provides a unique opportunity to understand which one dominates when, and to develop a unified understanding of what controls the effectiveness of magnetic reconnection. The three categories are discussed in turn.

Inflow conditions. Changes in the reconnection inflow conditions can result from changing plasma populations, plasma properties, the magnetic field, or magnetic geometry. One prominent example is the involvement of cold, dense, plasma or beams in the inflow region(s) (Hesse and Birn, 2004; Borovsky and Denton, 2006; McFadden et al., 2008; Markidis et al., 2011; Garcia-Sage et al., 2015, Andre et al., 2016, Toledo-Redondo et al., 2016, Liu et al., 2014; Liang et al., 2017; Tenfjord et al., 2018).

The Alfvén speed changes induced by higher inflow mass densities are expected to reduce the reconnection rate, but dramatic changes – a rate reduction of a factor of ten requires a mass density increase of 100 - may not be achievable. Furthermore, on a kinetic level, inflowing ions need to be re-magnetized in reconnected flux tubes, or electrostatically coupled to magnetized electrons, to provide effective mass loading of the outflow jet.

Finally, the outflow partition of inflowing energy flux depends on the incoming plasma temperature – more precisely, on the plasma beta in the inflow region (Birn et al., 2011) – because any incoming plasma population has to be heated sufficiently to provide force balance with the inflow regions. It is

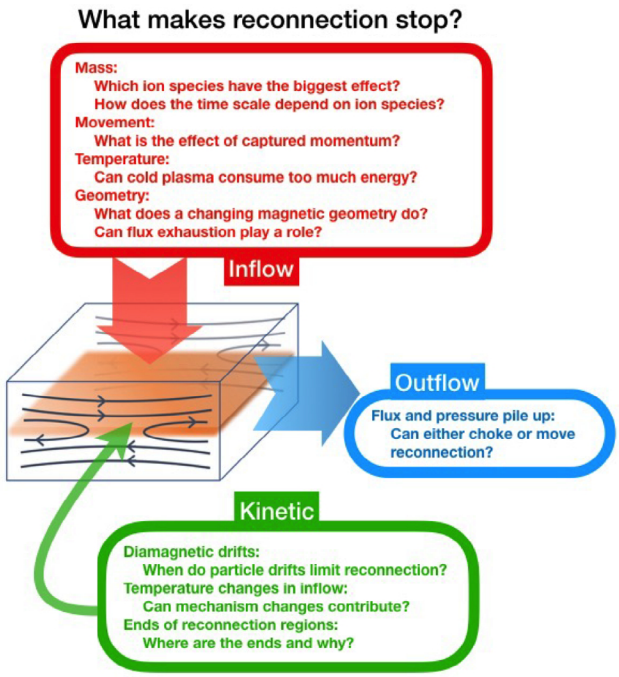

Figure 2.2: Overview of magnetic reconnection cession processes.

thought that this level of heating will be more difficult for lower plasma pressure in the inflow region, when more of the inflowing energy has to be spent on plasma heating, which would then make less energy available for outflow kinetic energy. This dependence, in itself, may not lead to a cessation of reconnection but may lead to reduced rates in combination with other factors. In conclusion, it is not clear which inflow population change has the biggest effect, or how much the rate will be reduced, and over which time scales. MMS has the opportunity to answer these questions.

On the nightside, and the high-latitude magnetopause, MMS plans to further investigate the interaction of reconnection with broader plasma flows. MHD modelling (Labelle-Hamer et al., 1995) indicates that super-Alfvénic shear flows suppress magnetic reconnection, and that slower shear flows can convect high-latitude reconnection regions anti-sunward. A similar scenario is likely to apply to reconnection in the magnetotail, where streaming mantle plasma may become involved, as reconnection is bound to encounter flux tubes filled with flowing mantle plasma at some time if the process lasts long enough. Like before, its density will tend to decrease reconnection rates, but its overall, tailward-directed momentum should generate a tailward motion of a reconnection region once sufficient mantle plasma

has been captured on reconnected flux tubes. Similarly, the tailward-moving magnetosheath plasma will impact its momentum on high-latitude magnetopause reconnection.

Dynamic changes, including magnetic rotation and flux reduction, in the inflow region are also excellent candidates to affect the reconnection rate. At the dayside magnetopause the impact of the shocked solar wind on the magnetopause wouldn't permit magnetic energy reductions in the inflow region although it may be different on the nightside, where the Bernoulli effect of the tangential magnetosheath flow may, at times, create flux reduction conditions. Here, fast reconnection may locally strongly reduce the magnetic flux in the inflow regions above and below, which can lead to a significant reduction of the reconnection rate (Liu et al, 2017). At the magnetopause, interplanetary magnetic field changes may locally cause a rotation of the inflowing magnetic field, similar to the solar corona, where magnetic shears can change reconnection from anti-parallel into strongly sheared geometries (e.g., Karpen et al., 2012). Since the direction of the reconnection line depends on the orientation of the magnetic field in the inflow region (e.g., Hesse et al., 2013), any significant changes to the latter likely require substantial re-orientations of the reconnection geometry. Not only is the dynamics of such re-orientation unknown on a kinetic level, but also the likely temporary or longer-term reduction of the reconnection rate is unknown. In conclusion, how inflow conditions affect the reconnection rate and the time scales involved are open questions to be resolved. MMS is ideally suited to investigate these processes, particularly in its multiscale configuration.

Outflow conditions. In order for magnetic reconnection to proceed, reconnected flux needs to be transported away continuously. Reconnection in the solar corona as well as in the plasma sheet of the Earth's magnetotail faces one closed boundary and hence the potential of backpressure by postflare loops (e.g., Longcope et al., 2009) or by the dipolarizing magnetic field, respectively. The asymmetric backpressure creates both macroscopically and microscopically an asymmetric reconnection scenario, which may lead to motion of the reconnection region seen in simulations (e.g., Karpen et al., 2012) and inferred from observations in the magnetosphere (Oka et al., 2011; Baumjohann et al., 1999). In the frame of reference of a moving reconnection region, the inflowing plasma will move, which can lead to a reconnection rate reduction. In addition, the reconnection region may move into regions of weaker inflow magnetic field by the flaring of the magnetotail, or the coronal altitude profile in the solar case. The flux pile-up may give rise to secondary instabilities, such as the ballooning mode (e.g., Pritchett and Coroniti, 2013), which can lead to fracturing of the reconnection line by backpressure effects. These processes can create reductions in overall reconnection efficiency, which will be investigated by MMS.

Kinetic conditions. The processes forming the reconnection diffusion region may change under varying physical conditions and influence the overall reconnection rate. For example, diamagnetic drift effects have the potential to prevent magnetic reconnection (Swisdak et al., 2003, Liu and Hesse, 2016). If not previously present, such drifts can be generated by magnetic field rotations in the inflow region and suppress an on-going reconnection process.

The diffusion region physics depends on the kinetic properties of the inflowing particle populations. How efficiently magnetic reconnection operates depends on parameters such as the ratio of drift and thermal speeds, with the latter depending on inflow parameters. MMS observations provide unique insights into this dependence. Observations (e.g., Ergun et al., 2016) support the idea that fluctuations may play a role in the reconnection process, and that fluctuating and laminar regions may couple.

Reconnection is often bursty within a limited extent of the reconnection region and appears to be common to both symmetric and asymmetric reconnection. In the magnetotail, for example, the so-called bursty bulk flows are deemed to be the consequence of reconnection with lateral scale sizes of at most a few Earth radii (Angelopoulos et al., 1992; Baumjohann et al., 1990), and similar inferences have been made regarding flux transfer events at the magnetopause (e.g., Owen et al., 2008). Therefore, the electron- and ion-centred X-line expansion processes noted in the literature (Lapenta et al., 2006) must be limited by local conditions (Liu et al., 2019). This limitation implies that the kinetic physics of the electron and ion diffusion regions has to cease to operate at the lateral "ends" of the reconnection region, for example, by a complicated change of kinetic parameters or magnetic geometry. This termi-

nation of a reconnection line is conceptually related to the cessation in that a spatial gradient of physical conditions must exist to permit reconnection to operate in one location, yet prevent it at an adjacent location. MMS multi-scale spacecraft configurations enable investigations of this scenario.

2.2.2. How is energy dissipated outside of diffusion regions? Owing to the diminutive size of diffusion regions, the vast majority of reconnection energy conversion has to occur elsewhere. It is believed that much of the associated heating and energization occurs at or around separatrices, but there are indications of additional thermalization in outflow jets. During reconnection, electrons are preheated in the inflow regions (Norgren et al., 2016, Khotyaintsev et al., 2020). The heating, acceleration, and thermalization processes that constitute electron and ion dissipation of magnetic energy often involve interactions of the particles with a variety of wave modes (c.f. Wilder et al., 2019; Hesse et al., 2018; Norgren et al., 2020) or pickup processes (Drake et al., 2009). It remains an open question to date which process, if any, dominates the conversion of magnetic energy into ion and electron thermal and kinetic energy outside of the electron and ion diffusion regions – a problem in urgent need of resolution. Further, fundamental questions remain regarding the coupling of the multi-scale processes that comprise dissipation of magnetic energy during reconnection, including a complete view of the role whistler waves play in reconnection, and how this energy conversion may depend on overall geometry and driving. During its extended mission, MMS attains new configurations, which are excellently suited to study and relate to each other the key kinetic processes at multiple locations from EDR to reconnection outflow.

2.2.3. How do multiple X-lines develop and interact? At large scales, field line merging and energy conversion may be mediated by reconnection at multiple X-lines. Multiple X-line reconnection is thought to mix plasmas and convert energy more efficiently than single X-line reconnection. Converging jets and reconnected flux tubes from multiple adjacent X-lines may be important sites of particle acceleration (Drake et al. 2006). The extended mission of MMS provides a unique opportunity to extend our understanding of individual reconnection sites and address fundamental system-level questions regarding the causes and impacts of multiple X-line reconnection.

Multiple X-line reconnection is thought to occur more frequently in turbulent current sheets (Genestreti et al. 2022), where secondary X lines develop to efficiently reconnect fluctuating magnetic fields. Multiple X-line reconnection may also be a natural consequence of certain initial conditions in laminar current sheets, namely temperature gradients across the current sheet (Lu et al. 2019) or small current sheet aspect ratios. Lastly, reconnection may occur at multiple X lines when the global and local forces, which dictate the X-line location and orientation, are in conflict; such a scenario is considered a regular feature of anti-parallel magnetopause reconnection dawnward and duskward of the subsolar point (Fuselier et al. 2021). These scenarios are all hypothesized and based on theory, models, and/or past MMS observations in a tight, electron-scale tetrahedron. The MMS configurations proposed here offer an excellent opportunity to understand at a fundamental kinetic level, under which conditions multiple X-line reconnection occurs, how multiple X-lines interact and evolve, e.g., merge, and how efficient multiple X-line reconnection is in energy conversion and in particle acceleration.

2.2.4. What are the dominant wave-particle interactions during magnetic reconnection and their large-scale impact? Reconnection-related wave-particle interactions can contribute to plasma heating, anomalous resistivity, and particle scattering and diffusion. Hence it is incumbent on space plasma research to develop a deeper understanding of the phenomenology, causality, and impacts of the waves in reconnection. MMS provides the best available research tool for these studies. For kinetic Alfvén waves and lower-hybrid waves, the highest resolution particle distributions and moments resolve the fluctuations associated with these waves, enabling wave-particle interactions to be characterized (e.g., Chen et al., 2020; Gershman et al., 2017; Graham et al., 2022; Wang et al., 2022). Likewise, recent observations show that MMS is capable of resolving wave-particle interactions associated with electron holes (Mozer, 2018; Norgren et. al., 2022) and whistler waves (Kitamura et al., 2022) with millisecond timescales. Larger-scale consequences of these wave-particle interactions, including heating at the separatrices of magnetic reconnection, require further

investigation.

The MMS Theory and Modeling team continues to place a significant amount of attention on three-dimensional effects associated with magnetic reconnection. The interplay between observations and prediction is key to efficient advancement in understanding. Simulations have shown that in three dimensions lower-hybrid waves can enhance electron heating in asymmetric reconnection and broaden the separatrix regions from electron scales to a hybrid scale between ion and electron spatial scales (Le et al., 2017; Price et al., 2020). For magnetopause reconnection, the simulations showed that the waves lead to mixing of the magnetospheric and magnetosheath plasmas. This mixing has been confirmed with observations from MMS, which showed significant electron diffusion across reconnection boundaries (Graham et al., 2022). However, the relative importance of wave-particle interactions versus large-scale electric fields associated with reconnection for electron heating is yet to be assessed. In addition, electromagnetic lower hybrid waves can develop in the diffusion region, leading to a kinking of the current sheet near the diffusion region and separatrices (Cozzani et al., 2021). At ion scales, kinking has been investigated by MMS (e.g., Richard et al., 2021). However, several unresolved questions remain, such as the generation mechanism of the kinking, the ion behavior, and what balances current sheet thinning. These three-dimensional effects on reconnection require further investigation, and they are readily accessible to MMS observations.

For reconnection exhausts, instabilities such as the electron and ion firehose instabilities have been proposed to constrain the temperature anisotropies that develop. While these waves have been reported in kinetic reconnection simulations, direct observations still need to be pursued. Direct measurements of these waves and the associated wave-particle interactions is a crucial step toward understanding the constraints on temperature anisotropies in these regions as well as an understanding of the overall energy conversion.

MMS is poised to break new ground on the large-scale impact of wave-particle interactions. One further example concerns ion waves and turbulence at the bow shock. Electromagnetic waves gyro-resonant with ions are predicted by simulations to be amplified in the magnetosheath and present large-scale negative Bz regions that can trigger magnetopause reconnection even when the Sun is quiet and the IMF Bz is northward (Chen et al., 2021b). Similarly, magnetosheath jets, whose generation mechanism is an open question, can impact the magnetopause, leading to local reconnection (Plaschke, 2018; Ng et al., 2021). Observational work is needed to validate these predictions. To investigate such processes, conjunctions between MMS and other HSO spacecraft are important. For example, recent conjunctions between MMS and Cluster were able to simultaneously observe reconnection at the subsolar magnetopause and flanks (Toledo-Redondo, 2021) and thereby investigate the effect of magnetosheath jets on the magnetopause (Escoubet, 2020).

2.2.5: How is magnetopause reconnection connected to the physics of the cusps and associated diamagnetic cavities? Magnetosheath plasma has the most direct access to the ionosphere through the high-altitude cusps owing to magnetic reconnection operating in the vicinity of the exterior cusp funnel. Cusp signatures differ depending on altitude and IMF orientation. The four spacecraft Cluster mission revealed the general structure of the high-altitude cusps on ion scales. MMS detected the presence of energized and trapped O^{+} from the ionosphere and trapped He^{++} from the solar wind at the high-latitude magnetopause (Nykyri et al., 2019). These observations were used to determine the distance from the MMS spacecraft to the reconnection site and to assess the size of an inferred magnetic bottle. To address the nature (e.g., reconnection rate) and global consequences of magnetopause reconnection, MMS observations through the cusp funnel and analysis of ion dispersions with composition measurements are needed. String-of-pearls MMS observations of the cusp help distinguish the relative contribution of the suggested sources for the high energy particles observed in the cusp-associated diamagnetic cavities (DMCs): 1) local acceleration via 'turbulence' in DMCs, 2) quasi-parallel bow-shock, 3) magnetospheric source, or 4) local acceleration via particle trapping and drifting in a reconnection quasi potential.

2.2.6. Researching these topics with MMS. The science questions listed under SO2 require MMS measurements that resolve the evolution of waves and particle distributions. For studying the evolution and heating of electrons in the separatrices of

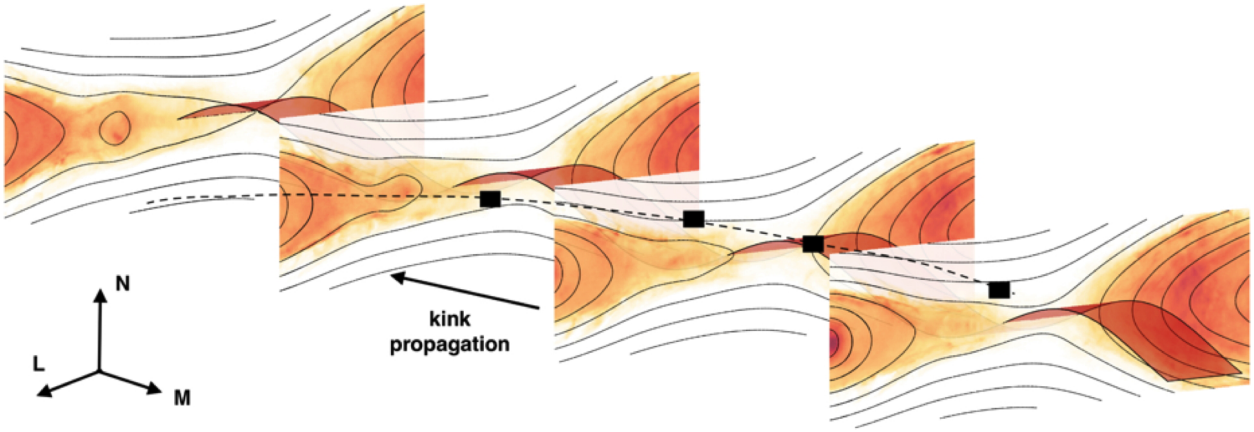

Figure 2.3. Illustration of current sheet kinking. Spacecraft along a string of pearls configuration in Earth's magnetotail provides a unique opportunity to investigate drift waves and kinking of the current sheet.

the magnetotail, a string-of-pearls configuration along the GSM x-direction is implemented (separations ranging from ~10 km to ~100 km) and can be achieved for the inbound and outbound orbits in the magnetotail phase (Figure 2.3). This configuration provides simultaneous measurements along the magnetic field to study how these waves and particle distributions evolve along the separatrices. The highest resolution FPI data and EDI measurements will quantify the wave-particle interactions. These measurements will provide new insight into electron heating in the reconnection separatrices.

The same spacecraft configuration can shed new light on waves near the diffusion region of magnetotail reconnection. At apogee the spacecraft can be separated along the out-of-plane direction. This separation enables the study of localized drift waves and perturbations in the diffusion region along the out-of-plane direction to be directly measured and helps clarify the three-dimensional effects, such as kinking in and near the diffusion region, on magnetic reconnection. Larger ion-scale flapping and kinking observed in the magnetotail requires larger spacecraft separations. In the magnetotail, the spacecraft separations have been well below ion spatial scales. Future ion- and MHD-scale spacecraft separations enable these unresolved questions to be addressed.

From 2022 to 2025, the apogee latitude increases, and cusp and high latitude magnetopause encounters increase. The full complement of high-resolution fields and particle measurements combined with energetic particle and composition measurements enables cusp physics and formation of the cusp associated DMCs to be understood from ion to electron scales. The string-of-pearls configuration is ideal for tracking the motion of the reconnected field lines through the cusp, establishing the formation of the DMCs, and distinguishing between different proposed acceleration mechanisms and particle sources.

2.2.7. Extensions via the HSO. The MMS spacecraft routinely observe the magnetopause, magnetosheath and solar wind, enabling validation of simulation predictions of the effects of ion waves on dayside reconnection. Conjunctions with other missions, such as Cluster and THEMIS, provide simultaneous observations of the ion foreshock, magnetosheath, and/or the magnetopause, which are crucial for studying the development of nonlinear structures from ion foreshock waves, as well as the effects of these structures and magnetosheath jets on the dayside magnetopause. MMS conjunctions with the upcoming TRACERS mission (planned launch 2024) can determine spatiotemporal variations of magnetopause reconnection and the impact of foreshock waves on the cusp ionosphere through magnetopause reconnection.

Having four MMS spacecraft in the high-altitude cusp region in the string-of-pearls configuration while having THEMIS at the low-latitude dayside magnetosheath-magnetopause, and ARTEMIS upstream of the bow shock provides additional opportunities to directly relate solar wind, bow shock, magnetospheric, and locally accelerated sources of plasma in the cusp. MMS conjunctions with the TRACERS mission allow for further assessments of

magnetopause reconnection, in particular important properties such as extent of a reconnection line.

2.3 SO3: Understand particle acceleration processes in the magnetotail and their relationship to magnetic reconnection.

Understanding particle energization and acceleration remains a compelling objective owing to relevance to space weather and its general importance in a variety of space and astrophysical contexts. Therefore, it remains an objective of MMS to understand particle acceleration directly or indirectly related to magnetic reconnection. The magnetosphere is an effective and efficient accelerator of energetic ions and relativistic electrons, and the magnetotail in particular is an ideal and accessible natural laboratory for studies of energetic ion and relativistic electron acceleration associated with magnetic reconnection.

2.3.1. How does magnetotail reconnection inject energetic particles to the inner magnetosphere? Recent observational and modeling studies have revealed that injections of higher energy (>300 keV) particles are not commonly observed at or within geostationary orbit though they are frequently seen farther out in the magnetosphere. A hypothesis has been recently put forth in the literature suggesting that this may be associated with the energy-dependent dynamics of particles in magnetic islands associated with earthward-moving dipolarizing flux bundles (e. g., Zhou et al., 2018). Testing this "leaky bucket" hypothesis with theoretical, observational, and simulation studies provides important information about how reconnection – and the energization of particles resulting from it – affect global magnetospheric transport. Understanding this process at Earth provides critical insight into how similar transport and acceleration processes may operate in other planetary magnetospheres and astrophysical systems with different configurations.

MMS is now the only mission that can measure particle distributions in the critical range of energies (i.e., in the 10s to 100s of keV range) from within the heart of the outer radiation belt to well into the central plasma sheet. This capability provides a wide range of radial distances and L-shells over which the "leaky bucket" hypothesis can be observed. Furthermore, MMS provides critical energetic ion composition observations that will enable study of how this potential transport and energization mechanism differs by mass.

2.3.2. What processes dominate ion energization in the magnetotail? The past decade has revealed a wealth of information about the potential mechanisms that may contribute to the energization and acceleration of ions in the magnetotail. However, it remains unclear which of these processes are most significant and how their significance may vary under certain conditions. For example, direct observational evidence has been found of ion acceleration in the tail by betatron acceleration, current sheet scattering, pickup acceleration, and Fermi reflection. In particular, the simulations further support the hypothesis that the latter two mechanisms may occur within or near transient structures associated with the global reconnection exhaust in the magnetotail. Understanding the nature, prevalence, and driving conditions of these ion acceleration processes in the magnetotail is necessary to inform understanding of universal energization mechanisms that may be at play, as well as the meso- and large-scale effects of reconnection on the magnetosphere.

MMS provides unique magnetospheric suprathermal and energetic ion mass composition measurements that are necessary to understand the potential mass-dependent nature of these acceleration processes. Furthermore, its comprehensive electric and magnetic field measurements and significant orbital coverage (e.g., radial distance, MLT) provide critical information about how and where these acceleration mechanisms apply.

2.3.3. Does reconnection energize electrons directly or via secondary processes? Magnetic reconnection is a universal process in which energy is transferred from magnetic fields to particles. However, it remains unclear whether this transfer of energy includes the direct energization of electrons to high energies (i.e., >10s of keV) or if it arises from secondary effects resulting from reconnection. Measurements and simulations have provided evidence for many mechanisms that may result in electron local acceleration at or near electron diffusion regions (Figure 2.4), including betatron acceleration and current-sheet scattering in very thin local current sheets. However, even more mechanisms have been identified that may drive acceleration from secondary processes that result from reconnection (i.e., exhaust transient structures); these include Fermi reflection and acceleration and trapping in turbulent field structures (Ergun et al., 2020a,b). Understand-

ing the relative frequency and potential dominance of these different mechanisms provides fundamental information about how Earth's radiation belts may be sourced and how energetic electrons may be produced generally in many astrophysical settings.

2.3.4. Researching these topics with MMS. MMS is now the only mission that can measure particle distributions in the critical range of energies (i.e., in the 10s to 100s of keV range) from within the heart of the outer radiation belt to well into the central plasma sheet. This capability provides a wide range of radial distances and L-shells over which the "leaky bucket" hypothesis can be observed. Furthermore, MMS provides critical energetic ion composition observations that will enable study of how this potential transport and energization mechanism differs by mass.

MMS's remarkable temporal and angular observations of energetic electrons provides the best opportunity to explore the nature and characteristics of electron energization throughout the magnetotail. This capability, coupled with the high-resolution plasma and fields observations, across the four MMS spacecraft enables novel investigation of electron energization processes.

2.3.4. Extension via HSO To address these questions, observations from MMS will be combined with complementary measurements from Arase (ERG), THEMIS, and/or Cluster conjunctions to examine the cross-scale evolution and impacts of reconnection on the magnetosphere and its particle populations.

2.4 SO4: Understand the fundamental nature of kinetic-scale turbulence, including its coupling to larger scales.

Understanding the role of turbulence in near-Earth space remains one of the main priorities of the MMS mission. Turbulence is present in most plasma systems, often having a major impact on the global dynamics. Plasma turbulence channels energy from large scale flows into small-scale fluctuations. It is an inherently multi-scale process, through which magnetic field energy is dissipated, leading to plasma heating and particle acceleration. Major open questions remain regarding how energy is exchanged across these scales. Answers to these questions will yield an understanding of the crucial role of turbulence in geospace dynamics and represent a fundamental contribution to plasma physics applicable to coronal and solar wind heating, cosmic

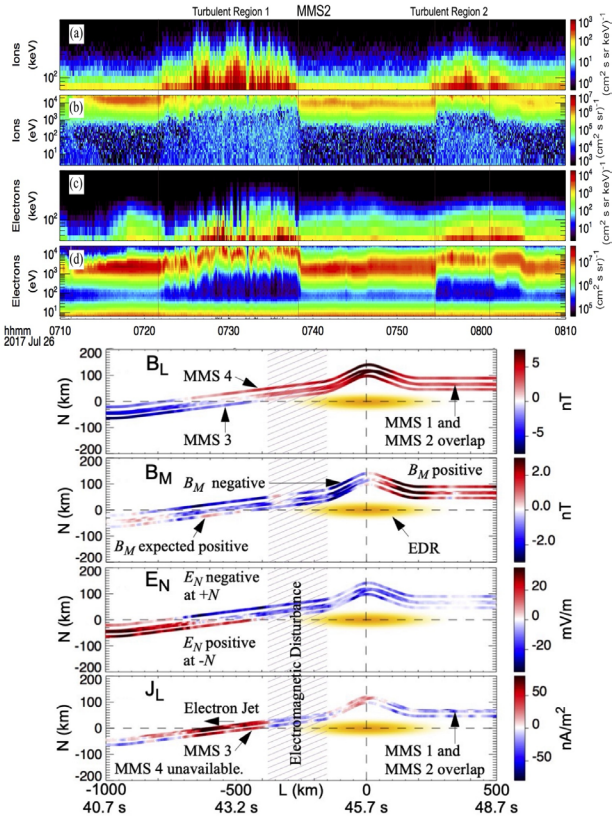

Figure 2.4 MMS discoveries of intense electron and ion acceleration in magnetotail turbulence (top panels, Ergun et al., 2020a,b) motivates the investigations in sections 2.3.2 and 2.3.3. The EDR embedded in the observed turbulence exhibits the same characteristics as in 2D, anti-parallel reconnection (bottom panels, Ergun et al., 2022), except for the short interruption due to an electromagnetic disturbance (shaded interval).

ray particle acceleration, and plasma turbulence in magnetic confinement fusion.

2.4.1 How do the drivers of turbulence impact the small-scale dissipation and particle acceleration? The turbulent energy cascade rate in the magnetosheath, downstream of the bow shock, exceeds that of the solar wind by three orders of magnitude. This energy drives reconnection at ion and electron scales, with wave-particle interactions generating streams of hot plasma and energetic particles. As MMS continues to gather observations under different conditions, we will examine how these turbulent processes are controlled by the different large-scale drivers at play. Specifically, we will address how the upstream solar wind conditions, the bow-shock configuration and the local turbulence dynamics each influence the small-scale dissipation and energization. While we have observed strong turbulence generated behind the quasi-parallel bow-shock, developing to the typical Kolmogorov turbulence as it relaxes towards

the flanks, MMS is able to use varying configurations to examine the generation and evolution of turbulence and the interplay of the different dissipative mechanisms that channel the cross-scale energy transfer. As we head to a solar maximum, the increased variability of solar wind conditions offers a unique opportunity to understand how small-scale turbulent dissipation is influenced by such large-scale drivers, and it alters their impact on our planet.

2.4.2 Which turbulent processes heat and accelerate plasma? The unprecedented capabilities of MMS revealed the wide variety of kinetic-scale mechanisms that mediate the energy exchange in turbulent plasmas. Examples range from novel observations of electron-only magnetic reconnection (Phan et al., 2018), to direct observations of wave-particle interactions within ion-scale current sheets, and measurements of kinetic dissipation associated with complex non-Maxwellian velocity-space structure revealing a cascade-like process in velocity space (Servidio et al., 2017; Chasapis et al., 2018a). As an illustration of these effects, Figure 2.5 shows how bulk velocity, resulting from the conversion of electromagnetic energy to particle energy in reconnection (J•E)cascades to plasma thermal energy through the pressure stress interaction. This chain of processes is followed by MMS measurements with intriguing results including spatial separation of the sites of particle acceleration and plasma heating (Bandyopadhyay, et al., 2021).

As such observations are extended in different regions and under different upstream conditions, we are able to examine which of those processes contribute to significant dissipation and particle acceleration. Moreover, using different spacecraft formation configurations we can examine under which conditions such mechanisms become efficient pathways of turbulent energy exchange. The outstanding question of the partition of this energy into the thermal and non-thermal parts of the different species are also addressed, helping us better understand how turbulence can contribute to heating and particle acceleration.

2.4.3. Researching these topics with MMS. The unique capabilities and flexibility of the MMS payload and mission offer continued opportunities for fundamental science using both established and novel observational strategies. As outlined above, there are many remaining open questions in plasma

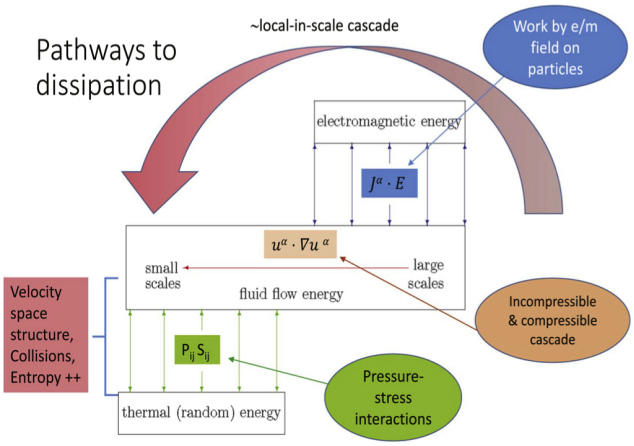

Figure 2.5 Diagram illustrating the pathways to dissipation (From Chasapis et al., 2018a). Velocity cascades transfer energy across spatial scales, while electromagnetic work exchanges energy with the flow velocities of each species. The pressure-stress interactions convert kinetic energy between flows and internal energy.

turbulence that MMS can address in order to better understand the nature of turbulent energy dissipation. While some aspects relate to individual events that have been studied previously, statistical surveys are required, or at least much larger samples, to arrive at more robust and enduring conclusions. There is also an issue of spacecraft formation and separations. For some studies a near ideal tetrahedron is optimal, such as those requiring three dimensional spatial derivatives- (such as curl operations). Useful studies can also be accomplished using multiscale sampling, including colinear spacecraft formations, or by sampling of three dimensions with more asymmetric arrangements.

Nongyrotropy. A survey of the degree of nongyrotropy in a large sample of magnetosheath turbulence intervals is a basic plasma physics study that cannot be done by any other mission. Nongyrotropy can be quantified in a number of ways, making use of the capabilities of the FPI instruments to resolve the velocity space structure of the electron and proton distributions. Major progress can be achieved by quantifying not only nongyrotropy itself (which focuses on the magnetic field direction, which could be locally averaged or more regionally averaged) (Swisdak, 2021; Scudder and Daughton, 2008; Aunai et al., 2013)) but also the dependence of measured nongyrotropies on additional preferred directions such as vorticity, eigenvectors of the strain tensor (Del Sarto et al., 2016; Del Sarto and Pegoraro, 2018). MMS has unique capabilities to measure

these quantities. Nongyrotropy also can be related to the magnetosheath dissipation functions: pressure strain and pressure dilatation surveys have been started in previous campaigns but so far there has not been sufficient work on decomposition into gyrotropic and nongyrotropic contributions (Bacchini et al., 2018; Du et al., 2018; Zhou et al., 2018). Such a survey can provide strong constraints on development of theoretical descriptions of processes leading to dissipation.

Curvature. Some basic theory is available to describe magnetic field-line curvature (Yang et al., 2019), a property that underlies some of the more prominent theories of particle energization (Jokipii, 1982; Guo et al. 2014; Dahlin et al., 2014, 2017; Li et al., 2015, 2017; Wang et al., 2016, 2017; Beresnyak et al., 2016; Lu et al., 2018). Magnetic curvature has been extensively studied in reconnecton events (Bandyopadhyay et al., 2020), but much less so in samples of turbulence such as what is available with surveys of the turbulent magnetosheath.

Topology of small-scale coherent structures. Coherent structures are sites of dissipation and other important processes in turbulent plasmas. The relationship between the different invariants of gradient tensor (of velocity and magnetic field) can reveal the nature of coherent structures at observed scales (Yang et al., 2017; Dallas and Alexakis, 2013; Meneveau, 2011; Blackburn et al., 1996; Consolini et al., 2015, 2018; Quattrociocchi et al., 2019). MMS, with high resolution data and 4 spacecraft, has the unique capability of exploring these issues.

Electron-proton heating rates. The fundamental physical principles that determine how turbulence apportions its dissipated energy into protons and electrons remains an actively discussed topic at a theoretical level (Wu et al., 2013; Matthaeus et al., 2016; Howes, 2010; Parashar et al., 2018; Wan et al., 2015). MMS has the capability to substantially constrain these discussions (Bandyopadhyay et al., 2021; Vech et al., 2017).

Compressive vs incompressive heating. It has been known for some time that standard simulations of "Alfvenic turbulence", meaning here quasi-equipartition turbulence as seen in the solar wind, generally evolve and dissipate largely through incompressive channels (Yang et al., 2022). However, the observations reported until now have suggested that magnetosheath turbulence is different. Measurements of compressive dissipation ("p-theta") appear to be systematically much larger than the incompressive dissipation channels ("Pi-D") (Chasapis et al., 2018a; Bandyopadhyay et al., 2021; Wang et al., 2021). (i) Additional studies in which a large collection of samples of magnetosheath turbulence is evaluated for compressive vs incompressive effects and compared with models of the state of the magnetosphere is needed to resolve this issue, which may have implications for plasma turbulence in many other venues, including astrophysical plasmas. Conditions that may influence the degree of compressional effects include shock type and proximity (Wang et al., 2021), solar wind streams, expansion of magnetospheric magnetic field configuration, etc. (ii) Dependence of compressive-incompressive heating ratios in a magnetosheath survey can be meaningfully compared with plasma simulations with varying parameters, to better understand how this ratio varied with local turbulence parameters such as plasma beta, mean field strength, etc.

Effect of energy fluxes in space. The basic quantities, J•E (Zenitani et al., 2011); PiD/ptheta (Yang et al., 2017); heat and enthalpy fluxes (Fadanelli et al., 2021) each can in principle be related with varying degrees of correlation, to local temperature variations or increments. This kind of study is complementary to recent work on evaluating the terms in the Vlasov equation and the terms in Ohm's Law (Stawarz et al., 2021). MMS in the magnetosheath is ideal for attempting to understand these relationships, which strongly influence the energy budgets in plasma turbulence. Again requiring a survey of many turbulence intervals, this analysis will clarify differences between what is meant by heating and what's meant by dissipation.

Signatures of local relaxation processes. Relaxation processes (Chandrasekhar, and Woltjer, 1958; Woltjer, 1958; Montgomery et al., 1979; Stribling and Matthaeus, 1991) are seen in hydrodynamic turbulence and in MHD simulations (Pelz et al., 1985; Servidio et al., 2008a,b), as well as, with limitations coming from single-spacecraft measurement, or less precise measurements due to spacecraft separation (Osman et al., 2011; Servidio et al., 2014). Recent work has indicated that these several interesting types of local relaxations lead to distinctive correlations that are also seen, in preliminary results, with MMS data obtained in the magnetosheath. These

locally generated correlations might include pressure balances, Beltrami flows, Alfvenic states, and forever-free states. How common are these in the magnetosheath? There are no reported data in these as far as we are aware, other than a few selected "events". A full survey is needed and only MMS can enable this fundamental research.

Closure in collisionless plasma. For collisional plasma the standard view is that simple closures are not normally available in the way they are for collision-dominated gasses and high-density plasmas. However, some recent studies, both in simulations (Wan et al., 2015, 2016) and MMS observations (Chasapis et al., 2018b) suggest that a kind of statistical closure may be available, at least in some cases. For example, why do the statistical values of electromagnetic work scale similarly to the collisional case? We do not yet know how frequently this kind of scaling of J•E occurs in the magnetosheath. Does this collisional-like dissipation extend also to a viscous like scaling? Additional MMS observations of magnetosheath (or magnetotail) turbulence are needed to provide answers to these questions.

Velocity space cascade. Only a few in-depth observational studies have been carried out so far on this fundamental plasma physics problem (Servidio et al., 2017), in contrast to the intense theoretical interest in this subject (Meyrand et al., 2019; Cerri et al., 2018). MMS is unique in its capability to study the velocity scale structure in the highly dynamic magnetosphere owing to the refined quality of the FPI instrument. The data is most useful when the fine scales in the VDF are well covered. Accumulation of more useful intervals in the magnetosheath by MMS presents a unique opportunity for establishing a benchmark characterization of this very important property of dynamic and turbulent collisionless plasmas in which the distortions of the VDFs are essential contributors to dissipation while also being responsible for many instabilities.

Increase in knowledge of standard turbulence measures. In addition to the specialized topics above, MMS remains the best configured space mission for examining spectra, correlation functions and intermittency at kinetic scales. Understanding of these basic physical properties of turbulence is essential for interpreting spacecraft data, for inputs to modeling, for particle scattering and energization applications, and for space weather. Such studies have remained active throughout the mission so far and will benefit from an increased catalog of available datasets in the next phase of MMS.

MMS plans to execute a magnetosheath turbulence campaign for a designated dayside mission phase to downlink regular intervals of burst data whenever the spacecraft is in the magnetosheath to enable statistical studies of turbulence.

2.4.4 Extensions via HSO. The question of how turbulence drivers impact kinetic scale dissipation and particle acceleration benefits from combining MMS with HSO to extend the scale-size coverage and distinguish effects of large-scale drivers. In addition to working with other existing missions (e.g., THEMIS and Cluster) which have MHD scale interspacecraft separations, the multi-point ion- and electron-scale plasma distribution measurements unique to MMS have the power to transform the state-of-the-art knowledge of turbulence.

2.5 SO5: Understand the role of kinetic physics in the bow shock and interplanetary shocks.

Through its unprecedented high cadence measurements, MMS opens up a new realm of possibilities to study the role of kinetic physics in the bow shock and interplanetary shocks. The interplay between magnetic reconnection and shock-driven turbulence, as well as the large-scale impact of this complex interaction are among the lines of investigation made possible by MMS. Below are major directions in which MMS will further explore shock physics with new multi-scale spacecraft configurations.

2.5.1 Shock driven turbulence at kinetic scales and its cross-scale consequences. The bow shock is a strongly-driven environment hosting turbulence with multiple energy injection scales (Figure 2.6; note the multiple spectral peaks in the magnetic spectra). At the foreshock, bow shock transition, and downstream from the quasi-parallel shock in the magnetosheath, abundant reconnecting current sheets reside (e.g., Phan et al., 2018; Gingell et al., 2021; Stawarz et al., 2022), showing the prevalence of reconnection in releasing locally unbearable magnetic stress and accelerating/thermalizing the plasma. The observations have inspired MMS theory and modeling team simulations to discover new ways in which reconnection occurs under shock-driven turbulence (e.g., Bessho et al., 2022; Ng et al., 2022a). For ex-

ample, reconnection is predicted to occur with only electron jets, one-sided jets, and plasma distribution functions distinct from those in standard laminar reconnection. The motivating fundamental questions include (a) the distinct dynamics of reconnection in strong magnetic turbulence and its impact on particle acceleration, heating, and wave generation and (b) to what degree reconnection contributes to the primary function of the shock in converting bulk flow energies into heat.

2.5.2 Large-scale impact of shock-driven reconnection. How shock-driven reconnection impacts the bow shock and magnetopause is an important question in both shock physics and space weather. If reconnection can occur unrestricted in the shock layer in the same manner as that at the magnetopause, it will modify the large-scale structure of the bow shock just like dayside magnetopause reconnection erodes the magnetosphere and contributes to the flux circulation dynamics of the magnetosphere. An example of a well-developed reconnection layer is observed in the electron temperature ramp at a nearly perpendicular shock (Figure 2.7). Can such a reconnection layer modify the large-scale structure of the bow shock?

Intense foreshock wave structures are expected to be omni-present in front of the quasi-parallel bow shock. The 3D bow shock always has a quasi-parallel part, and as the IMF changes direction, the quasi-parallel part moves to different region of the bow shock. The capability of MMS to resolve ion distributions in foreshock waves and solitary magnetic structures reveals how ion-ion kinetic instability at the bow shock have potential large-scale impact on the study of planetary magnetospheres, both intrinsic ones like the Earth's and induced ones like Mars' (Chen et al., 2022a). MMS shows that even when the IMF Bz is northward and constant, planet-sized regions of southward Bz with density enhancements (Figure 2.8, left panel) can develop from the electromagnetic waves gyro-resonant with the solar wind ions (Chen et al., 2020). The observations motivated global hybrid simulations to investigate the impact of these southward Bz regions. The simulations (Chen et al., 2021, Ng et al., 2022b) predict that the structures are amplified in the magnetosheath and present large-scale southward Bz regions at the magnetopause (Figure 2.8, middle panel) that can trigger magnetic reconnection even

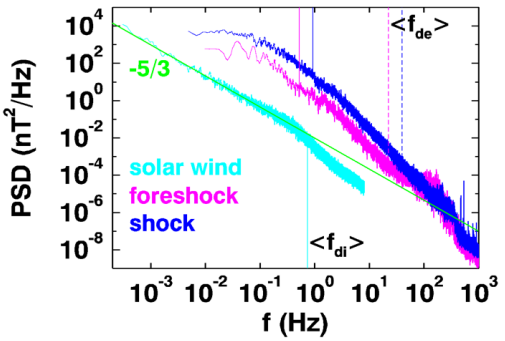

Figure 2.6. Magnetic field spectra from the foreshock and a bow shock observed by MMS showing strongly driven shock turbulence. The strong foreshock and shock magnetic turbulence is orders of magnitude higher in power spectral density (PSD) than solar wind turbulence. Shock turbulence is convected into and further compressed in the magnetosheath where MMS observes kinetic-scale current sheets reconnect (Stawarz et al., 2022). Solid vertical lines mark the frequencies corresponding to the ion skin depth, and dotted lines those corresponding to the electron skin depth. Being the only mission capable of resolving the electron kinetic scales with plasma measurements, MMS explores strongly driven turbulence and its cross-scale impact in the extended mission.

when the Sun is quiet and the IMF Bz is northward (Figure 2.8, right panel).

2.5.3. *Interplanetary shocks.* Interplanetary (IP) shocks expand the range of shock parameters down to the subcritical regime where the underlying physics of the required energy conversion differs from that of the bow shock. Owing to their larger scale than planetary shocks, IP shocks often create vastly extended foreshock regions populated by shock-accelerated particles, providing a rare regime to study shock-driven turbulence on kinetic scales. Researching the broad category of shocks provides a unique opportunity to understand how collisionless shocks operate throughout the universe.

The IP shock studies MMS will pursue during the proposed extended mission include the following:

1. Spatial structures and temporal variations of IP shocks and their impact: how do the variations differ for supercritical and subcritical IP shocks? how do the variations affect particle acceleration and interaction with Earth's bow shock and magnetosphere?
2. Identify types and roles of wave-particle interaction in IP shocks: how do they contribute to energy dissipation and particle energization?
3. Further investigate the nature of cross shock potential associated with IP shocks: what fraction of the cross-shock potential is achieved by

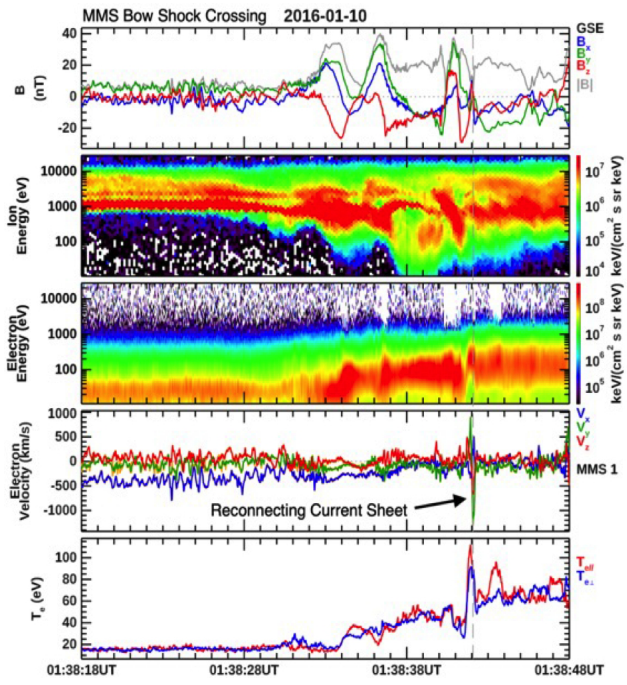

Figure 2.7 An MMS example showing how reconnection may modify the bow shock structure. A reconnecting current sheet (vertical dashed line) marked by sharp magnetic field gradients occurs within the shock ramp), and exhibits strong electron jets and intense heating. Features of electron distribution functions (not shown) are similar to those in a fully developed electron diffusion region at the magnetopause, suggesting that reconnection may have large-scale impact on the bow shock like what happens at the magnetopause. This possibility is investigated with the multi-scale spacecraft configuration in the proposed extended mission. The results have implications on how collisionless shocks in planetary environment and astrophysical systems achieve their function of energy conversion. From Chen et al. (2022b).

kinetic-scale electric fields? MMS observations of an IP shock raised controvercies regarding the nonlinear (Cohen et al., 2019) or linear (Hansen et al., 2019) nature of the cross-shock potential, highlighting the need for new observations and further analysis of IP shocks.

2.5.4 Researching these topics with MMS. In the extended mission more use is made of string-of-pearls types of formations, which are well-suited to diagnose the time-evolution of shocks. During a test of this method in 2019, Turner et al. (2021a) examined in detail observations of the reformation of a fast magnetosonic shock observed on the upstream edge of a foreshock transient structure upstream of Earth's bow shock (Figure 2.9). The four MMS spacecraft were separated by several hundred kilometers, comparable to suprathermal ion gyroradius scales or several ion inertial lengths. At least half of the shock reformation cycle was observed, with a new shock ramp rising up out of the "foot" region of the original shock ramp. Their analysis showed that the growth rate increases during reformation, electron-scale physics play an important role in the shock reformation, and energy conversion processes also undergo the same cyclical periodicity as reformation.

2.5.5. Extensions via the HSO. MMS leads the HSO (e.g., ARTEMIS/THEMIS and Cluster) and ground assets to explore how shock driven turbulence, especially shock-driven reconnection, may result in self-

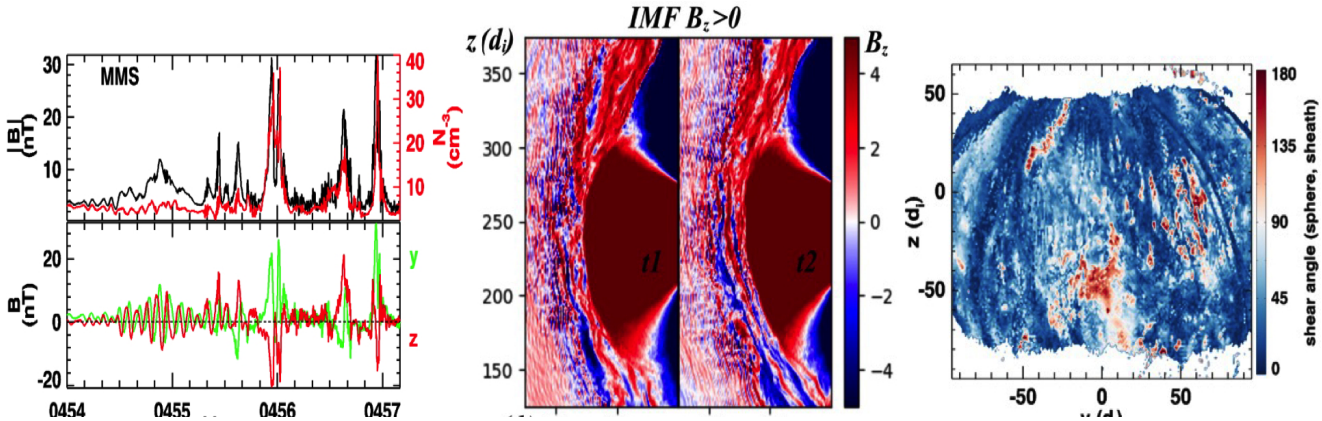

Figure 2.8 MMS observed Earth-sized solitary structures with magnetic field (B) and plasma density (N) enhancements as part of the shock-driven turbulence (Left). Using the MMS observed conditions (constant solar wind and IMF with Bz>0 and dominant Bx), global hybrid simulations predict that foreshock waves develop into planet-sized regions of enhanced Bz (middle). The southward Bz structures intensify and reach the magnetopause, leading to high magnetic shear angles that are conducive to magnetic reconnection near the subsolar region (right). MMS, in conjunction with HSO, tests the simulation predictions of bursty magnetopause reconnection occurring at places not expected in the standard picture.

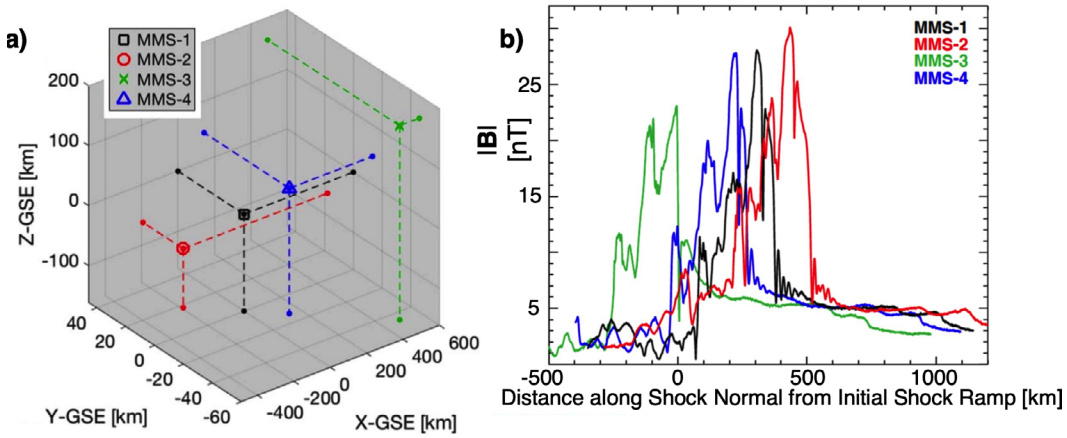

Figure 2.9 (a) MMS formation in GSE coordinates centered on MMS-1 location, which was at [14.5, 5.1, 2.5] RE in GSE at 04:39:25 UT on 30 January 2019. (b) magnetic field magnitude (B-Tot) measured as the shock moved at ~60 km/s from MMS2 to MMS3. Evolution of the shock ramp is seen as the trailing edges of the B-Tot traces. (Adapted from Turner et al., 2021a).

generated space weather that affects magnetospheric plasma escape.

MMS measurements are central to investigation of the nonlocal shock physics when combined with observations from ACE, Wind, and ARTEMIS. Non-planarity and non-stationarity from MHD to kinetic scales impact particle trapping and acceleration both at the bow shock, the IP shock, and IP shock interaction with the bow shock and magnetopause.

Solar observations provide predictive capability on a time scale of weeks to target short campaigns. MMS capabilities answer the primary questions related to kinetic processes, electromagnetic fields and waves, and shock acceleration. The likelihood of encountering IP shocks is enhanced during designated campaigns in the rising solar phase, and in particular, during campaigns conducted in coordination with Parker Solar Probe and Solar Orbiter.

3 Contribution to Heliophysics System Observatory

3.1 Relevance to NASA's Heliophysics Strategic Goals

With new multi-scale flight configurations and increasing solar activity, this MMS extended mission is poised to substantially advance the Heliophysics goal to "understand the Sun and its interactions with Earth, the solar system and the interstellar medium, including space weather". Utilizing the traditional goal structure, the following paragraphs summarize how MMS addresses the objectives listed in the 2020 SMD Science Plan to discover (G1) the fundamental physics governing how the universe works, (G2) what the coupled solar-terrestrial system teaches us about the habitability of planets in other stellar systems throughout the universe, and (G3) the physics that helps protect our technology and astronauts in space from the impacts of space weather.

Fundamental Processes: As described in Section 2, the most important MMS advances will result from the new kinetic- and cross-scale studies of magnetic reconnection, shocks, turbulence, and particle acceleration to be conducted across a range of plasma conditions, latitudes, and spacecraft formations than were previously available. Of equal interest is that the findings are applicable to similar energy conversion and transport-of-energy processes known to occur in other planetary magnetospheres, interplanetary plasmas, and at the Sun. MMS science is tightly aligned with the 2013 Heliophysics Decadal Survey Priority: "Establish how magnetic reconnection is triggered and how it evolves to drive mass, momentum, and energy transport".

Coupled Solar-Terrestrial System: MMS data comes in two forms, Fast Survey and Burst. While the burst data are key to the electron- and ion-scale studies at the heart of its success, the nearly full-orbit fast survey data are equivalent in resolution and quality to most all other in-situ magnetosphere missions. This broader dataset is widely used in larger-scale studies

including the transmission of solar wind energy into the magnetopause, energy/particle injections from the magnetotail to the inner magnetosphere, and the role of ionospheric-source plasmas. Of far-reaching impact are the studies concerning the relative importance of reconnection, shocks, and turbulence in establishing the energization and transport linkages between domains within a planetary magnetosphere.

Space Weather Prediction: MMS serves a vital role in developing our space weather predictive capabilities by quantifying the behavior of reconnection, which powers these space weather events. The rising phase and maximum of solar cycle 25 will bring an increasing frequency of intense space weather events. The MMS team is confident its instrument suite will remain healthy through FY25 such that a full solar cycle of kinetic-scale observations can be archived for the benefit of the community.

3.2 Role in the Heliophysics System Observatory

MMS plays a key role in the HSO as the fleet's sole "microscope". When MMS observations are aligned with other observatories, our community is able –for a short while– to approximate a cross-scale mission that resolves multiple plasma scales and regions of geospace simultaneously. In addition to the discussion below, please also note the "Extensions via the HSO" sections for each MMS science objective presented in Section 2.

Each season, MMS works closely with other mission leaders to incorporate conjunction opportunities into its science operations planning. Lists of potential conjunctions are provided to the MMS SITLs who search for and select burst data segments of broader scientific interest for downlink. If not for our MMS SITLs, far fewer "external team" publications would be possible.

Fortunately for all, conjunctions in the coming years will be more frequent and interesting than previously. Figure 3.1 is an example of what can be expected in the extended mission timeframe. MMS, in conjunction with other HSO missions, reveals structures and dynamics of the 3D magnetosphere. Enhanced solar activity is expected to provide several opportunities for MMS and the HSO to observe reconfigurations of the magnetosphere in response to strong solar driving conditions. Of great interest is the opportunity for MMS to serve as a companion to the upcoming TRACERS mission. Scheduled for launch in 2024, many conjunction opportunities are anticipated as TRACERS samples the low-altitude cusp while MMS samples the dayside magnetopause, high altitude cusp, and surrounding boundary layers. The two missions, working in tandem and observing signatures of magnetic reconnection in their respective regions at both macro- and micro-scales, will lead to major breakthroughs in understanding the nature and dynamics of magnetopause reconnection.

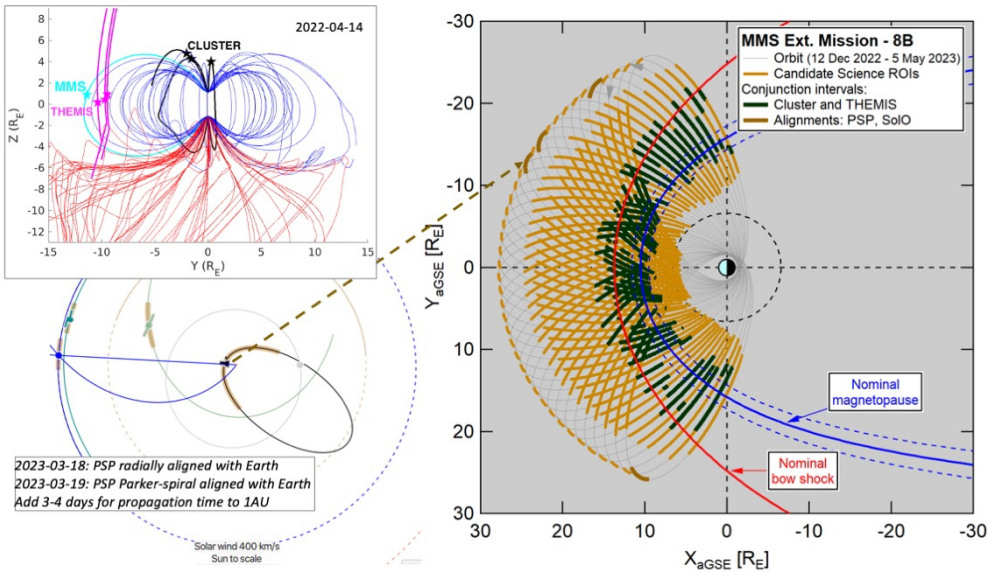

Figure 3.1: (right) Projections of 2022 dayside MMS orbits, science regions-of-interest, along with Cluster, Themis, PSP, and SolO conjunctions – as an example of the joint science operations performed among HSO missions each season. (left) Example 2022 storm-time conjunction of MMS (cyan), THEMIS (magenta), and Cluster (black), illustrated with closed magnetosphere (blue) and open (red) field lines.

4 Technical Implementation

4a Anticipated Mission Operations

Orbits and Campaigns

The MMS spacecraft are in a 1.8 x 28.8 R_E orbit that precesses over 24 hours local time in approximately one year (~3.5 day orbit period). Figure 4a.1 shows the MMS orbits (green) projected on the X-Y_{GSE} plane, highlighting encounters with the boundary regions targeted by our science objectives. The clockwise rotation of the apogee starting with the duskside flank provides a natural division of each year's orbits into the four campaigns described in Table 4a.1. Instrument modes and burst data collection regions (max 46 hrs/orbit) are matched to the science targets during each campaign. In the magnetotail, parts of individual orbits are color-coded when the spacecraft are within 0.5 R_E of the plasma sheet (grey) and the neutral sheet (black). These times are important for magnetotail reconnection and bursty bulk flow science. Magnetic reconnection figures prominently in all campaigns.

Figure 4a.2 shows the orbit inclination over time; perturbations torque the apogee slightly out of the ecliptic plane, reaching a maximum in 2023 and then returning to the ecliptic plane. This, combined with the time of year of the dayside sweep, results in encounters with the southern magnetospheric cusp over several years. The cusps were the target of the Cluster prime mission, and their investigation of ion-scale physics was a significant accomplishment. During this new extended mission, MMS will provide the first-ever electron-scale observations of high-latitude magnetopause reconnection and cusp dynamics. Based on the insights provided by MMS studies of electron-scale physics at the low-latitude magnetopause, these observations at higher-latitude will prove to be intriguing and lead to scientific understanding.

As the nightside orbital plane returns to the near-ecliptic, encounters with the plasma sheet and neutral sheet again shift toward the long dwell times at apogee. Of particular interest is magnetotail reconnection during the rising phase and maximum of solar cycle 25. Observations will be contrasted against those taken during the late MMS prime mission (2017), when MMS was in a comparable position during the Cycle 24 deep minimum. The scientific return is expected to be substantial, providing insight as to how kinetic processes in the deep magnetotail may or may not vary under strong solar driving.

Observatory Formations

The MMS spacecraft formation is designed to maximize science return with respect to the proposed science objectives. To date, MMS has kept the spacecraft in the tight tetrahedron formation optimal for exploring kinetic-scale reconnection in the magnetotail (avg 40km separation) and for resolving reconnection at the magnetopause crossings that occur approximately half-way to apogee on the outbound and inbound orbit legs (avg 20km separation). The intent is to remain in this formation at least through CY2023, especially as MMS accesses the high-latitude dayside and flank magnetopause, which are important sites for investigating reconnection, particularly in the presence of flow shears.

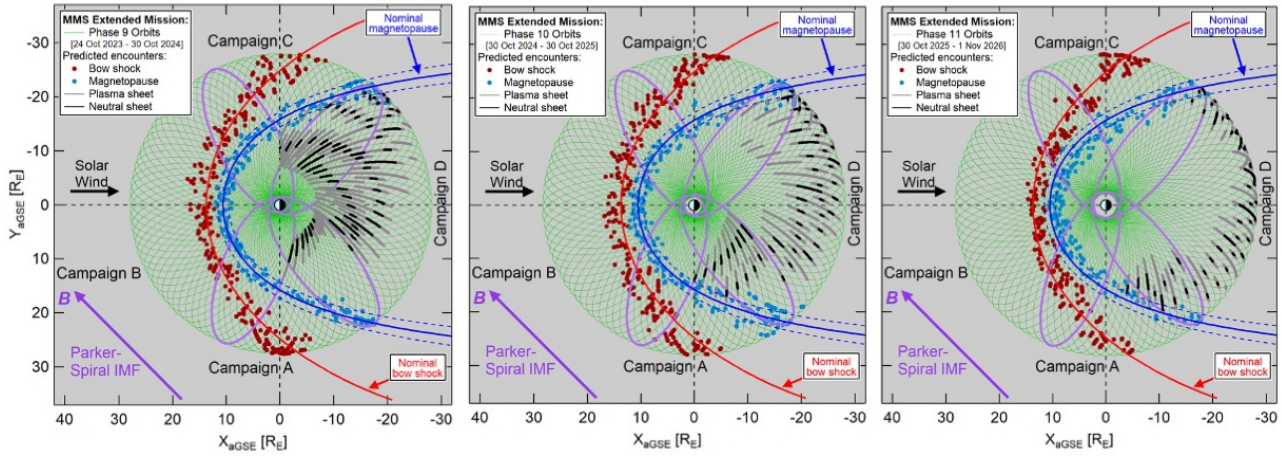

Figure 4a.1: Each year, MMS orbits (green) are divided into four observing campaigns, with the start of each marked by purple orbits. Magnetopause(blue), bow shock (red), plasma sheet (grey) and neutral sheet (black) encounters are prioritized for burst data collection, along with solar wind observing as data storage permits. Orbit precession repeatedly sweeps plasma sheet encounters across an ideal range of tail distances over time. Note that on completion of year/phase 11, MMS will have completed a full solar cycle of reconnection observation.

In the FY24-FY26 extended mission, we propose to add "formation change" periods to investigate the cross-scale physics that couple electron-kinetic processes to the surrounding environment in which they occur. Changes to the spacecraft constellation will be executed over many weeks with minimal maneuvers, both to avoid disruption to science data collection and to collect observations over a range of spacecraft distance. The proposal for the first campaign (nominally in FY24 for ~9 months) is a logarithmic string-of-pearls configuration. Starting with an ion-scale formation ideal for studying the coupling between the ion-kinetic structure of the magnetopause boundary and the electron-kinetic physics of diffusion regions, the formation would evolve to peak separation in the deep magnetotail to provide coverage over a variety of scales ranging from two spacecraft separated by electron-kinetic scales to 5 pairs of spacecraft with ion-to-MHD-scale separations. Minimal development is expected as a similar observing configuration was necessarily adopted during a 1-month period in February 2019 when the MMS apogee was raised from 25 to 29RE. After each formation change period, the intent is to return to the nominal tetrahedron formation. Subsequent formation changes would depend on the scientific success of previous campaigns.

The only expendable on the spacecraft is hydrazine with about 116kg left in the fuel tanks of each s/c as of October 2022, which is enough to maintain tetrahedron formations for 20+ years (~1kg/MMS/0.5yr). Fuel reserves support at least three science-focused formation changes (~2-9kg/MMS/formation depending on configuration, timing, and duration), plus a perigee raise (~16kg) to extend the mission beyond 2030, and later the forced reentry (21kg). Small apogee-adjusts are applied ~annually to minimize long-duration eclipses. See also Table 4.b.4.

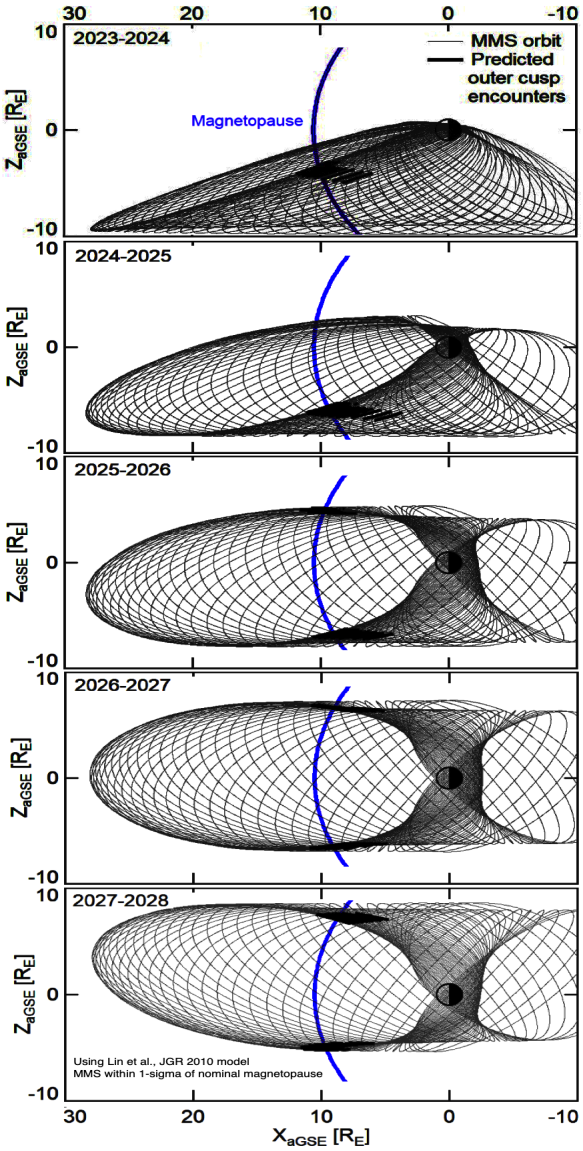

Figure 4a.2: MMS inclination drifts yeild the first-ever electron-scale observations of high-latitude magnetopause reconnection and outer cusp dynamics. Later, important conjunction opportunities occur as TRACERS at ~550km altitude, samples the low-altitude cusp while MMS samples the dayside magnetopause, high-altitude cusp, and surrounding boundary layers.

Table 4a.1: Each year is divided into four observing campaigns with specific science targets

Campaign	#Months	Orbit Description	Science Topics
A	1.5	Duskside magnetopause skimming	Flank reconnection, Kelvin-Helmholtz, quasi-parallel bow shock, magnetosheath turbulence, dusk magnetosphere
B	6	Duskside magnetopause, bow shock and pristine solar wind, dayside magnetopause, bow shock and ion/electron foreshock, dawnside magnetopause	Dayside magnetopause reconnection, magnetosheath flow bursts, quasi-perpendicular and quasi-parallel bow shock, foreshock dynamics, solar wind turbulence
C	1.5	Dawnside magnetopause skimming	High-flow-shear reconnection, Kelvin-Helmholtz, dawn magnetosphere
D	3	Magnetotail	Magnetotail reconnection, plasma sheet transients, bursty bulk flows, dipolarization fronts

4b Current Mission Status

The MMS payload continues to perform exceptionally well with remarkably few failures considering the number of instruments and the mission age. Because not every element is simultaneously required on each spacecraft, the 100+ instrumentation components continue to provide nearly full Level-1 performance (Table 4b.1) and appear capable of continuing this performance for several more years. There are no open subsystem or hardware risks, providing confidence in continued reliability for the next extended mission. Specific issues and their mitigations are detailed below.

Table 4b.1: Instrument Level 1 Performance

L1 Req	Measurement	Range	Resolution			Meets?
M10, M30	FIELDS **B** field	DC - 6kHz	0.1 nT	10ms	3D	✓
M20, M30	FIELDS **E** field	DC-100 kHz	0.5 mV/m	1 ms	3D	✓
M40	FPI Electrons	6 eV-30 keV	20%	30 ms	12°	✓ 3s/c
M50	FPI Ions	2 eV-30 keV	20%	150 ms	12°	✓
M60	HPCA Composition	10 eV-30 keV	20%	10 sec	12°	✓
M70	EPD Ions/Electrons	to 500 KeV	n/a	10 sec	12°	✓
M80	EPD Composition	to 500 keV	n/a	30 sec	12°	✓
I70	Potential Control	< 4 V	< 0.1 V	20 sec	n/a	✓

Note that four fully functioning spacecraft, while ideal, has never been an MMS L1 requirement, nor necessary for robust reconnection science.

4b.1 Instrument Status

All instruments are operating nominally with few exceptions (Table 4b.2). Details of the instrument operations are:

FPI DES/DIS: Sixty of the sixty-four Fast Plasma Investigation 16-channel spectrometers are operating nominally, measuring 2eV-30keV ions and 6eV-30keV electrons, and delivering >95% lossless data through their compression chips. The statistical and systematic uncertainties have been quantified. The Level-2 data products provide high-fidelity current density calculations from each spacecraft, enabling not-otherwise-possible studies of kinetic-scale physics. FPI uses a refined energy sweep table for solar wind observations (ions: 197eV-9222 eV; electrons: 4eV-940eV).

In summer 2018, two of the four MMS4 dual electron spectrometers suffered HV801 optocoupler failures; both are non-operational. MMS4 continues to provide half-sky 30ms electron observations, which remain of high value albeit requiring event-by-event analysis and the application of assumptions regarding the missing half-sky. One MMS3 dual ion spectrometer operates to max energy of 11 keV, with no appreciable loss to moment accuracies. Weekly monitoring indicates no further optocoupler issues. MMS maintains a near constant temperature for these detectors, which has been successful in maintaining their health, even through deep eclipse. FPI anticipates uninterrupted operations throughout this extended mission.

FIELDS E-Field: Full 3D electric field measurements continue within specifications for all spacecraft. In June 2016, a micrometeoroid severed a single bias wire of Probe 4 (SDP4) on MMS4 and is no longer accurate in the frequency range DC- ~600 Hz. For this range, the FIELDS team successfully implemented a post-processing routine using the remaining probes to determine the E-field components in the spin plane. Comparison data from before June

MMS1								
Central Data Processer				DFG		AFG	SCM	BField
SDP1	SDP2	SDP3	SDP4	ADP1	ADP2	EDI1	EDI2	EField
DIS0	DIS1	DIS2	DIS3	DES0	DES1	DES2	DES3	Fast Electrons/Ions
FEEPS1				FEEPS2				Electrons
EIS (SSD OFF)				HPCA				Ions/Comp
A1E1	A1E2	A1E3	A1E4	A2E1	A2E2	A2E3	A2E4	ASPOC

MMS2								
Central Data Processer				DFG		AFG	SCM	BField
SDP1	SDP2	SDP3	SDP4	ADP1	ADP2	EDI1	EDI2	EField
DIS0	DIS1	DIS2	DIS3	DES0	DES1	DES2	DES3	Fast Electrons/Ions
FEEPS1				FEEPS2				Electrons
EIS				HPCA				Ions/Comp
A1E1	A1E2	A1E3	A1E4	A2E1	A2E2	A2E3	A2E4	ASPOC

MMS3								
Central Data Processer				DFG		AFG	SCM	BField
SDP1	SDP2	SDP3	SDP4	ADP1	ADP2	EDI1	EDI2	EField
DIS0	DIS1	DIS2	DIS3	DES0	DES1	DES2	DES3	Fast Electrons/Ions
FEEPS1				FEEPS2				Electrons
EIS				HPCA				Ions/Comp
A1E1	A1E2	A1E3	A1E4	A2E1	A2E2	A2E3	A2E4	ASPOC

MMS4								
Central Data Processer				DFG		AFG	SCM	BField
SDP1	SDP2	SDP3	SDP4	ADP1	ADP2	EDI1	EDI2	EField
DIS0	DIS1	DIS2	DIS3	DES0	DES1	DES2	DES3	Fast Electrons/Ions
FEEPS1				FEEPS2				Electrons
EIS				HPCA				Ions/Comp
A1E1	A1E2	A1E3	A1E4	A2E1	A2E2	A2E3	A2E4	ASPOC

Green = nominal ops
Yellow = partial ops

Table 4b.2 Instrument Status

Grey = on hold as backup
White = non-operational

2016, documented in the CMAD, shows that the resulting accuracy change, remains less than the 0.5 mV/m mission success requirement with only a modest increase in the noise floor. A second micrometeoroid impact occurred in Sept 2018 to Probe2 (SDP2) on MMS2 which severed its 12V power. A flight software mod in early Oct 2018 reconfigured signals from the three remaining SDP probes to continue MMS2 spacecraft potential calculations, several burst trigger quantities, and the 1% duty cycled AC E-field, keeping MMS2 within specifications. More recently, on 8 May 8 2022, a micrometeoroid impacted MMS3 on probe 2, resulting in loss of function of that probe. Once again, the remaining 3 probes were configured so that full L1 performance continues. Thus, all four spacecraft are still returning the full science performance requirement.

FIELDS B-Field: All magnetometers on all spacecraft are operating nominally.

FIELDS EDI: Some HV optocouplers in the Electron Drift Instrument (EDI) deflection system are known to exhibit a higher than expected degradation with time. When a HV amplifier reaches the limit of its drive capability due to a degrading opto-coupler, the impact on operations and science return depends on the affected system. The energy for the Ambient Electron Mode (AEM) was reduced from 500eV to 250eV in Oct 2019 to reduce drive currents and lower the optocoupler degradation rate. Various other restrictions on either ambient mode or electric field mode have been implemented to carefully manage the estimated remaining run-time hours. Table 4b.3 summarizes the current status. Otherwise, the functions of EDI continue unabated and essentially at full success. Calibrations for E and B are well understood, and updates are stable over time; periodic calibrations can be expected to continue throughout the mission's lifetime.HPCA: The Hot Plasma Composition Analyzers on all spacecraft are operating nominally. At the start of Phase 1B (Sept 2016), the RF energy range (used to reduce the high proton fluxes without affecting the heavier ion fluxes) was expanded from the original 0.5 to ~4 keV to 0.2 to ~4 keV to reduce fluxes of magnetosheath protons in the range 0.2 to 0.5 keV. The RF proton flux reduction for MMS1 and MMS2 is approximately 50%, and the reduction for MMS3 and MMS4 is approximately 90%. The spacecraft are operated differently to bracket the range of proton fluxes in the magnetosphere, boundary layers, and magnetosheath. In the magnetotail, flux reduction is unnecessary and the RF is disabled. Gain tests are conducted twice yearly, it has not been necessary to increase detector microchannel plate (MCPs) voltages in the past two years.

EPD: With one exception, the Energetic Particle Detectors on all spacecraft are operating nominally. On 31 Jan 2016, one Energetic Ion Spectrometer unit (EIS1) disabled high voltage after sensing a microdischarge in its high voltage circuitry. On 31 Jan 2018, the EIS1 high voltage was restored, and no further issues have been encountered. There is light contamination in some Fly's Eye Energetic Particle Spectrometer (FEEPS) detectors due to penetration of the aluminum entrance foils used to prevent protons from striking the electron detectors. The burst data

Table 4b.3 Status of EDI subsystems and projected remaining life

Spacecraft	Affected Units*		EDI Subsystem	Technical Impact	Science Impact
	EDI1	EDI2			
MMS1	Jan2022	4 yrs	Gun Deflection	General Impact: When B is rapidly varying, loss of beam return at some spin phases.	Less frequent E and B intra-instrument calibrations
MMS2	N/A	N/A			
MMS3	N/A	Sep2019			
MMS4	>10 yrs	5 yrs			
MMS1	2 yrs	4 yrs	Electron Beam Generation	Operational Impacts: No electric field mode on MMS2. Electric field mode limited to one gun on MMS3, which provides data for flux gate calibration. Ambient mode continues, as below.	Impact is currently benign; flux gate spin axis offset determiniation continues with EDI time-of-flight data from MMS1, MMS3, and MMS4.
MMS2	Feb2022	Nov2016			
MMS3	May2017	< 1yr			
MMS4	5 yrs	5 yrs			
MMS1	5 yrs	> 10 yrs	Electrostatic Optics	General Impact: Potential loss of geometric factor and signal return detection for poleward direction. Operational Impacts: Ambient Mode restricted to field aligned (perpendicular) sampling on MMS2 (MMS3); No Ambient Mode on MMS4.	Impact is currently benign
MMS2	4 yrs	> 10 yrs			
MMS3	>10 yrs	> 10 yrs			
MMS4	4 yrs	4 yrs			

*status or estimated remaining life in years at 10 hours E-Field Mode per orbit and 50% ambient electron mode

is easily filtered on the ground and masking tables are uploaded to provide comprehensive survey data from all spacecraft; thus, the impact is manageable. In December 2019, the energy range on one EIS4 was shifted higher, complementing FEEPS electron data and enabling additional inner magnetospheric studies after decommissioning of the VAP mission. Recently, the precession of the MMS orbit resulted in multiple L=5 crossings each orbit; this complicated EIS operations as HV must be disabled/enabled to shield the detectors from high fluxes within the inner magnetosphere. The result has been more frequent EIS HV anomalies, though these pose no health and safety risk and recovery has been automated.

ASPOC: The Active Spacecraft Potential Control ion emitters have consumed far less indium to date than expected (~20%) owing to the lower level of ion currents (10 μA per unit), which enable high values of beam efficiency (larger than 96%), and shorter operation times compared to original planning. Only two emitters (MMS2 A1E1 and MMS4 A1E3) have expended their supply. With two ASPOC units on each spacecraft, each with four emitters, these unit failures do not impact mission science. Because of this low consumption, ASPOC continues to meet its L1 requirements, and the current level of operation can be maintained throughout the proposed extended mission.

4b.2 Spacecraft System Status

All four spacecraft are performing well, continue to meet requirements, and far exceed the engineering design. There are no open subsystem or hardware risks. All spacecraft operations are on Side A; Side B remains available for future need. The primary consumable is hydrazine propellant, used to maintain orbit and attitude and the observatory formation (Tables 4b.4 and 4b.5). Delta-V analysis shows MMS can complete a 5-year extended mission with sufficient propellant reserve to meet the 25-year reentry requirement (current predicted Earth reentry ~August 2030). Any fuel not consumed for science campaigns is available for potential mission extensions past the current planned 2030 EOM date. A tentative plan has demonstrated feasibility to delay reentry to 2037, although this is not proposed at this time.

There have been few on-orbit anomalies to date. In February 2016 a suspected micrometeoroid impact damaged one of five parallel shunt resistors on the bottom deck of MMS4, which has not presented a concern. In March 2019 MMS1 Star Tracker camera head A exhibited voltage and temperature fluctuations requiring that head be turned off. There is no impact to navigation as there are 2 other functional camera heads and only one is required. Only 2 spacecraft processor resets have occurred (MMS4 in Jan 2019 and MMS3 in Jun 2019). In Dec 2021, the circuit that generates the health and safety telemetry for the Navigator board on MMS2 began reporting intermittent spurious values. The Navigator continues to provide quality solutions that meet mission requirements and can be monitored using its solution output. While the telemetry and data generated by this circuit may be intermittently degraded, they are not used for fault detection nor do they impact the ability to command or control the Navigator system onboard.

Table 4b.4: MMS Fuel Budget to 2030 Reentry

S/C	Current Fuel Mass (kg)	Tetrahedron Formation & Eclipse (kg)	Perigee Raises (kg)	Science Campaigns (kg)	Exigencies (kg)	Remaining for EOM 2030 (kg)
MMS1	118.4	14	6	27	6	65
MMS2	116.4	14	6	27	6	63
MMS3	116.0	14	6	27	6	63
MMS4	116.0	14	6	27	6	63

The Mission Director tracks all risks using standard NASA risk management tools. The Continuous Risk Management (CRM) methodology is used to identify, analyze, plan, track, and control all risks. Operational mitigation techniques have been applied to maximize the likelihood that all four MMS observatories continue to operate reliably through the extended mission

4b.3 Mission Operations Status

The MMS Payload Operations Center (POC), located at LASP in Boulder, Colorado, operates the MMS science payload in coordination with the instrument teams. POC functions include routine planning and scheduling, command generation and uplink via the Mission Operations Center (MOC), health and safety assessment, contingency response, onboard and ground-based data management, and dissemination of data. The MOC and the Flight Dynamics Operations Areas are both co-located at Goddard Space Flight Center (GSFC) and perform all MMS spacecraft bus operations, including mission planning, real-time pass operations, systems

Table 4b.5: Orbit Adjustments to 2030 Reentry			
Date	Δ Period (min)	Δ Peri Height (km)	Adjustment Type (apogee/perigee)
11/1/23	5.68	150	Perigee
10/12/25	24.79	N/A	Apogee
10/11/26	-30.04	N/A	Apogee
10/14/27	-15.36	N/A	Apogee
10/2/29	7.57	200	Perigee
5/1/30	7.57	200	Perigee

and networks administration, IT security, observatory data trending, orbit determination, maneuver planning, and systems engineering support.

MMS telemetry is captured by the MOC and relayed, as they are received, to the POC using a high reliability private operational network. In addition to telemetry data transfers, ancillary data are provided to the POC via the MOC interface. The POC provides a real-time flow of data to the instrument teams to support commanding activities.

Addressing the need to refresh aging MOC hardware, in August 2022 the MOC transitioned most of its computer system's infrastructure to be run as virtual machines hosted by the GSFC Space Science Mission Operations (SSMO) virtualized Multi-Mission Operations Center (vMMOC). The infrastructure change coupled with standardization across SSMO missions offers reductions of future sustainment costs despite rapidly increasing inflation. The MOC leverages the vMMOC infrastructure to test and upgrade Operating Systems to adhere to NASA's increasing Information Technology security policies and directives.

Onboard burst data management is a critical function performed by the POC. Downlinked Fast Survey data are used to generate default burst data selections, which are made available to a Scientist-in-the-Loop (SITL) interface operated by the SDC and maintained in collaboration with UCB. Designed SITL scientists examine the fast survey data to assign figures of merit (FOMs) to time intervals that fall in-line with seasonal science guidelines. These improved selections, which are submitted to the POC and are processed/checked there, are used to produce a revised downlink plan. The system maximizes the downlink of the highest value science data.

MMS utilizes DSN, Space Network (SN), and the Near-Earth Network (NEN) via standard NASA services to provide ~5 DSN contacts every orbit (3.5 days) and 3 contacts spread across the SN and NEN. DSN contacts have remained at ~8 hours per week since 2019, although in 2022 continuing DSN maintenance and subscription pressures have negatively impacted downlinked burst data volumes. While MMS can fully meet its objectives, events of broader interest are hindered. While the MMS payload remains at prime mission quality, the Senior Review may want to consider the cost/benefit of recommending additional MMS downlink time to enable further burst data downlinks in support of HSO-related studies.

Starting in 2019, eclipse durations exceeding the original design limit of 3.85 hours were unavoidable. Besides the substantial operational measures required to manage power during these events, annual thermal and power analyses are required to ensure the instruments stay as thermally stable as possible to minimize the risk of HV801 optocoupler delamination. A custom set of operations for each eclipse season includes the power state (on, off, low power) of spacecraft subsystems and the Instrument Suite, custom sequences of heater operation, as well as a tilt of the instrument decks toward the Sun. The MMS Flight Dynamics team performs extensive analysis to minimize eclipse durations via small annual adjustments to spacecraft apogee. These measures mitigate eclipses significantly. All 4 observatories have performed these yearly eclipse operation sequences with no issues since 2019.

5 Management Plan

MMS is managed by GSFC, as the Project Management and Mission Operations organization, and Southwest Research Institute for Science Payload and Science Management. A full org chart and team list is maintained at https://lasp.colorado.edu/galaxy/x/MIAj. GSFC project management includes administration and reporting, science operations coordination, budgeting, contract and grant administration, mission operations, and a minimal science component. SwRI is under contract to GSFC and leads the Solving Magnetospheric Acceleration, Reconnection, and Turbulence (SMART) Science investigation. This work includes science research and publication, instrument payload operations, theory and modeling, data processing and analysis, data archiving and community science support. This division of responsibility is as selected via AO-02-OSS-03 and confirmed at the MMS KDP-C in July 2009. No changes are planned to the management structure in the extended mission.

The MMS leadership team has extensive experience. MMS Project Scientist, Barbara Giles, served as PS (and/or the HQ Program Scientist) for the Polar Mission, the Radiation Belt Storm Probes, MMS, and the Explorer Program. Similarly, Payload PI, James Burch, served as PI for numerous flight projects including the IMAGE mission, Rosetta's Ion and Electron Sensor, and for the MMS science payload. Both Dr. Giles and Dr. Burch have held management roles at their organizations. Recently, Deputy PI, Roy Torbert, stepped aside in favor of promoting a MMS DPI-in-Training candidate into the position, Kevin Genestreti. Dr. Torbert continues as Fields Lead Co-I and mentors Dr. Genestreti in his new role. Dr. Guan Le has served as MMS Deputy PS for many years, she was Geotail PS and is now PI for a GDC magnetometer proposal currently in Phase A competition. Our MMS Project Manager, James Clapsadle, has almost 30 years of mission operations experience across 10 different NASA missions

Building on the MMS Leadership Training Program presented in our 2020 SR proposal, key positions have deputies (or deputies-in-training) identified for the purpose of succession planning and for the purpose of training future PIs and PSs for other missions. Table 5.1 shows the status of those approved via the 2020 Senior Review – six promotions into full leadership already – and the new leadership trainees submitted for approval via this SR proposal. The deputies-in-training participate as ex-officio members of the MMS Science Working Group (SWG), which is the executive decision-making body for the broader MMS Science Working Team (SWT). These new-and-future leaders are early- to mid-career and have significant MMS experience by having started with the mission as graduate students or postdocs, which should serve the mission exceptionally well during extended flight. Fresh science perspectives and innovative management are already evident (e.g., the developing ISSI volume https://www.issibern.ch/workshops/magnetgeospace/).

Table 5.1: MMS Leadership Training and Succession Planning

2020 SR	Current Status	Leaders in Training	Previous Role	Current (or Proposed) Role
	Promoted	Gina Lafferty–LASP	Deputy POC Lead	POC Lead
2018	Promoted	Ian Cohen–JHU/APL	Deputy Lead–EPD	Lead–EPD
2019	Promoted	Dan Gershman–GSFC	Deputy Lead–FPI	Lead–FPI
Proposed	2021	Li-Jen Chen–NASA/GSFC	Deputy PS in training	Deputy PS in training
Proposed	Promoted	Kevin Genestreti–SwRI	Deputy PI in training	Deputy PI
Proposed	2021	Kyoung (Joo) Hwang–SwRI	Deputy PI in training	Deputy PI in training
	Proposed	Kristie Llera–SwRI	Team Scientist	Deputy PI in training
Proposed	2021	James Webster–Rice	Deputy Lead–HPCA in training	Deputy Lead–HPCA in training
Proposed	2021	Matthew Argall–UNH	Deputy Lead–FIELDS in training	Deputy Lead–FIELDS in training
Proposed	2021	Narges Ahmadi–LASP	Deputy Lead–ADP in training	Deputy Lead–ADP in training
Proposed	Promoted	Rick Wilder–LASP	Deputy Lead–Burst Mode	Lead–Burst Mode
Proposed	2021	Yi-Hsin Liu–Dartmouth	Deputy Lead–T&M	Deputy Lead–T&M
	Promoted	Christopher Riley–GSFC	Deputy SE Lead–MOC	Manager
	Promoted	Carl Phillips –GSFC	Real-Time Operations Engineer	Deputy Technical Lead - MOC

6 Data and Code Management Plan

Maximum science output requires rapid access to quality science data products along with the tools to perform advanced analysis of those data sets. MMS established, early on, a robust ground system to provide this service and is continually evolving that system as our instrument teams develop new products and tools. MMS is fully committed to the policies concerning open access as outlined under OMB memo M-13-13, as well as the 'NASA Plan for Increasing Access to the Results of Scientific Research' and the Heliophysics Division Science Data Management Policy.

As noted in Section 4b, MMS has been extremely fortunate in being able to maintain prime-mission data quality for its entire operations period. The value of the survey- and burst-resolution data to the long-term heliophysics data archive is extraordinary and MMS is dedicated to ensuring an archive of the highest quality. All science-quality data is available as open access within 30 days of downlink, with many products available much sooner. This is the time required to apply the cross-instrument calibrations and processing algorithms. Burst data are stored onboard and "trickled" to the ground by priority, often over many weeks, depending on downlink availability. This may lead to the impression of a release delay, even though data are being made available as quickly as technically feasible.

Data Management: MMS continues a vigorous flight calibration program to ensure maximum science data quality. Calibration and correction techniques are mature and the products exceed Level-1 requirements. Cross-calibrations utilize independently computed parameters such as currents or densities (e.g., FIELDS values of upper hybrid frequency compared with FPI/HPCA densities, EPD/FPI/HPCA continuity of particle spectra, Ve-ixB values compared to E, and others). This cross-calibration greatly enhances confidence in data accuracies.

As was required for MMS at launch, a Project Data Management Plan (PDMP) was developed and approved by the HQ Heliophysics Division. The archival data products and algorithms for the processing and calibration of the data are described in a new Calibration and Measurement Algorithms Document (CMAD). This document will continue to be expanded as teams further their analysis methodologies.

The MMS Science Data Center (SDC) (https://lasp.colorado.edu/mms/sdc/public/) serves as the central hub for MMS data related activities, including processing, archiving, visualization, and distribution. The SDC provides a large array of public-access web-based data access tools supporting multiple platforms and methods. Interfaces are provided that can be used from a web browser, command-line, or via scripts or other software, for maximum versatility. There are MMS data visualizations, including orbit plots, observatory formations, and auto-generated QuickLook data plots, which serve as a convenient first glimpse of new data within ~24 hours. Data are stored in Common Data Format (CDF) with full SPASE descriptions that were peer reviewed for maximum accessibility.

MMS partners with the Space Physics Data Facility (SPDF) for implementation of its open science requirements. The designated final archive for the MMS is the SPDF, which receives the MMS science data products on an ongoing basis. MMS employs a dedicated liaison to the SPDF, Scott Boardsen, to ensure compliance with all data policies. Open data initiatives in 2022 include (1) Digital Object Identifiers (DOI) along with a SPASE document resource available for all the L2 and L3 MMS datasets, and (2) a data product quality/documentation review utilizing a toolset originally developed for the Cluster mission for a similar purpose.

Code Management: MMS provides funding to UCLA to provide publicly available data analysis codes through the Space Physics Environment Data Analysis Software (SPEDAS) framework. SPEDAS is fully documented online (e.g., http://spedas.org) and Python-based SPEDAS tools for MMS are now available along with instrument-specific tutorial scripts. Training sessions and webinars on the use of SPEDAS with MMS data are regularly held at community workshops.

MMS adheres to HQ guidelines for legacy missions concerning open-source software. All data product processing codes will be archived at end of mission to ensure data reproducibility. Because the MMS ground data processing codes were developed at each instrument institution prior to the 2014 launch, using a wide variety of local protocols, languages, and proprietary toolkits, it is not possible to switch the codes to open source at this point in the mission.

7 Budget Narrative

MMS is managed by GSFC, as the Project Science, Project Management and Mission Operations organization. Southwest Research Institute (SwRI) is responsible for Payload and Science Management through the Solving Magnetospheric Acceleration, Reconnection, and Turbulence (SMART) investigation awarded via AO-02-OSS-03. Responsibilities are as detailed in Section 5. Throughout its operations, MMS spending has been kept well within the funding appropriations and has been carefully managed. The organization chart maintained at https://lasp.colorado.edu/galaxy/x/MIAj illustrates the funding flows.

Two budget spreadsheets are provided. The first spreadsheet proposes a guideline budget covering fiscal years 2024-2028 and the second details an over-guideline budget for the same period. Budgets for FY22 and FY23, already past or in progress, are provided for reference. Both budgets are grass-roots estimates based on averaged actual costs over the years FY19-FY22 and – for requirements-based operational components – incorporate inflation factors as provided by the 2022 NASA New Start Inflation Index.

The guideline budget supports the proposed payload and mission operations but results in termination of funding for the Early Career Scientist initiative and Outreach efforts after FY23 and the MMS Theory and Modeling (T&M) Team after FY24. Priority is placed on maintaining instrument team funding through FY26 to ensure the proposed multi-scale campaigns are supported as planned. Regardless, in the guideline scenario, all science investigation by the instrument teams would be terminated after FY26.

The over-guideline budget supports the proposed payload and mission operations and scientific research, including the T&M team, through FY28. The Early Career Scientist initiative and Outreach continues through FY24. This budget gradually ramps down by ~$1M per year from FY23 to FY26 until settling on a constant baseline budget of $20.2M.

The MMS budget is dominated by two major operational endeavors, the Mission Operations Center and the SMART payload/science activity. The MOC budget is entirely requirements-based; FY24 estimated costs are based on averaged prior actuals with future years simply inflated via the standard NASA table noted above. The non-research component of the SMART payload/science budget is also requirements-based and includes simple inflation. This budget component also reflects a commitment to reduce or further automate several operational and data processing processes. Further reductions to these two components would require changes to the operational requirements (e.g., elimination of the planned formation changes or, depending on the level of reduction, tetrahedron formation flying).MMS-SMART Budget. SMART funding supports project activities at SwRI and several subcontractor institutions as well as government contributions (FPI at GSFC/MSFC and EPD at LANL) that are overseen by SwRI. Several efforts – including T&M, MEC, early career, and SITL – have their grants/contracts administered by the Project Scientist office to minimize overhead. The over-guideline budget supports continued operations and scientific research at levels comparable to, but somewhat lower than, those of the highly successful prime phase and first two extended missions.

Budget for GSFC Management and Mission Operations. The MMS budget supports mission management functions at GSFC within the Heliophysics Science Division, the Space Sciences Mission Operations (SSMO) Project office, and the Mission Validation and Operations Branch, including flight ops contracted services. Future mission operational costs are based on experience with MMS tetrahedron formation flying operations during Phase E and the present extended mission. The operations remain challenging in terms of the number and frequency of maneuvers required to maintain the four spacecraft in scientifically viable orbits. An estimate of required High End Computing Resources is included to support the state-of-the-art kinetic modeling proposed, in close association with MMS measurements

The MMS project remains cognizant of the need to reduce its operational costs. To date, in spite of increased operational complexities (flight dynamics, anomaly mitigations, long eclipses), operational costs have been held approximately level with the exception of labor inflationary pressures. This unique science payload has endured for much longer than anticipated and it is a project value to continue collecting the full range of burst resolution data for as many scientifically valuable events-of-interest as possible, until the time that the payload degrades to the level of Heliophysics' other magnetospheric in-situ observatories.

Appendix A: MMS Acronym List

Acronym	Definition
ABS	Automatic Burst Selection
AC	Alternating Current
ACE	Advanced Composition Explorer
AEM	Ambient Electron Mode
AFG	Analog Flux Gate
AI	Artificial Intelligence
ARASE	Formerly ERG
ARTEMIS	Acceleration, Reconnection, Turbulence and Electrodynamics of the Moon's Interaction with the Sun
ASCII	American Standard Code for Information Interchange
ASPOC	Active Spacecraft Potential Control
AU	Astronomical Unit
CDF	Common Data Format s
CIR	Corotating Interaction Region
CMAD	Calibration and Measurement Algorithms Document
CPS	Central Plasma Sheet
CRM	Continuous Risk Management
DC	Direct Current
DES	Dual Electron Sensor
DF	Dipolarization Front
DFG	Digital Fluxgate
DIS	Dual Ion Sensor
DL	Double Layer
DMC	Diamagnetic Cavity
DSA	Diffusive Shock Acceleration
DSCOVR	Deep Space Climate Observatory
DSN	Deep Space Network
EDI	Electron Drift Instrument
EDR	Electron Diffusion Region
EIS	Energetic Ion Spectrometer
EMIC	Electromagnetic Ion Cyclotron
EOM	End of Mission
EPD	Energetic Particle Detectors
ERG	Exploration of Energization and Radiation in Geospace
ESW	Electrostatic Waves
FB	Foreshock Bubble
FDOA	Flight Dynamics Operations Area
FEEPS	Fly’s Eye Energetic Particle Spectrometer
FGM	Flux-Gate Magnetometer
FIELDS	MMS suite of electric and magnetic field instruments
FOT	Flight Operations Team
FOM	Figures of Merit
FPI	Fast Plasma Instrument
FTE	Flux Transfer Event
FY	Fiscal Year
GOES	Geostationary Operational Environmental Satellite
GOLD	Global-scale Observations of the Limb and Disk

GLS ..... Ground Loop System
GSE ..... Geocentric Solar Ecliptic
GSFC..... Goddard Space Flight Center
GSM..... Geocentric Solar Magnetospheric
HFA..... Hot Flow Anomaly
HPCA..... Hot Plasma Composition Analyzer
HSD..... Heliophysics Science Division
HSO..... Heliophysics System Observatory
HV..... High Voltage
IBEX ..... Interstellar Boundary Explorer
ICON..... Ionosphere Connection Explorer
IDR..... Ion Diffusion Region
IMAP..... Interstellar Mapping and Acceleration Probe
IMF ..... Interplanetary Magnetic Field
IP ..... Interplanetary
IT..... Information Technology
ITM ..... Ionosphere, Thermosphere, Mesosphere
JAXA..... Japan Aerospace Exploration Agency
KDP..... Key Decision Point
KH..... Kelvin-Helmholtz
KHV..... Kelvin-Helmholtz Vortex
LANL..... Los Alamos National Laboratory
LASP..... Laboratory for Atmospheric and Space Physics
LEO..... Low Earth Orbit
LHW..... Lower-Hybrid Waves
LMN..... Boundary Normal Coordinates
LT ..... Local Time
MCP ..... Microchannel Plate
MEC..... Magnetic Ephemeris Coordinates
MHD ..... Magnetohydrodynamics
MLT..... Magnetic Local Time
MMOC..... Multi-Mission Operations Center
MMS ..... Magnetospheric Multiscale Mission
MOC ..... Mission Operations Center
MSFC..... Marshall Space Flight Center
N/A..... Not Applicable
NAS..... National Academy of Sciences
NASA..... National Aeronautics and Space Administration
NEN ..... Near Earth Network
NISM..... Near Interstellar Medium
OMB ..... Office of Management and Budget
P&SS..... Planetary and Space Science
PDF ..... Portable Document Format
PDMP..... Project Data Management Plan
PI..... Principal Investigator
POC..... Payload Operations Center
PS ..... Project Scientist
PSD ..... Power Spectral Density
PSBL ..... Plasma Sheet Boundary Layer

PSG ..... Prioritized Science Goal
PSP ..... Parker Solar Probe
PUI ..... Pickup Ion
RE ..... Earth Radii
RF ..... Radio Frequency
ROI ..... Regions of Interest
S/C ..... Spacecraft
SCM ..... Search Coil Magnetometer
SDA ..... Shock Drift Acceleration
SDC ..... Science Data Center
SDP ..... Spin-plane Double Probe
SG ..... Science Goal
SITL ..... Scientist-in-the-Loop
SLAM ..... Short Large Amplitude Magnetic structure
SMART ..... Solving Magnetospheric Acceleration, Reconnection, and Turbulence
SMD ..... Science Mission Directorate
SN ..... Space Network
SO ..... Science Objective
SOC ..... Science Operations Center
SOHO ..... Solar and Heliospheric Observatory
SPASE ..... Space Physics Archive Search and Extract
SPDF ..... Space Physics Data Facility
SPEDAS ..... Space Physics Environment Data Analysis Software
SR ..... Senior Review
SROI ..... Science Regions of Interest
SSCWeb ..... Satellite Situation Center Web
SSMO ..... Space Science Mission Operations
STEM ..... Science, Technology, Engineering and Mathematics
SW ..... Solar Wind
SWG ..... Science working group
SwRI ..... Southwest Research Institute
SWT ..... Science Working Team
T&M ..... Theory and Modeling
THEMIS ..... Time History of Events and Macroscale Interactions during Substorms mission
TRACERS ..... Tandem Reconnection and Cusp Electrodynamics Reconnaissance Satellites
TWINS ..... Two Wide-Angle Imaging Neutral-Atom Spectrometers
UCB ..... University of California – Berkeley
UCLA ..... University of California – Los Angeles
ULF ..... Ultra-Low Frequency
UNH ..... University of New Hampshire
USAF ..... United States Air Force
VAP ..... Van Allen Probes
VDF ..... Velocity Distribution Function
vMMOC ..... Virtualized Multi-Mission Operations Center
XML ..... Extensible Markup Language

Appendix C: References

Afshari, A. S., et al. (2021). The importance of electron Landau damping for the dissipation of turbulent energy in terrestrial magnetosheath plasma. Journal of Geophysical Research: Space Physics, 126, e2021JA029578. doi: 10.1029/2021JA029578

Amano, T., et al. (2020). Observational evidence for stochastic shock drift acceleration of electrons at the Earth's bow shock. Physical Review Letters, 124(6), 065101. doi: 10.1103/PhysRevLett.124.065101

André, M., et al. (2016). Magnetic reconnection and modification of the Hall physics due to cold ions at the magnetopause. Geophys. Res. Lett., 43, 6705–6712, doi:10.1002/2016GL069665

Angelopoulos, V., et al., (1992). Bursty bulk flows in the inner central plasma sheet. J. Geophys. Res., 97(A4), 4027–4039. doi:10.1029/91JA02701

Artemyev, A., et al. (2021). Configuration of the Earth's magnetotail current sheet. Geophysical Research Letters, 48, e2020GL092153. https://doi.org/10.1029/2020GL092153

Aunai, N., et al. (2013). Electron nongyrotropy in the context of collisionless magnetic reconnection. Physics of Plasmas 20.9: 092903. doi: 10.1063/1.4820953

Bacchini, Fabio, et al. (2022). Kinetic heating by Alfvén waves in magnetic shears. Physical Review Letters 128.2: 025101. doi: 10.1103/PhysRevLett.128.025101

Bandyopadhyay, R., et al. (2021). Energy dissipation in turbulent reconnection. Physics of Plasmas 28.11: 112305. doi: 10.1063/5.0071015

Bandyopadhyay, R., et al. (2020). In situ measurement of curvature of magnetic field in turbulent space plasmas: a statistical study. The Astrophysical Journal Letters 893.1: L25. doi: 10.3847/2041-8213/ab846e

Baumjohann, W., et al., (1990). Characteristics of high-speed ion flows in the plasma sheet J. Geophys. Res., 95(A4), 3801–3809, doi:10.1029/JA095iA04p03801

Baumjohann, W., et al. (1999). Substorm dipolarization and recovery. J. Geophys. Res., 104(A11), 24995–25000, doi:10.1029/1999JA900282

Beresnyak, A., and Li, H. (2016). First-order particle acceleration in magnetically driven flows. The Astrophysical Journal 819.2: 90. doi: 10.3847/0004-637X/819/2/90

Bessho, N., L.-J. Chen, S. Wang et al. (2020), Magnetic reconnection and kinetic waves generated in the Earth's quasi-parallel bow shock, Phys. Plasmas, 27, 092901, doi: 10.1063/5.0012443

Bessho, N., L.-J. Chen, J. E. Stawarz et al. (2022), Strong reconnection electric fields in shock-driven turbulence, Phys. Plasmas, 29, 042304, doi: 10.1063/5.0077529

Birn, J., M. Hesse, and S. Zenitani. (2011). Reconnection in compressible plasmas: Extended conversion region. Phys. Plasmas, 18, 111202. doi: 10.1063/1.3626836

Blackburn, H. M., Mansour, N. N., and Cantwell, B. J. (1996). Topology of fine-scale motions in turbulent channel flow. Journal of Fluid Mechanics, 310, 269-292. doi:10.1017/S0022112096001802

Borovsky, J. E., and Denton, M. H. (2006), Geophys. Res. Lett., 33, L20101, doi:10.1029/2006GL026519

Burch, J. L., et al. (2020). Electron inflow velocities and reconnection rates at Earth's magnetopause and magnetosheath. Geophysical Research Letters, 47, e2020GL089082. doi: 10.1029/2020GL089082

Burch, J. L., et al. (2022). The EDR inflow region of a reconnecting current sheet in the geomagnetic tail. Physics of Plasmas 29, 052903. doi: 10.1063/5.0083169

Cassak, P. and Otto, A. (2011). Scaling of the magnetic reconnection rate with symmetric shear flow, Phys. Plasmas, 18, 074501. doi: 10.1063/1.3609771

Cerri, S. S. et al. Dual phase-space cascades in 3D hybrid-Vlasov–Maxwell turbulence. The Astrophysical Journal Letters 856, no. 1 (2018): L13. doi: 10.3847/2041-8213/aab557

Chandrasekhar, S., & Woltjer, L. (1958). On force-free magnetic fields. Proceedings of the National Acad-

emy of Sciences, 44(4), 285-289. doi: 10.1073/pnas.44.4

Chasapis, A., et al. (2018a). Energy conversion and collisionless plasma dissipation channels in the turbulent magnetosheath observed by the Magnetospheric Multiscale Mission. The Astrophysical Journal 862.1: 32. doi: 10.3847/1538-4357/aac775

Chasapis, A., et al. (2018b). In situ observation of intermittent dissipation at kinetic scales in the Earth's magnetosheath. The Astrophysical Journal Letters 856.1: L19. doi: 10.3847/2041-8213/aaadf8

Chen, L.-J., et al., (2020) Lower-hybrid drift waves driving electron nongyrotropic heating and vortical flows in a magnetic reconnection layer, Physical Review Letters, 125, 025103. doi:10.1103/PhysRevLett.125.025103

Chen, L. J., et al. (2021a). Solitary magnetic structures at quasi-parallel collisionless shocks: Formation. Geophysical Research Letters, 48, e2020GL090800. doi: 10.1029/2020GL090800

Chen, L.-J., et al., (2021b) Magnetopause reconnection and indents induced

by foreshock turbulence. Geophysical Research Letters, 48, doi:10.1029/2021GL093029

Chen, L., et al. (2022a). "Solitary Magnetic Structures Developed From Gyro-Resonance With Solar Wind Ions at Mars and Earth." Geophysical Research Letters, 49 (3): [10.1029/2021gl097600]

Chen, L.-J. et al. (2022b). Reconnection diffusion region in the temperature ramp of a near-perpendicular bow shock, in preparation.

Cohen, I. J., et al. (2019). High-resolution measurements of the cross-shock potential, ion reflection, and electron heating at an interplanetary shock by MMS. Journal of Geophysical Research: Space Physics, 124, 3961– 3978. doi: 10.1029/2018JA026197

Cohen, I. J. et al. (2021). Investigating the link between outer radiation belt losses and energetic electron escape at the magnetopause: A case study using multi-mission observations and simulations. Journal of Geophysical Research: Space Physics, 126, e2021JA029261. doi: 10.1029/2021JA029261

Consolini, G., et al. (2015). Statistics of the velocity gradient tensor in space plasma turbulent flows. The Astrophysical Journal, 812(1), 84. doi: 10.1088/0004-637X/812/1/84

Consolini, G., et al. (2018). On the magnetic field topology in reconnection region. In Journal of Physics: Conference Series (Vol. 1100, No. 1, p. 012007). doi: 10.1088/1742-6596/1100/1/012007

Cozzani, G., et al., (2021) Structure of a Perturbed Magnetic Reconnection Electron Diffusion Region in the Earth's Magnetotail, Physical Review Letters, 127, 215101. doi:10.1103/PhysRevLett.127.215101

Dahlin, J. T., J. F. Drake, and M. Swisdak (2014). The mechanisms of electron heating and acceleration during magnetic reconnection. Physics of Plasmas 21.9: 092304. doi:10.48550/arXiv.1406.0831

Dahlin, J. T., J. F. Drake, and M. Swisdak (2017). The role of three-dimensional transport in driving enhanced electron acceleration during magnetic reconnection. Physics of Plasmas 24.9 (2017): 092110. doi: 10.48550/arXiv.1706.00481

Dallas, V., and Alexakis, A. (2013). Structures and dynamics of small scales in decaying magnetohydrodynamic turbulence. Physics of Fluids, 25(10), 105106. doi: 10.1063/1.4824195

Del Sarto, D., et al. (2016). Pressure anisotropy and small spatial scales induced by velocity shear. Physical Review E 93.5: 053203. doi: 10.1103/PhysRevE.93.053203

Del Sarto, D., and Pegoraro, F. (2018). Shear-induced pressure anisotropization and correlation with fluid vorticity in a low collisionality plasma. Monthly Notices of the Royal Astronomical Society 475.1: 181-192. doi: 10.1093/mnras/stx3083

Drake, J. F., et al. (2006). Electron acceleration from contracting magnetic islands during reconnection. Nature, Volume 443, Issue 7111, pp. 553-556. doi: 10.1038/nature05116

Drake, J. F., et al., (2009), Journal of Geophysical Research-Space Physics, 114, doi:10.1029/2008JA013701

Du, S., et al. (2018). Plasma energization in colliding magnetic flux ropes. The Astrophysical Journal 867.1: 16. doi: 10.3847/1538-4357/aae30e

Ergun, R. E., et al. (2016). Magnetospheric Multiscale observations of large-amplitude, parallel, electrostatic waves associated with magnetic reconnection at the magnetopause. Geophys. Res. Lett., 43, 5626–5634, doi:10.1002/2016GL068992

Ergun, R. E., et al. (2018). Magnetic reconnection, turbulence, and particle acceleration: Observations in the Earth's magnetotail. GRL, 45, 3338–3347. doi: 10.1002/ 2018GL076993

Ergun, R. E., et al. (2020a). Observations of Particle Acceleration in Magnetic Reconnection–driven Turbulence. The Astrophysical Journal, 898(2), 154. doi: 10.3847/1538-4357/ab9ab6

Ergun, R. E., et al. (2020b). Particle acceleration in strong turbulence in the Earth's magnetotail. The Astrophysical Journal, 898(2), 153. doi: 10.3847/1538-4357/ab9ab5

Ergun, R.E., et al., (2022), Observation of Magnetic Reconnection in a Region of Strong Turbulence, Astrophysical Journal Letters, 935 L8. doi: 10.3847/2041-8213/ac81d4

Eriksson, E., et al. (2020). Electron acceleration in a magnetotail reconnection outflow region using Magnetospheric MultiScale data. Geophysical Research Letters, 47, e2019GL085080. https://doi.org/10.1029/2019GL085080

Eriksson, S., et al. (2016). Magnetospheric Multiscale observations of magnetic reconnection associated with Kelvin-Helmholtz waves, Geophys. Res. Lett., 43, 5606–5615, doi:10.1002/2016GL068783

Escoubet, C. P., et al. (2020). Cluster and MMS Simultaneous Observations of Magnetosheath High Speed Jets and Their Impact on the Magnetopause. Front. Astron. Space Sci. 6:78. doi: 10.3389/fspas.2019.00078

Fadanelli, S. et al. (2021). Energy conversions associated with magnetic reconnection. Journal of Geophysical Research: Space Physics 126.1: e2020JA028333. doi: 10.1029/2020JA028333

Fargette, N., et al. (2020). On the ubiquity of magnetic reconnection inside flux transfer event-like structures at the Earth's magnetopause. Geophysical Research Letters, 47, e2019GL086726. doi: 10.1029/2019GL086726

Fuselier, S. A., et al. (2020). Neutral atom imaging of the solar wind magnetosphere- exosphere interaction near the subsolar magnetopause. Geophysical Research Letters, 47, e2020GL089362. doi: 10.1029/2020GL089362

Fuselier, S. A., et al. (2021). Reconnection X-line orientations at the Earth's magnetopause. Journal of Geophysical Research: Space Physics, 126, e2021JA029789. doi: 10.1029/2021JA029789

Garcia-Sage, K., et al. (2015). Modeling the effects of ionospheric oxygen outflow on bursty magnetotail flows. J. Geophys. Res. Space Physics, 120, 8723, doi:10.1002/2015JA021228

Genestreti, K. G., et al. (2014). The location and rate of occurrence of near-Earth magnetotail reconnection as observed by Cluster and Geotail. Journal of Atmospheric and Solar-Terrestrial Physics. Volume 121, Part A, December 2014, Pages 98-109. doi: 10.1016/j.jastp.2014.10.005

Genestreti, K. J., et al. (2020). Multiscale coupling during magnetopause reconnection: Interface between the electron and ion diffusion regions. Journal of Geographical Research: Space Physics,125, e2020JA027985. doi: 10.1029/2020JA027985

Genestreti, K. G., et al. (2022). On the origin of "patchy" energy conversion in electron diffusion regions. Phys. Plasmas 29, 082107. doi: 10.1063/5.0090275

Gershman, D. J., et al., (2017) Wave-particle energy exchange directly observed in a kinetic Alfven-branch wave, Nature Communications, 8, 14719. doi:10.1038/ncomms14719

Gingell, I., et al. (2020), Statistics of Reconnecting Current Sheets in the Transition Region of Earth's Bow Shock, J. Geophys. Res., 125, e2019JA027119, doi: 10.1029/2019JA027119

Gingell, I., et al. (2021), Observing the prevalence of thin current sheets downstream of Earth's bow shock,

Phys. Plasmas 28, 102902, doi: 10.1063/5.0062520

Goldstein, J., et al. (2020). Global ENA imaging and in situ observations of substorm dipolarization on 10 August 2016. Journal of Geophysical Research: Space Physics, 125, e2019JA027733. doi: 10.1029/2019JA027733

Graham, D.B., et al. (2022). Direct observations of anomalous resistivity and diffusion in collisionless plasma, Nature Communications 13, 2954. doi:10.1038/s41467-022-30561-8

Guo, Fan, et al. (2014). Formation of hard power laws in the energetic particle spectra resulting from relativistic magnetic reconnection. Physical Review Letters 113.15: 155005. doi: 10.1103/PhysRevLett.113.155005

Hanson, E. L. M., et al. (2019). Cross-shock potential in rippled versus planar quasi-perpendicular shocks observed by MMS. Geophysical Research Letters, 46, 2381–2389. doi: 10.1029/2018GL080240

Hasegawa, H., et al. (2022). Magnetic field annihilation in a magnetotail electron diffusion region with electron-scale magnetic island. Journal of Geophysical Research: Space Physics, 127, e2022JA030408. doi: 10.1029/2022JA030408

Hasegawa, H., et al. (2020). Generation of turbulence in Kelvin-Helmholtz vortices at the Earth's magnetopause: Magnetospheric Multiscale observations. Journal of Geophysical Research: Space Physics, 125, e2019JA027595. doi: 10.1029/2019JA027595

Hesse, M, and J. Birn (2004). On the cessation of magnetic reconnection Annales Geophysicae, 22, 2, 603-612. doi: 10.5194/angeo-22-603-2004

Hesse, M. et al. (2013). Aspects of collisionless magnetic reconnection in asymmetric systems. Physics of Plasmas, 20, 6, 61210. doi: 10.1063/1.4811467

Hesse, M. et al. (2018). The physical foundation of the reconnection electric field. Phys. Plasmas, 25, 032901, doi: 10.1063/1.5021461

Holmes, J. C., et al. (2021). Wave activity in a dynamically evolving reconnection separatrix. Journal of Geophysical Research: Space Physics, 126, e2020JA028520. doi: 10.1029/2020JA028520

Howes, Gregory G. A prescription for the turbulent heating of astrophysical plasmas. Monthly Notices of the Royal Astronomical Society: Letters 409.1 (2010): L104-L108. doi: 10.1111/j.1745-3933.2010.00958.x

Hwang, K. J., et al. (2021). Microscale Processes Determining Macroscale Evolution of Magnetic Flux Tubes along Earth's Magnetopause. The Astrophysical Journal, 914(1), 26. doi: 10.3847/1538-4357/abf8b1

Jia, Y.-D., Qi, Y., Lu, S., and Russell, C. T. (2021). Temporal evolution of flux rope/tube entanglement in 3-D Hall MHD simulations. Journal of Geophysical Research: Space Physics, 126, e2020JA028698. doi: 10.1029/2020JA028698

Jokipii, J. R. (1982) Particle drift, diffusion, and acceleration at shocks. The Astrophysical Journal 255: 716-720. doi: 10.1086/159870

Karpen, J. T., S. K. Antiochos, and C. R. DeVore, (2012). The mechanisms for the onset and explosive eruption of coronal mass ejections and eruptive flares. Astrophysical Journal, 760: 81, doi: 10.1088/0004-637X/760/1/81

Kitamura, N., et al. (2022) Direct observations of energy transfer from resonant electrons to whistler-mode waves in magnetosheath of Earth. Nat Commun 13, 6259. https://doi.org/10.1038/s41467-022-33604-2

Khoutyaintsev, Y., et al. (2020). Electron Heating by Debye-Scale Turbulence in Guide-Field Reconnection. Physical Review Letters, Volume 124, Issue 4, article id.045101. doi: 10.1103/PhysRevLett.124.045101

Kieokaew, R., et al. (2020). Magnetic reconnection inside a flux transfer event-like structure in magnetopause Kelvin-Helmholtz waves. Journal of Geophysical Research: Space Physics, 125, e2019JA027527. doi: 10.1029/2019JA027527

Labelle-Hamer, A., et al. (1995). Magnetic reconnection in the presence of sheared flow and density asym-

metry: Applications to the Earth's magnetopause J. Geophys. Res., 100,11875. doi:10.1029/95JA00969

Lapenta, G. et al. (2006). Kinetic simulations of x-line expansion in 3D reconnection. Geophysical Research Letters, 33, L10102, doi:10.1029/2005GL025124

Le, A., et al., (2017) Enhanced electron mixing and heating in 3-D asymmetric reconnection at the Earth's magnetopause, Geophys. Res. Lett., 44, 2096–2104, doi:10.1002/2017GL072522.

Li, X., et al. (2015). Nonthermally dominated electron acceleration during magnetic reconnection in a low-β plasma. The Astrophysical Journal Letters 811.2 (2015): L24. doi: 10.1088/2041-8205/811/2/L24

Li, X., et al. (2017). Particle acceleration during magnetic reconnection in a low-beta plasma. The Astrophysical Journal 843.1 (2017): 21. doi: 10.3847/1538-4357/aa745e

Liang, H., et al. (2017). Oxygen acceleration in magnetotail reconnection. J. Geophys. Res., 122, 618. doi:10.1002/2016JA023060

Lichko, E., and Egedal, J. (2020). Magnetic pumping model for energizing superthermal particles applied to observations of the Earth's bow shock, Nat. Commun. 11, 2942 (2020). doi: 10.1038/s41467-020-16660-4

Liu, T. Z., et al. (2020). Magnetospheric Multiscale (MMS) Observations of Magnetic Reconnection in Foreshock Transients, J. Geophys. Res. 125, e2020JA027822. doi: 10.1029/2020JA027822

Liu, Y.-H., and M. Hesse (2016). Suppression of collisionless magnetic reconnection in asymmetric current sheets. Physics of Plasmas, 23(6). doi:10.1063/1.4954818.

Liu, Y-H. et al., (2014). Onset of reconnection in the near magnetotail: PIC simulations. Journal of Geophysical Research: Space Physics, 119, 12, 9773-9789. doi: 10.1002/2014JA020492

Liu, Y.-H., et al. (2017). Why does steady-state magnetic reconnection have a maximum local rate of order 0.1? Physical Review Letters 118 (8), 085101. doi: 10.1103/PhysRevLett.118.085101

Liu Y.-H., et al. (2018). Strongly localized magnetic reconnection by the out-of-plane super-Alfvénic shear flow, Phys. Plasmas, 25, 08070. doi: 10.1063/1.5042539

Liu, Y.-H. et al. (2019). Three-dimensional magnetic reconnection with a spatially confined x-line extent: implications for dipolarizing flux bundles and the dawn-dusk asymmetry. Journal of Geophysical Research: Space Physics, Volume 124, Issue 4, pp. 2819-2830. doi: 10.1029/2019JA026539

Longcope, D. W., et al. (2009). Gas-dynamic shock heating of post-flare loops due to retraction following localized, impulsive reconnection. Astrophys. J., 690:L18–L22. doi:10.1088/0004-637X/690/1/L18

Lu, Q., et al. (2018). Formation of power law spectra of energetic electrons during multiple X line magnetic reconnection with a guide field. Physics of Plasmas 25.7: 072126. doi: 10.1063/1.5034012

Lu, S., et al. (2019). The Hall electric field in Earth's magnetotail thin current sheet. Journal of Geophysical Research: Space Physics, 124, 1052–1062. doi: 10.1029/2018JA026202

Man, H.Y., et al. (2020). Observations of electron-only magnetic reconnection associated with macroscopic flux ropes. Geophysical Research Letters, 47, e2020GL089659. doi: 10.1029/2020GL089659

Markidis, S., et al. (2011). Kinetic simulations of magnetic reconnection in presence of a background O+ population. J. Geophys. Res, 116, A00K16. doi:10.1029/2011JA016429

Marshall, A. T., et al. (2020). Asymmetric reconnection within a flux rope-type dipolarization front., e2019JA027296. doi: 10.1029/2019JA027296

Matthaeus, William H., et al. Turbulence and proton–electron heating in kinetic plasma. The Astrophysical Journal Letters 827.1 (2016): L7. doi: 10.3847/2041-8205/827/1/L7

McFadden, J., et al., (2008). Structure of plasmaspheric plumes and their participation in magnetopause reconnection: First results from THEMIS Geophys. Res. Lett., 35, L17S10. doi:10.1029/2008GL033677

Meneveau, C. (2011). Lagrangian dynamics and models of the velocity gradient tensor in turbulent flows. Annual Review of Fluid Mechanics, 43(1), 219-245. doi: 10.1146/annurev-fluid-122109-160708

Meyrand, R. et al. (2019). Fluidization of collisionless plasma turbulence. Proceedings of the National Academy of Sciences 116, no. 4: 1185-1194. doi: 10.1073/pnas.1813913116

Montgomery, D., Turner, L., & Vahala, G. (1978). Three-dimensional magnetohydrodynamic turbulence in cylindrical geometry. The Physics of Fluids, 21(5), 757-764. doi: 10.1063/1.862295

Mozer, F. S., (2018). Direct Observation of Electron Distributions inside Millisecond Duration Electron Holes, Physical Review Letters, 121, 135102. doi:10.1103/PhysRevLett.121.135102

Ng, J., L.-J. Chen, N. Bessho et al. (2022a). Electron-Scale Reconnection in Three-Dimensional Shock Turbulence, Geophys. Res. Lett. 49, e2022GL099544. doi: 10.1029/2022GL099544

Ng, J., et al., (2022b). "Hybrid Simulations of the Cusp and Dayside Magnetosheath Dynamics Under Quasi-Radial Interplanetary Magnetic Fields." Journal of Geophysical Research: Space Physics, 127 (10): [10.1029/2022ja030359]

Norgren, C., et al. (2016). Finite gyroradius effects in the electron outflow of asymmetric magnetic reconnection. Geophysical Research Letters, 43:6724–6733. doi:10.1002/2016GL069205

Norgren, C., et al. (2020). Electron acceleration and thermalization at magnetotail separatrices. Journal of Geophysical Research: Space Physics, 125, e2019JA027440. doi: 10.1029/2019JA027440

Norgren, C., et al. (2022). Millisecond observations of nonlinear wave-electron interaction in electron phase space holes, Physics of Plasmas, 29, 012309. doi:10.1063/5.0073097

Nykyri, K., et al. (2019). First MMS observation of energetic particles trapped in high-latitude magnetic field depressions. Journal of Geophysical Research: Space Physics, 124, 197–210. doi: 10.1029/2018JA026131

Øieroset, M., et al. (2021). Spatial evolution of magnetic reconnection diffusion region structures with distance from the X-line", Physics of Plasmas 28, 122901. doi: 10.1063/5.0072182

Oka, M. et al. (2011). Magnetic reconnection X-line retreat associated with dipolarization of the Earth's magnetosphere. Geophys. Res. Lett. doi: 10.1029/2011GL049350

Osman, K. T., et al. (2011). Directional alignment and non-Gaussian statistics in solar wind turbulence. The Astrophysical Journal, 741(2), 75. doi: 10.1088/0004-637X/741/2/75

Owen, C. J.,et al. (2008). Cluster observations of “crater” flux transfer events at the dayside high-latitude magnetopause. J. Geophys. Res., 113, A07S04. doi:10.1029/2007JA012701

Parashar, T. N., Matthaeus, W. H., and Shay, M. A. (2018). Dependence of kinetic plasma turbulence on plasma β. The Astrophysical Journal Letters 864.1: L21. doi: https://doi.org/10.3847/2041-8213/aadb8b

Payne, D. S., et al. (2021). Origin and structure of electromagnetic generator regions at the edge of the electron diffusion region. Physics of Plasmas 28, 112901. doi: 10.1063/5.0068317

Pelz, R. B., et al. (1985). Velocity-vorticity patterns in turbulent flow. Physical review letters, 54(23), 2505. doi: 10.1103/PhysRevLett.54.2505

Pesses, M. E., Jokipii, J. R., and Eichler, D. (1981). Cosmic ray drift, shock wave acceleration and the anomalous component of cosmic rays. Astrophysical Journal, Part 2 - Letters to the Editor, vol. 246, June 1, 1981, p. L85-L88. doi: 10.1086/183559

Phan, T.D., et al. (2018). Electron magnetic reconnection without ion coupling in Earth’s turbulent magnetosheath. Nature 557, 202–206. doi: 10.1038/s41586-018-0091-5

Plaschke, F., et al., (2018). Jets Downstream of Collisionless Shocks, Space Sci Rev, 214:81. doi:10.1007/s11214-018-0516-3

Price, L., et al., (2020). Turbulence and transport during guide field reconnection at the magnetopause. Journal of Geophysical Research: Space Physics, 125. doi:10.1029/2019JA027498

Pritchett, P. L., and F. V. Coroniti (2013). Structure and consequences of the kinetic ballooning/interchange instability in the magnetotail. J. Geophys. Res. Space Physics, 118, 146–159. doi:10.1029/2012JA018143

Pyakurel, P. S., et al. (2021). Faster Form of Electron Magnetic Reconnection with a Finite Length X-Line. Physical Review Letters, 127(15), 155101. doi: 10.1103/PhysRevLett.127.155101

Quattrociocchi, V., et al. (2019). On geometrical invariants of the magnetic field gradient tensor in turbulent space plasmas: Scale variability in the inertial range. The Astrophysical Journal, 878(2), 124. doi: 10.3847/1538-4357/ab1e47

Richard, L., et al., (2021). Observations of short-period ion-scale current sheet flapping. Journal of Geophysical Research: Space Physics, 126. doi:10.1029/2021JA029152

Russell, C. T., and Qi, Y. (2020). Flux ropes are born in pairs: An outcome of interlinked, reconnecting flux tubes. Geophysical Research Letters, 47, e2020GL087620. doi: 10.1029/2020GL087620

Schwartz, S. J., et al. (2021). Energy conversion within current sheets in the earth's quasi-parallel magnetosheath. Geophysical Research Letters, 48, e2020GL091859. doi: 10.1029/2020GL09185

Scudder, J,, and Daughton, W. (2008). Illuminating electron diffusion regions of collisionless magnetic reconnection using electron agyrotropy. Journal of Geophysical Research: Space Physics 113.A6. doi: 10.1029/2008JA013035

Servidio, S., et al. (2008a). Depression of nonlinearity in decaying isotropic MHD turbulence. Physical review letters, 100(9), 095005. doi: 10.1103/PhysRevLett.100.095005

Servidio, S., et al. (2008b). Statistical properties of ideal three-dimensional Hall magnetohydrodynamics: The spectral structure of the equilibrium ensemble. Physics of Plasmas, 15(4), 042314. doi: 10.1063/1.2907789

Servidio, S., et al. (2014). Relaxation processes in solar wind turbulence. The Astrophysical Journal Letters, 789(2), L44. doi: 10.1088/2041-8205/789/2/L44

Servidio, S., et al. (2017). Magnetospheric Multiscale observation of plasma velocity-space cascade: Hermite representation and theory. Physical Review Letters 119, no. 20: 205101. doi: 10.1103/PhysRevLett.119.205101

Staples, F. A., et al. (2022). Resolving magnetopause shadowing using multimission measurements of phase space density. Journal of Geophysical Research: Space Physics, 127, e2021JA029298. doi: 10.1029/2021JA029298

Starkey, M. J. et al. (2022). Determining the near-instantaneous curvature of Earth's bow shock using simultaneous IBEX and MMS observations. Journal of Geophysical Research: Space Physics, 127, e2021JA030036. doi: 10.1029/2021JA030036

Stawarz, Julia E., et al. (2021). Comparative analysis of the various generalized Ohm's law terms in magnetosheath turbulence as observed by Magnetospheric Multiscale. Journal of Geophysical Research: Space Physics 126.1. doi: 2020JA028447.

Stawarz, J. E., et al. (2022). Turbulence-driven magnetic reconnection and the magnetic correlation length: Observations from Magnetospheric Multiscale in Earth's magnetosheath, Phys. Plasmas 29, 012302. doi: 10.1063/5.0071106

Stribling, T., & Matthaeus, W. H. (1991). Relaxation processes in a low-order three-dimensional magnetohydrodynamics model. Physics of Fluids B: Plasma Physics, 3(8), 1848-1864. doi: 10.1063/1.859654

Swisdak, M. (2016). Quantifying gyrotropy in magnetic reconnection. Geophysical Research Letters 43.1: 43-49.in magnetic reconnection. doi: 10.1002/2015GL066980

Swisdak, M., et al. (2003). Diamagnetic suppression of component magnetic reconnection at the magnetopause. J. Geophys. Res., 108, 1218. doi:10.1029/2002JA009726

Tenfjord, P., Hesse, M., & Norgren, C. (2018). The formation of an oxygen wave by magnetic reconnection. J. Geophys. Res., 123, 9370– 9380. doi: 10.1029/2018JA026026

Toledo-Redondo, S., et al. (2016). Cold ion demagnetization near the X-line of magnetic reconnection. Geophys. Res. Lett., 43, 6759–676. doi:10.1002/2016GL069877

Toledo-Redondo, S., et al. (2021). Solar wind—Magnetosphere coupling during radial interplanetary magnetic field conditions: Simultaneous multi-point observations. Journal of Geophysical Research: Space Physics, 126. doi:10.1029/2021JA029506

Torbert, R. B., et al. (2020). A new method of 3-D magnetic field reconstruction. Geophysical Research Letters, 47, e2019GL085542. doi: 10.1029/2019GL085542

Turner, D. L., et al. (2021a), Direct Multipoint Observations Capturing the Reformation of a Supercritical Fast Magnetosonic Shock, ApJL 911 L31, DOI 10.3847/2041-8213/abec78

Turner, D. L. et al. (2021b). Can Earth's magnetotail plasma sheet produce a source of relativistic electrons for the radiation belts? Geophysical Research Letters, 48, e2021GL095495. doi: 10.1029/2021GL095495

Vasko, I. Y., et al. (2020). On the nature and origin of bipolar electrostatic structures in the Earth's bow shock. Frontiers in Physics, 8, 156. doi: 10.3389/fphy.2020.00156

Vech, D., et al. (2017). Nature of stochastic ion heating in the solar wind: testing the dependence on plasma beta and turbulence amplitude. The Astrophysical Journal Letters 850.1: L11. doi: 10.3847/2041-8213/aa9887

Wan, M., et al. (2015). Intermittent dissipation and heating in 3D kinetic plasma turbulence. Physical review letters 114.17: 175002. doi: 10.1103/PhysRevLett.114.175002

Wan, M., et al. (2016). Intermittency, coherent structures and dissipation in plasma turbulence. Physics of Plasmas 23.4: 042307. doi: 10.1063/1.4945631

Wang, H., et al. (2016). The mechanisms of electron acceleration during multiple X line magnetic reconnection with a guide field. The Astrophysical Journal 821.2: 84. doi: 0.3847/0004-637X/821/2/84

Wang, H., et al. (2017). Electron acceleration in a secondary magnetic island formed during magnetic reconnection with a guide field. Physics of Plasmas 24.5: 052113. doi: 10.1063/1.4982813

Wang, R., et al. (2020). Electrostatic turbulence and Debye-scale structures in collisionless shocks. The Astrophysical Journal Letters, 889(1), L9. doi: 10.3847/2041-8213/ab6582

Wang, R., et al. (2021). Electrostatic solitary waves in the Earth's bow shock: Nature, properties, lifetimes, and origin. Journal of Geophysical Research: Space Physics, 126, e2021JA029357. doi: 10.1029/2021JA029357

Wang, S., et al. (2020). Ion-scale Current Structures in Short Large-amplitude Magnetic Structures, Astrophys. J. 898, 121. doi: 10.3847/1538-4357/ab9b8b

Wang, S., et al. (2022). Lower-hybrid wave structures and interactions with electrons observed in magnetotail reconnection diffusion regions. Journal of Geophysical Research: Space Physics, 127. doi:10.1029/2021JA030109

Wang, Y., et al. (2021). Statistical survey of collisionless dissipation in the terrestrial magnetosheath. Journal of Geophysical Research: Space Physics 126.6: e2020JA029000. doi: 10.1029/2020JA029000

Wilder, F. et al. (2014). Observation of a retreating x line and magnetic islands poleward of the cusp during northward interplanetary magnetic field conditions. Journal of Geophysical Research: Space Physics, Volume 119, Issue 12, pp. 9643-9657. doi: 10.1002/2014JA020453

Wilder, F. D., et al. (2019), A survey of plasma waves appearing near dayside magnetopause electron diffusion region events, Journal of Geophysical Research: Space Physics, 124, 7837–7849. doi: 10.1029/2019JA027060

Wilder F. D., et al. (2021). The Occurrence and Prevalence of Time Domain Structures in the Kelvin- Helmholtz Instability at Different Positions Along the Earth’s Magnetospheric Flanks. Front. Astron. Space Sci. 8:756563. doi: 10.3389/fspas.2021.756563

Woltjer, L. (1958). A theorem on force-free magnetic fields. Proceedings of the National Academy of Sciences, 44(6), 489-491. doi: 10.1073/pnas.44.6.489

Wu, P., et al. (2013). von Kármán energy decay and heating of protons and electrons in a kinetic turbulent

plasma. Physical review letters 111.12: 121105. doi: 10.1103/PhysRevLett.111.121105

Yang, Y., et al. (2017). Energy transfer, pressure tensor, and heating of kinetic plasma, Phys. Plasmas, 24, 072306. doi:10.1063/1.4990421

Yang, Y., et al. (2019). Role of magnetic field curvature in magnetohydrodynamic turbulence. Physics of Plasmas 26.7: 072306. doi: 10.1063/1.5099360

Yang, Y., et al. (2022). Pressure–Strain Interaction as the Energy Dissipation Estimate in Collisionless Plasma. The Astrophysical Journal 929.2: 142. doi: 10.3847/1538-4357/ac5d3e

Yordanova, E., et al. (2020). Current sheet statistics in the magnetosheath. Frontiers in Astronomy and Space Sciences, 2. doi: 10.3389/fspas.2020.00002

Zenitani, S., et al. (2011). New measure of the dissipation region in collisionless magnetic reconnection. Physical Review Letters 106.19: 195003. doi: 10.1103/PhysRevLett.106.195003

Zhou, M., et al. (2021). Measurements of Energy Dissipation in the Electron Diffusion Region. Geophysical Research Letters 48.24: e2021GL096372. doi: 10.1029/2021GL096372

Zhou, X.-Z. et al. (2018). On the Acceleration and Anisotropy of Ions Within Magnetotail Dipolarizing Flux Bundles. J. Geophys. Res.: Space Phys., 123. doi: 10.1002/2017JA024901

APPENDIX D: PUBLICATION LIST – TEAM

The full list of MMS publications can be accessed at https://lasp.colorado.edu/galaxy/x/p0e9Aw, which has indicators – to the best of our ability – for (1) student/early career first authors, (2) studies utilizing NASA's HSO; (3) non-MMS team first authors, and (4) instrumentation/technology papers. MMS also maintains publication lists at the Web of Science site (https://www.webofscience.com/wos/author/record/J-5393-2013) and the Google Scholar site (https://scholar.google.com/citations?user=OWZfs-4AAAAJ) with citation metrics constantly updating.

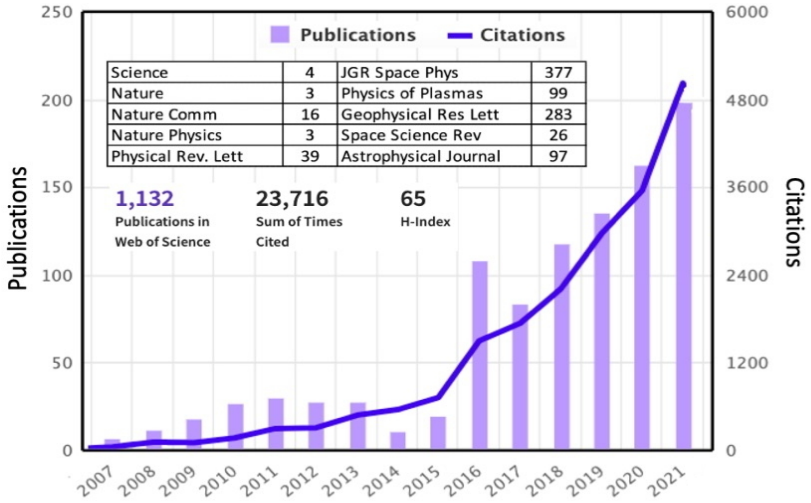

MMS Publication statistics show the early impact of its theory/ modeling program and, more recently, extensive utilization of the data by the world's space and plasma physics communities.

2022

[Note: 2022 list is incomplete. Updates for the Senior Review were completed mid-October 2022 and may not include all publications completing review or pending full publication].

Ahmadi, N., Eriksson, S., Newman, D., Andersson, L., Ergun, R. E., and Wilder, F. D. (2022). Observations of electron vorticity and phase space holes in the magnetopause reconnection separatrix. *Journal of Geophysical Research: Space Physics*, 127, e2022JA030702. https://doi.org/10.1029/2022JA030702

Alqeeq, S. W., Le Contel, O., Canu, P., Retinò, A., Chust, T., Mirioni, L., Richard, L., Aït-Si-Ahmed, Y., Alexandrova, A., Chuvatin, A., Ahmadi, N.,Baraka, S. M., Nakamura, R., Wilder, F. D., Gershman, D. J., Lindqvist, P. A., Khotyaintsev, Yu. V., Ergun, R. E., Burch, J. L., Torbert, R. B., Russell, C. T., Magnes, W., Strangeway, R. J., Bromund, K. R., Wei, H., Plaschke, F., Anderson, B. J., Giles, B. L., Fuselier, S. A., Saito, Y., and Lavraud, B. (2022) Investigation of the homogeneity of energy conversion processes at dipolarization fronts from MMS measurements. Physics of Plasmas 29, 012906. https://doi.org/10.1063/5.0069432

Argall, M. R., Barbhuiya, M. H., Cassak, P. A., Wang, S., Shuster, J., Liang, H., Gershman, D. J., Torbert, R. B., and Burch, J. L. (2022) Theory, observations, and simulations of kinetic entropy in a magnetotail electron diffusion region. Physics of Plasmas 29, 022902. https://doi.org/10.1063/5.0073248

Beedle, J. M. H., Gershman, D. J., Uritsky, V. M., Phan, T. D., and Giles, B. L. (2022). A systematic look at the temperature gradient contribution to the dayside magnetopause current. Geophysical Research Letters, 49, e2021GL097547. https://doi.org/10.1029/2021GL097547

Bessho, N., L.-J. Chen, J. E. Stawarz, S. Wang, M. Hesse, L. B. Wilson III, and J. Ng (2022), Strong reconnection electric fields in shock-driven turbulence, Physics of Plasmas 29, 042304; https://doi.org/10.1063/5.0077529

Birn, J., Hesse, M., Runov, A., Turner, D. L., Cohen, I., and Slavin, J. A. (2022). Energetic ions downtail of the reconnection site. Journal of Geophysical Research: Space Physics, 127, e2021JA029892. https://doi.org/10.1029/2021JA029892

Blasl, K. A., Nakamura, T. K. M., Plaschke, F., Nakamura, R., Hasegawa, H., Stawarz, J. E., Liu, Y.-H., Peery, S., Holmes, J. C., Hosner, M., Schmid, D., Roberts, O. W., and Volwerk, M. (2022) Multi-scale observations of the magnetopause Kelvin–Helmholtz waves during southward IMF. Physics of Plasmas 29, 012105. https://doi.org/10.1063/5.0067370

Burch, J.L., Hesse, M., Webster, J. M., Genestreti, K. J., Torbert, R. B., Denton, R. E., Ergun, R. E., Giles, B. L., Gershman, D. J., Russell, C. T., Wang, *S.,* Chen, L.-J., Dokgo, K., Hwang, K.-J., and Pollock, C. J. (2022) The EDR inflow region of a reconnecting current sheet in the geomagnetic tail", Physics of Plasmas 29, 052903. https://doi.org/10.1063/5.0083169

Chen, L.-J., Halekas, J., Wang, S., DiBraccio, G. A., Romanelli, N., Ng, J., Russell, C. T., Schwartz, S. J., Sibeck, D. G., Farrell, W., Pollock, C., Gershman, D., Giles, B., Collado-Vega Y. M. (2022). Solitary magnetic structures developed from gyro-resonance with solar wind ions at Mars and Earth. Geophysical Research Letters, 49, e2021GL097600. https://doi.org/10.1029/2021GL097600

Chepuri, S., Jaynes, A., Baker, D., Mauk, B., Cohen, I., Leonard, T., Turner, D., Blake, J., and Fennell, J. (2022). A Statistical Study of Magnetopause Boundary Layer Energetic Electron Enhancements Using MMS, Front. Astron. Space Sci., 9:926660. https://doi.org/10.3389/fspas.2022.926660

Choi, S., Bessho, N., Wang, S., Chen, L.-J., and Hesse, M. (2022) Whistler waves generated by nongyrotropic and gyrotropic electron beams during asymmetric guide field reconnection. Physics of Plasmas 29, 012903. https://doi.org/10.1063/5.0059884

Denton, Richard E., Yi-Hsin Liu, Hiroshi Hasegawa, Roy B. Torbert, Wenya Li, Stephen Fuselier, and James L. Burch (2022), Polynomial reconstruction of the magnetic field observed by multiple spacecraft with integrated velocity determination, J. Geophys. Res. Space Physics, doi:10.1029/2022JA030512

Dimmock, A. P., Yordanova, E., Graham, D. B., Khotyaintsev, Y. V., Blanco-Cano, X., Kajdič, P., et al. (2022). Mirror mode storms observed by Solar Orbiter. *Journal of Geophysical Research: Space Physics*, 127, e2022JA030754. https://doi.org/10.1029/2022JA030754

Ergun, R. E., Usanova, M. E., Turner, D. L., and Stawarz, J. E. (2022). Bursty bulk flow turbulence as a source of energetic particles to the outer radiation belt. *Geophysical Research Letters*, 49, e2022GL098113. https://doi.org/10.1029/2022GL098113

Fuselier, S. A., Kletzing, C. A., Petrinec, S. M., Trattner, K. J., George, D., Bounds, S. R., Sawyer, R. P., Bonnell, J. W., Burch, J. L., Giles, B. L., and Strangeway, R. J. (2022). Multiple reconnection X-lines at the magnetopause and overlapping cusp ion injections. *Journal of Geophysical Research: Space Physics*, 127, e2022JA030354. https://doi.org/10.1029/2022JA030354

Graham, D. B., Khotyaintsev, Y. V., André, M., Vaivads, A., Divin, A., Drake, J. F., Norgren, C., Le Contel, O., Lindqvist, P.-A., Rager, A. C., Gershman, D. J., Russell, C. T., Burch, J. L., Hwang, K.-J., and Dokgo, K. (2022). Direct observations of anomalous resistivity and diffusion in collisionless plasma. *Nature Communications*, *13*(1), 1-9. https://doi.org/10.1038/s41467-022-30561-8

Genestreti, K.J., X. Li, Y.-H. Liu, J.L. Burch, R.B. Torbert, S.A. Fuselier, TKM Nakamura, B.L. Giles, D.J. Gershman, R.E. Ergun, C.T. Russell, and R.J. Strangeway (2022), On the origin of "patchy" energy conversion in electron diffusion regions, *Physics of Plasmas* 29, 082107 https://doi.org/10.1063/5.0090275

Goldstein, J., Burch, J. L., Fuselier, S.A., Kim, M. J., Gomez, R., Gonzalez, C.A., Mukherjee, J., Turner, N.E., and Wilson, M.E. (2022). MMS Observations of Dayside Warm (Several eV to 100 eV) Ions in the Middle and Outer Magnetosphere, J. Geophys. Res. https://doi.org/10.1029/2022JA031051

Hasegawa, H., Denton, R. E., Nakamura, T. K. M., Genestreti, K. J., Phan, T. D., Nakamura, R., et al. (2022). Magnetic field annihilation in a magnetotail electron diffusion region with electron-scale magnetic island. *Journal of Geophysical Research: Space Physics*, 127, e2022JA030408. https://doi.org/10.1029/2022JA030408

Hosner, M., Nakamura, R., Nakamura, T. K. M., Schmid, D., Panov, E. V., and Plaschke, F. (2022). Statistical investigation of electric field fluctuations around the lower-hybrid frequency range at dipolarization fronts in the near-earth magnetotail. *Physics of Plasmas*, 29(1), 012111. https://doi.org/10.1063/5.0067382

Huang, K., Liu, Y.-H., Lu, Q., Hu, Z., Lynch, K. A., Hesse, M., et al. (2022). Auroral spiral structure formation through magnetic reconnection in the auroral acceleration region. Geophysical Research Letters, 49, e2022GL100466. https://doi.org/10.1029/2022GL100466

Hubbert, M., Russell, C. T., Qi, Y., Lu, S., Burch, J. L., Giles, B. L., and Moore, T. E. (2022). Electron-only reconnection as a transition phase from quiet magnetotail current sheets to traditional magnetotail reconnection. *Journal of Geophysical Research: Space Physics*, 127, e2021JA029584. https://doi.org/10.1029/2021JA029584

Hughes, J., Blay, R., Ziegler, J., Anderson, P., Armijo, W., Maxwell, J., and Kendra, J. (2022). Free-Space Dynamics and Control of the Rotary-Motion Extended Array Synthesis Spacecraft Concept. *Journal of Spacecraft and Rockets*, 59(1), 129-139. https://doi.org/10.2514/1.A35118

Kim, M. J., Goldstein, J., Fuselier, S. A., and Burch, J. L. (2022). H^+ pitch angle distributions in the outer magnetosphere observed by MMS HPCA. *Journal of Geophysical Research: Space Physics*, 127, e2021JA029648. https://doi.org/10.1029/2021JA029648

Kitamura, N., Amano, T., Omura, Y. *et al.* (2022). Direct observations of energy transfer from resonant electrons to whistler-mode waves in magnetosheath of Earth. *Nat Commun* **13**, 6259. https://doi.org/10.1038/s41467-022-33604-2

Lalti, A., Khotyaintsev, Yu. V., Dimmock, A. P., Johlander, A., Graham, D. B., & Olshevsky, V. (2022). A database of MMS bow shock crossings compiled using machine learning. *Journal of Geophysical Research: Space Physics*, 127, e2022JA030454. https://doi.org/10.1029/2022JA030454

Lalti, A., Khotyaintsev, Y. V., Graham, D. B., Vaivads, A., Steinvall, K., and Russell, C. T. (2022). Whistler waves in the foot of quasi-perpendicular supercritical shocks. *Journal of Geophysical Research: Space Physics*, 127, e2021JA029969. https://doi.org/10.1029/2021JA029969

Lindberg, M., Vaivads, A., Raptis, S., Lindqvist, P.-A., Giles, B.L., Gershman, D.J. (2022). Electron Kinetic Entropy across Quasi-Perpendicular Shocks. *Entropy,* 24(6), 745. https://doi.org/10.3390/e24060745

Lipatov, A. S., Avanov, L. A., and Giles, B. L. (2022). Hybrid kinetic model of the interaction between the dense plasma clouds and magnetospheric plasma on large time and spatial scales, and comparison with MMS observations. *Journal of Geophysical Research: Space Physics*, 127, e2022JA030493. https://doi.org/10.1029/2022JA030493

Liu, C. M., Vaivads, A., Khotyaintsev, Y. V., Fu, H. S., Graham, D. B., Steinvall, K., Liu, Y.-Y., and Burch, J. L. (2022). Cross-scale Dynamics Driven by Plasma Jet Braking in Space. The Astrophysical Journal, 926(2), 198. https://doi.org/10.3847/1538-4357/ac4979

Liu, T. Z., Zhang, H., Turner, D., Vu, A., and Angelopoulos, V. (2022). Statistical study of favorable foreshock ion properties for the formation of hot flow anomalies and foreshock bubbles. *Journal of Geophysical Research: Space Physics*, 127, e2022JA030273. https://doi.org/10.1029/2022JA030273

Liu, Y. H., Cassak, P., Li, X., Hesse, M., Lin, S. C., and Genestreti, K. (2022). First-principles theory of the rate of magnetic reconnection in magnetospheric and solar plasmas. *Communications Physics*, *5*(1), 1-9. https://doi.org/10.1038/s42005-022-00854-x

Lu, S., Lu, Q., Wang, R., Pritchett, P. L., Hubbert, M., Qi, Y., et al. (2022). Electron-only reconnection as a transition from quiet current sheet to standard reconnection in Earth's magnetotail: Particle-in-cell simulation and application to MMS data. *Geophysical Research Letters*, 49, e2022GL098547. https://doi.org/10.1029/2022GL098547

Lu, X., Zhang, H., Liu, T., Vu, A., Pollock, C., and Wang, B. (2022). Statistical study of foreshock density holes. *Journal of Geophysical Research: Space Physics*, 127, e2021JA029981. https://doi.org/10.1029/2021JA029981

Marshall, A. T., Burch, J. L., Reiff, P. H., Webster, J. M., Denton, R. E., Rastaetter, L., Torbert, R. B., Ergun, R. E., Russell, C. T., and Gershman, D. J. (2022) Lower hybrid drift wave motion at a dayside magnetopause x-line with energy conversion dominated by a parallel electric field. Physics of Plasmas 29, 012905. https://doi.org/10.1063/5.0071159

Motoba, T., Sitnov, M. I., Stephens, G. K., and Gershman, D. J. (2022). A new perspective on magnetotail electron and ion divergent flows: MMS observations. Journal of Geophysical Research: Space Physics, 127, e2022JA030514. https://doi.org/10.1029/2022JA030514

Nakamura, T. K. M., Blasl, K. A., Liu, Y.-H., and Peery, S. A. (2022) Diffusive Plasma Transport by the Magnetopause Kelvin-Helmholtz Instability During Southward IMF. Front. Astron. Space Sci. 8:809045. http://doi.org/10.3389/fspas.2021.809045

Nakamura, T. K. M., Blasl, K. A., Hasegawa, H., Umeda, T., Liu, Y.-H., Peery, S. A., Plaschke, F., Nakamura, R., Holmes, J. C., Stawarz, J. E., and Nystrom, W. D. (2022) Multi-scale evolution of Kelvin–Helmholtz waves at the Earth's magnetopause during southward IMF periods. Physics of Plasmas 29, 012901. https://doi.org/10.1063/5.0067391

Ng, J., Chen, L.-J., Bessho, N., Shuster, J., Burkholder, B., & Yoo, J. (2022). Electron-scale reconnection in three-dimensional shock turbulence. *Geophysical Research Letters*, 49, e2022GL099544. https://doi.org/10.1029/2022GL099544

Ng, J., Chen, L.-J., Omelchenko, Y., Zou, Y., & Lavraud, B. (2022). Hybrid simulations of the cusp and dayside magnetosheath dynamics under quasi-radial interplanetary magnetic fields. Journal of Geophysical Research: Space Physics, 127, e2022JA030359. https://doi.org/10.1029/2022JA030359

Nguyen, G., Aunai, N., Michotte de Welle, B., Jeandet, A., Lavraud, B., and Fontaine, D. (2022d). Massive multi-mission statistical study and analytical modeling of the Earth's magnetopause: 4. On the near-cusp magnetopause indentation. Journal of Geophysical Research: Space Physics, 127, e2021JA029776. https://doi.org/10.1029/2021JA029776

Nguyen, G., Aunai, N., Michotte de Welle, B., Jeandet, A., Lavraud, B., and Fontaine, D. (2022c). Massive multi-mission statistical study and analytical modeling of the Earth's magnetopause: 3. An Asymmetric Non Indented Magnetopause Analytical Model. Journal of Geophysical Research: Space Physics, 127, e2021JA030112. https://doi.org/10.1029/2021JA030112

Nguyen, G., Aunai, N., Michotte de Welle, B., Jeandet, A., Lavraud, B., and Fontaine, D. (2022b). Massive multi-mission statistical study and analytical modeling of the Earth's magnetopause: 2. Shape and Location. Journal of Geophysical Research: Space Physics, 127, e2021JA029774. https://doi.org/10.1029/2021JA029774

Nguyen, G., Aunai, N., Michotte de Welle, B., Jeandet, A., Lavraud, B., and Fontaine, D. (2022a). Massive multi-mission statistical study and analytical modeling of the Earth's magnetopause: 1. A Gradient Boosting Based Automatic Detection of Near-Earth Regions. Journal of Geophysical Research: Space Physics, 127, e2021JA029773. https://doi.org/10.1029/2021JA029773

Norgren, C., Graham, D. B., Argall, M. R., Steinvall, K., Hesse, M., Khotyaintsev Yu. V., Vaivads, A., Tenfjord, P., Gershman, D. J., Lindqvist, P.-A., Burch, J. L., and Plaschke, F. (2022) Millisecond observations of nonlinear wave–electron interaction in electron phase space holes, Physics of Plasmas 29, 012309. https://doi.org/10.1063/5.0073097

Oka, M., T. D. Phan, M. Øieroset, D. L. Turner, J. F. Drake, X. Li, S. A. Fuselier, D. J. Gershman, B. L. Giles, R. E. Ergun, R. B. Torbert, H. Y. Wei, R. J. Strangeway, C. T. Russell, and J. L. Burch (2022). Electron energization and thermal to non-thermal energy partition during earth's magnetotail reconnection, Physics of Plasmas 29, 052904. https://doi.org/10.1063/5.0085647

Petrinec SM, Wing S, Johnson JR and Zhang Y. (2022) Multi-Spacecraft Observations of Fluctuations Occurring Along the Dusk Flank Magnetopause, and Testing the Connection to an Observed Ionospheric Bead. *Front. Astron. Space Sci.* 9:827612. https://doi.org/10.3389/fspas.2022.827612

Petrinec, S. M., Burch, J. L., Fuselier, S. A., Trattner, K. J., Giles, B. L., and Strangeway, R. J. (2022). On the occurrence of magnetic reconnection along the terrestrial magnetopause, using Magnetospheric Multiscale (MMS) observations in proximity to the reconnection site. *Journal of Geophysical Research: Space Physics*, 127, e2021JA029669. https://doi.org/10.1029/2021JA029669

Pollock, C,J., Chen, L.-J., Schwartz, S.J., Wang, S., Avanov, L., Burch, J.L., Gershman, D.J., Giles, B.L., Raptis, S., and Russell, C.T. (2022). Dynamics of Earth's bow shock under near-radial interplanetary magnetic field conditions, Physics of Plasmas 29, 112902. https://doi.org/10.1063/5.0089937

Qi, Y., Chu Li, T., Russell, C., Ergun, R., Jia, Y., and Hubbert, M. (2022). Magnetic Flux Transport Identification of Active Reconnection: MMS Observations in Earth's Magnetosphere. The Astrophysical Journal Letters, 926(2), L34. https://doi.org/10.3847/2041-8213/ac5181

Raptis, S., Karlsson, T., Vaivads, A., Pollock, C., Plaschke, F., Johlander, A., Trollvik, H., and Lindqvist, P.-A. Downstream high-speed plasma jet generation as a direct consequence of shock reformation. Nat Commun 13, 598 (2022). https://doi.org/10.1038/s41467-022-28110-4

Raptis, S., Karlsson, T., Vaivads, A., Lindberg, M., Johlander, A., & Trollvik, H. (2022). On magnetosheath jet kinetic structure and plasma properties. Geophysical Research Letters, 49, e2022GL100678. https://doi.org/10.1029/2022GL100678

Rice, R. C., Nykyri, K., Ma, X., and Burkholder, B. L. (2022). Characteristics of Kelvin–Helmholtz waves as observed by the MMS from September 2015 to March 2020. *Journal of Geophysical Research: Space Physics*, 127, e2021JA029685. https://doi.org/10.1029/2021JA029685

Richard, L., Khotyaintsev, Yu. V., Graham, D. B., Vaivads, A., Nikoukar, R., Cohen, I. J., et al. (2022). Proton and helium ion acceleration at magnetotail plasma jets. *Journal of Geophysical Research: Space Physics*, 127, e2022JA030430. https://doi.org/10.1029/2022JA030430

Roberts, O. W., Narita, Y., Nakamura, R., Vörös, Z., and Verscharen, D. (2022) The kinetic Alfvén-like nature of turbulent fluctuations in the Earth's magnetosheath: MMS measurement of the electron Alfvén ratio. Physics of Plasmas 29, 012308. https://doi.org/10.1063/5.0068828

Rufai, O. R., Khazanov, G. V., Singh, S. V., and Lakhina, G. S. (2022). Large-amplitude electrostatic fluctuations at the Earth's magnetopause with a vortex-like distribution of hot electrons. Results in Physics, 105343. https://doi.org/10.1016/j.rinp.2022.105343

Schwartz, S. J., Goodrich, K. A., Wilson, L. B., Turner, D. L., Trattner, K. J., Kucharek, H., et al. (2022). Energy partition at collisionless supercritical quasi-perpendicular shocks. Journal of Geophysical Research: Space Physics, 127, e2022JA030637. https://doi.org/10.1029/2022JA030637

Settino, A., Khotyaintsev, Y. V., Graham, D. B., Perrone, D., and Valentini, F. (2022). Characterizing satellite path through Kelvin-Helmholtz instability using a mixing parameter. Journal of Geophysical Research: Space Physics, 127, e2021JA029758. https://doi.org/10.1029/2021JA029758

Shen, Y., Artemyev, A. V., Zhang, X.-J., Angelopoulos, V., Vasko, I., Turner, D., et al. (2022). Tens to hundreds of keV electron precipitation driven by kinetic Alfvén waves during an electron injection. *Journal of Geophysical Research: Space Physics*, 127, e2022JA030360. https://doi.org/10.1029/2022JA030360

Starkey, M. J. and Dayeh, M. A. and Fuselier, S. A. and Petrinec, S. M. and McComas, D. J. and Ogasawara, K. and Szalay, J. R. and Schwadron, N. A. (2022). Determining the near-instantaneous curvature of Earth's bow shock using simultaneous IBEX and MMS observations. *Journal of Geophysical Research: Space Physics*, 127, e2021JA030036. https://doi.org/10.1029/2021JA030036

Stawarz, J. E., Eastwood, J. P., Phan, T. D., Gingell, I. L., Pyakurel, P. S., Shay, M. A., Robertson, S. L., Russell, C. T., and Le Contel, O. (2022) Turbulence-driven magnetic reconnection and the magnetic correlation length: Observations from Magnetospheric Multiscale in Earth's magnetosheath. Physics of Plasmas 29, 012302. https://doi.org/10.1063/5.0071106

Steinvall, K., Khotyaintsev, Y. V., and Graham, D. B. (2022). On the applicability of single-spacecraft interferometry methods using electric field probes. *Journal of Geophysical Research: Space Physics*, 127, e2021JA030143. https://doi.org/10.1029/2021JA030143

Svenningsson, I., Yordanova, E., Cozzani, G., Khotyaintsev, Yu. V., & André, M. (2022). Kinetic generation of whistler waves in the turbulent magnetosheath. Geophysical Research Letters, 49, e2022GL099065. https://doi.org/10.1029/2022GL099065

Ukhorskiy, A. Y., Sorathia, K. A., Merkin, V. G., Crabtree, C., Fletcher, A. C., Malaspina, D. M., and Schwartz, S. J. (2022), Scientific Reports, 12, 4446. Cross-scale energy cascade powered by magnetospheric convection. Sci Rep 12, 4446 (2022). https://doi.org/10.1038/s41598-022-08038-x

Vasko, I. Y., Mozer, F. S., Bale, S. D., and Artemyev, A. V. (2022). Ion-acoustic waves in a quasi-perpendicular Earth's bow shock. *Geophysical Research Letters*, 49, e2022GL098640. https://doi.org/10.1029/2022GL098640

Wang, S., Bessho, N., Graham, D. B., Le Contel, O., Wilder, F. D., Khotyaintsev, Y. V., et al. (2022). Whistler waves associated with electron beams in magnetopause reconnection diffusion regions. *Journal of Geophysical Research: Space Physics*, 127, e2022JA030882. https://doi.org/10.1029/2022JA030882

Wetherton, B. A., Egedal, J., Le, A., and Daughton, W. (2022). Generation of a strong parallel electric field and embedded electron jet in the exhaust of moderate guide field reconnection. *Geophysical Research Letters*, 49, e2022GL098907. https://doi.org/10.1029/2022GL098907

Wilder, F. D., Conley, M., Ergun, R. E., Newman, D. L., Chasapis, A., Ahmadi, N., et al. (2022). Magnetospheric multiscale observations of waves and parallel electric fields in reconnecting current sheets in the turbulent magnetosheath. Journal of Geophysical Research: Space Physics, 127, e2022JA030511. https://doi.org/10.1029/2022JA030511

Wilson III, L.B., Goodrich, K.A., Turner, D.L., Cohen, I.J., Whittlesey, P.L., and Schwartz, S.J. (2022), The need for accurate measurements of thermal velocity distribution functions in the solar wind, Front. Astron. Space Sci., Accepted on Nov. 7, 2022

Wood, P. B., Schaub, A. (2022) Analysis of CFDP Performance for the MMS Mission CIDP. *IEEE Aerospace Conference (AERO)*, 1-8. https://doi.org/10.1109/AERO53065.2022.9843669

Yang, Y., Matthaeus, W. H., Roy, S., Roytershteyn, V., Parashar, T. N., Bandyopadhyay, R., and Wan, M. (2022). Pressure–Strain Interaction as the Energy Dissipation Estimate in Collisionless Plasma. *The Astrophysical Journal*, *929*(2), 142. https://doi.org/10.3847/1538-4357/ac5d3e

Zhu X., Cohen I.J., Mauk B.H., Nikoukar R., Turner, D.L. and Torbert, R.B. (2022) A New Three-Dimensional Empirical Reconstruction Model Using a Stochastic Optimization Method. *Front. Astron. Space Sci.* 9:878403. https://doi.org/10.3389/fspas.2022.878403

2021

Afshari, A. S., Howes, G. G., Kletzing, C. A., Hartley, D. P., and Boardsen, S. A. (2021). The importance of electron Landau damping for the dissipation of turbulent energy in terrestrial magnetosheath plasma. Journal of Geophysical Research: Space Physics, 126, e2021JA029578. https://doi.org/10.1029/2021JA029578

Artemyev, A., Lu, S., El-Alaoui, M., Lin, Y., Angelopoulos, V., Zhang, X.-J., Runov, A., Vasko, I., Zelenyi, L., and Russell, C. (2021). Configuration of the Earth's magnetotail current sheet. Geophysical Research Letters, 48, e2020GL092153. https://doi.org/10.1029/2020GL092153

Bandyopadhyay, R., Chasapis, A., Matthaeus, W.H., Parashar, T.N., Haggerty, C.C, Shay, M.A., Gershman, D.J., Giles, B.L., and Burch, J.L. (2021) Energy dissipation in turbulent reconnection. Physics of Plasmas 28, 112305. https://doi.org/10.1063/5.0071015

Bandyopadhyay, R., Chasapis, A., Gershman, D. J., Giles, B. L., Russell, C. T., Strangeway, R. J., Le Contel, O., Argall, M. R., and Burch, J. L. (2021). Observation of an inertial-range energy cascade within a reconnection jet in the Earth's magnetotail. *Monthly Notices of the Royal Astronomical Society: Letters*, *500*(1), L6-L10. https://doi.org/10.1093/mnrasl/slaa171

Barrie, A. C., Schiff, C., Gershman, D. J., Giles, B. L., and Rand, D. (2021). Calibrating electrostatic deflection of charged particle sensors using ambient plasma measurements. Journal of Geophysical Research: Space Physics, 126, e2021JA029149. https://doi.org/10.1029/2021JA029149

Bingham, S. T., Nikoukar, R., Cohen, I. J., Mauk, B. H., Turner, D. L., Mitchell, D. G., Burch, J. L., Gomez, R. G., Fuselier, S. A., and Torbert, R. B. (2021). Evidence for nonadiabatic oxygen energization in the near-Earth magnetotail from MMS. Geophysical Research Letters, 48, e2020GL091697. https://doi.org/10.1029/2020GL091697

Birn, J., Hesse, M., Bingham, S. T., Turner, D. L., and Nakamura, R. (2021). Acceleration of oxygen ions in dipolarization events: 1. CPS distributions. *Journal of Geophysical Research: Space Physics*, 126, e2021JA029184. https://doi.org/10.1029/2021JA029184

Birn, J., Hesse, M., Bingham, S. T., Turner, D. L., and Nakamura, R. (2021). Acceleration of Oxygen Ions in Dipolarization Events: 2. PSBL distributions. *Journal of Geophysical Research: Space Physics*, 126, e2021JA029143. https://doi.org/10.1029/2021JA029143

Birn, J., Runov, A. and Khotyaintsev, Y. (2021). Magnetotail Processes. In Magnetospheres in the Solar System (eds R. Maggiolo, N. André, H. Hasegawa, D.T. Welling, Y. Zhang and L.J. Paxton). https://doi.org/10.1002/9781119815624.ch17

Burch, J.L. and Hwang, K.-J. (2021). Exploring Small Scales with MMS. In Magnetospheres in the Solar System (eds R. Maggiolo, N. André, H. Hasegawa, D.T. Welling, Y. Zhang and L.J. Paxton). https://doi.org/10.1002/9781119815624.ch41

Burkholder, B. L., Nykyri, K., and Ma, X. (2021). Magnetospheric multiscale statistics of high energy electrons trapped in diamagnetic cavities. Journal of Geophysical Research: Space Physics, 126, e2020JA028341. https://doi.org/10.1029/2020JA028341

Burkholder, B. L., Nykyri, K., Ma, X., Sorathia, K., Michael, A., Otto, A., and Merkin, V. (2021). The structure of the cusp diamagnetic cavity and test particle energization in the GAMERA global MHD simulation. Journal of Geophysical Research: Space Physics, 126, e2021JA029738. https://doi.org/10.1029/2021JA029738

Catapano, F., Retino, A., Zimbardo, G., Alexandrova, A., Cohen, I. J., Turner, D. L., Le Contel, O., Cozzan, G., Perri, S., Greco, A., Breuillard, H., Delcourt, D., Mirioni, L., Khotyaintsev, Y., Vaivads, A., Giles, B. L., Mauk, B. H., Fuselier, S. A., Torbert, R. B., Russell, C. T., Lindqvist, P. A., Ergun, R. E., Moore, T., and Burch, J. L. (2021). In situ evidence of ion acceleration between consecutive reconnection jet fronts. The Astrophysical Journal, 908(1), 73. https://doi.org/10.3847/1538-4357/abce5a

Chandler, M. O., Schwartz, S. J., Avanov, L. A., Coffey, V. N., Giles, B. L., Moore, T. E., Pollock, C. J., Burch, J. L., Russell, C. T., Torbert, R. B. (2021). Observations of mirror mode structures in the dawn-side magnetosphere. Journal of Geophysical Research: Space Physics, 126, e2020JA028649. https://doi.org/10.1029/2020JA028649

Chappell, C. R., Glocer, A., Giles, B. L., Moore, T. E., Huddleston, M. M., and Gallagher, D. L. (2021). The Key Role of Cold Ionospheric Ions As a Source of Hot Magnetospheric Plasma and As a Driver of the Dynamics of Substorms and Storms. *Frontiers in Astronomy and Space Sciences*, 181. https://doi.org/10.3389/fspas.2021.746283

Chaston, C. C., and Travnicek, P. (2021). Ion scattering and energization in filamentary structures through Earth's magnetosheath. Geophysical Research Letters, 48, e2021GL094029. https://doi.org/10.1029/2021GL094029

Chen, L.-J., Ng, J., Omelchenko, Y., and Wang, S. (2021). Magnetopause reconnection and indents induced by foreshock turbulence. Geophysical Research Letters, 48, e2021GL093029. https://doi.org/10.1029/2021GL093029

Chen, L. J., Wang, S., Ng, J., Bessho, N., Tang, J. M., Fung, S. F., Le, G., Gershman, D., Giles, B., Russell, C. T., Torbert, R., Burch, J. (2021). Solitary magnetic structures at quasi-parallel collisionless shocks: Formation. Geophysical Research Letters, 48, e2020GL090800. https://doi.org/10.1029/2020GL090800

Cohen, I. J., Turner, D. L., Mauk, B. H., Bingham, S. T., Blake, J. B., Fennell, J. F., Burch, J. L. (2021). Characteristics of energetic electrons near active magnetotail reconnection sites: Statistical evidence for local Energization. Geophysical Research Letters, 48, e2020GL090087. https://doi.org/10.1029/2020GL090087

Cohen, I. J., Turner, D. L., Michael, A. T., Sorathia, K. A., and Ukhorskiy, A. Y. (2021). Investigating the link between outer radiation belt losses and energetic electron escape at the magnetopause: A case study using multi-mission observations and simulations. Journal of Geophysical Research: Space Physics, 126, e2021JA029261. https://doi.org/10.1029/2021JA029261

Cozzani, G., Khotyaintsev, Y. V., Graham, D. B., Egedal, J., André, M., Vaivads, A., Alexandrova, A., Le Contel, O., Nakamura, R., Fuselier, S. A., Russell, C. T., and Burch, J. L. (2021). Structure of a Perturbed Magnetic Reconnection Electron Diffusion Region in the Earth's Magnetotail. *Physical review letters*, *127*(21), 215101. https://doi.org/10.1103/PhysRevLett.127.215101

da Silva, D., Gershman, D., Barrie, A., Elkington, S., Li, X., Kirk, M., Giles, B., Avanov, L., Shuster, J., Paterson, B., Schiff, C., Chen, L. J. (2021). Three solar irradiance proxies for aperture photoelectron detections in top-hat ESAs coated with Ebonol-C. Journal of Geophysical Research: Space Physics, 126, e2020JA028960. https://doi.org/10.1029/2020JA028960

Denton, R. E., Torbert, R. B., Hasegawa, H., Genestreti, K. J., Manuzzo, R., Belmont, G., Rezeau, L., Califano, F., Nakamura, R., Egedal, J., Le Contel, O., Burch, J. L., Gershman, D. J., Dors, I., Argall, M. R., Russell, C. T., Strangeway, R. J., Giles, B. L. (2021). Two-dimensional velocity of the magnetic structure

observed on July 11, 2017 by the Magnetospheric Multiscale spacecraft. Journal of Geophysical Research: Space Physics, 126, e2020JA028705. https://doi.org/10.1029/2020JA028705

Farrugia, C. J., Rogers, A. J., Torbert, R. B., Genestreti, K. J., Nakamura, T. K. M., Lavraud, B., Montag, P., Egedal, J., Payne, D., Keesee, A., Ahmadi, N., Ergun, R., Reiff, P., Argall, M., Matsui, H., Wilson III, L. B., Lugaz, N., Burch, J. L., Russell, C. T., Fuselier, S. A., and Dors, I. (2021). An encounter with the ion and electron diffusion regions at a flapping and twisted tail current sheet. *Journal of Geophysical Research: Space Physics*, 126, e2020JA028903. https://doi.org/10.1029/2020JA028903

Fuselier, S. A., Haaland, S., Tenfjord, P., Paschmann, G., Toledo-Redondo, S., Malaspina, D., Kim, M. J., Trattner, K. J., Petrinec, S. M., Giles, B. L., Goldstein, J., Burch, J. L., and Strangeway, R. J. (2021). High-density magnetospheric He+ at the dayside magnetopause and its effect on magnetic reconnection. *Journal of Geophysical Research: Space Physics*, 126, e2020JA028722. https://doi.org/10.1029/2020JA028722

Fuselier, S. A., Webster, J. M., Trattner, K. J., Petrinec, S. M., Genestreti, K. J., Pritchard, K. R., Llera, K., Broll, J. M., Burch, J. L., Strangeway, R. J. (2021). Reconnection X-line orientations at the Earth's magnetopause. *Journal of Geophysical Research: Space Physics*, 126, e2021JA029789. https://doi.org/10.1029/2021JA029789

Gingell, I., Schwartz, S. J., Kucharek, H., Farrugia, C. J., and Trattner, K. J. (2021) Observing the prevalence of thin current sheets downstream of Earth's bow shock. *Physics of Plasmas* 28, 102902. https://doi.org/10.1063/5.0062520

Goldman, M. V., Newman, D. L., Eastwood, J. P., Lapenta, G., Burch, J. L., and Giles, B. (2021) Multi-beam energy moments of measured compound ion velocity distributions. *Physics of Plasmas* 28, 102305. https://doi.org/10.1063/5.0063431

Gomez, R. G., Fuselier, S. A., Sokół, J. M., Burch, J. L., Malaspina, D. M., Trattner, K. J., et al. (2021). Multipoint density measurements of geocoronal pickup ions. Geophysical Research Letters, 48, e2021GL093695. https://doi.org/10.1029/2021GL093695

Graham, D. B., Khotyaintsev, Y. V., André, M., Vaivads, A., Chasapis, A., Matthaeus, W. H., Retinò, A., Valentini, F., and Gershman, D. J. (2021). Non-Maxwellianity of electron distributions near Earth's magnetopause. *Journal of Geophysical Research: Space Physics*, 126, e2021JA029260. https://doi.org/10.1029/2021JA029260

Hansel, P. J., Wilder, F. D., Malaspina, D. M., Ergun, R. E., Ahmadi, N., Holmes, J. C., Goodrich, K. A., Fuselier, S., Giles, B., Russell, C. T., Torbert, R., Strangeway, R., Khotyaintsev, Y., Lindqvist, P.-A., and Burch, J. L. (2021). Mapping MMS observations of solitary waves in Earth's magnetic field. *Journal of Geophysical Research: Space Physics*, 126, e2021JA029389. https://doi.org/10.1029/2021JA029389

Hasegawa, H., Nakamura, T. K. M., and Denton, R. E. (2021). Reconstruction of the electron diffusion region with inertia and compressibility effects. *Journal of Geophysical Research: Space Physics*, 126, e2021JA029841. https://doi.org/10.1029/2021JA029841

Hesse, M., Norgren, C., Tenfjord, P., Burch, J. L., Liu, Y.-H., Bessho, N., Chen, L.-J., Wang, S., Kolstø, H., Spinnangr, S. F., Ergun, R. E., Moretto, T., and Kwagala, N. K. (2021). A new look at the electron diffusion region in asymmetric magnetic reconnection. *Journal of Geophysical Research: Space Physics*, 126, e2020JA028456. https://doi.org/10.1029/2020JA028456

Hoilijoki, S., Pucci, F., Ergun, R. E., Schwartz, S. J., Wilder, F. D., Eriksson, S., Chasapis, A., Ahmadi, N., Webster, J. M., Burch, J. L., Torbert, R. B., Strangeway, R. J., and Giles, B. L. (2021). Origin of electron-scale magnetic fluctuations close to an electron diffusion region. *Journal of Geophysical Research: Space Physics*, 126, e2020JA029046. https://doi.org/10.1029/2020JA029046

Holmes, J. C., Nakamura, R., Schmid, D., Nakamura, T. K. M., Roberts, O., and Vörös, Z. (2021). Wave activity in a dynamically evolving reconnection separatrix. *Journal of Geophysical Research: Space Physics*, 126, e2020JA028520. https://doi.org/10.1029/2020JA028520

Hosseini, P., Agapitov, O., Harid, V., and Gołkowski, M. (2021). Evidence of small scale plasma irregularity effects on whistler mode chorus propagation. *Geophysical Research Letters*, 48, e2021GL092850. https://doi.org/10.1029/2021GL092850

Hubbert, M., Qi, Y., Russell, C. T., Burch, J. L., Giles, B. L., and Moore, T. E. (2021). Electron-only tail current sheets and their temporal evolution. *Geophysical Research Letters*, 48, e2020GL091364. https://doi.org/10.1029/2020GL091364

Hwang, K. J., Burch, J. L., Russell, C. T., Choi, E., Dokgo, K., Fear, R. C., Fuselier, S. A., Petrinec, S. M., Sibeck, D. G., Hasegawa, H., Fu, H., Øieroset, M., Escoubet, C. P., Giles, B. L., Khotyaintsev, Y., Graham, D. B., Gershman, D. J., Pollock, C. J., Ergun, R. E., Torbert, R. B., and Broll, J. (2021). Microscale Processes Determining Macroscale Evolution of Magnetic Flux Tubes along Earth's Magnetopause. *The Astrophysical Journal*, *914*(1), 26. https://doi.org/10.3847/1538-4357/abf8b1

Kajdič, P., Raptis, S., Blanco-Cano, X., and Karlsson, T. (2021). Causes of jets in the quasi-perpendicular magnetosheath. Geophysical Research Letters, 48, e2021GL093173. https://doi.org/10.1029/2021GL093173

Kamaletdinov, S. R., Hutchinson, I. H., Vasko, I. Y., Artemyev, A. V., Lotekar, A., and Mozer, F. (2021). Spacecraft observations and theoretical understanding of slow electron holes. Physical review letters, *127*(16), 165101. https://doi.org/10.1103/PhysRevLett.127.165101

Keesee, A. M., Buzulukova, N., Mouikis, C., and Scime, E. E. (2021). Mesoscale structures in Earth's magnetotail observed using energetic neutral atom imaging. Geophysical Research Letters, 48, e2020GL091467. https://doi.org/10.1029/2020GL091467

Kieokaew, R., Lavraud, B., Fargette, N., Marchaudon, A., Génot, V., Jacquey, C., Gershman, D., Giles, B., Toberst, R., Burch, J. (2021). Statistical relationship between interplanetary magnetic field conditions and the helicity sign of flux transfer event flux ropes. Geophysical Research Letters, 48, e2020GL091257. https://doi.org/10.1029/2020GL091257

Kitamura, N., M. Shoji, S. Nakamura, M. Kitahara, T. Amano, Y. Omura, H. Hasegawa, S. A. Boardsen, Y. Miyoshi, Y. Katoh, M. Teramoto, Y. Saito, S. Yokota, M. Hirahara, D. J. Gershman, B. L. Giles, C. T. Russell, R. J. Strangeway, N. Ahmadi, P.-A. Lindqvist, R. E. Ergun, S. A. Fuselier, and J. L. Burch (2021). Energy transfer between hot protons and electromagnetic ion cyclotron waves in compressional Pc5 ultra-low frequency waves. Journal of Geophysical Research: Space Physics, 126, e2020JA028912. https://doi.org/10.1029/2020JA028912

Kolstø, H. M., Norgren, C., Hesse, M., Chen, L.-J., Tenfjord, P., Spinnangr, S. F., and Kwagala, N. (2021). Magnetospheric multiscale observations of an expanding oxygen wave in magnetic reconnection. Geophysical Research Letters, 48, e2021GL095065. https://doi.org/10.1029/2021GL095065

Korovinskiy, D. B., Kiehas, S. A., Panov, E. V., Semenov, V. S., Erkaev, N. V., Divin, A. V., and Kubyshkin, I. V. (2021). The inertia-based model for reconstruction of the electron diffusion region. Journal of Geophysical Research: Space Physics, 126, e2020JA029045. https://doi.org/10.1029/2020JA029045

Lakhina, G. S., Singh, S. V., and Rubia, R. (2021). A mechanism for electrostatic solitary waves observed in the reconnection jet region of the Earth's magnetotail. *Advances in Space Research*, *68*(4), 1864-1875. https://doi.org/10.1016/j.asr.2021.04.026

LaMoury, A. T., Hietala, H., Plaschke, F., Vuorinen, L., and Eastwood, J. P. (2021). Solar wind control of magnetosheath jet formation and propagation to the magnetopause. Journal of Geophysical Research: Space Physics, 126, e2021JA029592. https://doi.org/10.1029/2021JA029592

Le, G., Chi, P. J., Strangeway, R. J., Russell, C. T., Slavin, J. A., Anderson, B., R. Nakamura, F. Plaschke, R. Torbert, and F. Wilder (2021). MMS observations of field line resonances under disturbed solar wind conditions. *Journal of Geophysical Research: Space Physics*, 126, e2020JA028936. https://doi.org/10.1029/2020JA028936

Lee, J. H., Turner, D. L., Vines, S. K., Allen, R. C., Toledo-Redondo, S., Bingham, S. T., Fuselier, S. A., Cohen, I. J., Starkey, M. J., Graham, D. B., Khotyaintsev, Y. V., Mauk, B. H., Pollock, C. J., Ergun, R. E., Lindqvist, P-A, Torbert, R. B., and Burch, J. L. (2021). Application of cold and hot plasma composition measurements to investigate impacts on dusk-side electromagnetic ion cyclotron waves. Journal of Geophysical Research: Space Physics, 126, e2020JA028650. https://doi.org/10.1029/2020JA028650

Lee, S. H., Sibeck, D. G., Omidi, N., Silveira, M. V. D., Giles, B. L., Torbert, R. B., Wei, H., Burch, J. L. (2021). Comparison of MMS observations of foreshock bubbles with a global hybrid simulation. Journal of Geophysical Research: Space Physics, 126, e2020JA028848. https://doi.org/10.1029/2020JA028848

Lenouvel, Q., Génot, V., Garnier, P., Toledo-Redondo, S., Lavraud, B., Aunai, N., Nguyen, G., Gershman, D. J., Ergun R. E., Lindqvist P.-A., Giles B., and Burch J. L. (2021). Identification of electron diffusion regions with a machine learning approach on MMS data at the Earth's magnetopause. Earth and Space Science, 8, e2020EA001530. https://doi.org/10.1029/2020EA001530

Leonenko, M. V., Grigorenko, E. E., and Zelenyi, L. M. (2021). Spatial Scales of Super Thin Current Sheets with MMS Observations in the Earth's Magnetotail. Geomagnetism and Aeronomy, 61(5), 688-695. https://doi.org/10.1134/S0016793221050091

Li, K., Haaland, S., and Wei, Y. (2021). A new concept to measure the ambipolar electric field driving ionospheric outflow. Journal of Geophysical Research: Space Physics, 126, e2020JA028409. https://doi.org/10.1029/2020JA028409

Li, W.-Y., Khotyaintsev, Y. V., Tang, B.-B., Graham, D. B., Norgren, C., Vaivads, A., André, M., Le, A., Egedal, J., Dokgo, K., Fujimoto, K., He, J.-S., Burch, J. L., Lindqvist, P.-A., Ergun, R. E., Torbert, R. B., Le Contel, O., Gershman, D. J., Giles, B. L., Lavraud, B., Fuselier, S., Plaschke, F., Russell, C. T., Guo, X.-C., Lu, Q.-M., and Wang, C. (2021). Upper-hybrid waves driven by meandering electrons around magnetic reconnection X line. Geophysical Research Letters, 48, e2021GL093164. https://doi.org/10.1029/2021GL093164

Li, X. and Liu, Y.-H. (2021). The effect of thermal pressure on collisionless magnetic reconnection rate. The Astrophysical Journal, 912, 152. https://doi.org/10.3847/1538-4357/abf48c

Li, Y., Li, W., Tang, B., Norgren, C., He, J., Wang, C., Zong, Q., André, M., Chappell, C., Dargent, J., Fuselier, S. A., Glocer, A., Graham, D. B., Haaland, S., Kistler, L., Lavraud, B., Moore, T. E., Tenfjord, P., Vines, S. K., Burch, J. (2021). Quantification of Cold-Ion Beams in a Magnetic Reconnection Jet. Frontiers in Astronomy and Space Sciences. https://doi.org/10.3389/fspas.2021.745264

Lin, S.-C., Liu, Y.-H., and Li, X. (2021) Fast magnetic reconnection induced by resistivity gradients in 2D magnetohydrodynamics, Phys. Plasmas 28, 072109. https://doi.org/10.1063/5.0052317

Lipatov, A. S., Avanov, L. A., and Giles, B. L. (2021). Particle acceleration by dense impulsive structures moving in ambient magnetospheric plasma. 3-D hybrid kinetic modeling and MMS observations. Geophysical Research Letters, 48, e2020GL088590. https://doi.org/10.1029/2020GL088590

Liu, T. Z., Zhang, H., Turner, D. L., Goodrich, K. A., An, X., and Zhang, X. (2021). Kinetic-scale magnetic holes inside foreshock transients. Journal of Geophysical Research: Space Physics, 126, e2021JA029748. https://doi.org/10.1029/2021JA029748

Liu, T. Z., Hao, Y., Wilson, L. B. III, Turner, D. L., and Zhang, H. (2021). Magnetospheric multiscale observations of Earth's oblique bow shock reformation by foreshock ultralow-frequency waves. Geophysical Research Letters, 47, e2020GL091184. https://doi.org/10.1029/2020GL091184

Liu, T. Z., Zhang, H., Wang, C.-P., Angelopoulos, V., Vu, A., Wang, X., and Lin, Y. (2021). Statistical study of foreshock transients in the midtail foreshock. Journal of Geophysical Research: Space Physics, 126, e2021JA029156. https://doi.org/10.1029/2021JA029156

Madanian, H., Schwartz, S.J., Fuselier, S.A., Burgess, D., Turner, D.L., Chen, L.-J., Desai, M.I., & Starkey, M.J. (2021). Direct Evidence for Magnetic Reflection of Heavy Ions from High Mach Number Collisionless Shocks. The Astrophysical Journal, 915 (1), L19. https://doi.org/10.3847/2041-8213/ac0aee

Madanian, H., Desai M. I., Schwartz S. J., Wilson III, L. B., Fuselier, S. A., Burch, J. L., Le Contel, O., Turner, D. L., Ogasawara, K., Brosius, A. L., Russell, C. T., Ergun,R. E., Ahmadi, N., Gershman, D. J., and Lindqvist, P.-A. (2021), The Dynamics of a High Mach Number Quasi-perpendicular Shock: MMS Observations, The Astrophysical Journal, 908:40 (11pp). https://doi.org/10.3847/1538-4357/abcb88

Matsui, H., Torbert, R. B., Spence, H. E., Argall, M. R., Cohen, I. J., Cooper, M. B., Ergun, R. E., Farrugia, C. J., Fennell, J. F., Fuselier, S. A., Gkioulidou, M., Khotyaintsev, Yu. V., Lindqvist, P.-A., Matsuoka, A., Russell, C. T., Shoji, M., Strangeway, R. J., Turner, D. L., Vaith, H., and Wygant, J. R. (2021). A multi-instrument study of a dipolarization event in the inner magnetosphere. Journal of Geophysical Research: Space Physics, 126, e2021JA029294. https://doi.org/10.1029/2021JA029294

Matthaeus, W. H. (2021). Turbulence in space plasmas: Who needs it?. *Physics of Plasmas*, *28*(3), 032306. https://doi.org/10.1063/5.0041540

Michael, A. T., Sorathia, K. A., Merkin, V. G., Nykyri, K., Burkholder, B., Ma, X., Ukhorskiy A. Y., and Garretson, J. (2021). Modeling KelvinHelmholtz instability at the high-latitude boundary layer in a global magnetosphere simulation. Geophysical Research Letters, 48, e2021GL094002. https://doi.org/10.1029/2021GL094002

Nakamura, R., Baumjohann, W., Nakamura, T. K. M., Panov, E. V., Schmid, D., Varsani, A., Apatenkov, S., Sergeev, V. A., Birn, J., Nagai, T., Gabrielse, C., André, M., Burch, J. L., Carr, C., Dandouras, I. S., Escoubet, C. P., Fazakerley, A. N., Giles, B. L., Le Contel, O., Russell, C. T., and Torbert, R. B. (2021). Thin current sheet behind the dipolarization front. Journal of Geophysical Research: Space Physics, 126, e2021JA029518. https://doi.org/10.1029/2021JA029518

Nakamura, T. K. M., Hasegawa, H., Genestreti, K. J., Denton, R. E., Phan, T. D., Stawarz, J. E., Nakamura, R., and Nystrom, W. D. (2021). Fast cross-scale energy transfer during turbulent magnetic reconnection. Geophysical Research Letters, 48, e2021GL093524. https://doi.org/10.1029/2021GL093524

Ng, J., Chen, L.-J., and Omelchenko, Y. A. (2021) Bursty magnetic reconnection at the Earth's magnetopause triggered by high-speed jets. Physics of Plasmas 28, 092902. https://doi.org/10.1063/5.0054394

Nishino, M. N., Hasegawa, H., Saito, Y., Kitamura, N., Miyashita, Y., Nagai, T., Yokota, S., Russell, C. T., Gershman, D. J., and Giles, B. L. (2022). Transport path of cold-dense plasmas in the dusk magnetotail plasma sheet: MMS observations. Journal of Geophysical Research: Space Physics, 127, e2021JA029747. https://doi.org/10.1029/2021JA029747

Norgren, C., Tenfjord, P., Hesse, M., Li, W., Xu, Y., Kwagala, N. K., Spinnangr, S., Kolstø, H., & Moretto, T. (2021). On the Presence and Thermalization of Cold Ions in the Exhaust of Antiparallel Symmetric Reconnection. Frontiers in Astronomy and Space Sciences. https://doi.org/10.3389/fspas.2021.730061

Nykyri, K., Ma, X., Burkholder, B., Rice, R., Johnson, J. R., Kim, E.-K., Delamere, P., Michael, A., Sorathia, K., Lin, D., Merkin, S., Fuselier, S., Broll, J., Le Contel, O., Gershman, D., Cohen, I., Giles, B., Strangeway, R. J., Russell, C. T., and Burch, J. L. (2021). MMS observations of the multiscale wave

structures and parallel electron heating in the vicinity of the southern exterior cusp. Journal of Geophysical Research: Space Physics, 126, e2019JA027698. https://doi.org/10.1029/2019JA027698

Nykyri, K., Johnson, J., Kronberg, E., Turner, D., Wing, S., Cohen, I., Sorathia, K., Ma, X., Burkholder, B., Reeves, G., Fennell, J. (2021). Magnetospheric multiscale observations of the source region of energetic electron microinjections along the duskside, high-latitude magnetopause boundary layer. Geophysical Research Letters, 48, e2021GL092466. https://doi.org/10.1029/2021GL092466

Øieroset, M., Phan, T. D., Ergun, R., Ahmadi, N., Genestreti, K., Drake, J. F., Liu, Y.-H., Haggerty, C., Eastwood, J. P., Shay, M. A., Pyakurel, P. S., Haaland, S., Oka, M., Goodbred, M., Eriksson, S., Burch, J. L., Torbert, R. B., Khotyaintsev, Y., Russell, C. T., Strangeway, R. J., Gershman, D. J., and Giles, B. L. (20211) Spatial evolution of magnetic reconnection diffusion region structures with distance from the X-line", Physics of Plasmas 28, 122901.https://doi.org/10.1063/5.0072182

Olshevsky, V., Khotyaintsev, Y. V., Lalti, A., Divin, A., Delzanno, G. L., Anderzén, S., Herman, P., Chien, S. W. D., Avanov, L., Dimmock, A. P., and Markidis, S. (2021). Automated classification of plasma regions using 3D particle energy distributions. Journal of Geophysical Research: Space Physics, 126, e2021JA029620. https://doi.org/10.1029/2021JA029620

Omelchenko, Y. A., Chen, L.-J., and Ng, J. (2021). 3D space-time adaptive hybrid simulations of magnetosheath high-speed jets. Journal of Geophysical Research: Space Physics, 126, e2020JA029035. https://doi.org/10.1029/2020JA029035

Page, B., Vasko, I. Y., Artemyev, A. V., and Bale, S. D. (2021). Generation of High-frequency Whistler Waves in the Earth's Quasi-perpendicular Bow Shock. *The Astrophysical Journal Letters*, *919*(2), L17. https://doi.org/10.3847/2041-8213/ac2748

Paschmann, G., Sonnerup, B. U. Ö., Phan, T., Fuselier, S. A., Haaland, S., Denton, R. E., Burch, J. L., Trattner, K. J., Giles, B. L., Gershman, D. J., Cohen, I. J., Russell, C. T. (2021). Anomalous reconnection layer at Earth's dayside magnetopause. Journal of Geophysical Research: Space Physics, 126, e2021JA029678. https://doi.org/10.1029/2021JA029678

Payne, D. S., Farrugia, C. J., Torbert, R. B., Germaschewski, K., Rogers A. R., and Argall, M. R. (2021). Origin and structure of electromagnetic generator regions at the edge of the electron diffusion region", Physics of Plasmas 28, 112901. https://doi.org/10.1063/5.0068317

Pyakurel, P. S., Shay, M. A., Drake, J. F., Phan, T. D., Cassak, P. A., and Verniero, J. L. (2021). Faster Form of Electron Magnetic Reconnection with a Finite Length X-Line. *Physical Review Letters*, *127*(15), 155101. https://doi.org/10.1103/PhysRevLett.127.155101

Quijia P., Fraternale F., Stawarz J. E., Vásconez C. L., Perri S., Marino R., Yordanova E., and Sorriso-Valvo L. (2012). Comparing turbulence in a Kelvin-Helmholtz instability region across the terrestrial magnetopause, Monthly Notices of the Royal Astronomical Society, 503, 4815. https://doi.org/10.1093/mnras/stab319

Retinò, A., Khotyaintsev, Y., Le Contel, O., Marcucci, M. F., Plaschke, F., Vaivads, A., Angelopoulos, V., Blasi, P., Burch, J., De Keyser, J., Dunlop, M., Dai, L., Eastwood, J., Fu, H., Haaland, S., Hoshino, M., Johlander, A., Kepko, L., Kucharek, H., Lapenta, G., Lavraud, B., Malandraki, O., Matthaeus, W., McWilliams, K., Petrukovich, A., Pinçon, J.-L., Saito, Y., Sorriso-Valvo, L., Vainio, R., and Wimmer-Schweingruber, R. (2021), Particle energization in space plasmas: towards a multi-point, multi-scale plasma observatory. Exp Astron. https://doi.org/10.1007/s10686-021-09797-7

Richard, L., Khotyaintsev, Y. V., Graham, D. B., Sitnov, M. I., Le Contel, O., & Lindqvist, P.-A. (2021). Observations of short-period ion-scale current sheet flapping. Journal of Geophysical Research: Space Physics, 126, e2021JA029152. https://doi.org/10.1029/2021JA029152

Roberts, O. W. and Nakamura, R. and Coffey, V. N. and Gershman, D. J. and Volwerk, M. and Varsani, A. and Giles, B. L. and Dorelli, J. C. and Pollock, C. (2021). A study of the solar wind ion and electron measurements from the magnetospheric multiscale mission's fast plasma investigation. Journal of Geophysical Research: Space Physics, 126, e2021JA029784. https://doi.org/10.1029/2021JA029784

Robertson, S. L. and Eastwood, J. P. and Stawarz, J. E. and Hietala, H. and Phan, T. D. and Lavraud, B. and Burch, J. L. and Giles, B. and Gershman, D. J. and Torbert, R. and Lindqvist, P.-A. and Ergun, R. E. and Russell, C. T. and Strangeway, R. J. (2021). Electron trapping in magnetic mirror structures at the edge of magnetopause flux ropes. Journal of Geophysical Research: Space Physics, 126, e2021JA029182. https://doi.org/10.1029/2021JA029182

Rufai, O. R., G. V. Khazanov, S. V. Singh (2021), Finite amplitude electron-acoustic waves in the electron diffusion region, Results in Physics, 24, 104041. https://doi.org/10.1016/j.rinp.2021.104041

Runov, A., Angelopoulos, V., Artemyev, A. V., Weygand, J. M., Lu, S., Lin, Y., and Zhang, X. J. (2021). Global and local processes of thin current sheet formation during substorm growth phase. Journal of Atmospheric and Solar-Terrestrial Physics, 220, 105671. https://doi.org/10.1016/j.jastp.2021.105671

Sawyer, R. P. and Fuselier, S. A. and Kletzing, C. A. and Bonnell, J. W. and Roglans, R. and Bounds, S. R. and Kim, M. J. and Vines, S. K. and Cairns, I. H. and Moser, C. and LaBelle, J. and Moen, J. I. and Trattner, K. J. and Petrinec, S. M. and Burch, J. L. and Giles, B. L. and George, D. (2021). TRICE 2 observations of low-energy magnetospheric ions within the cusp. Journal of Geophysical Research: Space Physics, 126, e2021JA029382. https://doi.org/10.1029/2021JA029382

Schwartz, S. J., Kucharek, H., Farrugia, C. J., Trattner, K., Gingell, I., Ergun, R. E., Strangeway, R., Gershman D. (2021). Energy conversion within current sheets in the earth's quasi-parallel magnetosheath. Geophysical Research Letters, 48, e2020GL091859. https://doi.org/10.1029/2020GL09185

Schwartz, S. J., Ergun, R., Kucharek, H., Wilson, L., Chen, L.-J., Goodrich, K., Turner, D., Gingell, I., Madanian, H., Gershman, D., Strangeway R. (2021). Evaluating the deHoffmann-Teller cross-shock potential at real collisionless shocks. Journal of Geophysical Research: Space Physics, 126, e2021JA029295. https://doi.org/10.1029/2021JA029295

Scudder, J. D. (2021). Measuring particle current density J on NASA’s magnetospheric multiscale mission (MMS). Journal of Geophysical Research: Space Physics, 126, e2020JA028619. https://doi.org/10.1029/2020JA028619

Shen, Y., Vasko, I. Y., Artemyev, A., Malaspina, D. M., Chu, X., Angelopoulos, V., and Zhang, X.-J. (2021). Realistic electron diffusion rates and lifetimes due to scattering by electron holes. Journal of Geophysical Research: Space Physics, 126, e2021JA029380. https://doi.org/10.1029/2021JA029380

Shuster, J.R., Bessho, N., Wang, S., and Ng, J. (2021) Electron-scale temperature gradients in kinetic equilibrium: MMS observations and Vlasov–Maxwell solutions. Physics of Plasmas 28, 122902. https://doi.org/10.1063/5.0069559

Shuster, J.R., Gershman, D.J., Dorelli, J.C., Giles, B. L., Wang, S., Bessho, N., Chen, L.-J., Cassak, P. A., Schwartz, S. J., Denton, R. E., Uritsky, V. M., Paterson, W. R., Schiff, C., Viñas, A. F., Ng, J., Avanov, L. A., da Silva, D. E. and Torbert, R. B. (2021) Structures in the terms of the Vlasov equation observed at Earth’s magnetopause. Nat. Phys. 17, 1056–1065. https://doi.org/10.1038/s41567-021-01280-6

Sisti, M., Fadanelli, S., Cerri, S. S., Faganello, M., Califano, F., and Agullo, O. (2021). Characterizing current structures in 3D hybrid-kinetic simulations of plasma turbulence. Astronomy and Astrophysics, *655*, A107. https://doi.org/10.1051/0004-6361/202141902

Sitnov, M. I., Motoba, T., and Swisdak, M. (2021). Multiscale nature of the magnetotail reconnection onset. Geophysical Research Letters, 48, e2021GL093065. https://doi.org/10.1029/2021GL093065

Spinnangr, S. F., Tenfjord, P., Hesse, M., Norgren, C., Kolstø, H. M., Kwagala, N. K., J., T. Moretto and P.-C. Jiménez, J. (2021). Asymmetrically varying guide field during magnetic reconnection: Particle-in-cell simulations. Journal of Geophysical Research: Space Physics, 127, e2021JA029955. https://doi.org/10.1029/2021JA029955

Spinnangr, S. F., Hesse, M., Tenfjord, P., Norgren, C., Kolstø, H. M., Kwagala, N. K., and Jørgensen, T. M. (2021). The micro-macro coupling of mass-loading in symmetric magnetic reconnection with cold ions. Geophysical Research Letters, 48, e2020GL090690. https://doi.org/10.1029/2020GL090690

Starkey, M. J., Fuselier, S. A., Desai, M. I., Schwartz, S. J., Russell, C. T., Wei, H., ... and Wilson III, L. B. (2021). MMS Observations of Energized He+ Pickup Ions at Quasiperpendicular Shocks. *The Astrophysical Journal*, *913*(2), 112. https://doi.org/10.3847/1538-4357/abf4d9

Stawarz, J. E. and Matteini, L. and Parashar, T. N. and Franci, L. and Eastwood, J. P. and Gonzalez, C. A. and Gingell, I. L. and Burch, J. L. and Ergun, R. E. and Ahmadi, N. and Giles, B. L. and Gershman, D. J. and Le Contel, O. and Lindqvist, P.-A. and Russell, C. T. and Strangeway, R. J. and Torbert, R. B. (2021). Comparative analysis of the various generalized Ohm's law terms in magnetosheath turbulence as observed by Magnetospheric Multiscale. Journal of Geophysical Research: Space Physics, 126, e2020JA028447. https://doi.org/10.1029/2020JA028447

Steinvall, K., Khotyaintsev, Y. V., Graham, D. B., Vaivads, A., André, M., and Russell, C. T. (2021). Large amplitude electrostatic proton plasma frequency waves in the magnetospheric separatrix and outflow regions during magnetic reconnection. Geophysical Research Letters, 48, e2020GL090286. https://doi.org/10.1029/2020GL090286

Toledo-Redondo, S. and André, M. and Aunai, N. and Chappell, C. R. and Dargent, J. and Fuselier, S. A. and Glocer, A. and Graham, D. B. and Haaland, S. and Hesse, M. and Kistler, L. M. and Lavraud, B. and Li, W. and Moore, T. E. and Tenfjord, P. and Vines, S. K. (2021). Impacts of ionospheric ions on magnetic reconnection and Earth's magnetosphere dynamics. Reviews of Geophysics, 59, e2020RG000707. https://doi.org/10.1029/2020RG00

Toledo-Redondo, S. and Lee, J. H. and Vines, S. K. and Turner, D. L. and Allen, R. C. and André, M. and Boardsen, S. A. and Burch, J. L. and Denton, R. E. and Fu, H. S. and Fuselier, S. A. and Gershman, D. J. and Giles, B. and Graham, D. B. and Kitamura, N. and Khotyaintsev, Yu. V. and Lavraud, B.and Le Contel, O. and Li, W. Y. and Moore, T. E. and Navarro, E. A. and Portí, J. and Salinas, A. and Vinas, A. (2021). Kinetic interaction of cold and hot protons with an oblique EMIC wave near the dayside reconnecting magnetopause. Geophysical Research Letters, 48, e2021GL092376. https://doi.org/10.1029/2021GL092376

Toledo-Redondo , S. and Hwang , K.-J. and Escoubet , C. P. and Lavraud , B. and Fornieles , J. and Aunai , N. and Fear , R. C. and Dargent , J. and Fu, H. S. and Fuselier , S. A. and Genestreti , K. J. and Khotyaintsev , Yu V. and Li, W. Y. and Norgren , C. and Phan , T. D. (2021). Solar wind—Magnetosphere coupling during radial interplanetary magnetic field conditions: Simultaneous multi-point observations. Journal of Geophysical Research: Space Physics, 126, e2021JA029506. https://doi.org/10.1029/2021JA029506

Trattner, K. J., Fuselier, S. A., Petrinec, S. M., Burch, J. L., Ergun, R., and Grimes, E. W. (2021). Long and active magnetopause reconnection X-lines during changing IMF conditions. Journal of Geophysical Research: Space Physics, 126, e2020JA028926. https://doi.org/10.1029/2020JA028926

Trattner, K.J., Petrinec, S.M. and Fuselier, S.A. The Location of Magnetic Reconnection at Earth's Magnetopause. Space Sci Rev 217, 41 (2021). https://doi.org/10.1007/s11214-021-00817-8

Turner, Drew L. and Cohen, Ian J. and Michael, Adam and Sorathia, Kareem and Merkin, Slava and Mauk, Barry H. and Ukhorskiy, Sasha and Murphy, Kyle R. and Gabrielse, Christine and Boyd, Alexander J. and Fennell, Joseph F. and Blake, J. Bernard and Claudepierre, Seth G. and Drozdov, Alexander Y. and Jaynes,

Allison N. and Ripoll, Jean-François and Reeves, Geoffrey D. (2021). Can Earth's magnetotail plasma sheet produce a source of relativistic electrons for the radiation belts? Geophysical Research Letters, 48, e2021GL095495. https://doi.org/10.1029/2021GL095495

Turner, Drew L. and Cohen, Ian J. and Bingham, Samuel T. and Stephens, Grant K. and Sitnov, Mikhail I. and Mauk, Barry H. and Denton, Richard E. and Leonard, Trevor W. and Fennell, Joseph F. and Blake, J. Bernard and Torbert, Roy B. and Burch, James L. (2021). Characteristics of energetic electrons near active magnetotail reconnection sites: Tracers of a complex magnetic topology and evidence of localized acceleration. Geophysical Research Letters, 48, e2020GL090089. https://doi.org/10.1029/2020GL090089

Turner, D. L., L. B. Wilson III, K. A. Goodrich, H. Madanian, S. J. Schwartz, T. Z. Liu, A. Johlander, D. Caprioli, I. J. Cohen, D. Gershman (2021), Direct Multipoint Observations Capturing the Reformation of a Supercritical Fast Magnetosonic Shock, The Astrophysical Journal Letters, 911:L31 (11pp). https://doi.org/10.3847/2041-8213/abec78

Vidal-Luengo, S. E., and Moldwin, M. B. (2021). Global magnetosphere response to solar wind dynamic pressure pulses during northward IMF using the heliophysics system observatory. Journal of Geophysical Research: Space Physics, 126, e2020JA028587. https://doi.org/10.1029/2020JA028587

Vines, S. K., Anderson, B. J., Allen, R. C., Denton, R. E., Engebretson, M. J., Johnson, J. R., Toledo-Redondo, S., Lee, J. H., Turner, D. L., Ergun, R. E., Strangeway, R. J., Russell, C. T., Wei, H., Torbert, R. B., Fuselier, S. A., Giles, B. L., Burch, J. L. (2021). Determining EMIC wave vector properties through multi-point measurements: The wave curl analysis. Journal of Geophysical Research: Space Physics, 126, e2020JA028922. https://doi.org/10.1029/2020JA028922

Wang, R., Vasko, I. Y., Mozer, F. S., Bale, S. D., Kuzichev, I. V., Artemyev, A. V., Steinvall, K., Ergun, R., Giles, B., Khotyaintsev, Y., Lindqvist, P.-A., Russell, C. T., Strangeway, R. (2021). Electrostatic solitary waves in the Earth's bow shock: Nature, properties, lifetimes, and origin. Journal of Geophysical Research: Space Physics, 126, e2021JA029357. https://doi.org/10.1029/2021JA029357

Wang, S., Chen, L.J., Ng, J., Bessho, N., Le, G., Fung, S.F., Gershman, D.J., and Giles, B.L., "A statistical study of three-second foreshock ULF waves observed by the Magnetospheric Multiscale mission", Physics of Plasmas 28, 082901 (2021) https://doi.org/10.1063/5.0055972

Wang, S., Wang, R., Lu, Q., Burch, J. L., and Wang, S. (2021). Energy dissipation via magnetic reconnection within the coherent structures of the magnetosheath turbulence. Journal of Geophysical Research: Space Physics, 126, e2020JA028860. https://doi.org/10.1029/2020JA028860

Wang, S., Wang, R., Lu, Q., Russell, C. T., Ergun, R. E., and Wang, S. (2021). Large-scale parallel electric field colocated in an extended electron diffusion region during the magnetosheath magnetic reconnection. Geophysical Research Letters, 48, e2021GL094879. https://doi.org/10.1029/2021GL094879

Wang, Y., Bandyopadhyay, R., Chhiber, R., Matthaeus, W. H., Chasapis, A., Yang, Y., Wilder, F.D., Gershman, D.J., Giles, B.L., Pollock, C. J., Dorelli, J., Russell, C. T., Strangeway, R. J., Torbert, R. T., Moore, T. E., Burch, J. L. (2021). Statistical survey of collisionless dissipation in the terrestrial magnetosheath. Journal of Geophysical Research: Space Physics, 126, e2020JA029000. https://doi.org/10.1029/2020JA029000

Wellenzohn, S., Nakamura, R., Nakamura, T. K. M., Varsani, A., Sergeev, V. A., Apatenkov, S. V., Holmes, J. C., Grigorenko, E. E., Burch, J. L., Giles, B. L., Torbert, R. B., (2021). Remote sensing of magnetic reconnection in the magnetotail using in situ multipoint observations at the plasma sheet boundary layer. Journal of Geophysical Research: Space Physics, 126, e2020JA028917. https://doi.org/10.1029/2020JA028917

Wetherton, B. A., Egedal, J., Le, A., and Daughton, W. (2021). Anisotropic electron fluid closure validated by in situ spacecraft observations in the far exhaust of guide-field reconnection. Journal of Geophysical Research: Space Physics, 125, e2020JA028604. https://doi.org/10.1029/2020JA028604

Wilder F.D., Ergun R.E., Gove D., Eriksson S., Hansel P., Ahmadi N., Malaspina D.M., Burch J.L., Torbert R.B., Strangeway R.J. and Giles B.L. (2021) The Occurrence and Prevalence of Time Domain Structures in the Kelvin- Helmholtz Instability at Different Positions Along the Earth's Magnetospheric Flanks. Front. Astron. Space Sci. 8:756563. https://doi.org/10.3389/fspas.2021.756563

Wilson III, L.B., Chen, L.-J., and Roytershteyn, V. (2021), The discrepancy between simulation and observation of electric fields in collisionless shocks, Front. Astron. Space Sci., 7:592634, https://doi.org/10.3389/fspas.2020.592634

2020

Adhikari, S., Shay, M. A., Parashar, T. N., Pyakurel, P. S., Matthaeus, W. H., Godzieba, D., ... and Dahlin, J. T. (2020). Reconnection from a turbulence perspective. *Physics of Plasmas*, *27*(4), 042305. https://doi.org/10.1063/1.5128376

Akhavan-Tafti, M., Palmroth, M., Slavin, J. A., Battarbee, M., Ganse, U., Grandin, M., et al. (2020). Comparative analysis of the Vlasiator simulations and MMS observations of multiple X-line reconnection and flux transfer events. Journal of Geophysical Research: Space Physics, 125, e2019JA027410. https://doi.org/10.1029/2019JA027410

Akhavan-Tafti, M., Fontaine, D., Slavin, J. A., Le Contel, O., and Turner, D. (2020). Cross-scale quantification of storm-time dayside magnetospheric magnetic flux content. Journal of Geophysical Research: Space Physics, 125, e2020JA028027. https://doi.org/10.1029/2020JA028027

Amano, T., Katou, T., Kitamura, N., Oka, M., Matsumoto, Y., Hoshino, M., ... and Blake, J. B. (2020). Observational evidence for stochastic shock drift acceleration of electrons at the Earth's bow shock. *Physical Review Letters*, *124*(6), 065101. https://doi.org/10.1103/PhysRevLett.124.065101

Argall, M. R., Small, C. R., Piatt, S., Breen, L., Petrik, M., Kokkonen, K., ... and Burch, J. L. (2020). MMS SITL Ground Loop: Automating the burst data selection process. *Frontiers in astronomy and space sciences*, 54. https://doi.org/10.3389/fspas.2020.00054

Bandyopadhyay, R., W. H. Matthaeus, A. Chasapis, C. T. Russell, R. J. Strangeway, R. B. Torbert, B. L. Giles, D. J. Gershman, C. J. Pollock, J. L. Burch (2020), Direct measurement of the solar-wind taylor microscale using MMS turbulence campaign data, The Astrophysical Journal, 899:63 (6pp). https://doi.org/10.3847/1538-4357/ab9ebe

Bandyopadhyay, R., Yang, Y., Matthaeus, W. H., Chasapis, A., Parashar, T. N., Russell, C. T., ... and Burch, J. L. (2020). In Situ Measurement of Curvature of Magnetic Field in Turbulent Space Plasmas: A Statistical Study. *The Astrophysical Journal Letters*, *893*(1), L25. https://doi.org/10.3847/2041-8213/ab846e

Bandyopadhyay, R., L. Sorriso-Valvo, A. Chasapis, P. Hellinger, W. H. Matthaeus, A. Verdini, S. Landi, L. Franci, L. Matteini, B. L. Giles, D. J. Gershman, T. E. Moore, C. J. Pollock, C. T. Russell, R. J. Strangeway, R. B. Torbert, and J. L. Burch (2020), In Situ Observation of Hall Magnetohydrodynamic Cascade in Space Plasma Phys. Rev. Lett. 124, 225101. https://doi.org/10.1103/PhysRevLett.124.225101

Bandyopadhyay, R., W. H. Matthaeus, T. N. Parashar, Y. Yang, A. Chasapis, B. L. Giles, D. J. Gershman, C. J. Pollock, C. T. Russell, R. J. Strangeway, R. B. Torbert, T. E. Moore, and J. L. Burch (2020), Statistics of Kinetic Dissipation in the Earth's Magnetosheath: MMS Observations, Phys. Rev. Lett. 124, 255101. https://doi.org/10.1103/PhysRevLett.124.255101

Bessho, N., L.-J. Chen, S. Wang, M. Hesse, L. B. Wilson III, and J. Ng (2020), Magnetic reconnection and kinetic waves generated in the Earth's quasi-parallel bow shock, Physics of Plasmas, 27, 092901; https://doi.org/10.1063/5.0012443

Bingham, S. T., Cohen, I. J., Mauk, B. H., Turner, D. L., Mitchell, D. G., Vines, S. K., et al. (2020). Charge- state-dependent energization of suprathermal ions during substorm injections observed by MMS in

the magnetotail. Journal of Geophysical Research: Space Physics, 125, e2020JA028144. https://doi.org/10.1029/2020JA028144

Birn, J., M. Chandler, and R. Nakamura (2020), Ion Beams in the Plasma Sheet Boundary Layer: MMS Observations and Test Particle Simulations, J. Geophys. Res., 125, e2019JA027113. https://doi.org/10.1029/2019JA027113

Birn, J., Borovsky, J. E., Hesse, M., and Kepko, L. (2020). Substorm current wedge: Energy conversion and current diversion. *Journal of Geophysical Research: Space Physics*, 125, e2020JA028073. https://doi.org/10.1029/2020JA028073

Burch, J. L., Webster, J. M., Hesse, M., Genestreti, K. J., Denton, R. E., and Phan, T. D., et al. (2020). Electron inflow velocities and reconnection rates at Earth's magnetopause and magnetosheath. *Geophysical Research Letters*, *47*, e2020GL089082. https://doi.org/10.1029/2020GL089082

Burkholder, B. L., K. Nykyri, X. Ma, R. Rice, S. A. Fuselier, K. J. Trattner, K. R. Pritchard, J. L. Burch, and S. M. Petrinec (2020), Magnetospheric Multiscale observation of an electron diffusion region at high latitudes, Geophysical Research Letters, 47, e2020GL087268. https://doi.org/10.1029/2020GL087268

Chasapis, A., W. H. Matthaeus, R. Bandyopadhyay, R. Chhiber, N. Ahmadi, R. E. Ergun, C. T. Russell, R. J. Strangeway, B. L. Giles, D. J. Gershman, C. J. Pollock, and J. L. Burch (2020), Scaling and Anisotropy of Solar Wind Turbulence at Kinetic Scales during the MMS Turbulence Campaign, The Astrophysical Journal, 903:127 (7pp). https://doi.org/10.3847/1538-4357/abb948

Chaston, C. C., Travnicek, P., and Russell, C. T. (2020). Turbulent wavefield morphology and ion scattering in the magnetosheath. Geophysical Research Letters, 47, e2020GL089613. https://doi.org/10.1029/2020GL089613

Chen, L. J., Wang, S., Le Contel, O., Rager, A., Hesse, M., Drake, J., ... and Avanov, L. (2020). Lower-hybrid drift waves driving electron nongyrotropic heating and vortical flows in a magnetic reconnection layer. *Physical Review Letters*, *125*(2), 025103. https://doi.org/10.1103/PhysRevLett.125.025103

Cozzani, G. (2020). In situ spacecraft observations of a structured electron diffusion region during magnetopause reconnection. In *Microphysics of Magnetic Reconnection in Near-Earth Space* (pp. 77-102). Springer, Cham. https://doi.org/10.1007/978-3-030-56142-0_7

Dahlin, J. T. (2020). Adiabatic acceleration in a magnetotail flux rope. Geophysical Research Letters, 47, e2020GL087918. https://doi.org/10.1029/2020GL087918

da Silva, D., Barrie, A., Gershman, D., Elkington, S., Dorelli, J., Giles, B., and Paterson, W. (2020). Neural network repair of Lossy compression Artifacts in the September 2015 to March 2016 duration of the MMS/FPI data set. Journal of Geophysical Research: Space Physics, 125, e2019JA027181. https://doi.org/10.1029/2019JA027181

Denton, R. E., R. B. Torbert, H. Hasegawa, I.Dors, K. J. Genestreti, M. R. Argall, D. Gershman, O. Le Contel, J. L. Burch, C. T. Russell, R. J. Strangeway, B. L. Giles, and D. Fischer (2020), Polynomial reconstruction of the reconnection magnetic field observed by multiple spacecraft, Journal of Geophysical Research: Space Physics,125, e2019JA027481. https://doi.org/10.1029/2019JA027481

Dokgo, K., Hwang, K.-J., Burch, J. L., Yoon, P. H., Graham, D. B., and Li, W. (2020). High-frequency waves driven by agyrotropic electrons near the electron diffusion region. Geophysical Research Letters, 47, e2020GL087111. https://doi.org/10.1029/2020GL087111

Dokgo, K., Hwang, K.-J., Burch, J.L., Yoon, P.H.,Graham,D.B.,&Li,W. (2020).The effects of upper-hybrid waves on energy dissipation in the electron diffusion region. Geophysical Research Letters, 47, e2020GL089778.https://doi.org/10.1029/2020GL089778

Eastwood, J. P., Goldman, M. V., Phan, T. D., Stawarz, J. E., Cassak, P. A., Drake, J. F., ... and Russell, C. T. (2020). Energy flux densities near the electron dissipation region in asymmetric magnetopause reconnection. Physical Review Letters, 125(26), 265102. https://doi.org/10.1103/PhysRevLett.125.265102

Ergun, R. E., Ahmadi, N., Kromyda, L., Schwartz, S. J., Chasapis, A., Hoilijoki, S., ... and Giles, B. L. (2020). Observations of Particle Acceleration in Magnetic Reconnection–driven Turbulence. *The Astrophysical Journal*, *898*(2), 154. https://doi.org/10.3847/1538-4357/ab9ab6

Ergun, R. E., Ahmadi, N., Kromyda, L., Schwartz, S. J., Chasapis, A., Hoilijoki, S., ... and Burch, J. L. (2020). Particle acceleration in strong turbulence in the Earth's magnetotail. *The Astrophysical Journal*, *898*(2), 153. https://doi.org/10.3847/1538-4357/ab9ab5

Eriksson, E., Vaivads, A., Alm, L., Graham, D. B., Khotyaintsev, Y. V., and André, M. (2020). Electron acceleration in a magnetotail reconnection outflow region using Magnetospheric MultiScale data. Geophysical Research Letters, 47, e2019GL085080. https://doi.org/10.1029/2019GL085080

Escoubet, C. P., Hwang, K. J., Toledo-Redondo, S., Turc, L., Haaland, S. E., Aunai, N., ... and Torbert, R. B. (2020). Cluster and MMS simultaneous observations of magnetosheath high speed jets and their impact on the magnetopause. *Frontiers in Astronomy and Space Sciences*, 78. https://doi.org/10.3389/fspas.2019.00078

Fargette, N., Lavraud, B., Øieroset, M., Phan, T. D., Toledo-Redondo, S., Kieokaew, R., et al. (2020), On the ubiquity of magnetic reconnection inside flux transfer event-like structures at the Earth's magnetopause, Geophysical Research Letters, 47, e2019GL086726. https://doi.org/10.1029/2019GL086726

Franci, L., S. Landi, J. E. Stawarz, E. Papini, P. Hellinger, T. Nakamura, D. Burgess, A. Verdini, L. Matteini, R. Ergun, O. Le Contel, and P.-A. Lindqvist (2020), Modeling MMS observations at the Earth's magnetopause with hybrid simulations of Alfvénic turbulence, The Astrophysical Journal, 898:175 (10pp). https://doi.org/10.3847/1538-4357/ab9a47

Fuselier, S. A., Ionospheric Oxygen ions in the dayside magnetosphere, Journal of Atmospheric and Solar-Terrestrial Physics, 210 (2020), 104338. https://doi.org/10.1016/j.jastp.2020.105448

Fuselier, S. A., Dayeh, M. A., Galli, A., Funsten, H. O., Schwadron, N. A.,Petrinec, S. M., et al. (2020). Neutral atom imaging of the solar wind magnetosphere- exosphere interaction near the subsolar magnetopause. Geophysical Research Letters, 47, e2020GL089362. https://doi.org/10.1029/2020GL089362

Genestreti, K. J., Liu, Y.-H., Phan, T.-D., Denton, R. E., Torbert, R. B., Burch, J. L., et al. (2020). Multiscale coupling during magnetopause reconnection: Interface between the electron and ion diffusion regions. Journal of Geographical Research: Space Physics,125, e2020JA027985. https://doi.org/10.1029/2020JA027985

Gingell I., Schwartz, S. T., Eastwood, J. P., Stawarz, J. E., Burch, J. L., Ergun, R. E., et al. (2020). Statistics of reconnecting current sheets in the transition region of earth's bow shock. Journal of Geophysical Research: Space Physics, 125, e2019JA027119. https://doi.org/10.1029/2019JA027119

Goldman, M. V., Newman, D. L., Eastwood, J. P., and Lapenta, G. (2020). Multibeam energy moments of multibeam particle velocity distributions. Journal of Geophysical Research: Space Physics, 125, e2020JA028340. https://doi.org/10.1029/2020JA028340

Goldstein, J., Valek, P. W., McComas, D. J., Redfern, J., Spence, H., Skoug, R. M., et al. (2020). Global ENA imaging and in situ observations of substorm dipolarization on 10 August 2016. *Journal of Geophysical Research: Space Physics*, *125*, e2019JA027733. https://doi.org/10.1029/2019JA027733

Haaland, S., Paschmann, G., Øieroset, M., Phan, T., Hasegawa, H., Fuselier, S. et al. (2020). Characteristics of the flank magnetopause: MMS results. *Journal of Geophysical Research: Space Physics*, *125*, e2019JA027623. https://doi.org/10.1029/2019JA027623

Hanson, E. L. M., Agapitov, O. V., Vasko, I. Y., Mozer, F. S., Krasnoselskikh,V., Bale, S. D., Avanov, L., Khotyaintsev, Y., and Giles, B. (2020), Shock Drift Acceleration of Ions in an Interplanetary Shock Observed by *MMS,* The Astrophysical Journal Letters, 891:L26 (8pp). https://doi.org/10.3847/2041-8213/ab7761

Hanson, E. L. M., Agapitov, O. V., Mozer, F. S., Krasnoselskikh, V., Bale, S. D., Avanov, L., et al. (2020). Terrestrial bow shock parameters from MMS measurements: Dependence on upstream and downstream time ranges. Journal of Geophysical Research: Space Physics, 125, e2019JA027231. https://doi.org/10.1029/2019JA027231

Hasegawa, H., Nakamura, T. K. M., Gershman, D. J., Nariyuki, Y., Viñas, A. F., Giles, B. L., et al. (2020). Generation of turbulence in Kelvin-Helmholtz vortices at the Earth's magnetopause: Magnetospheric Multiscale observations. Journal of Geophysical Research: Space Physics, 125, e2019JA027595. https://doi.org/10.1029/2019JA027595

Hesse, M., and P. A. Cassak (2020), Magnetic Reconnection in the Space Sciences: Past, Present, and Future, Journal of Geophysical Research: Space Physics, 125, e2018JA025935. https://doi.org/10.1029/2018JA025935

Horvath, S. A., G. G. Howes, and A. J. McCubbin (2020), Electron Landau damping of kinetic Alfvén waves in simulated magnetosheath turbulence, Phys. Plasmas 27, 102901. https://doi.org/10.1063/5.0021727

Huang, K., Liu, Y.-H., Lu, Q., & Hesse, M. (2020). Scaling of magnetic reconnection with a limited x-line extent. Geophysical Research Letters, 47, e2020GL088147. https://doi.org/10.1029/2020GL088147

Hull, A. J., L. Muschietti, O. Le Contel, J. C. Dorelli, and P.-A. Lindqvist (2020), MMS Observations of Intense Whistler Waves Within Earth's Supercritical Bow Shock: Source Mechanism and Impact on Shock Structure and Plasma Transport, Journal of Geophysical Research: Space Physics, 125, e2019JA027290. https://doi.org/10.1029/2019JA027290

Hwang, K.-J., Nishimura, Y., Coster, A. J., Gillies, R. G., Fear, R. C., Fuselier, S. A., et al. (2020). Sequential observations of flux transfer events, poleward-moving auroral forms, and polar cap patches. *Journal of Geophysical Research: Space Physics*, *125*, e2019JA027674. https://doi.org/10.1029/2019JA027674

Khotyaintsev, Yu. V., D. B. Graham, K. Steinvall, L. Alm, A. Vaivads, A. Johlander, C. Norgren, W. Li, A. Divin, H. S. Fu, K.-J. Hwang, J. L. Burch, N. Ahmadi, O. Le Contel, D. J. Gershman, C. T. Russell, and R. B. Torbert (2020), Electron Heating by Debye-Scale Turbulence in Guide-Field Reconnection, Phys. Rev. Lett. 124, 045101. https://doi.org/10.1103/PhysRevLett.124.045101

Kieokaew, R., Lavraud, B., Foullon, C., Toledo-Redondo, S., Fargette, N., Hwang, K.-J., et al. (2020). Magnetic reconnection inside a flux transfer event-like structure in magnetopause kelvin-helmholtz waves. *Journal of Geophysical Research: Space Physics*, *125*, e2019JA027527. https://doi.org/10.1029/2019JA027527

Kitamura, N., Y. Omura, S. Nakamura, T. Amano, S. A. Boardsen, N. Ahmadi, O. Le Contel, P.-A. Lindqvist, R. E. Ergun, Y. Saito, S. Yokota, D. J. Gershman, W. R. Paterson, C. J. Pollock, B. L. Giles, C. T. Russell, R. J. Strangeway, and J. L. Burch (2020). Observations of the source region of whistler mode waves in magnetosheath mirror structures. Journal of Geophysical Research: Space Physics, 125, e2019JA0274. https://doi.org/10.1029/2019JA027488

Kolstø, H. M., Hesse, M., Norgren, C., Tenfjord, P., Spinnangr, S. F., and Kwagala, N.(2020), Collisionless magnetic reconnection in an asymmetric oxygen density configuration, Geophysical Research Letters, 47, e2019GL085359. https://DOI.org/10.1029/2019GL085359

Lai, H. R., Russell, C. T., Jia, Y. D.,and Blanco-Cano, X. (2020). Solar wind conditions during the first 42 months of Magnetospheric Multiscale Mission. Journal of Geophysical Research: Space Physics, 125, e2020JA028207. https://doi.org/10.1029/2020JA028207

Lee, S. H., Sibeck, D. G., Lin, Y., Guo, Z., Adrian, M. L., Silveira, M. V. D., et al. (2020). Characteristics of escaping magnetospheric ions associated with magnetic field fluctuations. *Journal of Geophysical Research: Space Physics*, *125*, e2019JA027337. https://doi.org/10.1029/2019JA027337

Lichko, E., and J. Egedal (2020), Magnetic pumping model for energizing superthermal particles applied to observations of the Earth's bow shock, Nat. Commun 11, 2942 (2020). https://doi.org/10.1038/s41467-020-16660-4

Liu, T. Z., Wang, C.-P., Wang, B., Wang, X., Zhang, H., Lin, Y., and Angelopoulos, V. (2020). ARTEMIS observations of foreshock transients in the midtail foreshock. Geophysical Research Letters, 47, e2020GL090393. https://doi.org/10.1029/2020GL090393

Liu, T. Z., Lu, S., Turner, D. L., Gingell, I., Angelopoulos, V., Zhang, H., et al. (2020). Magnetospheric Multiscale (MMS) observations of magnetic reconnection in foreshock transients. Journal of Geophysical Research: Space Physics, 125, e2020JA027822. https://doi.org/10.1029/2020JA027822

Liu, T. Z., X. An, H. Zhang, and D. Turner (2020), Magnetospheric Multiscale observations of foreshock transients at their very early stage, The Astrophysical Journal, 902:5 (15pp). https://doi.org/10.3847/1538-4357/abb249

Liu, Y.-H., S.-C. Lin, M. Hesse, F. Guo, X. Li, H. Zhang, and S. Peery (2020), The Critical Role of Collisionless Plasma Energization on the Structure of Relativistic Magnetic Reconnection, The Astrophysical Journal Letters, 892:L13 (5pp). https://doi.org/10.3847/2041-8213/ab7d3f

Lotekar, A., Vasko, I. Y., Mozer, F. S., Hutchinson, I., Artemyev, A. V., Bale, S. D., et al. (2020). Multisatellite MMS analysis of electron holes in the Earth's magnetotail: Origin, properties, velocity gap, and transverse instability. Journal of Geophysical Research: Space Physics, 125, e2020JA028066. https://doi.org/10.1029/2020JA028066

Marshall, A. T., Burch, J. L., Reiff, P. H., Webster, J. M., Torbert, R. B., Ergun, R. E., et al. (2020). Asymmetric reconnection within a flux rope-type dipolarization front. *Journal of Geophysical Research: Space Physics*, *125*, e2019JA027296. https://doi.org/10.1029/2019JA027296

Nakamura, T. K. M., Stawarz, J. E., Hasegawa, H., Narita, Y., Franci, L., Wilder, F. D. et al. (2020). Effects of fluctuating magnetic field on the growth of the Kelvin-Helmholtz instability at the Earth's magnetopause. Journal of Geophysical Research: Space Physics, 125, e2019JA027515. https://doi.org/10.1029/2019JA027515

Ng, J., Chen, L.-J., Le, A., Stanier, A., Wang, S., & Bessho, N.(2020). Lower-Hybrid-Drift Vortices in the Electron-Scale Magnetic Reconnection Layer. Geophysical Research Letters, 47, e2020GL090726. https://doi.org/10.1029/2020GL090726

Norgren, C., Hesse, M., Graham, D. B., Khotyaintsev, Y. V., Tenfjord, P., Vaivads, A., et al. (2020). Electron acceleration and thermalization at magnetotail separatrices. Journal of Geophysical Research: Space Physics, 125, e2019JA027440. https://doi.org/10.1029/2019JA027440

Paschmann, G., Sonnerup, B. U. Ö., Haaland, S. E., Phan, T.-D., and Denton, R. E. (2020). Comparison of quality measures for Walén relation. *Journal of Geophysical Research: Space Physics*, 125, e2020JA028044. https://doi.org/10.1029/2020JA028044

Payne, D. S., Genestreti, K. J., Germaschewski, K., Argall, M. R., Torbert, R. B., Dors, I., et al. (2020). Energy balance and time dependence of a magnetotail electron diffusion region. *Journal of Geophysical Research: Space Physics*, 125, e2020JA028290. https://doi.org/10.1029/2020JA028290

Petrinec, S. M., Burch, J. L., Chandler, M., Farrugia, C. J., Fuselier, S. A., Giles, B. L., et al. (2020). Characteristics of minor ions and electrons in flux transfer events observed by the Magnetospheric Multiscale Mission. Journal of Geophysical Research: Space Physics, 125, e2020JA027778. https://doi.org/10.1029/2020JA027778

Plaschke, F., Jernej, M., Hietala, H., and Vuorinen, L. (2020, March). On the alignment of velocity and magnetic fields within magnetosheath jets. In *Annales geophysicae* (Vol. 38, No. 2, pp. 287-296). Copernicus GmbH. https://doi.org/10.5194/angeo-38-287-2020

Price, L., M. Swisdak, J. F. Drake, and D. B. Graham (2020), Turbulence and transport during guide-field reconnection atthe magnetopause JournalofGeophysicalResearch: SpacePhysics, 125, e2019JA027498.https://doi.org/10.1029/2019JA027498

Qi, Y., Russel, C. T., Jia, Y.-D., and Hubbert, M. (2020). Temporal evolution of flux tube entanglement at the magnetopause as observed by the MMS satellites. Geophysical Research Letters, 47, e2020GL090314. https://doi.org/10.1029/2020GL090314

Qudsi, R. A., Bandyopadhyay, R., Maruca, B. A., Parashar, T. N., Matthaeus, W. H., Chasapis, A., ... and Burch, J. L. (2020). Intermittency and Ion Temperature–Anisotropy Instabilities: Simulation and Magnetosheath Observation. *The Astrophysical Journal*, *895*(2), 83. https://doi.org/10.3847/1538-4357/ab89ad

Raptis, S., Aminalragia-Giamini, S., Karlsson, T., and Lindberg, M. (2020) Classification of Magnetosheath Jets Using Neural Networks and High Resolution OMNI (HRO) Data. Front. Astron. Space Sci. 7:24. https://doi.org/10.3389/fspas.2020.00024

Raptis,S., Karlsson,T., Plaschke,F., Kullen,A., and Lindqvist,P.-A. (2020). Classifying Magnetosheath Jets Using MMS: Statistical Properties. Journal of Geophysical Research : Space Physics, 125, e2019JA027754. https://doi.org/10.1029/2019JA027754

Roberts, O. W., Nakamura, R., Torkar, K., Graham, D. B., Gershman, D. J., Holmes, J. C., et al. (2020). Estimation of the electron density from spacecraft potential during high-frequency electric field fluctuations. Journal of Geophysical Research: Space Physics, 125, e2020JA027854. https://doi.org/10.1029/2020JA027854

Roberts, O. W., Thwaites, J., Sorriso-Valvo, L., Nakamura, R., and Vörös, Z. (2020). Higher-order statistics in compressive solar wind plasma turbulence: High-resolution density observations from the magnetospheric multiscale mission. *Frontiers in Physics*, 464. https://doi.org/10.3389/fphy.2020.584063

Roberts, O. W., Verscharen, D., Narita, Y., Nakamura, R., Vörös, Z., and Plaschke, F. (2020). Possible coexistence of kinetic Alfvén and ion Bernstein modes in sub-ion scale compressive turbulence in the solar wind. *Physical Review Research*, *2*(4), 043253. https://doi.org/10.1103/PhysRevResearch.2.043253

Roberts, O. W., R. Nakamura, K. Torkar, Y. Narita, J. C. Holmes, Z. Vörös, C. Lhotka, C. P. Escoubet, D. B. Graham, D. J. Gershman, Y. Khotyaintsev, and P.-A. Lindqvist (2020), Sub-ion Scale Compressive Turbulence in the Solar Wind: MMS Spacecraft Potential Observations, The Astrophysical Journal Supplement Series, 250:35 (20pp). https://doi.org/10.3847/1538-4365/abb45d

Russell, C. T., and Qi, Y. (2020). Flux ropes are born in pairs: An outcome of interlinked, reconnecting flux tubes. Geophysical Research Letters, 47, e2020GL087620. https://doi.org/10.1029/2020GL087620

Sahraoui, F., Hadid, L., and Huang, S. (2020). Magnetohydrodynamic and kinetic scale turbulence in the near-Earth space plasmas: a (short) biased review. *Reviews of Modern Plasma Physics*, *4*(1), 1-33. https://doi.org/10.1007/s41614-020-0040-2

Silveira, M. D., Sibeck, D. G.,Lee, S. H., Koga, D., Souza, V. M.,Gonzalez, W. D., and Russell, C. T.(2020). Flux transfer event with an electron-scale substructure observedby the Magnetospheric

Multiscale mission. Journal of Geophysical Research: Space Physics,125, e2019JA027308. https://doi.org/10.1029/2019JA027308

Starkey, M., S. A. Fuselier, M. I. Desai, S. J. Schwartz, R. G. Gomez, J. Mukherjee, I. J. Cohen, and C. T. Russell (2020), MMS **o**bservations of **a**ccelerated **i**nterstellar **p**ickup He^{+} **i**ons at an **i**nterplanetary **s**hock**,** The Astrophysical Journal, 897:6 (10pp). https://doi.org/10.3847/1538-4357/ab960c

Stasiewicz, K., and Eliasson, B. (2020). Quasi-adiabatic and stochastic heating and particle acceleration at quasi-perpendicular shocks. *The Astrophysical Journal*, *903*(1), 57. https://doi.org/10.3847/1538-4357/abb825

Stasiewicz, K., and Eliasson, B. (2020). Stochastic and quasi-adiabatic electron heating in quasi-parallel shocks. *The Astrophysical Journal*, *904*(2), 173. https://doi.org/10.3847/1538-4357/abbffa

Trattner, K. J., Burch J. L., Fuselier, S. A., Petrinec, S. M., and Vines, S. K. (2020). The 18 November 2015 magnetopause crossing: The GEM dayside kinetic challenge event observed by MMS/HPCA. *Journal of Geophysical Research: Space Physics*, *125*, e2019JA027617. https://doi.org/10.1029/2019JA027617

Turner, D. L., Liu, T. Z., Wilson, L. B., III, Cohen, I. J., Gershman, D. G., Fennell, J. F., et al. (2020). Microscopic, multipoint characterization of foreshock bubbles with Magnetospheric Multiscale (MMS). Journal of Geophysical Research: Space Physics, 125, e2019JA027707. https://doi.org/10.1029/2019JA027707

Vasko, I. Y., Wang, R., Mozer, F. S., Bale, S. D., and Artemyev, A. V. (2020). On the nature and origin of bipolar electrostatic structures in the Earth's bow shock. *Frontiers in Physics*, *8*, 156. https://doi.org/10.3389/fphy.2020.00156

Vernisse, Y., Lavraud, B., Faganello, M., Fadanelli, S., Sisti, M., Califano, F., et al. (2020). Latitudinal dependence of the Kelvin-Helmholtz instability and beta dependence of vortex-induced high-guide field magnetic reconnection. Journal of Geophysical Research: Space Physics, 125, e2019JA027333. https://doi.org/10.1029/2019JA027333

Wang, R., Vasko, I. Y., Mozer, F. S., Bale, S. D., Artemyev, A. V., Bonnell, J. W., ... and Strangeway, R. (2020). Electrostatic turbulence and Debye-scale structures in collisionless shocks. *The Astrophysical Journal Letters*, *889*(1), L9. https://doi.org/10.3847/2041-8213/ab6582

Wang, S., Chen, L.-J., Ng, J., Bessho, N., Le, G., Fung, S. F., et al. (2020). A case study of nonresonant mode 3-s ULF waves observed by MMS. Journal of Geophysical Research: Space Physics, 125, e2020JA028557. https://doi.org/10.1029/2020JA028557

Wang, S., Wang, R., Lu, Q. *et al.* Direct evidence of secondary reconnection inside filamentary currents of magnetic flux ropes during magnetic reconnection. *Nat Commun* **11,** 3964 (2020). https://doi.org/10.1038/s41467-020-17803-3

Wang, S., Chen, L. J., Bessho, N., Hesse, M., Wilson, L. B., Denton, R., ... and Burch, J. (2020). Ion-scale current structures in short large-amplitude magnetic structures. *The Astrophysical Journal*, *898*(2), 121. https://doi.org/10.3847/1538-4357/ab9b8b

Wilder, F. D., Schwartz, S. J., Ergun, R. E., Eriksson, S., Ahmadi, N., Chasapis, A., et al. (2020). Parallel electrostatic waves associated with turbulent plasma mixing in the Kelvin-Helmholtz instability. Geophysical Research Letters, 46, e2020GL087837. https://doi.org/10.1029/2020GL087837

Williams, T., Palmer, E., and Ottenstein, N. (2020, August 9-12). Non-Tetrahedral Formations for Cusp Science Collection during the MMS Extended Mission. Paper AAS 20-764, AAS/AIAA Astrodynamics Specialist Conference, held remotely.

Williams, T., Shulman, S., Ottenstein, N., Palmer, E., Riley, C., Letourneau, S., Hollister, J., Tedla, Y., and Godine, D. (2020, March 7-14). Operational Techniques for Dealing with Long Eclipses during the MMS

Extended Mission. IEEE Aerospace Conference, Big Sky, MT. https://doi.org/10.1109/AERO47225.2020.9172276

Wilson, L. B., Chen, L. J., Wang, S., Schwartz, S. J., Turner, D. L., Stevens, M. L., ... and Goodrich, K. A. (2020). Electron energy partition across interplanetary shocks. III. Analysis. *The Astrophysical Journal*, *893*(1), 22. https://doi.org/10.3847/1538-4357/ab7d39

Yoo, J., Ji, J.-Y., Ambat, M. V., Wang, S., Ji, H., Lo, J., et al. (2020). Lower hybrid drift waves during guide field reconnection. Geophysical Research Letters, 47, e2020GL087192. https://doi.org/10.1029/2020GL087192

Yordanova, E., Vörös, Z., Raptis, S., and Karlsson, T. (2020). Current sheet statistics in the magnetosheath. *Frontiers in Astronomy and Space Sciences*, 2. https://doi.org/10.3389/fspas.2020.00002

2019

Akhavan-Tafti, M., Slavin, J. A., Eastwood, J. P., Cassak, P. A., and Gershman, D. J. (2019), MMS multi-point analysis of FTE evolution: Physical characteristics and dynamics, Journal of Geophysical Research: Space Physics, 124, 5376–5395. https://doi.org/10.1029/2018JA026311

Akhavan-Tafti, M., Slavin, J. A., Sun, W. J., Le, G., and Gershman, D. J. (2019), MMS Observations of Plasma Heating Associated with FTE Growth, Geophysical Research Letters, 46, 12,654-12,664. https://doi.org/10.1029/2019GL084843

Alm, L., Andr'e, M., Graham, D. B., Khotyaintsev, Y. V., Vaivads, A., Chappell, C. R., Dargent, J., Fuselier, S. A., Haaland, S., Lavaraud, B., Li, W., Tenfjord, P., Toledo-Redondo, S., and Vines, S. K. (2019), MMS observations of multiscale Hall physics in the magnetotail. Geophysical Research Letters, 46, 10,230-10,239. https://doi.org/10.1029/2019GL084137

Andrés, N., F. Sahraoui, S. Galtier, L. Z. Hadid, R. Ferrand, and S. Y. Huang (2019), Energy Cascade Rate Measured in a Collisionless Space Plasma with MMS Data and Compressible Hall Magnetohydrodynamic Turbulence Theory, Phys. Rev. Lett. 123, 245101. https://doi.org/10.1103/PhysRevLett.123.245101.

Artemyev, A. V., Angelopoulos, V., Vasko, I. Y., Runov, A., Avanov, L. A., Giles, B. L., et al. (2019). On the kinetic nature of solar wind discontinuities. Geophysical Research Letters, 46, 1185–1194. https://doi.org/10.1029/2018GL079906

Barrie, A. C., Smith, D. L., Elkington, S. R., Sternovsky, Z., Silva, D., Giles, B. L., and Schiff, C. (2019),Wavelet compression performance of MMS/FPI plasma count data with plasma environment, Earth and Space Science,6, 116–135. https://doi.org/10.1029/2018EA000430

Bessho, N., L.-J. Chen, S. Wang, and M. Hesse (2019), Effects of the guide field on electron distribution functions in the diffusion region of asymmetric reconnection, Physics of Plasmas 26, 082310; https://doi.org/10.1063/1.5092809

Bessho, N., Chen, L.-J., Wang, S., Hesse, M., and Wilson, L. B. (2019), Magnetic reconnection in a quasi-parallel shock: Two-dimensional local particle-in-cell simulation. Geophysical Research Letters, 46. https://doi.org/10.1029/2019GL083397

Birn, J., Liu, J., Runov, A., Kepko, L., and Angelopoulos, V. (2019), On the contribution of dipolarizing flux bundles to the substorm current wedge and to flux and energy transport. *Journal of Geophysical Research: Space Physics*, *124*, 5408–5420. https://doi.org/10.1029/2019JA026658

Blake, J. B., Fennell, J. F., Turner, D. L., Cohen, I. J., and Mauk, B. H. (2019). Delayed arrival of energetic solar particles at MMS on 16 July 2017. Journal of Geophysical Research: Space Physics, 124, 2711–2719. https://doi.org/10.1029/2018JA026341

Burch, J. L., Dokgo, K., Hwang, K. J., Torbert, R. B., Graham, D. B., Webster, J. M., Ergun, R. E., Giles, B. L., Allen, R. C., Chen, L.-J., Wang, S., Genestreti, K. J., Russell, C. T., Strangeway, R. J., Le Contel, O.

(2019), High-frequency wave generation in magnetotail reconnection: Linear dispersion analysis. Geophysical Research Letters, 46, 4089–4097. https://d oi.org/10.1029/2019GL082471

Chen, L.-J., Wang, S., Hesse, M., Ergun, R. E., Moore, T., Giles, B., Bessho, N., Russell, C., Burch, J., Torbert, R. B., Genestreti, K. J., Paterson, W., Pollock, C., Lavraud, B., Le Contel, O., Strangeway, R., Khotyaintsev, Yu. V., Lindqvist, P.-A. (2019), Electron diffusion regions in magnetotail reconnection under varying guide fields. Geophysical Research Letters, 46, 6230– 6238. https://doi.org/10.1029/2019GL082393

Cohen, I. J., Mauk, B. H., Turner, D. L., Fennell, J. F., Blake, J. B., Reeves, G. D., Leonard, T. W., Baker, D. N., Jaynes, A. N., Spence, H. E., Gabrielse, C. (2019), Drift-dispersed flux dropouts of energetic electrons observed in Earth's middle magnetosphere by the Magnetospheric Multiscale (MMS) mission, Geophysical Research Letters, 46, 3069–3078. https://doi.org/10.1029/2019GL082008

Cohen, I. J., Schwartz, S. J., Goodrich, K. A., Ahmadi, N., Ergun, R. E., Fuselier, S. A., Desai, M. I., Christian, E. R., McComas, D. J., Zank, G. P., Shuster, J. R., Vines, S. K., Mauk, B. H., Decker, R. B., Anderson, B. J., Westlake, J. H., Le Contel, O., Breuillard H., Giles, B. L., Torbert, R. B., Burch, J. L. (2019), High-resolution measurements of the cross-shock potential, ion reflection, and electron heating at an interplanetary shock by MMS. Journal of Geophysical Research: Space Physics,124, 3961–3978. https://doi.org/10.1029/2018JA026197

Cozzani, G., A. Retinò, F. Califano, A. Alexandrova, O. Le Contel, Y. Khotyaintsev, A. Vaivads, H. S. Fu, F. Catapano, H. Breuillard, N. Ahmadi, P.-A. Lindqvist, R. E. Ergun, R. B. Torbert, B. L. Giles, C. T. Russell, R. Nakamura, S. Fuselier, B. H. Mauk, T. Moore, and J. L. Burch (2019), In situ spacecraft observations of a structured electron diffusion region during magnetopause reconnection, Phys. Rev. E 99, 043204. http://doi.org/10.1103/PHYSREVE.99.043204

Delano, K., Fuselier, S. A., Elliott, H. A., Burch, J. L., Mukherjee, J., Petrinec, S., et al. (2019). The He++/H+ density ratio across earth's subsolar magnetopause and its implications for the presence of a mass-dependent reflection coefficient. Journal of Geophysical Research: Space Physics, 124, https://doi.org/10.1029/2019JA027182

Dokgo, K., Hwang, K.-J., Burch, J. L., Choi, E., Yoon, P. H., Sibeck, D. G., and Graham, D. B. (2019). High-frequency wave generation in magnetotail reconnection: Nonlinear harmonics of upper hybrid waves. Geophysical Research Letters, 46, 7873–7882. https://doi.org/10.1029/2019GL083361

Ergun, R. E., S. Hoilijoki, N. Ahmadi, S. J. Schwartz, F. D. Wilder, J. F. Drake, M. Hesse, M. A. Shay, H. Ji, M. Yamada, D. B. Graham, P. A. Cassak, M. Swisdak, J. L. Burch, R. B. Torbert, J. C. Holmes, J. E. Stawarz, K. A. Goodrich, S. Eriksson, R. J. Strangeway, and O. LeContel (2019), Magnetic reconnection in three dimensions: Modeling and analysis of electromagnetic drift waves in the adjacent current sheet, J. Geophys. Res., 124, 10,085-10,103. https://doi.org/10.1029/2019JA027275

Ergun, R. E., Hoilijoki, S., Ahmadi, N., Schwartz, S. J., Wilder, F. D., Burch, J. L., et al. (2019). Magnetic reconnection in three dimensions: observations of electromagnetic drift waves in the adjacent current sheet. *Journal of Geophysical Research: Space Physics*, 124, 10104– 10118. https://doi.org/10.1029/2019JA027228

Fadanelli, S., Lavraud, B., Califano, F., Jacquey, C., Vernisse, Y., Kacem, I., et al. (2019), Four-spacecraft measurements of the shape and dimensionality of magnetic structures in the near-Earth plasma environment, Journal of Geophysical Research: SpacePhysics, 124, 6850–6868. https://doi.org/10.1029/2019JA026747

Fuselier, S. A., K. J. Trattner, S. M. Petrinec, M. H. Denton, S. Toledo-Redondo, M. André, N. Aunai, C. R. Chappell, A. Glocer, S. Haaland, M. Hesse, L. M. Kistler, B. Lavraud, W. Li, T. E. Moore, D. Graham, L. Alm, P. Tenfjord, J. Dargent, S. K. Vines, K. Nykyri, J. L. Burch, and R. J. Strangeway (2019), Mass-

loading the Earth's dayside magnetopause boundary layer and its effect on magnetic reconnection, *Geophys. Res. Lett., 46,* 6204–6213. https://doi.org/10.1029/2019GL08238

Fuselier, S. A., Trattner, K. J., Petrinec, S. M., Pritchard, K. R., Burch, J. L., Cassak, P. A., Giles, B. L., Lavraud, B., Strangeway, R. J. (2019). Stationarity of the Reconnection X-Line at Earth's Magnetopause for Southward IMF. *Journal of Geophysical Research: Space Physics*, 124. https://doi.org/10.1029/2019JA027143

Fuselier, S. A., J. Mukherjee, M. H. Denton, S. M. Petrinec, K. J. Trattner, S. Toledo-Redondo, S., M. André, N. Aunai, C. R. Chappell, A. Glocer, S. Haaland, M. Hesse, L. M. Kistler, B. Lavraud, W. Y. Li, T. E. Moore, D. Graham, P. Tenfjord, J. Dargent, S. K. Vines,R. J. Strangeway, and J. L. Burch (2019), High-density O^+ in Earth's outer magnetosphere and its effect on dayside magnetopause magnetic reconnection, Journal of Geophysical Research: SpacePhysics, 124. https://doi.org/10.1029/2019JA027396

Gershman, D. J., Dorelli, J. C., Avanov, L. A., Gliese, U., Barrie, A., Schiff, C., et al. (2019). Systematic uncertainties in plasma parameters reported by the fast plasma investigation on NASA's magnetospheric multiscale mission. Journal of Geophysical Research: Space Physics, 124, https://doi.org/10.1029/2019JA026980

Gingell, I., S. J. Schwartz, J. P. Eastwood, J. L. Burch, R. E. Ergun, S. Fuselier, D. J. Gershman, B. L. Giles, Y. V. Khotyaintsev, B. Lavraud, P.-A. Lindqvist, W. R. Paterson, T. D. Phan, C. T. Russell, J. E. Stawarz, R. J. Strangeway, R. B. Torbert, and F. Wilder (2019). Observations of magnetic reconnection in the transition region of quasi-parallel shocks. Geophysical Research Letters,46, 1177–1184. https://doi.org/10.1029/2018GL081804

Gomez, R. G., Fuselier, S. A., Mukherjee, J., Gonzalez, C. A., Burch,J. L., Strangeway, R. J., and Starkey, M. J.(2019). The extra-magnetospheric ion environment as observed by the Magnetospheric Multiscale mission hot plasma composition analyzer (MMS-HPCA). Journal of Geophysical Research: Space Physics,124,1509–1524. https://doi.org/10.1029/2018JA025392

Goodrich, K. A., Ergun, R., Schwartz, S. J., Wilson, L. B. III, Johlander, A., Newman, D., Wilder, F. D., Holmes, J., Burch, J., Torbert, R., Khotyaintsev, Y., Lindqvist, P.-A., Strangeway, R., Gershman, D., Giles, B. (2019). Impulsively reflected ions: A plausible mechanism for ion acoustic wave growth in collisionless shocks. Journal of Geophysical Research: Space Physics,124, 1855–1865. https://doi.org/10.1029/2018JA026436

Graham, D. B., Khotyaintsev, Y. V., Norgren, C., Vaivads, A., André, M., Drake, J. F., Egedal, J., Zhou, M., Le Contel, O., Webster, J. M., Lavraud, B., Kacem, I., Génot, V., Jacquey, C., Rager, A. C., Gershman, D. J., Burch, J. L., Ergun, R. E.(2019). Universality of lower hybrid waves at Earth's magnetopause, Journal of Geophysical Research: Space Physics,124. https://doi.org/10.1029/2019JA027155

Hanson, E. L. M., Agapitov, O. V., Mozer, F. S., Krasnoselskikh, V., Bale, S. D., Avanov, L., Khotyaintsev, Y., Giles, B. (2019). Cross-shock potential in rippled versus planar quasi-perpendicular shocks observed by MMS. Geophysical Research Letters,46, 2381–2389.https://doi.org/10.1029/2018GL080240

Hasegawa, H., Denton, R. E., Nakamura, R., Genestreti, K. J., Nakamura, T. K. M., Hwang, K.-J., Phan, T. D., Torbert, R. B., Burch, J. L., Giles, B. L., Gershman, D. J., Russell, C. T., Strangeway, R. J., Lindqvist, P.-A., Khotyaintsev, Y., Ergun, R. E., Kitamura, N., Saito, Y. (2019). Reconstruction of the electron diffusion region of magnetotail reconnection seen by the MMS spacecraft on 11 July 2017.Journalof Geophysical Research: Space Physics,124,122–138.https://doi.org/10.1029/2018JA026051

Hoilijoki, S., R. E. Ergun, S. J. Schwartz, S. Eriksson, F. D. Wilder, J. M. Webster, N. Ahmadi, O. Le Contel, J. L. Burch, R. B. Torbert, R. J. Strangeway, and B. L. Giles al. (2019), Electron-scale magnetic structure observed adjacent to an electron diffusion region at the dayside magnetopause, Journal of Geophysical Research: Space Physics, 124, 10,153-10,169. https://doi.org/10.1029/2019JA027192

Holmes, J. C., Ergun, R. E., Nakamura, R., Roberts, O., Wilder, F. D., and Newman, D. L. (2019), Structure of electron-scale plasma mixing along the dayside reconnection separatrix, Journal of Geophysical Research: Space Physics, 124, 8788-8803. https://doi.org/10.1029/2019JA026974

Hwang, K.-J., Choi, E., Dokgo, K., Burch, J. L., Sibeck, D. G., Giles, B. L., Goldstein, M. L., Paterson, W. R., Pollock, C. J., Shi, Q. Q., Fu, H., Hasegawa, H., Gershman, D. J., Khotyaintsev, Y., Torbert, R. B., Ergun, R. E., Dorelli, J. C., Avanov, L., Russell, C. T., Strangeway, R. J. (2019). Electron vorticity indicative of the electron diffusion region of magnetic reconnection. Geophysical Research Letters, 46, 6287–6296.https://doi.org/10.1029/2019GL082710

Kistler, L. M., Mouikis, C. G., Asamura, K., Yokota, S., Kasahara, S., Miyoshi, Y., et al. (2019). Cusp and nightside auroral sources of O+ in the plasma sheet. Journal of Geophysical Research: Space Physics, 124, 10036– 10047. https://doi.org/10.1029/2019JA027061

Lee, J. H., D. L. Turner, S. Toledo-Redondo, S. K. Vines, R. C. Allen, S. A. Fuselier, et al. (2019). MMS measurements and modeling of peculiar electromagnetic ion cyclotron waves, Geophysical Research Letters, 46, 11,622-11,631. https://doi.org/10.1029/2019GL085182

Liang, H., P. A. Cassak, S. Servidio, M. A. Shay, J. F. Drake, M. Swisdak, M. R. Argall, J. C. Dorelli, E. E. Scime, W. H. Matthaeus, V. Roytershteyn, and G. L. Delzanno (2019), Decomposition of Plasma Kinetic Entropy into Position and Velocity Space and the Use of Kinetic Entropy in Particle-in-Cell Simulations, Phys. Plasmas, 26, 082903. https://doi.org/10.1063/1.5098888

Liu, Y.-H., T. C. Li, M. Hesse, W. J. Sun, J. Liu, J. Burch, J. A. Slavin and K. Huang (2019), Three-dimensional magnetic reconnection with a spatially confined x-line extent — Implications for Dipolarizing Flux Bundles and the Dawn-Dusk Asymmetry Journal ofGeophysical Research: Space Physics,124, 2819–2830. https://doi.org/10.1029/2019JA026539

Lu, S., Artemyev, A. V., Angelopoulos, V., Lin, Y., Zhang, X.-J., Liu, J., et al. (2019). The Hall electric field in Earth's magnetotail thin current sheet. Journal of Geophysical Research: Space Physics, 124, 1052–1062. https://doi.org/10.1029/2018JA026202

Macek, W. M., M. V. D. Silveira, D. G. Sibeck, B. L. Giles, and J. L. Burch (2019), Mechanism of Reconnection on Kinetic Scales Based on Magnetospheric Multiscale Mission Observations, The Astrophysical Journal Letters, 885:L26 (6pp). https://doi.org/10.3847/2041-8213/ab4b5a

Macek, W. M., M. V. D. Silveira, D. G. Sibeck, B. L. Giles, and J. L. Burch (2019), Magnetospheric multiscale mission observations of reconnecting electric fields in the magnetotail on kinetic scales, Geophys. Res. Lett., 46, 10295-10302. https://doi.org/10.1029/2019GL083782

Manuzzo, R., G. Belmont, L. Rezeau, F. Califano, and R. E. Denton (2019), Crossing of plasma structures by spacecraft: A path calculator, J. Geophys. Res. Space Physics, 124, 10.119-10.140. https://doi.org/10.1029/2019JA026632

Marshall, A. T., Burch, J. L., Reiff, P. H., Webster, J. M., Torbert, R. B., Ergun, R. E., et al. (2020). Asymmetric reconnection within a flux rope-type dipolarization front. Journal of Geophysical Research: Space Physics, 125, e2019JA027296. https://doi.org/10.1029/2019JA027296

Matsui, H., Farrugia, C. J., Goldstein, J., Torbert, R. B., Argall, M. R., Vaith, H., et al. (2019). Velocity rotation events in the outer magnetosphere near the magnetopause. Journal of Geophysical Research: Space Physics, 124, 4137–4156. https://doi.org/10.1029/2019JA026548

Mauk, B. H., I. J. Cohen, D. K. Haggerty, G. B. Hospodarsky, J. E. P. Connerney, B. J. Anderson, F. Bagenal, R. W. Ebert, S. J. Bolton, J. L. Burch, S. M. Levin, R. B. Torbert, S. K. Vines, and J. H. Westlake (2019), Investigation of mass/charge-dependent escape of energetic ions across the magnetopauses of Earth and Jupiter, J. Geophys. Res. Space Physics, 124, https://doi.org/10.1029/2019JA026626.

Merkin, V. G., Panov, E. V., Sorathia, K., and Ukhorskiy, A. Y. (2019). Contribution of bursty bulk flows to the global dipolarization of the magnetotail during an isolated substorm. Journal of Geophysical Research: Space Physics, 124, https://doi.org/10.1029/2019JA026872

Nakamura, R., Genestreti, K. J., Nakamura, T., Baumjohann, W., Varsani, A., Nagai, T., Bessho, N., Burch, J. L., Denton, R. E., Eastwood, J. P., Ergun, R. E., Gershman, D. J., Giles, B. L., Hasegawa, H., Hesse, M., Lindqvist, P.-A., Russell, C. T., Stawarz, J. E., Strangeway, R. J., Torbert, R. B. (2019). Structure of the current sheet in the 11 July 2017 Electron Diffusion Region event. Journal of Geophysical Research: Space Physics, 124, 1173–1186. https://doi.org/10.1029/2018JA026028

Nakamura, T. K. M, T. Umeda, R. Nakamura, H. S. Fu, and M. Oka (2019), Disturbance of the Front Region of Magnetic Reconnection Outflow Jets due to the Lower-Hybrid Drift Instability, Phys. Rev. Lett. 123, 235101. https://doi.org/10.1103/PhysRevLett.123.235101

Nykyri, K., Bengtson, M., Angelopoulos, V., Nishimura, Y. T., and Wing, S. (2019). Can enhanced flux loading by high-speed jets lead to a substorm? Multipoint detection of the Christmas Day substorm onset at 08:17 UT, 2015. *Journal of Geophysical Research: Space Physics*, 124, 4314– 4340. https://doi.org/10.1029/2018JA026357

Nykyri, K., Chu, C., Ma, X., Fuselier, S. A., and Rice, R. (2019). First MMS observation of energetic particles trapped in high-latitude magnetic field depressions. Journal of Geophysical Research: Space Physics, 124, 197–210. https://doi.org/10.1029/2018JA026131

Øieroset, M., Phan, T. D., Drake, J. F., Eastwood, J. P., Fuselier, S. A., Strangeway, R. J., Hagerty, C., Shay, M. A., Oka, M., Wang, S., Chen, L.-J., I. Kacem, Lavraud, B., Angelopoulos, V., Burch, J. L., Torbert, R. B., Ergun, R. E., Khotyaintsev, Y., Lindqvist, P. A., Gershman, D. J., Giles, B. L., Pollock, C., Moore, T. E., Russell, C. T., Saito, Y., Avanov, L. A., Paterson, W. (2019). Reconnection with magnetic flux pileup at the interface of converging jets at the magnetopause. Geophysical Research Letters,46, 1937–1946. https://doi.org/10.1029/2018GL080994

Oka, M., Otsuka, F., Matsukiyo, S., Wilson, L. B., Argall, M. R., Amano, T., ... and Lindqvist, P. A. (2019). Electron scattering by low-frequency Whistler waves at Earth's bow shock. *The Astrophysical Journal*, *886*(1), 53. https://doi.org/10.3847/1538-4357/ab4a81

Panov, E. V., Baumjohann, W., Nakamura, R., Weygand, J. M., Giles, B. L., Russell, C. T., Reeves, G., Kubyshkina, M. V. (2019). Continent-wide R1/R2 current system and ohmic losses by broad dipolarization-injection fronts. Journal of Geophysical Research: Space Physics, 124, 4064-4082. https://doi.org/10.1029/2019JA026521

Poh, G., Slavin, J. A., Lu, S., Le, G., Ozturk, D. S., Sun, W.-J., Zou, S., Eastwood, J. P., Nakamura, R., Baumjohann, W., Russell, C. T., Gershman, D. J., Giles, B. L., Pollock, C. J., Moore, T. E., Torbert, R. B., Burch, J. L. (2019).Dissipation of earthward propagating flux rope through re-reconnection with geomagnetic field: An MMS case study.Journal of Geophysical Research: SpacePhysics,124, 7477–7493. https://doi.org/10.1029/2018JA026451

Pritchard, K. R., Burch, J. L., Fuselier, S.A., Webster, J. M., Torbert, R. B., Argall,M. R., Broll, J., Genestreti, K. J., Giles, B. L., Le Contrel, O., Mukherjee, J., Phan, T. D., Rager, A. C., Russell, C. T., Strangeway, R. J. (2019). Energy conversion and electron acceleration in the magnetopause reconnection diffusion region. Geophysical Research Letters, 46, 10,274-10,282. https://doi.org/10.1029/2019GL084636

Roberts, O. W, Y. Narita, R. Nakamura, Z. Vörös and D. Gershman (2019), Anisotropy of the Spectral Index in Ion Scale Compressible Turbulence: MMS Observations in the Magnetosheath, Front. Phys., 20. https://doi.org/10.3389/fphy.2019.00184

Rogers, A. J., Farrugia, C. J., and Torbert, R. B. (2019), Numerical algorithm for detecting ion diffusion regions in the geomagnetic tail with applications to MMS tail season 1 May to 30 September 2017, Journal of Geophysical Research: Space Physics,124, 6487–6503. https://doi.org/10.1029/2018JA026429

Schmid, D., Volwerk, M., Plaschke, F., Nakamura, R., Baumjohann, W., Wang, G., Wu, M. Y., Zhang, T. L. (2019). A statistical study on the properties of dips ahead of dipolarization fronts observed by MMS. Journal of Geophysical Research: Space Physics, 124, 139–150. https://doi.org/10.1029/2018JA026062

Sharma Pyakurel, P., Shay, M. A., Phan, T. D., Matthaeus, W. H., Drake, J. F., TenBarge, J. M., ... and Chasapis, A. (2019). Transition from ion-coupled to electron-only reconnection: Basic physics and implications for plasma turbulence. *Physics of plasmas*, *26*(8), 082307. https://doi.org/10.1063/1.5090403

Shuster, J. R., D. J. Gershman, L.-J. Chen, S. Wang, N. Bessho, J. C. Dorelli, D. E. da Silva, B. L. Giles, W. R. Paterson, R. E. Denton, S. J. Schwartz, C. Norgren, F. D. Wilder, P. A. Cassak, M. Swisdak, V. Uritsky, C. Schiff, A. C. Rager, S. Smith, L. A. Avanov, and A. F. Viñas (2019), MMS measurements of the Vlasov equation: Probing the electron pressure divergence within thin current sheets, Geophys. Res. Lett., 46, 7862-7872. https://doi.org/10.1029/2019GL083549

Sitnov, M., Birn, J., Ferdousi, B. Gordeev, E., Khotyaintsev, Y., Merkin, V., Motoba, T., Otto, A., Panov, E., Pritchett, P., Pucci, F., Raeder, J., Runov, A., Sergeev, V., Velli, M., Zhou, X. (2019), Explosive Magnetotail Activity, Space Sci. Rev., 215: 31. https://doi.org/10.1007/s11214-019-0599-5

Sitnov, M., Birn, J., Ferdousi, B., Gordeev, E., Khotyaintsev, Y., Merkin, V., ... and Zhou, X. (2019). Explosive magnetotail activity. *Space science reviews*, *215*(4), 1-95. https://doi.org/10.1007/s11214-019-0599-5

Starkey, M. J., Fuselier, S. A., Desai, M. I., Burch, J. L., Gomez, R. G., Mukherjee, J., et al. (2019). Acceleration of interstellar pickup He+ at Earth's perpendicular bow shock. Geophysical Research Letters, 46, 10,735–10,743. https://doi.org/10.1029/2019GL084198

Stawarz, J. E., J. P. Eastwood, T. D. Phan, I. L. Gingell, M. A. Shay, J. L. Burch, R. E. Ergun, B. L. Giles, D. J. Gershman, O. Le Contel, P.-A. Lindqvist, C. T. Russell, R. J. Strangeway, R. B. Torbert, M. R. Argall, D. Fischer, W. Magnes, and L. Franci (2019), Properties of the Turbulence Associated with Electron-only Magnetic Reconnection in Earth's Magnetosheath, The Astrophysical Journal Letters, 877(2). https://doi.org/10.3847/2041-8213/ab21c8

Steinvall, K., Khotyaintsev, Y. V., Graham, D. B., Vaivads, A., Lindqvist, P.-A., Russell, C. T., and Burch, J. L. (2019). Multispacecraft analysis of electron holes. Geophysical Research Letters, 46, 55–63. https://doi.org/10.1029/2018GL080757

Steinvall, K., Khotyaintsev, Y. V., Graham, D. B., Vaivads, A., Le Contel, O., and Russell, C. T. (2019). Observations of electromagnetic electron holes and evidence of Cherenkov whistler emission. *Physical Review Letters*, *123*(25), 255101. https://doi.org/10.1103/PhysRevLett.123.255101

Sun, W. J., Slavin, J. A., Tian, A. M.,Bai, S. C., Poh, G. K., Akhavan-Tafti, M., Lu, S., Yao, S. T., Le, G., Nakamura, R., Giles, B. L., Burch, J. L. (2019). MMS study of the structure of ion-scale flux ropes in the Earth's cross-tail current sheet. Geophysical Research Letters,46, 6168–6177. https://doi.org/10.1029/2019GL083301

Tenfjord, P., Hesse, M., Norgren, C., Spinnangr, S. F., and Kolstø, H. (2019). The impact of oxygen on the reconnection rate. Geophysical Research Letters, 46, 6195– 6203. https://doi.org/10.1029/2019GL082175

Toledo-Redondo, S., Lavraud, B., Fuselier, S. A., André, M., Khotyaintsev, Y. V., Nakamura, N., et al. (2019). Electrostatic spacecraft potential structure and wake formation effects for characterization of cold ion beams in the Earth's magnetosphere. Journal of Geophysical Research: Space Physics, 124, https://doi.org/10.1029/2019JA027145

Torkar, K., R. Nakamura, S. Wellenzohn, H. Jeszenszky, R. B. Torbert, Lindqvist, P.-A., Ergun, R. E., Giles, B. L. (2019), Improved Determination of Plasma Density Based on Spacecraft Potential of the Magnetospheric Multiscale Mission Under Active Potential Control, IEEE Transactions on Plasma Science, 47(8). https://doi.org/10.1109/TPS.2019.2911425

Vines, S. K., Allen, R. C., Anderson, B. J., Engebretson, M. J., Fuselier, S. A., Russell, C. T., Strangeway, R. J., Ergun, R. E., Lindqvist, P. A., Torbert, R. B., Burch, J. L. (2019). EMIC waves in the outer magnetosphere: Observations of an off-equator source region. Geophysical Research Letters, 46, 5707–5716. https://doi.org/10.1029/2019GL082152

Vörös, Z., Yordanova, E., Graham, D. B., Khotyaintsev, Y. V., and Narita, Y. (2019), MMS observations of whistler and lower hybrid drift waves associated with magnetic reconnection in the turbulent magnetosheath, Journal of Geophysical Research: Space Physics,124, 8551-8563. https://doi.org/10.1029/2019JA027028

Wang, S., Chen, L.-J., Bessho, N., Hesse, M., Wilson, L. B., III, Giles, B., Moore, T. E., Russell, C. T., Torbert, R. B., Burch, J. L. (2019). Observational evidence of magnetic reconnection in the terrestrial bow shock transition region. Geophysical Research Letters, 46, 562–570. https://doi.org/10.1029/2018GL080944

Wang, S., Chen, L.-J., Bessho, N., Hesse, M., Giles, B. L., and Moore, T. E. (2019). Ion behaviors in the reconnection diffusion region of a corrugated magnetotail current sheet. Geophysical Research Letters, 46, 5014– 5020. https://doi.org/10.1029/2019GL082226

Watanabe, K., Keika, K., Hoshino, M., Kitamura, N., Saito, Y., Giles, B. L., and Paterson, W. R. (2019). Statistical study on electron and ion temperatures in the near-Earth reconnection and magnetic pileup regions. *Geophysical Research Letters*, *46*, 14,223–14,229. https://doi.org/10.1029/2019GL084837

Wetherton, B. A., Egedal, J., Lê, A., and Daughton, W. S. (2019). Validation of anisotropic electron fluid closure through in situ spacecraft observations of magnetic reconnection. Geophysical Research Letters, 46, 6223–6229. https://doi.org/10.1029/2019GL083119

Wilder, F. D., Ergun, R. E., Hoilijoki, S., Webster, J., Argall, M. R., Ahmadi, N., et al. (2019), A survey of plasma waves appearing near dayside magnetopause electron diffusion region events, Journal of Geophysical Research: Space Physics, 124, 7837–7849 https://doi.org/10.1029/2019JA027060

Williams, T., Palmer, E., Hollister, J., Godine, D., Ottenstein, N., and Burns, R. (2019, August). Lunisolar Perturbations of High-Eccentricity Orbits such as the Magnetospheric Multiscale Mission. In *AAS/AIAA Astrodynamics Specialist Conference* (No. AAS 19-914), Portland, ME. https://ntrs.nasa.gov/api/citations/20190029165/downloads/20190029165.pdf

Williams, T., Palmer, E., Godine, D., Hollister, J., Ottenstein, N., & Vint, B. (2019, August). MMS Extended Mission Eclipse Mitigation and Solar Wind Turbulence Science Campaign. In AAS/AIAA Astrodynamics Specialist Conference, Portland, ME.

Wilson, L. B., Chen, L. J., Wang, S., Schwartz, S. J., Turner, D. L., Stevens, M. L., ... & Goodrich, K. A. (2019). Electron energy partition across interplanetary shocks. II. Statistics. The Astrophysical Journal Supplement Series, 243(1), 8. https://doi.org/10.3847/1538-4365/ab22bd

Wilson, L. B., Chen, L. J., Wang, S., Schwartz, S. J., Turner, D. L., Stevens, M. L., ... and Goodrich, K. A. (2019). Electron energy partition across interplanetary shocks. II. Statistics. *The Astrophysical Journal Supplement Series*, *245*(2), 24. https://doi.org/10.3847/1538-4365/ab5445

2018

Ahmadi, N., Wilder, F. D., Ergun, R. E., Argall, M., Usanova, M. E., Breuillard, H., Malaspina, D., Paulson, K., Germaschewski, K., Eriksson, S., Goodrich, K., Torbert, R., Le Contel, O., Strangeway, R. J., Russell, C. T., Burch, J., Giles, B. (2018). Generation of electron whistler waves at the mirror mode magnetic holes: MMS observations and PIC simulation. Journal of Geophysical Research: Space Physics,123, 6383–6393.https://doi.org/10.1029/2018JA025452

Akhavan-Tafti, M., Slavin, J. A., Le, G., Eastwood, J. P., Strangeway, R. J., Russell, C. T., Nakamure, R., Baumjohann, W., Torbert, R. B., Giles, B. L., Gershmann, D. J., Burch J. L. (2018). MMS examination of

FTEs at the Earth's subsolar magnetopause. Journal of Geophysical Research: Space Physics, 123, 1224–1241. https://doi.org/10.1002/2017JA024681

Alm, L., Farrugia, C. J., Paulson, K. W., Argall, M. R., Torbert, R. B., Burch, J. L.,...Giles, B. L. (2018). Differing properties of two ion-scale magnetopause fluxropes. Journal of Geophysical Research: Space Physics,123, 114–131. https://doi.org/10.1002/2017JA024525

Alm, L., André. M., Vaivads, A., Khotyaintsev, Y. V., Torbert, R. B., and Burch, J. L. (2018). Magnetotail Hall physics in the presence of cold ions. Geophysical Research Letters, 45, 10,941–10,950. https://doi.org/10.1029/2018GL079857

Andriopoulou, M., Nakamura, R., Wellenzohn, S., Torkar, K., Baumjohann, W., Torbert, R. B., Lindqvist, P.-A., Khotyaintsev, Y., Dorelli, J., Burch, J. L. (2018). Plasma density estimates from spacecraft potential using MMS observations in the dayside magnetosphere. Journal of Geophysical Research: SpacePhysics, 123, 2620–2629. https://doi.org/10.1002/2017JA025086

Argall, M. R., Paulson, K., Alm, L., Rager, A., Dorelli, J., Shuster, J., Ahmadi, N. (2018). Electron dynamics within the electron diffusion region of asymmetric reconnection. Journal of Geophysical Research: Space Physics,123, 146–162.https://doi.org/10.1002/2017JA024524

Artemyev, A. V., Pritchett, P. L., Angelopoulos, V., Zhang, X.-J., Nakamura, R., Lu, S., Runov, A., Fuselier, S. A., Wellenzohn, S., Plaschke, F., Russell, C. T., Strangeway, R. J., Lindqvist, P.-A., Ergun, R. E. (2018). Field-aligned currents originating from the magnetic reconnection region: Conjugate MMS-ARTEMIS observations. Geophysical Research Letters,45, 5836–5844. https://doi.org/10.1029/2018GL078206

Bandyopadhyay, R., Chasapis, A., Chhiber, R., Parashar, T. N., Matthaeus, W. H., Shay, M. A., ... and Strangeway, R. J. (2018). Incompressive energy transfer in the earth's magnetosheath: magnetospheric multiscale observations. *The Astrophysical Journal*, *866*(2), 106. https://doi.org/10.3847/1538-4357/aade04

Bandyopadhyay, R., A. Chasapis, R. Chhiber, T. N. Parashar, B. A. Maruca, W. H. Matthaeus, S. J. Schwartz, S. Eriksson, O. Le Contel, H. Breuillard, J. L. Burch, T. E. Moore, C. J. Pollock, B. L. Giles, W. R. Paterson, J. Dorelli, D. J. Gershman, R. B. Torbert, C. T. Russell, and R. J. Strangeway (2018), Solar Wind Turbulence Studies Using MMS Fast Plasma Investigation Data, The Astrophysical Journal, Volume 866, Number 2. http://doi.org/10.3847/1538-4357/AADE93

Bessho, N., Chen, L.-J., Wang, S., and Hesse, M. (2018). Effect of the reconnection electric field on electron distribution functions in the diffusion region of magnetotail reconnection. Geophysical Research Letters, 45, 12,142–12, 152. https://doi.org/10.1029/2018GL081216

Birn, J., V. G. Merkin, M. I. Sitnov, and A. Otto (2018), MHD Stability of Magnetotail Configurations With a Bz Hump, J. Geophys. Res.: Space Physics, 123. https://doi.org/10.1029/2018JA025290

Breuillard, H., O. Le Contel, M. Berthomier, S.Y. Huang, A. Retino, R. Nakamura, W. Baumjohann, G. Cozzani, F. Catapano, A. Alexandrova, L. Mirioni, T. Chust, D. B. Graham, M. R. Argall, D. Fischer, F. D. Wilder, D. J. Gershman, A. Varsani, P.-A. Lindqvist, Yu. V. Khotyaintsev, C. Norgren, G. Marklund, R. E. Ergun, K. A. Goodrich, J. L. Burch, R. B. Torbert, J. Needell, M. Chutter, D. Rau, I. Dors, C. T. Russell, W. Magnes, R. J. Strangeway, K. R. Bromund, H. Wei, F. Plaschke, B. J. Anderson, G. Le, T. E. Moore, B. L. Giles, W. R. Paterson, C. J. Pollock, J. C. Dorelli, L. A. Avanov, Y. Saito, B. Lavraud, S. A. Fuselier, B. H. Mauk, I. J. Cohen, D. L. Turner, J. F. Fennell (2018), The properties of lion roars and electron dynamics in mirror-mode waves observed by the Magnetospheric MultiScale mission, *J. Geophys. Res., 123,* 93-103. https://doi.org/10.1002/2017JA024551

Breuillard, H., Matteini, L., Argall, M.R., Sahraoui, F., Andriopoulou, M., Contel, O.L., Retinò, A., Mirioni, L., Huang, S.Y., Gershman, D.J., Ergun, R.E., Wilder, F.D., Goodrich, K.A., Ahmadi, N., Yordanova, E., Vaivads, A., Turner, D.L., Khotyaintsev, Y.V., Graham, D.B., Lindqvist, P.A., Chasapis, A.G., Burch, J.L., Torbert, R.B., Russell, C.T., Magnes, W., Strangeway, R.J., Plaschke, F., Moore, T.E.,

Giles, B.L., Paterson, W.R., Pollock, C.J., Lavraud, B., Fuselier, S.A., and Cohen, I.J. (2018). New Insights into the Nature of Turbulence in the Earth's Magnetosheath Using Magnetospheric MultiScale Mission Data, The Astrophysical Journal, 859 (2). http://doi.org/10.3847/1538-4357/AABAE8

Broll, J. M., Fuselier, S. A., Trattner, K. J., Schwartz, S. J., Burch, J. L., Giles, B. L.,and Anderson, B. J. (2018). MMS observation of shock-reflected He++at Earth's quasi-perpendicular bow shock. Geophysical Research Letters,45, 49–55. https://doi.org/10.1002/2017GL075411

Burch, J. L., Ergun, R. E., Cassak, P. A., Webster, J. M., Torbert, R. B., Giles, B. L., Dorelli, J. C., Rager, A. C., Hwang, K.-J., Phan, T. D., Genestreti, K. J., Allen, R. C., Chen, L.-J., Wang, S., Gershman, D., LE Contel, O., Russell, C. T., Strangeway, R. J., Wilder, F. D., Graham, D. B., Hesse, M., Drake, J. F., Swisdak, M., Price, L. M., Shay, M. A., Lindqvist, P.-A., Pollock, C. J., Renton, R. E., Newman, D. L. (2018). Localized oscillatory energy conversion in magnetopause reconnection. Geophysical Research Letters,45,1237–1245. https://doi.org/10.1002/2017GL076809

Burch, J. L., J. M. Webster, K. J. Genestreti, R. B. Torbert, B. L. Giles, S. A. Fuselier, J. C. Dorelli, A. C. Rager, T. D. Phan, R. C. Allen, L.-J. Chen, S. Wang, O. Le Contel, C. T. Russell, R. J. Strangeway, R. E. Ergun, A. N. Jaynes, P.-A. Lindqvist, D. B. Graham, F. D. Wilder, K.-J. Hwang, J. Goldstein (2018). Wave phenomena and beam-plasma interactions at the magnetopause reconnection region. Journal of Geophysical Research: Space Physics,123,1118–1133. https://doi.org/10.1002/2017JA024789

Chasapis, A., Y. Yang, W. H. Matthaeus, T. N. Parashar, C. C. Haggerty, J. L. Burch, T. E. Moore, C. J. Pollock, J. Dorelli, D. J. Gershman, R. B. Torbert, and C. T. Russell (2018), Energy Conversion and Collisionless Plasma Dissipation Channels in the Turbulent Magnetosheath Observed by the Magnetospheric Multiscale Mission, The American Astronomical Society. All rights reserved. The Astrophysical Journal, 862 (1). http://doi.org/10.3847/1538-4357/AAC775

Chasapis, A., W. H. Matthaeus, T. N. Parashar, M. Wan, C. C. Haggerty, C. J. Pollock, B. L. Giles, W. R. Paterson, J. Dorelli, D. J. Gershman, R. B. Torbert, C. T. Russell, P.-A. Lindqvist, Y. Khotyaintsev, T. E. Moore, R. E. Ergun, and J. L. Burch (2018), In Situ Observation of Intermittent Dissipation at Kinetic Scales in the Earth's Magnetosheath, The Astrophysical Journal Letters, 856(1). http://doi.org/10.3847/2041-8213/AAADF8

Chen, L. J., S. Wang,L. B. Wilson III,S. Schwartz,N. Bessho, T. Moore, D. Gershman, B. Giles, D. Malaspina, F. D. Wilder,R. E. Ergun,M. Hesse, H. Lai,C. Russell, R. Strangeway,R. B. Torbert,A. F.-Vinas,J. Burch,S. Lee,C. Pollock,J. Dorelli, W. Paterson,N. Ahmadi,K. Goodrich,B. Lavraud,O. Le Contel,Yu. V. Khotyaintsev,P.-A. Lindqvist, S. Boardsen, H. Wei,A. Le,and L. Avanov (2018), Electron Bulk Acceleration and Thermalization at Earth's Quasiperpendicular Bow Shock, Phys. Rev. Lett. 120, 225101. http://doi.org/10.1103/PhysRevLett.120.225101

Chhiber, R., Chasapis, A., Bandyopadhyay, R., Parashar, T. N., Matthaeus, W. H., Maruca, B. A., Moore, T. E, Burch, J. L., Torbert, R. B., Russell, C. T., Le Contel, O., Argall, M. R., Fischer, D., Mirioni, L., Strangeway, R. J., Pollock, C. J., Giles, B. L., Gershman, D. J. (2018). Higher-order turbulence statistics in the Earth's magnetosheath and the solar wind using Magnetospheric Multiscale observations. Journal of Geophysical Research: Space Physics, 123, 9941–9954. https://doi.org/10.1029/2018JA025768

Denton, R. E., Sonnerup, B. U. Ö., Russell, C. T., Hasegawa, H., Phan, T.-D., Strangeway, R. J., Giles, B. L., Ergun, R. E., Lindqvist, P.-A., Torbert, R. B., Burch, J. L., Vines, S. K. (2018). Determining L-M-N current sheet coordinates at the magnetopause from Magnetospheric Multiscaledata. Journal of Geophysical Research: Space Physics, 123, 2274–2295. https://doi.org/10.1002/2017JA024619

Eastwood, J. P., Mistry, R., Phan, T. D., Schwartz, S. J., Ergun, R. E., Drake, J. F., Øieroset, M., Stawarz, J. E., Goldman, M. V., Haggerty, C., Shay, M. A., Burch, J. L., Gershman, D. J., Giles, B. L., Lindqvist, P. A., Torbert, R. B., Strangeway, R. J., Russell, C. T. (2018). Guide field reconnection: Exhaust structure and heating. Geophysical Research Letters, 45, 4569–4577. https://doi.org/10.1029/2018GL077670

Ergun, R. E., Goodrich, K. A., Wilder, F. D., Ahmadi, N., Holmes, J. C., Eriksson, S., Stawarz, J. E., Nakamura, R., Genestreti, K. J., Hesse, M., Burch, Torbert, R. B., Phan, T. D., Schwartz, S. J., Eastwood, J. P., Strangeway, R. J., Le Contel, O., Russell, C. T., Argall, M. R., Lindqvist, P.-V., Chen, L. J., Cassak, P. A., Giles, B. L., Dorelli, J. C., Gershman, D., Leonard, T. W., Lavraud, B., Retino, A., Matthaeus, W., Vaivads, A. (2018). Magnetic reconnection, turbulence, and particle acceleration: Observations in the Earth's magnetotail. Geophysical Research Letters,45,3338–3347. https://doi.org/10.1002/2018GL076993

Eriksson, E., Vaivads, A., Graham, D. B., Divin, A., Khotyaintsev, Y. V., Yordanova, E., Andre, M., Giles, B. L., Pollock, C. J., Russell, C. T., Le Contel, O., Torbert, R. B., Ergun, R. E., Lindqvist, P.-A., Burch, J. L. (2018). Electron energization at a reconnecting magnetosheath current sheet. Geophysical Research Letters,45, 8081–8090. https://doi.org/10.1029/2018GL078660

Farrugia, C. J., I. J. Cohen, B. J. Vasquez, N. Lugaz, L. Alm, R. B. Torbert, M. R. Argall, K. Paulson, B. Lavraud, D. J. Gershman, F. T. Gratton, H. Matsui, A. Rogers, T. Forbes, D. Payne, R. E. Ergun, B. Mauk, J. L. Burch, C. T. Russell, R. J. Strangeway, S. Shuster, R. Nakamura, S. A. Fuselier, B. L. Giles, T. D. Phan, Y. V. Khotyaintsev, P. A. Lindqvist, G. T. Marklund, J. P.Eastwood, S. M. Petrinec, and C. J. Pollock (2018), Effects in the near-Magnetopause Magnetosheath Elicited by Large-Amplitude Alfvenic Fluctuations Terminating in a Field and Flow Discontinuity, J. Geophys. Res., 123, 8983-9004. https://doi.org/10.1029/2018JA025724

Fuselier, S. A., Petrinec, S. M., Trattner, K. J., Broll, J. M., Burch, J. L., Giles, B. L., Strangeway, R. J., Russell, C. T., Lavraud, B., Øieroset, M., Torbert, R. B., Farrugia, C. J., Vines, S. K., Gomez, R. G., Muhherjee, J., Cassak, P. A. (2018). Observational evidence of large-scale multiple reconnection at the Earth's dayside magnetopause. Journal of Geophysical Research: Space Physics,123, 8407–8421. https://doi.org/10.1029/2018JA025681

Genestreti, K. J., Varsani, A., Burch, J. L., Cassak, P. A., Torbert, R. B., Nakamura, R., Ergun, R. E., Phan, T.-D., Toledo-Redondo, S., Hesse, M., Wang, S., Giles, B. L., Russell, C. T., Voros, Z., Hwang, K.-J., Eastwood, J. P., Lavraud, B., Escoubet, C. P., Fear, R. C., Khotyaintsev, Y., Nakamura, T. K. M., Webster, J. M., Baumjohann, W. (2018). MMS observation of asymmetric reconnection supported by 3-D electron pressure divergence. Journal of Geophysical Research: Space Physics, 123, 1806–1821. https://doi.org/10.1002/2017JA025019

Genestreti, K. J., Cassak, P. A., Varsani, A., Burch, J. L., Nakamura, R., and Wang, S. (2018). Assessing thetime dependence of reconnection with Poynting's theorem: MMS observations. Geophysical Research Letters,45, 2886–2892. https://doi.org/10.1002/2017GL076808

Genestreti, K. J., Nakamura, T. K. M., Nakamura, R., Denton, R. E., Torbert, R. B., Burch, J. L., Plaschke, F., Fuselier, S. A., Ergun, R. E., Giles, B. L., Russell, C. T. (2018). How accurately can we measure the reconnection rate E_M for the MMS diffusion region event of 11 July2017?. Journal of Geophysical Research: Space Physics,123, 9130–9149. https://doi.org/10.1029/2018JA025711

Gershman. D. J., Adolfo F.-Viñas, John C. Dorelli, Melvyn L. Goldstein, Jason Shuster, Levon A. Avanov, Scott A. Boardsen, Julia E. Stawarz, Steven J. Schwartz, Conrad Schiff, Benoit Lavraud, Yoshifumi Saito, William R. Paterson, Barbara L. Giles, Craig J. Pollock, Robert J. Strangeway, Christopher T. Russell, Roy B. Torbert, Thomas E. Moore, and James L. Burch (2018), Energy partitioning constraints at kinetic scales in low-β turbulence, Phys. Plasmas 25, 022303. https://doi.org/10.1063/1.5009158

Goodrich, K. A., Ergun, R.,Schwartz, S. J., Wilson, L. B. III., Newman, D., Wilder, F. D., Holmes, J., Johlander, A., Burch, J., Torbert, Khotyaintsev, Y., Lindqvist, P.-A., Strangeway, R., Russell, C., Gershman, D., Giles, B., Andersson, L. (2018). MMS observations of electrostatic waves in an oblique shock crossing. Journal of Geophysical Research: Space Physics,123, 9430–9442. https://doi.org/10.1029/2018JA025830

Graham, D. B., Vaivads, A., Khotyaintsev, Y. V., Eriksson, A. I., André, M., Malaspina, D. M., et al. (2018). Enhanced escape of spacecraft photoelectrons caused by Langmuir and upper hybrid waves. Journal of Geophysical Research: Space Physics, 123, 7534– 7553. https://doi.org/10.1029/2018JA025874

Graham, D. B., Vaivads, A., Khotyaintsev, Y. V., André, M., Le Contel, O., Malaspina, D. M., Lindqvist, P.-A., Wilder, F. D., Ergun, R. E., Gershman, D. J., Giles, B. L., Magnes, W., Russell, C. T., Burch, J. L., Torbert, R. B. (2018). Large-amplitude high-frequency waves at Earth's magnetopause. Journal of Geophysical Research: SpacePhysics,123, 2630–2657. https://doi.org/10.1002/2017JA025034

Hesse, M., Y.-H. Liu, L.-J. Chen, N. Bessho, S. Wang, J. L. Burch, T. Moretto, C. Norgren, K. J. Genestreti, T. D. Phan, and P. Tenfjord (2018), The physical foundation of the reconnection electric field, Phys. Plasmas 25, 032901. https://doi.org/10.1063/1.5021461

Hesse, M., C. Norgren, P. Tenfjord, J. Burch, Y-H. Liu, L.-J. Chen, N. Bessho, S. Wang, R. Nakamura, J. Eastwood, M. Hoshino, R. Torbert, and R. Ergun (2018), On the Role of Separatrix Instabilities in Heating the Reconnection Outflow Region, Physics of Plasmas, 25, 122902. https://doi.org/10.1063/1.5054100

Holmes, J. C., Ergun, R. E., Newman, D. L., Wilder, F. D., Sturner, A. P., Goodrich, K. A.,... Burch, J. L. (2018). Negative potential solitary structures in the magnetosheath with large parallel width. Journal of Geophysical Research: Space Physics,123, 132–145. https://doi.org/10.1002/2017JA024890

Holmes, J. C., Ergun, R. E., Newman, D. L., Ahmadi, N., Andersson, L., LeContel, O., Torbert, R. B., Giles, B. L., Strangeway, R. J., Burch, J. L. (2018). Electron phase-space holes in three dimensions: Multispacecraft observations by Magnetospheric Multiscale. Journal of Geophysical Research: Space Physics, 123, 9963– 9978. https://doi.org/10.1029/2018JA025750

Johlander, A., Andris Vaivads, Yuri V Khotyaintsev, Imogen Gingell, Steven J Schwartz, Barbara L Giles, Roy B Torbert and Christopher T Russell (2018), Shock ripples observed by the MMS spacecraft: ion reflection and dispersive properties, Plasma Physics and Controlled Fusion, 60(12). http://doi.org/10.1088/1361-6587/AAE920

Kacem, I., C. Jacquey, V. Génot, B. Lavraud, Y. Vernisse, A. Marchaudon, O. Le Contel, H. Breuillard, T. D. Phan, H. Hasegawa, M. Oka, K. J. Trattner, C. J. Farrugia, K. Paulson, J. P. Eastwood, S. A. Fuselier, D. Turner, S. Eriksson, F. Wilder, C. T. Russell, M. Øieroset, J. Burch, D. B. Graham, J.-A. Sauvaud, L. Avanov, M. Chandler, V. Coffey, J. Dorelli, D. J. Gershman, B. L. Giles, T. E. Moore, Y. Saito, L.-J. Chen, and E. Penou (2018). Magnetic reconnection at a thin current sheet separating two interlaced flux tubes at the Earth's magnetopause. Journal of Geophysical Research: SpacePhysics, 123, 1779–1793. https://doi.org/10.1002/2017JA024537

Karlsson, T., Plaschke, F., Hietala, H., Archer, M., Blanco-Cano, X., Kajdič, P., ... and Gershman, D. J. (2018, April). Investigating the anatomy of magnetosheath jets–MMS observations. In *Annales geophysicae* (Vol. 36, No. 2, pp. 655-677). Copernicus GmbH. https://doi.org/10.5194/angeo-36-655-2018

Kavosi, S., Spence, H. E., Fennell, J. F., Turner, D. L., Connor, H. K., and Raeder, J. (2018). MMS/FEEPS observations of electron microinjections due to Kelvin-Helmholtz waves and flux transfer events: A case study. Journal of Geophysical Research: Space Physics, 123, 5364– 5378. https://doi.org/10.1029/2018JA025244

Kitamura, N., M. Kitahara, M. Shoji, Y. Miyoshi, H. Hasegawa, S. Nakamura, Y. Katoh, Y. Saito, S. Yokota, D. J. Gershman, A. F. Vinas, B. L. Giles, T. E. Moore, W. R. Paterson, C. J. Pollock, C. T. Russell, R. J. Strangeway, S. A. Fuselier, and J. L. Burch (2018), Direct measurements of two-way wave-particle energy transfer in a collisionless space plasma, Science, 361(6406), 1000-1003. http://doi.org/10.1126/SCIENCE.AAP8730

Lavraud, B., C. Jacquey, T. Achilli, S. A. Fuselier, E. Grigorenko, T. D. Phan, M. Øieroset, J. McFadden, and V. Angelopoulos (2018), Concomitant double ion and electron populations in the Earth's

magnetopause boundary layers from double reconnection with lobe and closed field lines*, J. Geophys. Res., 123,* 5407-5419. https://doi.org/10.1029/2017JA025152

Le, A., W. Daughton, O. Ohia, L. -J. Chen, Y. -H. Liu, S. Wang, W. D. Nystrom and R. Bird (2018), Drift turbulence, Particle transport, and anomalous dissipation at the reconnecting magnetopause, Phys. Plasmas, 25, 062103. https://doi.org/10.1063/1.5027086

Liu, Y.-H., M. Hesse, F. Guo, H. Li and T. K. M. Nakamura (2018), Strongly localized magnetic reconnection by the out-of-plane super-Alfvenic shear flow, Phys. Plasmas, 25, 080701. https://doi.org/10.1063/1.5042539

Liu, Y.-H., Hesse, M., Li, T. C.,Kuznetsova, M., and Le, A. (2018). Orientation and stability of asymmetric magnetic reconnection x-line.Journal of Geophysical Research:Space Physics,123, 4908–4920. https://doi.org/10.1029/2018JA025410

Liu, Y.-H., Hesse, M., Cassak, P. A.,Shay, M. A., Wang, S., and Chen,L.-J. (2018). On the collision-less asymmetric magnetic reconnection rate. GeophysicalResearch Letters, 45, 3311–3318. https://doi.org/10.1002/2017GL076460

Mackler, D., L.bAvanov, A. Barrie, D. Chornay, D. Gershman, B. Giles, C. Pollock, A. Rager, and S. Smith (2018), Microchannel plate lifetime experiment for the DIS and DES instruments on the Magnetospheric Multiscale Mission, Planetary and Space Sci., 161, 92-98. https://doi.org/10.1016/j.pss.2018.05.005

Maruca, B. A., A. Chasapis, S. P. Gary, R. Bandyopadhyay, R. Chhiber, T. N. Parashar, W. H. Matthaeus, M. A. Shay, J. L. Burch, T. E. Moore, C. J. Pollock, B. J. Giles, W. R. Paterson, J. Dorelli, D. J. Gershman, R. B. Torbert, C. T. Russell, and R. J. Strangeway (2018), MMS Observations of Beta-dependent Constraints on Ion Temperature Anisotropy in Earth's Magnetosheath, The Astrophysical Journal, 866(1). http://doi.org/10.3847/1538-4357/AADDFB

Mozer, F. S., O. V. Agapitov, B. Giles, and I. Vasko (2018), Direct Observation of Electron Distributions inside Millisecond Duration Electron Holes, Phys. Rev. Lett. 121, 135102. http://doi.org/10.1103/PHYSREVLETT.121.135102

Nakamura, R., A. Varsani, K. J. Genestreti, O. Le Contel, T. Nakamura, W. Baumjohann, T. Nagai, A. Artemyev, J. Birn, V. A. Sergeev, S. Apatenkov, R. E. Ergun, S. A. Fuselier, D. J. Gershman, B. J. Giles, Y. V. Khotyaintsev, P.-A. Lindqvist, W. Magnes, B. Mauk, A. Petrukovich, C. T. Russell, J. Stawarz, R. J. Strangeway, B. Anderson, J. L. Burch, K. R. Bromund, I. Cohen, D. Fischer, A. Jaynes, L. Kepko, G. Le, F. Plaschke, G. Reeves, H. J. Singer, J. A. Slavin, R. B. Torbert, D. L. Turner (2018). Multiscale currents observed by MMS in the flow braking region. Journal of Geophysical Research: Space Physics,123, 1260–1278. https://doi.org/10.1002/2017JA024686

Nakamura, T. K. M., K. J. Genestreti, Y-H. Liu, R. Nakamura, W. -L. Teh, H. Hasegawa, W. Daughton, M. Hesse, R. B. Tobert, J. L. Burch and B. L. Giles (2018), Measurement of the magnetic reconnection rate in the Earth's magnetotail, Journal of Geophysical Research: Space Physics, 123, 9150–9168. https://doi.org/10.1029/2018JA025713

Nakamura, T. K. M., Nakamura, R., Varsani, A., Genestreti, K. J., Baumjohann, W., and Liu, Y.-H. (2018). Remote sensing of the reconnection electric field from in situ multipoint observations of the separatrix boundary. Geophysical Research Letters,45,3829–3837. https://doi.org/10.1029/2018GL078340

Nakamura, T. K. M., Genestreti, K. J., Liu, Y.-H., Nakamura, R., Teh, W.-L., Hasegawa, H., Daughton, W., Hesse, M., Torbert, R. B., Burch, J. L., Giles, B. L. (2018). Measurement of the magnetic reconnection rate in the Earth's magnetotail. Journal of Geophysical Research: Space Physics, 123, 9150–9168. https://doi.org/10.1029/2018JA025713

Norgren, C., D. B. Graham, Yu. V. Khotyaintsev, M. André, A. Vaivads, M. Hesse, E. Eriksson, P.-A. Lindqvist, B. Lavraud, J. Burch, S. Fuselier, W. Magnes, D. J. Gershman, C. T. Russell (2018), Electron reconnection in the magnetopause current layer, *J. Geophys. Res., 123,* 9222-9238. https://doi.org/10.1029/2018JA025676

Oka, M., Birn, J., Battaglia, M. *et al.* Electron Power-Law Spectra in Solar and Space Plasmas. *Space Sci Rev* **214,** 82 (2018). https://doi.org/10.1007/s11214-018-0515-4

Pan, D.-X., Khotyaintsev, Y. V.,Graham, D. B., Vaivads, A., Zhou, X.-Z.,André, M., Lindqvist, P.-A., Ergun, R. E., Le Contel, O., Russell, C. T., Torbert, R. B., Giles, B., Burch, J. L. (2018). Rippled electron-scale structure of a dipolarization front. Geophysical Research Letters,45, 12,116–12,124.https://doi.org/10.1029/2018GL080826

Parashar, T. N., Matthaeus, W. H., and Shay, M. A. (2018). Dependence of kinetic plasma turbulence on plasma β. *The Astrophysical Journal Letters*, *864*(1), L21. https://doi.org/10.3847/2041-8213/aadb8b

Parashar, T. N., Alexandros Chasapis, Riddhi Bandyopadhyay, Rohit Chhiber, W. H. Matthaeus, B. Maruca, M. A. Shay, J. L. Burch, T. E. Moore, B. L. Giles, D. J. Gershman, C. J. Pollock, R. B. Torbert, C. T. Russell, R. J. Strangeway, and Vadim Roytershteyn (2018), Kinetic Range Spectral Features of Cross Helicity Using the Magnetospheric Multiscale Spacecraft, Phys. Rev. Lett. 121, 265101. http://doi.org/10.1103/PHYSREVLETT.121.265101

Phan, T. D., J. P. Eastwood, M. Shay, J. F. Drake, B. U. Ö. Sonnerup, M. Fujimoto, P. Cassak, M. Øieroset, J. L. Burch, R. Torbert, A. C. Rager, J. C. Dorelli, D. J. Gershman, C. Pollock, P. S. Pyakurel, C. C. Haggerty, Y. Khotyaintsev, B. Lavraud, Y. Saito, M. Oka, R. E. Ergun, A. Retino, O. Le Contel, M. R. Argall, B. L. Giles, T. E. Moore, F. D. Wilder, R. J. Strangeway, C. T. Russell, P. A. Lindqvist, and W, Magnes (2018). Electron magnetic reconnection without ion coupling in Earth's turbulent magnetosheath. Nature. 557. http://doi.org/10.1038/s41586-018-0091-5

Pollock, C.J., J.L. Burch, A. Chasapis, B.L. Giles, D.A. Mackler, W.H. Matthaeus, C.T. Russell (2018), Magnetospheric Multiscale observations of turbulent magnetic and electron velocity fluctuations in Earth's magnetosheath downstream of a quasi-parallel bow shock, J. Atmos. Solar-Terr. Phys., 177, SI, 84-91. http://doi.org/10.1016/j.jastp.2017.12.006

Roberts, O. W., Toledo-Redondo, S., Perrone, D., Zhao, J., Narita, Y., Gershman, D., Nakamura, R., Lavraud, B., Escoubet, C. P., Giles, B., Dorelli, J., Pollock, C., Burch, J. (2018). Ion-scale kinetic Alfvén turbulence: MMS measurements of the Alfvén ratio in the magnetosheath. Geophysical Research Letters,45, 7974–7984. https://doi.org/10.1029/2018GL078498

Schwartz, S. J., L. Avanov, D. Turner, H. Zhang, I. Gingell, J. P. Eastwood, D. J. Gershman, A. Johlander, C. T. Russell, J. L. Burch, J. C. Dorelli, S. Eriksson, R. E. Ergun, S. A. Fuselier, B. L. Giles, K. A. Goodrich, J. T. Gosling, Y. V. Khotyaintsev, B. Lavraud, P.-A. Lindqvist, M. Oka, T. D. Phan, R. J. Strangeway, K. Trattner, R. B. Torbert, A. Vaivads, H. Wei, F. Wilder (2018). Ion kinetics in a hot flow anomaly: MMS observations. Geophysical Research Letters, 45, 11,520–11,529. https://doi.org/10.1029/2018GL080189

Sedlak, J.E. and Vint, B. (2018, August). Change of Inertia Tensor Due to a Severed Radial Boom for Spinning Spacecraft. AAS/AIAA Astrodynamics Specialist Conference, Snowbird, UT. https://ntrs.nasa.gov/api/citations/20180006157/downloads/20180006157.pdf

Shay, M. A., Haggerty, C. C., Matthaeus, W. H., Parashar, T. N., Wan, M., and Wu, P. (2018). Turbulent heating due to magnetic reconnection. *Physics of Plasmas*, *25*(1), 012304. https://doi.org/10.1063/1.4993423

Sonnerup, B. U. Ö., Haaland, S. E., Paschmann, G., and Denton, R. E.(2018). Quality Measure for the Walén Relation. Journal of Geophysical Research: Space Physics,123, 9979–9990. https://doi.org/10.1029/2018JA025677

Stawarz, J. E., J. P. Eastwood, K. J. Genestreti, R. Nakamura, R. E. Ergun, D. Burgess, J. L. Burch, S. A. Fuselier, D. J. Gershman, B. L. Giles, O. Le Contel, P.-A. Lindqvist, C. T. Russell, R. B. Torbert (2018). Intense electric fields and electron-scale substructure within magnetotail flux ropes as revealed by the Magnetospheric Multiscale mission. Geophysical Research Letters,45, 8783–8792. https://doi.org/10.1029/2018GL079095

Sturner, A. P., Eriksson, S., Nakamura, T., Gershman, D. J., Plaschke, F., Ergun, R. E., Wilder, F. D., Giles, B., Pollock, C., Paterson, W. R., Strangeway, R. J., Baumjohann, W., Burch, J. L.(2018). On multiple Hall-like electron currents and tripolar guide magnetic field perturbations during Kelvin-Helmholtz waves. Journal of Geophysical Research: Space Physics, 123, 1305–1324. https://doi.org/10.1002/2017JA024155

Swisdak, M., Drake, J. F., Price, L., Burch, J. L., Cassak, P. A., and Phan, T.-D.(2018). Localized and intense energy conversion in the diffusion region of asymmetric magnetic reconnection. Geophysical Research Letters, 45, 5260–5267. https://doi.org/10.1029/2017GL076862

Tenfjord, P., Hesse, M., and Norgren, C. (2018). The formation of an oxygen wave by magnetic reconnection. Journal of Geophysical Research: Space Physics, 123, 9370– 9380. https://doi.org/10.1029/2018JA026026

Toledo-Redondo, S., Dargent, J., Aunai, N., Lavraud, B., André, M., Li, W., Giles, B., Lindqvist, P.-A., Ergun, R. E., Russell, C. T., Burch, J. L. (2018). Perpendicular current reduction caused by cold ions of ionospheric origin in magnetic reconnection at the magnetopause: Particle-in-cell simulations and spacecraft observations. Geophysical Research Letters,45, 10,033–10,042. https://doi.org/10.1029/2018GL079051

Tong, Y., Vasko, I., Mozer, F. S., Bale, S. D., Roth, I., Artemyev, A. V., et al. (2018). Simultaneous multispacecraft probing of electron phase space holes. Geophysical Research Letters, 45, 11,513–11,519. https://doi.org/10.1029/2018GL079044

Torbert, R. B., J. L. Burch, T. D. Phan, M. Hesse, M. R. Argall, J. Shuster, R. E. Ergun, L. Alm, R. Nakamura, K. J. Genestreti, D. J. Gershman, W. R. Paterson, D. L. Turner, I. Cohen, B. L. Giles, C. J. Pollock, S. Wang, L.-J. Chen, J. E. Stawarz, J. P. Eastwood, K. J. Hwang, C. Farrugia, I. Dors, H. Vaith, C. Mouikis, A. Ardakani, B. H. Mauk, S. A. Fuselier, C. T. Russell, R. J. Strangeway, T. E. Moore, J. F. Drake, M. A. Shay, Yuri V. Khotyaintsev, P.-A. Lindqvist, W. Baumjohann, F. D. Wilder, N. Ahmadi, J. C. Dorelli, L. A. Avanov, M. Oka, D. N. Baker, J. F. Fennell, J. B. Blake, A. N. Jaynes, O. Le Contel, S. M. Petrinec, B. Lavraud, Y. Saito (2018), Electron-scale dynamics of the diffusion region during symmetric magnetic reconnection in space, Science, 362(6421), 1391-1395. http://doi.org/10.1126/science.aat2998

Trattner, K. J., J. L. Burch, P. A. Cassak, R. Ergun, S. Eriksson, S. A. Fuselier, B. L. Giles, R. G. Gomez, E. W. Grimes, S. M. Petrinec, J. M. Webster, and F. D. Wilder (2018), The transition between antiparallel and component magnetic reconnection at Earth's dayside magnetopause, J. Geophys. Res., 123. https://doi.org/10.1029/2018JA026081

Turner, D. L., Wilson, L. B., Liu, T. Z., Cohen, I. J., Schwartz, S. J., Osmane, A., Fennell, J. F., Clemmons, J. H., Blake, J. B., Westlake, J., Mauk, B. H., Jaynes, A. N., Leonard, T., Baker, D. N., Strangeway, R. J., Russell, C. T., Gershman, D. J., Avanov, L., Giles, B. L., Torbert, R. B., Broll, J., Gomez, R. G., Fuselier, S. A., and Burch, J. L. (2018). Autogenous and efficient acceleration of energetic ions upstream of Earth's bow shock. Nature, 561, 206-210. http://doi.org/10.1038/S41586-018-0472-9

Usanova, M. E., N. Ahmadi, D. M. Malaspina, R. E. Ergun, K. J. Trattner, Q. Reece, T. Leonard, O. Le Contel, S. A. Fuselier, R. B. Torbert, C. T. Russell, J. L. Burch (2018). MMS observations of harmonic electromagnetic ion cyclotron waves. Geophysical Research Letters,45,8764–8772. https://doi.org/10.1029/2018GL079006

Wang, S., L.-J. Chen, N. Bessho, M. Hesse, J. Yoo, M. Yamada, Y. -H. Liu, D. Gershman, B. Giles and T. Moore (2018), Energy conversion and partitionin the asymmetric reconnection diffusion region. Journal of Geophysical Research: Space Physics,123, 8185–8205. https://doi.org/10.1029/2018JA025519

Webster, J. M., J. L. Burch, P. H. Reiff, D. B. Graham, R. B. Torbert, R. E. Ergun, A. G. Daou, S. Y. Sazykin, A. Marshall, L-J. Chen, S. Wang, T. D. Phan, K. J. Genestreti, B. L. Giles, T. E. Moore, S. A. Fuselier, G. Cozzani, C. T. Russell, S. Eriksson, A. C. Rager, J. M. Broll, K. Goodrich, and F. Wilder (2018). Magnetospheric Multiscale dayside reconnection electron diffusion region events. Journal of Geophysical Research: Space Physics, 123, 4858–4878. https://doi.org/10.1029/2018JA025245

Wendel, D. E., Liu, Y.-H., Giles, B. L., and Torbert, R. B. (2018). Violation of field line conservation and associated spatial scales in particle-in-cell simulations and MMS data. Journal of Geophysical Research: Space Physics,123, 1853–1884, https://doi.org/10.1002/2017JA024467

Wilder, F. D., Ergun, R. E., Burch, J. L., Ahmadi, N., Eriksson, S., Phan, T. D., Goodrich, K. A., Shuster, J., Rager, A. C., Torbert, R. B., Giles, B. L., Strangeway, R. J., Plaschke, F., Magnes, W. (2018). The role of the parallel electric field in electron-scale dissipation at reconnecting currents in the magnetosheath. Journal of Geophysical Research: Space Physics,123, 6533–6547. https://doi.org/10.1029/2018JA025529

Williams, T., Godine, D., Palmer, E., Patel, I., Ottenstein, N., Winternitz, L., and Petrinec, S. (2018, August). MMS Extended Mission Design: Evaluation of a Lunar Gravity Assist Option. Paper AAS 18-250, AAS/AIAA Astrodynamics Specialist Conference, Snowbird, UT. https://ntrs.nasa.gov/api/citations/20180006445/downloads/20180006445.pdf

Yamada, M., L.-J. Chen, J. Yo, S. Wang, W. Fox, J. Jara-Almonte, H. Ji, W. Daughton, A. Le, J. Burch, B. Giles, M. Hesse, T. Mooreand R. Torbert (2018), The two-fluid dynamics and energetics of the asymmetric magnetic reconnection in laboratory and space plasmas, Nature Communications, volume 9, Article number: 5223. https://doi.org/10.1038/s41467-018-07680-2

Yoo, J., Jara-Almonte, J., Yerger, E., Wang, S., Qian, T., Le, A., et al. (2018). Whistler wave generation by anisotropic tail electrons during asymmetric magnetic reconnection in space and laboratory. Geophysical Research Letters, 45, 8054– 8061. https://doi.org/10.1029/2018GL079278

2017

Allen, R. C., S. A. Livi, S. K. Vines, J. Goldstein, I. Cohen, S. A. Fuselier, B. H. Mauk, and H. E. Spence (2017), Storm time empirical model of O+ and O6+ distributions in the magnetosphere, J. Geophys. Res. Space Physics,122,8353–8374. http://doi.org/10.1002/2017JA024245

Alm, L., Argall, M. R., Torbert, R. B., Farrugia, C. J., Burch, J. L., Ergun, R. E., Russell, C. T., Strangeway, R. J., Khotyaintsev, Y., Lindqvist, P.-A., Marklund, G. T., Giles, B. L., Shuster, J. (2017), EDR signatures observed by MMS in the 16 October event presented in a 2-D parametric space, J. Geophys. Res. Space Physics,122, 3262–3276. http://doi.org/10.1002/2016JA023788

Barrie, A. C., S. E. Smith, J. C. Dorelli, D. J. Gershman, P. Yeh, C. Schiff, and L. A. Avanov (2017), Performance of a space-based wavelet compressor for plasma count data on the MMS Fast Plasma Investigation, J. Geophys. Res. Space Physics, 122, 765–779, http://doi.org/10.1002/2016JA022645

Bessho, N., L.-J. Chen, M. Hesse, and S. Wang (2017), The effect of reconnection electric field on crescent and U-shaped distribution functions in asymmetric reconnection with no guide field, Physics of Plasmas 24 (7), 072903. https://doi.org/10.1063/1.4989737

Birn, J., A. Runov, and X.-Z. Zhou (2017), Ion Velocity Distributions in Dipolarization Events: Distributions in the Central Plasma Sheet, J. Geophys. Res., 122, 8014-8025. https://doi.org/10.1002/2017JA024230

Birn, J., M. Chandler, T. Moore, and A. Runov (2017), Ion Velocity Distributions in Dipolarization Events: Beams in the Vicinity of the Plasma Sheet Boundary, J. Geophys. Res., 122, 8026-8036. https://doi.org/10.1002/2017JA024231

Broll, J. M., S. A. Fuselier, and K. J. Trattner (2017), Locating dayside magnetopause reconnection with exhaust ion distributions, *J. Geophys. Res., 122,* 5105-5113. http://doi.org/10.1002/2016JA023590

Cassak, P. A. K. J. Genestreti, J. L. Burch, T.-D. Phan, M. A. Shay, M. Swisdak, J. F. Drake, L. Price, S. Eriksson, R. E. Ergun, B. J. Anderson, V. G. Merkin and C. M. Komar (2017), The effect of a guide field on local energy conversion during asymmetric magnetic reconnection: Particle-in-cell simulations. Journal of Geophysical Research: Space Physics, 122, 11,523–11,542. https://doi.org/10.1002/2017JA024555

Cassak, P. A., Y. -H. Liu and M. A. Shay (2017), A review of the 0.1 reconnection rate problem, J. Plasma Phys. 83, 715830501. https://doi.org/10.1017/S0022377817000666

Catapano, F., Zimbardo, G., Perri, S., Greco, A., Delcourt, D., Retino, A., & Cohen, I. J. (2017). Charge proportional and weakly mass-dependent acceleration of different ion species in the Earth's magnetotail. Geophysical Research Letters, 44, 10,108– 10,115. https://doi.org/10.1002/2017GL075092

Chasapis, A., W. H. Matthaeus, T. N. Parashar, O. LeContel, A. Retinò, H. Breuillard, Y. Khotyaintsev, A. Vaivads, B. Lavraud, E. Eriksson, et. al. (2017), Electron Heating at Kinetic Scales in Magnetosheath Turbulence, The Astrophysical Journal, 836(2). http://doi.org/10.3847/1538-4357/836/2/247

Chasapis, A., W. H. Matthaeus, T. N. Parashar, S. A. Fuselier, B. A. Maruca, T. D. Phan, J. L. Burch, T. E. Moore, C. J. Pollock, D. J. Gershman, Torbert, R. B., Russell, C. T., Strangeway, R. J. (2017), High-resolution Statistics of Solar Wind Turbulence at Kinetic Scales Using the Magnetospheric Multiscale Mission, The Astrophysical Journal Letters, 844(1). http://doi.org/10.3847/2041-8213/AA7DDD

Chen, L.-J., Hesse, M., Wang, S., Gershman, D., Ergun, R. E., Burch, J., Bessho, N., Torbert, R. B., Giles, B., Webster, J., Pollock, C., Dorelli, J., Moore, T., Paterson, W., Lavraud, B., Strangeway, R., Russell, C., Khotyaintsev, Y., Lindqvist, P.-A., Avanov, L. (2017), Electron diffusion region during magnetopause reconnection with an intermediate guide field: Magnetospheric multiscale observations, J. Geophys. Res. Space Physics,122, 5235–5246. http://doi.org/10.1002/2017JA024004

Chen, Y., G. Toth, P. A. Cassak, X. Jia, T. I. Gombosi, J. Slavin, S. Markidis, I. B. Peng, V. K. Jordanova, and M. G. Henderson (2017), Global three-dimensional simulation of Earth's dayside reconnection using a two-way coupled magnetohydrodynamics with embedded particle-in-cell model: Initial results, Journal of Geophysical Research: Space Physics, 122, 10,318–10,335. https://doi.org/10.1002/2017JA024186

Cohen, I. J., Mitchell, D. G., Kistler, L. M., Mauk, B. H., Anderson, B. J., Westlake, J. H., Ohtani, S., Hamilton, D. C., Turner, D. L., Blake, J. B., Fennell, J. F., Jaynes, A. N., Leonard, T. W., Gerrard, A. J., Lanzerotti, L. J., Allen, R. C., Burch, J. L. (2017), Dominance of high-energy (>150 keV) heavy ion intensities in Earth's middle to outer magnetosphere, J. Geophys. Res. SpacePhysics, 122, 9282–9293. http://doi.org/10.1002/2017JA024351

Cohen, I. J., Mauk, B. H., Anderson, B. J., Westlake, J. H., Sibeck, D. G., Turner, D. L., Fennell, J. F., Blake, J. B., Jaynes, A. N., Leonard, T. W., Baker, D. N., Spence, H. E., Reeves, G. D., Giles, B. J., Strangeway, R. J., Torbert, R. B., Burch, J. L. (2017), Statistical analysis of MMS observations of energetic electron escape observed at/beyond the dayside magnetopause, J. Geophys. Res. SpacePhysics,122, 9440–9463. http://doi.org/10.1002/2017JA024401

Ergun, R. E., Chen, L.-J., Wilder, F. D., Ahmadi, N., Eriksson, S., Usanova, M. E., Goodrich, K. A., Holmes, J. C., Sturner, A. P., Malaspina, D. M., Newman, D. L., Torbert, R. B., Argall, M. R.,Lindqvist, P.-A., Burch, J. L., Webster, J. M., Drake, J. F., Price, L., Cassak, P. A., Swisdak, M., Shay, M. A., Graham, D. B., Strangeway, R. J., Russell, C. T., Giles, B. L., Dorelli, J. C., Gershman, D., Avanov, L., Hesse, M., Lavraud, B., Le Contel, O., Retino, A., Phan, T. D., Goldman, M. V., Stawarz, J. E., Schwartz, S. J., Eastwood, J. P., Hwang, K.-J., Nakamure, R., Wang, S. (2017), Drift waves, intense parallel electric

fields, and turbulence associated with asymmetric magnetic reconnection at the magnetopause, Geophys. Res. Lett., 44, 2978–2986. http://doi.org/10.1002/2016GL072493

Farrugia, C. J., Lugaz, N., Alm, L., Vasquez, B., Argall, M. R., Kucharek, H.,...Pollock, C. J. (2017). MMS observations of reconnection at dayside magnetopause crossings during transitions of the solar wind to sub-Alfvénic flow. Journal of Geophysical Research: Space Physics, 122, 9934–9951. https://doi.org/10.1002/2017JA024563

Fuselier, S. A., S. K. Vines, J. L. Burch, S. M. Petrinec, K. J. Trattner, P. A. Cassak, L.-J. Chen, R. E. Ergun, S. Eriksson, B. L. Giles, D. B. Graham, Yu. V. Khotyaintsev, B. Lavraud, W. S. Lewis, J. Mukherjee, C. Norgren, T.-D. Phan, C. T. Russell, R. J. Strangeway, R. B. Torbert, J. M. Webster (2017), Large-scale characteristics of reconnection diffusion regions and associated magnetopause crossings observed by MMS, *J. Geophys. Res., 122,* 5466-5486. http://doi.org/10.1002/2017JA024024

Fuselier, S. A., J. L. Burch, J. Mukherjee, K. J. Genestreti, S. K. Vines, R. Gomez, J. Goldstein, K. J. Trattner, S. M. Petrinec, B. Lavraud, and R. J. Strangeway (2017), Magnetospheric ion influence at the dayside magnetopause, J. Geophys. Res. Space Physics,122, 8617–8631. http://doi.org/10.1002/2017JA024515Genestreti, K. J., Burch, J. L., Cassak, P. A., Torbert, R. B., Ergun, R. E., Varsani, A.,...Allen, R. C. (2017). The effect of a guide field on local energy conversion during asymmetric magnetic reconnection: MMS observations. Journal of Geophysical Research: Space Physics,122, 11,342–11,353. https://doi.org/10.1002/2017JA024247

Gershman, D, J. Adolfo F-Viñas, John C. Dorelli, Scott A. Boardsen, Levon A. Avanov, Paul M. Bellan, Steven J. Schwartz, Benoit Lavraud, Victoria N. Coffey, Michael O. Chandler, Yoshifumi Saito, William R. Paterson, Stephen A. Fuselier, Robert E. Ergun, Robert J. Strangeway, Christopher T. Russell, Barbara L. Giles, Craig J. Pollock, Roy B. Torbert and James L. Burch (2017), Wave-particle energy exchange directly observed in a kinetic Alfvén-branch wave, Nature Communications volume 8, Article number: 14719. http://doi.org/10.1038/NCOMMS14719

Gershman, D. J., Avanov, L. A., Boardsen,S. A., Dorelli, J. C., Gliese, U., Barrie, A. C.,...Pollock, C. J. (2017). Spacecraft and instrument photoelectrons measured by the dual electron spectrometers on MMS. Journal of Geophysical Research: Space Physics,122, 11,548–11,558. https://doi.org/10.1002/2017JA024518

Gingell, I., Schwartz, S. J., Burgess, D., Johlander, A., Russell, C. T., Burch, J. L.,...Wilder, F. (2017). MMS observations and hybrid simulations of surface ripples at a marginally quasi-parallel shock. Journal of Geophysical Research: Space Physics,122, 11,003–11,017. https://doi.org/10.1002/2017JA024538

Graham, D. B., Khotyaintsev, Y., Norgren, C., Vaivads, A., Andre, M., Toledo-Redondo, S., Lindqvist, P.-A., Marklund, G. T., Ergun, R. E., Paterson, W. R., Gershman, D. J., Giles, B. L., Pollock, C. J., Dorelli, J. C., Avanov, L. A., Lavraud, B., Saito, Y., Magnes, W., Russel, C. T., Strangeway, R. J., Torbert, R. B., Burch, J. L. (2017), Lower hybrid waves in the ion diffusion and magnetospheric inflow regions, J. Geophys. Res. Space Physics,122,517–533. http://doi.org/10.1002/2016JA023572

Graham, D. B., Yu. V. Khotyaintsev, A. Vaivads, C. Norgren, M. André, J. M. Webster, J. L. Burch, P.-A. Lindqvist, R. E. Ergun, R. B. Torbert, W. R. Paterson, D. J. Gershman, B. L. Giles, W. Magnes, and C. T. Russell (2017), Instability of Agyrotropic Electron Beams near the Electron Diffusion Region, Phys. Rev. Lett. 119, 025101. http://doi.org/10.1103/PHYSREVLETT.119.025101

Hasegawa, H., Sonnerup, B. U. O., Denton, R. E., Phan, T.-D., Nakamura, T. K. M., Giles, B. L., Gershman, D. J., Dorelli, J. C., Burch, J. L., Torbert, R. B., Russell, C. T., Strangeway, R. J., Lindqvist, P.-A., Khotyaintsev, Y. V., Ergun, R. E., Cassak, P. A., Kitamura, N., Saito, Y. (2017), Reconstruction of the electron diffusion region observed by the Magnetospheric Multiscale spacecraft: First results, Geophys. Res. Lett.,44, 4566–4574. http://doi.org/10.1002/2017GL073163

Hesse, M., L. J. Chen, Y.-H. Liu, N. Bessho, and J. L. Burch (2017), Population Mixing in Asymmetric Magnetic Reconnection with a Guide Field, Phys. Rev. Lett. 118, 145101. http://doi.org/10.1103/PHYSREVLETT.118.145101

Hwang, K.-J., Sibeck, D. G., Choi, E., Chen, L.-J., Ergun, R. E., Khotyaintsev, Y., Giles, B. L., Pollock, C. J., Gershman, D., Dorelli, J. C., Avanov, L., Paterson W. R., Burch, J. L., Russell, C. T., Strangeway, R. J., Torbert, R. B. (2017), Magnetospheric Multiscale mission observations of the outer electron diffusion region, Geophys. Res. Lett.,44,2049–2059. http://doi.org/10.1002/2017GL072830

Lapenta, G., Berchem, J., Zhou, M., Walker, R. J., El-Alaoui, M., Goldstein, M. L., Paterson, W. R., Giles, B. L., Pollock, C. J., Russell, C. T., Strangeway, R. J., Ergun, R. E., Khotyaintsev, Y. V., Torbert, R. B., Burch, J. L. (2017), On the origin of the crescent-shaped distributions observed by MMS at the magnetopause, J. Geophys. Res. Space Physics, 122, 2024–2039. http://doi.org/10.1002/2016JA023290

Le, A., W. Daughton, L.-J. Chen, and J. Egedal (2017), Enhanced electron mixing and heating in 3-D asymmetric reconnection at the Earth's magnetopause, Geophys. Res. Lett., 44, 2096–2104, https://doi.org/10.1002/2017GL072522

Le, G., Chi, P. J., Strangeway, R. J., Russell, C. T., Slavin, J. A., Takahshi, K., Singer, H. J., Anderson, B. J., Bromund, K., Fischer, D., Kepko, E. L., Magnes, W., Nakamura, R., Plaschke, F., Torbert, R. B. (2017), Global observations of magnetospheric high-m poloidal waves during the 22 June 2015 magnetic storm, Geophys. Res. Lett., 44, 3456–3464. http://doi.org/10.1002/2017GL073048

Le Contel, O., R. Nakamura, H. Breuillard, M. R. Argall, D. B. Graham, D. Fischer, A. Retinò, M. Berthomier, R. Pottelette, L. Mirioni, T. Chust, F. D. Wilder, D. J. Gershman, A. Varsani, P.-A. Lindqvist, Yu. V. Khotyaintsev, C. Norgren, R. E. Ergun, K. A. Goodrich, J. L. Burch, R. B. Torbert, J. Needell, M. Chutter, D. Rau, I. Dors, C. T. Russell, W. Magnes, R. J. Strangeway, K. R. Bromund, H. Wei, F. Plaschke, B. J. Anderson, G. Le, T. E. Moore, B. L. Giles, W. R. Paterson, C. J. Pollock, J. C. Dorelli, L. A. Avanov, Y. Saito, B. Lavraud, S. A. Fuselier, B. H. Mauk, I. J. Cohen, D. L. Turner, J. F. Fennell (2017). Lower hybrid drift waves and electromagnetic electron space-phase holes associated with dipolarization fronts and field-aligned currents observed by the Magnetospheric Multiscale mission during a substorm. Journal of Geophysical Research: Space Physics,122, 12,236–12,257. https://doi.org/10.1002/2017JA024550

Lee, S. H., Sibeck, D. G., K.-J. Hwang, Wang, Y., Silveira, M. V. D., Chu, C., Mauk, B. H., Cohen, I. J., Ho, G. C., Mason, G. M., Gold, R. E., Burch, J. L., Torbert, R. B., Russell, C. T., Wei, H. (2017), MMS observation of inverse energy dispersion in shock drift accelerated ions, J. Geophys. Res. Space Physics,122, 3232–3246. http://doi.org/10.1002/2016JA023694

Li, W. Y., André, M., Khotyaintsev, Y. V., Vaivads, A., Fuselier, S. A., Graham, D. B.,...Burch, J. (2017). Cold ionospheric ions in the magnetic reconnection outflow region. Journal of Geophysical Research: Space Physics,122, 10,194–10,202. https://doi.org/10.1002/2017JA024287

Liu, Y.-H., M. Hesse, F. Guo, W. Daughton, H. Li, P. A. Cassak and M. A. Shay (2017), Why does steady-state magnetic reconnection have a maximum local rate of order 0.1?, Phys. Rev. Lett. 118, 085101. https://doi.org/10.1103/PhysRevLett.118.085101

Matsui, H., Torbert, R. B., Spence, H. E., Argall, M. R., Alm, L., Farrugia, C. J.,...Lindqvist, P.-A. (2017). Relativistic electron increase during chorus wave activities on the 6–8March 2016 geomagnetic storm. Journal of Geophysical Research: Space Physics,122, 11,302–11,319. https://doi.org/10.1002/2017JA024540

Nakamura, R., K. Torkar, M. Andriopoulou, H. Jeszenszky, C. P. Escoubet, F. Cipriani, P. A. Lindqvist, S. A. Fuselier, C. J. Pollock, B. L. Giles, Y. Khotyaintsev (2017), Initial Results From the Active Spacecraft Potential Control Onboard Magnetospheric Multiscale Mission, IEEE Transactions on Plasma Science, 45 (8), 1847-1852. http://doi.org/10.1109/TPS.2017.2694223

Nakamura, R., T. Nagai; J. Birn; V. A. Sergeev; O. Le Contel; A. Varsani; W. Baumjohann; T. Nakamura; S. Apatenkov; A. Artemyev; R. E. Ergun; S. A. Fuselier; D. J. Gershman; B. J. Giles; Y. V. Khotyaintsev; P.-A. Lindqvist; W. Magnes; B. Mauk; C. T. Russell; H. J. Singer; J. Stawarz; R. J. Strangeway; B. Anderson; K. R. Bromund; D. Fischer; L. Kepko; G. Le; F. Plaschke; J. A. Slavin; I. Cohen; A. Jaynes; D. L. Turner (2017), Near-Earth plasma sheet boundary dynamics during substorm dipolarization, Earth, Planets and Space, 69(129). http://doi.org/10.1186/S40623-017-0707-2

Nakamura, T. K. M., Eriksson, S., Hasegawa, H., Zenitani, S., Li, W. Y., Genestreti, K. J.,...Daughton, W. (2017). Mass and energy transfer across the Earth's magnetopause caused by vortex-induced reconnection. Journal of Geophysical Research: Space Physics,122,11,505–11,522. https://doi.org/10.1002/2017JA024346

Nakamura, T. K., Hasegawa, H., Daughton, W., Eriksson, S., Li, W. Y., and Nakamura, R. (2017), Turbulent mass transfer caused by vortex induced reconnection in collisionless magnetospheric plasmas, Nature Communications, volume 8, Article number: 1582 (2017). http://doi.org/10.1038/S41467-017-01579-0

Oka, M., L. B. Wilson III, T. D. Phan, A. J. Hull, T. Amano, M. Hoshino, M. R. Argall, O. Le Contel, O. Agapitov, D. J. Gershman, et. al. (2017), Electron Scattering by High-frequency Whistler Waves at Earth's Bow Shock, The Astrophysical Journal Letters, 842(2). http://doi.org/10.3847/2041-8213/AA7759

Plaschke, F., Karlsson, T., Hietala, H., Archer, M., Vörös, Z., Nakamura, R.,...Giles, B. L. (2017). Magnetosheath high-speed jets: Internal structure and interaction with ambient plasma. Journalof Geophysical Research: SpacePhysics, 122, 10,157–10,175. https://doi.org/10.1002/2017JA024471

Price, L., Swisdak, M., Drake, J. F., Burch, J. L., Cassak, P. A., and Ergun, R. E. (2017). Turbulence in three-dimensional simulations of magnetopause reconnection. Journal of Geophysical Research: Space Physics, 122, 11,086–11,099. https://doi.org/10.1002/2017JA024227

Russell, C. T., R. J. Strangeway,C. Zhao,B. J. Anderson,W. Baumjohann, K. R. Bromund,D. Fischer,L. Kepko,G. Le,W. Magnes,R. Nakamura,F. Plaschke,J. A. Slavin,R. B. Torbert,T. E. Moore,W. R. Paterson,C. J. Pollock,J. L. Burch (2017), Structure, force balance, and topology of Earth's magnetopause, Science, 356(6341), 960-963. http://doi.org/10.1126/SCIENCE.AAG3112

Servidio, S., A. Chasapis, W. H. Matthaeus, D. Perrone, F. Valentini, T. N. Parashar, P. Veltri, D. Gershman, C. T. Russell, B. Giles, S. A. Fuselier, T. D. Phan, and J. Burch (2017), Magnetospheric Multiscale Observation of Plasma Velocity-Space Cascade: Hermite Representation and Theory, Phys. Rev. Lett. 119, 205101. http://doi.org/10.1103/PHYSREVLETT.119.205101

Shuster, J. R., Argall, M. R., Torbert, R. E., Chen, L.-J., Farrugia, C. J., Alm, L., Wang, S., Daughton, W., Gershman, D. J., Giles, B. L., Burch, J. L., Pollock, C. J. (2017), Hodographic approach for determining spacecraft trajectories through magnetic reconnection diffusion regions, Geophys. Res. Lett., 44, 1625-1633. http://doi.org/10.1002/2017GL072570

Sorathia, K. A., V. G. Merkin, A. Y. Ukhorskiy, B. H. Mauk, and D. G. Sibeck (2017), Energetic particle loss through the magnetopause: A combined global MHD and test-particle study, J. Geophys. Res. Space Physics, 122, 9329–9343, http://doi.org/10.1002/2017JA024268

Stawarz, J. E., Eastwood, J. P., Varsani, A., Ergun, E. R., Shay, M. A., Nakamura, R., Phan, T. D., Burch, J. L., Gershman, D. J., Giles, B. L., Goodrich, K. A., Khotyaintsev, Y. V., Lindqvist, P.-A., Russell, C. T., Strangeway, R. J., Torbert, R. B. (2017), Magnetospheric Multiscale analysis of intense field-aligned Poynting fluxnear the Earth's plasma sheet boundary, Geophys. Res. Lett.,44, 7106–7113. http://doi.org/10.1002/2017GL073685

Toledo-Redondo, S., M. Andre, Y. V. Khotyaintsev, B. Lavraud, A. Vaivads, D. B. Graham, W. Li, D. Perrone, S. Fuselier, D. J. Gershman, N. Aunai, J. Dargent, B. Giles, O. Le Contel, P.-A. Lindqvist, R. E. Ergun, C. T. Russell, and J. L. Burch (2017), Energy budget and mechanisms of cold plasma heating in

asymmetric magnetic reconnection, *J. Geophys. Res., 122,* 9396-9413. http://doi.og/10.1002/2017JA024553

Torbert, R. B., Burch, J. L., Argall, M. R., Alm, L., Farrugia, C. J., Forbes, T. G.,...Khotyaintsev, Y. (2017). Structure and dissipation characteristics of an electron diffusion region observed by MMS during a rapid, normal-incidence magnetopause crossing. Journal of Geophysical Research: Space Physics, 122, 11,901–11,916. https://doi.org/10.1002/2017JA024579

Torkar, K., Nakamura, R., Andriopoulou, M., Giles, B. L., Jeszenszky, H., Khotyaintsev, Y. V.,...Torbert, R. B.(2017). Influence of the ambient electric field on measurements of the actively controlled spacecraft potential by MMS. Journal of Geophysical Research: SpacePhysics, 122, 12,019–12,030. https://doi.org/10.1002/2017JA024724

Trattner, K. J., S. Thresher, L. Trenchi, S. A. Fuselier, S. M. Petrinec, W. K. Peterson, and M. F. Marcucci (2017), On the occurrence of magnetic reconnection equatorward of the cusps a the Earth's magnetopause during northward IMF conditions, *J. Geophys. Res., 122,* 605-617. http://doi.org/10.1002/2016JA023398

Trattner, K. J., J. L. Burch, R. Ergun, S. Eriksson, S. A. Fuselier, B. L. Giles, R. G. Gomez, E. W. Grimes, W. S. Lewis, B. Mauk, S. M. Petrinec, C. T. Russell, R. J. Strangeway, L. Trenchi,and F. D. Wilder (2017). The MMS dayside magnetic reconnection locations during phase 1 and their relation to the predictions of the maximum magnetic shear model. Journal of Geophysical Research: Space Physics, 122, 11,991–12,005. https://doi.org/10.1002/2017JA024488

Turner, D. L., Lee, J. H., Claudepierre, S. G., Fennell, J. F., Blake, J. B., Jaynes, A. N.,...Santolik, O. (2017). Examining coherency scales, substructure, and propagation of whistler mode chorus elements with Magnetospheric Multiscale (MMS). Journal of Geophysical Research: SpacePhysics,122, 11,201–11,226. https://doi.org/10.1002/2017JA024474

Turner, D. L., Fennell, J. F., Blake, J. B., Claudepierre, S. G., Clemmons, J. H., Jaynes, A. N.,...Reeves, G. D. (2017). Multipoint observations of energetic particle injections and substorm activity during a conjunction between Magnetospheric Multiscale (MMS) and Van Allen Probes. Journal of Geophysical Research: Space Physics,122,11,481–11,504. https://doi.org/10.1002/2017JA024554

Varsani, A., Nakamura, R., Sergeev, V. A., Baumjohann, W., Owen, C. J., Petrukovich, A. A.,...Ergun, R. E. (2017). Simultaneous remote observations of intense reconnection effects by DMSP and MMS spacecraft during a stormtime substorm. Journal of Geophysical Research: Space Physics,122,10,891–10,909. https://doi.org/10.1002/2017JA024547

Vines, S. K., Fuselier, S. A., Trattner, K. J., Burch, J. L., Allen, R. C., Petrinec, S. M.,...Russell, C. T. (2017). Magnetospheric ion evolution across the low-latitude boundary layer separatrix. Journal of Geophysical Research: Space Physics,122, 10,247–10,262. https://doi.org/10.1002/2017JA024061

Vörös, Z., Yordanova, E., Varsani, A., Genestreti, K. J., Khotyaintsev, Y. V., Li, W.,...Saito, Y.(2017). MMS observation of magnetic reconnection in the turbulent magnetosheath. Journal of Geophysical Research: SpacePhysics, 122, 11,442–11,467. https://doi.org/10.1002/2017JA024535

Wang, R., Rumi Nakamura, Quanming Lu, Wolfgang Baumjohann, R. E. Ergun, J. L. Burch, Martin Volwerk, Ali Varsani, Takuma Nakamura, Walter Gonzalez, Barbara Giles, Dan Gershman, and Shui Wang (2017), Electron-Scale Quadrants of the Hall Magnetic Field Observed by the Magnetospheric Multiscale spacecraft during Asymmetric Reconnection, Phys. Rev. Lett. 118, 175101. http://doi.org/10.1103/PHYSREVLETT.118.175101

Wang, S., L.J. Chen, M. Hesse, Wilson, L. B., Bessho, N., Gershman, D. J., Ergun, R. E., Phan, T. D., Burch, J. L., Dorelli, J. C., Giles, B. L., Torbert, R. B., Pollock, C. J., Russell, C. T., Strangeway, R., Avanov, L., Lavraud, B., Moore, T. E. (2017), Parallel electron heating in the magnetospheric inflow region, Geophys. Res. Lett., 44, 4384–4392, https://doi.org/10.1002/2017GL073404

Wilder, F. D., R. E. Ergun, S. Eriksson, T. D. Phan, J. L. Burch, N. Ahmadi, K. A. Goodrich, D. L. Newman, K. J. Trattner, R. B. Torbert, B. L. Giles, R. J. Strangeway, W. Magnes, P.-A. Lindqvist, and Yu-V. Khotyaintsev (2017), Multipoint Measurements of the Electron Jet of Symmetric Magnetic Reconnection with a Moderate Guide Field, Phys. Rev. Lett. 118, 265101. http://doi.org/10.1103/PHYSREVLETT.118.265101

Wilder, F. D., Ergun, R. E., Newman, D. L., Goodrich, K. A., Trattner, K. J., Goldman, M. V., Eriksson, Jaynes, A. N., Leonard, T., Malaspina, D. M., Ahmadi, N., Schwartz, S. J., Burch, J. L., Torbert, R. B., Aragall, M. R., Giles, B. L., Phan, T. D., Le Contel, O., Graham, D. B., Khotyaintsev, Y. V., Strangeway, R. J., Russell, C. T., Magnes, W., Plaschke, F., Lindqvist, P.-A. (2017), The nonlinear behavior of whistler waves at the reconnecting dayside magnetopause as observed by the Magnetospheric Multiscale mission: A case study, J. Geophys. Res. Space Physics, 122, 5487–5501. http://doi.org/10.1002/2017JA024062

Williams, T., Ottenstein, N., Palmer, E., and Godine, D. (2017, June). Satellite Formation Flight Results from Phase 1 of the Magnetospheric Multiscale Mission. 9th International Workshop on Satellite Constellations and Formation Flying, Boulder, CO. https://ntrs.nasa.gov/api/citations/20170005560/downloads/20170005560.pdf

Williams, T.W., Carpenter, J.R., Farahmand, M., Ottenstein, N.A., Demoret, M., and Godine, D. (2017, June). Conjunction Assessment Techniques and Operational Results from the Magnetospheric Multiscale Mission. 9th International Workshop on Satellite Constellations and Formation Flying, Boulder, CO. https://ntrs.nasa.gov/api/citations/20170005561/downloads/20170005561.pdf

Williams, T., Ottenstein, N., Palmer, E., and Hollister, J. (2017, August). Results of the Apogee-Raising Campaign of the Magnetospheric Multiscale Mission. Paper AAS 17-760, AAS/AIAA Astrodynamics Specialist Conference, Stevenson, WA. https://ntrs.nasa.gov/api/citations/20170007741/downloads/20170007741.pdf

Winternitz, L. B. W.A. Bamford, S.R. Price, J.R. Carpenter, A.C. Long and M. Farahmand, (2017) Global Positioning System Navigation Above 76,000 km for NASA's Magnetospheric Multiscale Mission, Journal of the Institute of Navigation, 64(2), 289-300. https://doi.org/10.1002/navi.198

Zhou, M., J. Berchem, R. J. Walker, M. El-Alaoui, X. Deng, E. Cazzola, G. Lapenta, M. L. Goldstein, W. R. Paterson, Y. Pang, R. E. Ergun, B. Lavraud, H. Liang, C. T. Russell, R. J. Strangeway, C. Zhao, B. L. Giles, C. J. Pollock, P.-A. Lindqvist, G. Marklund, F. D. Wilder, Y. V. Khotyaintsev, R. B. Torbert, and J. L. Burch (2017), Coalescence of Macroscopic Flux Ropes at the Subsolar Magnetopause: Magnetospheric Multiscale Observations, Phys. Rev. Lett. 119, 055101. http://doi.org/10.1103/PHYSREVLETT.119.055101

2016

Anderson, B. J., Russell, C. T., Strangeway, R. J., Plaschke, F., Magnes, W., Fischer, D., Merkin, V. G., Barnes, R. J., Waters, C. L., Cohen, I. J., Westlake, J. H., Mauk, B. H., Leinweber, H. K., Gershman, D. J., Giles, B. L., Le, G., Torbert, R. B., Burch, J. B. (2016), Electrodynamic context of magnetopause dynamics observed by magnetospheric multiscale, Geophysical Research Letters, 43(12), 5988-5996, https://doi.org/10.1002/2016GL069577.

Andre, M., W. Li, S. Toledo-Redondo, Yu. V. Khotyaintsev, A. Vaivads, D. B. Graham, C. Norgren, J. Burch, P.-A. Lindqvist, G. Marklund, R. Ergun, R. Torbert, W. Magnes, C. T. Russell, B. Giles, T. E. Moore, M. O. Chandler, C. Pollock, D. T. Young, L. A. Avanov, J. C. Dorelli, D. J. Gershman, W. R. Paterson, B. Lavraud, Y. Saito (2016), Magnetic reconnection and modification of the Hall physics due to cold ions at the magnetopause, Geophysical Research Letters, 43(13), 6705-6712, https://doi.org/10.1002/2016GL069665.

Andriopoulou, M., R. Nakamura, K. Torkar, W. Baumjohann, R. B. Torbert, P.-A. Lindqvist, Y. V. Khotyaintsev, J. Dorelli, J. L. Burch, and C. T. Russell (2016), Study of the spacecraft potential under

active control and plasma density estimates during the MMS commissioning phase, Geophysical Research Letters, 43(10), 4858-4864, https://doi.org/10.1002/2016GL068529.

Ashour-Abdalla, M., G. Lapenta, R. Walker, M. El-Alaoui, H. Liang, M. Zhou, J. Berchem, and M. L. Goldstein (2016), Identifying the electron diffusion region in a realistic simulation of Earth's magnetotail, Geophysical Research Letters, 43(12), 6005-6011, https://doi.org/10.1002/2016GL069355.

Aunai, N., M. Hesse, B. Lavraud, J. Dargent, and R. Smets (2016), Orientation of the X-line in asymmetric magnetic reconnection, Journal of Plasma Physics, 82, https://doi.org/10.1017/S0022377816000647.

Baker, D., L. Riesberg, C. Pankratz, R. Panneton, B. Giles, F. Wilder, and R. Ergun (2016a), Magnetospheric Multiscale Instrument Suite Operations and Data System, Space Science Reviews, 199(1-4), 545-575, https://doi.org/10.1007/s11214-014-0128-5.

Baker, D. N., A. N. Jaynes, D. L. Turner, R. Nakamura, D. Schmid, B. H. Mauk, I. J. Cohen, J. F. Fennell, J. B. Blake, R. J. Strangeway, C. T. Russell, R. B. Torbert, J. C. Dorelli, D. J. Gershman, B. L. Giles, J. L. Burch (2016b), A telescopic and microscopic examination of acceleration in the June 2015 geomagnetic storm: Magnetospheric Multiscale and Van Allen Probes study of substorm particle injection, Geophysical Research Letters, 43(12), 6051-6059, https://doi.org/10.1002/2016GL069643.

Bessho, N., L.-J. Chen, and M. Hesse (2016), Electron distribution functions in the diffusion region of asymmetric magnetic reconnection, Geophysical Research Letters, 43(5), 1828-1836, https://doi.org/10.1002/2016GL067886.

Blake, J., B. H. Mauk, D. N. Baker, P. Carranza, J. H. Clemmons, J. Craft, W. R. Crain Jr., A. Crew, Y. Dotan, J. F. Fennell, R. H. Friedel, L. M. Friesen, F. Fuentes, R. Galvan, C. Ibscher, A. Jaynes, N. Katz, M. Lalic, A. Y. Lin, D. M. Mabry, T. Nguyen, C. Pancratz, M. Redding, G. D. Reeves, S. Smith, H. E. Spence, J. Westlake (2016), The Fly's Eye Energetic Particle Spectrometer (FEEPS) Sensors for the Magnetospheric Multiscale (MMS) Mission, Space Science Reviews, 199(1-4), 309-329, https://doi.org/10.1007/s11214-015-0163-x

Breuillard, H., O. Le Contel, A. Retino, A. Chasapis, T. Chust, L. Mirioni, D. B. Graham, F. D. Wilder, I. Cohen, A. Vaivads, Yu. V. Khotyaintsev, P.-A. Lindqvist, G. T. Marklund, J. L. Burch, R. B. Torbert, R. E. Ergun, K. A. Goodrich, J. Macri, J. Needell, M. Chutter, D. Rau, I. Dors, C. T. Russell, W. Magnes, R. J. Strangeway, K. R. Bromund, F. Plaschke, D. Fischer, H. K. Leinweber, B. J. Anderson, G. Le, J. A. Slavin, E. L. Kepko, W. Baumjohann, B. Mauk, S. A. Fuselier, R. Nakamura (2016), Multispacecraft analysis of dipolarization fronts and associated whistler wave emissions using MMS data, Geophysical Research Letters, 43(14), 7279-7286, https://doi.org/10.1002/2016GL069188.

Burch, J., T. Moore, R. Torbert, and B. Giles (2016a), Magnetospheric Multiscale Overview and Science Objectives, Space Science Reviews, 199(1-4), 5-21, https://doi.org/10.1007/s11214-015-0164-9

Burch, J. L., and T. D. Phan (2016), Magnetic reconnection at the dayside magnetopause: Advances with MMS, Geophysical Research Letters, 43(16), 8327-8338, https://doi.org/10.1002/2016GL069787

Burch, J. L., and R. B. Torbert (2016), Preface, Space Science Reviews, 199(1-4), 1-3, https://doi.org/10.1007/s11214-015-0153-z

Burch, J. L., R. B. Torbert, T. D. Phan, L.-J. Chen, T. E. Moore, R. E. Ergun, J. P. Eastwood, D. J. Gershman, P. A. Cassak, M. R. Argall, S. Wang, M. Hesse, C. J. Pollock, B. L. Giles, R. Nakamura, B. H. Mauk, S. A. Fuselier, C. T. Russell, R. J. Strangeway, J. F. Drake, M. A. Shay, Yu. V. Khotyaintsev, P.-A. Lindqvist, G. Marklund, F. D. Wilder, D. T. Young, K. Torkar, J. Goldstein, J. C. Dorelli, L. A. Avanov, M. Oka, D. N. Baker, A. N. Jaynes, K. A. Goodrich, I. J. Cohen, D. L. Turner, J. F. Fennell, J. B. Blake, J. Clemmons, M. Goldman, D. Newman, S. M. Petrinec, K. J. Trattner, B. Lavraud, P. H. Reiff, W. Baumjohann, W. Magnes, M. Steller, W. Lewis, Y. Saito, V. Coffey, M. Chandler (2016b), Electron-scale measurements of magnetic reconnection in space, Science, 352(6290), 1189-+, https://doi.org/10.1126/science.aaf2939

Cassak, P. (2016), Inside the Black Box: Magnetic Reconnection and the Magnetospheric Multiscale Mission, Space Weather-the International Journal of Research and Applications, 14(3), 186-197, https://doi.org/10.1002/2015SW001313

Cazzola, E., M. E. Innocenti, M. V Goldman, D. L. Newman, S. Markidis, and G. Lapenta (2016), On the electron agyrotropy during rapid asymmetric magnetic island coalescence in presence of a guide field, Geophys. Res. Lett., 43, 7840–7849, https://doi.org/10.1002/2016GL070195

Chen, L.-J., M. Hesse, S. Wang, N. Bessho, and W. Daughton (2016a), Electron energization and structure of the diffusion region during asymmetric reconnection, Geophysical Research Letters, 43(6), 2405-2412, https://doi.org/10.1002/2016GL068243

Chen, L.-J., Hesse, M., Wang, S., Gershman, D., Ergun, R., Pollock, C., Torbert, R., Bessho, N., DAughton, W., Dorelli, J., Giles, B., Strangeway, R., Russell, C., Khotyaintsev, Y., Burch, J., Moore, T. E., Lavraud, B., Phan, T., Avanov, L. (2016b), Electron energization and mixing observed by MMS in the vicinity of an electron diffusion region during magnetopause reconnection, Geophysical Research Letters, 43(12), 6036-6043, https://doi.org/10.1002/2016GL069215

Clark, G., I. Cohen, J. H. Westlake, G. B. Andrews, P. Brandt, R. E. Gold, M. A. Gkioulidou, R. Hacala, D. Haggerty, M. E. Hill, G. C. Ho, S. E. Jaskulek, P. Kollmann, B. H. Mauk, R. L. McNutt Jr., D. G. Mitchell, K. S. Nelson, C. Paranicas, N. Paschalidis, C. E. Schlemm, (2016), The “Puck” energetic charged particle detector: Design, heritage, and advancements, J. Geophys. Res. Space Physics, 121, 7900–7913, https://doi.org/10.1002/2016JA022579

Cohen, I. J., B. H. Mauk, B. J. Anderson, J. H. Westlake, D. G. Sibeck, B. L. Giles, C. J. Pollock, D. L. Turner, J. F. Fennell, J. B. Blake, J. H. Clemmons, A. N. Jaynes, D. N. Baker, J. V. Craft, H. E. Spence, J. T. Niehof, G. D. Reeves, R. B. Torbert, C. T. Russell R. J. Strangeway, W. Magnes, K. J. Trattner, S. A. Fuselier, J. L. Burch (2016), Observations of energetic particle escape at the magnetopause: Early results from the MMS Energetic Ion Spectrometer (EIS), Geophysical Research Letters, 43(12), 5960-5968, https://doi.org/10.1002/2016GL068689

Collinson, G. A., J. P. McFadden, D. J. Chornay, D. Gershman, and T. E. Moore (2016), Constraining electric fields from electrostatic deflector plates: A brief report and case study from the Fast Plasma Investigation for the Magnetospheric Multiscale Mission, J. Geophys. Res. Space Physics, 121, 7887–7894, http://doi.org/10.1002/2016JA022590

Denton, R. E., B. U. O. Sonnerup, H. Hasegawa, T. D. Phan, C. T. Russell, R. J. Strangeway, B. L. Giles, D. Gershman, and R. B. Torbert (2016a), Motion of the MMS spacecraft relative to the magnetic reconnection structure observed on 16 October 2015 at 1307UT, Geophysical Research Letters, 43(11), 5589-5596, https://doi.org/10.1002/2016GL069214

Denton, R. E., B. U. O. Sonnerup, H. Hasegawa, T. D. Phan, C. T. Russell, R. J. Strangeway, B. L. Giles, and R. B. Torbert (2016b), Reconnection guide field and quadrupolar structure observed by MMS on 16 October 2015 at 1307 UT, Journal of Geophysical Research-Space Physics, 121(10), 9880-9887, https://doi.org/10.1002/2016JA023323

Eastwood, J. P., T. D. Phan, P. A. Cassak, D. J. Gershman, C. Haggerty, K. Malakit, M. A. Shay, R. Mistry, M. Øieroset, C. T. Russell, J. A. Slavin, M. R. Argall, L. A. Avanov, J. L. Burch, L. J. Chen, J. C. Dorelli, R. E. Ergun, B. L. Giles, Y. Khotyaintsev, B. Lavraud, P. A. Lindqvist, T. E. Moore, R. Nakamura, W. Paterson, C. Pollock, R. J. Strangeway, R. B. Torbert, S. Wang (2016), Ion-scale secondary flux ropes generated by magnetopause reconnection as resolved by MMS, Geophysical Research Letters, 43(10), 4716-4724, https://doi.org/10.1002/2016GL068747

Ergun, R., S. Tucker, J. Westfall, K. A. Goodrich, D. M. Malaspina, D. Summers, J. Wallace, M. Karlsson, J. Mack, N. Brennan, B. Pyke, P. Withnell, R. Torbert, J. Macri, D. Rau, I. Dors, J. Needell, P.-A.

Lindqvist, G. Olsson, C. M. Cully (2016a), The Axial Double Probe and Fields Signal Processing for the MMS Mission, Space Science Reviews, 199(1-4), 167-188, https://doi.org/10.1007/s11214-014-0115-x

Ergun, R. E., K. A. Goodrich, F. D. Wilder, J. C. Holmes, J. E. Stawarz, S. Eriksson, A. P. Sturner, D. M. Malaspina, M. E. Usanova1, R. B. Torbert, P.-A. Lindqvist, Y. Khotyaintsev, J. L. Burch, R. J. Strangeway, C. T. Russell, C. J. Pollock, B. L. Giles, M. Hesse, L. J. Chen, G. Lapenta, M. V. Goldman, D. L. Newman, S. J. Schwartz, J. P. Eastwood, T. D. Phan, F. S. Mozer, J. Drake, M. A. Shay, P. A. Cassak, R. Nakamura, and G. Marklund (2016b), Magnetospheric Multiscale Satellites Observations of Parallel Electric Fields Associated with Magnetic Reconnection, Physical Review Letters, 116(23), https://doi.org/10.1103/PhysRevLett.116.235102

Ergun, R. E., J. C. Holmes, K. A. Goodrich, F. D. Wilder, J. E Stawarz, S. Eriksson, D. L. Newman, S. J. Schwartz, M. V. Goldman, A. P. Sturner, D. M. Malaspina, M. E. Usanova, R. B. Torbert, M. Argall, P.-A. Lindqvist, Y. Khotyaintsev, J. L. Burch, R. J. Strangeway, C. T. Russell, C. J. Pollock, B. L. Giles, J. J. C. Dorelli, L. Avanov, M. Hesse, L. J. Chen, B. Lavraud, O. Le Contel, A. Retino, T. D. Phan, J. P. Eastwood, M. Oieroset, J. Drake, M. A. Shay, P. A. Cassak, R. Nakamura, M. Zhou, M. Ashour-Abdalla, M. André, (2016c), Magnetospheric Multiscale observations of large-amplitude, parallel, electrostatic waves associated with magnetic reconnection at the magnetopause, Geophysical Research Letters, 43(11), 5626-5634, https://doi.org/10.1002/2016GL068992

Erickson, P. J., H. Matsui, J. C. Foster, R. B. Torbert, R. E. Ergun, Yu. V. Khotyaintsev, P.-A. Lindqvist, M. R. Argall, C. J. Farrugia, K. W. Paulson, R. J. Strangeway, W. Magnes (2016), Multipoint MMS observations of fine-scale SAPS structure in the inner magnetosphere, Geophysical Research Letters, 43(14), 7294-7300, https://doi.org/10.1002/2016GL069174

Eriksson, E., A. Vaivads, D. B. Graham, Yu. V. Khotyaintsev, E. Yordanova, H. Hietala, M. André, L. A. Avanov, J. C. Dorelli, D. J. Gershman, B. L. Giles, B. Lavraud, W. R. Paterson, C. J. Pollock, Y. Saito, W. Magnes, C. Russell, R. Torbert, R. Ergun, P-A. Lindqvist, J. Burch (2016a), Strong current sheet at a magnetosheath jet: Kinetic structure and electron acceleration, Journal of Geophysical Research-Space Physics, 121(10), 9608-9618, https://doi.org/10.1002/2016JA023146

Eriksson, S., B. Lavraud, F. D. Wilder, J. E. Stawarz, B. L. Giles, J. L. Burch, W. Baumjohann, R. E. Ergun, P.-A. Lindqvist, W. Magnes, C. J. Pollock, C. T. Russell, Y. Saito, R. J. Strangeway, R. B. Torbert, D. J. Gershman, Yu. V. Khotyaintsev, J. C. Dorelli, S. J. Schwartz, L. Avanov, E. Grimes, Y. Vernisse, A. P. Sturner, T. D. Phan, G. T. Marklund, T. E. Moore, W. R. Paterson, K. A. Goodrich (2016b), Magnetospheric Multiscale observations of magnetic reconnection associated with Kelvin-Helmholtz waves, Geophysical Research Letters, 43(11), 5606-5615, https://doi.org/10.1002/2016GL068783

Eriksson, S., F. D. Wilder, R. E. Ergun, S. J. Schwartz, P. A. Cassak, J. L. Burch, L.-J. Chen, R. B. Torbert, T. D. Phan, B. Lavraud, K. A. Goodrich, J. C. Holmes, J. E. Stawarz, A. P. Sturner, D. M. Malaspina, M. E. Usanova1, K. J. Trattner, R. J. Strangeway, C. T. Russell, C. J. Pollock, B. L. Giles, M. Hesse, P.-A. Lindqvist, J. F. Drake, M. A. Shay, R. Nakamura, and G. T. Marklund (2016c), Magnetospheric Multiscale Observations of the Electron Diffusion Region of Large Guide Field Magnetic Reconnection, Physical Review Letters, 117(1), https://doi.org/10.1103/PhysRevLett.117.015001

Farrugia, C. J., B. Lavraud, R. B. Torbert, M. Argall, I. Kacem, W. Yu, L. Alm, J. Burch, C. T. Russell, J. Shuster, J. Dorelli, J. P. Eastwood, R. E. Ergun, S. Fuselier, D. Gershman, B. L. Giles, Y. V. Khotyaintsev, P. A. Lindqvist, H. Matsui, G. T. Marklund, T. D. Phan, K. Paulson, C. Pollock, R. J. Strangeway (2016), Magnetospheric Multiscale Mission observations and non-force free modeling of a flux transfer event immersed in a super-Alfvenic flow, Geophysical Research Letters, 43(12), 6070-6077, https://doi.org/10.1002/2016GL068758

Fennell, J. F., D. L. Turner, C. L. Lemon, J. B. Blake, J. H. Clemmons, B. H. Mauk, A. N. Jaynes, I. J. Cohen, J. H. Westlake, D. N. Baker, J. V. Craft, H. E. Spence, G. D. Reeves, R. B. Torbert, J. L. Burch, B. L. Giles, W. R. Paterson, R. J. Strangeway (2016), Microinjections observed by MMS FEEPS in the dusk

to midnight region, Geophysical Research Letters, 43(12), 6078-6086, https://doi.org/10.1002/2016GL069207

Fischer, D., Werner Magnes, Christian Hagen, Ivan Dors, Mark W. Chutter, Jerry Needell, Roy B. Torbert, Olivier Le Contel, Robert J. Strangeway, Gernot Kubin, Aris Valavanoglou, Ferdinand Plaschke, Rumi Nakamura, Laurent Mirioni, Christopher T. Russell, Hannes K. Leinweber, Kenneth R. Bromund, Guan Le, Lawrence Kepko, Brian J. Anderson, James A. Slavin, and Wolfgang Baumjohann (2016), Optimized merging of search coil and fluxgate data for MMS, Geoscientific Instrumentation Methods and Data Systems, 5(2), 521-530, https://doi.org/10.5194/gi-5-521-2016

Fuselier, S., J. L. Burch, P. A. Cassak, J. Goldstein, R. G. Gomez, K. Goodrich, W. S. Lewis, D. Malaspina, J. Mukherjee, R. Nakamura, S. M. Petrinec, C. T. Russell, R. J. Strangeway, R. B. Torbert, K. J. Trattner, P. Valek (2016a), Magnetospheric ion influence on magnetic reconnection at the duskside magnetopause, Geophysical Research Letters, 43(4), 1435-1442, https://doi.org/10.1002/2015GL067358

Fuselier, S., W. Lewis, C. Schiff, R. Ergun, J. Burch, S. Petrinec, and K. Trattner (2016b), Magnetospheric Multiscale Science Mission Profile and Operations, Space Science Reviews, 199(1-4), 77-103, https://doi.org/10.1007/s11214-014-0087-x

Gershman, D. J., John C. Dorelli, Adolfo F. Viñas, Levon A. Avanov, Ulrik Gliese, Alexander C. Barrie, Victoria Coffey, Michael Chandler, Charles Dickson, Elizabeth A. MacDonald, Chad Salo, Matthew Holland, Yoshifumi Saito, Jean-Andre Sauvaud, Benoit Lavraud, William R. Paterson, Roy Torbert, Li-Jen Chen, Katherine Goodrich, Christopher T. Russell, Robert J. Strangeway, Barbara L. Giles, Craig J. Pollock, Thomas E. Moore, James L. Burch (2016), Electron dynamics in a subproton-gyroscale magnetic hole, Geophysical Research Letters, 43(9), 4112-4118, https://doi.org/10.1002/2016GL068545

Goldman, M. V., D. L. Newman, and G. Lapenta (2016), What Can We Learn about Magnetotail Reconnection from 2D PIC Harris-Sheet Simulations?, Space Science Reviews, 199(1-4), 651-688, https://doi.org/10.1007/s11214-015-0154-y

Goldstein, M. L., Maha Ashour-Abdalla, Adolfo F. Viñas, John Dorelli, Deirdre Wendel, Alex Klimas, Kyoung-Joo Hwang, Mostafa El-Alaoui, Raymond J. Walker, Qingjiang Pan, Haoming Liang (2016), Mission Oriented Support and Theory (MOST) for MMS-the Goddard Space Flight Center/University of California Los Angeles Interdisciplinary Science Program, Space Science Reviews, 199(1-4), 689-719, https://doi.org/10.1007/s11214-014-0127-6

Gomez, R. G., S. K. Vines, S. A. Fuselier, P. A. Cassak, R. J. Strangeway, S. M. Petrinec, J. L. Burch, K. J. Trattner, C. T. Russell, R. B. Torbert, C. Pollock, D. T. Young, W. S. Lewis, J. Mukherjee (2016), Stable reconnection at the dusk flank magnetopause, Geophysical Research Letters, 43(18), 9374-9382, https://doi.org/10.1002/2016GL069692

Goodrich, K. A., Robert E. Ergun, Frederick D. Wilder, James Burch, Roy Torbert, Yuri Khotyaintsev, Per-Arne Lindqvist, Christopher Russell, Robert Strangeway, Werner Magnes, Daniel Gershman, Barbara Giles, Rumi Nakamura, Julia Stawarz, Justin Holmes, Andrew Sturner, David M. Malaspina (2016), MMS Multipoint electric field observations of small-scale magnetic holes, Geophysical Research Letters, 43(12), 5953-5959, https://doi.org/10.1002/2016GL069157

Graham, D. B., Yu. V. Khotyaintsev, C. Norgren, A. Vaivads, M. André, P.-A. Lindqvist, G. T. Marklund, R. E. Ergun, W. R. Paterson, D. J. Gershman, B. L. Giles, C. J. Pollock, J. C. Dorelli, L. A. Avanov, B. Lavraud, Y. Saito, W. Magnes, C. T. Russell, R. J. Strangeway, R. B. Torbert, J. L. Burch (2016), Electron currents and heating in the ion diffusion region of asymmetric reconnection, Geophysical Research Letters, 43(10), 4691-4700, https://doi.org/10.1002/2016GL068613

Hasegawa, H., N. Kitamura, Y. Saito, T. Nagai, I. Shinohara, S. Yokota, C. J. Pollock, B. L. Giles, J. C. Dorelli, D. J. Gershman, L. A. Avanov, S. Kreisler, W. R. Paterson, M. O. Chandler, V. Coffey, J. L. Burch, R. B. Torbert, T. E. Moore, C. T. Russell, R. J. Strangeway, G. Le, M. Oka, T. D. Phan, B. Lavraud,

S. Zenitani, M. Hesse (2016), Decay of mesoscale flux transfer events during quasi-continuous spatially extended reconnection at the magnetopause, Geophysical Research Letters, 43(10), 4755-4762, https://doi.org/10.1002/2016GL069225

Hesse, M., N. Aunai, J. Birn, P. Cassak, R. E. Denton, J. F. Drake, T. Gombosi, M. Hoshino, W. Matthaeus, D. Sibeck, S. Zenitani (2016a), Theory and Modeling for the Magnetospheric Multiscale Mission, Space Science Reviews, 199(1-4), 577-630, https://doi.org/10.1007/s11214-014-0078-y

Hesse, M., Y.-H. Liu, L.-J. Chen, N. Bessho, M. Kuznetsova, J. Birn, and J. L. Burch (2016b), On the electron diffusion region in asymmetric reconnection with a guide magnetic field, Geophysical Research Letters, 43(6), 2359-2364, https://doi.org/10.1002/2016GL068373

Hwang, K.-J., D. G. Sibeck, B. L. Giles, C. J. Pollock, D. Gershman, L. Avanov, W. R. Paterson, J. C. Dorelli, R. E. Ergun, C. T. Russell, R. J. Strangeway, B. Mauk, I. J. Cohen, R. B. Torbert, J. L. Burch (2016), The substructure of a flux transfer event observed by the MMS spacecraft, Geophysical Research Letters, 43(18), 9434-9443, https://doi.org/10.1002/2016GL070934

Jaynes, A. N., D. L. Turner, F. D. Wilder, A. Osmane, D. N. Baker, J. B. Blake, J. F. Fennell, I. J. Cohen, B. H. Mauk, G. D. Reeves, R. E. Ergun, B. L. Giles, D. J. Gershman, R. B. Torbert, J. L. Burch (2016), Energetic electron acceleration observed by MMS in the vicinity of an X-line crossing, Geophysical Research Letters, 43(14), 7356-7363, https://doi.org/10.1002/2016GL069206

Johlander, A., S. J. Schwartz, A. Vaivads, Yu. V. Khotyaintsev, I. Gingell, I. B. Peng, S. Markidis, P.-A. Lindqvist, R. E. Ergun, G. T. Marklund, F. Plaschke, W. Magnes, R. J. Strangeway, C. T. Russell, H. Wei, R. B. Torbert, W. R. Paterson, D. J. Gershman, J. C. Dorelli, L. A. Avanov, B. Lavraud, Y. Saito, B. L. Giles, C. J. Pollock, J. L. Burch (2016), Rippled Quasiperpendicular Shock Observed by the Magnetospheric Multiscale Spacecraft, Physical Review Letters, 117(16), https://doi.org/10.1103/PhysRevLett.117.165101

Khotyaintsev, Y. V., Yu. V. Khotyaintsev, D. B. Graham, C. Norgren, E. Eriksson, W. Li, A. Johlander, A. Vaivads, M. André, P. L. Pritchett, A. Retinò, T. D. Phan, R. E. Ergun, K. Goodrich, P.-A. Lindqvist, G. T. Marklund, O. Le Contel, F. Plaschke, W. Magnes, R. J. Strangeway, C. T. Russell, H. Vaith, M. R. Argall, C. A. Kletzing, R. Nakamura, R. B. Torbert, W. R. Paterson, D. J. Gershman, J. C. Dorelli, L. A. Avanov, B. Lavraud, Y. Saito, B. L. Giles, C. J. Pollock, D. L. Turner, J. D. Blake, J. F. Fennell, A. Jaynes, B. H. Mauk, J. L. Burch (2016), Electron jet of asymmetric reconnection, Geophysical Research Letters, 43(11), 5571-5580, https://doi.org/10.1002/2016GL069064

Kitamura, N., H. Hasegawa, Y. Saito, I. Shinohara, S. Yokota, T. Nagai, C. J. Pollock, B. L. Giles, T. E. Moore, J. C. Dorelli, D. J. Gershman, L. A. Avanov, W. R. Paterson, V. N. Coffey, M. O. Chandle,r J. A. Sauvaud, B. Lavraud, R. B. Torbert, C. T. Russell, R. J. Strangeway, J. L. Burch (2016), Shift of the magnetopause reconnection line to the winter hemisphere under southward IMF conditions: Geotail and MMS observations, Geophysical Research Letters, 43(11), 5581-5588, https://doi.org/10.1002/2016GL069095

Klein, K. G., and Howes, G. G. (2016). Measuring collisionless damping in heliospheric plasmas using field–particle correlations. *The Astrophysical Journal Letters*, *826*(2), L30. http://dx.doi.org/10.3847/2041-8205/826/2/L30

Lapenta, G, M. Goldman, D. Newman, and S. Markidis (2016), Where should MMS look for electron diffusion regions?, 10th International Conference On Numerical Modeling Of Space Plasma Flows: ASTRONUM-2015, Journal of Physics Conference Series, 719(1), https://doi.org/10.1088/1742-6596/719/1/012011

Lavraud, B., Y. C. Zhang, Y. Vernisse, D. J. Gershman, J. Dorelli, P. A. Cassak, J. Dargent, C. Pollock, B. Giles, N. Aunai, M. Argall, L. Avanov, A. Barrie, J. Burch, M. Chandler, L.-J. Chen, G. Clark, I. Cohen, V. Coffey, J. P. Eastwood, J. Egedal, S. Eriksson, R. Ergun, C. J. Farrugia, S. A. Fuselier, V. Génot, D.

Graham, E. Grigorenko, H. Hasegawa, C. Jacquey, I. Kacem, Y. Khotyaintsev, E. MacDonald, W. Magnes, A. Marchaudon, B. Mauk, T. E. Moore, T. Mukai, R. Nakamura, W. Paterson, E. Penou, T. D. Phan, A. Rager, A. Retino, Z. J. Rong, C. T. Russell, Y. Saito, J.-A. Sauvaud, S. J. Schwartz, C. Shen, S. Smith, R. Strangeway, S. Toledo-Redondo, R. Torbert, D. L. Turner, S. Wang, S. Yokota (2016), Currents and associated electron scattering and bouncing near the diffusion region at Earth's magnetopause, Geophysical Research Letters, 43(7), 3042-3050, https://doi.org/10.1002/2016GL068359

Le Contel, O., P. Leroy, A. Roux, C. Coillot, D. Alison, A. Bouabdellah, L. Mirioni, L. Meslier, A. Galic, M. C. Vassal, R. B. Torbert, J. Needell, D. Rau, I. Dors, R. E. Ergun, J. Westfall, D. Summers, J. Wallace, W. Magnes, A. Valavanoglou, G. Olsson, M. Chutter, J. Macri, S. Myers, S. Turco, J. Nolin, D. Bodet, K. Rowe, M. Tanguy, B. de la Porte (2016a), The Search-Coil Magnetometer for MMS, Space Science Reviews, 199(1-4), 257-282, https://doi.org/10.1007/s11214-014-0096-9

Le Contel, O., A. Retinò, H. Breuillard, L. Mirioni, P. Robert, A. Chasapis, B. Lavraud, T. Chust, L. Rezeau, F. D. Wilder, D. B. Graham, M. R. Argall, D. J. Gershman, P.-A. Lindqvist, Y. V. Khotyaintsev, G. Marklund, R. E. Ergun, K. A. Goodrich, J. L. Burch, R. B. Torbert, J. Needell, M. Chutter, D. Rau, I. Dors, C. T. Russell, W. Magnes, R. J. Strangeway, K. R. Bromund, H. K. Leinweber, F. Plaschke, D. Fischer, B. J. Anderson, G. Le, T. E. Moore, C. J. Pollock, B. L. Giles, J. C. Dorelli, L. Avanov, Y. Saito (2016b), Whistler mode waves and Hall fields detected by MMS during a dayside magnetopause crossing, Geophysical Research Letters, 43(12), 5943-5952, https://doi.org/10.1002/2016GL068968

Le, G., H. Lühr, B. J. Anderson, R. J. Strangeway, C. T. Russell, H. Singer, J. A. Slavin, Y. Zhang, T. Huang, K. Bromund, P. J. Chi, G. Lu, D. Fischer, E. L. Kepko, H. K. Leinweber, W. Magnes, R. Nakamura, F. Plaschke, J. Park, J. Rauberg, C. Stolle, R. B. Torbert (2016), Magnetopause erosion during the 17 March 2015 magnetic storm: Combined field-aligned currents, auroral oval, and magnetopause observations, Geophysical Research Letters, 43(6), 2396-2404, https://doi.org/10.1002/2016GL068257

Lee, S. H., D. G. Sibeck, K.-J. Hwang, Y. Wang, M. V. D. Silveira, M.-C. Fok, B. H. Mauk, I. J. Cohen, J. M. Ruohoniemi, N. Kitamura, J. L. Burch, B. L. Giles, R. B. Torbert, C. T. Russell, M. Lester (2016), Inverse energy dispersion of energetic ions observed in the magnetosheath, Geophysical Research Letters, 43(14), 7338-7347, https://doi.org/10.1002/2016GL069840

Li, W., M. André Yu, V. Khotyaintsev, A. Vaivads, D. B. Graham, S. Toledo-Redondo, C. Norgren, P. Henri, C. Wang, B. B. Tang, B. Lavraud, Y. Vernisse, D. L. Turner, J. Burch, R. Torbert, W. Magnes, C. T. Russell, J. B. Blake, B. Mauk, B. Giles, C. Pollock, J. Fennell A. Jaynes, L. A. Avanov, J. C. Dorelli, D. J. Gershman, W. R. Paterson, Y. Saito, R. J. Strangeway (2016), Kinetic evidence of magnetic reconnection due to Kelvin-Helmholtz waves, Geophysical Research Letters, 43(11), 5635-5643, https://doi.org/10.1002/2016GL069192

Lindqvist, P., G. Olsson, R. B. Torbert, B. King, M. Granoff, D. Rau, G. Needell, S. Turco, I. Dors, P. Beckman, J. Macri, C. Frost, J. Salwen, A. Eriksson, L. Åhlén, Y. V. Khotyaintsev, J. Porter, K. Lappalainen, R. E. Ergun, W. Wermeer, S. Tucker (2016), The Spin-Plane Double Probe Electric Field Instrument for MMS, Space Science Reviews, 199(1-4), 137-165, https://doi.org/10.1007/s11214-014-0116-9

Liu, Y.-H., and M. Hesse (2016), Suppression of collisionless magnetic reconnection in asymmetric current sheets, Physics of Plasmas, 23(6), https://doi.org/10.1063/1.4954818

Matsui, H., P. J. Erickson, J. C. Foster, R. B. Torbert, M. R. Argall, B. J. Anderson, J. B. Blake, I. J. Cohen, R. E. Ergun, C. J. Farrugia, Yu. V. Khotyaintsev, H. Korth, P.-A. Lindqvist, W. Magnes, G. T. Marklund, B. H. Mauk, K. W. Paulson, C. T. Russell, R. J. Strangeway, D. L. Turner (2016), Dipolarization in the inner magnetosphere during a geomagnetic storm on 7 October 2015, Geophysical Research Letters, 43(18), 9397-9405, https://doi.org/10.1002/2016GL070677

Mauk, B., J. B. Blake, D. N. Baker, J. H. Clemmons, G. D. Reeves, H. E. Spence, S. E. Jaskulek, C. E. Schlemm, L. E. Brown, S. A. Cooper, J. V. Craft, J. F. Fennell, R. S. Gurnee, C. M. Hammock, J. R. Hayes, P. A. Hill, G. C. Ho, J. C. Hutcheson, A. D. Jacques, S. Kerem, D. G. Mitchell, K. S. Nelson, N. P. Paschalidis, E. Rossano, M. R. Stokes, J. H. Westlake (2016a), The Energetic Particle Detector (EPD) Investigation and the Energetic Ion Spectrometer (EIS) for the Magnetospheric Multiscale (MMS) Mission, Space Science Reviews, 199(1-4), 471-514, https://doi.org/10.1007/s11214-014-0055-5

Mauk, B. H., I. J. Cohen, J. H. Westlake, and B. J. Anderson (2016b), Modeling magnetospheric energetic particle escape across Earth's magnetopause as observed by the MMS mission, Geophysical Research Letters, 43(9), 4081-4088, https://doi.org/10.1002/2016GL068856

Mozer, F., O. Agapitov, A. Artemyev, J. Burch, R. Ergun, B. Giles, D. Mourenas, R. Torbert, T. Phan, and I. Vasko (2016), Magnetospheric Multiscale Satellite Observations of Parallel Electron Acceleration in Magnetic Field Reconnection by Fermi Reflection from Time Domain Structures, Physical Review Letters, 116(14), https://doi.org/10.1103/PhysRevLett.116.145101

Nakamura, R., V. A. Sergeev, W. Baumjohann, F. Plaschke, W. Magnes, D. Fischer, A. Varsani, D. Schmid, T. K. M. Nakamura, C. T. Russell, R. J. Strangeway, H. K. Leinweber, G. Le, K. R. Bromund, C. J. Pollock, B. L. Giles, J. C. Dorelli, D. J. Gershman, W. Paterson, L. A. Avanov, S. A. Fuselier, K. Genestreti, J. L. Burch, R. B. Torbert, M. Chutter, M. R. Argall, B. J. Anderson, P.-A. Lindqvist, G. T. Marklund, Y. V. Khotyaintsev, B. H. Mauk, I. J. Cohen, D. N. Baker, A. N. Jaynes, R. E. Ergun, H. J. Singer, J. A Slavin, E. L. Kepko, T. E. Moore, B. Lavraud, V. Coffey, Y. Saito (2016a), Transient, small-scale field-aligned currents in the plasma sheet boundary layer during storm time substorms, Geophysical Research Letters, 43(10), 4841-4849, https://doi.org/10.1002/2016GL068768

Nakamura, T., R. Nakamura, and H. Haseagwa (2016b), Spatial dimensions of the electron diffusion region in anti-parallel magnetic reconnection, Annales Geophysicae, 34(3), 357-367, https://doi.org/10.5194/angeo-34-357-2016

Nakamura, T. K. M., R. Nakamura, W. Baumjohann, T. Umeda, and I. Shinohara (2016), Three-dimensional development of front region of plasma jets generated by magnetic reconnection, Geophys. Res. Lett., 43, 8356–8364, http://doi.org/10.1002/2016GL070215

Narita, Y., R. Nakamur, W. Baumjohann, K.-H. Glassmeier, U. Motschmann, B. Giles, W. Magnes, D. Fischer, R. B. Torbert, C. T. Russell, R. J. Strangeway, J. L. Burch, Y. Nariyuki, S. Saito, and S. P. Gary (2016a), ON ELECTRON-SCALE WHISTLER TURBULENCE IN THE SOLAR WIND, Astrophysical Journal Letters, 827(1),https://doi.org/10.3847/2041-8205/827/1/L8

Narita, Y., F. Plaschke, R. Nakamura, W. Baumjohann, W. Magnes, D. Fischer, Z. Vörös, R. B. Torbert, C. T. Russell, R. J. Strangeway, H. K. Leinweber, K. R. Bromund, B. J. Anderson, G. Le, M. Chutter, J. A. Slavin, E. L. Kepko, J. L. Burch, U. Motschmann, I. Richter, K.-H. Glassmeier (2016b), Wave telescope technique for MMS magnetometer, Geophysical Research Letters, 43(10), 4774-4780, https://doi.org/10.1002/2016GL069035

Norgren, C., D. B. Graham Yu, V. Khotyaintsev, M. André, A. Vaivads, L.-J. Chen, P.-A. Lindqvist, G. T. Marklund, R. E. Ergun, W. Magnes, R. J. Strangeway, C. T. Russell,R. B. Torbert, W. R. Paterson, D. J. Gershman, J. C. Dorelli, L. A. Avanov, B. Lavraud, Y. Saito, B. L. Giles, C. J. Pollock, J. L. Burch (2016), Finite gyroradius effects in the electron outflow of asymmetric magnetic reconnection, Geophysical Research Letters, 43(13), 6724-6733, https://doi.org/10.1002/2016GL069205

Oieroset, M., T. D. Phan, C. Haggerty, M. A. Shay, J. P. Eastwood, D. J. Gershman, J. F. Drake, M. Fujimoto, R. E. Ergun, F. S. Mozer, M. Oka, R. B. Torbert, J. L. Burch, S. Wang, L. J. Chen, M. Swisdak, C. Pollock, J. C. Dorelli, S. A. Fuselier, B. Lavraud, B. L. Giles, T. E. Moore, Y. Saito, L. A. Avanov, W. Paterson, R. J. Strangeway, C. T. Russell, Y. Khotyaintsev, P. A. Lindqvist, K. Malakit (2016), MMS observations of large guide field symmetric reconnection between colliding reconnection jets at the center

of a magnetic flux rope at the magnetopause, Geophysical Research Letters, 43(11), 5536-5544, https://doi.org/10.1002/2016GL069166

Petrinec, S. M., J. L. Burch, S. A. Fuselier, R. G. Gomez, W. Lewis, K. J. Trattner, R. Ergun, B. Mauk, C. J. Pollock, C. Schiff, R. J. Strangeway, C. T. Russell, T.-D. Phan, D. Young. First published: 07 June 2016 (2016), Comparison of Magnetospheric Multiscale ion jet signatures with predicted reconnection site locations at the magnetopause, Geophysical Research Letters, 43(12), 5997-6004, https://doi.org/10.1002/2016GL069626

Phan, T., M. Shay, J. Eastwood, V. Angelopoulos, M. Oieroset, M. Oka, and M. Fujimoto (2016a), Establishing the Context for Reconnection Diffusion Region Encounters and Strategies for the Capture and Transmission of Diffusion Region Burst Data by MMS, Space Science Reviews, 199(1-4), 631-650, https://doi.org/10.1007/s11214-015-0150-2

Phan, T. D., J. P. Eastwood, P. A. Cassak, M. Øieroset, J. T. Gosling, D. J. Gershman, F. S. Mozer, M. A, Shay, M. Fujimoto, W. Daughton, J. F. Drake, J. L. Burch, R. B. Torbert, R. E. Ergun, L. J. Chen, S. Wang, C. Pollock, J. C. Dorelli, B. Lavraud, B. L. Giles, T. E. Moore, Y. Saito, L. A. Avanov, W. Paterson, R. J. Strangeway, C. T. Russell, Y. Khotyaintsev, P. A. Lindqvist, M. Oka, F. D. Wilder (2016b), MMS observations of electron-scale filamentary currents in the reconnection exhaust and near the X line, Geophysical Research Letters, 43(12), 6060-6069, https://doi.org/10.1002/2016GL069212

Plaschke, F., N. Kahr, D. Fischer, R. Nakamura, W. Baumjohann, W. Magnes, J. L. Burch, R. B. Torbert, C. T. Russell, B. L. Giles, R. J. Strangeway, H. K. Leinweber, K. R. Bromund, B. J. Anderson, G. Le, M. Chutter, J. A. Slavin, E. L. Kepko (2016), Steepening of waves at the duskside magnetopause, Geophysical Research Letters, 43(14), 7373-7380, https://doi.org/10.1002/2016GL070003

Pollock, C., T. Moore, A. Jacques, J. Burch, U. Gliese, Y. Saito, T. Omoto, L. Avanov, A. Barrie, V. Coffey, J. Dorelli, D. Gershman, B. Giles, T. Rosnack, C. Salo, S. Yokota, M. Adrian, C. Aoustin, C. Auletti, S. Aung, V. Bigio, N. Cao, M. Chandler, D. Chornay, K. Christian, G. Clark, G. Collinson, T. Corris, A. De Los Santos, R. Devlin, T. Diaz, T. Dickerson, C. Dickson, A. Diekmann, F. Diggs, C. Duncan, A. Figueroa-Vinas, C. Firman, M. Freeman, N. Galassi, K. Garcia, G. Goodhart, D. Guererro, J. Hageman, J. Hanley, E. Hemminger, M. Holland, M. Hutchins, T. James, W. Jones, S. Kreisler, J. Kujawski, V. Lavu, J. Lobell, E. LeCompte, A. Lukemire, E. MacDonald, A. Mariano, T. Mukai, K. Narayanan, Q. Nguyan, M. Onizuka, W. Paterson, S. Persyn, B. Piepgrass, F. Cheney, A. Rager, T. Raghuram, A. Ramil, L. Reichenthal, H. Rodriguez, J. Rouzaud, A. Rucker, Y. Saito, M. Samara, J.-A. Sauvaud, D. Schuster, M. Shappirio, K. Shelton, D. Sher, D. Smith, K. Smith, S. Smith, D. Steinfeld, R. Szymkiewicz, K. Tanimoto, J. Taylor, C. Tucker, K. Tull, A. Uhl, J. Vloet, P. Walpole, S. Weidner, D. White, G. Winkert, P.-S. Yeh, M. Zeuch (2016), Fast Plasma Investigation for Magnetospheric Multiscale, Space Science Reviews, 199(1-4), 331-406, https://doi.org/10.1007/s11214-016-0245-4

Price, L., M. Swisdak, J. F. Drake, P. A. Cassak, J. T. Dahlin, and R. E. Ergun (2016), The effects of turbulence on three-dimensional magnetic reconnection at the magnetopause, Geophysical Research Letters, 43(12), 6020-6027, https://doi.org/10.1002/2016GL069578

Reiff, P., and T. Cline (2016), Education and Communication for the Magnetospheric Multiscale Mission, Space Science Reviews, 199(1-4), 721-747, https://doi.org/10.1007/s11214-015-0166-7

Reiff, P. H., A. G. Daou, S. Y. Sazykin, R. Nakamura, M. R. Hairston, V. Coffey, M. O. Chandler, B. J. Anderson, C. T. Russell, D. Welling, S. A. Fuselier, K. J. Genestreti (2016), Multispacecraft observations and modeling of the 22/23 June 2015 geomagnetic storm, Geophysical Research Letters, 43(14), 7311-7318, https://doi.org/10.1002/2016GL069154

Russell, C., B. J. Anderson, W. Baumjohann, K. R. Bromund, D. Dearborn, D. Fischer, G. Le, H. K. Leinweber, D. Leneman, W. Magnes, J. D. Means, M. B. Moldwin, R. Nakamura, D. Pierce, F. Plaschke, K. M. Rowe, J. A. Slavin, R. J. Strangeway, R. Torbert, C. Hagen, I. Jernej, A. Valavanoglou, I. Richter

(2016), The Magnetospheric Multiscale Magnetometers, Space Science Reviews, 199(1-4), 189-256, https://doi.org/10.1007/s11214-014-0057-3

Schmid, D., R. Nakamura, M. Volwerk, F. Plaschke, Y. Narita, W. Baumjohann, W. Magnes, D. Fischer, H. U. Eichelberger, R. B. Torbert, C. T. Russell, R. J. Strangeway, H. K. Leinweber, G. Le, K. R. Bromund, B. J. Anderson, J. A. Slavin, E. L. Kepko (2016), A comparative study of dipolarization fronts at MMS and Cluster, Geophysical Research Letters, 43(12), 6012-6019, https://doi.org/10.1002/2016GL069520

Sedlak, J.E. (2016, September). Center of Mass Estimation for a Spinning Spacecraft Using Doppler Shift of the GPS Carrier Frequency. AAS/AIAA Astrodynamics Specialist Conference, Long Beach, CA. https://arc.aiaa.org/doi/pdf/10.2514/6.2016-5519

Shay, M. A., T. D. Phan, C. C. Haggerty, M. Fujimoto, J. F. Drake, K. Malakit, P. A. Cassak, and M. Swisdak (2016), Kinetic signatures of the region surrounding the X line in asymmetric (magnetopause) reconnection, Geophysical Research Letters, 43(9), 4145-4154, https://doi.org/10.1002/2016GL069034

Sonnerup, B. U. O., H. Hasegawa, R. E. Denton, and T. K. M. Nakamura (2016), Reconstruction of the electron diffusion region, Journal of Geophysical Research-Space Physics, 121(5), 4279-4290, https://doi.org/10.1002/2016JA022430

Stawarz, J. E., S. Eriksson, F. D. Wilder, R. E. Ergun, S. J. Schwartz, A. Pouquet, J. L. Burch, B. L. Giles, Y. Khotyaintsev, O. Le Contel, P.-A. Lindqvist, W. Magnes, C. J. Pollock, C. T. Russell, R. J. Strangeway, R. B. Torbert, L. A. Avanov, J. C. Dorelli, J. P. Eastwood, D. J. Gershman, K. A. Goodrich, D. M. Malaspina, G. T. Marklund, L. Mirioni, A. P. Sturner, (2016), Observations of turbulence in a Kelvin-Helmholtz event on 8 September 2015 by the Magnetospheric Multiscale mission, Journal of Geophysical Research-Space Physics, 121(11), 11021-11034, https://doi.org/10.1002/2016JA023458

Toledo-Redondo, S., Andre, M., Khotyaintsev, Y. V., Vaidas, A., Walsh, A., Li, W., Graham, D. B., Lavraud, B., Masson, A., Aunai, N., Divin, A., Dargent, J., Fuselier, S., Gershman, D. J., Dorelli, J., Giles, B., Avanov, L., Pollock, C., Saito, Y., Moore, T. E., Coffey, V., Chandler, M. O., Lindqvist, P.-A., Torbert, R., Russell, C. T. (2016), Cold ion demagnetization near the X-line of magnetic reconnection, Geophysical Research Letters, 43(13), 6759-6767, https://doi.org/10.1002/2016GL069877

Tooley, C., R. Black, B. Robertson, J. Stone, S. Pope, and G. Davis (2016), The Magnetospheric Multiscale Constellation, Space Science Reviews, 199(1-4), 23-76, https://doi.org/10.1007/s11214-015-0220-5

Torbert, R., C. T. Russell, W. Magnes, R. E. Ergun, P.-A. Lindqvist, O. Le Contel, H. Vaith, J. Macri, S. Myers, D. Rau, J. Needell, B. King, M. Granoff, M. Chutter, I. Dors, G. Olsson, Y. V. Khotyaintsev, A. Eriksson, C. A. Kletzing, S. Bounds, B. Anderson, W. Baumjohann, M. Steller, K. Bromund, Guan Le, R. Nakamura, R. J. Strangeway, H. K. Leinweber, S. Tucker, J. Westfall, D. Fischer, F. Plaschke, J. Porter, K. Lappalainen (2016a), The FIELDS Instrument Suite on MMS: Scientific Objectives, Measurements, and Data Products, Space Science Reviews, 199(1-4), 105-135, https://doi.org/10.1007/s11214-014-0109-8

Torbert, R., H. Vaith, M. Granoff, M. Widholm, J. A. Gaidos, B. H. Briggs, I. G. Dors, M. W. Chutter, J. Macri, M. Argall, D. Bodet, J. Needell, M. B. Steller, W. Baumjohann, R. Nakamura, F. Plaschke, H. Ottacher, J. Hasiba, K. Hofmann, C. A. Kletzing, S. R. Bounds, R. T. Dvorsky, K. Sigsbee,V. Kooi (2016b), The Electron Drift Instrument for MMS, Space Science Reviews, 199(1-4), 283-305, https://doi.org/10.1007/s11214-015-0182-7

Torbert, R. B., J. L. Burch, B. L. Giles, D. Gershman, C. J. Pollock, J. Dorelli, L. Avanov, M. R. Argall, J. Shuster, R. J. Strangeway, C. T. Russell, R. E. Ergun, F. D. Wilder, K. Goodrich, H. A. Faith, C. J. Farrugia, P.-A. Lindqvist, T. Phan, Y. Khotyaintsev, T. E. Moore, G. Marklund,W. Daughton, W. Magnes, C. A. Kletzing, S. Bounds (2016c), Estimates of terms in Ohm's law during an encounter with an electron diffusion region, Geophysical Research Letters, 43(12), 5918-5925, https://doi.org/10.1002/2016GL069553

Torbert, R. B., H. Vaith, M. Granoff, M. Widholm, J. A. Gaidos, B. H. Briggs, I. G. Dors, M. W. Chutter, J. Macri, M. Argall, D. Bodet, J. Needell, M. B. Steller, W. Baumjohann, R. Nakamura, F. Plaschke, H. Ottacher, J. Hasiba, K. Hofmann, C. A. Kletzing, S. R. Bounds, R. T. Dvorsky, K. Sigsbee, V. Kooi (2016d), Erratum to: The Electron Drift Instrument for MMS (vol 199, pg 283, 2016), Space Science Reviews, 199(1-4), 307-308, https://doi.org/10.1007/s11214-016-0238-3

Torkar, K., R. Nakamura, M. Tajmar, C. Scharlemann, H. Jeszenszky, G. Laky, G. Fremuth, C. Escoubet, and K. Svenes (2016), Active Spacecraft Potential Control Investigation, Space Science Reviews, 199(1-4), 515-544, https://doi.org/10.1007/s11214-014-0049-3

Trattner, K. J., J. L. Burch, R. Ergun, S. A. Fuselier, R. G. Gomez, E. W. Grimes, W. S. Lewis, B. Mauk, S. M. Petrinec, C. J. Pollock, T. D. Phan, S. K. Vines, F. D. Wilder, D. T. Young (2016), The response time of the magnetopause reconnection location to changes in the solar wind: MMS case study, Geophysical Research Letters, 43(10), 4673-4682, https://doi.org/10.1002/2016GL068554

Turner, D. L., J. F. Fennell, J. B. Blake, J. H. Clemmons, B. H. Mauk, I. J. Cohen, A. N. Jaynes, J. V. Craft, F. D. Wilder, D. N. Baker, G. D. Reeves, D. J. Gershman, L. A. Avanov, J. C. Dorelli, B. L. Giles, C. J. Pollock, D. Schmid, R. Nakamura, R. J. Strangeway, C. T. Russell, A. V. Artemyev, A. Runov, V. Angelopoulos, H. E. Spence, R. B. Torbert, J. L. Burch (2016), Energy limits of electron acceleration in the plasma sheet during substorms: A case study with the Magnetospheric Multiscale (MMS) mission, Geophysical Research Letters, 43(15), 7785-7794, https://doi.org/10.1002/2016GL069691

Vernisse, Y., B. Lavraud, S. Eriksson, D. J. Gershman, J. Dorelli, C. Pollock, B. Giles, N. Aunai, L. Avanov, J. Burch, M. Chandler, V. Coffey, J. Dargent, R. E. Ergun, C. J. Farrugia, V. Génot, D. B. Graham, H. Hasegawa, C. Jacquey, I. Kacem, Y. Khotyaintsev, W. Li, W. Magnes, A. Marchaudon, T. Moore, W. Paterson, E. Penou, T. D. Phan, A. Retino, C. T. Russell, Y. Saito, J.-A. Sauvaud, R. Torbert, F. D. Wilder, S. Yokota (2016), Signatures of complex magnetic topologies from multiple reconnection sites induced by Kelvin-Helmholtz instability, Journal of Geophysical Research-Space Physics, 121(10), 9926-9939, https://doi.org/10.1002/2016JA023051

Wang, S., L.-J. Chen, N. Bessho, L. M. Kistler, J. R. Shuster, and R. Guo (2016a), Electron heating in the exhaust of magnetic reconnection with negligible guide field, Journal of Geophysical Research-Space Physics, 121(3), 2104-2130, https://doi.org/10.1002/2015JA021892

Wang, S., Chen, L.-J., Hesse, M., Bessho, N., Gershman, D. J., Dorelli, J., Giles, B., Torbert, R. B., Pollock, C. J., Strangeway, R., Ergun, R. E., Burch, J. L., Avanov, L., Lavraud, B., Moore, T. E., Saito, Y. (2016b), Two-scale ion meandering caused by the polarization electric field during asymmetric reconnection, Geophysical Research Letters, 43(15), 7831-7839, https://doi.org/10.1002/2016GL069842

Wang, S., Chen, L.-J., Hesse, M., Gershman, D. J., Dorelli, J., Giles, B., Torbert, R. B., Pollock, Strangeway, R., Ergun, R. E., Burch, J. L., Avanov, L., Moore, T. E., Saito, Y. (2016c), Ion demagnetization in the magnetopause current layer observed by MMS, Geophysical Research Letters, 43(10), 4850-4857, https://doi.org/10.1002/2016GL069406

Wendel, D. E., M. Hesse, N. Bessho, M. L. Adrian, and M. Kuznetsova (2016), Nongyrotropic electrons in guide field reconnection, Physics of Plasmas, 23(2), https://doi.org/10.1063/1.4942031

Westlake, J. H., I. J. Cohen, B. H. Mauk, B. J. Anderson, D. G. Mitchell, M. Gkioulidou, B. M. Walsh, L. J. Lanzerotti, R. J. Strangeway, and C. T. Russell (2016), The permeability of the magnetopause to a multispecies substorm injection of energetic particles, Geophysical Research Letters, 43(18), 9453-9460, https://doi.org/10.1002/2016GL070189

Wilder, F. D., R. E. Ergun, K. A. Goodrich, M. V. Goldman, D. L. Newman, D. M. Malaspina, A. N. Jaynes, S. J. Schwartz, K. J. Trattner, J. L. Burch, M. R. Argall, R. B. Torbert, P.-A. Lindqvist, G. Marklund, O. Le Contel, L. Mirioni, Yu. V. Khotyaintsev, R. J. Strangeway, C. T. Russell, C. J. Pollock, B. L. Giles, F. Plaschke, W. Magnes, S. Eriksson, J. E. Stawarz, A. P. Sturner, J. C. Holmes (2016a),

Observations of whistler mode waves with nonlinear parallel electric fields near the dayside magnetic reconnection separatrix by the Magnetospheric Multiscale mission, Geophysical Research Letters, 43(12), 5909-5917, https://doi.org/10.1002/2016GL069473

Wilder, F. D., R. E. Ergun, S. J. Schwartz, D. L. Newman, S. Eriksson, J. E. Stawarz, M. V. Goldman, K. A. Goodrich, D. J. Gershman, D. M. Malaspina, J. C. Holmes, A. P. Sturner, J. L. Burch, R. B. Torbert, P.-A. Lindqvist, G. T. Marklund, Y. Khotyaintsev, R. J. Strangeway, C. T. Russell, C. J. Pollock, B. L. Giles, J. C. Dorrelli, L. A. Avanov, W. R. Patterson, F. Plaschke, W. Magnes (2016b), Observations of large-amplitude, parallel, electrostatic waves associated with the Kelvin-Helmholtz instability by the magnetospheric multiscale mission, Geophysical Research Letters, 43(17), 8859-8866, https://doi.org/10.1002/2016GL070404

Williams, T., N. Ottenstein, E. Palmer and M. Farahmand (2016), Initial Satellite Formation Flight Results from the Magnetospheric Multiscale Mission, Paper AIAA 2016-5505, AIAA SPACE-2016, Long Beach, CA, Sept. 2016. https://doi.org/10.2514/6.2016-5505

Williams, T., S. Shulman, J. Sedlak, N. Ottenstein and B. Lounsbury (2016), Magnetospheric Multiscale Mission Attitude Dynamics: Observations from Flight Data, Paper AIAA 2016-5505, AIAA SPACE-2016, Long Beach, CA, Sept. 2016. https://doi.org/10.2514/6.2016-5675

Yordanova, E., Z. Vörös, A. Varsani, D. B. Graham, C. Norgren, Yu. V. Khotyaintsev, A. Vaivads, E. Eriksson, R. Nakamura, P.-A. Lindqvist, G. Marklund, R. E. Ergun, W. Magnes, W. Baumjohann, D. Fischer, F. Plaschke, Y. Narita, C. T. Russell, R. J. Strangeway, O. Le Contel, C. Pollock, R. B. Torbert, B. J. Giles, J. L. Burch, L. A. Avanov, J. C. Dorelli, D. J. Gershman, W. R. Paterson, B. Lavraud, Y. Saito (2016), Electron scale structures and magnetic reconnection signatures in the turbulent magnetosheath, Geophysical Research Letters, 43(12), 5969-5978, https://doi.org/10.1002/2016GL069191

Young, D., J. L. Burch, R. G. Gomez, A. De Los Santos, G. P. Miller, P. Wilson IV, N. Paschalidis, S. A. Fuselier, K. Pickens, E. Hertzberg, C. J. Pollock, J. Scherrer, P. B. Wood, E. T. Donald, D. Aaron, J. Furman, D. George, R. S. Gurnee, R. S. Hourani, A. Jacques, T. Johnson, T. Orr, K. S. Pan, S. Persyn, S. Pope, J. Roberts, M. R. Stokes, K. J. Trattner, J. M. Webster (2016), Hot Plasma Composition Analyzer for the Magnetospheric Multiscale Mission, Space Science Reviews, 199(1-4), 407-470, https://doi.org/10.1007/s11214-014-0119-6

Zhao, C., C. T. Russell, R. J. Strangeway, S. M. Petrinec, W. R. Paterson, M. Zhou, B. J. Anderson,W. Baumjohann, K. R. Bromund, M. Chutter, D. Fischer, G. Le, R. Nakamura, F. Plaschke, J. A. Slavin, R. B. Torbert, H. Y. Wei (2016), Force balance at the magnetopause determined with MMS: Application to flux transfer events, Geophys. Res. Lett., 43, 11,941–11,947, https://doi.org/10.1002/2016GL071568

Zhou, M., M. Ashour-Abdalla, J. Berchem, R. J. Walker, H. Liang, M. El-Alaoui, M. L. Goldstein, P.-A. Lindqvist, G. Marklund, Y. V. Khotyaintsev, R. E. Ergun, F. D. Wilder, C. T. Russell, R. J. Strangeway, C. Zhao, W. R. Paterson, B. L. Giles, C. J. Pollock, R. B. Torbert, J. L. Burch, J. C. Dorelli, D. J. Gershman, L. A. Avanov, B. Lavraud, M. O. Chandler (2016), Observation of high-frequency electrostatic waves in the vicinity of the reconnection ion diffusion region by the spacecraft of the Magnetospheric Multiscale (MMS) mission, Geophysical Research Letters, 43(10), 4808-4815, https://doi.org/10.1002/2016GL069010

2015

Andriopoulou, M., R. Nakamura, K. Torkar, W. Baumjohann, and B. Hoelzl (2015), Deriving plasma densities in tenuous plasma regions, with the spacecraft potential under active control, Journal of Geophysical Research-Space Physics, 120(11), 9594-9616, https://doi.org/10.1002/2015JA021472

Ashour-Abdalla, M., G. Lapenta, R. Walker, M. El-Alaoui, and H. Liang (2015), Multiscale study of electron energization during unsteady reconnection events, Journal of Geophysical Research-Space Physics, 120(6), 4784-4799, https://doi.org/10.1002/2014JA020316

Bessho, N., L.-J. Chen, K. Germaschewski, and A. Bhattacharjee (2015), Electron acceleration by parallel and perpendicular electric fields during magnetic reconnection without guide field, Journal of Geophysical Research-Space Physics, 120(11), 9355-9367, https://doi.org/10.1002/2015JA021548

Birn, J., M. Hesse, A. Runov, and X.-Z. Zhou (2015a), Ion beams in the plasma sheet boundary layer, Journal of Geophysical Research-Space Physics, 120(9), 7522-7535, https://doi.org/10.1002/2015JA021573

Birn, J., Y.-H. Liu, W. Daughton, M. Hesse, and K. Schindler (2015b), Reconnection and interchange instability in the near magnetotail, Earth Planets and Space, 67, https://doi.org/10.1186/s40623-015-0282-3

Birn, J., A. Runov, and M. Hesse (2015c), Energetic ions in dipolarization events, Journal of Geophysical Research-Space Physics, 120(9), 7698-7717, https://doi.org/10.1002/2015JA021372

Farahmand, M., Long, A., and Carpenter, R. (2015, October). Magnetospheric Multiscale Mission Navigation Performance Using the Goddard Enhanced Onboard Navigation System. 25th International Symposium on Space Flight Dynamics, Munich, Germany. https://issfd.org/2015/files/downloads/papers/024_Farahmand.pdf

Goldstein, M., M. L. Goldstein, P. Escoubet, K.-Joo Hwang, D. E. Wendel, A.-F. Viñas, S. F. Fung, S. Perri, S. Servidio, J. S. Pickett, G. K. Parks, F. Sahraoui, C. Gurgiolo, W. Matthaeus, J. M. Weygand (2015), Multipoint observations of plasma phenomena made in space by Cluster, Journal of Plasma Physics, 81, https://doi.org/10.1017/S0022377815000185

Hesse, M., Aunai, N., Kuznetsova, M., Zenitani, S. and Birn, J. (2015) Magnetic Reconnection in Different Environments, in Magnetotails in the Solar System (eds A. Keiling, C. M. Jackman and P. A. Delamere), John Wiley and Sons, Inc, Hoboken, NJ. https://doi.org/10.1002/9781118842324ch15

Lapenta, G., S. Markidis, M. Goldman, and D. Newman (2015), Secondary reconnection sites in reconnection-generated flux ropes and reconnection fronts, Nature Physics, 11(8), 690-+, https://doi.org/10.1038/NPHYS3406

Liu, Y.-H., M. Hesse, and M. Kuznetsova (2015a), Orientation of X lines in asymmetric magnetic reconnection- Mass ratio dependency, Journal of Geophysical Research-Space Physics, 120(9), 7331-7341, https://doi.org/10.1002/2015JA021324

Liu, Y.-H., F. Guo, W. Daughton, H. Li, and M. Hesse (2015b), Scaling of Magnetic Reconnection in Relativistic Collisionless Pair Plasmas, Physical Review Letters, 114(9), https://doi.org/10.1103/PhysRevLett.114.095002

Moore, T. E., J. L. Burch, and R. B. Torbert (2015), Magnetic reconnection, Nature Physics, 11(8), 611-613.

Queen, S. Z. (2015, October). A Kalman Filter for Mass Property and Thrust Identification of the Spin-Stabilized Magnetospheric Multiscale Formation. 25th International Symposium on Spaceflight Dynamics, Munich, Germany. https://ntrs.nasa.gov/api/citations/20150019913/downloads/20150019913.pdf

Raymond, J.C., Sedlak, J.E., and Vint, B. (2015, October). Attitude Ground System (AGS) for the Magnetospheric Multiscale (MMS) Mission. 25th International Symposium on Spaceflight Dynamics, Munich, Germany. https://ntrs.nasa.gov/api/citations/20110014284/downloads/20110014284.pdf

Shuster, J. R., L.-J. Chen, M. Hesse, M. R. Argall, W. Daughton, R. B. Torbert, and N. Bessho (2015), Spatiotemporal evolution of electron characteristics in the electron diffusion region of magnetic reconnection: Implications for acceleration and heating, Geophysical Research Letters, 42(8), 2586-2593, https://doi.org/10.1002/2015GL063601

Torkar, K., R. Nakamura, and M. Andriopoulou (2015), Interdependencies Between the Actively Controlled Cluster Spacecraft Potential, Ambient Plasma, and Electric Field Measurements, Ieee Transactions on Plasma Science, 43(9), 3054-3063, https://doi.org/10.1109/TPS.2015.2422733

Vines, S. K., S. A. Fuselier, K. J. Trattner, S. M. Petrinec, and J. F. Drake (2015), Ion acceleration dependence on magnetic shear angle in dayside magnetopause reconnection, Journal of Geophysical Research-Space Physics, 120(9), 7255-7269, https://doi.org/10.1002/2015JA021464

Wyper, P. F., and M. Hesse (2015), Quantifying three dimensional reconnection in fragmented current layers, Physics of Plasmas, 22(4), https://doi.org/10.1063/1.4918335

2014

Bessho, N., L.-J. Chen, J. R. Shuster, and S. Wang (2014), Electron distribution functions in the electron diffusion region of magnetic reconnection: Physics behind the fine structures, Geophysical Research Letters, 41(24), 8688-8695, https://doi.org/10.1002/2014GL062034

Birn, J., and M. Hesse (2014a), Forced reconnection in the near magnetotail: Onset and energy conversion in PIC and MHD simulations, Journal of Geophysical Research-Space Physics, 119(1), 290-309, https://doi.org/10.1002/2013JA019354

Birn, J., and M. Hesse (2014b), The substorm current wedge: Further insights from MHD simulations, Journal of Geophysical Research-Space Physics, 119(5), 3503-3513, https://doi.org/10.1002/2014JA019863

Birn, J., A. Runov, and M. Hesse (2014), Energetic electrons in dipolarization events: Spatial properties and anisotropy, Journal of Geophysical Research-Space Physics, 119(5), 3604-3616, https://doi.org/10.1002/2013JA019738

Genestreti, K., S. Fuselier, J. Goldstein, T. Nagai, and J. Eastwood (2014), The location and rate of occurrence of near-Earth magnetotail reconnection as observed by Cluster and Geotail, Journal of Atmospheric and Solar-Terrestrial Physics, 121, 98-109, https://doi.org/10.1016/j.jastp.2014.10.005

Hesse, M., N. Aunai, D. Sibeck, and J. Birn (2014), On the electron diffusion region in planar, asymmetric, systems, Geophysical Research Letters, 41(24), 8673-8680, https://doi.org/10.1002/2014GL061586

Liu, Y.-H., J. Birn, W. Daughton, M. Hesse, and K. Schindler (2014), Onset of reconnection in the near magnetotail: PIC simulations, Journal of Geophysical Research-Space Physics, 119(12), https://doi.org/10.1002/2014JA020492

Shuster, J. R., L.-J. Chen, W. S. Daughton, L. C. Lee, K. H. Lee, N. Bessho, R. B. Torbert, G. Li, and M. R. Argall (2014), Highly structured electron anisotropy in collisionless reconnection exhausts, Geophysical Research Letters, 41(15), 5389-5395, https://doi.org/10.1002/2014GL060608

Zenitani, S., and T. Umeda (2014), Some remarks on the diffusion regions in magnetic reconnection, Physics of Plasmas, 21(3), https://doi.org/10.1063/1.4869717

Zenitani, S., M. Hesse, A. Klimas, C. Black, and M. Kuznetsova (2014), The inner structure of collisionless magnetic reconnection: The electron-frame dissipation measure and Hall fields (vol 18, 122108, 2011), Physics of Plasmas, 21(12). https://doi.org/10.1063/1.4905516

2013

Aunai, N., M. Hesse, C. Black, R. Evans, and M. Kuznetsova (2013a), Influence of the dissipation mechanism on collisionless magnetic reconnection in symmetric and asymmetric current layers, Physics of Plasmas, 20(4), https://doi.org/10.1063/1.4795727

Aunai, N., M. Hesse, and M. Kuznetsova (2013b), Electron nongyrotropy in the context of collisionless magnetic reconnection, Physics of Plasmas, 20(9), https://doi.org/10.1063/1.4820953

Aunai, N., M. Hesse, S. Zenitani, M. Kuznetsova, C. Black, R. Evans, and R. Smets (2013c), Comparison between hybrid and fully kinetic models of asymmetric magnetic reconnection: Coplanar and guide field configurations, Physics of Plasmas, 20(2), https://doi.org/10.1063/1.4792250

Birn, J., and M. Hesse (2013), The substorm current wedge in MHD simulations, Journal of Geophysical Research-Space Physics, 118(6), 3364-3376, https://doi.org/10.1002/jgra.50187

Birn, J., M. Hesse, R. Nakamura, and S. Zaharia (2013a), Particle acceleration in dipolarization events, Journal of Geophysical Research-Space Physics, 118(5), 1960-1971, https://doi.org/10.1002/jgra.50132

Birn, J., R. Nakamura, and M. Hesse (2013b), On the propagation of blobs in the magnetotail: MHD simulations, Journal of Geophysical Research-Space Physics, 118(9), 5497-5505, https://doi.org/10.1002/jgra.50521

Che, H., J. F. Drake, M. Swisdak, and M. L. Goldstein (2013), The adiabatic phase mixing and heating of electrons in Buneman turbulence, Physics of Plasmas, 20(6), https://doi.org/10.1063/1.4811137

Eastwood, J. P., T. D. Phan, M. Oieroset, M. A. Shay, K. Malakit, M. Swisdak, J. F. Drake, and A. Masters (2013), Influence of asymmetries and guide fields on the magnetic reconnection diffusion region in collisionless space plasmas, Plasma Physics and Controlled Fusion, 55(12), https://doi.org/10.1088/0741-3335/55/12/124001

Genestreti, K. J., S. A. Fuselier, J. Goldstein, and T. Nagai (2013), An empirical model for the location and occurrence rate of near-Earth magnetotail reconnection, Journal of Geophysical Research-Space Physics, 118(10), 6389-6396, https://doi.org/10.1002/2013JA019125

Hesse, M., N. Aunai, S. Zenitani, M. Kuznetsova, and J. Birn (2013), Aspects of collisionless magnetic reconnection in asymmetric systems, Physics of Plasmas, 20(6), https://doi.org/10.1063/1.4811467

Hunana, P., M. L. Goldstein, T. Passot, P. L. Sulem, D. Laveder, and G. P. Zank (2013a), POLARIZATION AND COMPRESSIBILITY OF OBLIQUE KINETIC ALFVEN WAVES, Astrophysical Journal, 766(2), https://doi.org/10.1088/0004-637X/766/2/93

Hunana, P., Goldstein, M. L., Passot, T., Laveder, D., Zank, G. P. (2013b), Properties of kinetic Alfven waves : a comparison of fluid models with kinetic theory, Proceedings of the Thirteenth International Solar Wind Conference (Solar Wind 13), 1539, 179-182, https://doi.org/10.1063/1.4811017

Klar, R. A., S. A. Miller, M. L. Brysch, A. R. Bertrand, and Ieee (2013), Performance of the Magnetospheric Multiscale Central Instrument Data Handling, in 2013 Ieee Aerospace Conference, edited.

Lyatsky, W., and M. L. Goldstein (2013), Effect of interchange instability on magnetic reconnection, Nonlinear Processes in Geophysics, 20(3), 365-377, https://doi.org/10.5194/npg-20-365-2013

Malakit, K., M. A. Shay, P. A. Cassak, and D. Ruffolo (2013), New Electric Field in Asymmetric Magnetic Reconnection, Physical Review Letters, 111(13), https://doi.org/10.1103/PhysRevLett.111.135001

Malaspina, D. M., D. L. Newman, L. B. Willson, III, K. Goetz, P. J. Kellogg, and K. Kerstin (2013), Electrostatic Solitary Waves in the Solar Wind: Evidence for Instability at Solar Wind Current Sheets, Journal of Geophysical Research-Space Physics, 118(2), 591-599, https://doi.org/10.1002/jgra.50102

Moore, T. E., J. L. Burch, W. S. Daughton, S. A. Fuselier, H. Hasegawa, S. M. Petrinec, and Z. Y. Pu (2013), Multiscale studies of the three-dimensional dayside X-line, Journal of Atmospheric and Solar-Terrestrial Physics, 99, 32-40, https://doi.org/10.1016/j.jastp.2012.10.004

Oka, M., S. Ishikawa, P. Saint-Hilaire, S. Krucker, and R. P. Lin (2013), KAPPA DISTRIBUTION MODEL FOR HARD X-RAY CORONAL SOURCES OF SOLAR FLARES, Astrophysical Journal, 764(1), https://doi.org/10.1088/0004-637X/764/1/6

Phan, T. D., G. Paschmann, J. T. Gosling, M. Oieroset, M. Fujimoto, J. F. Drake, and V. Angelopoulos (2013), The dependence of magnetic reconnection on plasma beta and magnetic shear: Evidence from magnetopause observations, Geophysical Research Letters, 40(1), 11-16, https://doi.org/10.1029/2012GL054528

Roscoe, C., S. Vadali, and K. Alfriend (2013a), Third-Body Perturbation Effects on Satellite Formations, Journal of the Astronautical Sciences, 60(3-4), 408-433, https://doi.org/10.1007/s40295-015-0057-x

Roscoe, C. W. T., S. R. Vadali, K. T. Alfriend, and U. P. Desai (2013b), Satellite formation design in orbits of high eccentricity with performance constraints specified over a region of interest: MMS phase II, Acta Astronautica, 82(1), 16-24, https://doi.org/10.1016/j.actaastro.2012.07.028

Rose, D., R. Panneton, R. Klar, and Ieee (2013), The MMS Burst System; Co-operative Concept of Flight Ground Operations to Maximize Burst System Science Data Return, in 2013 Ieee Aerospace Conference, edited.

Sonnerup, B. U. O., R. E. Denton, H. Hasegawa, and M. Swisdak (2013), Axis and velocity determination for quasi two-dimensional plasma/field structures from Faraday's law: A second look, Journal of Geophysical Research-Space Physics, 118(5), 2073-2086, https://doi.org/10.1002/jgra.50211

Torkar, K., and M. Tajmar (2013), Qualification of the Liquid Metal Ion Source Instruments for the NASA MMS Mission, Ieee Transactions on Plasma Science, 41(12), 3512-3519, https://doi.org/10.1109/TPS.2013.2282177

Vapirev, A. E., G. Lapenta, A. Divin, S. Markidis, P. Henri, M. Goldman, and D. Newman (2013), Formation of a transient front structure near reconnection point in 3-D PIC simulations, Journal of Geophysical Research-Space Physics, 118(4), 1435-1449, https://doi.org/10.1002/jgra.50136

Wan, M., W. H. Matthaeus, S. Servidio, and S. Oughton (2013), Generation of X-points and secondary islands in 2D magnetohydrodynamic turbulence, Physics of Plasmas, 20(4), https://doi.org/10.1063/1.4802985

Wendel, D. E., D. K. Olson, M. Hesse, N. Aunai, M. Kuznetsova, H. Karimabadi, W. Daughton, and M. L. Adrian (2013), The relation between reconnected flux, the parallel electric field, and the reconnection rate in a three-dimensional kinetic simulation of magnetic reconnection, Physics of Plasmas, 20(12), https://doi.org/10.1063/1.4833675

Williams, T. (2013, January/February). Launch Window Analysis for the Magnetospheric Multiscale Mission. Paper AAS 12-255, AAS/AIAA Space Flight Mechanics Meeting, Charleston, SC. https://ntrs.nasa.gov/api/citations/20140010795/downloads/20140010795.pdf

Zenitani, S., I. Shinohara, T. Nagai, and T. Wada (2013), Kinetic aspects of the ion current layer in a reconnection outflow exhaust, Physics of Plasmas, 20(9), https://doi.org/10.1063/1.4821963

2012

Birn, J., J. E. Borovsky, and M. Hesse (2012a), The role of compressibility in energy release by magnetic reconnection, Physics of Plasmas, 19(8), https://doi.org/10.1063/1.4742314

Birn, J., K. Schindler, M. Hesse, A. Keiling, E. Donovan, F. Bagenal, and T. Karlsson (2012b), Magnetotail Aurora Connection: The Role of Thin Current Sheets, in Auroral Phenomenology and Magnetospheric Processes: Earth and Other Planets, edited, pp. 337-346, https://doi.org/10.1029/2011GM001182.

Brysch, M. L., R. A. Klar, and C. D. Sauer (2012), Implementation for central data handling within a Multi-Instrument Suite, IEEE Aerospace Conference Proceedings. 1-9. https://doi.org/10.1109/AERO.2012.6187223

Chen, L.-J., W. Daughton, A. Bhattacharjee, R. B. Torbert, V. Roytershteyn, and N. Bessho (2012), In-plane electric fields in magnetic islands during collisionless magnetic reconnection, Physics of Plasmas, 19(11), https://doi.org/10.1063/1.4767645

Collinson, G., Dorelli, J. C., Avanov, L. A., Lewis, G. R., Moore, T. E., Pollock, C., Kataria, D. O., Bedington, R., Arridge, C. S., Chornay, D. J., Gliese, U., Mariano, A., Barrie, A. C., Tucker, C., Owen, C. J., Walsh, A. P., Shappirio, M. D., Adrian, M. L. (2012), The geometric factor of electrostatic plasma analyzers: A case study from the Fast Plasma Investigation for the Magnetospheric Multiscale mission, Review of Scientific Instruments, 83(3). https://doi.org/10.1063/1.3687021

Davis, V. A., M. J. Mandell, N. R. Baker, M. Brown-Hayes, G. T. Davis, R. H. Maurer, and C. Herrmann (2012), Surface-Charging Analysis of the Radiation Belt Storm Probe and Magnetospheric MultiScale Spacecraft, Ieee Transactions on Plasma Science, 40(2), 262-273. https://doi.org/10.1109/tps.2011.2178615

Denton, R. E., B. U. O. Sonnerup, M. Swisdak, J. Birn, J. F. Drake, and M. Hesse (2012), Test of Shi et al. method to infer the magnetic reconnection geometry from spacecraft data: MHD simulation with guide field and antiparallel kinetic simulation, Journal of Geophysical Research-Space Physics, 117, https://doi.org/10.1029/2012JA017877

Divin, A., G. Lapenta, S. Markidis, D. L. Newman, and M. V. Goldman (2012), Numerical simulations of separatrix instabilities in collisionless magnetic reconnection, Physics of Plasmas, 19(4), https://doi.org/10.1063/1.3698621

Eastwood, J. P., T. D. Phan, R. C. Fear, D. G. Sibeck, V. Angelopoulos, M. Oieroset, and M. A. Shay (2012), Survival of flux transfer event (FTE) flux ropes far along the tail magnetopause, Journal of Geophysical Research-Space Physics, 117, https://doi.org/10.1029/2012JA017722

El-Alaoui, M., R. L. Richard, M. Ashour-Abdalla, R. J. Walker, and M. L. Goldstein (2012), Turbulence in a global magnetohydrodynamic simulation of the Earth's magnetosphere during northward and southward interplanetary magnetic field, Nonlinear Processes in Geophysics, 19(2), 165-175, https://doi.org/10.5194/npg-19-165-2012

Hwang, K.-J., M. L. Goldstein, M. M. Kuznetsova, Y. Wang, A. F. Vinas, and D. G. Sibeck (2012), The first in situ observation of Kelvin-Helmholtz waves at high-latitude magnetopause during strongly dawnward interplanetary magnetic field conditions, Journal of Geophysical Research-Space Physics, 117, https://doi.org/10.1029/2011JA017256

Jenkins, B., M. W. L. Thein, and Ieee (2012), On-Board and/or Ground-Based Gyroless Accelerometer Calibration for NASA's Magnetospheric MultiScale (MMS) Mission, in 2012 American Control Conference, edited, pp. 179-184.

Klimas, A., M. Hesse, and S. Zenitani (2012), Particle-in-cell simulation of collisionless undriven reconnection with open boundaries, Physics of Plasmas, 19(4), https://doi.org/10.1063/1.3699032

Lapenta, G. (2012), Particle simulations of space weather, Journal of Computational Physics, 231(3), 795-821, https://doi.org/10.1016/j.jcp.2011.03.035

Leinweber, H. K., C. T. Russell, and K. Torkar (2012), In-flight calibration of the spin axis offset of a fluxgate magnetometer with an electron drift instrument, Measurement Science and Technology, 23(10), https://doi.org/10.1088/0957-0233/23/10/105003

Liu, Y.-H., J. F. Drake, and M. Swisdak (2012), The structure of the magnetic reconnection exhaust boundary, Physics of Plasmas, 19(2), https://doi.org/10.1063/1.3685755

Mandell, M. J., V. A. Davis, G. T. Davis, R. H. Maurer, and C. Herrmann (2012), Photoemission Driven Charging in Tenuous Plasma, Ieee Transactions on Plasma Science, 40(2), 209-216, https://doi.org/10.1109/tps.2011.2179675

Markidis, S., P. Henri, G. Lapenta, A. Divin, M. V. Goldman, D. Newman, and S. Eriksson (2012a), Collisionless magnetic reconnection in a plasmoid chain, Nonlinear Processes in Geophysics, 19(1), 145-153, https://doi.org/10.5194/npg-19-145-2012

Markidis, S., G. Lapenta, A. Divin, M. Goldman, D. Newman, and L. Andersson (2012b), Three dimensional density cavities in guide field collisionless magnetic reconnection, Physics of Plasmas, 19(3), https://doi.org/10.1063/1.3697976

Olson, C., C. Wright, and A. Long (2012), EXPECTED NAVIGATION FLIGHT PERFORMANCE FOR THE MAGNETOSPHERIC MULTISCALE (MMS) MISSION, in Spaceflight Mechanics 2012, edited by J. V. McAdams, D. P. McKinley, M. M. Berry and K. L. Jenkins, pp. 1437-1456.

Pan, Q., M. Ashour-Abdalla, M. El-Alaoui, R. J. Walker, and M. L. Goldstein (2012), Adiabatic acceleration of suprathermal electrons associated with dipolarization fronts, Journal of Geophysical Research-Space Physics, 117, https://doi.org/10.1029/2012JA018156

Roemer, T. J., N. F. Aubut, J. Chabot, W. K. Holmes, A. Jenkins, M. Johnson, and M. W. L. Thein (2012), USING THE MAGNETOSPHERIC MULTISCALE (MMS) TABLESAT IB FOR THE ANALYSIS OF ATTITUDE CONTROL AND FLEXIBLE BOOM DYNAMICS FOR MMS MISSION SPACECRAFT, in Spaceflight Mechanics 2012, edited by J. V. McAdams, D. P. McKinley, M. M. Berry and K. L. Jenkins, pp. 2115-2124.

Roscoe, C., S. Vadali, and K. Alfriend (2012), Design of Satellite Formations in Orbits of High Eccentricity with Performance Constraints Specified over a Region of Interest, Journal of the Astronautical Sciences, 59(1-2), 145-164.

Schindler, K., J. Birn, and M. Hesse (2012), Kinetic model of electric potentials in localized collisionless plasma structures under steady quasi-gyrotropic conditions, Physics of Plasmas, 19(8), https://doi.org/10.1063/1.4747162

Torkar, K., M. Tajmar, C. P. Escoubet, and K. Svenes (2012), Active Spacecraft Potential Control for the Magnetospheric Multiscale Mission, Ieee Transactions on Plasma Science, 40(2), 394-401, https://doi.org/10.1109/TPS.2011.2178867

Williams, T. (2012), LAUNCH WINDOW ANALYSIS FOR THE MAGNETOSPHERIC MULTISCALE MISSION, in Spaceflight Mechanics 2012, edited by J. V. McAdams, D. P. McKinley, M. M. Berry and K. L. Jenkins, pp. 2273-2291.

Zenitani, S., I. Shinohara, and T. Nagai (2012), Evidence for the dissipation region in magnetotail reconnection, Geophysical Research Letters, 39, https://doi.org/10.1029/2012GL051938

2011

Ashour-Abdalla, M., M. El-Alaoui, M. L. Goldstein, M. Zhou, D. Schriver, R. Richard, R. Walker, M. G. Kivelson, and K.-J. Hwang (2011), Observations and simulations of non-local acceleration of electrons in magnetotail magnetic reconnection events, Nature Physics, 7(4), 360-365, https://doi.org/10.1038/nphys1903

Birn, J., M. Hesse, and S. Zenitani (2011a), Reconnection in compressible plasmas: Extended conversion region, Physics of Plasmas, 18(11), https://doi.org/10.1063/1.3626836

Birn, J., R. Nakamura, E. V. Panov, and M. Hesse (2011b), Bursty bulk flows and dipolarization in MHD simulations of magnetotail reconnection, Journal of Geophysical Research-Space Physics, 116, https://doi.org/10.1029/2010JA016083

Che, H., J. F. Drake, and M. Swisdak (2011a), A current filamentation mechanism for breaking magnetic field lines during reconnection, Nature, 474(7350), 184-187, https://doi.org/10.1038/nature10091

Che, H., M. V. Goldman, and D. L. Newman (2011b), Buneman instability in a magnetized current-carrying plasma with velocity shear, Physics of Plasmas, 18(5), https://doi.org/10.1063/1.3590879

Chen, L.-J., W. S. Daughton, B. Lefebvre, and R. B. Torbert (2011), The inversion layer of electric fields and electron phase-space-hole structure during two-dimensional collisionless magnetic reconnection, Physics of Plasmas, 18(1), https://doi.org/10.1063/1.3529365

El-Alaoui, M., M. Ashour-Abdalla, R. L. Richard, M. L. Goldstein, J. M. Weygand, and R. J. Walker (2011), Global magnetohydrodynamic simulation of reconnection and turbulence in the plasma sheet (vol 116, A04206, 2011), Journal of Geophysical Research-Space Physics, 116, https://doi.org/10.1029/2011JA016601

Fuselier, S., and W. Lewis (2011), Properties of Near-Earth Magnetic Reconnection from In-Situ Observations, Space Science Reviews, 160(1-4), 95-121, https://doi.org/10.1007/s11214-011-9820-x

Goldman, M. V., G. Lapenta, D. L. Newman, S. Markidis, and H. Che (2011), Jet Deflection by Very Weak Guide Fields during Magnetic Reconnection, Physical Review Letters, 107(13), https://doi.org/10.1103/PhysRevLett.107.135001

Gosling, J. T., H. Tian, and T. D. Phan (2011), PULSED ALFVEN WAVES IN THE SOLAR WIND, Astrophysical Journal Letters, 737(2), https://doi.org/10.1088/2041-8205/737/2/L35

Griffiths, S. T., S. M. Petrinec, K. J. Trattner, S. A. Fuselier, J. L. Burch, T. D. Phan, and V. Angelopoulos (2011), A probability assessment of encountering dayside magnetopause diffusion regions, Journal of Geophysical Research-Space Physics, 116, https://doi.org/10.1029/2010JA015316

Hesse, M., J. Birn, and S. Zenitani (2011a), Magnetic reconnection in a compressible MHD plasma, Physics of Plasmas, 18(4), https://doi.org/10.1063/1.3581077

Hesse, M., T. Neukirch, K. Schindler, M. Kuznetsova, and S. Zenitani (2011b), The Diffusion Region in Collisionless Magnetic Reconnection, Space Science Reviews, 160(1-4), 3-23, https://doi.org/10.1007/s11214-010-9740-1

Hwang, K.-J., M. L. Goldstein, E. Lee, and J. S. Pickett (2011a), Cluster observations of multiple dipolarization fronts, Journal of Geophysical Research-Space Physics, 116, https://doi.org/10.1029/2010JA015742

Hwang, K.-J., M. M. Kuznetsova, F. Sahraoui, M. L. Goldstein, E. Lee, and G. K. Parks (2011b), Kelvin-Helmholtz waves under southward interplanetary magnetic field, Journal of Geophysical Research-Space Physics, 116, https://doi.org/10.1029/2011JA016596

Jenkins, Benjamin M., "Accelerometer calibration for NASA's magnetospheric multiscale mission spacecraft" (2011). Master's Theses and Capstones. 659. https://scholars.unh.edu/thesis/659

Lapenta, G., and L. Bettarini (2011a), Self-consistent seeding of the interchange instability in dipolarization fronts, Geophysical Research Letters, 38, https://doi.org/10.1029/2011GL047742

Lapenta, G., and L. Bettarini (2011b), Spontaneous transition to a fast 3D turbulent reconnection regime, Epl, 93(6), https://doi.org/10.1209/0295-5075/93/65001

Lapenta, G., S. Markidis, A. Divin, M. V. Goldman, and D. L. Newman (2011), Bipolar electric field signatures of reconnection separatrices for a hydrogen plasma at realistic guide fields, Geophysical Research Letters, 38, https://doi.org/10.1029/2011GL048572

Liu, Y.-H., J. F. Drake, and M. Swisdak (2011), The effects of strong temperature anisotropy on the kinetic structure of collisionless slow shocks and reconnection exhausts. II. Theory, Physics of Plasmas, 18(9), https://doi.org/10.1063/1.3627147

Markidis, S., G. Lapenta, L. Bettarini, M. Goldman, D. Newman, and L. Andersson (2011), Kinetic simulations of magnetic reconnection in presence of a background O+ population, Journal of Geophysical Research-Space Physics, 116, https://doi.org/10.1029/2011JA016429

Oieroset, M., T. D. Phan, J. P. Eastwood, M. Fujimoto, W. Daughton, M. A. Shay, V. Angelopoulos, F. S. Mozer, J. P. McFadden, D. E. Larson, K.-H. Glassmeier (2011), Direct Evidence for a Three-Dimensional Magnetic Flux Rope Flanked by Two Active Magnetic Reconnection X Lines at Earth's Magnetopause, Physical Review Letters, 107(16), https://doi.org/10.1103/PhysRevLett.107.165007

Oka, M., T.-D. Phan, J. P. Eastwood, V. Angelopoulos, N. A. Murphy, M. Oieroset, Y. Miyashita, M. Fujimoto, J. McFadden, and D. Larson (2011), Magnetic reconnection X-line retreat associated with dipolarization of the Earth's magnetosphere, Geophysical Research Letters, 38, https://doi.org/10.1029/2011GL049350

Olson, C., A. Long, and J. R. Carpenter (2011), SENSITIVITY OF MAGNETOSPHERIC MULTI-SCALE (MMS) MISSION NAVIGATION ACCURACY TO MAJOR ERROR SOURCES, in Spaceflight Mechanics 2011, Pts I-Iii, edited by M. K. Jah, Y. P. Guo, A. L. Bowes and P. C. Lai, pp. 1495-1512.

Phan, T. D., T. E. Love, J. T. Gosling, G. Paschmann, J. P. Eastwood, M. Oieroset, V. Angelopoulos, J. P. McFadden, D. Larson, and U. Auster (2011), Triggering of magnetic reconnection in a magnetosheath current sheet due to compression against the magnetopause, Geophysical Research Letters, 38, https://doi.org/10.1029/2011GL048586

Roscoe, C. W. T., S. R. Vadali, and K. T. Alfriend (2011a), DESIGN OF SATELLITE FORMATIONS IN ORBITS OF HIGH ECCENTRICITY WITH PERFORMANCE CONSTRAINTS SPECIFIED OVER A REGION OF INTEREST, in Kyle T. Alfriend Astrodynamics Symposium, edited by S. L. Coffey, J. L. Junkins, K. K. Luu, I. M. Ross, C. Sabol and P. W. Schumacher, pp. 145-162.

Roscoe, C. W. T., S. R. Vadali, K. T. Alfriend, and U. P. Desai (2011b), Optimal Formation Design for Magnetospheric Multiscale Mission Using Differential Orbital Elements, Journal of Guidance Control and Dynamics, 34(4), 1070-1080, https://doi.org/10.2514/1.52484

Sedlak, J.E., Superfin, E.A., and Raymond, J.C. (2011, February). Magnetospheric Multiscale (MMS) Mission Attitude Ground System Design. 22nd International Symposium on Spaceflight Dynamics, INPE, São José dos Campos, SP, Brazil. https://ntrs.nasa.gov/api/citations/20110014284/downloads/20110014284.pdf

Tao, J. B., R. E. Ergun, L. Andersson, J. W. Bonnell, A. Roux, O. Le Contel, V. Angelopoulos, J. P. McFadden, D. E. Larson, C. M. Cully, H.-U. Auster, K.-H. Glassmeier, (2011), A model of electromagnetic electron phase-space holes and its application, Journal of Geophysical Research-Space Physics, 116, https://doi.org/10.1029/2010JA016054

Wu, P., M. A. Shay, T. D. Phan, M. Oieroset, and M. Oka (2011), Effect of inflow density on ion diffusion region of magnetic reconnection: Particle-in-cell simulations, Physics of Plasmas, 18(11), https://doi.org/10.1063/1.3641964

Zenitani, S., M. Hesse, A. Klimas, C. Black, and M. Kuznetsova (2011a), The inner structure of collisionless magnetic reconnection: The electron-frame dissipation measure and Hall fields, Physics of Plasmas, 18(12), https://doi.org/10.1063/1.3662430

Zenitani, S., M. Hesse, A. Klimas, and M. Kuznetsova (2011b), New Measure of the Dissipation Region in Collisionless Magnetic Reconnection, Physical Review Letters, 106(19), https://doi.org/10.1103/PhysRevLett.106.195003

Zenitani, S., M. Hesse, A. Klimas, V. Florinski, J. Heerikhuisen, G. Zank, and D. Gallagher (2011c), Fluid and Magnetofluid Modeling of Relativistic Magnetic Reconnection, Partially Ionized Plasmas Throughout the Cosmos - Proceedings of the 2010 Huntsville Workshop, 1366, https://doi.org/10.1063/1.3625599

2010

Birn, J., and M. Hesse (2010), Energy release and transfer in guide field reconnection, Physics of Plasmas, 17(1), https://doi.org/10.1063/1.3299388

Birn, J., J. E. Borovsky, M. Hesse, and K. Schindler (2010), Scaling of asymmetric reconnection in compressible plasmas, Physics of Plasmas, 17(5), https://doi.org/10.1063/1.3429676

Brieda, L., A. Barrie, D. Hughes, and T. Errigo (2010), Analysis of Particulate Contamination During Launch of MMS Mission, in Optical System Contamination: Effects, Measurements, and Control 2010, edited by S. A. Straka and N. Carosso, https://doi.org/77940p10.1117/12.864331

Che, H., J. F. Drake, M. Swisdak, and P. H. Yoon (2010), Electron holes and heating in the reconnection dissipation region, Geophysical Research Letters, 37, https://doi.org/10.1029/2010GL043608

Chung, L. R., S. Novak, A. Long, and C. Gramling (2010), MAGNETOSPHERIC MULTISCALE (MMS) MISSION COMMISSIONING PHASE ORBIT DETERMINATION ERROR ANALYSIS, in Astrodynamics 2009, Vol 135, Pts 1-3, edited by A. V. Rao, T. A. Lovell, F. K. Chan and L. A. Cangahuala, pp. 355-374.

Denton, R. E., B. U. O. Sonnerup, J. Birn, W.-L. Teh, J. F. Drake, M. Swisdak, M. Hesse, and W. Baumjohann (2010), Test of methods to infer the magnetic reconnection geometry from spacecraft data, Journal of Geophysical Research-Space Physics, 115, https://doi.org/10.1029/2010JA015420

Divin, A., S. Markidis, G. Lapenta, V. S. Semenov, N. V. Erkaev, and H. K. Biernat (2010), Model of electron pressure anisotropy in the electron diffusion region of collisionless magnetic reconnection, Physics of Plasmas, 17(12), https://doi.org/10.1063/1.3521576

Eastwood, J. P., T. D. Phan, M. Oieroset, and M. A. Shay (2010a), Average properties of the magnetic reconnection ion diffusion region in the Earth's magnetotail: The 2001-2005 Cluster observations and comparison with simulations, Journal of Geophysical Research-Space Physics, 115, https://doi.org/10.1029/2009JA014962

Eastwood, J. P., M. A. Shay, T. D. Phan, and M. Oieroset (2010b), Asymmetry of the Ion Diffusion Region Hall Electric and Magnetic Fields during Guide Field Reconnection: Observations and Comparison with Simulations, Physical Review Letters, 104(20), https://doi.org/10.1103/PhysRevLett.104.205001

El-Alaoui, M., Ashour-Abdalla, M., Richard, R. L., Goldstein, M. L., Weygand, J. M., and Walker, R. J. (2010), Global magnetohydrodynamic simulation of reconnection and turbulence in the plasma sheet, *J. Geophys. Res.*, 115, A12236, http://doi.org/10.1029/2010JA015653

Gramling, C. J. (2010), OVERVIEW OF THE MAGNETOSPHERIC MULTISCALE FORMATION FLYING MISSION, in Astrodynamics 2009, Vol 135, Pts 1-3, edited by A. V. Rao, T. A. Lovell, F. K. Chan and L. A. Cangahuala, pp. 407-417.

Hesse, M., S. Zenitani, M. Kuznetsova, and A. Klimas (2010), A simple, analytical model of collisionless magnetic reconnection in a pair plasma (vol 16, 102106, 2009), Physics of Plasmas, 17(7), https://doi.org/10.1063/1.3450300

Hughes, S. P. (2010), OPTIMAL CONTROL AND NEAR OPTIMAL GUIDANCE FOR THE MAGNETOSPHERIC MULTISCALE MISSION (MMS), in Astrodynamics 2009, Vol 135, Pts 1-3, edited by A. V. Rao, T. A. Lovell, F. K. Chan and L. A. Cangahuala, pp. 439-462.

Klimas, A., M. Hesse, S. Zenitani, and M. Kuznetsova (2010), Particle-in-cell simulation of collisionless driven reconnection with open boundaries, Physics of Plasmas, 17(11), https://doi.org/10.1063/1.3510480

Lapenta, G., S. Markidis, A. Divin, M. Goldman, and D. Newman (2010), Scales of guide field reconnection at the hydrogen mass ratio, Physics of Plasmas, 17(8), https://doi.org/10.1063/1.3467503

Malakit, K., M. A. Shay, P. A. Cassak, and C. Bard (2010), Scaling of asymmetric magnetic reconnection: Kinetic particle-in-cell simulations, Journal of Geophysical Research-Space Physics, 115, https://doi.org/10.1029/2010JA015452

Mann, L. M., J. Tichy, and C. J. Gramling (2010), LAUNCH WINDOW OPPORTUNITY ASSESSMENT FOR THE MAGNETOSPHERIC MULTISCALE MISSION, in Astrodynamics 2009, Vol 135, Pts 1-3, edited by A. V. Rao, T. A. Lovell, F. K. Chan and L. A. Cangahuala, pp. 395-406.

Oka, M., M. Fujimoto, I. Shinohara, and T. D. Phan (2010a), "Island surfing" mechanism of electron acceleration during magnetic reconnection, Journal of Geophysical Research-Space Physics, 115, https://doi.org/10.1029/2010JA015392

Oka, M., T.-D. Phan, S. Krucker, M. Fujimoto, and I. Shinohara (2010b), ELECTRON ACCELERATION BY MULTI-ISLAND COALESCENCE, Astrophysical Journal, 714(1), 915-926, https://doi.org/10.1088/0004-637X/714/1/915

Phan, T. D., J. T. Gosling, G. Paschmann, C. Pasma, J. F. Drake, M. Oieroset, D. Larson, R. P. Lin, and M. S. Davis (2010), THE DEPENDENCE OF MAGNETIC RECONNECTION ON PLASMA beta AND MAGNETIC SHEAR: EVIDENCE FROM SOLAR WIND OBSERVATIONS, Astrophysical Journal Letters, 719(2), L199-L203, https://doi.org/10.1088/2041-8205/719/2/L199

Roberts, C. E., J. Tichy, and C. J. Gramling (2010), APOGEE RAISING TECHNIQUE FOR THE MAGNETOSPHERIC MULTISCALE FORMATION FLYING MISSION, in Astrodynamics 2009, Vol 135, Pts 1-3, edited by A. V. Rao, T. A. Lovell, F. K. Chan and L. A. Cangahuala, pp. 419-437.

Sahraoui, F., G. Belmont, M. L. Goldstein, and L. Rezeau (2010), Limitations of multispacecraft data techniques in measuring wave number spectra of space plasma turbulence, Journal of Geophysical Research-Space Physics, 115, https://doi.org/10.1029/2009ja014724

Scaperoth, P. T., A. Long, and J. R. Carpenter (2010), MAGNETOSPHERIC MULTISCALE MISSION (MMS) PHASE 2B NAVIGATION PERFORMANCE, in Astrodynamics 2009, Vol 135, Pts 1-3, edited by A. V. Rao, T. A. Lovell, F. K. Chan and L. A. Cangahuala, pp. 335-353.

Schindler, K., and M. Hesse (2010), Conditions for the formation of nongyrotropic current sheets in slowly evolving plasmas, Physics of Plasmas, 17(8), https://doi.org/10.1063/1.3464198

Waterhouse, D., M. Dunstan, M. Kramer, J. Kite, B. Jenkins, and M. W. Thein (2010), TABLESAT II FOR NASA'S MAGNETOSPHERIC MULTISCALE (MMS) MISSION - A PROBLEM IN ORBIT AND ATTITUDE DETERMINATION AND CONTROL, in Spaceflight Mechanics 2010, Pts I-Iii, edited by D. Mortari, T. F. Starchville, A. J. Trask and J. K. Miller, pp. 2295-2306.

Zenitani, S., M. Hesse, and A. Klimas (2010a), RESISTIVE MAGNETOHYDRODYNAMIC SIMULATIONS OF RELATIVISTIC MAGNETIC RECONNECTION, Astrophysical Journal Letters, 716(2), L214-L218, https://doi.org/10.1088/2041-8205/716/2/L214

Zenitani, S., M. Hesse, and A. Klimas (2010b), SCALING OF THE ANOMALOUS BOOST IN RELATIVISTIC JET BOUNDARY LAYER, Astrophysical Journal, 712(2), 951-956, https://doi.org/10.1088/0004-637X/712/2/951

Zenitani, S., M. Hesse, and A. Klimas (2010c), TWO-FLUID MAGNETOHYDRODYNAMIC SIMULATIONS OF RELATIVISTIC MAGNETIC RECONNECTION (vol 696, pg 1385, 2009), Astrophysical Journal, 722(1), 968-969, https://doi.org/10.1088/0004-637X/722/1/968

2009

Andersson, L., R. E. Ergun, J. Tao, A. Roux, O. LeContel, V. Angelopoulos, J. Bonnell, J. P. McFadden, D. E. Larson, S. Eriksson, T. Johansson, C. M. Cully, D. L. Newman, M. V. Goldman, K.-H.

Glassmeier,W. Baumjohann (2009), New Features of Electron Phase Space Holes Observed by the THEMIS Mission, Physical Review Letters, 102(22), https://doi.org/10.1103/PhysRevLett.102.225004

Birn, J., and M. Hesse (2009), Reconnection in substorms and solar flares: analogies and differences, Annales Geophysicae, 27(3), 1067-1078.

Birn, J., L. Fletcher, M. Hesse, and T. Neukirch (2009a), ENERGY RELEASE AND TRANSFER IN SOLAR FLARES: SIMULATIONS OF THREE-DIMENSIONAL RECONNECTION, Astrophysical Journal, 695(2), 1151-1162, https://doi.org/10.1088/0004-637X/695/2/1151

Birn, J., M. Hesse, K. Schindler, and S. Zaharia (2009b), Role of entropy in magnetotail dynamics, Journal of Geophysical Research-Space Physics, 114, https://doi.org/10.1029/2008JA014015

Cassak, P. A., and M. A. Shay (2009), Structure of the dissipation region in fluid simulations of asymmetric magnetic reconnection, Physics of Plasmas, 16(5), https://doi.org/10.1063/1.3086867

Chen, L.-J., Bessho, N., Lefebvre, B., Vaith, H., Asnes, A., Santolik, O., Fazakerley, A., Puhl-Quinn, P., Bhattacharjee, A., Khotyaintsev, Y., Daly, P., Torbert, R. (2009), Multispacecraft observations of the electron current sheet, neighboring magnetic islands, and electron acceleration during magnetotail reconnection, Physics of Plasmas, 16(5), https://doi.org/10.1063/1.3112744

Chung, L. R., Novak, S., Long, A., and Gramling, C. MAGNETOSPHERIC MULTISCALE (MMS) MISSION COMMISSIONING PHASE ORBIT DETERMINATION ERROR ANALYSIS.

Drake, J. F., M. Swisdak, T. D. Phan, P. A. Cassak, M. A. Shay, S. T. Lepri, R. P. Lin, E. Quataert, and T. H. Zurbuchen (2009), Ion heating resulting from pickup in magnetic reconnection exhausts, Journal of Geophysical Research-Space Physics, 114, https://doi.org/10.1029/2008JA013701

Eastwood, J. P., T. D. Phan, S. D. Bale, and A. Tjulin (2009), Observations of Turbulence Generated by Magnetic Reconnection, Physical Review Letters, 102(3), https://doi.org/10.1103/PhysRevLett.102.035001.

Ergun, R. E., L. Andersson, J. Tao, V. Angelopoulos, J. Bonnell, J. P. McFadden, D. E. Larson, S. Eriksson, T. Johansson, C. M. Cully, D. N. Newman, M. V. Goldman, A. Roux, O. LeContel, K.-H. Glassmeier, W. Baumjohann (2009), Observations of Double Layers in Earth's Plasma Sheet, Physical Review Letters, 102(15), https://doi.org/10.1103/PhysRevLett.102.155002

Eriksson, S., J. T. Gosling, T. D. Phan, L. M. Blush, K. D. C. Simunac, D. Krauss-Varban, A. Szabo, J. G. Luhmann, C. T. Russell, A. B. Galvin, M. H. Acuña (2009), Asymmetric shear flow effects on magnetic field configuration within oppositely directed solar wind reconnection exhausts, Journal of Geophysical Research-Space Physics, 114, https://doi.org/10.1029/2008JA013990

Folkner, W. M., Williams, J. G., and Boggs, D. H. (2009). The planetary and lunar ephemeris DE 421. IPN progress report, 42(178), 1-34.

Hasegawa, H., et al. (2009), Kelvin-Helmholtz waves at the Earth’s magnetopause: Multiscale development and associated reconnection, J. Geophys. Res., 114, A12207, http://doi.org/10.1029/2009JA014042

Hesse, M., S. Zenitani, M. Kuznetsova, and A. Klimas (2009a), A simple, analytical model of collisionless magnetic reconnection in a pair plasma, Physics of Plasmas, 16(10), https://doi.org/10.1063/1.3246005

Hesse, M., S. Zenitani, M. Kuznetsova, and A. Klimas (2009b), A simple, analytical model of collisionless magnetic reconnection in a pair plasma (vol 16, 102106, 2009), Physics of Plasmas, 16(12), https://doi.org/10.1063/1.3275791

Hughes, S. P. (2009). OPTIMAL CONTROL AND NEAR OPTIMAL GUIDANCE FOR THE MAGNETOSPHERIC MULTISCALE MISSION(MMS). *Advances in the Astronautical Sciences*, *135*(1), 439-462.

Kuznetsova, M. M., D. G. Sibeck, M. Hesse, Y. Wang, L. Rastaetter, G. Toth, and A. Ridley (2009), Cavities of weak magnetic field strength in the wake of FTEs: Results from global magnetospheric MHD simulations, Geophysical Research Letters, 36, https://doi.org/10.1029/2009GL037489

Lapenta, G. (2009), Large-scale momentum exchange by microinstabilities: a process happening in laboratory and space plasmas, Physica Scripta, 80(3), https://doi.org/10.1088/0031-8949/80/03/035507

Mann, L. M., Tichy, J., and Gramling, C. J. (2009). LAUNCH WINDOW OPPORTUNITY ASSESSMENT FOR THE MAGNETOSPHERIC MULTISCALE MISSION. *Advances in the Astronautical Sciences*, *135*(1), 395-406.

Roberts, C. E., Tichy, J., and Gramling, C. J. (2009). Apogee Raising Technique for the Magnetospheric Multiscale Formation Flying Mission. *Advances in the Astronautical Sciences*, *135*(1), 419-437.

Scaperoth, P. T., Long, A., and Carpenter, R. (2009, August). Magnetospheric Multiscale Mission (MMS) Phase 2B Navigation Performance. In *2009 AAS/AIAA Astrodynamics Specialist Conference*.

Winternitz, L. M. B., W. A. Bamford, and G. W. Heckler (2009), A GPS Receiver for High-Altitude Satellite Navigation, Ieee Journal of Selected Topics in Signal Processing, 3(4), 541-556, https://doi.org/10.1109/jstsp.2009.2023352

Zenitani, S., M. Hesse, and A. Klimas (2009a), RELATIVISTIC TWO-FLUID SIMULATIONS OF GUIDE FIELD MAGNETIC RECONNECTION, Astrophysical Journal, 705(1), 907-913, https://doi.org/10.1088/0004-637X/705/1/907

Zenitani, S., M. Hesse, and A. Klimas (2009b), TWO-FLUID MAGNETOHYDRODYNAMIC SIMULATIONS OF RELATIVISTIC MAGNETIC RECONNECTION, Astrophysical Journal, 696(2), 1385-1401, https://doi.org/10.1088/0004-637X/696/2/1385

2008

Birn, J., J. E. Borovsky, and M. Hesse (2008), Properties of asymmetric magnetic reconnection, Physics of Plasmas, 15(3), https://doi.org/10.1063/1.2888491

Borovsky, J. E., M. Hesse, J. Birn, and M. M. Kuznetsova (2008), What determines the reconnection rate at the dayside magnetosphere?, Journal of Geophysical Research-Space Physics, 113(A7), https://doi.org/10.1029/2007JA012645

Goldman, M. V., D. L. Newman, and P. Pritchett (2008), Vlasov simulations of electron holes driven by particle distributions from PIC reconnection simulations with a guide field, Geophysical Research Letters, 35(22), https://doi.org/10.1029/2008GL035608

Hesse, M., S. Zenitani, and A. Klimas (2008), The structure of the electron outflow jet in collisionless magnetic reconnection, Physics of Plasmas, 15(11), https://doi.org/10.1063/1.3006341

Hughes, S. P. (2008), General method for optimal guidance of spacecraft formations, Journal of Guidance Control and Dynamics, 31(2), 414-423, https://doi.org/10.2514/1.23731

Klimas, A., M. Hesse, and S. Zenitani (2008), Particle-in-cell simulation of collisionless reconnection with open outflow boundaries, Physics of Plasmas, 15(8), https://doi.org/10.1063/1.2965826

Schindler, K., and M. Hesse (2008), Formation of thin bifurcated current sheets by quasisteady compression, Physics of Plasmas, 15(4), https://doi.org/10.1063/1.2907359

Scudder, J. D., R. D. Holdaway, R. Glassberg, and S. L. Rodriguez (2008), Electron diffusion region and thermal demagnetization, Journal of Geophysical Research-Space Physics, 113(A10), https://doi.org/10.1029/2008ja013361

Zenitani, S., and M. Hesse (2008a), Self-regulation of the reconnecting current layer in relativistic pair plasma reconnection, Astrophysical Journal, 684(2), 1477-1485, https://doi.org/10.1086/590425

Zenitani, S., and M. Hesse (2008b), The role of the Weibel instability at the reconnection jet front in relativistic pair plasma reconnection, Physics of Plasmas, 15(2), https://doi.org/10.1063/1.2836623

Zenitani, S., and M. Hesse (2008c), The role of the Weibel instability at the reconnection jet front in relativistic pair plasma reconnection (vol 15, art no 022101, 2008), Physics of Plasmas, 15(4), https://doi.org/10.1063/1.2891088

Zenitani, S., and M. Hesse (2008d), The role of the Weibel instability at the reconnection jet front in relativistic pair plasma reconnection (vol 15, artn no 022101, 2008), Physics of Plasmas, 15(8), https://doi.org/10.1063/1.2965501

2007

Birn, J., and M. Hesse (2007), Reconnection rates in driven magnetic reconnection, Physics of Plasmas, 14(8), https://doi.org/10.1063/1.2752510

Borovsky, J. E., and M. Hesse (2007), The reconnection of magnetic fields between plasmas with different densities: Scaling relations, Physics of Plasmas, 14(10), https://doi.org/10.1063/1.2772619

Eastwood, J. P., T.-D. Phan, F. S. Mozer, M. A. Shay, M. Fujimoto, A. Retino, M. Hesse, A. Balogh, E. A. Lucek, and I. Dandouras (2007), Multi-point observations of the Hall electromagnetic field and secondary island formation during magnetic reconnection, Journal of Geophysical Research-Space Physics, 112(A6), https://doi.org/10.1029/2006JA012158

Hesse, M., and S. Zenitani (2007), Dissipation in relativistic pair-plasma reconnection, Physics of Plasmas, 14(11), https://doi.org/10.1063/1.2801482

Hoskins, A. B., and E. M. Atkins (2007), Satellite formation mission optimization with a multi-impulse design, Journal of Spacecraft and Rockets, 44(2), 425-433, https://doi.org/10.2514/1.19984

Kuznetsova, M. M., M. Hesse, L. Rastaetter, A. Taktakishvili, G. Toth, D. L. De Zeeuw, A. Ridley, and T. I. Gombosi (2007), Multiscale modeling of magnetospheric reconnection, Journal of Geophysical Research-Space Physics, 112(A10), https://doi.org/10.1029/2007JA012316.

2006

Birn, J., T. G. Forbes, and M. Hesse (2006a), Stability and dynamic evolution of three-dimensional flux ropes, Astrophysical Journal, 645(1), 732-741, https://doi.org/10.1086/504280.

Birn, J., M. Hesse, and K. Schindler (2006b), Entropy conservation in simulations of magnetic reconnection, Physics of Plasmas, 13(9), https://doi.org/10.1063/1.2349440

Birn, J., M. Hesse, and K. Schindler (2006c), Modeling of the magnetospheric response to the dynamic solar wind, Space Science Reviews, 124(1-4), 103-116, https://doi.org/10.1007/s11214-006-9100-3

Hesse, M. (2006), Dissipation in magnetic reconnection with a guide magnetic field, Physics of Plasmas, 13(12), https://doi.org/10.1063/1.2403784

2005

Birn, J., K. Galsgaard, M. Hesse, M. Hoshino, J. Huba, G. Lapenta, P. L. Pritchett, K. Schindler, L. Yin, J. Büchner, T. Neukirch, E. R. Priest (2005), Forced magnetic reconnection, Geophysical Research Letters, 32(6), https://doi.org/10.1029/2004GL022058

Birn, J., and M. Hesse (2005), Energy release and conversion by reconnection in the magnetotail, Annales Geophysicae, 23(10), 3365-3373.

Clemente, D. C., and E. M. Atkins (2005), Optimization of a tetrahedral satellite formation, Journal of Spacecraft and Rockets, 42(4), 699-710.

Curtis, S. A., P. E. Clark, and C. Y. Cheung (2005), The central role of reconnection in space plasma phenomena targeted by the magnetospheric multiscale mission, 473-486 pp., https://doi.org/10.1016/b978-044451881-1/50035-6

Gim, D. W., and K. T. Alfriend (2005), Criteria for best configuration and sub-optimal reconfiguration for MMS mission, in Spaceflight Mechanics 2004, Vol 119, Pt 1-3, edited by S. L. Coffey, A. P. Mazzoleni, K. K. Luu and R. A. Glover, pp. 947-968.

Hesse, M., T. Forbes, and J. Birn (2005a), On the relation between reconnected magnetic flux and parallel electric fields in the solar corona, Astrophysical Journal, 631(2), 1227-1238, https://doi.org/10.1086/432677

Hesse, M., M. Kuznetsova, K. Schindler, and J. Birn (2005b), Three-dimensional modeling of electron quasiviscous dissipation in guide-field magnetic reconnection, Physics of Plasmas, 12(10), https://doi.org/10.1063/1.2114350

Mueller, J. B., and S. J. Thomas (2005), Decentralized formation flying control in a multiple-team hierarchy, in New Trends in Astrodynamics and Applications, edited by E. Belbruno, pp. 112-138, https://doi.org/10.1196/annals.1370.014

2004

Gim, D., and Alfriend, K. (2004, February). Criteria for best configuration and sub-optimal reconfiguration for mms mission. In AAS Spaceflight Mechanics Meeting, Maui, HI.

Gramling, C., R. Carpenter, T. Lee, and A. Long (2004), Relative navigation strategies for the magnetospheric multiscale mission, in Proceedings of the 18th International Symposium on Space Flight Dynamics, edited by O. Montenbruck and B. Battrick, pp. 435-440.

Guzman, J. J., A. Edery, and ieee (2004), Mission design for the MMS tetrahedron formation, in 2004 Ieee Aerospace Conference Proceedings, Vols 1-6, edited, pp. 533-540, https://doi.org/10.1109/aero.2004.1367637

Hasegawa, H., Fujimoto, M., Phan, TD. et al. Transport of solar wind into Earth's magnetosphere through rolled-up Kelvin–Helmholtz vortices. Nature 430, 755–758 (2004). https://doi.org/10.1038/nature02799

Hughes, S. P. (2004), Orbit design for phase I and II of the magnetospheric multiscale mission, in Guidance and Control 2004, edited by J. D. Chapel and R. D. Culp, pp. 255-274

2003

Edery, A. (2003), Designing phase 2 for the double-lunar swingby of the Magnetospheric Multiscale mission (MMS), in Spaceflight Mechanics 2003, Pts 1-3, edited by D. J. Scheeres, M. E. Pittelkau, R. J. Proulx and L. A. Cangahuala, pp. 2089-2099

2002

Fränz, M., and Harper, D. (2002). Heliospheric coordinate systems. *Planetary and Space Science*, *50*(2), 217-233. https://doi.org/10.1016/S0032-0633(01)00119-2

1999

Curtis, S. (1999). The magnetospheric multiscale mission: Resolving fundamental processes in space plasmas: Report of the NASA science and technology definition team for the magnetospheric multiscale (MMS) mission. The magnetospheric multiscale mission: resolving fundamental processes in space plasmas: report of the NASA Science and Technology Definition Team for the Magnetospheric Multiscale (MMS) Mission/S. Curtis. Greenbelt.

Mauk, B. H., Mcentire, R. W., Heelis, R. A. and Pfaff, R. F. (1999) Magnetospheric Multiscale and Global Electrodynamics Missions, in Sun-Earth Plasma Connections (eds J. L. Burch, R. L. Carovillano and S. K.

Antiochos), Geophysical Monograph 109, American Geophysical Union, Washington, D. C. pp 225-235, https://doi.org/10.1029/GM109p0225

1995

Hapgood, M. A. (1995, July). Space physics coordinate transformations: the role of precession. In *Annales Geophysicae* (Vol. 13, No. 7, pp. 713-716). Copernicus GmbH. https://doi.org/10.1007/s00585-995-0713-8

END OF LIST

APPENDIX E: PUBLICATION LIST – EXTERNAL

2022

[Note: 2022 list is incomplete. Updates for Senior Review were completed mid-October 2022 and may not include all publications completing review or pending full publication].

Alho, M., Battarbee, M., Pfau-Kempf, Y., Khotyaintsev, Yu. V., Nakamura, R., Cozzani, G., et al. (2022). Electron signatures of reconnection in a global eVlasiator simulation. *Geophysical Research Letters*, 49, e2022GL098329. https://doi.org/10.1029/2022GL098329

Allmann-Rahn, F., Lautenbach, S., and Grauer, R. (2022). An energy conserving Vlasov solver that tolerates coarse velocity space resolutions: Simulation of MMS reconnection events. Journal of Geophysical Research: Space Physics, 127, e2021JA029976. https://doi.org/10.1029/2021JA029976

Barani, M., Tu, W., Hudson, M. K., and Sarris, T. (2022). High-fidelity analysis of ULF wave mode structure following interplanetary shock compression of the dayside magnetopause using MMS multi-point observations. *Journal of Geophysical Research: Space Physics*, 127, e2021JA030116. https://doi.org/10.1029/2021JA030116

Bharuthram, R., Rufai, O. R., and Maharaj, S. K. (2022). Theoretical studies of low and high frequency electrostatic solitary waves in the magnetopause associated with asymmetric magnetic reconnection. Advances in Space Research. https://doi.org/10.1016/j.asr.2022.01.034

Chandra, S., Goswami, J., Sarkar, J., Das, C., Nandi, D., and Ghosh, B. (2022) Formation of electron acoustic shock wave in inner magnetospheric plasma. Indian J Phys. https://doi.org/10.1007/s12648-021-02276-x

Chen, G. W., and Hau, L. N. (2022). Evidence of Magnetic Reconnection with Multiple X Lines and Flux Ropes in Thin Magnetotail Currents Observed by the MMS Spacecraft: Results of Grad–Shafranov Reconstruction. *The Astrophysical Journal*, *928*(2), 133. https://doi.org/10.3847/1538-4357/ac5746

Chen, R., Gao, X., Lu, Q., Tsurutani, B. T., Chen, H., and Wang, S. (2022). First observation of electron cyclotron harmonic waves inside mirror mode structures in the Earth's outer magnetosphere. Geophysical Research Letters, 49, e2021GL097592. https://doi.org/10.1029/2021GL097592

Chen, Y. Q., Wang, G. Q., Wu, M. Y., Xiao, S. D., and Zhang, T. L. (2022). Study of the electron-scale magnetic peaks in the magnetotail current sheet observed by the Magnetospheric Multiscale mission. *Journal of Geophysical Research: Space Physics*, 127, e2021JA030135. https://doi.org/10.1029/2021JA030135

Chen, Z. Z., Fu, H. S., Cao, J. B., Cui, J., Lu, Q. M., Li, W. Y., ... and Liu, Y. Y. (2022). Magnetospheric Multiscale Mission Observations of Lower-hybrid Drift Waves in Terrestrial Magnetotail Reconnection with Moderate Guide Field and Asymmetric Plasma Density. *The Astrophysical Journal*, *933*(2), 208. https://doi.org/10.3847/1538-4357/ac75e9

Chong, G. S., Pitkänen, T., Hamrin, M., and Kullen, A. (2022). Dawn-dusk ion flow asymmetry in the plasma sheet: Interplanetary magnetic field B_y versus distance with respect to the neutral sheet. *Journal of Geophysical Research: Space Physics*, 127, e2021JA030208. https://doi.org/10.1029/2021JA030208

Faganello, M., Sisti, M., Califano, F., and Lavraud, B. (2022). Kelvin-Helmholtz instability and induced magnetic reconnection at the Earth's magnetopause: a 3D simulation based on satellite data. *Plasma Physics and Controlled Fusion*, *64*(4), 044014. https://doi.org/10.1088/1361-6587/ac43f0

Fu, W. D., Fu, H. S., Cao, J. B., Yu, Y., Chen, Z. Z., and Xu, Y. (2022). Formation of rolling-pin distribution of suprathermal electrons behind dipolarization fronts. Journal of Geophysical Research: Space Physics, 127, e2021JA029642. https://doi.org/10.1029/2021JA029642

Guo, R., Pu, Z., Wang, X., Xiao, C., and He, J. (2022). 3D reconnection geometries with magnetic nulls: Multispacecraft observations and reconstructions. *Journal of Geophysical Research: Space Physics*, 127, e2021JA030248. https://doi.org/10.1029/2021JA030248

Huang, H., Yu, Y., Chen, Z., Liu, C., Cao, J., and Yu, T. (2022). On the magnetic dip ahead of the dipolarization fronts. *Journal of Geophysical Research: Space Physics*, 127, e2021JA029783. https://doi.org/10.1029/2021JA029783

Huang, S. Y., Zhang, J., Yuan, Z. G., Jiang, K., Wei, Y. Y., Xu, S. B., Xiong, Q. Y., Zhang, Z. H., Lin, R. T., and Yu, L. (2022). Intermittent dissipation at kinetic scales in the turbulent reconnection outflow. *Geophysical Research Letters*, 49, e2021GL096403. https://doi.org/10.1029/2021GL096403

Huang, S. Y., Wei, Y. Y., Zhao, J. S., Yuan, Z. G., Deng, X. H., Jiang, K., Xu, S. B., Zhang, J., Xiong, Q. Y., Zhang, Z. H., Yu, L., and Lin, R. T. (2022). Kinetic-size magnetic holes in the terrestrial foreshock region. *Geophysical Research Letters*, 49, e2021GL093813. https://doi.org/10.1029/2021GL093813

Ji, H., Daughton, W., Jara-Almonte, J., Le, A., Stanier, A., and Yoo, J. (2022). Magnetic reconnection in the era of exascale computing and multiscale experiments. *Nature Reviews Physics*, 4, 263-282. https://doi.org/10.1038/s42254-021-00419-x

Jiang, K., Huang, S. Y., Yuan, Z. G., Deng, X. H., Wei, Y. Y., Xiong, Q. Y., Xu, S. B., Zhang, J., Zhang, Z. H., Lin, R. T., and Yu, L. (2022). Sub-structures of the separatrix region during magnetic reconnection. *Geophysical Research Letters*, 49, e2022GL097909. https://doi.org/10.1029/2022GL097909

Jiang, W., D. Verscharen, H. Li, C. Wang, and K. G. Klein (2022). Whistler Waves as a Signature of Converging Magnetic Holes in Space Plasmas, The Astrophysical Journal, 935, 169. https://doi.org/10.3847/1538-4357/ac7ce2

Jin, R., Zhou, M., Pang, Y., Deng, X., and Yi, Y. (2022). Characteristics of Turbulence Driven by Transient Magnetic Reconnection in the Terrestrial Magnetotail. *The Astrophysical Journal*, 925(1), 17. https://doi.org/10.3847/1538-4357/ac390c

Johlander, A., Battarbee, M., Turc, L., Ganse, U., Pfau-Kempf, Y., Grandin, M., Suni, J., Tarvus, V., Bussov, M., Zhou, H., Alho, M., Dubart, M., George, H., Papadakis, K., Palmroth, M. (2022). Quasi-parallel shock reformation seen by Magnetospheric Multiscale and ion-kinetic simulations. *Geophysical Research Letters*, 49, e2021GL096335. https://doi.org/10.1029/2021GL096335

Keika, K., Asami, R., Hoshino, M., and Fuselier, S. A. (2022). Global characteristics of cold protons around midnight in the magnetotail: Implication for efficient heating and origin. *Journal of Geophysical Research: Space Physics*, 127, e2021JA029576. https://doi.org/10.1029/2021JA029576

Khabarova, O., Büchner, J., Jain, N., Sagitov, T., Malova, H., and Kislov, R. (2022). Electron-to-ion Bulk Speed Ratio as a Parameter Reflecting the Occurrence of Strong Electron-dominated Current Sheets in the Solar Wind. *The Astrophysical Journal*, *933*(1), 97. https://doi.org/10.3847/1538-4357/ac71ab

Li, X., Wang, R., Huang, C., Lu, Q., Lu, S., Burch, J. L., and Wang, S. (2022). Energy Conversion and Partition in Plasma Turbulence Driven by Magnetotail Reconnection. *The Astrophysical Journal*, *936*(1), 34. https://doi.org/10.3847/1538-4357/ac84d7

Li, X., Wang, R., Lu, Q., Russell, C. T., Lu, S., Cohen, I. J., ... and Wang, S. (2022). Three-dimensional network of filamentary currents and super-thermal electrons during magnetotail magnetic reconnection. *Nature Communications*, *13*(1), 1-10. https://doi.org/10.1038/s41467-022-31025-9

Li, X.-Y., Liu, Z.-Y., Zong, Q.-G., Liu, J.-J., Fu, S.-Y., Zhou, X.-Z., Hao, Y.-X., Pollock, C. J., Russell, C. T., Ergun, R. E., and Lindqvist, P.-A. (2022). ULF wave-induced ion pitch angle evolution in the dayside outer magnetosphere. *Geophysical Research Letters*, 49, e2022GL098108. https://doi.org/10.1029/2022GL098108

Liu, Y. Y., Fu, H. S., Cao, J. B., Wang, Z., He, R. J., Guo, Z. Z., Xu, Y., and Yu, Y. (2022). Magnetic Discontinuities in the Solar Wind and Magnetosheath: Magnetospheric Multiscale Mission (MMS) Observations. *The Astrophysical Journal*, *930*(1), 63. https://doi.org/10.3847/1538-4357/ac62d2

Liu, Y. Y., Wang, Z., Chen, G., Yu, Y., Guo, Z. Z., and Xiong, X. (2022). Testing the Linearity of Vector Fields in Cold and Dense Space Plasmas. *The Astrophysical Journal*, *929*(2), 155. https://doi.org/10.3847/1538-4357/ac5d4b

Liu, Z.-Y., Zong, Q.-G., Zhang, H., Zhao, J.-T., Rankin, R., Pollock, C. J., and Le, G. (2022). Ion behavior at shocklets: A case study of MMS observations. Geophysical Research Letters, 49, e2022GL100449. https://doi.org/10.1029/2022GL100449

Liu, ZY., Zong, QG., Rankin, R. *et al.* Simultaneous macroscale and microscale wave–ion interaction in near-earth space plasmas. *Nat Commun* **13**, 5593 (2022). https://doi.org/10.1038/s41467-022-33298-6

Luo, Q., Zhu, X., He, J., Cui, J., Lai, H., Verscharen, D., and Duan, D. (2022). Coherence of Ion Cyclotron Resonance in Damped Ion Cyclotron Waves in Space Plasmas. *The Astrophysical Journal*, *928*(1), 36. https://doi.org/10.3847/1538-4357/ac52a9

Luo, Z., Xie, L., Fu, S., Pu, Z., Xiong, Y., Zhou, X., et al. (2022). Energetic electron microinjections observed by MMS in the dusk plasma sheet and drift resonance interpretation. *Geophysical Research Letters*, 49, e2022GL098652. https://doi.org/10.1029/2022GL098652

Ma, W., Zhou, M., Zhong, Z., and Deng, X. (2022). Contrasting the Mechanisms of Reconnection-driven Electron Acceleration with In Situ Observations from MMS in the Terrestrial Magnetotail. *The Astrophysical Journal*, *931*(2), 135. https://doi.org/10.3847/1538-4357/ac6be6

Ma, Y., Wang, S., Shen, C., Ren, N., Chen, T., Shao, P., et al. (2022). Rotational discontinuities in the magnetopause of an open magnetosphere. *Journal of Geophysical Research: Space Physics*, 127, e2021JA029126. https://doi.org/10.1029/2021JA029126

Man, H., Zhou, M., Zhong, Z., and Deng, X. (2022). Intense energy conversion events at the magnetopause boundary layer. *Geophysical Research Letters*, 49, e2022GL098069. https://doi.org/10.1029/2022GL098069

Mostafa, N., Ghamry, E., Ellithi, A., Gobashy, M., Fathy, A. (2022) Multi-space observations of the storm sudden commencement (September 2017) and its effect on the geomagnetic field, Advances in Space Research. https://doi.org/10.1016/j.asr.2022.04.023

Pouquet A, Yokoi N. (2022) Helical fluid and (Hall)-MHD turbulence: a brief review.Phil. Trans. R. Soc. A 380: 20210087. https://doi.org/10.1098/rsta.2021.0087

Rae, J., Forsyth, C., Dunlop, M. et al. (2022). What are the fundamental modes of energy transfer and partitioning in the coupled Magnetosphere-Ionosphere system?. Exp Astron. https://doi.org/10.1007/s10686-022-09861-w

Ren, Y., Dai, L., Wang, C., and Lavraud, B. (2022). Parallel Electron Heating through Landau Resonance with Lower Hybrid Waves at the Edge of Reconnection Ion Jets. *The Astrophysical Journal*, *928*(1), 5. https://doi.org/10.3847/1538-4357/ac53fb

Schroeder, J. M., Egedal, J., Cozzani, G., Khotyaintsev, Y. V., Daughton, W., Denton, R. E., and Burch, J. L.(2022). 2D reconstruction of magnetotail electron diffusion region measured by MMS. Geophysical Research Letters, 49, e2022GL100384. https://doi.org/10.1029/2022GL100384

Shamir, M., Khan, I. A., and Murtaza, G. (2022). Charged particles energization during magnetic reconnection in the Earth's magnetosphere by double layers: an analytical approach. Monthly Notices of the Royal Astronomical Society, 509(3), 3703-3708. https://doi.org/10.1093/mnras/stab3236

Staples, F. A., Kellerman, A., Murphy, K. R., Rae, I. J., Sandhu, J. K., and Forsyth, C. (2022). Resolving magnetopause shadowing using multimission measurements of phase space density. Journal of Geophysical Research: Space Physics, 127, e2021JA029298. https://doi.org/10.1029/2021JA029298

Stasiewicz, K., and Kłos, Z. (2022). Fine structure and motion of the bow shock, and particle energisation mechanisms inferred from MMS observations. Annales Geophysicae Discussions, 1-16. https://doi.org/10.5194/angeo-40-315-2022

Stasiewicz, K., and Kłos, Z. (2022). On the formation of quasi-parallel shocks, magnetic and electric field turbulence, and the ion energization mechanism. *Monthly Notices of the Royal Astronomical Society*, *513*(4), 5892-5899. https://doi.org/10.1093/mnras/stac1193

Tang, B.-B., Li, W. Y., Khotyaintsev, Y. V., Graham, D. B., Gao, C. H., Chen, Z. Z., et al. (2022). Fine structures of the electron current sheet in magnetotail guide-field reconnection. *Geophysical Research Letters*, 49, e2021GL097573. https://doi.org/10.1029/2021GL097573

Teh, W. L. (2022). Effects of Pressure Anisotropy on the Geometry of Magnetic Flux Rope. *The Astrophysical Journal*, *930*(1), 22. https://doi.org/10.3847/1538-4357/ac62d1

Teh, W.-L., Nakamura, T., Nakamura, R., and Umeda, T. (2018). Oblique ion-scale magnetotail flux ropes generated by secondary tearing modes. Journal of Geophysical Research: Space Physics, 123, 8122– 8130. https://doi.org/10.1029/2018JA025775

Terres, M., and Li, G. (2022). Relating the Solar Wind Turbulence Spectral Break at the Dissipation Range with an Upstream Spectral Bump at Planetary Bow Shocks. The Astrophysical Journal, 924(2), 53. https://doi.org/10.3847/1538-4357/ac400c

Tian, A., Degeling, A. W., Park, J.-S., Shi, Q., Nowada, M., Pitkänen, T., Li, W., and Xiao, C. (2022), Structure of Pc 5 compressional waves observed in the duskside outer magnetosphere: MMS observations. Journal of Geophysical Research: Space Physics, 127, e2021JA029817. https://doi.org/10.1029/2021JA029817

Tsai, E., Artemyev, A., Zhang, X., and Angelopoulos, V. (2022). Relativistic electron precipitation driven by nonlinear resonance with whistler-mode waves. *Journal of Geophysical Research: Space Physics*, 127, e2022JA030338. https://doi.org/10.1029/2022JA030338

Vu, A., Liu, T. Z., Zhang, H., and Pollock, C. (2022). Statistical study of foreshock bubbles, hot flow anomalies, and spontaneous hot flow anomalies and their substructures observed by MMS. Journal of Geophysical Research: Space Physics, 127, e2021JA030029. https://doi.org/10.1029/2021JA030029

Wang, C.-P., Xing, X., Wang, X., Avanov, L. A., Lin, Y., Strangeway, R. J., and Wei, H. Y. (2022). Effect of IMF B_y on the entry of solar wind ions into the near-Earth tail lobe: Global hybrid simulation and MMS observation. *Journal of Geophysical Research: Space Physics*, 127, e2022JA030800. https://doi.org/10.1029/2022JA030800

Wang, G. Q., Volwerk, M., Xiao, S. D., Wu, M. Y., Chen, Y. Q., and Zhang, T. L. (2022). Electron-scale current sheet as the boundary of a linear magnetic hole in the terrestrial current sheet observed by the Magnetospheric Multiscale mission. *Journal of Geophysical Research: Space Physics*, 127, e2021JA029707. https://doi.org/10.1029/2021JA029707

Wang, G., and Pan, Z. (2022). Fluxgate Magnetometer Offset Vector Determination Using Current Sheets in the Solar Wind. *The Astrophysical Journal*, *926*(1), 12. https://doi.org/10.3847/1538-4357/ac3d8f

Wang, L., Huang, C., Du, A., and Ge, Y. (2022). Hall nature ahead of Dipolarization Fronts in the Earth's magnetotail: A statistical study for MMS data. Geophysical Research Letters, 49, e2021GL097075. https://doi.org/10.1029/2021GL097075

Wang, R., Vasko, I. Y., Artemyev, A. V., Holley, L. C., Kamaletdinov, S. R., Lotekar, A., and Mozer, F. S. (2022). Multisatellite observations of ion holes in the Earth's plasma sheet. *Geophysical Research Letters*, 49, e2022GL097919. https://doi.org/10.1029/2022GL097919

Wei, Y. Y., Huang, S. Y., Yuan, Z. G., Jiang, K., Xu, S. B., Deng, X. H., Deng, X. H., Zhang, J., Zhang, Z. H., Xiong, Q. Y., Yu, L., and Lin, T. R. (2022). Observations of pitch angle changes of electrons and high-frequency wave activities in the magnetotail plasma bubble. Journal of Geophysical Research: Space Physics, 127, e2021JA029761. https://doi.org/10.1029/2021JA029761

Xiong, Q. Y., Huang, S. Y., Zhou, M., Yuan, Z. G., Deng, X. H., Jiang, K., et al. (2022). Distribution of negative $J{\cdot}E'$ in the inflow edge of the inner electron diffusion region during tail magnetic reconnection:

Simulations vs. observations. *Geophysical Research Letters*, 49, e2022GL098445. https://doi.org/10.1029/2022GL098445

Xiong, Q. Y., Huang, S. Y., Zhou, M., Yuan, Z. G., Deng, X. H., Jiang, K., K. Jiang, Wei, Y.Y., Xu, S. B., Zhang, J., Zhang, Z. H., Yu, L., Lin, R.T., (2022). Formation of negative J · E′ in the outer electron diffusion region during magnetic reconnection. Journal of Geophysical Research: Space Physics, 127, e2022JA030264. https://doi.org/10.1029/2022JA030264

Yang, F., Zhou, X. Z., Li, J. H., Zong, Q. G., Yao, S. T., Shi, Q. Q., and Artemyev, A. V. (2022). Kinetic-scale flux ropes: Observations and applications of kinetic equilibrium models. The Astrophysical Journal, 926(2), 208. https://doi.org/10.3847/1538-4357/ac47f9

Yu, Y., Fu, H. S., Cao, J. B., Liu, Y. Y., and Wang, Z. (2022). Electron Rolling-pin Distribution Inside Magnetic Hole. The Astrophysical Journal, 926(2), 199. https://doi.org/10.3847/1538-4357/ac497a

Yu, Y., Fu, H. S., Cao, J. B., Liu, C. M., and Wang, Z. (2022). Electron Thermalization and Electrostatic Turbulence Caused by Flow Reversal in Dipolarizing Flux Tubes. The Astrophysical Journal, 926(1), 22. https://doi.org/10.3847/1538-4357/ac42c5

Yuan, Z., Dong, Y., Huang, S., Xue, Z., and Yu, X. (2022). Direct observation of acceleration and thermalization of beam electrons caused by double layers in the Earth's plasma sheet. *Geophysical Research Letters*, 49, e2022GL099483. https://doi.org/10.1029/2022GL099483

Zhang, H., Zhong, Z., Tang, R., Liu, C., Deng, X., Zhou, M., and Wang, D. (2022). Observations of Whistler-mode Waves and Large-amplitude Electrostatic Waves Associated with a Dipolarization Front in the Bursty Bulk Flow. *The Astrophysical Journal*, *933*(1), 105. https://doi.org/10.3847/1538-4357/ac739d

Zhang, L. Q., Wang, C., Dai, L., Baumjohann, W., Burch, J. L., Khotyaintsev, Y. V., and Wang, J. Y. (2022). Turbulent current sheet frozen in bursty bulk flow: observation and model. *Scientific Reports*, *12*(1), 1-8. https://doi.org/10.1038/s41598-022-19266-6

Zhang, L. Q., Wang, C., Dai, L., Baumjohann, W., Lui, A. T. Y., Burch, J. L., Khotyaintsev, Y. V., Ren, Y. (2022). Vorticity within bursty bulk flows: Convective versus kinetic. *Journal of Geophysical Research: Space Physics*, 127, e2020JA028934. https://doi.org/10.1029/2020JA028934

Zhang, W, Z., H. S. Fu, J. B. Cao, Y. Y. Liu, J. S. Zhao, Z. Z. Guo, Z. Wang, and T. Y. Wang (2022). DRAFT: A Method for Wave Analyses in Space Plasmas, The Astrophysical Journal, 936, 176. https://doi.org/10.3847/1538-4357/ac8872

Zhang, Z., Yuan, Z., Huang, S., Yu, X., Xue, Z., Deng, D., and Huang, Z. (2022). Observations of kinetic Alfvén waves and associated electron acceleration in the plasma sheet boundary layer. *Earth and Planetary Physics*, *6*. http://doi.org/10.26464/epp2022041

Zhong, Z. H., Zhou, M., Graham, D. B., Khotyaintsev, Y. V., Wu, Y. F., Le Contel, O., Li, H. M., Tao, X., Tang, R. X., Deng, X. H. (2022). Evidence for whistler waves propagating into the electron diffusion region of collisionless magnetic reconnection. *Geophysical Research Letters*, 49, e2021GL097387. https://doi.org/10.1029/2021GL097387

Zhong, Z. H., Zhou, M., Liu, Y. H., Deng, X. H., Tang, R. X., Graham, D. B., Song L.J., Man, H.Y., Pang, Y., and Khotyaintsev, Y. V. (2022). Stacked Electron Diffusion Regions and Electron Kelvin–Helmholtz Vortices within the Ion Diffusion Region of Collisionless Magnetic Reconnection. The Astrophysical Journal Letters, 926(2), L27. https://doi.org/10.3847/2041-8213/ac4dee

2021

Abid, A. A., Lu, Q., Gao, X. L., Alotaibi, B. M., Ali, S., Qureshi, M. N. S., Al-Hadeethi, Y., and Wang, S. (2021). Energization of cold ions by electromagnetic ion cyclotron waves: Magnetospheric multiscale (MMS) observations. Physics of Plasmas 28, 072901. https://doi.org/10.1063/5.0046764

Alberti, T., Faranda, D., Donner, R. V., Caby, T., Carbone, V., Consolini, G., Dubrulle, B., and Vaienti, S. (2021). Small-scale Induced Large-scale Transitions in Solar Wind Magnetic Field. The Astrophysical journal letters, 914(1), L6. https://doi.org/10.3847/2041-8213/ac0148

Aravindakshan, H., Kakad, A., Kakad, B., and Yoon, P. H. (2021). Structural Characteristics of Ion Holes in Plasma. Plasma, 4(3), 435-449. https://doi.org/10.3390/plasma4030032

Bashir, M. F., and Ilie, R. (2021). The first observation of N+ electromagnetic ion cyclotron waves. Journal of Geophysical Research: Space Physics, 126, e2020JA028716. https://doi.org/10.1029/2020JA028716

Battarbee, M., Brito, T., Alho, M., Pfau-Kempf, Y., Grandin, M., Ganse, U., Papadakis, K., Johlander, A., Turc, L., Dubart, M., and Palmroth, M. (2021). Vlasov simulation of electrons in the context of hybrid global models: an eVlasiator approach, Ann. Geophys., 39, 85–103. https://doi.org/10.5194/angeo-39-85-2021

Blum, L. W., Koval, A., Richardson, I. G., Wilson, L. B., Malaspina, D., Greeley, A., and Jaynes, A. N. (2021). Prompt response of the dayside magnetosphere to discrete structures within the sheath region of a coronal mass ejection. Geophysical Research Letters, 48, e2021GL092700. https://doi.org/10.1029/2021GL092700

Chang, C., Huang, K., Lu, Q., Sang, L., Lu, S., Wang, R., Gao, X., Wang, S. (2021). Particle-in-cell simulations of electrostatic solitary waves in asymmetric magnetic reconnection. Journal of Geophysical Research: Space Physics, 126, e2021JA029290. https://doi.org/10.1029/2021JA029290

Chen, Y. Q., Wu, M., Zhang, T. L., Huang, Y., Wang, G. Q., Nakamura, R., Baumjohann, W., Russell, C. T., Giles, B. J., Burch, J. L. (2021). Statistical characteristics of field-aligned currents in the plasma sheet boundary layer. Journal of Geophysical Research: Space Physics, 126, e2020JA028319. https://doi.org/10.1029/2020JA028319

Chen, Z. Z., Fu, H. S., Wang, Z., Guo, Z. Z., Xu, Y., and Liu, C. M. (2021). First observation of magnetic flux rope inside electron diffusion region. Geophysical Research Letters, 48, e2020GL089722. https://doi.org/10.1029/2020GL089722

Chong, G. S., Pitkänen, T., Hamrin, M., and Schillings, A. (2021). Ion convection as a function of distance to the neutral sheet in Earth's magnetotail. Journal of Geophysical Research: Space Physics, 126, e2021JA029694. https://doi.org/10.1029/2021JA029694

Dong, X.-C., Dunlop, M. W., Wang, T.-Y., Zhao, J.-S., Fu, H.-S., Chen, Z.-Z., Russell, C. T., Giles, B., Ergun, R., Lindqvist, P. (2021). Observation of nonuniform energy dissipation in the electron diffusion region of magnetopause reconnection. Geophysical Research Letters, 48, e2020GL091928. https://doi.org/10.1029/2020GL091928

Gao, C.-H., Tang, B.-B., Li, W. Y., Wang, C., Khotyaintsev, Y. V., Graham, D. B., Gershman, D. J., Rager, A. C., Giles, B. L., Lindqvist, P.-A., Ergun, R. E., Russell, C. T., and Burch, J. L. (2021). Effect of the electric field on the agyrotropic electron distributions. *Geophysical Research Letters*, 48, e2020GL091437. https://doi.org/10.1029/2020GL091437

Guo, J., Lu, S., Lu, Q., Lin, Y., Wang, X., Huang, K., Wang, R., and Wang, S. (2021). Re-reconnection processes of magnetopause flux ropes: Three-dimensional global hybrid simulations. *Journal of Geophysical Research: Space Physics*, 126, e2021JA029388. https://doi.org/10.1029/2021JA029388

Guo, J., Lu, S., Lu, Q., Lin, Y., Wang, X., Huang, K., Wang, R., and Wang, S. (2021). Structure and coalescence of magnetopause flux ropes and their dependence on IMF clock angle: Three-dimensional global hybrid simulations. Journal of Geophysical Research: Space Physics, 126, e2020JA028670. https://doi.org/10.1029/2020JA028670

Guo, Z. Z., Fu, H. S., Cao, J. B., Yu, Y., Chen, Z. Z., Xu, Y., Liu, Y. Y., Wang, Z., Chen, G., and Xiong, X. (2021). Broadband electrostatic waves behind dipolarization front: Observations and analyses. *Journal of Geophysical Research: Space Physics*, 126, e2021JA029900. https://doi.org/10.1029/2021JA029900

Hart, S. T., Dayeh, M. A., Reisenfeld, D. B., Janzen, P. H., McComas, D. J., Allegrini, F., Fuselier, S. A., Ogasawara, K., Szalay, J. R., Funsten, H. O., and Petrinec, S. M. (2021). Probing the magnetosheath boundaries using Interstellar Boundary Explorer (IBEX) orbital encounters. *Journal of Geophysical Research: Space Physics*, 126, e2021JA029278. https://doi.org/10.1029/2021JA029278

Hau, L.-N., Chang, C.-K., and Wang, B.-J. (2021). Do there exist energy closures to the observed mirror waves? *Geophysical Research Letters*, 48, e2021GL095483. https://doi.org/10.1029/2021GL095483

He, R. J., Fu, H. S., Liu, Y. Y., Wang, Z., and Liu, C. M. (2021). Subion-scale flux rope nested inside ion-scale flux rope in Earth's magnetotail. *Geophysical Research Letters*, 48, e2021GL096169. https://doi.org/10.1029/2021GL096169

Hou, C., He, J., Zhu, X., and Wang, Y. (2021). Contribution of magnetic reconnection events to energy dissipation in space plasma turbulence. *The Astrophysical Journal*, 908(2), 237. https://doi.org/10.3847/1538-4357/abd6f3

Huang, S. Y., Xiong, Q. Y., Song, L. F., Nan, J., Yuan, Z. G., Jiang, K., Deng, X. H., and Yu, L. (2021). Electron-only Reconnection in an Ion-scale Current Sheet at the Magnetopause. *The Astrophysical Journal*, *922*(1), 54. https://doi.org/10.3847/1538-4357/ac2668

Huang, S. Y., Xiong, Q. Y., Yuan, Z. G., Zhan, H. L., Deng, X. H., Jiang, K., Zhao, P. F., Zhang, J., Xu, S. B., Wei, Y. Y., Yu, L., and Lin, T. R. (2021). Multi-spacecraft measurement of anisotropic spatial correlation functions at kinetic range in the magnetosheath turbulence. *Journal of Geophysical Research: Space Physics*, 126, e2020JA028780. https://doi.org/10.1029/2020JA028780

Jia, Y.-D., Qi, Y., Lu, S., and Russell, C. T. (2021). Temporal evolution of flux rope/tube entanglement in 3-D Hall MHD simulations. *Journal of Geophysical Research: Space Physics*, 126, e2020JA028698. https://doi.org/10.1029/2020JA028698

Jiang, K., Huang, S. Y., Fu, H. S., Yuan, Z. G., Deng, X. H., Wang, Z., ... and Yu, L. (2021). Observational Evidence of Magnetic Reconnection in the Terrestrial Foreshock Region. *The Astrophysical Journal*, *922*(1), 56. https://doi.org/10.3847/1538-4357/ac2500

Jiang, K., Huang, S. Y., Yuan, Z. G., Deng, X. H., Wei, Y. Y., Xiong, Q. Y., Xu, S. B., Zhang, J., Zhang, Z. H., Lin, R. T., and Yu, L. (2021). Statistical properties of current, energy conversion, and electron acceleration in flux ropes in the terrestrial magnetotail. *Geophysical Research Letters*, 48, e2021GL093458. https://doi.org/10.1029/2021GL093458

Johlander, A., Battarbee, M., Vaivads, A., Turc, L., Pfau-Kempf, Y., Ganse, U., Grandin, M., Dubart, M., Khotyaintsev, Y. V., Caprioli, D., Haggerty, C., Schwartz, S. J., Giles, B. L., and Palmroth, M. (2021). Ion Acceleration Efficiency at the Earth's Bow Shock: Observations and Simulation Results. *The Astrophysical Journal*, *914*(2), 82. https://doi.org/10.3847/1538-4357/abfafc

Jun, C.-W., Miyoshi, Y., Kurita, S., Yue, C., Bortnik, J., Lyons, L., Nakamura, S., Shoji, M., Imajo, S., Kletzing, C., Kasahara, Y., Kasaba, Y., Matsuda, S., Tsuchiya, F., Kumamoto, A., Matsuoka, A., Shinohara, I. (2021). The characteristics of EMIC waves in the magnetosphere based on the Van Allen Probes and Arase observations. *Journal of Geophysical Research: Space Physics*, 126, e2020JA029001. https://doi.org/10.1029/2020JA029001

Li, J.-H., Zhou, X.-Z., Yang, F., Artemyev, A. V., and Zong, Q.-G. (2021). Helical magnetic cavities: Kinetic model and comparison with MMS observations. Geophysical Research Letters, 48, e2021GL092383. https://doi.org/10.1029/2021GL092383

Li, J.-H., Zhou, X.-Z., Zong, Q.-G., Yang, F., Fu, S., Yao, S., Liu, J., and Shi, Q. (2021). On the origin of donut-shaped electron distributions within magnetic cavities. Geophysical Research Letters, 48, e2020GL091613. https://doi.org/10.1029/2020GL091613

Li, X.-Y., Liu, Z.-Y., Zong, Q.-G., Zhou, X.-Z., Hao, Y.-X., Pollock, C. J., Russell, C. L., and Lindquist, P.-A. (2021). Off-equatorial minima effects on ULF wave-ion interaction in the dayside outer

magnetosphere. Geophysical Research Letters, 48, e2021GL095648. https://doi.org/10.1029/2021GL095648

Liu, C. M., Fu, H. S., and Liu, Y. Y. (2021). Electron vorticity at dipolarization fronts. *The Astrophysical Journal*, *911*(2), 122. https://doi.org/10.3847/1538-4357/abee1c

Liu, C. M., Fu, H. S., Yu, Y. Q., Lu, H. Y., Liu, W. L., Xu, Y., Giles, B. L., Burch, J. L. (2021). Energy flux densities at dipolarization fronts. Geophysical Research Letters, 48, e2021GL094932. https://doi.org/10.1029/2021GL094932

Liu, C. M., Fu, H. S., Liu, Y. Y., and Xu, Y. (2021). Kinetics of magnetic hole behind dipolarization front. Geophysical Research Letters, 48, e2021GL093174. https://doi.org/10.1029/2021GL093174

Liu, Z.-Y., Wang, B., Zong, Q.-G., Yao, S. T., Pollock, C. J., and Le, G. (2021). Thermal electron behavior in obliquely propagating whistler waves: MMS observations in the solar wind. Geophysical Research Letters, 48, e2021GL094099. https://doi.org/10.1029/2021GL094099

Lou, Y., Cao, X., Ni, B., Tu, W., Gu, X., Fu, S., Xiang, Z., and Ma, X. (2021). Diffuse auroral electron scattering by electrostatic electron cyclotron harmonic waves in the dayside magnetosphere. Geophysical Research Letters, 48, e2020GL092208. https://doi.org/10.1029/2020GL092208

Lu, Q., Yang, Z., Wang, H., Wang, R., Huang, K., Lu, S., and Wang, S. (2021). Two-dimensional Particle-in-cell Simulation of Magnetic Reconnection in the Downstream of a Quasi-perpendicular Shock. The Astrophysical Journal, 919(1), 28. https://doi.org/10.3847/1538-4357/ac18c0

Malykhin, A. Y., Grigorenko, E. E., Shklyar, D. R., Panov, E. V., Le Contel, O., Avanov, L., and Giles, B. (2021). Characteristics of resonant electrons interacting with whistler waves in the nearest dipolarizing magnetotail. Journal of Geophysical Research: Space Physics, 126, e2021JA029440. https://doi.org/10.1029/2021JA029440

Malykhin, A.Y., Grigorenko, E.E. and Shklyar, D.R. MMS Observations of Narrow-Band Quasi-Parallel Whistler Waves in the Flow Braking Region in Near-Earth Magnetotail. Cosmic Res 59, 6–14 (2021). https://doi.org/10.1134/S0010952521010044

Malykhin, A.Y., and Grigorenko, E.E. (2021). Observation of Small-Scale Magnetic and Current Structures During Prolonged Dipolarizations in the Near Geomagnetic Tail by MMS Mission. Plasma Phys. Rep. 47, 427–439. https://doi.org/10.1134/S1063780X21050068

Man, H., Zhou, M., Zhong, Z., Deng, X., and Li, H. (2021). Statistics of the intense current structure in the dayside magnetopause boundary layer. Journal of Geophysical Research: Space Physics, 126, e2021JA029890. https://doi.org/10.1029/2021JA029890

Norenius, L., Hamrin, M., Goncharov, O., Gunell, H., Opgenoorth, H., Pitkänen, T., Chong, S., Partamies, N., and Baddeley L. (2021). Ground-based magnetometer response to impacting magnetosheath jets. Journal of Geophysical Research: Space Physics, 126, e2021JA029115. https://doi.org/10.1029/2021JA029115

Palmroth, M., Raptis, S., Suni, J., Karlsson, T., Turc, L., Johlander, A., Ganse, U., Pfau-Kempf, Y., Blanco-Cano, X., Akhavan-Tafti, M., Battarbee, M., Dubart, M., Grandin, M., Tarvus, V., and Osmane, A. (2021). Magnetosheath jet evolution as a function of lifetime: global hybrid-Vlasov simulations compared to MMS observations, Ann. Geophys., 39, 289–308. https://doi.org/10.5194/angeo-39-289-2021

Panasyuk, M. I., Zhukova, E. I., Kalegaev, V. V., Malova, H. V., Popov, V. Y., Vlasova, N. A., and Zelenyi, L. M. (2021). Earth's magnetotail as the reservoir of accelerated singleand multicharged oxygen ions replenishing radiation belts. Journal of Geophysical Research: Space Physics, 126, e2020JA028217. https://doi.org/10.1029/2020JA028217

Perri, S., Perrone, D., Roberts, O., Settino, A., Yordanova, E., Sorriso-Valvo, L., Veltri, P., and Valentini, F. (2021). Nature of electrostatic fluctuations in the terrestrial magnetosheath. The Astrophysical Journal, 919(2), 75. https://doi.org/10.3847/1538-4357/ac13a2

Petrukovich, A. A., and Chugunova, O. M. (2021). Detailed structure of very high-β Earth bow shock. Journal of Geophysical Research: Space Physics, 126, e2020JA029004. https://doi.org/10.1029/2020JA029004

Pezzi, O., Liang, H., Juno, J. L., Cassak, P. A., Vásconez, C. L., Sorriso-Valvo, L., Perrone, D., Servidio, S., Roytershteyn, V., TenBarge, J. M., and Matthaeus, W. H. (2021). Dissipation measures in weakly collisional plasmas. *Monthly Notices of the Royal Astronomical Society*, *505*(4), 4857-4873. https://doi.org/10.1093/mnras/stab1516

Pitkänen, T., Hamrin, M., Chong, G. S., and Kullen, A. (2021). Relevance of the north-south electric field component in the propagation of fast convective earthward flows in the magnetotail: An event study. Journal of Geophysical Research: Space Physics, 126, e2021JA029233. https://doi.org/10.1029/2021JA029233

Ren, Y., Dai, L., Wang, C., Li, W., Tao, X., Lavraud, B., and Le Contel, O. (2021). Statistical characteristics in the spectrum of whistler waves near the diffusion region of dayside magnetopause reconnection. Geophysical Research Letters, 48, e2020GL090816. https://doi.org/10.1029/2020GL090816

Settino, A., Perrone, D., Khotyaintsev, Y. V., Graham, D. B., and Valentini, F. (2021). Kinetic Features for the Identification of Kelvin–Helmholtz Vortices in In Situ Observations. The Astrophysical Journal, 912(2), 154. https://doi.org/10.3847/1538-4357/abf1f5

Shen, C., Zhou, Y., Gao, L., Wang, X., Pu, Z., Escoubet, C. P., and Burch, J. L. (2021). Measurements of the net charge density of space plasmas. Journal of Geophysical Research: Space Physics, 126, e2021JA029511. https://doi.org/10.1029/2021JA029511

Shustov, P.I., Kuzichev, I.V., Vasko, I.Y., Artemyev, A.V., and Gerrard, A,J. (2021) The dynamics of electron holes in current sheets. Physics of Plasmas 28, 012902. https://doi.org/10.1063/5.0029999

Stasiewicz, K., Eliasson, B., Cohen, I. J., Turner, D. L., & Ergun, R. E. (2021). Local acceleration of protons to 100 keV in a quasi-parallel bow shock. *Journal of Geophysical Research: Space Physics*, 126, e2021JA029477. https://doi.org/10.1029/2021JA029477

Tang, S. Y., Zhang, Y. C., Dai, L., Chen, T., and Wang, C. (2021). MMS Observation of the Hall Field in an Asymmetric Magnetic Reconnection with Guide Field. The Astrophysical Journal, *922*(2), 96. https://doi.org/10.3847/1538-4357/ac31b1

Teh, W.-L., and Zenitani, S. (2021). Two-dimensional reconstruction of a time-dependent mirror structure from double-polytropic MHD simulation. Earth and Space Science, 8, e2020EA001449. https://doi.org/10.1029/2020EA001449

Vaverka, J., Pavlů, J., Nouzák, L., Šafránková, J., Němeček, Z., Antonsen, T., .Mann, I., and Lindqvist (2021). Ion Cloud Expansion after Hyper-velocity Dust Impacts Detected by the Magnetospheric Multiscale Mission Electric Probes in the Dipole Configuration. *The Astrophysical Journal*, *921*(2), 127. https://doi.org/10.3847/1538-4357/ac1944

Vech, D., and Malaspina, D. M. (2021). A novel machine learning technique to identify and categorize plasma waves in spacecraft measurements. Journal of Geophysical Research: Space Physics, 126, e2021JA029567. https://doi.org/10.1029/2021JA029567

Vech, D., Malaspina, D. M., Cattell, C., Schwartz, S. J., Ergun, R. E., Klein, K. G., Kromyda, L., Chasapis, A. (2021). Experimental determination of ion acoustic wave dispersion relation with interferometric analysis. Journal of Geophysical Research: Space Physics, 126, e2021JA029221. https://doi.org/10.1029/2021JA029221

Volwerk, M., D. Mautner, C. S. Wedlund, C. Goetz, F. Plaschke, T. Karlsson, D. Schmid, D. Rojas-Castillo, O. W. Roberts, and A. Varsani (2021), Statistical study of linear magnetic hole structures near Earth, Ann. Geophys., 39, 239–253. https://doi.org/10.5194/angeo-39-239-2021

Vörös, Z., Varsani, A., Yordanova, E., Sasunov, Y. L., Roberts, O. W., Kis, Á., Nakamura, R., Narita, Y. (2021). Magnetic reconnection within the boundary layer of a magnetic cloud in the solar wind. Journal of Geophysical Research: Space Physics, 126, e2021JA029415. https://doi.org/10.1029/2021JA029415

Vuorinen, L., Hietala, H., Plaschke, F., and LaMoury, A. T. (2021). Magnetic field in magnetosheath jets: A statistical study of BZ near the magnetopause. Journal of Geophysical Research: Space Physics, 126, e2021JA029188. https://doi.org/10.1029/2021JA029188

Wang, B., Zhang, H., Liu, Z., Liu, T., Li, X., and Angelopoulos, V. (2021) Energy Modulations of Magnetospheric Ion Induced by Foreshock Transient-Driven ULF Waves. Geophysical Research Letters, 48, e2021GL093913. https://doi.org/10.1029/2021GL093913

Wang, G. Q., and Pan, Z. H. (2021). A new method to calculate the fluxgate magnetometer offset in the interplanetary magnetic field: 1. Using Alfvén waves. Journal of Geophysical Research: Space Physics, 126, e2020JA028893. https://doi.org/10.1029/2020JA028893

Wang, G. Q., Volwerk, M., Xiao, S. D., Wu, M. Y., Chen, Y. Q., and Zhang, T. L. (2021). Electron-scale Magnetic Peaks Upstream of the Terrestrial Bow Shock Observed by the Magnetospheric Multiscale Mission. *The Astrophysical Journal*, *914*(2), 101. https://doi.org/10.3847/1538-4357/abfaa1

Wang, G. Q., Zhang, T. L., Wu, M. Y., Xiao, S. D., Wang, G., Chen, Y. Q., Sun, J. C., Volwerk, M. (2021). Field-aligned currents originating from the chaotic motion of electrons in the tilted current sheet: MMS observations. Geophysical Research Letters, 48, e2020GL088841. https://doi.org/10.1029/2020GL088841

Wang, G. Q., M. Volwerk, M. Y. Wu, Y. F. Hao, S. D. Xiao, G. Wang, L. J. Liu, Y. Q. Chen, and T. L. Zhang (2021), First Observations of an Ion Vortex in a Magnetic Hole in the Solar Wind by MMS, The Astronomical Journal, 161:110 (4pp). https://doi.org/10.3847/1538-3881/abd632

Wang, G. Q., Volwerk, M., Xiao, S. D., Wu, M. Y., Chen, Y. Q., and Zhang, T. L. (2021). Foreshock as a Source Region of Electron-scale Magnetic Holes in the Solar Wind at 1 au. *The Astrophysical Journal*, *915*(1), 3. https://doi.org/10.3847/1538-4357/abfd31

Wang, G. Q., Volwerk, M., Xiao, S. D., Wu, M. Y., Chen, Y. Q., and Zhang, T. L. (2021). Statistical Properties of Electron-scale Magnetic Peaks in the Solar Wind at 1 au. *The Astrophysical Journal*, *921*(2), 152. https://doi.org/10.3847/1538-4357/ac1c6c

Wei, Y. Y., Huang, S. Y., Yuan, Z. G., Deng, X. H., Jiang, K., Xu, S. B., Zhang, J., Zhang, Z. H., Xiong, Q. Y., Yu, L., Lin, R. T. (2021). Observation of high-frequency electrostatic waves in the dip region ahead of dipolarization front. Journal of Geophysical Research: Space Physics, 126, e2021JA029408. https://doi.org/10.1029/2021JA029408

Xu, Y., Fu, H., Cao, J., Liu, C., Norgren, C., and Chen, Z. (2021). Electron-scale measurements of antidipolarization front. Geophysical Research Letters, 48, e2020GL092232. https://doi.org/10.1029/2020GL092232.

Xue, Z., Yuan, Z., and Yu, X. (2021). Prompt emergence and disappearance of EMIC waves driven by the sequentially enhanced solar wind dynamic pressure. Geophysical Research Letters, 48, e2020GL091479. https://doi.org/10.1029/2020GL091479.

Yao, S. T., Shi, Q. Q., Zong, Q. G., Degeling, A. W., Guo, R. L., Li, L., Li, J. X., Tian, A. M., Zhang, H., Yao, Z. H., Fu, H. S., Liu, C. M., Sun, W. J., Niu, Z., Li, W. Y., Liu, Z. Y., Le Contel, O., Zhang, S., Xiao, C., Shang, W. S., Torbert, R. B., Ergun, R. E., Lindqvist, P.-A., Pollock, C. J. (2021). Low-frequency Whistler Waves Modulate Electrons and Generate Higher-frequency Whistler Waves in the Solar Wind. *The Astrophysical Journal*, *923*(2), 216. https://doi.org/10.3847/1538-4357/ac2e97

Yao, S. T., Yue, Z. S., Shi, Q. Q., Degeling, A. W., Fu, H. S., Tian, A. M., Zhang, H., Vu, A., Guo, R. L., Yao, Z., Liu, J., Zong, Q.-G., Zhou, X., Li, J., Li, W., Hu, H., Liu, Y., Sun, W. J., (2021). Statistical properties of kinetic-scale magnetic holes in terrestrial space. Earth Planet. Phys., 5(1), 63–72. http://doi.org/10.26464/epp2021011

Yoon, Y.D., Yun, G.S., Wendel, D.E., Burch, J. L. (2021) Collisionless relaxation of a disequilibrated current sheet and implications for bifurcated structures. Nat Commun 12, 3774. https://doi.org/10.1038/s41467-021-24006-x

Yordanova, E., Vörös, Z., Sorriso-Valvo, L., Dimmock, A. P., and Kilpua, E. (2021). A possible link between turbulence and plasma heating. The Astrophysical Journal, 921(1), 65. https://doi.org/10.3847/1538-4357/ac1942

Yu, X., Lu, Q., Wang, R., Huang, K., Gao, X., and Wang, S. (2021). MMS observations of broadband electrostatic waves in electron diffusion region of magnetotail reconnection. Journal of Geophysical Research: Space Physics, 126, e2020JA028882. https://doi.org/10.1029/2020JA028882.

Yu, X., Lu, Q., Wang, R., Gao, X., Sang, L., and Wang, S. (2021). Simultaneous observation of whistler waves and electron cyclotron harmonic waves in the separatrix region of magnetopause reconnection. Journal of Geophysical Research: Space Physics, 126, e2021JA029609. https://doi.org/10.1029/2021JA029609.

Zhang, H., Zhong, Z., Tang, R., Deng, X., Li, H., and Wang, D. (2021). Modulation of whistler mode waves by ultra-low frequency wave in a macroscale magnetic hole: MMS observations. Geophysical Research Letters, 48, e2021GL096056. https://doi.org/10.1029/2021GL096056

Zhang, L. Q., Wang, C., Dai, L., Fu, H. S., Lui, A. T. Y., Baumjohann, W., Yu, Y., Ren, Y., Burch, J. L., Khotyaintsev, Yu. V. (2021). MMS observation on the cross-tail current sheet roll-up at the dipolarization front. Journal of Geophysical Research: Space Physics, 126, e2020JA028796. https://doi.org/10.1029/2020JA028796

Zhao, S. Q., Zhang, H., Liu, T. Z., Yan, H., Xiao, C. J., Liu, M., Zong, Q.-G., Wang, X., Shi, M., Teng, S., Wang, H., Rankin, R., Pollock, C., Le, G. (2021). Observations of an electron-cold ion component reconnection at the edge of an ion-scale antiparallel reconnection at the dayside magnetopause. Journal of Geophysical Research: Space Physics, 126, e2021JA029390. https://doi.org/10.1029/2021JA029390.

Zhao, S. Q., Xiao, C. J., Liu, T. Z., Chen, H., Zhang, H., Shi, M. J., Teng, S., Zhang, H. S., Wang, X. G., Pu, Z. Y., Liu, M. Z. (2021). Observations of the beam-driven whistler mode waves in the magnetic reconnection region at the dayside magnetopause. Journal of Geophysical Research: Space Physics, 126. https://doi.org/10.1029/2020JA028525

Zhong, Z. H., Zhou, M., Deng, X. H., Song, L. J., Graham, D. B., Tang, R. X., Man, H. Y., Pang, Y., Khotyaintsev, Yu V., Giles, B. L. (2021). Three-dimensional electron-scale magnetic reconnection in Earth's magnetosphere. Geophysical Research Letters, 48, e2020GL090946. https://doi.org/10.1029/2020GL090946

Zhong, Z. H., Graham, D. B., Khotyaintsev, Y. V., Zhou, M., Le Contel, O., Tang, R. X., and Deng, X. H. (2021). Whistler and broadband electrostatic waves in the multiple X-line reconnection at the magnetopause. Geophysical Research Letters, 48, e2020GL091320. https://doi.org/10.1029/2020GL091320.

Zhou, M., Man, H., Yang, Y., Zhong, Z., and Deng, X. (2021). Measurements of energy dissipation in the electron diffusion region. Geophysical Research Letters, 48, e2021GL096372. https://doi.org/10.1029/2021GL096372.

Zhou, M., Man, H. Y., Deng, X. H., Pang, Y., Khotyaintsev, Y., Lapenta, G., Yi, Y.Y., Zhong, Z.H., Ma W.Q. (2021). Observations of secondary magnetic reconnection in the turbulent reconnection outflow. Geophysical Research Letters, 48, e2020GL091215. https://doi.org/10.1029/2020GL091215

Zhou, X.-Z., Zhang, X., Li, J.-H., and Zong, Q.-G. (2021). On the species dependence of ion escapes across the magnetopause. Geophysical Research Letters, 48, e2021GL093115. https://doi.org/10.1029/2021GL093115

Zhu, X., Wang, M., Shi, Q., Zhang, H., Tian, A., Yao, S., Guo, R., Liu, J., Bai, S., Degeling, A. W., Zhang, S., Niu, Z., Zhao, J., Xiao, Y., Shang, W., (2021). Motion of classic and spontaneous hot flow anomalies

observed by Cluster. Journal of Geophysical Research: Space Physics, 126, e2021JA029418. https://doi.org/10.1029/2021JA029418

2020

Bai, S.-C., Shi, Q., Liu, T. Z., Zhang, H., Yue, C., Sun, W.-J., et al. (2020). Ion-scale flux rope observed inside a hot flow anomaly. Geophysical Research Letters, 47, e2019GL085933. https://doi.org/10.1029/2019GL085933

Behar, E., Sahraoui, F., and Berčič, L. (2020). Resonant whistler-electron interactions: MMS observations versus test-particle simulation. Journal of Geophysical Research: Space Physics,125, e2020JA028040. https://doi.org/10.1029/2020JA028040

Bergstedt, K., Ji, H., Jara-Almonte, J., Yoo, J., Ergun, R. E., and Chen, L.-J. (2020). Statistical properties of magnetic structures and energy dissipation during turbulent reconnection in the Earth's magnetotail. Geophysical Research Letters, 47, e2020GL088540. https:// doi.org/10.1029/2020GL088540

Briggs,J.K.,Fasel,G.J.,Silveira,M., Sibeck,D.G.,Lin,Y.,andSigernes,F. (2020).Daysideauroralobservation resultingfromarapidlocalized compressionoftheEarth'smagnetic field.Geophysical Research Letters, 47, e2020GL088995.https://doi.org/10.1029/2020GL088995

Dong, X.-C., Dunlop, M. W., Wang, T.-Y., Trattner, K. J., Russell, C. T., and Giles, B. (2020). MMS observation of secondary magnetic reconnection beside ion-scale flux rope at the magnetopause. *Geophysical Research Letters*, *47*, e2020GL089075. https://doi.org/10.1029/2020GL089075

Fu, H. S., Chen, F., Chen, Z. Z., Xu, Y., Wang, Z., Liu, Y. Y., ... and Burch, J. L. (2020). First measurements of electrons and waves inside an electrostatic solitary wave. *Physical review letters*, *124*(9), 095101. https://doi.org/10.1103/PhysRevLett.124.095101

Goncharov, O., Gunell, H., Hamrin, M., and Chong, S. (2020). Evolution of high-speed jets and plasmoids downstream of the quasi-perpendicular bow shock. *Journal of Geophysical Research: Space Physics*, *125*, e2019JA027667. https://doi.org/10.1029/2019JA027667

Greco, A., Perrone, D., Lavraud, B., and Chasapis, A. (2020). Improving the Understanding of Kinetic Processes in Solar Wind and Magnetosphere: From CLUSTER to Magnetospheric Multiscale Mission. *Frontiers in Astronomy and Space Sciences*, 87. https://doi.org/10.3389/fspas.2020.549935

Grigorenko, E. E., Malykhin, A. Y., Shklyar, D. R., Fadanelli, S., Lavraud, B., Panov, E. V., et al. (2020). Investigation of electron distribution functions associated with whistler waves at dipolarization fronts in the Earth's magnetotail: MMS observations. Journal of Geophysical Research: Space Physics, 125, e2020JA028268. https://doi.org/10.1029/2020JA028268

Guo, Z., Lin, Y., Wang, X., Vines, S. K., Lee, S. H., and Chen, Y. (2020). Magnetopause reconnection as influenced by the dipole tilt under southward IMF conditions: Hybrid simulation and MMS observation. Journal of Geophysical Research: Space Physics, 125, e2020JA027795. https://doi.org/10.1029/2020JA027795

Hau, L.-N., G.-W. Chen, and C.-K. Chang (2020), Mirror Mode Waves Immersed in Magnetic Reconnection, The Astrophysical Journal Letters, 903:L12 (8pp). https://doi.org/10.3847/2041-8213/abbf4a

Hau, L. N., Chang, C. K., and Chen, G. W. (2020). Mirror-wave Structures in the Solar Wind: Grad–Shafranov Reconstruction, MHD, and Hall MHD Simulations with Double-polytropic Energy Closures. The Astrophysical Journal, 900(2), 97. https://doi.org/10.3847/1538-4357/aba2d0

He, J. X. Zhu, D. Verscharen, D. Duan, J. Zhao, and T. Wang (2020), Spectra of Diffusion, Dispersion, and Dissipation for Kinetic Alfvénic and Compressive Turbulence: Comparison between Kinetic Theory and Measurements from MMS, The Astrophysical Journal, 898:43 (12pp). https://doi.org/10.3847/1538-4357/ab9174

Huang, S. Y., S. B. Xu, L. H. He, K. Jiang, Z. G. Yuan, X. H. Deng, Y. Y. Wei, J. Zhang, Z. H. Zhang (2020), Excitation of Whistler waves through the bidirectional field-aligned electron beams with electron

temperature anisotropy: MMS observations, Geophysical Research Letters, 47, e2020GL087515. https://doi.org/10.1029/2020GL087515

Huang, S. Y., Deng, D., Yuan, Z. G., Jiang, K., Li, J. X., Deng, X. H., et al. (2020). First observations of magnetosonic waves with nonlinear harmonics. Journal of Geophysical Research: Space Physics, 125, e2019JA027724. https://doi.org/10.1029/2019JA027724

Huang, S. Y., Zhang, J., Sahraoui, F., Yuan, Z. G., Deng, X. H., Jiang, K., ... and Zhang, Z. H. (2020). Observations of magnetic field line curvature and its role in the space plasma turbulence. *The Astrophysical Journal Letters*, *898*(1), L18. https://doi.org/10.3847/2041-8213/aba263

Jiang, K., Huang, S. Y., Yuan, Z. G., Deng, X. H., Xu, S. B., Wei, Y. Y., et al. (2020). Observations of electron vortex at the dipolarization front. Geophysical Research Letters, 47, e2020GL088448. https://doi.org/10.1029/2020GL088448

Li, H., C. Zhu, L. Guo, Q. Cheng, and O. Le Contel (2020), Magnetospheric Multiscale observations of the off-equatorial dipolarization front dynamics in the terrestrial magnetotail, The Astrophysical Journal, 899:125 (13pp). https://doi.org/10.3847/1538-4357/aba8a7

Li, H., W. Jiang, C. Wang, D. Verscharen, C. Zeng, C. T. Russell, B. Giles, and J. L. Burch (2020), Evolution of the Earth's Magnetosheath Turbulence: A Statistical Study Based on MMS Observations, The Astrophysical Journal Letters, 898:L43 (10pp). https://doi.org/10.3847/2041-8213/aba531

Li, H., Peng, Q., Tang, R., Zhang, H., Zhong, Z., Deng, X., and Wang, D. (2020). Statistical characteristics of electronpitch angle distributions inside themagnetopasue based on MMS observations. Journal of GeophysicalResearch: Space Physics, 125, e2020JA028291. https://doi.org/10.1029/2020JA028291

Li, JH., Yang, F., Zhou, XZ. *et al.* Self-consistent kinetic model of nested electron- and ion-scale magnetic cavities in space plasmas. *Nat Commun* **11,** 5616 (2020). https://doi.org/10.1038/s41467-020-19442-0

Li, L.-F., Tu, W., Dai, L., Tang, B.-B., Wang, C., Barani, M., et al (2020). Quantifying event-specific radial diffusion coefficients of radiation belt electrons with the PPMLR-MHD simulation. Journal of Geophysical Research: Space Physics, 125, e2019JA027634. https://doi.org/10.1029/2019JA027634

Li, Z. (2020). In Situ Evidence of a Magnetic Hole Downstream of the Magnetic Reconnection in the Magnetopause Reconnection. *The Astrophysical Journal*, *901*(1), 20. https://doi.org/10.3847/1538-4357/abad33

Liu, J., Yao, S. T., Shi, Q. Q., Wang, X. G., Zong, Q. G., Feng, Y. Y., ... and Giles, B. L. (2020). Electron energization and energy dissipation in microscale electromagnetic environments. *The Astrophysical Journal Letters*, *899*(2), L31. https://doi.org/10.3847/2041-8213/abab92

Liu, Y. Y., Fu, H. S., Zong, Q. G., Wang, Z., Liu, C. M., Huang, S. Y., et al. (2020). First topology of electron-scale magnetic hole. Geophysical Research Letters, 47, e2020GL088374. https://doi.org/10.1029/2020GL088374

Liu, Z., Wang, L., Shi, Q., Oka, M., Yang, L., Wimmer-Schweingruber, R. F., ... and Bale, S. D. (2020). Case Study of Solar Wind Suprathermal Electron Acceleration at the Earth's Bow Shock. *The Astrophysical Journal Letters*, *889*(1), L2. https://doi.org/10.3847/2041-8213/ab64d0

Liu, Z.-Y., Zong, Q.-G., and Blake, J. B. (2020). On phase space density and its radial gradient of outer radiation belt seed electrons: MMS/FEEPS observations. *Journal of Geophysical Research: Space Physics*, *125*, e2019JA027711. https://doi.org/10.1029/2019JA027711

Loureiro, N. F., and Boldyrev, S. (2020), Nonlinear Reconnection in Magnetized Turbulence, The Astrophysical Journal, 890:55 (6pp). https://doi.org/10.3847/1538-4357/ab6a95

Lu, Q., Wang, H., Wang, X., Lu, S., Wang, R., Gao, X., and Wang, S., (2020). Turbulence-driven magnetic reconnection in the magnetosheath downstream of a quasi-parallel shock: A three-dimensional global hybrid simulation. Geophysical Research Letters, 47, e2019GL085661. https://doi.org/10.1029/2019GL085661

Lu, S., Wang, R., Lu, Q. *et al.* Magnetotail reconnection onset caused by electron kinetics with a strong external driver. *Nat Commun* **11,** 5049 (2020). https://doi.org/10.1038/s41467-020-18787-w

Lukin,A.S.,Panov,E.V., Artemyev,A.V.,Petrukovich,A.A., Haaland,S.,Nakamura,R.,etal. (2020).Comparison of the flank magnetopause at near-Earth and lunar distances: MMS and ARTEMIS observations. Journal of Geophysical Research: Space Physics, 125, e2020JA028406. https://doi.org/10.1029/2020JA028406

Luo, Q., He, J., Cui, J., Zhu, X., Duan, D., and Verscharen, D. (2020). Energy Conversion between Ions and Electrons through Ion Cyclotron Waves and Embedded Ion-scale Rotational Discontinuity in Collisionless Space Plasmas. *The Astrophysical Journal Letters*, *904*(2), L16. https://doi.org/10.3847/2041-8213/abc75a

Ma, W., Zhou, M., Zhong, Z., and Deng, X. (2020). Electron acceleration rate at Dipolarization Fronts. *The Astrophysical Journal*, *903*(2), 84. https://doi.org/10.3847/1538-4357/abb8cc

Ma, Y. D., Yang, J., Dunlop, M. W., Rae, I. J., and Yang, J. Y. (2020), Energy Budget of High-speed Plasma Flows in the Terrestrial Magnetotail, The Astrophysical Journal, 894:16 (12pp). https://doi.org/10.3847/1538-4357/ab83fd

Man, H., Zhong, Z. and Li, H. Internal structures of the ion-scale flux rope associated with dayside magnetopause reconnection. *Astrophys Space Sci* **365,** 87 (2020). https://doi.org/10.1007/s10509-020-03803-8

Man,H.Y.,Zhou,M.,Yi,Y.Y., Zhong,Z.H.,Tian,A.M.,Deng,X.H., etal.(2020).Observationsof electron-onlymagneticreconnection associatedwithmacroscopicflux ropes. Geophysical Research Letters, 47, e2020GL089659. https://doi.org/10.1029/2020GL089659

Manuzzo, R., Califano, F., Belmont, G., and Rezeau, L. (2020), A multi-fluid model of the magnetopause, Ann. Geophys., 38, 275–286, 2020. https://doi.org/10.5194/angeo-38-275-2020

Nishimura, Y., Wang, B., Zou, Y., Donovan, E.F., Angelopoulos, V., Moen, J.I., Clausen, L.B. and Nagatsuma, T. (2020). Transient Solar Wind–Magnetosphere–Ionosphere Interaction Associated with Foreshock and Magnetosheath Transients and Localized Magnetopause Reconnection. In Dayside Magnetosphere Interactions (eds Q. Zong, P. Escoubet, D. Sibeck, G. Le and H. Zhang). https://doi.org/10.1002/9781119509592.ch3

Oimatsu, S., Nosé, M., Le, G., Fuselier, S. A., Ergun, R. E., Lindqvist, P.-A., and Sormakov, D. (2020). Selective acceleration of O+ by drift-bounce resonance in the Earth's magnetosphere: MMS observations. *Journal of Geophysical Research: Space Physics*, *125*, e2019JA027686. https://doi.org/10.1029/2019JA027686

Peng, Q., Li, H., Tang, R., Zhong, Z., Zhang, H., and Li, Q. (2020). Variation of dayside chorus waves associated with solar wind dynamic pressure based on MMS observations. *Advances in Space Research*, *65*(11), 2551-2558. https://doi.org/10.1016/j.asr.2020.03.006

Perri, S., D. Perrone, E. Yordanova, L. Sorriso-Valvo, W. R. Paterson, D. J. Gershman, B. L. Giles, C. J. Pollock, J. C. Dorelli, L. A. Avanov, B. Lavraud, Y. Saito, R. Nakamura, D. Fischer, W. Baumjohann, F. Plaschke, Y. Narita, W. Magnes, C. T. Russell, R. J. Strangeway, O. Le Contel, Y. Khotyaintsev and F. Valentini (2020), On the deviation from Maxwellian of the ion velocity distribution functions in the turbulent magnetosheath, *J. Plasma Phys.* (2020), v*ol*. 86, 905860108. https://doi.org/10.1017/S0022377820000021

Pucci, F., Velli, M., Shi, C., Singh, K. A. P., Tenerani, A., Alladio, F., ... and Schwartz, S. (2020). Onset of fast magnetic reconnection and particle energization in laboratory and space plasmas. *Journal of Plasma Physics*, *86*(6). https://doi.org/10.1017/S0022377820001373

Qin, P., Y. Ge, A. Du, C. Huang, Y. Zhang, H. Luo, J. Ou, T. Zhang, and L. shan (2020), Coupling between the magnetospheric dipolarization Front and the Earth's ionosphere by ultralow-frequency Waves, The Astrophysical Journal Letters, 895:L13 (8pp). https://doi.org/10.3847/2041-8213/ab8e48

Settino, A., Malara, F., Pezzi, O., Onofri, M., Perrone, D., and Valentini, F. (2020). Kelvin–Helmholtz instability at proton scales with an exact kinetic equilibrium. *The Astrophysical Journal*, *901*(1), 17. https://doi.org/10.3847/1538-4357/abada9

Shi, C., Zhao, J., Huang, C., Wang, T., and Dunlop, M. W. (2020). Modulation of ionospheric outflow ions by EMIC waves in the dayside outer magnetosphere. *Physics of Plasmas*, *27*(3), 032902. https://doi.org/10.1063/1.5142686

Tang, B. B., W. Y. Li, A. Le, D. B. Graham, Y.-F. Wu, C. Wang, Yu. V. Khotyaintsev, J. Egedal, X. Tao, D. J. Gershman, B. L. Giles, P.-A. Lindqvist, R. E. Ergun, C. T. Russell, and J. L. Burch (2020), Electron mixing and isotropization in the exhaust of asymmetric magnetic reconnection with a guide field, Geophysical Research Letters, 47, e2020GL087159. https://doi.org/10.1029/2020GL087159

Tang, B.,-B., Li, W. Y., Graham, D. B., Wang,C.,Khotyaintsev,Y.V.,Le,A., etal.(2020).Lower hybrid waves at the magnetosheath separatrix region. Geophysical Research Letters, 47, e2020GL089880. https://doi.org/10.1029/2020GL089880

Teh, W.-L., and Zenitani, S. (2020), Thermodynamics of Dipolarization Fronts of Magnetic Reconnection in Anisotropic Plasma: MMS Observations and Resistive Double-polytropic MHD Simulations, The Astrophysical Journal, 890:114 (7pp). https://doi.org/10.3847/1538-4357/ab6d6b

Tian, A., Xiao, K., Degeling, A. W., Shi, Q., Park, J. S., Nowada, M., and Pitkänen, T. (2020). Reconstruction of plasma structure with anisotropic pressure: Application to Pc5 compressional wave. *The Astrophysical Journal*, *889*(1), 35. https://doi.org/10.3847/1538-4357/ab6296

Tsurutani, B. T., Lakhina, G. S., and Hajra, R. (2020), The physics of space weather/solar-terrestrial physics (STP): what we know now and what the current and future challenges are, Nonlin. Processes Geophys., 27, 75–119. https://doi.org/10.5194/npg-27-75-2020

Wang, G. Q., Zhang, T. L., Wu, M. Y., Schmid, D. N., Hao, Y. F., and Volmerk, M. (2020), Roles of electrons and ions in formation of the current in mirror-mode structures in the terrestrial plasma sheet: Magnetospheric Multiscale observations, Ann. Geophys., 38, 309–318. https://doi.org/10.5194/angeo-38-309-2020

Wang, G. Q., Zhang, T. L., Xiao, S. D., Wu, M. Y., Wang, G., Liu, L. J., et al. (2020). Statistical properties of sub-ion magnetic holes in the solar wind at 1 AU. Journal of Geophysical Research: Space Physics, 125, e2020JA028320. https://doi.org/10.1029/2020JA028320

Wang, G. Q., Zhang, T. L., Wu, M. Y., Hao, Y. F., Xiao, S. D., Wang, G., et al.(2020). Study of the electron velocity inside sub-ion-scale magnetic holes in the solar wind by MMS observations. Journal of Geophysical Research: Space Physics, 125, e2020JA028386. https://doi.org/10.1029/2020JA028386

Wang, G. Q., Volwerk, M., Xiao, S. D., Wu, M. Y., Hao, Y. F., Liu, L. J., ... and Zhang, T. L. (2020). Three-dimensional Geometry of the Electron-scale Magnetic Hole in the Solar Wind. *The Astrophysical Journal Letters*, *904*(1), L11. https://doi.org/10.3847/2041-8213/abc553

Wang, L., Huang, C., Cao, X., Du, A., andGe, Y. S. (2020). Magnetic energy conversion and transport in the terrestrial magnetotail due to dipolarization fronts. Journal of Geophysical Research: Space Physics,125, e2020JA028568. https://doi.org/10.1029/2020JA028568

Wang, R., Lu, Q., Lu, S., Russell, C. T., Burch, J. L., Gershman, D. J., et al. (2020). Physical implication of two types of reconnection electron diffusion regions with and without ion-coupling in the magnetotail current sheet. Geophysical Research Letters, 47, e2020GL088761. https://doi.org/10.1029/2020GL088761

Wang, T., He, J., Alexandrova, O., Dunlop, M., and Perrone, D. (2020). Observational quantification of three-dimensional anisotropies and scalings of space plasma turbulence at kinetic scales. *The Astrophysical Journal*, *898*(1), 91. https://doi.org/10.3847/1538-4357/ab99ca

Wang, Z., Fu, H. S., Vaivads, A., Burch, J. L., Yu, Y., and Cao, J. B. (2020). Monitoring the Spatio-temporal Evolution of a Reconnection X-line in Space. *The Astrophysical Journal Letters*, *899*(2), L34. https://doi.org/10.3847/2041-8213/abad2c

Xu, J., Peng, F. Z., Russell, C. T., Giles, B., Lindqvist, P. A., Torbert, R. B., ... and Burch, J. L. (2020). Observation of energy conversion near the x-line in asymmetric guide-field reconnection. *The Astrophysical Journal Letters*, *895*(1), L10. https://doi.org/10.3847/2041-8213/ab8e31

Yang, Z. Y. D. Liu, A. Johlander, G. K. Parks, B. Lavraud, E. Lee, W. Baumjohann, R. Wang, and J. L. Burch (2020), MMS direct observations of kinetic-scale shock self-reformation, The Astrophysical Journal Letters, 901:L6 (6pp). https://doi.org/10.3847/2041-8213/abb3ff

Yao, S. T., Q. Q. Shi, R. L. Guo, Z. H. Yao, H. S. Fu, A. W. Degeling, Q. G. Zong, X. G. Wang, C. T. Russell, A. M. Tian, Y. C. Xiao, H. Zhang, S. M. Wang, H. Q. Hu, J. Liu, H. Liu, B. Li, and B. L. Giles (2020), Kinetic-scale flux rope in the magnetosheath boundary layer, The Astrophysical Journal, 897:137 (12pp). https://doi.org/10.3847/1538-4357/ab9620

Yao, S. T., Hamrin, M., Shi, Q. Q., Yao, Z. H., Degeling, A. W., Zong, Q.-G., et al. (2020). Propagating and dynamic properties of magnetic dips in the dayside magnetosheath: MMS observations. Journal of Geophysical Research: Space Physics, 124, e2019JA026736. https://doi.org/10.1029/2019JA026736

Yu, J., J. Wang, L. Y. Li, J. Cui, J. B. Cao, and Z. G. He (2020), Electron diffusion by coexisting plasmaspheric hiss and chorus waves: Multisatellite observations and simulations, Geophysical Research Letters, 47, e2020GL088753. https://doi.org/10.1029/2020GL088753

Yu, Y., Z. Chen, F. Chen (2020), Cold and Dense Plasma Sheet Caused by Solar Wind Entry: Direct Evidence, *Atmosphere*, *11*, 831. https://doi.org/10.3390/atmos11080831

Zeng, C., Duan, S., Chi Wang, C., Dai, L., Fuselier, S., Burch, J., Torbert, R., Giles, B., and Russell, C., (2020), Magnetospheric Multiscale observations of energetic oxygen ions at the duskside magnetopause during intense substorms, Ann. Geophys., 38, 123–135. https://doi.org/10.5194/angeo-38-123-2020

Zeng, C., C. Wang, S. Duan, L. Dai, S. A. Fuselier, J. L. Burch, R. B. Torbert, and B. Giles (2020), Statistical Study of Oxygen Ions Abundance and Spatial Distribution in the Dayside Magnetopause Boundary Layer: MMS Observations, Journal of Geophysical Research: Space Physics, 125, e2019JA027323. https://doi.org/10.1029/2019JA027323

Zhang, C., Z. Rong, C. Shen, L. Klinger, J. Gao, J. A. Slavin, Y. Zhang, J. Cui, and Y. Wei (2020), Examining the Magnetic Geometry of Magnetic Flux Ropes from the View of Single-point Analysis, The Astrophysical Journal, 903:53 (15pp). https://doi.org/10.3847/1538-4357/abba16

Zhang, L. Q., Lui, A. T. Y., Baumjohann, W., Wang, C., Burch, J. L., and Khotyaintsev, Y. V. (2020). Anisotropic vorticity within bursty bulk flow turbulence. Journal of Geophysical Research: Space Physics, 125, e2020JA028255. https://doi.org/10.1029/2020JA028255

Zhang, M., Wang, R., Lu, Q., and Wang, S. (2020). Observation of the tailward electron flows commonly detected at the flow boundary of the earthward ion bursty bulk flows in the magnetotail. *The Astrophysical Journal*, *891*(2), 175. https://doi.org/10.3847/1538-4357/ab72a8

Zhao, J., Wang, T., Graham, D. B., He, J., Liu, W., Dunlop, M. W., and Wu, D. (2020). Identification of the Nature of Electromagnetic Waves near the Proton-cyclotron Frequency in Solar-terrestrial Plasmas. *The Astrophysical Journal*, *890*(1), 17. https://doi.org/10.3847/1538-4357/ab672f

Zhong, Z. H., Zhou, M., Tang, R. X., Deng, X. H., Turner, D. L., Cohen, I. J., et al (2020). Direct evidence for electron acceleration within ion-scale flux rope. Geophysical Research Letters, 47, e2019GL085141. https://doi.org/10.1029/2019GL085141

Zhong, Z. H., Zhou, M., Tang, R. X., Deng, X. H., Khotyaintsev, Y. V., Giles, B. L., ... and Burch, J. L. (2020). Extension of the electron diffusion region in a guide field magnetic reconnection at magnetopause. *The Astrophysical Journal Letters*, *892*(1), L5. https://doi.org/10.3847/2041-8213/ab7b7c

Zhu, X., He, J., Wang, Y., and Sorriso-Valvo, L. (2020). Difference of intermittency between electric field and magnetic field fluctuations from ion scale down to sub-electron scale in the magnetosheath turbulence. *The Astrophysical Journal*, *893*(2), 124. https://doi.org/10.3847/1538-4357/ab7815

2019

Bai, S.-C., Shi, Q., Zong, Q.-G., Wang, X., Tian, A., Degeling, A. W., et al. (2019). Electron dispersion and parallel electron beam observed near the separatrix, Journal of Geophysical Research: Space Physics, 124, 7494–7504. https://doi.org/10.1029/2019JA026836

Chen, C.H.K., Klein, K.G. and Howes, G.G. Evidence for electron Landau damping in space plasma turbulence. Nat Commun 10, 740 (2019). https://doi.org/10.1038/s41467-019-08435-3

Chen, Y. Q., Wu, M., Wang, G., Schmid, D., Zhang, T., Nakamura, R., Baumjohann W., Burch, J. L., Giles, B. L., Russell, C. T. (2019), Carriers of the field-aligned currents in the plasma sheet boundary layer: An MMS multicase study, Journal of Geophysical Research: SpacePhysics,124, 2873–2886. https://doi.org/10.1029/2018JA026216

Chen, Y., Zhang, T., Wu, M., Wang, G., Schmid, D., Baumjohann, W., et al. (2019). Small spatial-scale field-aligned currents in the plasma sheet boundary layer surveyed by magnetosphere multiscale spacecraft. Journal of Geophysical Research: Space Physics, 124, https://doi.org/10.1029/2019JA027027

Chen, Z. Z., Fu, H. S., Liu, C. M., Wang, T. Y., Ergun, R. E., Cozzani, G., Huang, S. Y., Khotyaintsev, Y. V., Le Contel, O., Giles, B. L., Burch, J. L. (2019), Electron-driven dissipation in a tailward flow burst, Geophysical Research Letters, 46, 5698–5706. https://doi.org/10.1029/2019GL082503

Chen, Z. Z., Fu, H. S., Wang, T. Y., Cao, D., Peng, F. Z., Yang, J., and Xu, Y. (2019), Reconstructing the flux-rope topology using the FOTE method, Science China Technological Sciences, 62(1), pp 144–150, http://doi.org/10.1007/S11431-017-9201-1

Chen, Z. Z., H. S. Fu, Z. Wang, C. M. Liu, and Y. Xu, (2019), Evidence of magnetic nulls in the reconnection at bow shock, Geophysical Research Letters, 46, 10,209-10,218. https://doi.org/10.1029/2019GL084360

Dong, X.-C., Dunlop, M. W., Trattner, K. J., Wang, T.-Y., Pu, Z. Y., Zhao, J.-S., et al. (2019). Electron sublayers and the associated magnetic topologies in the inner low-latitude boundary layer. Geophysical Research Letters, 46, 5746–5753. https://doi.org/10.1029/2019GL081998

Fletcher, A. C., Crabtree, C., Ganguli, G., Malaspina, D., Tejero, E., and Chu, X. (2019). Kinetic equilibrium and stability analysis of dipolarization fronts. Journal of Geophysical Research: Space Physics, 124, 2010–2028. https://doi.org/10.1029/2018JA026433

Fu, H. S., Peng, F. Z., Liu, C. M., Burch, J. L., Gershman, D. G., and Le Contel, O. (2019). Evidence of electron acceleration at a reconnecting magnetopause. Geophysical Research Letters, 46, 5645–5652. https://doi.org/ 10.1029/2019GL083032

Grošelj, D. C. H. K. Chen, A. Mallet, R. Samtaney, K. Schneider, and F. Jenko (2019), Kinetic Turbulence in Astrophysical Plasmas: Waves and/or Structures? Phys. Rev. X, 9, 031037. https://doi.org/10.1103/PhysRevX.9.031037

Hamrin, M., H. Gunell, O. Goncharov, A. De Spiegeleer, S. Fuselier, J. Mukherjee, A. Vaivads, T. Pitkänen1, R. B. Torbert, and B. Giles (2019), Can reconnection be triggered as a solar wind directional discontinuity crosses the bow shock? A case of asymmetric reconnection, Journal of Geophysical Research: Space Physics, 124. https://doi.org/10.1029/2019JA027006

He, J., Duan, D., Wang, T., Zhu, X., Li, W., Verscharen, D., ... and Burch, J. (2019). Direct measurement of the dissipation rate spectrum around ion kinetic scales in space plasma turbulence. *The Astrophysical Journal*, *880*(2), 121. https://doi.org/10.3847/1538-4357/ab2a79

Huang, S. Y., L. H. He, Z. G. Yuan, F. Sahraoui, O. Le Contel, X. H. Deng, M. Zhou, H. S. Fu, K. Jiang, X. D. Yu, H. M. Li, D. Deng, C. J. Pollock, R. B. Torbert, and J. L. Burch (2019), MMS Observations of

Kinetic-size Magnetic Holes in the Terrestrial Magnetotail Plasma Sheet, The Astrophysical Journal, 875(2).http://doi.org/10.3847/1538-4357/AB0F2F

Huang, S. Y., Jiang, K., Yuan, Z. G., Zhou, M., Sahraoui, F., Fu, H. S.,Deng X. H., Khotyaintsev, Y., Yu, X. D., He, L. H., Deng, D., Pollock, C. J., Torbert R. B., Burch, J. L.(2019). Observations of flux ropes with strong energy dissipation in the magnetotail. Geophysical ResearchLetters,46, 580–589.https://doi.org/10.1029/2018GL081099

Huang, S. Y., Jiang, K., Fu, H. S., Yuan, Z. G., Deng, X. H., Li, H. M., et al (2019). Periodical dipolarization processes in Earth's magnetotail. Geophysical Research Letters, 46, 13,640–13,648. https://doi.org/10.1029/2019GL086136

Jiang, K., Huang, S.Y., Yuan, Z.G. et al. (2019). Observations of whistler waves in two sequential flux ropes at the magnetopause. Astrophys Space Sci 364, 168. https://doi.org/10.1007/s10509-019-3647-4

Jiang, K., S. Y. Huang, Z. G. Yuan, F. Sahraoui, X. H. Deng, X. D. Yu, L. H. He, D. Deng, Y. Y. Wei, and S. B. Xu (2019), The Role of Upper Hybrid Waves in the Magnetotail Reconnection Electron Diffusion Region, The Astrophysical Journal Letters, 881(2), L28. https://DOI.org/10.3847/2041-8213/ab36b9

Li, B., Han, D.-S., Hu, Z.-J., Hu, H.-Q., Liu, J.-J., Dai, L., Liu, D., Escoubert, C. P., Dunlop, M. W., Ergun, R. E., Lindqvist, P.-A., Torbert, R. B., Russell, C. T. (2019). Magnetospheric multiscale observations of ULF waves and correlated low-energy ion monoenergetic acceleration. Journal of Geophysical Research: Space Physics,124, 2788–2794. https://doi.org/10.1029/2018JA026372

Li, X., Wang, R., Lu, Q., Hwang, K.-J., Zong, Q., Russell, C. T., and Wang, S. (2019). Observation of nongyrotropic electron distribution across the electron diffusion region in the magnetotail reconnection. Geophysical Research Letters, 46 https://doi.org/10.1029/2019GL085014

Li, Z., Lu, Q. M., Wang, R. S., Gao, X. L., and Chen, H. Y. (2019). In situ evidence of resonant interactions between energetic electrons and whistler waves in magnetopause reconnection. Earth Planet. Phys., 3(6), 467–473. http://doi.org/10.26464/epp2019048

Liu, C. M., Vaivads, A., Graham, D. B., Khotyaintsev, Y. V., Fu, H. S., Johlander, A., et al (2019). Ion-Beam-Driven Intense Electrostatic Solitary Waves in Reconnection Jet. Geophysical Research Letters, 46, 12,702–12,710. https://doi.org/10.1029/2019GL085419

Liu, H., Q.-G. Zong, H. Zhang, C.J. Xiao, Q.Q. Shi, S.T. Yao, J.S. He, X.-Z. Zhou, C. Pollock, W.J. Sun, G. Le, J.L. Burch, and R. Rankin (2019). MMS observations of electron scale magnetic cavity embedded in proton scale magnetic cavity, Nature Communications, volume 10, Article number: 1040. https://doi.org/10.1038/s41467-019-08971-y

Liu, H., Zong, Q.-G., Zhang, H., Sun, W. J., Zhou, X.-Z., Gershman, D. J., Shi C., Zhang K., Le G., and Pollock C. (2019). The geometry of an electron scale magnetic cavity in the plasma sheet. Geophysical Research Letters, 46, 9308–9317. https://doi.org/10.1029/2019GL083569

Liu, S., Xia, Z., Chen, L., Liu, Y., Liao, Z., and Zhu, H. (2019). Magnetospheric Multiscale Observation of quasiperiodic EMIC waves associated with enhanced solar wind pressure. Geophysical Research Letters, 46, 7096–7104. https://doi.org/10.1029/2019GL083421

Liu, Y. Y., H. S. Fu, C. M. Liu, Z. Wang, P. Escoubet, K.-J. Hwang, J. L. Burch, and B. L. Giles (2019), Parallel Electron Heating by Tangential Discontinuity in the Turbulent Magnetosheath, The Astrophysical Journal Letters, 877(2). http://doi.org/10.3847/2041-8213/AB1FE6

Liu, Z.-Y., Zong, Q.-G., Zhou, X.-Z., Hao, Y. X., Yau, A. W., Zhang, H., et al. (2019). ULF waves modulating and acting as mass spectrometer for dayside ionospheric outflow ions. Geophysical Research Letters, 46, 8633–8642. https://doi.org/10.1029/2019GL083849

Lu, S. W., C. Wang, W. Y. Li, B. B. Tang, R. B. Torbert, B. L. Giles, C. T. Russell, J. L. Burch, J. P. McFadden, H. U. Auster, and V. Angelopoulos (2019), Prolonged Kelvin–Helmholtz Waves at Dawn and

Dusk Flank Magnetopause: Simultaneous Observations by MMS and THEMIS, The Astrophysical Journal, 875(1). http://doi.org/10.3847/1538-4357/AB0E76

Ozturk, D. S., Zou, S., Slavin, J. A., and Ridley, A. J. (2019). Response of the geospace system to the solar wind dynamic pressure decrease on 11 June 2017: Numerical models and observations. Journal of Geophysical Research: Space Physics, 124, 2613–2627. https://doi.org/10.1029/2018JA026315

Pecora, F., Greco, A., Hu, Q., Servidio, S., Chasapis, A. G., and Matthaeus, W. H. (2019). Single-spacecraft identification of flux tubes and current sheets in the solar wind. *The Astrophysical Journal Letters*, *881*(1), L11. https://doi.org/10.3847/2041-8213/ab32d9

Pezzi, O., Yang, Y., Valentini, F., Servidio, S., Chasapis, A., Matthaeus, W. H., and Veltri, P. (2019). Energy conversion in turbulent weakly collisional plasmas: Eulerian hybrid Vlasov-Maxwell simulations. *Physics of Plasmas*, *26*(7), 072301. https://doi.org/10.1063/1.5100125

Ren,Y., Dai, L., Li, W., Tao, X., Wang, C., Tang, B., Lavraud, B., Wu, Y., Burch, J. L., Giles, B., Le Contel, O., Torbert, R. B., Russell, C. T., Strangeway, R. J., Ergun, R. E., Lindqvist, P.-A. (2019). Whistler waves driven by field-aligned streaming electrons in the near-Earth magnetotail reconnection. Geophysical Research Letters,46, 5045–5054. https://doi.org/10.1029/2019GL083283

Sergeev, V. A., Apatenkov, S. V., Nakamura, R., Baumjohann, W., Khotyaintsev, Y. V., Kauristie, K., Van de Kamp, M., Burch, J. L., Ergun, R. E., Lindqvist, P.-A., Russell, C. T., Giles, B. L. (2019). Substorm-related near-Earth reconnection surge: Combining telescopic and microscopic views. Geophysical Research Letters, 46, 6239–6247. https://doi.org/10.1029/2019GL083057

Sorriso-Valvo L., Catapano F., Retinò A., Le Contel O., Perrone D., Roberts O. W., Coburn J. T., Panebianco V., Valentini F., Perri S., Greco A., Malara F., Carbone V., Veltri P., Pezzi O.,Fraternale F., Di Mare F., Marino R., Giles B. L., Moore T. E., Russell C. T., Torbert R. B., Burch J. L., Khotyaintsev Y. V. (2019), Turbulence-Driven Ion Beams in the Magnetospheric Kelvin-Helmholtz Instability, Physical Review Letters 122, 035102. http://doi.org/10.1103/PhysRevLett.122.035102

Tang, B.-B., Li, W. Y., Graham, D. B., Rager, A. C., Wang, C., Khotyaintsev, Y. V., Lavraud, B., Hasegawa, H., Zhang, Y.-C., Dai, L., Giles, B. L., Dorelli, J. C., Russell, C. T., Lindqvist, P.-A., Ergun, R. E., Burch, J. L. (2019). Crescent-shaped electron distributions at the nonreconnecting magnetopause: Magnetospheric multiscale observations. Geophysical ResearchLetters,46, 3024–3032. https://doi.org/10.1029/2019GL082231

Teh, W.-L. (2019), Two-dimensional reconstruction of magnetic mirror structures with pressure anisotropy: Theory and application, Journal of Geophysical Research: Space Physics, 124, 1644–1650. https://doi.org/10.1029/2018JA026416

Teh, W.-L. and S. Zenitani (2019), Thermodynamic Properties of Mirror Structures in the Magnetosheath: MMS Observations and Double-polytropic MHD Simulations, The Astrophysical Journal, 885:22 (6pp). https://doi.org/10.3847/1538-4357/ab4417

TenBarge, J. M., Ng, J., Juno, J., Wang, L., Hakim, A. H., and Bhattacharjee, A. (2019), An extended MHD study of the16 October 2015 MMS diffusion region crossing, Journal of Geophysical Research: Space Physics,124, 8474-8487. https://doi.org/10.1029/2019JA026731

Trenchi, L., J. C. Coxon, R. C. Fear, J. P. Eastwood, M. W. Dunlop, K. Trattner, D. J. Gershman, D. B. Graham, Yu. Khotyaintsev, and B. Lavraud (2019), Signatures of magnetic separatrices at the borders of a crater flux transfer event connected to an active X-line, Journal of Geophysical Research: Space Physics, 124. https://doi.org/10.1029/2018JA026126

Vaverka, J., Pavlu, J., Nouzá, L. k.,Safrankova, J., Nemecek, Z.,Mann, I. B., et al. (2019), One-year analysis of dust impact-like events onto the MMS spacecraft, Journal of Geophysical Research: Space Physics, 124, 8179-8190. https://doi.org/10.1029/2019JA027035

Wang, Chih-Ping, Stephen A. Fuselier, Marc Hairston, Xiao-jia Zhang, Shasha Zou, Levon A. Avanov, Robert J. Strangeway, Narges Ahmadi, and Jacob Bortnik (2019), Event studies of O^+ density variability within a quiet-time plasma sheet, *J. Geophys. Res., 124,* 4168–4187. https://doi.org/10.1029/2019JA026644

Wang, G. Q., Zhang, T. L., Wu, M. Y., Schmid, D., Cao, J. B., and Volwerk, M. (2019). Solar wind directional change triggering flapping motions of the current sheet: MMS observations. Geophysical Research Letters, 46, 64–70. https://doi.org/10.1029/2018GL080023

Wang, S., Wang, R., Yao, S. T., Lu, Q., Russell, C. T., and Wang, S. (2019). Anisotropic electron distributions and whistler waves in a series of the flux transfer events at the magnetopause. Journal of Geophysical Research: SpacePhysics,124, 1753–1769. https://doi.org/10.1029/2018JA026417

Wang, T., Alexandrova, O., Perrone, D., Dunlop, M., Dong, X., Bingham, R., ... and Burch, J. L. (2019). Magnetospheric multiscale observation of kinetic signatures in the Alfvén vortex. *The Astrophysical journal letters*, *871*(2), L22. https://doi.org/10.3847/2041-8213/aafe0d

Wang, Z., Fu, H. S., Liu, C. M., Liu, Y.Y., Cozzani, G., Giles, B. L., Hwang, K.-J., Burch, J. L. (2019). Electron distribution functions around a reconnection X-line resolved by the FOTE method. Geophysical ResearchLetters,46, 1195–1204. https://doi.org/10.1029/2018GL081708

Wei, C., Dai, L., Duan, S-P., Wang, C., Wang, Y-X. (2019). Multiple satellites observation evidence: High-*m* Poloidal ULF waves with time-varying polarization states. *Earth and Planetary Physics*, 3(3): 190-203. doi: 10.26464/epp2019021

Wei, Y. Y., S. Y. Huang, Z. J. Rong, Z. G. Yuan, K. Jiang, X. H. Deng, M. Zhou, H. S. Fu, X. D. Yu, S. B. Xu, L. H. He, and D. Deng (2019), Observations of Short-period Current Sheet Flapping Events in the Earth's Magnetotail, The Astrophysical Journal Letters, Volume 874, Number 2. http://doi.org/10.3847/2041-8213/AB0F28

Wu, H., Verscharen, D., Wicks, R. T., Chen, C. H., He, J., and Nicolaou, G. (2019). The fluid-like and kinetic behavior of kinetic Alfvén turbulence in space plasma. *The Astrophysical Journal*, *870*(2), 106. https://doi.org/10.3847/1538-4357/aaef77

Xu, Y., Fu, H. S., Norgren, C., Toledo-Redondo, S., Liu, C. M., and Dong, X. C. (2019), Ionospheric cold ions detected by MMS behind dipolarization fronts, Geophysical Research Letters, 46, 7883–7892. https://doi.org/10.1029/2019GL083885

Yang, Y., Wan, M., Matthaeus, W. H., Shi, Y., Parashar, T. N., Lu, Q., and Chen, S. (2019). Role of magnetic field curvature in magnetohydrodynamic turbulence. *Physics of Plasmas*, *26*(7), 072306. https://doi.org/10.1063/1.5099360

Yao, S. T., Shi, Q. Q., Yao, Z. H., Li, J. X., Yue, C., Tao, X., Degeling, A. W., Zong, Q. G., Wang, X. G., Tian, A. M., Russell, C. T., Zhou, X. Z., Guo, R. L., Rae, I. J., Fu, H. S., Zhang, H., Li, L., Le Contel, O., Torbert, R. B., Ergun, R. E., Lindqvist, P.-A., Pollock, C. J., Giles, B. L. (2019). Waves in kinetic-scale magnetic dips: MMS observations in the magnetosheath. Geophysical Research Letters,46,523–533. https://doi.org/10.1029/2018GL080696

Yao, S. T., Q. Q. Shi, Z. H. Yao, R. L. Guo, Q. G. Zong, X. G. Wang, A. W. Degeling, I. J. Rae, C. T. Russell, A. M. Tian, H. Zhang, H. Q. Hu, J. Liu, H. Liu, B. Li, and B. L. Giles (2019), Electron Mirror-mode Structure: Magnetospheric Multiscale Observations, The Astrophysical Journal Letters, 881(2):L31 (6pp). https://doi.org/10.3847/2041-8213/ab3398

Yoo, J., S. Wang, E. Yerger, J. Jara-Almonte, H. Ji, M. Yamada, L.-J. Chen, W. Fox, A. Goodman, and A. Alt (2019), Whistler wave generation by electron temperature anisotropy during magnetic reconnection at the magnetopause, Physics of Plasmas 26, 052902 (2019). https://doi.org/10.1063/1.5094636

Zhang, L. Q., Baumjohann, W., Dai, L., Khotyaintsev, Y. V., and Wang, C. (2019). Measurements of the vorticity in the bursty bulk flows. Geophysical Research Letters, 46. https://doi.org/10.1029/2019GL084597

Zhao, J. S., Wang, T. Y., Dunlop, M. W., Shi, C., He, J. S., Dong, X. C., et al. (2019). Large-amplitude electromagnetic ion cyclotron waves and density fluctuations in the flank of the Earth's magnetosheath. Geophysical Research Letters, 46, 4545–4553. https://doi.org/10.1029/2019GL081964

Zhao, M. J., Fu, H. S., Liu, C. M., Chen, Z. Z., Xu, Y., Giles, B. L., and Burch, J. L. (2019). Energy range of electron rolling in distribution behind depolarization front. Geophysical Research Letters,46,2390–2398. https://doi.org/10.1029/2019GL082100

Zhong, Z. H., Deng, X. H., Zhou, M., Ma, W. Q., Tang, R. X., Khotyaintsev, Y. V., et al. (2019). Energy conversion and dissipation at dipolarization fronts: a statistical overview. Geophysical Research Letters, 46, 12,693–12,701. https://doi.org/10.1029/2019GL085409

Zhong, Z. H., Zhou, M., Huang, S. Y., Tang, R. X., Deng, X. H., Pang, Y., and Chen, H. T. (2019). Observations of a kinetic-scale magnetic hole in a reconnection diffusion region. Geophysical Research Letters, 46, 6248–6257. https://doi.org/10.1029/2019GL082637

Zhou, M., J. Huang, H. Y. Man, X. H. Deng, Z. H. Zhong, C. T. Russell, W. R. Paterson, B. L. Giles, P.-A. Lindqvist, Y. V. Khotyaintsev, J. L. Burch(2019), Electron-scale Vertical Current Sheets in a Bursty Bulk Flow in the Terrestrial Magnetotail, The Astrophysical Journal Letters, 872 (2). https://doi.org/10.3847/2041-8213/ab0424

Zhou, M., Deng, X. H., Zhong, Z. H., Pang, Y., Tang, R. X., El-Alaoui, M., ... and Lindqvist, P. A. (2019). Observations of an electron diffusion region in symmetric reconnection with weak guide field. The Astrophysical Journal, 870(1), 34. https://doi.org/10.3847/1538-4357/aaf16f

Zhou, M., Man, H. Y., Zhong, Z. H., Deng, X. H., Pang, Y., Huang, S. Y., et al. (2019), Sub-ion-scale dynamics of the ion diffusion region in the magnetotail: MMS observations, Journal of Geophysical Research: Space Physics, 124, 7898-7911. https://doi.org/10.1029/2019JA026817

Zhu, C., Zhang, H., Fu, S., Ni, B., Strangeway, R. J., Giles, B. L., et al. (2019). Trapped and accelerated electrons within a magnetic mirror behind a flux rope on the magnetopause. Journal of Geophysical Research: Space Physics, 124, 3993–4008. https://doi.org/10.1029/2019JA026464

2018

Dong, X.-C., Dunlop, M. W., Wang, T.-Y., Cao, J.-B., Trattner, K. J., Bamford, R., Russell, C. T., Bingham, R., Strangeway, R. J., Fear, R. C., Giles, B. L., Torbert, R. B. (2018). Carriers and sources of magnetopause current: MMS case study. Journal of Geophysical Research: Space Physics,123, 5464–5475. https://doi.org/10.1029/2018JA025292

Egedal, J., A. Le, W. Daughton, B. Wetherton, P. A. Cassak, J. L. Burch, B. Lavraud, J. Dorelli, D. J. Gershman, and L. A. Avanov (2018), Spacecraft Observations of Oblique Electron Beams Breaking the Frozen-In Law During Asymmetric Reconnection, Phys. Rev. Lett. 120, 055101. http://doi.org/10.1103/PHYSREVLETT.120.055101

Engebretson, M. J., J. L. Posch, N. S. S. Capman, N. G. Campuzano, P. Bělik, R. C. Allen, S. K. Vines, B. J. Anderson, S. Tian, C. A. Cattell, J. R. Wygant, S. A. Fuselier, M. R. Argall, M. R. Lessard, R. B. Torbert, M. B. Moldwin, M. D. Hartinger, H. Kim, C. T. Russell, C. A. Kletzing, G. D. Reeves, and H. J. Singer (2018). MMS, Van Allen Probes, GOES 13, and ground-based magnetometer observations of EMICwave events before, during, and after a modest interplanetary shock. Journal of Geophysical Research: Space Physics,123,8331–8357. https://doi.org/10.1029/2018JA025984

Fox, W., Wilder, F. D., Eriksson, S., Jara-Almonte, J., Pucci, F., Yoo, J., et al. (2018). Energy conversion by parallel electric fields during guide field reconnection in scaled laboratory and space experiments. Geophysical Research Letters, 45, 12,677–12,684. https://doi.org/10.1029/2018GL079883

Ganguli, G., Crabtree, C., Fletcher, A.C. *et al.* (2018). Kinetic Equilibrium of Dipolarization Fronts. *Sci Rep* **8**, 17186. https://doi.org/10.1038/s41598-018-35349-9

Giagkiozis, S., Wilson, L. B., Burch, J. L., Le Contel, O., Ergun, R. E., Gershman, D. J., Lindqvist, P.-A., Mirioni, L., Moore, T. E., Strangeway, R. J. (2018). Statistical study of the properties of magnetosheath lion roars. Journal of Geophysical Research: Space Physics, 123, 5435–5451. https://doi.org/10.1029/2018JA025343

Gingell, I., Schwartz, S., Gershman, D. J., Paterson, W. R., Desai, R. T., Giles, B. L., Pollock, C. J., Avanov, L. A. (2018). Production of negative hydrogen ions within the MMS Fast Plasma Investigation due to solar wind bombardment. Journal of Geophysical Research: Space Physics, 123, 6161–6170. https://doi.org/10.1029/2018JA025341

Hamrin, M., Gunell, H., Lindkvist, J., Lindqvist, P.-A., Ergun, R. E., and Giles, B. L. (2018). Bow shock generator current systems: MMS observations of possible current closure. Journal of Geophysical Research: Space Physics,123, 242–258. https://doi.org/10.1002/2017JA024826

Han, De-Sheng, J. J. Liu, X.-C. Chen, T. Xu, B. Li, Z.-J. Hu, H.-Q. Hu, H. G. Yang, S. A. Fuselier, and C. J. Pollock (2018). Direct evidence for throat aurora being the ionospheric signature of magnetopause transient and reflecting localized magnetopause indentations. Journal of Geophysical Research: Space Physics,123, 2658–2667. https://doi.org/10.1002/2017JA024945

Huang, S. Y., F. Sahraoui, Z. G. Yuan, O. Le Contel, H. Breuillard, J. S. He, J. S. Zhao, H. S. Fu, M. Zhou, X. H. Deng, X. Y. Wang, J. W. Du, X. D. Yu, D. D. Wang, C. J. Pollock, R. B. Torbert, and J. L. Burch (2018), Observations of Whistler Waves Correlated with Electron-scale Coherent Structures in the Magnetosheath Turbulent Plasma, The Astrophysical Journal, 861(1). http://doi.org/10.3847/1538-4357/AAC831

Huang, S. Y., K. Jiang, Z. G. Yuan, F. Sahraoui, L. H. He, M. Zhou, H. S. Fu, X. H. Deng, J. S. He, D. Cao, X. D. Yu, D. D. Wang, J. L. Burch, C. J. Pollock, and R. B. Torbert (2018), Observations of the Electron Jet Generated by Secondary Reconnection in the Terrestrial Magnetotail, The Astrophysical Journal, 862(2). http://doi.org/10.3847/1538-4357/AACD4C

Li, J., Bortnik, J., An, X., Li, W., Russell, C. T., Zhou, M., BHerhcem, J., Zhao, C., Wang, S., Torbert, R. B., Le Contel, O., Ergun, R. E., Lindqvist, P.-A., Pollock, C. J., Burch, J. L. (2018). Local excitation of whistler mode waves and associated Langmuir waves at dayside reconnection regions. Geophysical Research Letters, 45, 8793–8802. https://doi.org/10.1029/2018GL078287

Liu, C. M., Fu, H. S., Vaivads, A., Khotyaintsev, Y. V., Gershman, D. J., Hwang, K.-J.,...Le Contel, O. (2018). Electron jet detected by MMS at dipolarization front. Geophysical Research Letters, 45, 556–564. https://doi.org/10.1002/2017GL076509

Liu, C. M., Fu, H. S., Xu, Y., Khotyaintsev, Y. V., Burch, J. L., Ergun, R. E., Gershman, Torbert, R. B. (2018). Electron-scale measurements of dipolarization front. Geophysical ResearchLetters, 45, 4628–4638. https://doi.org/10.1029/2018GL077928

Liu, S., Zhang, J., Chen, L., Zhu, H., and He, Z. (2018). Examining wave vector and minimum cyclotron resonant electron energy of EMIC waves with Magnetospheric Multiscale mission. Geophysical Research Letters, 45, 10,138–10,149. https://doi.org/10.1029/2018GL079737

Lou, Y., Gu, X., Summers, D., Ni, B., Liu, K.,Fu, S., Xiang, Z., Zou, Z., Cao, X., Zhang, W., Huang, H., He, Y. (2018). Statistical distributions of dayside ECH waves observed by MMS. Geophysical ResearchLetters,45, 12,730–12,738. https://doi.org/10.1029/2018GL080125

Lv, X., and W. L. Liu (2018), Measurements of convection electric field in the inner magnetosphere, Science China Technological Sciences, 61(12), 1866–1871. http://doi.org/10.1007/S11431-017-9200-6

Macek, W. M., A. Krasińska, M. V. D. Silveira, D. G. Sibeck, A. Wawrzaszek, J. L. Burch, and C. T. Russell (2018), Magnetospheric Multiscale Observations of Turbulence in the Magnetosheath on Kinetic Scales, The Astrophysical Journal Letters, 864(2). http://doi.org/10.3847/2041-8213/AAD9A8

Man, H. Y., Zhou, M., Deng, X. H., Fu, H. S., Zhong, Z. H., Chen, Z. Z., Russell, C. T., Strangeway, R. J., Paterson, W. R., Giles, B. L., Lindqvist, P.-A., Ergun, R. E., Burch, J. L. (2018). In situ observation of

magnetic reconnection between an earthward propagating flux rope and the geomagnetic field. Geophysical Research Letters, 45, 8729–8737. https://doi.org/10.1029/2018GL079778

Moretto, T., Hesse, M., Vennerstrøm, S., and Tenfjord, P. (2018). Estimating the rate of cessation of magnetospheric activity in AMPERE field-aligned currents. Geophysical Research Letters, 45, 12,713–12,719. https://doi.org/10.1029/2018GL080631

Oimatsu, S., Nosé, M., Teramoto, M.,Yamamoto, K., Matsuoka, A., Kasahara, S., Yokota, S., Keika, K., Le, G., Nomura, R., Fujimoto, A., Sormakov, D., Troshichev, O., Tanaka, Y.-M., Shinohara, M., Shinohara, I., Miyoshi, Y., Slavin, J. A., Ergun, R. A., Lindqvist, P.-A. (2018). Drift-bounce resonance between Pc5 pulsations and ions at multiple energies in the nightside magnetosphere: Arase and MMS observations. Geophysical Research Letters,45, 7277–7286. https://doi.org/10.1029/2018GL078961

Paschmann, G., S. E. Haaland, T. D. Phan, B. U. Ö. Sonnerup, J. L. Burch, R. B. Torbert, D. J. Gershman, J. C. Dorelli, B. L. Giles, C. Pollock, C. T. Russell, R. J. Strangeway, S. A. Fuselier (2018).Large-scale survey of the structureof the dayside magnetopauseby MMS.Journal of GeophysicalResearch: Space Physics,123, 2018–2033.https://doi.org/10.1002/2017JA025121

Pecora, F., Servidio, S., Greco, A., Matthaeus, W. H., Burgess, D., Haynes, C. T., ... and Veltri, P. (2018). Ion diffusion and acceleration in plasma turbulence. *Journal of Plasma Physics*, *84*(6). https://doi.org/10.1017/S0022377818000995

Pezzi, O., Servidio, S., Perrone, D., Valentini, F., Sorriso-Valvo, L., Greco, A., ... and Veltri, P. (2018). Velocity-space cascade in magnetized plasmas: Numerical simulations. *Physics of Plasmas*, *25*(6), 060704. https://doi.org/10.1063/1.5027685

Rezeau, L., Belmont, G., Manuzzo, R., Aunai, N., and Dargent, J. (2018). Analyzing the magnetopause internal structure: New possibilities offered by MMS tested in a case study. Journal of Geophysical Research: Space Physics, 123, 227– 241. https://doi.org/10.1002/2017JA024526

Roberts, O. W., Toledo-Redondo, S., Perrone, D., Zhao, J., Narita, Y., Gershman, D., Nakamura, R., Lavraud, B., Escoubet, C. P., Giles, B., Dorelli, J., Pollock, C., Burch, J. (2018). Ion-scale kinetic Alfvén turbulence: MMS measurements of the Alfvén ratio in the magnetosheath. Geophysical Research Letters,45, 7974–7984. https://doi.org/10.1029/2018GL078498

Tang, B. B., Li, W. Y., Wang, C., Dai, L., and Han, J. P. (2018). Effect of kinetic Alfvén waves on electron transport in an ion-scale flux rope. *Chinese Physics Letters*, *35*(11), 119401. https://doi.org/10.1088/0256-307X/35/11/119401

Tang, B., W. Li, C. Wang, L. Dai, Yuri Khotyaintsev, Per-Arne Lindqvist, Robert Ergun, Olivier Le Contel, Craig Pollock, Christopher Russell, and James Burch (2018), Magnetic depression and electron transport in an ion-scale flux rope associated with Kelvin–Helmholtz waves, Ann. Geophys., 36, 879–889. https://doi.org/10.5194/angeo-36-879-2018

Vasko, I. Y., Mozer, F. S., Krasnoselskikh, V. V., Artemyev, A. V., Agapitov, O. V., Bale, S. D., Avanov, L., Ergun, R., Giles, B., Lindqvist, P.-A., Russell, C. T., Strangeway, R., Torbert, R. (2018). Solitary waves across upper critical quasi-perpendicular shocks. Geophysical Research Letters, 45, 5809–5817. https://doi.org/10.1029/2018GL077835

Vaverka, J., Nakamura, T., Kero, J., Mann, I. B., De Spiegeleer, A., Hamrin, M., et al. (2018). Comparison of dust impact and solitary wave signatures detected by multiple electric field antennas onboard the MMS spacecraft. Space Physics, 123, 6119–6129. https://doi.org/10.1029/2018JA025380

Walia, N. K., Seki, K., Hoshino, M., Amano, T., Kitamura, N., Saito, Y., Yokota, S., Pollock C. J., Giles, B. L., Moore, T. E., Torbert, R. B., Russell, C. T., Burch, J. L. (2018). A statistical study of slow-mode shocks observed by MMS in the dayside magnetopause. Geophysical Research Letters, 45, 4675–4684. https://doi.org/10.1029/2018GL077580

Wang, R., Lu, Q., Nakamura, R., Baumjohann, W., Huang, C., Russell, C. T., Burch, J. L., Pollock, C. J., Gershman, D., Ergun, R. E. (2018). An electron-scale current sheet without bursty reconnection signatures

observed in the near-Earthtail. Geophysical Research Letters,45,4542–4549. https://doi.org/10.1002/2017GL076330

Yao, S. T., Shi, Q. Q., Guo, R. L., Yao, Z. H., Tian, A. M., Degeling, A. W.,Liu, H.(2018). Magnetospheric Multiscale observations of electron scale magnetic peak. Geophysical Research Letters, 45,527–537. https://doi.org/10.1002/2017GL075711

Yao, S. T., Shi, Q. Q., Liu, J., Yao, Z. H., Guo, R. L., Ahmadi, N., Degeling, A. W., Zong, Q. G., Wang, X. G., Tian, A. M., Russell, C. T., Fu, H. S., Pu, Z. Y., Fu, S. Y., Zhang, H., Sun, W. J., Li, L., Xiao, C. J., Feng, Y. Y., Giles, B. L. (2018). Electron dynamics in magnetosheath mirror-mode structures. Journal of Geophysical Research: Space Physics,123,5561–5570. https://doi.org/10.1029/2018JA025607

Zhao, J. S., T. Y. Wang, M. W. Dunlop, J. S. He, X. C. Dong, D. J. Wu, Yu. V. Khotyaintsev, R. E. Ergun, C. T. Russell, B. L. Giles, R. B. Torbert, and J. L. Burch (2018), Modulation of Ion and Electron Pitch Angle in the Presence of Large-amplitude, Low-frequency, Left-hand Circularly Polarized Electromagnetic Waves Observed by MMS, The Astrophysical Journal, Volume 867, Number 1. http://doi.org/10.3847/1538-4357/AAE097

Zhong, Z. H., R. X. Tang, M. Zhou, X. H. Deng, Y. Pang, W. R. Paterson, B. L. Giles, J. L. Burch, R. B. Tobert, R. E. Ergun, Y. V. Khotyaintsev, and P.-A. Lindquist (2018), Evidence for Secondary Flux Rope Generated by the Electron Kelvin-Helmholtz Instability in a Magnetic Reconnection Diffusion Region, Phys. Rev. Lett. 120, 075101. http://doi.org/10.1103/PHYSREVLETT.120.075101

Zhou, M., Berchem, J., Walker, R. J., El-Alaoui, M., Goldstein, M. L., Lapenta, G., Deng, X., Li, J., Le Contel, O., Graham, D. B., Lavraud, B., Paterson, W. R., Giles, B. L., Torbert, R. B., Russell, C. T., Strangeway, R. J., Zhao, C., Ergun, R. E., Lindqvist, P.-A., Marklund, G. (2018). Magnetospheric Multiscale observations of an ion diffusion region with large guide field at the magneto-pause: Current system, electron heating, and plasma waves. Journal of Geophysical Research: Space Physics,123,1834–1852. https://doi.org/10.1002/2017JA024517

2017

Allanson, O., F. Wilson, T. Neukirch, Y.-H. Liu, and J. D. B. Hodgson (2017), Exact Vlasov-Maxwell equilibria for asymmetric current sheets, Geophys. Res. Lett., 44, 8685–8695. https://doi.org/10.1002/2017GL074168

Cao, D., Fu, H. S., Cao, J. B., Wang, T. Y., Graham, D. B., Chen, Z. Z., Peng, F. Z., Huang, S. Y., Khotyaintsev, Y., Andre, M., Russell, C. T., Giles, B. L., Lindqvist, P.-A., Torbert, R. B., Ergun, R. E., Le Contel, O., Burch, J. L. (2017), MMS observations of whistler waves in electron diffusion region, Geophys.Res.Lett., 44, 3954–3962. http://doi.org/10.1002/2017GL072703

Cattell, C., Breneman, A., Colpitts, C., Dombeck, J., Thaller, S., Tian, S., Wygant, J., Fennell, J., Hudson, M. K., Ergun, R., Russell, C. T., Torbert, R., Lindqvist, P.-A., Burch, J. (2017), Dayside response of the magnetosphere to a small shock compression: Van Allen Probes, Magnetospheric MultiScale, and GOES-13, Geophys. Res. Lett., 44, 8712–8720, http://doi.org/10.1002/2017GL074895.

Dai, L., C. Wang, Y. Zhang, B. Lavraud, J. Burch, C. Pollock, and R. B. Torbert (2017), Kinetic Alfven wave explanation of the Hall fields in magnetic reconnection, Geophys. Res. Lett.,44, 634–640. http://doi.org/10.1002/2016GL071044

Dimmock, A. P., A. Osmane, T. I. Pulkkinen, K. Nykyri, and E. Kilpua (2017), Temperature variations in the dayside magnetosheath and their dependence on ion-scale magnetic structures: THEMIS statistics and measurements by MMS, J. Geophys. Res. Space Physics, 122, 6165–6184, http://doi.org/10.1002/2016JA023729

Dong, X.-C., Dunlop, M. W., Trattner, K. J., Phan, T. D., Fu, H.-S., Cao, J.-B., Russell, C. T., Giles, B. L., Torbert, R. B., Le, G., Burch, J. L. (2017), Structure and evolution of flux transfer events near dayside magnetic reconnection dissipation region: MMS observations, Geophys. Res. Lett.,44, 5951–5959. http://doi.org/10.1002/2017GL073411

Han, D.-S., Li, J.-X., Nishimura, Y., Lyons, L. R., Bortnik, J., Zhou, M., Liu, J.-J. Liu, Z.-J., Hu, Hu, H.-Q., Yang, H.-G., Fuselier, S. A., Le Contel, O., Ergun, R. E., Malaspina, D., Lindqvist, P.-A., Pollock, C. J. (2017), Coordinated observations of two types of diffuse auroras near magnetic local noon by Magnetospheric Multiscale mission and ground all-sky camera, Geophys. Res.Lett., 44, 8130–8139. http://doi.org/10.1002/2017GL074447

Huang, S. Y., F. Sahraoui, Z. G. Yuan, J. S. He, J. S. Zhao, O. Le Contel, X. H. Deng, M. Zhou, H. S. Fu, Q. Q. Shi, Lavraud, B., Pang, Y., Jang, J., Wang, D. D., Li, H. M., Yu, X. D., Pollock, C. J., Giles, B. L., Torbert, R. B., Russell, C. T., Goodrich, K. A., Gershman, D. J., Moore, T. E., Ergun, R. E., Khotyaintsev, Y. V., Lindqvist, P.-A., Strangeway, R. J., Magnes, W., Bromund, K., Leinweber, H., Plaschke, F., Anderson, B. J., Burch, J. L. (2017), Magnetospheric Multiscale Observations of Electron Vortex Magnetic Hole in the Turbulent Magnetosheath Plasma, The Astrophysical Journal Letters, Volume 836, Number 2. http://doi.org/10.3847/2041-8213/AA5F50

Huang, S. Y., Du, J. W., Sahraoui, F., Yuan, Z. G., He, J. S., Zhao, J. S., Le Contel, O., Breuillard, H., Wang, D. D., Yu, X. D., Deng, X. H., Fu, H. S., Zhou, M., Pollock, C. J., Torbert, R. B., Russell, C. T., Burch, J. L.(2017), A statistical study of kinetic-size magnetic holes in turbulent magnetosheath: MMS observations, J. Geophys. Res. Space Physics, 122, 8577–8588. http://doi.org/10.1002/2017JA024415

Li, J., Bortnik, J., Li, W., Ma, Q., Thorne, R. M., Kletzing, C. A., Kurth, W. S., Hospodarsky, G. B., Wygang, J., Breneman, A., Thaller, S., Funstein, H. O., Mitchell, D. G., Manweiller, J. W., Torbert, R. B., Le Contel, O., Ergun, R. E., Lindqvist, P.-A., Torkar, K., Andriopoulou, M., Russell, C. T. (2017), "Zipper-Like" Periodic Magnetosonic Waves: Van Allen Probes, THEMIS, and Magnetospheric Multiscale Observations, J. Geophys. Res. Space Physics, 122, http://doi.org/10.1002/2016JA023536

Peng, F. Z., Fu, H. S., Cao, J. B., Graham, D. B., Chen, Z. Z., Cao, D., Xu, Y., Huang, S. Y., Wang, T. Y., Khotyaintsev, Y. V., Andre, M., Russell, C. T., Giles, B., Lindqvist, P.-A., Torbert, R. B., Ergun, R. E., Burch, J. L. (2017), Quadrupolar pattern of the asymmetric guide-field reconnection, J. Geophys. Res. Space Physics, 122, 6349–6356. http://doi.org/10.1002/2016JA023666

Teh, W.-L., Nakamura, T. K. M., Nakamura, R., Baumjohann, W., Russell, C. T., Pollock, C., Lindqvist, P.-A., Ergun, R. E., Burch, J. L., Torbert, R. B., Giles, B. L. (2017), Evolution of atypical ion-scale magnetic flux rope caused by thermal pressure enhancement, J. Geophys. Res. Space Physics, 122, 2040–2050. http://doi.org/10.1002/2016JA023777.

Teh, W.L., R.E. Denton, B.U.O. Sonnerup, and C. Pollock (2017), MMS observations of oblique small-scale magnetopause flux ropes near the ion diffusion region during weak guide-field reconnection, Geophys. Res. Lett., 44 (13). https://doi.org/10.1002/2017gl074291

Wang, R., Lu, Q., Nakamura, R., Baumjohann, W., Russell, C. T., Burch, J. L.,Ergun, E. R., Gershman, D. (2017). Interaction of magnetic flux ropes via magnetic reconnection observed at the magnetopause. Journal of GeophysicalResearch: Space Physics,122,10,436–10,447. https://doi.org/10.1002/2017JA024482

Wang, X. Y., S. Y. Huang, R. C. Allen, H. S. Fu, X. H. Deng, M. Zhou, J. L. Burch, and R. B. Torbert (2017), The occurrence and wave properties of EMIC waves observed by the MagnetosphericMultiscale (MMS) mission, J. Geophys. Res. Space Physics, 122, 8228–8240. http://doi.org/10.1002/2017JA024237

Yao, S. T., X. G. Wang, Q. Q. Shi, T. Pitkänen, M. Hamrin, Z. H. Yao, Z. Y. Li, X. F. Ji, A. De Spiegeleer, Y. C. Xiao, A. M. Tian, Z. Y. Pu, Q. G. Zong, C. J. Xiao, S. Y. Fu, H. Zhang, C. T. Russell, B. L. Giles, R. L. Guo, W. J. Sun, W. Y. Li, X. Z. Zhou, S. Y. Huang, J. Vaverka, M. Nowada, S. C. Bai, M. M. Wang, J. Liu (2017), Observations of kinetic-size magnetic holes in the magnetosheath, J. Geophys. Res. SpacePhysics,122, 1990–2000. http://doi.org/10.1002/2016JA023858

Yao, Z., I. J. Rae, R. L. Guo, A. N. Fazakerley, C. J. Owen, R. Nakamura, W. Baumjohann, C. E. J. Watt, K. J. Hwang, B. L. Giles, C.T. Russell, R. B. Torbert, A. Varsani, H. S. Fu Q. Q. Shi, X.-J. Zhang (2017), A direct examination of the dynamics of depolarization fronts using MMS, J. Geophys. Res. Space Physics, 122, 4335–4347. http://doi.org/10.1002/2016JA023401

Yu, X., Z. Yuan, S. Huang, D. Wang, H. Li, Z. Qiao, and F. Yao (2017), EMIC waves covering wide L shells: MMS and Van Allen Probes observations, J. Geophys. Res. Space Physics, 122, 7387–7395, http://doi.org/10.1002/2017JA023982

Zhang, Y. C., B. Lavraud, L. Dai C. Wang, A. Marchaudon, L. Avanov, J. Burch, M. Chandler, J. Dorelli, S. P. Duan, R. E. Ergun, D. J. Gershman, B. Giles, Y. V. Khotyaintsev, P. A. Lindqvist, W. Paterson, C. T. Russell, C. Schiff, B. B. Tang, R. Torbert (2017), Quantitative analysis of a Hall system in the exhaust of asymmetric magnetic reconnection, J. Geophys. Res. Space Physics, 122, 5277–5289. http://doi.org/10.1002/2016JA023620

2016

Divin, A., V. Semenov, D. Korovinskiy, S. Markidis, J. Deca, V. Olshevsky, and G. Lapenta (2016), A new model for the electron pressure nongyrotropy in the outer electron diffusion region, Geophys. Res. Lett., 43, 10,565–10,573, http://doi.org/10.1002/2016GL070763

Fu, H. S., et al. (2016), Identifying magnetic reconnection events using the FOTE method, J. Geophys. Res. Space Physics, 121, 1263–1272. http://doi.org/10.1002/2015JA021701

Huang, S. Y., F. Sahraoui, A. Retino, O. Le Contel, Z. G. Yuan, A. Chasapis, N. Aunai, H. Breuillard, X. H. Deng, M. Zhou, H. S. Fu, Y. Pang, D. D. Wang, R. B. Torbert, K. A. Goodrich, R. E. Ergun, Y. V. Khotyaintsev, P.-A. Lindqvist, C. T. Russell, R. J. Strangeway, W. Magnes, K. Bromund, H. Leinweber, F. Plaschke, B. J. Anderson, C. J. Pollock, B. L. Giles, T. E. Moore, J. L. Burch (2016), MMS observations of ion-scale magnetic island in the magnetosheath turbulent plasma, Geophysical Research Letters, 43(15), 7850-7858, https://doi.org/10.1002/2016GL070033

Innocenti, M. E., C. Norgren, D. Newman, M. Goldman, S. Markidis, and G. Lapenta (2016), Study of electric and magnetic field fluctuations from lower hybrid drift instability waves in the terrestrial magnetotail with the fully kinetic, semi-implicit, adaptive multi level multi domain method, PHYSICS OF PLASMAS. 23 (5), https://doi.org/10.1063/1.4952630

Nagai, T., N. Kitamura, H. Hasegawa, I. Shinohara, S. Yokota, Y. Saito, R. Nakamura, B. L. Giles, C. Pollock, T. E. Moore, J. C. Dorelli, D. J. Gershman, W. R. Paterson, L. A. Avanov, M. O. Chandler, V. Coffey, J. A. Sauvaud, B. Lavraud, C. T. Russell, R. J. Strangeway, M. Oka, K. J. Genestreti, J. L. Burch (2016), Thick escaping magnetospheric ion layer in magnetopause reconnection with MMS observations, Geophysical Research Letters, 43(12), 6028-6035, https://doi.org/10.1002/2016GL069085

Zenitani, S., and T. Nagai (2016), Particle dynamics in the electron current layer in collisionless magnetic reconnection, Physics of Plasmas, 23(10), https://doi.org/10.1063/1.4963008

2015

Cazzola, E., M. Innocenti, S. Markidis, M. Goldman, D. Newman, and G. Lapenta (2015), On the electron dynamics during island coalescence in asymmetric magnetic reconnection, Physics of Plasmas, 22(9), https://doi.org/10.1063/1.4929847

Hamrin, M., L. Andersson, A. Vaivads, T. Pitkanen, and H. Gunell (2015), The use of the power density for identifying reconnection regions, Journal of Geophysical Research-Space Physics, 120(10), 8644-8662, https://doi.org/10.1002/2015JA021535

Olshevsky, V., A. Divin, E. Eriksson, S. Markidis, and G. Lapenta (2015), ENERGY DISSIPATION IN MAGNETIC NULL POINTS AT KINETIC SCALES, Astrophysical Journal, 807(2), https://doi.org/10.1088/0004-637X/807/2/155

Rai, R. K., S. Sharma, N. Yadav, M. L. Goldstein, and R. P. Sharma (2015), Effect of magnetic islands on the localization of kinetic Alfven wave, Physics of Plasmas, 22(12), https://doi.org/10.1063/1.4936873

Zhang, L., A. Lui, W. Baumjohann, and J. Wang (2015), Probabilities of magnetic reconnection encounter at different activity levels in the Earth's magnetotail, Advances in Space Research, 56(4), 736-741, https://doi.org/10.1016/j.asr.2015.05.001

2014

Huang, S., M. Zhou, Z. Yuan, X. Deng, F. Sahraoui, Y. Pang, and S. Fu (2014), Kinetic simulations of electric field structure within magnetic island during magnetic reconnection and their applications to the satellite observations, Journal of Geophysical Research-Space Physics, 119(9), https://doi.org/10.1002/2014JA020054

2013

Karimabadi, H., H. Karimabadi, V. Roytershteyn, M. Wan, W. H. Matthaeus, W. Daughton, P. Wu, M. Shay, B. Loring, J. Borovsky, E. Leonardis, S. C. Chapman, and T. K. M. Nakamura (2013), Coherent structures, intermittent turbulence, and dissipation in high-temperature plasmas, Physics of Plasmas, 20(1), https://doi.org/10.1063/1.4773205

END OF LIST

Magnetospheric Multiscale (MMS) Project

Project Data Management Plan (PDMP)

V2.0

Submitted: 22 November 2022

Goddard Space Flight Center
Greenbelt, Maryland

National Aeronautics and
Space Administration

MAGNETOSPHERIC MULTISCALE (MMS)
Project Data Management Plan (PDMP)

Dr. Barbara Giles, GSFC MMS Project Scientist — 14 November 2022 Date

Dr. James Burch, SwRI MMS Science PI — 21 November 2022 Date

By signing this document, signatories are certifying that the content herein is acceptable direction for managing the project's data and that they will ensure its implementation by those over whom they have authority.

Copy to: HQ Program Scientist

REVISION HISTORY

Revision Level	DESCRIPTION	EFFECTIVE DATE
Rev 0	SwRI Document No. 10160.18-PDMP-01 –export-controlled internal mission development document	30 Aug 2010
Rev 1	Draft, updated open-access PDMP	2 June 2020
Rev 2	V2.0 Public Release	22 Nov 2022

TABLE OF CONTENTS

LIST OF FIGURES

LIST OF TABLES

1. INTRODUCTION

1.1. Purpose and Scope

This document describes the Project Data Management Plan (PDMP) for the Magnetospheric Multiscale (MMS) mission. It describes the mission's data requirements and how the MMS data system is implemented in order to meet those requirements.

Described in this plan are:

- Overview of the MMS science objectives, mission concept, and instrumentation.
- Roles and responsibilities of all institutions expected to participate in MMS data production, dissemination, and archival activities.
- Identification and description of the various types of MMS data including data volume estimates.
- Description of data flow between key MMS project entities.
- Description of data distribution and access methods.
- Plans for mission data archival.

It is important to note that the MMS mission simultaneously supports four identically instrumented spacecraft flying in formation that operates in different data acquisition modes with significantly different data throughput and storage requirements.

1.2. Development, Maintenance, and Management Responsibility

Developing, maintaining and managing this PDMP is an MMS Project responsibility. The Science Operations Center (SOC) at the Laboratory for Atmospheric and Space Physics (LASP) has been designated responsibility for the development and maintenance of this plan under the direction of the MMS Principal Investigator (PI), Dr. James L. Burch, at the Southwest Research Institute (SwRI).

1.3. Change Control

This PDMP is an MMS Project-controlled document and is under change control once signed by all parties. The initial draft version was completed prior to the MMS Preliminary Design Review (PDR) and was baselined at the MMS Critical Design Review. The first significant update was initiated, as directed by NASA HQ, for the 2020 Senior Review. All changes to this document are submitted to the MMS Principal Investigator, who coordinates reviews of proposed changes.

1.4. Relevant Documents

Relevant documents that support details provided in this PDMP are listed in Table 1-1.

Document Reference	Title
461-PROJ-RQMT-0018	Program Level Requirements for the MMS Project - Appendix C to the STP Program Plan, MMS Level 1 Requirements
461-SYS-RQMT-0019	*MMS Mission Requirements Document (MRD)*
Version 1.2 - 04 October 2016	*NASA Heliophysics Science Data Management Policy*
461-PROJ-PLAN-0071	*MMS Concept of Operations*
461-GS-ICD-00134	*MOC/FDOA-SOC ICD*
461-GS-ICD-0014	*MMS MOC-SOC ICD*
SwI Document No. 10160.17-SOC-ITF-ICD	*MMS SOC-ITF ICD*
SwRI Document No. 10160.17-BADCO-01	*Burst Algorithm Definition and Concept of Operations (BADCO)*
461-PROJ-PLAN-0071	MMS Flight Operations Plan
POC Online Document	Instrument Suite Flight Operations Plan
TBD	*Calibration and Measurement Algorithm Document (CMAD)*

Table 1-1: *Relevant Documents*

2. MISSION OVERVIEW

2.1. Mission Objectives

The Magnetospheric Multiscale (MMS) mission is a National Aeronautics and Space Administration (NASA) Science Mission Directorate (SMD) Heliophysics Division flight project in the Solar Terrestrial Probes (STP) Program. MMS is a space physics research mission to discover the fundamental plasma physics processes of magnetic reconnection in the Earth's magnetosphere. Magnetic reconnection occurs when the charged particles and wave energy emanating from the sun in the Solar Wind interact with the Earth's magnetic field. Four identically instrumented satellites will measure electric and magnetic fields, fast plasma, energetic particles, and hot plasma composition at time scales of milliseconds to seconds and spatial scales of tens to hundreds of km. The satellites will fly in a tetrahedron formation to explore the dayside of the magnetopause and the night side of the magnetotail in three dimensions. The four satellites are launched together in a stacked configuration into an elliptical Earth orbit with an apogee of 12 Re.

The specific MMS science objectives are:

- Determine the role played by electron inertial effects and turbulent dissipation in driving magnetic reconnection in the electron diffusion region.
- Determine the rate of magnetic reconnection and the parameters that control it.
- Determine the role played by ion inertial effects in the physics of magnetic reconnection.

2.2. Mission Concept

The MMS mission employs four identically instrumented spinning spacecraft orbiting the Earth in a tetrahedral configuration to conduct definitive investigations of magnetic reconnection in key boundary regions of the Earth's magnetosphere. The process of magnetic reconnection, which controls the flow of energy, mass, and momentum within and across plasma boundaries, occurs throughout the universe and is fundamental to our understanding of astrophysical and solar system plasmas. It is only in the Earth's magnetosphere, however, that it is readily accessible for sustained study through the *in situ* measurement of plasma properties and of the electric and magnetic fields that govern the behavior of the plasmas.

Through high-resolution measurements made by each spacecraft, whose separations can be varied from tens of km to a few hundreds of kilometers, MMS probes the crucial microscopic physics involved in these fundamental processes; determines the 3-D geometry of the plasma, field, and current structures associated

with them; and relates their micro-scale dimension to phenomena occurring on the mesoscale. By acquiring data simultaneously at multiple points in space, MMS differentiates between spatial variations and temporal evolution, thus removing the space-time ambiguity that has limited single-spacecraft studies of magnetospheric plasma processes.

Over the lifetime of the mission, the MMS low-inclination orbit strategy probed the most likely reconnection sites on both the dayside magnetopause (Dayside mission phases) and in the magnetotail (nightside mission phases). Phase 1 consisted of an elliptical Earth orbit with an apogee of 12 R_E +/- 1 R_E. Prime mission Phase 2 consisted of an elliptical Earth orbit with an apogee of 25 R_E +/- 5 R_E (Figure 2-1). Each extended mission phase has balanced fuel usage, time in the reconnection regions of interest, and eclipse durations to maximize science return.

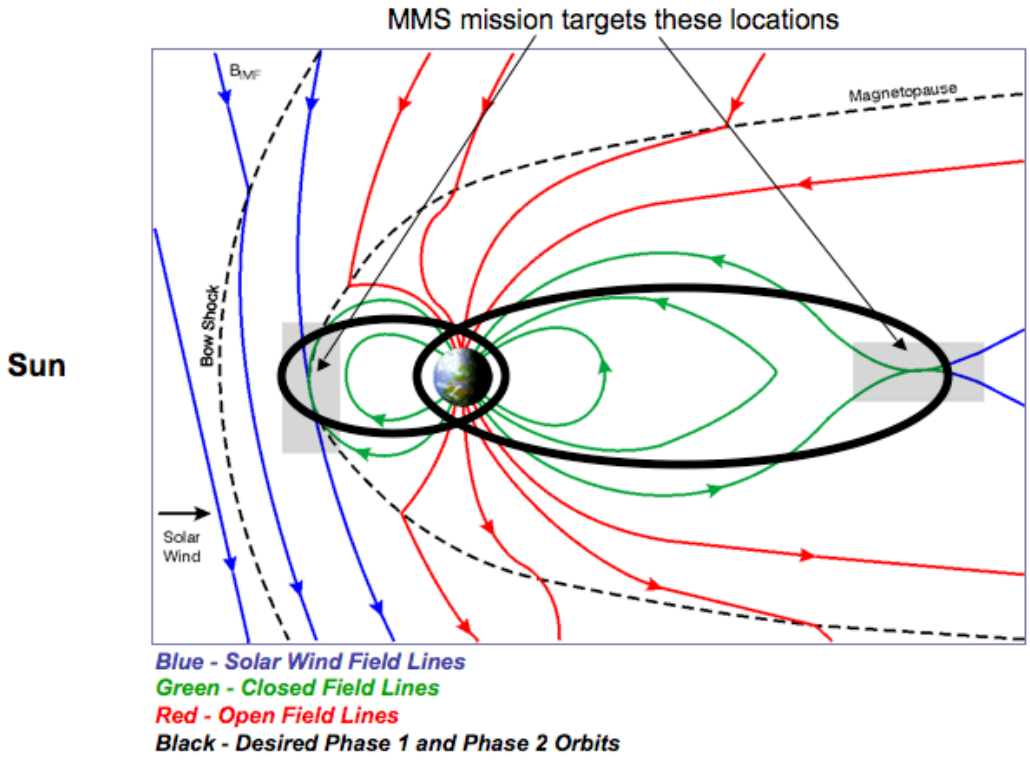

Figure 2-1: General Locations of Magnetic Reconnection for the Dayside/Nightside magnetosphere

Science Regions of Interest (SROI) with observatory formation requirements are defined for each dayside and nightside mission phase (geocentric apogee distances >9 R_E for Prime Mission Phase 1, and >15 R_E for Prime Mission Phase 2.) There are no (or relaxed) formation requirements for regions of science interest during Phase transitions (e.g. from Phase 1 to Phase 2.)

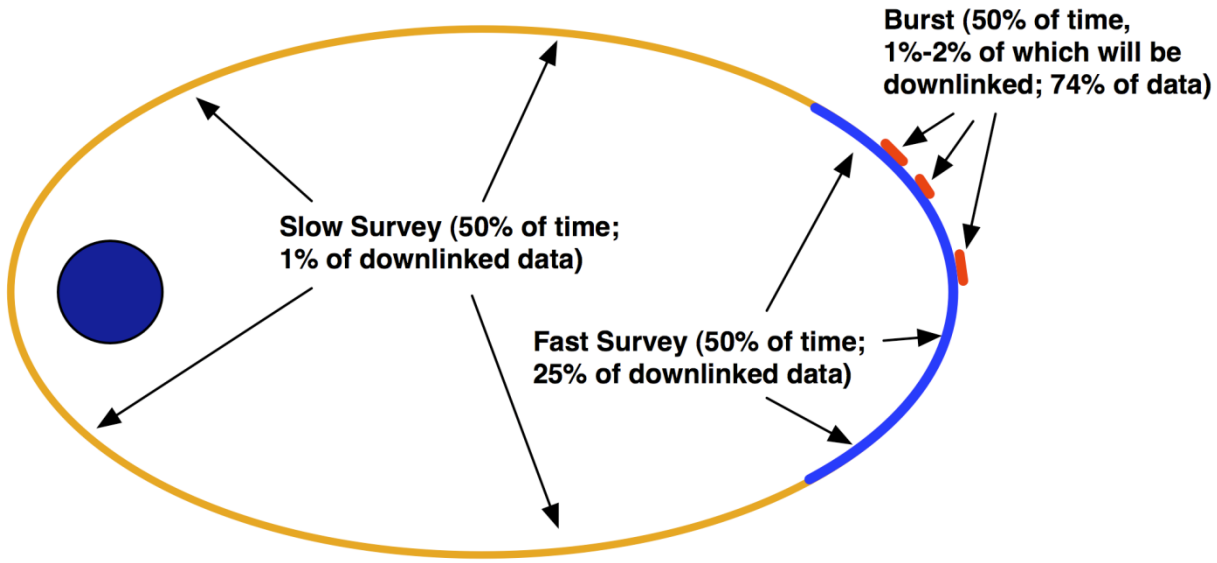

Tetrahedron configuration and burst data acquisition maintained throughout region of interest (> 9 R_E day side, > 15 R_E night side).

Figure 2-2: General *Data Collection Strategy: Low resolution – Nominal resolution – MMS resolution*

The four MMS spacecraft will operate in the Slow Survey mode approximately 50% of the time during each orbit. Fast Survey mode occurs within the primary science region of interest and is at a resolution equivalent to most previous missions. Burst data – the high resolution data that MMS is known for -- is collected throughout the Fast Survey period, although only a limited number of "SITL-selected segments" are able to be downlinked via the prescribed DSN antenna allocation. MMS continually advocates for additional DSN antenna contact time.

Data types used to meet the mission requirements are:

- *Survey data*: These data are collected continuously from all powered instrumentsand stored in the mass memory module of the CIDP. The orbit is divided into fast survey and slow survey periods. Fast survey data – at a resolution equivalent to most previous missions - are collected during the primary science regions of interest (SROI) period of the orbit while the slow survey data are collected at a lower resolution during the region of the orbit that is of low scientific interest. The fast and slow survey times are set by ground command.
- *Burst data*: The instruments provide a stream of the highest resolution data to the CIDP in parallel with the fast survey data. All burst data collected during the fast survey period are stored in the mass memory module of the CIDP. Burst information is tagged with quality information based on a spacecraft wide trigger system. Only a portion of this data is able to be downlinked via the prescribed DSN antenna allocation.

Trigger data are also generated by all instruments and are used by the CIDP to calculate quality information and by the Science Operations Center (SOC) to support the selection of the priority burst data to optimize science data downlink. Every instrument supplies a set of trigger data once every ~10 seconds.

Inter-spacecraft separation distances between the four spacecraft in the tetrahedron are changed from mission phase to phase (mostly, between 160 km and 10-20 km) by ground command to optimize the opportunities to capture reconnection events.

MMS Mission Phases are currently documented at https://lasp.colorado.edu/galaxy/x/yBQ_Ag and will be summarized in this document (or the CMAD as appropriate) during the proposed FY21 PDMP update.

2.3. Science Instrumentation

The SMART (Solving Magnetospheric Acceleration, Reconnection and Turbulence) Instrument Suite will make the required high-time resolution measurements of plasmas, electric fields and magnetic fields and provide important supporting measurements of energetic particles and ion composition. The SMART IS consists of the following complement of instruments:

- **The FIELDS investigation** includes a sensor suite consisting of axial and spin-plane double-probe electric-field sensors (ADP and SDP), two flux-gate magnetometers (AFG and DFG), a search-coil magnetometer (SCM), and two electron drift instruments (EDI) per spacecraft. These instruments measure DC magnetic field with a resolution of 10 ms, DC electric field with a resolution of 1 ms, electric plasma waves to 100 kHz, and magnetic plasma waves to 6 kHz.
- **The Energetic Particle Detector (EPD)** includes an Energetic Ion Spectrometer (EIS) and an all-sky particle sampler called the Fly's Eye Energetic Particle Sensor (FEEPS) per spacecraft. These instruments measure the energy-angle distribution and composition of ions (20 to 500 keV) at a time resolution of < 30 seconds, the energy-angle distribution of total ions (45 – 500 keV) at a time resolution of < 10 seconds, and the coarse and fine energy-angle distribution of energetic electrons (25 – 500 keV) at time resolutions of < 0.5 and < 10 seconds, respectively.
- **The Fast Plasma Instrument (FPI)** includes four dual electron spectrometers (DES) and four dual ion spectrometers (DIS) per spacecraft for a total of 64 plasma spectrometers across the observatories. These instruments measure the velocity-space distribution of electrons from 10 eV to 30 keV and ions from 10 eV to 30 keV with time resolution of 30 ms, and 150 ms, respectively
- **The Hot Plasma Composition Analyzer (HPCA)** on each spacecraft measures the composition-resolved velocity-space distribution of ions from 1 eV to 40 keV with time resolution of 10 – 15 seconds.
- **The Active Spacecraft Potential Control (ASPOC)** (two per spacecraft) generates beams of indium ions to limit positive spacecraft potentials to +4V in order to improve the measurements obtained by FPI, HPCA, ADP, and SDP.

The instrument suites on each spacecraft are supported by the Central Instrument Data Processor (CIDP), which collects and stores telemetry from each instrument and sends it to the spacecraft for downlink. The CIDP provides time and spin synchronization as well as switched power services to the instruments, and forwards commands received from the Spacecraft Avionics (Figure 2-3).

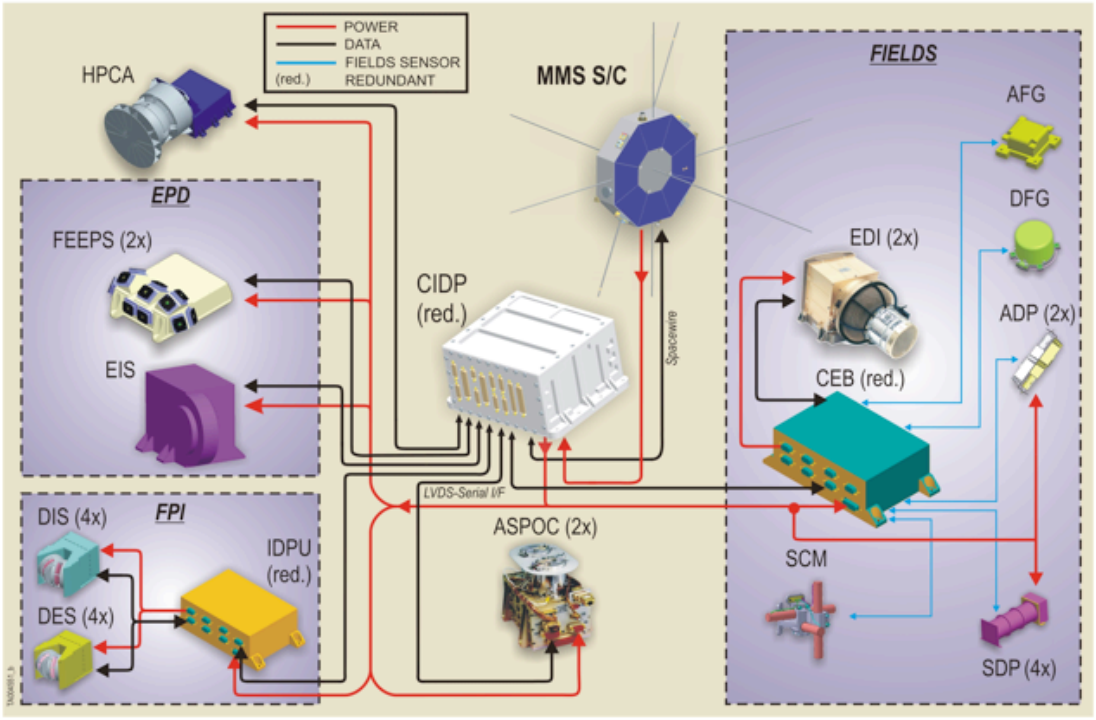

Figure 2-3: ***MMS-SMART Instrument Suite Architecture***

2.4. Orbit Phases and Mission Timeline

MMS's four satellites are launched together in a stacked configuration into an elliptical Earth orbit with an apogee of 12 Re. During the estimated 4-month checkout period, the perigee is raised to 1.2 Re via the spacecraft propulsion systems. At the end of the check out period the orbit apogee is near the dusk magnetopause. Phase 1 will commence at this point and last 16 months. During Phase 1 the MMS apogee will sweep across the dayside magnetopause twice (phase 1a and 1b). At the end of Phase 1b, the apogee is raised gradually to 25 Re. Phase 2 continues for an additional 5.5 months. The orbit is allowed to drift naturally throughout the mission lifetime (i.e., it will not be controlled). During the extended mission, the spacecraft remain in a tetrahedral formation with a 29 Re apogee (see Table 2.1).

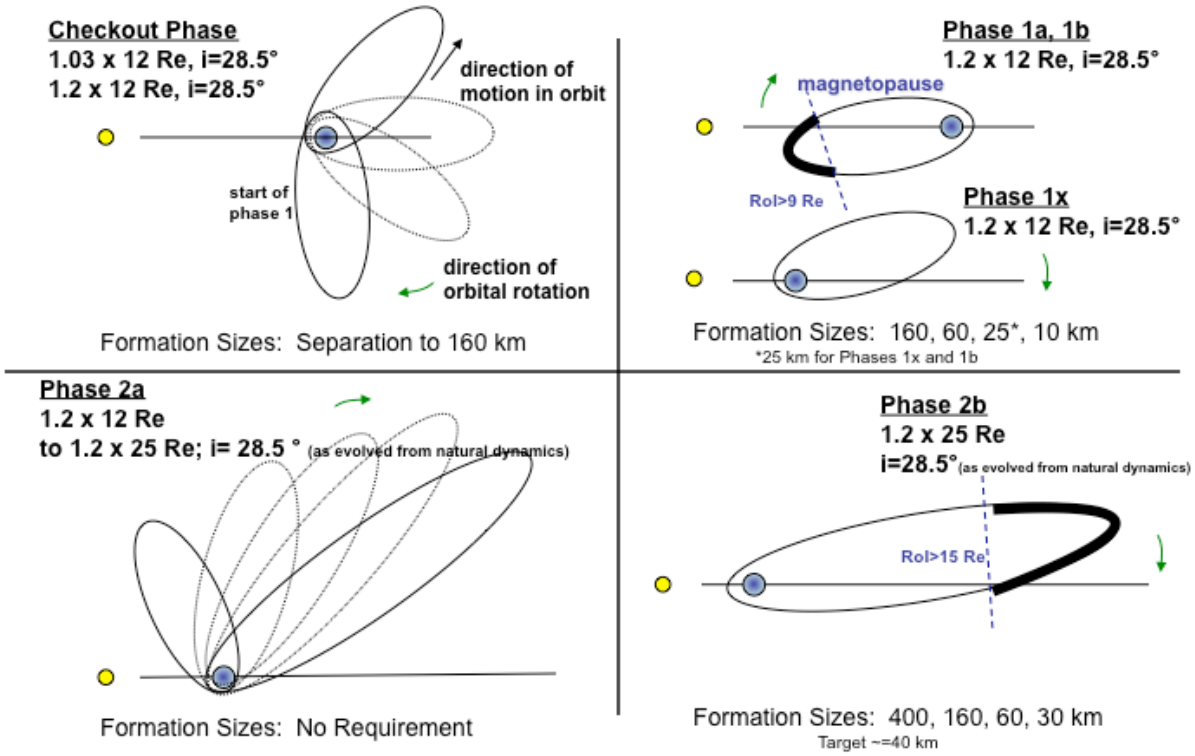

Figure 2-4: *MMS Orbit Phases*

The timeline for collection of science data during each of the MMS mission phases is shown in Figure 2-5.

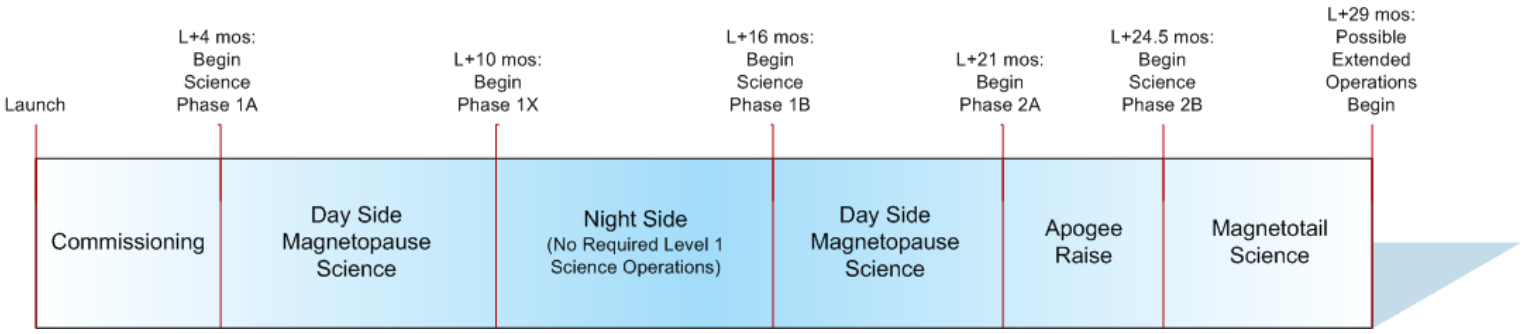

Figure 2-5: *MMS Science Acquisition Timeline*

	Phase	Region
Year 5	Extended Mission Year 3 Phase 5a: ~09/30/19-11/24/19	29 R_E Dusk Flank
	Phase 5b: ~11/24/2019 - 04/23/20	29 R_E Dayside
	Phase 5c: ~04/23/20-06/19/20	29 R_E Dawn Flank
	Phase 5d: ~06/22/20-10/02/20	29 R_E Nightside
Year 4	Extended Mission Year 2 Phase 4a – Sept 28, 2018	25R_E Dusk Flank
	Phase 4b – Nov 29, 2018	25R_E Dayside
	Phase 4c - ~April 16, 2019 - ~June 28, 2019	29R_E Dawn Flank
	Phase 4d - ~June 29, 2019 - ~July 25, 2019	1st 29R_E Nightside
Year 3	Extended Mission Year 1 Phase 3a – Sept 1, 2017	25R_E Dusk Flank
	Phase 3b – Nov 14, 2017	25R_E Dayside
	Phase 3c – Mar 13, 2018	25R_E Dawn Flank
	Phase 3d – May 25, 2018	2nd 25R_E Nightside
Year 2	Prime Mission Phase 2a – January 31, 2017	Apogee raise, Dawn
	Prime Mission Phase 2b – May 1, 2017	1st 25R_E Nightside Completion of Prime Mission
Year 1	Prime Mission Phase 1a – September 1, 2015	1st 12R_E Dayside
	Prime Mission Phase 1x – March 8, 2016	12R_E Dawn, Nightside, Dusk
	Prime Mission Phase 1b – Sept 12, 2016	2nd 12R_E Dayside
Commissioning	March 15, 2015 – Sept 15, 2015	Nightside --> Dusk Flank

Table 2-1: ***Mission Phases and Science Regions of Interest***

3. ROLES AND RESPONSIBILITIES

3.1. Overview of Ground System

The MMS ground system supports on-orbit operations of the MMS observatories, as well as the production, storage, management, and dissemination of MMS science data products. The MMS ground system consists of the following functional elements:

- Mission Operations Center (MOC). Located at Goddard Space Flight Center (GSFC) in Greenbelt, MD. Responsible for spacecraft operations and telemetry capture.

- Flight Dynamics Operations Area (FDOA). Located at Goddard Space Flight Center (GSFC) in Greenbelt, MD. Responsible for orbit and attitude determination and control.
- Science Operations Center (SOC). Located at the Laboratory for Atmospheric and Space Physics (LASP) at the University of Colorado in Boulder, CO. Responsible for Instrument Suite (IS) operations, instrument data processing, archiving, and distribution.
- SMART Instrument Team Facilities (ITF). Specific institutions are identified in Section 3-4. Instrument teams are responsible for data analysis and validation; instrument monitoring and special operations requests; software for producing data products; Level-2 data processing (FPI and HPCA only); analysis tools for publicly available data products.
- Education and Public Outreach (EPO). Located at Rice University. Responsible for dissemination of educational materials to schools and the general public.

Descriptions and operational responsibilities for each of these elements are summarized in Figure 3-1 and described in the sections that follow.

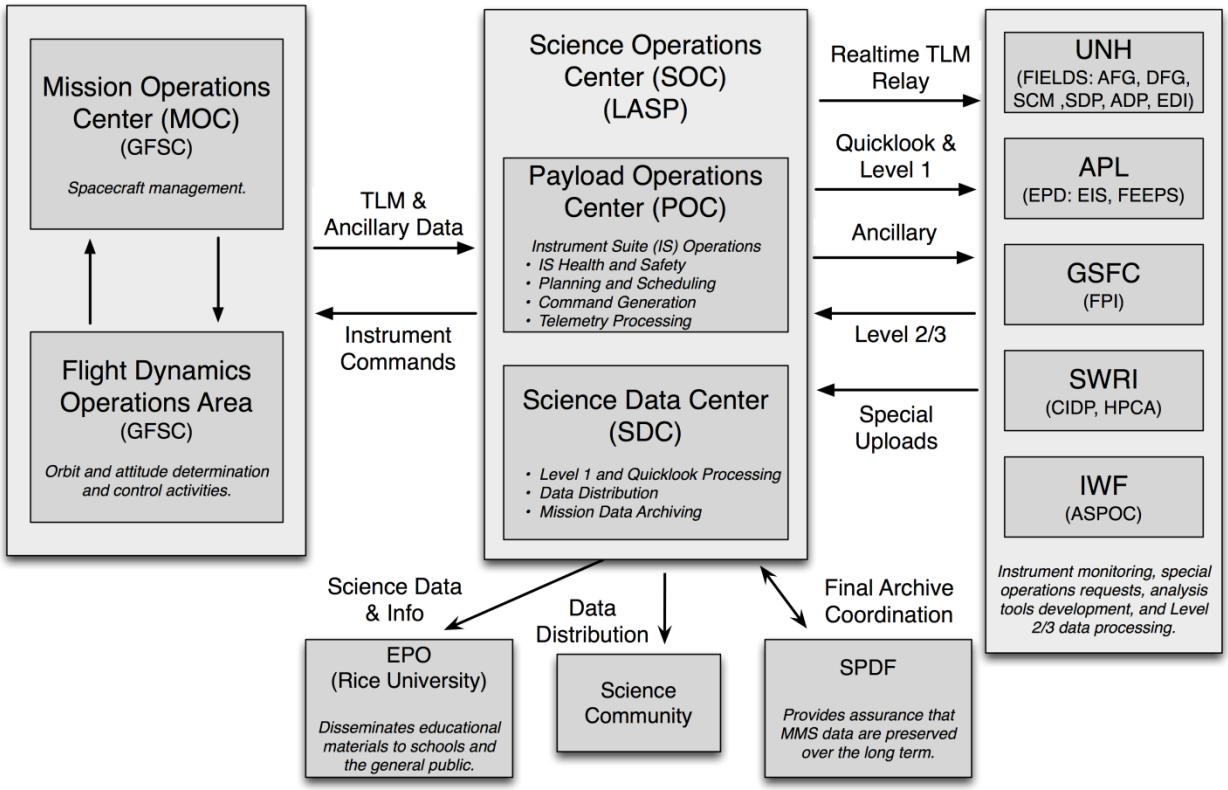

Figure 3-1: ***MMS Ground Data System Responsibilities***

3.2. Mission Operations Center (MOC)

The Mission Operations Center is located at Goddard Spaceflight Center (GSFC) and is responsible for all spacecraft-related operations. These functions include:

- Health and safety monitoring of the spacecraft bus and selected critical instrument safety parameters.
- Generation of spacecraft commands.
- Merge and uplink of spacecraft and Instrument Suite (IS) stored commands.

- Station pass planning and scheduling.
- Spacecraft and Instrument Suite engineering data capture.
- Engineering and Instrument Suite science data capture.
- Spacecraft engineering Level-0 data processing.
- Spacecraft telemetry/command definitions configuration management.

Additionally, the MOC is responsible for providing the SOC with various data, as outlined in the MOC-SOC ICD, including the following:

- All instrument telemetry and select spacecraft telemetry (real-time and playback).
- Planning aids/products.
- Spacecraft health/safety and status reports.
- Ancillary data.

3.2.1. Flight Dynamics Operations Area (FDOA)

The FDOA is co-located within the MOC at GSFC and is responsible for the following:

- All orbital dynamics.
- Constellation formation.
- Observatory spin axis and spin rate control.
- Definitive orbit and attitude determination, planning, calibration, and control.
- Tracking station acquisition.
- Data generation/distribution.
- NAV performance, calibration, configuration.
- Attitude/orbit related product generation.

3.3. Science Operations Center (SOC)

The Science Operations Center (SOC) is located at the University of Colorado in the Laboratory for Atmospheric and Space Physics (LASP). It is responsible for managing and conducting instrument operations and serves as the central hub for all instrument and ancillary data required for instrument suite operations support, data processing, data distribution, and science analysis. The SOC is also be responsible for archiving all MMS data during the active mission and will help plan and provide for subsequent archive phases prior to mission termination. Specific responsibilities include:

- All Instrument Suite operations including health and safety monitoring, IS operations planning and scheduling, and IS command generation/integration.
- Mission-level data storage.
- IS recorder management.
- Levels 0, 1, 2, and 3 data processing.
- IS calibration support.
- Mission data archiving/distribution.
- IS telemetry/command definition configuration management.
- Housing the Instrument Team during post-launch IS activation and checkout activities.
- Providing data in a variety of coordinate systems.

For organizational purposes, the SOC is functionally divided into a Payload Operations Center (POC) for operations-related functions and a Science Data Center (SDC) for data production, management, and distribution functions.

3.3.1. Payload Operations Center (POC)

The Payload Operations Center (POC) has primary responsibility for monitoring and controlling the MMS suite of instruments. The POC to MOC operational interface used for commanding the IS and receiving telemetry is described in the *MMS MOC-SOC ICD*.

In close collaboration with the ITFs and each instrument's PI and systems engineers, the POC establishes baselines of nominal operational and instrument calibration sequences given each mission phase, respective spacecraft state, and orbit location. The POC notifies the ITFs of anomalous conditions as they occur and wait for Anomaly Review Board (ARB) resolution before recovering an instrument and resuming nominal operations. The POC also notifies the ITFs of spacecraft, constellation, or ground segment configuration changes affecting previously established nominal operational command sequencing. To safely implement commanding, the POC works closely with the MOC to schedule and implement loading the ATS (Absolute Time Sequences) commands and the RTS (Relative Time Sequences) commands, as well as setting the needed Real-Time IS commanding windows. The POC works closely with the MMS science team to plan and prepare instrument observing sequences and command loads, and monitors and maintains the health and safety of the MMS instruments.

For a detailed description of the POC operations approach and implementation, see the *MMS Flight Operations Plan* and the *Instrument Suite Flight Operations Plan*. This list summarizes the principal POC responsibilities:

- Plan and schedule instrument activities.
- Generate and transmit instrument operational command loads (via the MOC).
- Deliver Level 0 data to the SDC.
- Monitor Instrument Suite health and safety.
- Support routine real-time operations and commissioning of the Instrument Suite.
- Produce and transmit real-time instrument suite commands (via the MOC).
- Relay IS health and safety telemetry to ITFs.
- Notify the ITFs of IS anomalous conditions and respond as instructed.
- Coordinate IS planning and commanding among the different instruments and MOC activities.
- Manage Instrument Suite command and telemetry definition.
- Produce POC-resident spacecraft telemetry definitions subset needed by the POC to monitor the spacecraft configuration.
- Produce MOC-resident IS telemetry definitions subset needed by the MOC to monitor the IS state or perform activities that could potentially affect the IS.
- Manage POC to MOC command and telemetry interface.
- Process and disseminate low-level instrument suite engineering telemetry.

3.3.2.Science Data Center (SDC)

The Science Data Center (SDC) is responsible for MMS science data management, distribution, and processing of selected data sets. In collaboration with the SMART-IS team, the SDC determines data storage and distribution mechanisms and ensures that data are processed and released to the public within the required timeframes (indicated in Table 5-1). In addition, the SDC develops web-based interfaces for accessing data and analysis tools, serves news items that are relevant to the MMS mission, and coordinates the development of data analysis and visualization tools with the MMS science team. These tools, higher level data products (Level 2+), and associated documentation are available to the science community via the Internet.

Specific SDC responsibilities are summarized as follows:

- Provide oversight and coordination of the distributed MMS data processing system.
- Generate Level-1, Quicklook, Level-2, and Level-3 science products.
- Provide ITFs access to all Level-0 data, Level-1 data, Quicklook science data, and ancillary data within 24-hours of receipt from each spacecraft.
- Provide tools to transform data into a variety of coordinate systems.
- Receive and manage processed science data products from ITFs.
- Collect and archive associated software and documentation from ITFs.
- Disseminate science data products to the science community via SDC web interfaces.

- Coordinate with NASA's Virtual Observatory (VxO) framework and the Space Physics Data Facility (SPDF) for additional dissemination of science products and analysis tools.

3.4. Instrument Team Facilities (ITF)

MMS-SMART Instrument Team Facilities (ITFs) are the principal institutions associated with each of the MMS-SMART science investigations. These facilities and their personnel provide support to the operation of their instruments and the overall data processing and distribution effort for MMS science data products.

The institutions listed in Table 3-1 have responsibility for each of the SMART investigations and their corresponding instruments, together constituting the MMS instrument suite:

MMS Investigation	Managing Institution
Fast Plasma Instrument (FPI)	Goddard Space Flight Center (GSFC)
Hot Plasma Composition Analyzer (HPCA)	Southwest Research Institute (SwRI)
Fields	University of New Hampshire (UNH)
Energetic Particle Detector System (EPD)	Johns Hopkins University (JHU) Applied Physics Laboratory (APL)
Active Spacecraft Potential Control (ASPOC)	Space Research Institute of the Austrian Academy of Sciences

Table 3-1: ***MMS-SMART Instrument Team Facilities (ITF)***

ITFs are responsible for the following:

- Operations Support:
  - Participate in the routine planning process, attend routine planning teleconferences, and review operational plans, as necessary.
  - Routinely perform detailed health and safety assessment of their respective instruments and provide the POC with instrument health and status reports.
  - Provide any needed instrument-planning requests and corresponding data to the POC for incorporation into instrument operations plans.
  - Maintain instrument flight software and tables and work with the SOC to facilitate uplink of any needed updates.
  - Support POC in developing flight procedures and scripts

- Science Data Production and Corresponding Support:
  - Provide the SDC with data product documentation.
  - Generate and maintain documentation of science algorithms and processing software systems.
  - Validate all science data that originate from their respective instruments.
  - Beginning as soon as possible but no later than 6-months after instrument commissioning, begin routinely generating Level-2 science data products and deliver to the SOC within 30 days of downlink from each spacecraft. Note that Level-2 processing for ASPOC and magnetometer (e.g. AFG/DFG) data are expected to be performed at the SDC instead of the ITF as described in Sec. 5.
  - Provide data access and visualization tools to the SDC. These tools will support SDC provided interfaces and will also be made available to the science community.
  - Provide the SDC with science product metadata as defined in the *MMS SOC-ITF ICD*. This metadata is compliant with the SPASE standard as per the *NASA Heliophysics Science Data Management Policy* document.
  - Provide the SDC with software needed for creating Quicklook products. The SDC works with ITF teams to adapt their software to execute on SDC computer systems, such that Quicklook

data products are routinely generated shortly after data downlink from each spacecraft. The ITFs assist the SDC in maintaining this software.
- Support end-to-end testing of interfaces with the SDC.
- Provide detailed descriptions of software and data version changes to the SDC so these changes can be communicated to the scientific community.
- Provide science news items to the SOC for posting on the SOC web site.

3.5. Education and Public Outreach (EPO)

The SMART EPO program, coordinated by Rice University, will focus on teacher training, educational software, and science videos for regular venues as well as planetariums during the primary mission. Student modules, museum exhibits, and planetarium and television shows are disseminated through an existing network of teachers and museums in coordination with ongoing programs. Additionally, the SMART EPO team will create a web site with up-to-date mission information, webcasts of major events, and educational broadcasts, utilizing data products and information provided through the SDC web site. Note that the EPO website is hosted at Rice University and serves a different audience than the data and analysis oriented website hosted at the SOC.

3.6. Space-Ground Network

Three ground tracking networks are used in support of MMS: Tracking and Data Relay Satellite System (TDRSS), Universal Space Network (USN, 13m dishes), and Deep Space Network (DSN, 34m dishes). TDRSS is used for launch and early orbit critical event coverage, Phase 0 (post launch checkout) Perigee coverage, backup command support, and Phase 2a orbit maneuver support. The USN is used for maneuver support. The Deep Space Network is used primarily for playback of recorded data, uplink of stored commands, and observatory health and safety monitoring.

All communications with the spacecraft (up/down) use S-Band frequency, and share a common frequency for all spacecraft. Protocols are in accordance with the Consultative Committee on Space Data Systems (CCSDS) recommendations.

3.7. Associated Organizations

Organization	Role
MMS Science Working Group	The MMS Science Working Group (SWG) is chartered by the Heliophysics Division at NASA Headquarters and provides scientific and technical findings to the MMS Project Scientist and the MMS Project Manager. The SMART PI will chair the SWG, the MMS Project Scientist is vice chair, and membership will include the five SMART Instrument Team Leaders, the SMART Theory and Modeling Team Lead, the SMART Burst System Lead, and the SMART Plasma Science Lead. Additionally, three Interdisciplinary Scientists (IDS), selected via *ROSES-2005 Appendix A.32,* are tasked by the SWG with specific deliverables. These IDS will serve as members of the MMS SWG in addition to conducting science investigations addressing the MMS science objectives independently of the SMART science efforts.
NASA HQ's Heliophysics Division	The goal of Heliophysics at NASA is to "Understand the Sun and its interactions with the Earth and the solar system". Early NASA spacecraft confirmed the theory that interplanetary space is completely filled with streams and clouds of material ejected by the Sun. Thus, a new view of our solar system was born. At its center is a magnetically variable star that governs the motions of the planets, drives the Earth's climate system, and modulates the interplanetary medium. From this view, the solar system appears as a heliosphere moving through interstellar space, the study of which NASA calls Heliophysics. The Heliophysics spaceflight strategy is to deploy modest-sized missions as frequently as possible to form a small fleet of solar, heliospheric, and geospace spacecraft that operate simultaneously to understand the coupled Sun-Earth system.
Space Physics Data Facility (SPDF)	The SPDF is a function of the Heliospheric Science Division (HSD) at NASA's Goddard Space Flight Center. The Facility supports data from most NASA Heliophysics missions to promote correlative and collaborative research across discipline and mission boundaries. The SPDF provides multi-mission data services such as CDAWeb, software tools used for working with CDF data files, and is responsible for long-term MMS data archival.
Virtual Observatories (VxO)	NASA's Heliophysics Virtual Observatories (VxO) provide simple, uniform access to data from distributed, heterogeneous sources. VxOs do not typically hold data but provide a framework for linking users to data and services that enhance the use of these data. In accordance with the NASA Heliophysics Science Data Management Policy, the MMS-SMART team will make its data available to NASA's VxO framework and is expected to work directly with the Virtual Magnetospheric Observatory.

Table 3-2: *MMS Associated Organizations*

4. DATA IDENTIFICATION

The MMS project uses the data level definitions indicated in Table 4-1.

Data Level	Brief Description
Raw	Raw telemetry data as received at the ground receiving station or ground test GSE, organized by contacts or ground test. Data sets may overlap and/or contain communication artifacts.
Level-0	Reconstructed, unprocessed instrument, payload, and spacecraft data; any and all communications artifacts, e.g. synchronization frames, communications headers, duplicate data are removed. These data will typically consist of binary CCSDS packets.
Level-1A	Fully decommutated but uncalibrated raw data at full resolution; time-referenced; "extracted telemetry items"
Level-1B	Level-1A (extracted telemetry items) to which engineering (e.g. simple polynomial) calibrations have been applied; data have been annotated with ancillary information (e.g., ephemeris, attitude data) and initial instrument-level science calibrations have been applied.
QuickLook	Scientific data products that are generated using simplified science processing algorithms and/or with provisional calibrations. These data are intended to provide basic scientific insight. Generation of these data will occur as quickly as possible, whereas routine production of Level-2 and Level-3 products may take considerably longer. In many cases, Level-1B products will serve as Quicklook data.
Level-2	Level-1 data that have been processed to physical units and/or derived geophysical parameters by combining calibration, ancillary, and other data. These data represent the lowest level of research grade scientific data, and exist at the same time and/or spatial resolution as Level-1 data.
Level-3	Mission Level Data Products. These data have been resampled spatially and/or temporally and may have been combined with measurements from other MMS instruments to produce a merged data set.

Table 4-1: *MMS-SMART Data Level Definitions*

4.1. Data Product File Formats

The SMART-IS team uses a common format for all publicly available MMS scientific data products. This facilitates the use of MMS data in multi-mission science studies and allows the data to be used with existing tools. The Common Data Format (CDF) was selected based on its proven capabilities, its familiarity to the instrument teams and corresponding scientific communities, its use and planned use by missions including Cluster, THEMIS and RBSP, and its status as a currently supported product of NASA's Space Physics Data Facility.

MMS produces and provides pre-processed, standard data product *files* that are versioned and directly traceable to algorithms, code, and calibration data used to generate them. In this fashion, publications that cite MMS data by version number enable provenance and reproducibility.

4.2. Calibration Data

Details about MMS instrument calibration data are included as part of the Calibration and Measurement Algorithm Document (CMAD).

4.3. Level-1 Data

Level-1 data products are fully decommutated but uncalibrated raw data at full resolution; time-referenced; "extracted telemetry items." Data volumes are identified in Table 4-13 and each instrument team's Level-1 products are described in the tables below:

Fast Plasma Instrument (FPI) Level-1 Products	
Sensor(s)	**Description**
DES	Efficiency/dead-time corrected, decompressed DES data [counts and/or $f(\boldsymbol{v})$]
DIS	Efficiency/dead-time corrected, decompressed DIS data [counts and/or $f(\boldsymbol{v})$]

Table 4-2 ***Fast Plasma Instrument (FPI) Level-1 Data Products***

Hot Plasma Composition Analyzer (HPCA) Level-1 Products	
Sensor(s)	**Description**
HPCA	Decompressed counting rates as a function of E, PO, AZ, TOF
HPCA	Gain, background, cal data

Table 4-3 ***Hot Plasma Composition Analyzer (HPCA) Level-1 Data Products***

FIELDS Level-1 Products	
Sensor(s)	**Description**
AFG	3-component B-field from Analog Flux Gate (AFG), to 128 vectors/sec
DFG	3-component B-field from Digital Flux Gate (DFG), to 128 vectors/sec
SDP	2-component E-field from Spin-plane Double Probe (SDP), to 8192 samples/sec
ADP	1-component E-field from Axial Double Probe (ADP), to 8192 samples/sec
SDP-ADP	Sweep calibration data from SDP and ADP
SDP-ADP	1 spacecraft potential sample from combination of ADP and SDP
SDP-ADP	3 sphere voltages from ADP and SDP
SDP-ADP	3-component Low Frequency (LF) electric Spectra
SDP-ADP	3 sampled Medium Frequency (MF) electric Waveform
SCM	3-component AC B-field from Search Coil Magnetometer (SCM)
SCM	Sweep calibration data
SCM	3-component LF magnetic Spectra
SCM	3-component sampled MF Magnetic waveform
EDI	Beam angles of successful Beam hits from Electron Drift Instrument (EDI)
EDI	Ambient electrons at two directions

Table 4-4: ***FIELDS Level-1 Data Products***

Energetic Particle Detector System (EPD) Level-1 Products	
Sensor(s)	**Description**
FEEPS	Burst: uncalibrated (counts) electron data cubes: Counts x Pseudo Energy x Detector versus time, sampled at the instrument sampling rate combined for both heads (18 detectors total) with each detector mapped to a Geophysical-Coordinate look direction (64 spin sectors).
FEEPS/EIS	Burst: uncalibrated (counts) Fast Ion data cube: Counts x Pseudo Energy x Detector versus time, at the slower of the 2 instrument sampling rates, combined 2 FEEPS heads (6 detectors) and the 1 EIS head (6 detectors) with each detector mapped to a Geophysical-Coordinate look direction (32 spin sectors).
FEEPS/EIS	Fast & Slow Survey: uncalibrated (Counts) electron data cubes: Counts x Pseudo Energy x Sector Elevation x Sector Longitude versus time, sampled at 1/8 spin period combined for both heads with each sector mapped to a Geophysical-Coordinate look direction.
FEEPS/EIS	Fast & Slow Survey: uncalibrated (Counts) Fast Ion data cube: Counts x Pseudo Energy x Sector Elevation x Sector Longitude versus time, at 1/8 spin period timing, combined 2 FEEPS heads (6 detectors) and the 1 EIS head (6 detectors) with each sector mapped to a Geophysical-Coordinate look direction.
EIS	Fast & Slow Survey: uncalibrated (Counts) Ion Composition data cube: Ion Species counts x Pseudo Energy x Sector Elevation x Sector Longitude versus time, with each 6 EIS sector mapped to a Geophysical-Coordinate look directions.
EIS	Burst: uncalibrated (Counts) Ion Composition data cube: Ion Species counts x Pseudo Energy x Sector Elevation x Sector Longitude versus time, with each 6 EIS sector mapped to a Geophysical-Coordinate look directions.

Table 4-5: ***Energetic Particle Detector System (EPD) Level-1 Data Products***

Active Spacecraft Potential Control (ASPOC) Level-1 Products	
Sensor(s)	**Description**
ASPOC	Ion and total beam current, ion beam energy and S/C potential value (provided by SDP) for each of the two ASPOC instruments at highest time resolution (1 second).
ASPOC	Status and housekeeping information (emitter heater current and voltage, secondary voltages, internal temperatures for each of the two ASPOCs (40 seconds resolution).
	All ASPOC Level-1 Data Product Files are generated at SDC.

Table 4-6: ***Active Spacecraft Potential Control (ASPOC) Level-1 Data Products***

4.4. Quicklook Data

Quicklook data are scientific data products that are generated using simplified science processing algorithms and/or with provisional calibrations. These data are intended to provide basic scientific insight. Generation of these data occurs as quickly as possible, whereas routine production of Level-2 and Level-3 products may take considerably longer. In many cases, Level-1B products serve as Quicklook data.

The MMS SDC routinely produces Quicklook science data products, which are readily browsed via a website interface hosted by the SOC. Quicklook data are made available to the science community within 24 hours of telemetry receipt at the SOC. These data products are generated using simplified science processing algorithms and/or provisional calibrations. While expected to be useful for providing scientific insight into recent magnetospheric activity, they are not appropriate for research use.

Data volumes are identified in Table 4-13 and Quicklook data products are described below:

Quicklook Data Products	
Investigation	**Description**
Fast Plasma Instrument (FPI)	Energy-azimuth-zenith angle vs. time spectrograms (survey "sky-maps"), and survey moment time-series including densities, velocities, and temperatures. Unpacked and de-spun FPI Trigger Terms (electron/ion "pseudo-moments").
Hot Plasma Composition Analyzer (HPCA)	Particle flux as a function of energy and ion species. Flux data are displayed primarily as spectrograms (energy vs. time for H^+, He^+, He^{++}, and O^+ ions).
FIELDS	DC electric field vector, DC magnetic field vector, spacecraft potential, E and B wave spectra, EDI ambient electron counts when available.
Energetic Particle Detector System (EPD)	Electron spectra, ion spectra, omni-directional intensities, selected energy angular distributions, selected-energy pitch angle distribution, ion composition index.
Active Spacecraft Potential Control (ASPOC)	Ion and total beam current, ion beam energy, S/C potential (as provided by SDP), filament power and impedance and the emission quality for each of the two ASPOC units. The ASPOC Quicklook Plots are generated at SDC.

Table 4-7: *MMS-SMART Quicklook Products*

4.5. Level-2 Data

Level-2 data are Level-1 data that have been processed to physical units and/or derived geophysical parameters by combining calibration, ancillary, and other data. These data represent the lowest level of research grade scientific data, and exist at the same time and/or spatial resolution as Level-1 data. All data products include data quality flags and uncertainties as appropriate to aid in accurate understanding of correct data use.

Production software to produce Level-2 science data products is the responsibility of each ITF. For convenience, some Level-2 data products are generated locally at the ITF (FIELDS, HPCA, FPI), with the remainder generated locally at the SDC. Data volumes are identified in Table 4-13 and Level-2 data products are described below:

Fast Plasma Instrument (FPI) Level-2 Science Products		
Sensor(s)	**Description**	**Notes**
DES/DIS	Energy, azimuth, zenith-angle spectrogram ("sky/burst-map") time-series supporting various levels of time axis zoom for survey and burst modes	• Files generated at ITF. • FPI's processed data volume is very large. An important and achievable goal is to minimize any unnecessary growth of this volume due to FPI-ITF re-processing.
DES/DIS	Velocity distribution functions in 3D per energy bin in despun body coordinate frame for survey and burst modes	
DES/DIS	Moments (density, velocity vector, temperature vector, pressure tensor, heat flux vector) with corrections (calibration, spacecraft potential, and photo-electron) for survey and burst modes	
DES/DIS	Partial moments (density, velocity vector, temperature vector, pressure tensor) integrated starting from each energy step for survey and burst modes	

Table 4-8 ***Fast Plasma Instrument (FPI) Level-2 Science Products***

HPCA Level-2 Science Products	
Description	**Notes**
Calibrated & background-corrected energy flux for H^+, He^+, He^{++}, and O^+ ions	• Files generated at ITF. • These are generated with varying fidelity depending on the operating mode of the instrument. In the highest resolution mode, each species will result in 18432 data values (64 Energy x Polar x 18 Azimuth at a ten second cadence.
Velocity distribution functions of H^+, He^+, He^{++}, and O^+ ions derived from j(E)	
Moments (density, velocity, temperature)	
Time of Flight (TOF) raw counts	

Table 4-9: ***Hot Plasma Composition Analyzer (HPCA) Level-2 Science Products***

FIELDS Level-2 Science Products		
Sensor(s)	**Description**	**Notes**
FGM	3-component B-field to 128 vectors/sec in GSE	Files generated at ITF
EDP	3-component E-field to 8192 samples/sec in GSE	Files generated at SDC
EDP	1 spacecraft potential	Files generated at SDC
EDP	3-component LF electric spectra	Files generated at SDC
EDP	3-component MF electric spectra	Files generated at SDC
SCM	3-component LF magnetic spectra	Files generated at SDC
SCM	3-component AC B-field	Files generated at SDC
EDI	3-component electric field	Files generated at ITF
EDI	Ambient electrons at two directions	Files generated at ITF

Table 4-10: ***FIELDS Level-2 Science Products***

Energetic Particle Detector System (EPD) Level-2 Science Products		
Sensor(s)	**Description**	**Notes**
EIS	Burst: Calibrated (intensity) Ion Composition ExTOF data cube - Ion Species Intensity x Energy (~50 – 500 keV) x Telescope versus time for each of the 6 telescopes, with each sector mapped to a Geophysical-Coordinate look direction (8 spin sectors) and magnetic field direction.	Files generated at ITF
EIS	Burst: Calibrated (intensity) Ion Composition PHxTOF data cube - Ion Species Intensity x Energy (~20 – 50 keV) x Telescope versus time for each of the 6 telescopes, with each sector mapped to a Geophysical-Coordinate look direction (8 spin sectors) and magnetic field direction.	Files generated at ITF
EIS	Burst: Calibrated (intensity) electron data cube – Electron Intensity x Energy x Telescope versus time for each of the 6 telescopes, with each sector mapped to a Geophysical-Coordinate look direction (8 spin sectors) and magnetic field direction.	Files generated at ITF
EIS	Fast & Slow Survey: Calibrated (intensity) Ion Composition ExTOF data cube - Ion Species Intensity x Energy (~50 – 500 keV) x Telescope versus time for each of the 6 telescopes, with each sector mapped to a Geophysical-Coordinate look direction (8 spin sectors) and magnetic field direction.	Files generated at ITF
EIS	Fast & Slow Survey: Calibrated (intensity) Ion Composition PHxTOF data cube - Ion Species Intensity x Energy (~20 – 50 keV) x Telescope versus time for each of the 6 telescopes, with each sector mapped to a Geophysical-Coordinate look direction (8 spin sectors) and magnetic field direction.	Files generated at ITF
EIS	Fast & Slow Survey: Calibrated (intensity) electron data cube - Electron Intensity x Energy x Telescope versus time for each of the 6 telescopes, with each sector mapped to a Geophysical-Coordinate look direction (8 spin sectors) and magnetic field direction.	Files generated at ITF

Table 4-11: ***Energetic Particle Detection System (EPD) Level-2 Science Products***

Active Spacecraft Potential Control (ASPOC) Level-2 Science Products	
Description	**Notes**
Interpolated ion beam current and energy for each of the two ASPOCs, as well as the sum of the individual beam currents (1 second resolution).	Files generated at SDC
Interpolated status information (modes of both ASPOCs, ON/OFF status) and data quality information at a resolution of 1 second.	

Table 4-12: ***Active Spacecraft Potential Control (ASPOC) Level-2 Science Products***

4.6. MMS Mission Level Science Products (Level-3)

The MMS Mission Level Data (MLD) products are combined from the instrument-specific Level-2 data products. MLDs specifically address the need for multi-instrument analyses central to the SMART project. Level-3 data may include other publicly available data products if they are of significance to the SMART science efforts *and* can be merged into the data system at the SDC (e.g. geomagnetic indices, solar UV fluxes, etc.).

Specific MMS Level-3 products, along with responsibility for their generation, are identified in the *MMS-SMART Instrument Suite Calibration and Measurement Algorithm Document.*

4.7. Data Volume

The MMS-SMART IS produces a substantial volume of data on a daily basis. Level-2, alone, accounts for more than 50 GB per day for all four observatories. Within the MMS team, systems are scaled accordingly to accommodate data transmission and storage needs. To facilitate use by the general science community, online analysis tools provide the ability to zero in on specific data of interest prior to download. For scientists working with the data, this can minimize the amount of data that needs to be downloaded and managed on local systems. The following table indicates the expected data volumes for each MMS-SMART investigation's data products.

MMS Data Volume (daily, per spacecraft)						
Instrument	**Raw Volume**	**Level-0 Volume**	**Level-1 Volume**	**Level-2 Volume**	**Level-3 Volume**	**Total**
Fast Plasma Instrument (FPI)	262 MB	262 MB	1310 MB	11200 MB	TBD	13034 MB
Hot Plasma Composition Analyzer (HPCA)	59 MB	59 MB	295 MB	443 MB	TBD	856 MB
Fluxgate magnetometer - AFG	3 MB	3 MB	15 MB	38 MB	TBD	59 MB
Fluxgate magnetometer - DFG	2 MB	2 MB	10 MB	32 MB	TBD	46 MB
Search-coil magnetometer (SCM)	35 MB	35 MB	175 MB	260 MB	TBD	505 MB
Spin-plane electric field instrument (SDP)	77 MB	77 MB	385 MB	600 MB	TBD	1139 MB
Axial double-probe electric field instrument (ADP)	39 MB	39 MB	195 MB	300 MB	TBD	573 MB
Electron-drift electric field instrument (EDI)	7 MB	7 MB	35 MB	100 MB	TBD	149 MB
EPD	5.0 MB	5.0 MB	25 MB	151 MB	TBD	186 MB
Active Spacecraft Potential Control (ASPOC)	1.2 MB	1.2 MB	8 MB	8 MB	0	18 MB
Total	.49 GB	.49 GB	2.5 GB	13.1 GB	TBD	16.6 GB

Table 4-13: *MMS-SMART Data Volume (daily, per spacecraft)*

Of the data volume numbers in the above table, approximately 74% are burst data, 25% are Fast Survey, and the remaining 1% is Slow Survey data.

5. DATA HANDLING

5.1. Overview of End-to-End Data Flow

Data capture of both instrument and spacecraft recorded telemetry occurs at the MOC. During ground station contacts, real-time telemetry are relayed from the MOC to the SOC. Following each ground station contact, the MOC provides the SOC with recorded telemetry frames containing instrument and spacecraft data, along with appropriate status and ancillary information. The SOC performs Level-0 processing on these data, dividing the telemetry data streams into packets. The packet sets are then processed at the SOC, using software developed by LASP and the investigator teams, to form Level-1 data products, which are used to monitor state-of-health and to support operations. Quicklook science data products are also be created to provide a preliminary view of MMS science measurements and are be accessible to the science community via the Internet. Generation of Level-1 data takes place within 6-hours of ground receipt, with Quicklook products nominally being generated within 24 hours.

Within one day of receipt, the SDC makes available telemetry and ancillary data to the ITFs for Level-2 data processing. Each ITF is responsible for ensuring the generation of Level-2 data products based on best current calibration factors and (where applicable) delivering these products to the SDC for distribution and archival within 30 days.

Since magnetometer and ASPOC data are needed by other ITFs to perform their Level-2 data processing, Level-2 magnetometer and ASPOC processing occur at the SDC in close collaboration with the corresponding ITF. In these cases, maintenance and development of the processing software, data validation, and calibrations are the responsibility of the ITF and the SDC will execute the provided Level-2 software on production systems. Subsequently, these data products are made available to all the teams within 24 hours of receipt of telemetry at the SOC.

Updates to calibrations, algorithms, and/or processing software occur regularly, resulting in appropriate production system updates followed by reprocessing of science data products. Systems at the SOC and ITFs are designed to handle these periodic version changes. Likewise, publicly available software tools are updated as needed.

Responsibilities for data product generation and dissemination are discussed in Section 3 and the timeline and schedule for production and availability of MMS data products is shown in Table 5-1. Details regarding data distribution to/from the ITFs, magnetometer and ASPOC Level-2 software deployment, data validation, and reprocessing strategies are provided in the *Calibration and Measurement Algorithm Document (CMAD).*

Data Level	Responsible Team	Availability Schedule
Level-0	MMS SOC	Beginning at the start of instrument commissioning, Level-0 data are routinely available within 6 hours of science telemetry receipt at the SOC.
Level-1	MMS SOC	Beginning at the start of instrument commissioning, Level-1 data are routinely available within 6 hours of science telemetry receipt at the SOC.
Quicklook	MMS SOC	Beginning at the start of instrument commissioning, Quicklook data are routinely available within 24 hours of science telemetry receipt at the SOC.

Data Level	Responsible Team	Availability Schedule
Level-2	Instrument Team Facilities (ITFs) are responsible for all Level 2 data production and validation. In the case of ASPOC and magnetometer data, Level 2 processing occurs at the SOC on behalf of the corresponding ITF. In these cases, the ITF provides the SOC with processing software, documentation, maintenance, and data validation as needed. Producing these data at the SOC allows for fast turnaround time of the products that the other ITFs depend on.	Beginning as soon as possible but no later than 6 months after commissioning, Level-2 products are routinely produced within 30 days of science telemetry receipt from each spacecraft. Further, since all teams depend on both ASPOC and magnetometer data, ASPOC and magnetometer data products are made available within 24 hours of the raw data being received at the SOC.
Level-3	Generation of Level-3 data products is the responsibility of individual instrument teams and is described within each team's Data Product Guides.	Beginning as soon as possible, Level-3 products are produced by individual instrument teams as developed.

Table 5-1: ***Timeline for Availability of MMS-SMART Data Products***

The SOC maintains an active archive of all MMS data levels, and provides direct access to the MMS science team and science community through the entire lifecycle of the MMS mission, beginning with management of telemetry data during observatory I&T. As is documented in the *MMS Mission Archive Plan*, following the operational phase of the mission MMS data products are expected to continue to be made available to the science community through an MMS Resident Archive, possibly the MMS SDC, to maintain continuity. Once it is no longer cost effective, the SOC is expected to transfer MMS data holdings to a Final Archive (the SPDF), which provides long-term preservation.

5.2. Data Acquisition

The MMS scientific questions require high-time-resolution measurements within boundary regions that often comprise only a small part of the MMS orbit. In the subsolar reconnection region, for example, high time resolution observations are needed for ~10 minute periods as the spacecraft cross the magnetopause regions, but only moderate time resolutions in the surrounding regions. Within the ion and electron diffusion regions, electron distributions at ~30 ms resolution are needed as well as electric and magnetic wave-form captures with resolution to 1-10 ms. The requirements in the magnetotail reconnection region are somewhat less stringent. To accommodate these different data acquisition needs while keeping within telemetry downlink limits, the SMART Instrument Suites generate two science data streams, Burst and Survey.

The Survey data stream is collected nearly continuously. When the spacecraft are not in or near targeted regions of scientific interest (about half of each orbit), data are collected in "Slow Survey" mode. In this mode, the instruments acquire data at significantly less than maximum data collection rates. As the four spacecraft approach targeted regions of scientific interest (the remaining half of each orbit), the instruments are configured in "Fast Survey" mode and acquire data at moderate time resolution. All of the data collected in survey mode is downlinked.

The Burst data stream is collected concurrently with the collection of Fast Survey data. Burst data are high time resolution, continuous data sets. At this resolution, the SMART IS produces scientific measurements many times faster than the orbit-averaged telemetry rate. Since it is not practical to downlink all of the burst data and since only a small fraction of the collected burst data are expected to be essential anyway, a buffer selection scheme is used to prioritize burst data for downlink. This scheme employs onboard algorithms to determine Cycle Data Quality factors (CDQs), which provide a quantitative measure of each

burst buffer's data values. The CDQs are much smaller than the data they represent and are easily transmitted to the ground. Once at the SOC, the CDQs are used to determine the periods of time that have the most valuable concurrent burst data on all 4 spacecraft.

This scheme focuses data collection on the most interesting parts of the orbit, helps to ensure that the best synchronous data is downlinked from all 4 spacecraft, and optimizes the 96 GB of on-board storage provided by the Central Instrument Data Processor (CIDP). For a detailed description of the burst buffer selection system, see the *Burst Algorithm Definition and Concept of Operations* (10160.17-BADCO-01).

5.3. MOC ⇔ POC Data Transfers

In order to support operations of the MMS Instrument Suites and capture and processing of science data, data and information exchanges between the MOC and the POC are necessary. The principal transfers are illustrated in Figure 5-1. Interfaces pertaining to science-related data flows are emphasized in this document; operations-related data flows are further described in the *MMS Concept of Operations* (461-PROJ-PLAN-0071), and are also indicated in Figure 5-1 and Figure 5-2.

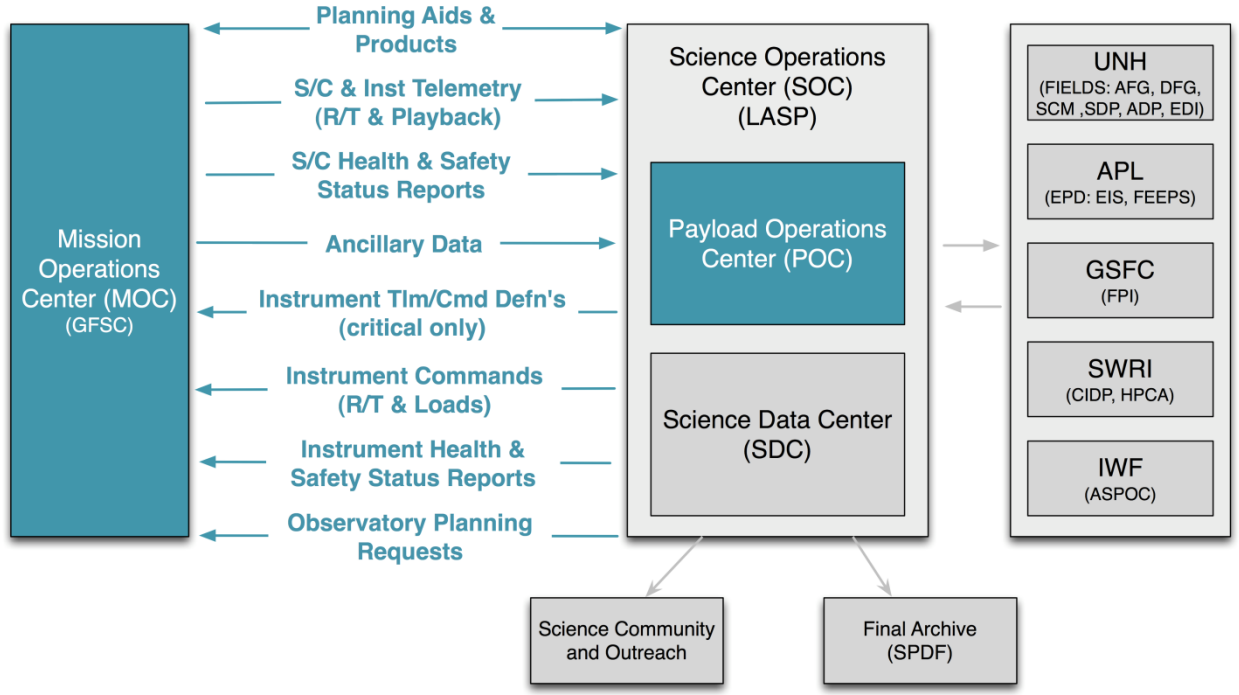

Figure 5-1: ***Key data flows between the MMS MOC and POC***

All MMS telemetry data (spacecraft and instrument housekeeping and science) are captured by the MMS MOC, and subsequently relayed or transferred to the POC. Immediately following a recorder dump pass, the MOC forwards all captured spacecraft and instrument telemetry files to the SOC/POC. Only minimal Level-0 processing and accounting is required, as the data are transferred in the reliable file mode of the CCSDS File Delivery Protocol (CFDP). All spacecraft, instrument, and ancillary data are transferred to the SOC/POC on an ongoing basis for archival and distribution; however, spacecraft data are also maintained in the MOC for the operational duration of the mission. The communications links used to support transfers between the MOC, SOC, and other ground system elements are documented in the *MMS MOC-SOC ICD*. Transfers between the SOC and other ground system sites (e.g. ITFs, science community) use the Internet.

The MOC transfers all real-time spacecraft and engineering telemetry to the SOC/POC using a private operational network, which is identified in the Project Service Level Agreement (PSLA). The MOC transfers all IS recorded telemetry files directly to the SOC/POC as it is received to allow the SOC to manage these data.

In addition to telemetry data transfers to the SOC, ancillary data are provided by the FDOA to the SOC via the MOC. The frequency and format of these data is documented in the *MOC/FDOA-SOC ICD*. These data will include:

- Predicted orbit ephemerides
- Definitive orbit ephemerides
- Definitive spin axis attitude - A definitive spin axis attitude file is computed from the downlinked spacecraft playback telemetry files and provided post-pass
- Definitive spin rate/spin phase angle
- Maneuver history

5.4. POC ⇔ Instrument Team Transfers

The POC makes available several data products to the ITFs to support operations of their instruments, including real-time telemetry data, contact schedules, planned activity summaries, and data availability notifications and quality reports. Similarly, operations support products and information are provided by ITFs to the POC, including detailed instrument state-of-health assessments, special planning requests, and any necessary special uploads (e.g. flight software updates). The principal data products transferred over this interface are indicated in Figure 5-2. The timelines for delivery of these products and formats used are documented in the *MMS SOC-ITF ICD.*

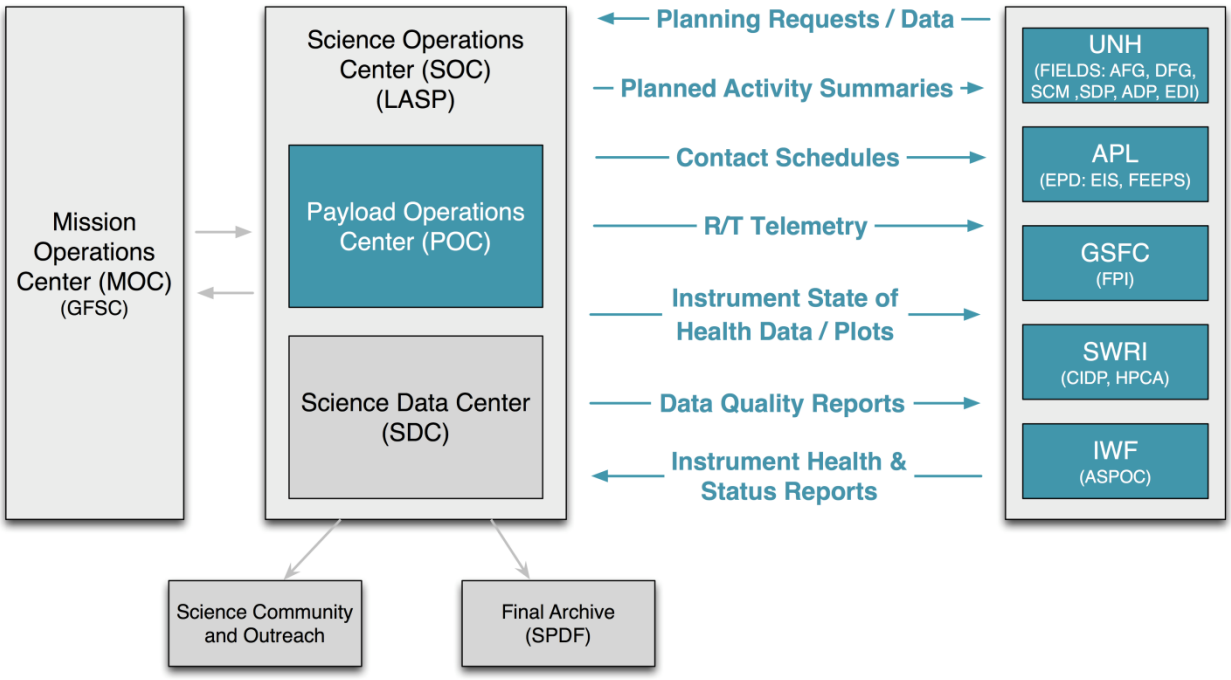

Figure 5-2: *POC-ITF Data Transfers*

5.5. SDC ⇔ Instrument Team Transfers

The interface between the SDC and the ITFs is designed to facilitate production, management, and dissemination of science data products. Low-level telemetry data, ancillary data, and Quicklook data are generated at the SOC and made available to the ITFs for generation of higher-level science products. Key data exchanges are indicated in Figure 5-3.

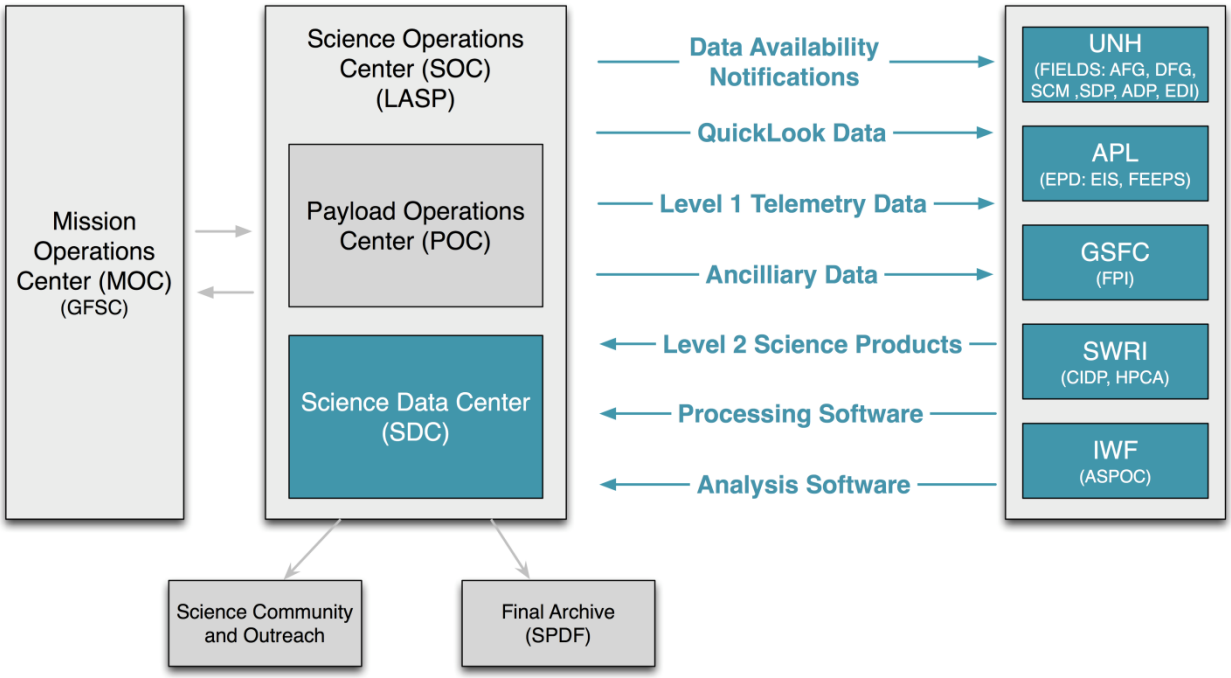

Figure 5-3: *SDC-ITF Data Transfers*

Within one day of acquisition, ITFs receive notification of the availability of Level-0 and Level-1 data. Each ITF then initiates transfer from the SDC of the telemetry and ancillary data needed for Level-2 production and data validation. Each ITF then returns Level-2 science data for their instrument to the SDC within 30 days. Level-2 data are in physical units for all appropriate quantities, based on best current calibration factors and analysis routines. Reprocessing of Level-2 data can occur throughout the operational mission as significant advances in instrument calibration and understanding warrant the production of a new data version. Version control systems are utilized by the SDC and the ITFs to ensure that changes in calibration and reprocessing of Level-2 data are tracked and are transparent to the scientific user receiving data from the SDC. Modeling data from the SMART theory efforts are also treated as Level-2 data and, after validation, can be maintained and disseminated by the SDC.

5.6. Science Data Production

In addition to raw telemetry and other ancillary data that are needed to support science processing by the ITFs, there are a number of interdependencies between instrument processing algorithms. Data products that other teams depend on (e.g. Level 2-Pre magnetometer data) are provided via programmer-level interfaces once that data is available at the SDC. For convenience, these interfaces work in much the same way as the interfaces that are used to access telemetry and ancillary data. Specific data processing needs and dependencies for each of the MMS investigations are detailed in the sections below.

5.6.1. FIELDS

Magnetometer science data from both AFG and DFG sensors are processed (to Level-2 Pre) by the SDC and provided to other ITFs for all scientific uses of the DC magnetic field. The FIELDS magnetometer team maintains and supervises this production. This Level-2 Pre Product is a preliminary version that is produced using an epoch-based set of calibration offset and matrices, with best available attitude information. These offset and matrices are refined over a period of 30 days and allow the production of a higher-fidelity Level 2 FGM product that combines AFG and DFG data into a single product that can be used for publication purposes. A Level 3 burst product, FSM (Fluxgate Search-Coil Merged), requires joint processing between AFG, DFG, and SCM to arrive at the final values.

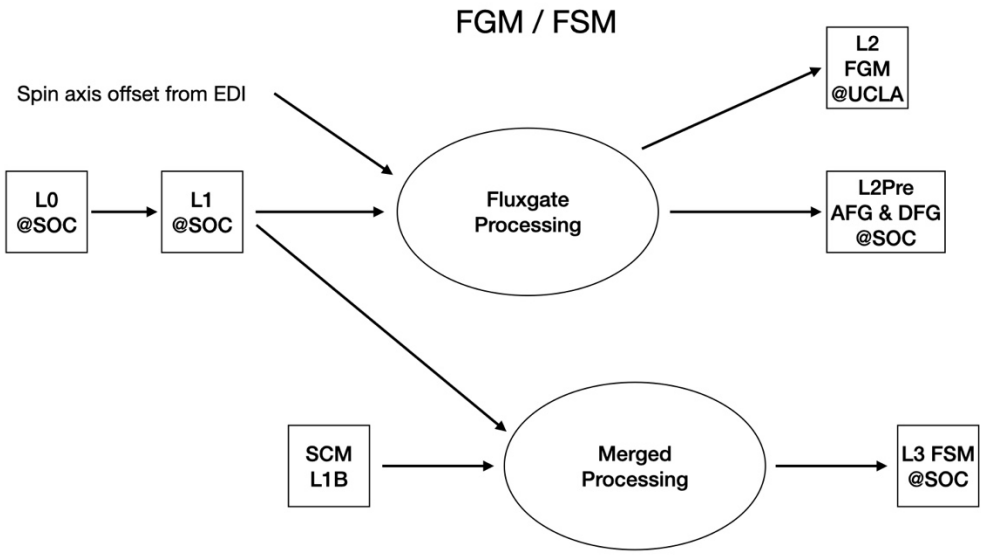

Figure 5-4: ***AFG / DFG /FGM / FSM Processing Flow***

For EDI, there is an existing software process, BESTARG, that is rather resource intensive and produces field and flow vectors for the "field" mode of EDI. Other processes, less intensive, produce time series of the electron flux, and magnetometer corrections.

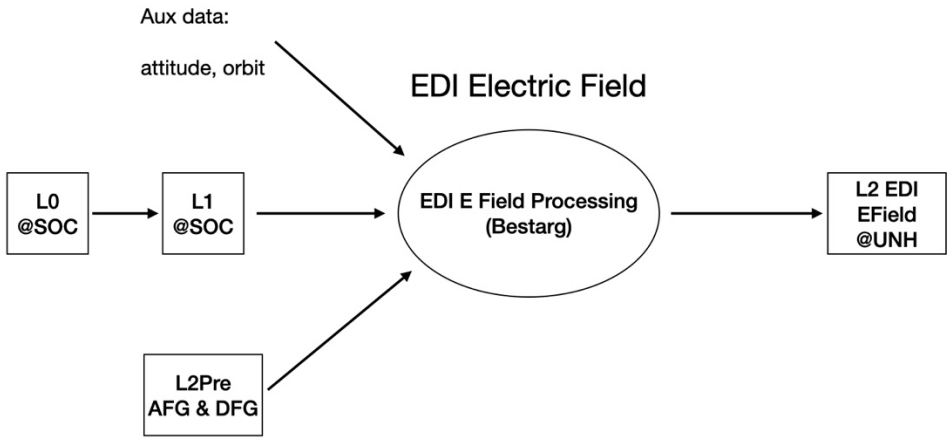

Figure 5-5: *EDI Bestarg Processing Flow*

EDI processes "Ambient mode" electron data using the L2Pre magnetometer data sets into a time-series of electron fluxes at one selected fixed energy (250 eV, 500 eV, and 1000 eV), as diagrammed in **Error! R eference source not found.**.

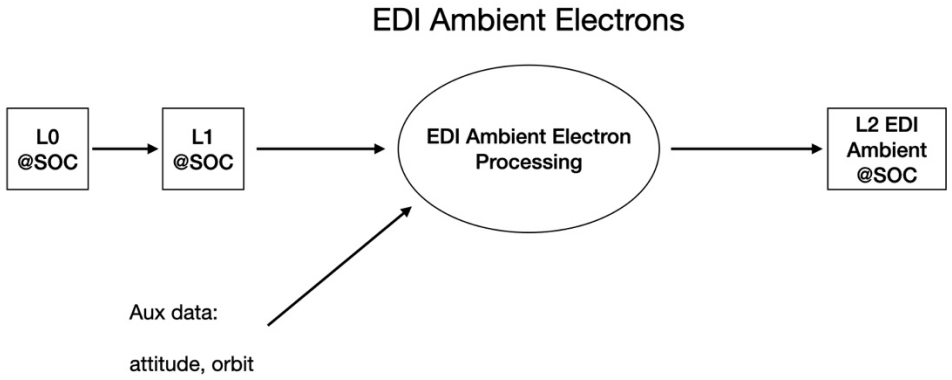

Figure 5-6: *EDI Ambient Electron Processing Flow*

EDP Level 2 Pre processing consists of offset removals and corrections of the ADP and SDP field components, data quality and error determination, and spin-period fits. EDP Level 2 processing includes EDI electric field data and FPI L2 ion moments data for higher fidelity electric field data as diagrammed in 5.7.

In addition, wave power and auto- and cross-correlation spectra are produced for the wave data.

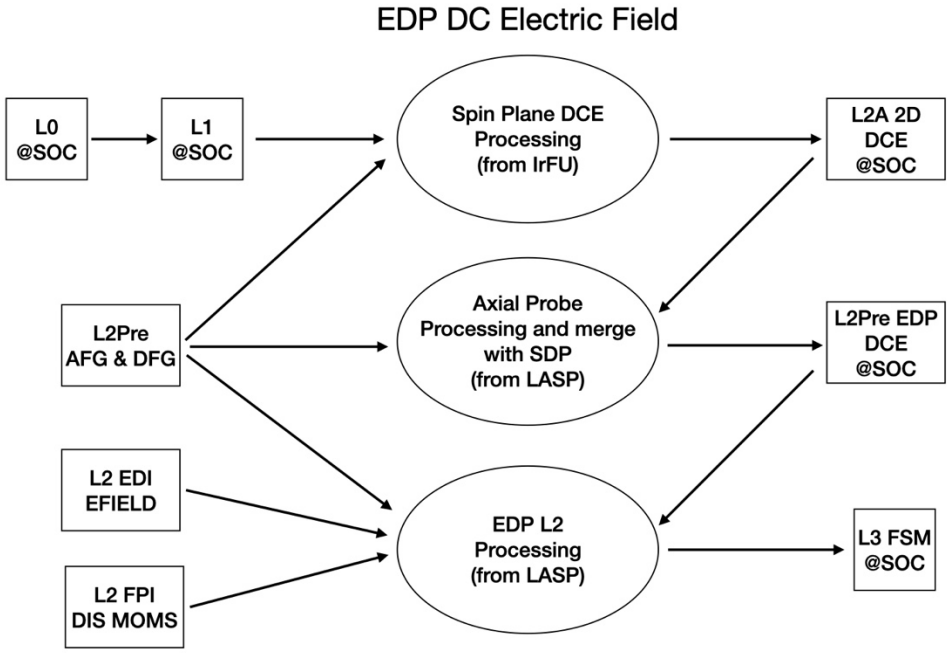

Figure 5-7: EDP / ADP / SDP Processing Flow

5.6.2. EPD

Figure 5-8 shows the flow of data and institutional responsibilities for the EPD data generation and processing functions. Primary data dependencies include accurate knowledge of the orientations of the EIS and FEEPS fields of view with respect to the local magnetic field vector and with respect to the Earth and Solar System coordinates, and accurate timing information between the EIS and FEEPS sampling (It is important that FEEPS sector "n" be accurately aligned with the very same EIS sector "n"). The EIS data are compressed on the spacecraft in two ways, and both types of compression must be inverted on the ground. Specifically, the EIS rate data are log-compressed from 16 or 24 bits to 10 bits. This compression is standard for particle detectors, but does generate loss of information. The error in intensity introduced by this process is < 2%. Secondly, a lossless compression algorithm is applied to data records. The FEEPS data is also log-compressed, but to 12 bits, for an error of < 1%. Figure 5-8 shows that the FEEPS data are validated by Aerospace (light orange box; with help from Boston University, now University of New Hampshire), and the EIS data are validated by APL, also with help from BU/University of New Hampshire (dark orange box). Standard particle detector plotting tools are generated, including intensity versus time line plots, energy versus time versus intensity color spectrograms, pitch angle versus time versus intensity

spectrograms, all-sky direction (2D) versus intensity displays, energy spectrum displays and pitch angle distributions displays.

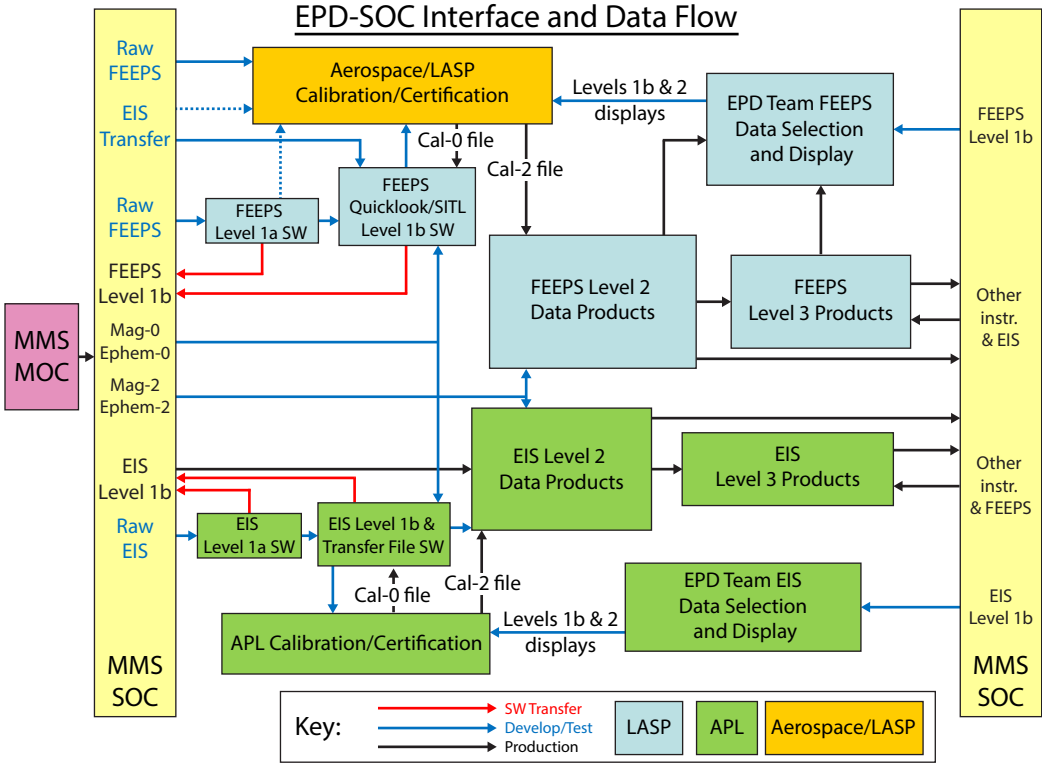

Figure 5-8: *EPD Processing Flow*

5.6.3. FPI

FPI Level-1 data products are produced using decoded and decompressed Level-0 data, plus current calibration and any ancillary data. The compression is done in hardware using a wavelet-based technique that ranges from essentially lossless to lossy, with a compression ratio varying accordingly. On orbit trades are made between burst data duration and velocity resolution, based on available telemetry allocation and experience, to assure overall data quality while maximizing the duration of telemetered high time resolution burst data. The result is fully time/energy/orientation-referenced (in spacecraft coordinates for bursts, de-spun spacecraft coordinates for survey products), associating a count (or "pixel") with the correct time, energy, and orientation (the one at which it was measured).

FPI Quicklook / Level-1B products include both the calibrated "flux skymaps" from Level-1 (all modes are available, but the results are provisional, particularly for burst-maps), and provisional moments (generated for fast-survey-mode data from the Level-1 product) which use spacecraft coordinates (albeit de-spun), and which incorporate older corrections and quality measures than those applied at Level-2.

Level-2 (and beyond) products use physical units, include all relevant (standards-compliant) metadata, and are submitted to the SOC after being certified "research grade" upon passing a set of quality tests (employing the best quality available B-field, spacecraft potential, FPI calibration data, reference densities from other instruments, etc.).

The basic set of moments consists of number density, velocity, temperature, pressure, and heat-flux parameters. Added to these moments are the associated uncertainties and some ancillary data, including spacecraft potential and "sun-sector". Differential energy fluxes for each energy are averaged over all directions as well as over various sky slices. Electron and ion distributions are phase-space-density (s/c-

potential-corrected f(**v**)) representations of instrument counts and are binned in their native instrument body coordinate frame (albeit de-spun). The Level-2 products are the native-resolution moments and canonical distributions (all modes, supporting any portrayals) for both DES (electrons) and DIS (ions).

Level-3 (derived from Level-2) products follow the same content and quality standards as Level-2. These can be as simple as re-sampled FPI products, or may be the result of merging FPI products with those of other instrument-suites.

A representation of FPI data processing flow is depicted in **Error! Reference source not found.**.

Figure 5-9: *FPI Processing Flow*

FPI data are organized and interpreted using data on the magnetic and electric fields. FPI analysis tools are provided for both diverse plotting methods as well as ASCII text (and various other useful formats) file dumps of any specified data array. In addition, all FPI algorithms, for example those used to compute moments, are version controlled but open to inspection and comment by anyone using the FPI data set. This combination of analysis tools provides the basis for development of additional tools of arbitrary sophistication limited only by the capabilities and resources of the interested investigator.

5.6.4. HPCA

HPCA data are compressed using a combination of table driven decimation together with a lossless compression step. Reversal of the lossless compression yields Level-0 data.

Level-1 data products consist of counting rates as function of energy, elevation, azimuth, mass/charge and time-of-flight. Gain and background data are generated.

Quicklook data products consist of particle flux as a function of energy and ion species. Flux data are formatted as time vs. energy spectrograms integrated over elevation and azimuthal angles. There is one spectrogram per species for H+, He+, He++, and O+ ions.

Level-2 data products are calibrated and background–corrected and provided for four ion species (H+, He+, He++, and O+) Data products for these species consist of: energy fluxes, velocity distribution functions,

pitch angle distributions, and moments (density, velocity, and temperature). Additionally, TOF raw counts are provided.

Level-3 data products are similar to level-2 but have been resampled and combined with measurements form other MMS instruments.

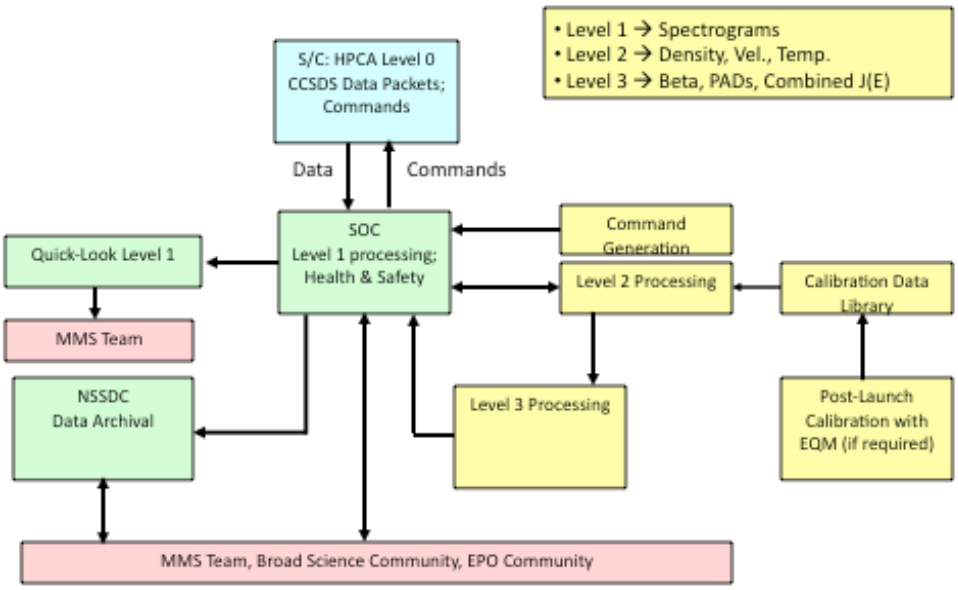

Figure 5-10: ***HPCA Processing Flow***

5.6.5. ASPOC

ASPOC data from both ASPOC instruments on each observatory are processed (to Level-2) by the SDC and provided to other ITFs for all scientific uses of the ion beam current and energy. The ASPOC team maintains and supervises this production.

Level-2 products include the current and voltage of the ion beam emitted by ASPOC using physical units. The processing consists of applying the current calibration, filtering, data quality and error determination. Data quality parameters are based on numerical analysis of the data (e.g., noise, presence of spikes). No compression is used.

As ASPOC is an active instrument, which influences the environment for other measurements, it is suggested to interpret this quality parameter (or to provide an additional quality parameter or flag) to describe the effectiveness of the control of the spacecraft potential. This parameter may be used by other ITFs together with the ASPOC L2 data to assess any cross-effect with other data.

Validation of the data are made by visual inspection of the data and by regular plausibility checks between the ASPOC L2 products on the one hand and spacecraft potential and plasma parameters on the other hand via spacecraft charging models.

Visualization software to facilitate the manual validation is provided, which delivers custom line plots of relevant parameters and support the plausibility checks mentioned before.

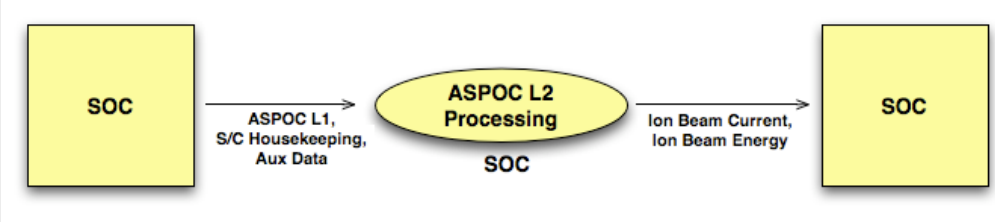

Figure 5-11: *ASPOC Processing Flow*

5.7. Science Analysis and News Reports

The SDC reports MMS related science news and data analysis summaries on the MMS SDC website. These news items may include descriptions of solar events, magnetospheric phenomenon, and MMS data highlights (such as reconnection events) as reported by the MMS science team.

5.8. Additional Data Flows

The general science community is able to access MMS science data products (Quicklook, Level 2, and Level 3) via a publicly accessible website, which is maintained and hosted at the SDC. The SDC also makes these data products available via a programmer level interface, which enables automated processing and analysis systems at other institutions as well as the retrieval needs of Virtual Observatories. In addition, appropriate MMS data are made available through existing SPDF multi-mission data services such as CDAWeb and orbit services such as SSCWeb to further enable multi-mission science studies using MMS data and to more easily use data from other missions to establish the larger context for given MMS observations.

6. CONFIGURATION MANAGEMENT / QA

The MMS SMART team is responsible for the production, analysis, and timely delivery of high-quality science data to the MMS Project. This is a standard expectation of NASA missions; however, the complexity of the MMS mission demands additional attention to software and data quality assurance strategies by both the SDC and the ITFs. With five science investigations onboard each of its four

spacecraft, MMS produces dozens of data products with many interdependencies. Data management challenges include:

- Software testing, data validation, defect tracking and data versioning is complicated by the fact that there are multiple investigations and multiple geographically dispersed teams.
- Calibration data are unique for each of the sensors. This data and its effect on Level-1, Level-2, and Level-3 (Mission Level Data) dependencies is carefully tracked.
- Changes in any of the Level-1 or Level-2 data products requires re-validating and re-releasing all affected software and data products. Affected data may include Level-1 data, Level-2 data, software products (e.g. "calibrators", analysis tools), and Mission Level Data products (Level-3).
- With dozens of data products, analysis tools, and on-the-fly data production tools (e.g. "calibrators"), staying informed of version updates may be challenging to users.

To address these challenges and ensure that the MMS project delivers correct, validated, and timely science data to the user community, a configuration management system is employed at each contributing institution for all of its science products, the data those products depend on (e.g. calibration data), and the software that is used to produce, distribute, and analyze them. Minimum configuration management includes versioning systems, release control procedures, issue/defect tracking, and documentation. Together, these configuration management systems and practices maintain a complete pedigree for each data product produced, and should also facilitate data reproducibility.

6.1. Information Preservation and Backup

As systems at the ITFs are not directly part of the Mission Archive at the SDC, adequate security and backup and recovery mechanisms are established at each ITF, if not already present. Backup and recovery mechanisms are generally documented along with contingency plans for ensuring a full recovery from catastrophic damage or failure. At a minimum this includes offline and offsite backup of all irreplaceable information, including software, calibration data, and other system dependencies.

6.2. Versioning

Each investigation has the responsibility of maintaining both an issue tracking and a version control system for its data production software, processing environment, analysis tools, data products and static calibration data. Two types of version tracking are employed in order to track revisions to both software and data products produced by software. These two types of versioning are described in the following sections.

6.2.1. Software Versioning

Teams are expected to use a source code management system for tracking code changes and other processing and data handling system dependencies (e.g. static calibration data). It is imperative that both software and calibration data are similarly revision controlled, and that the revision repository is backed up regularly and maintained off-site, as described in Section 6.1.

6.2.2. Data Versioning

MMS data users should be able to count on data of a specified version being consistent. This means that if anything changes in the processing system that produces a different data result, the version of that data product is incremented. Specifically:

- Changes to software or calibration data such that science results change for a specific time range indicates that the version number of the science data must change.
- When the version changes for a product that other products depend upon, the version must be incremented for the dependent products as well.

For clarity and consistency, version numbers included in data product file names. A consistent version numbering scheme is established and documented in each team's Data Product Guide.

6.3. Release Control

6.3.1. Validation

Ensuring the quality of the MMS science data products requires two types of validation efforts: that occurring prior to the production of data products (pre-production) and that which occurs after data products have been produced (post-production). Pre-production validation includes design reviews of algorithms and software that are used to produce and analyze data products. Production validation is best achieved through science data analysis using the archive products. All new version releases are validated by the contributing ITF and/or SDC team as appropriate, with the validation results being published and/or made available from the SDC-resident MMS data website.

6.3.2. Release Notes

Detailed release notes accompany all released software and data. At a minimum, release notes include the following information:

- Identification of the release (name, date, version number)
- Data product dependencies and corresponding versions.
- Requirements (required third-party platforms/modules/packages/etc)
- Features and changes (new features, defects corrected, etc)
- Outstanding issues (unresolved defects, work-arounds, installation issues, known issues, etc)
- Installation guide (if applicable)

6.3.3. New Release Notifications

In order to make sure that the *best* data products and tools are easily available for research and analysis, users need an easy way to be informed when new data versions and analysis tools become available. Strategies employed by the SDC include:

- Currently available version numbers are clearly indicated for all data and software products on the MMS SDC website.
- Version Release Notes for all data and software products are clearly available through the MMS SDC website.

The SDC work with applicable Virtual Observatories (e.g. Virtual Magnetospheric Observatory) to ensure that VxO users are also aware of when new releases are available.

6.4. Defect Tracking

A Defect Tracking System is established at the SDC and each ITF for tracking issues related to data products, data production software, and analysis tools. This system attaches a tracking number to all reported problems and allow for status changes (e.g. open/closed), the addition of comments, and filtered views (e.g. status, date reported, tags, etc). These systems are used for internal tracking at each ITF and need not be available for reporting by outside users.

Users from the general science community are encouraged to report any issues they might encounter through a web-based problem reporting system, which is implemented at the SDC and available through the MMS data access website, or via direct email to applicable ITF staff. The system is intended to guide users in the creation of effective problem reports, which includes user system details, activities causing problems, terminal output showing any error details, optional contact details, etc. These problem reports have a tracking number assigned to them and are communicated to the relevant instrument team(s) and the SDC manager for tracking and follow-up as needed.

7. DATA ACCESS AND AVAILABILITY

There are no proprietary periods associated with any of the MMS-SMART data products, and users have timely access to the scientifically useful products (Levels 2+). Additionally, users have access to science data analysis tools that aid in data access and analysis. To help ensure that the most recent data and software are easily available, access is centralized at the SDC. The SDC provides access to data and analysis tools via web-based interfaces and also supports data access through applicable Virtual Observatories. An overview of associated data flows is illustrated in Figure 7-1.

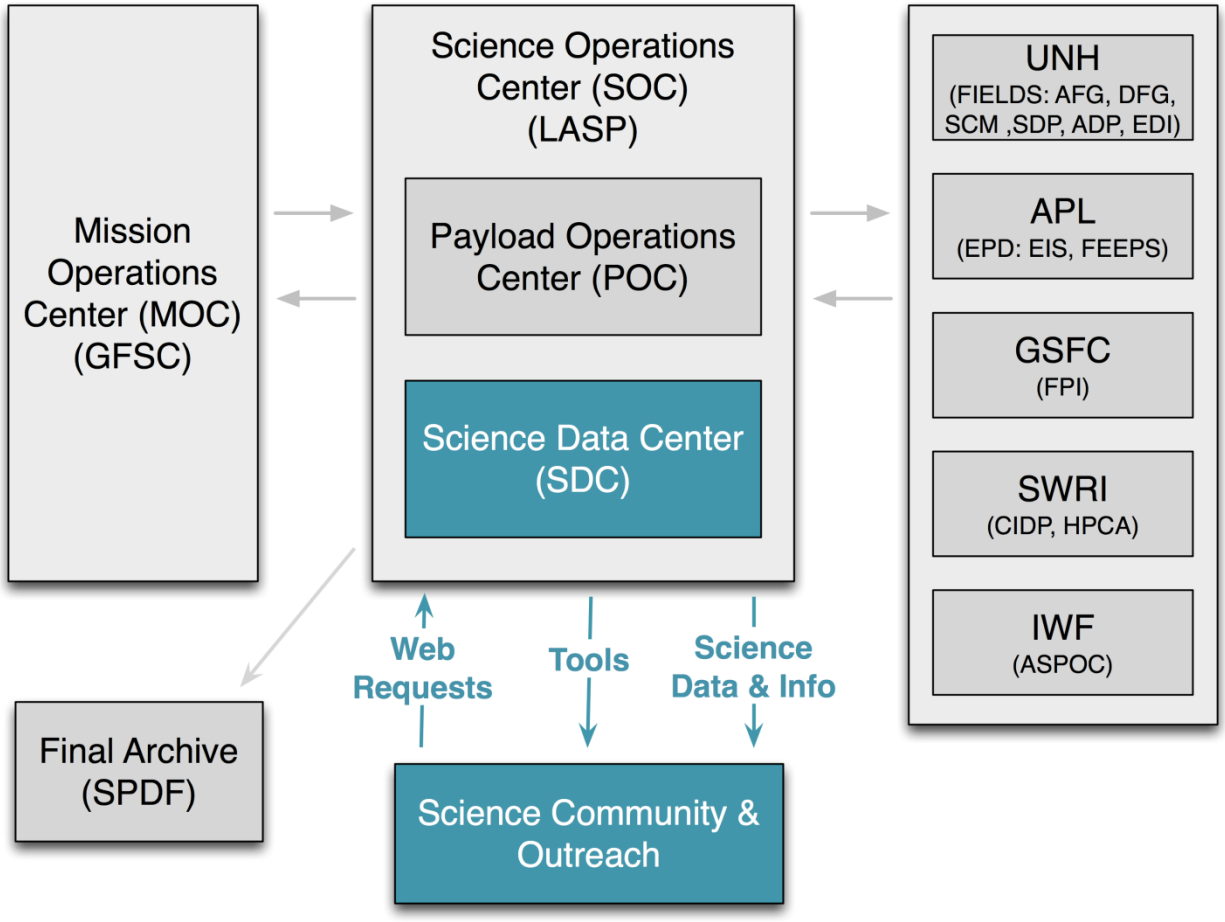

Figure 7-1: ***MMS-SMART Public Data Access***

The MMS science data system is designed to fully exploit the simultaneous measurements from all four MMS spacecraft. In close coordination with the MMS science groups, display tools are developed and provided at the SOC that are tailored for close association with modeling efforts and the broader science community. A timeline for MMS data availability is given in Table 5-1

7.1. Science Data

The SDC makes available Quicklook, Level-2, and Level-3 science data to the science community and general public. Instrument teams provide the SDC with software to produce Quicklook data products and Level-2 data files for archival and distribution and, in some cases, software 'calibrators' that allow users to produce Level-2 data on the fly.

In order to most effectively index, store, and distribute the MMS-SMART data, instrument teams are expected to provide the SDC with detailed documentation and metadata for each of their products. Specific metadata and documentation requirements are defined in the *MMS SDC-ITF ICD*. In part, these documentation and metadata requirements support the Space Physics Archive Search and Exchange (SPASE) data model so that the SDC can readily provide access to the data through Virtual Observatories. The SDC is responsible for identifying and collaborating with applicable Virtual Observatories to ensure that MMS data are accessible through these channels.

Additionally, the SDC is expected to maintain a record of spacecraft locations, instrument operating parameters, and version history notes for each data product and provide access to these data via its data access website.

7.2. Engineering Data

Spacecraft and instrument suite housekeeping/engineering data are provided to MMS team members and other designated individuals or organizations on a restricted basis.

7.3. Data Analysis Software

In coordination with the MMS science team, the SDC provides access to software tools to allow display, manipulation, and analysis of MMS data. Analysis tools that are unique to a specific dataset are developed by appropriate science team members and delivered to the SDC along with documentation for using the tools. These tools are made available to the science community via the SDC's data access website.

8. DATA ARCHIVAL

The SOC serves as the Mission Archive during the MMS mission, having responsibility for archiving all MMS mission data, and helps plan and provide for subsequent archive phases prior to mission termination. Resources archived at the SOC will include:

- Data – raw instrument and spacecraft telemetry (housekeeping and science); calibration data; ephemerides; attitude and other ancillary data needed to support scientific use and interpretation of MMS data; all levels of science data products.
- Metadata and Documentation describing data products (e.g. in SPASE terms), algorithms, instrument calibrations, validation, and data quality; also, command and telemetry definition information, descriptions of spacecraft and instrument design and operations, status reports, and other information needed for use of MMS data.
- Software and analysis tools, including software used for generation of scientific data products and corresponding metadata, as well as tools used for accessing, visualizing, and interpreting MMS science data.

Beginning with the observatory Integration and Test (I&T) phase and extending through launch, the SOC will collect and archive MMS data, principally telemetry data generated during ground testing and calibration activities. Following launch, as instruments are commissioned and begin routine science data collection, the SOC becomes actively responsible for data production and distribution activities and the archival function associated with management of science data sets. Throughout the mission, the SOC ensures that adequate security and backup/recovery mechanisms are established and documented, thereby maintaining the integrity of all data managed in the SOC repository and safeguarding them against loss. As responsibility for data processing and analysis activities is a distributed function on the MMS mission, each MMS-SMART instrument team also shares responsibility for maintaining the integrity of the MMS data during the active mission. The SOC and all Instrument Team Facilities (ITFs) establish backup/recovery mechanisms and document contingency plans for achieving a full recovery from catastrophic damage or failure. At a minimum, this includes offsite backup of raw telemetry, documentation/metadata, analysis

software, and any software that would be needed to reprocess, index, store, and distribute MMS data and analysis tools.

A *Mission Archive Plan* (MAP) is drafted by the SOC prior to the first Senior Review that guides the preparation of the final MMS archive. After the mission ends, MMS data, analysis tools, and the expertise to use them remains accessible through the SOC, as long as the SOC remains funded for its tailored dissemination of MMS data to the community. This ensures continuity of MMS data access mechanisms and tools to the scientific community. At some point after mission termination, once maintaining the SOC is no longer considered cost effective, full responsibility for maintaining and disseminating data will pass to a long-term archival facility determined in collaboration between the MMS program and the SPDF.

9. DATA RIGHTS AND RULES FOR DATA USE

The terms for distribution and use of the MMS data products are specified in the *NASA Heliophysics Science Data Management Policy* document, and are summarized here in terms of the MMS mission. These guidelines govern both the production and distribution of scientific data sets by the MMS program, and also use of the MMS data by the science community and general public, and are summarized below:

- MMS-SMART data products are open to all scientists and the public (Users).
- There are no proprietary periods associated with any of the MMS-SMART data products.
- Users shall have timely access to the scientifically useful data and analysis tools that are equivalent to the level that the MMS-SMART science team uses.
- Users should contact the MMS-SMART Principal Investigator (PI) or a designated lead investigator of an instrument or modeling group early in an analysis project to discuss the appropriate use of instrument data or model results. This applies to MMS-SMART team members, guest investigators, other members of the scientific community, and general public.
- Users that wish to publish the results derived from MMS data should normally offer co-authorship to the MMS-SMART PI and/or instrument PIs and science team members. Co-authorship may be declined.
- Users should heed the caveats of investigators as to the interpretation and limitations of data or model results. Investigators supplying data or models may insist that such caveats be published, even if co-authorship is declined. Data and model version numbers should also be specified.
- Users should acknowledge the sources of data used in all publications, presentations, and reports. Appropriate acknowledgement to institutions, personnel, and funding agencies should be given.
- Users are encouraged to provide the MMS-SMART PI and/or instrument PIs a copy of each manuscript that uses MMS-SMART data upon submission of that manuscript for consideration of publication. On publication the citation should be transmitted to the PI and any other providers of data.
- Pre-prints of publications and conference abstracts should be widely distributed to interested parties within the mission and related projects.
- Users are encouraged to make tools of general utility and/or value-added data products widely available to the community. Users are encouraged to notify the MMS-SMART PI of such utilities or products. The User should also clearly label the product as being different from the original MMS-SMART produced data product.

APPENDIX A - TABLE OF ACRONYMS

Acronym	Description
ADP	Axial Double Probe electric field instrument, part of FIELDS investigation
AFG	Analog Flux Gate Magnetometer, part of FIELDS investigation
APL	Applied Physics Laboratory
ARB	Anomaly Review Board
ASPOC	Active Spacecraft Potential Control
ATS	Absolute Time Sequence command
BADCO	Burst Algorithm Definition and Concept of Operations
CCSDS	Consultative Committee on Space Data Systems
CDF	Common Data Format
CDQ	Cycle Data Quality (burst buffer quality indicator calculated onboard each s/c)
CDR	Critical Design Review
CFDP	CCSDS File Delivery Protocol
CIDP	Central Instrument Data Processor
CMAD	Calibration and Measurement Algorithm Document
DES	Dual Electron Spectrometer, part of FPI investigation
DFG	Digital Flux Gate Magnetometer, part of FIELDS investigation
DIS	Dual Ion Spectrometer, part of FPI investigation
DSN	Deep Space Network
EDI	Electron Drift Instrument, part of FIELDS investigation
EDP	Electric Double Probe electric field instrument, combination of SDP and ADP
EIS	Energetic Ion Spectrometer, part of EPD investigation
EPD	Energetic Particle Detector System
EPO	Educational and Public Outreach
FDOA	Flight Dynamics Operations Area
FEEPS	Fly's Eye Energetic Particle Sensor, part of EPD investigation
FGM	Flux Gate Magnetometer, combination of AFG and DFG
FPI	Fast Plasma Instrument
FSM	Fluxgate Search Coil Merged, combination of AFG, DFG, and SCM
GSFC	Goddard Spaceflight Center
HPCA	Hot Plasma Composition Analyzer
HSD	Heliospheric Science Division
ICD	Interface Control Document
IDPU	Instrument Data Processor Unit (FPI)

IDS	Interdisciplinary Scientists
IS	Instrument Suite
ITF	Instrument Team Facility
IWF	Institut für Weltraumforschung (Space Research Institute of the Austrian Academy of Sciences)
JHU	Johns Hopkins University
L2	Level 2 Science (used to refer to data products and/or the software used to create Level 2 science products)
L3	Level 3 Science (used to refer to data products and/or the software used to create Level 3 science products)
LASP	Laboratory for Atmospheric and Space Physics
LF	Low Frequency
MAP	Mission Archive Plan
MF	Medium Frequency
MLD	Mission Level Data (Level 3)
MMS	Magnetospheric Multiscale
MOC	Mission Operations Center
MRD	Mission Requirements Document
NAV	Navigation
PDMP	Project Data Management Plan
PDR	Preliminary Design Review
PLSA	Project Level Service Agreement
POC	Payload Operations Center (located at the SOC)
QA	Quality Assurance
RA	Resident Archive
R_E	Unit of measure: 1 Earth Radius
ROI	Region of (science) Interest, defined as geocentric apogee distances > 9 R_E for Phase 1, and > 15 R_E for Phase 2.
RTS	Relative Time Sequence commands
SCM	Search Coil Magnetometer, part of FIELDS investigation
SDC	Science Data Center (located at the SOC)
SDP	Spin-plane Double Probe (part of FIELDS investigation)
SMART	Solving Magnetospheric Acceleration Reconnection and Turbulence
SOC	Science Operations Center
SPASE	Space Physics Archive Search and Exchange
SPDF	Space Physics Data Facility
STP	Solar Terrestrial Probes
SWG	Science Working Group
SwRI	Southwest Research Institute

TBC	To be Confirmed
TBD	To be Determined
TDRSS	Tracking and Data Relay Satellite System
TOF	Time of Flight
UNH	University of New Hampshire
USN	Universal Space Network
VMO	Virtual Magnetospheric Observatory
VxO	Virtual Observatory

670-MMS-Proj-Plan-CMAD
Revision 2

Magnetospheric Multiscale (MMS) Project

Calibration and Measurement Algorithms Document (CMAD)

V2.0

Submitted: 22 November 2022

Goddard Space Flight Center
Greenbelt, Maryland

National Aeronautics and
Space Administration

MAGNETOSPHERIC MULTISCALE (MMS)
Calibration and Measurement Algorithms Document (CMAD)

Dr. Barbara Giles, GSFC MMS Project Scientist — 14 November 2022 Date

Dr. James Burch, SwRI MMS Science PI — 21 November 2022 Date

By signing this document, signatories are certifying that the content herein is acceptable direction for managing the project's data and that they will ensure its implementation by those over whom they have authority.

Copy to: HQ Program Scientist

REVISION HISTORY

Revision Level	DESCRIPTION	EFFECTIVE DATE
Rev 0	Outline submitted to FY2020 Senior Review	2 June 2020
Rev 1	Full Draft, released for review and validation by MMS ITF Team	15 Feb 2022
Rev 2	V2.0 Public Release	22 Nov 2022

TABLE OF CONTENTS

1.0 INTRODUCTION

1.1 GENERAL INFORMATION

The Magnetospheric Multiscale (MMS) mission is the fourth mission of the Solar Terrestrial Probe (STP) program of the National Aeronautics and Space Administration (NASA). The MMS mission utilizes four identically instrumented observatories to perform the first definitive study of magnetic reconnection in space and tests critical hypotheses about reconnection. Magnetic reconnection is the primary process by which energy is transferred from the solar wind to the Earth's magnetosphere and is also fundamental to the explosive release of energy during substorms and solar flares.

The MMS mission studies magnetic reconnection in the Earth's magnetosphere, magnetosheath, bowshock, and heliosphere within $29R_E$. The four MMS observatories primarily fly in a tetrahedral formation to unambiguously determine the orientation of the magnetic reconnection layer.

1.2 PURPOSE

The MMS Calibration and Measurement Algorithm Document (CMAD) describes the overall concept for calibrating the many instruments onboard Magnetospheric Multiscale (MMS), including pre-flight and in-flight calibrations, and details the algorithms for converting instrument signals to physical quantities, including signal estimates, error analyses, and error budgets.

This document is not designed to be the only reference for these aspects of the MMS instrumentation. Other, more detailed documents and publications are referenced that describe the instrumentation designs, operations, ground systems, and data products. For example, a close companion to this document is the MMS Data Product Management Plan (PDMP) and this document does not repeat the materials therein.

1.3 CONTENTS

All plans and algorithms are described as they were known during the applicable extended mission period. Future changes in instrument operations and/or understanding of calibrations and algorithms may require modifications to this document. The document is organized as follows:

Table 1-1 Contents: Sections and Instrumentation

Section and Associated Instrumentation: Particles / Other					
Section	2	3	4	5	6
Instrument	ASPOC	MEC	FPI	HPCA	EPD
Subsystem			DES		FEEPS
			DIS		EIS

	Section and Associated Instrumentation: Fields					
Section	7	8	9	10	11	12
Instrument	FIELDS	FIELDS: FGM	FIELDS: SCM	FIELDS: EDI	FIELDS: EDP	FIELDS: FSM
Subsystem	Overview	AFG		E-Field	ADP	
	Fields Timing	DFG		Electrons	SDP	

Acronyms Defined in Table of Contents and in Acronym List

1.4 MISSION OVERVIEW STATUS

The status of the instruments throughout this mission can be broken down between the respective instrument groups as illustrated throughout this document; meanwhile, the below table represents the status of instruments collectively in relation to one another within each spacecraft. All instruments are operating nominally with, remarkably, few exceptions. For greater descriptions of the statuses of each instrument and the work of their corresponding groups, see sections 2.0 through 12.0 of this document. It is important to note that the information in the following table is subject to change over the mission lifespan.

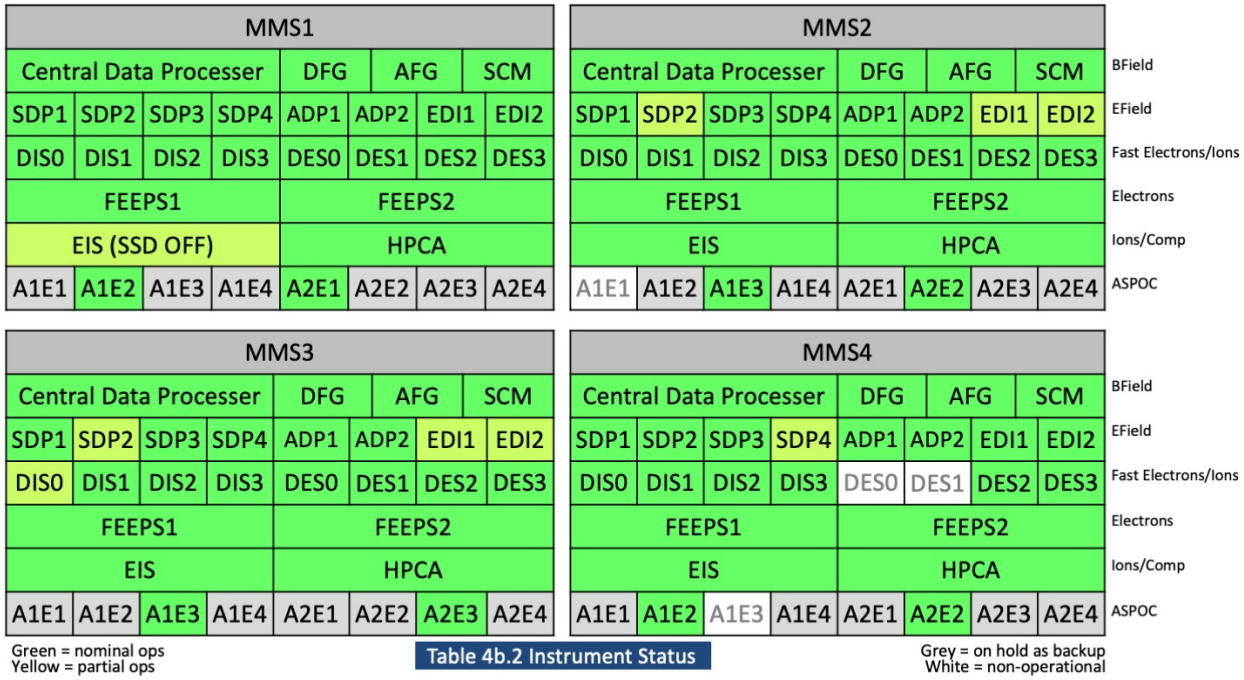

Table 1-2 Instrument Status Table

Throughout the lifespan of the mission, the spacecrafts have gone through, and continue to go through, the course of mission phases with each passing calendar year. Each mission phase determines varying science data collections and scheduled operations applicable to each individual instrument team. Within these phases, the mission orbits must satisfy certain engineering requirements with respect to and regard for the duration and depth of Earth's shadow that the spacecrafts are able to experience without restrain to their normal operations as well as with regard to the spacecraft's fuel usage, amongst other orbit constraints.

The mission phases based on particular start and end dates and differing descriptors and orbit ranges are demonstrated in the following table.

Mission Phase	Start	End	Phase Description	Orbit Range
Launch	n/a	March 15, 2015	n/a	n/a
Commissioning	March 15, 2015	Sept 1, 2015	Nightside -> Dusk Flank	1 – 173
Phase 1a	Sept 1, 2015	March 8, 2016	$12R_E$ Dayside	173 – 363

Phase 1x	March 8, 2016	Sept 12, 2016	12R_E Dayside, Nightside, Dusk	363 – 552
Phase 1b	Sept 12, 2016	Jan 31, 2017	12R_E Dayside	552 – 694
Phase 2a	Jan 31, 2016	May 1, 2017	Apogee Raise, Dawn	694 – 748
Phase 2b	May 1, 2017	Sept 1, 2017	25R_E Nightside	748 – 792
Phase 3a	Sept 1, 2017	Nov 14, 2017	25R_E Dusk Flank	792 – 818
Phase 3b	Nov 14, 2017	March 13, 2018	25R_E Dayside	818 – 860
Phase 3c	March 13, 2018	May 25, 2018	25R_E Dawn Flank	860 – 886
Phase 3d	May 25, 2018	Sept 28, 2018	25R_E Nightside	886 – 930
Phase 4a	Sept 28, 2018	Nov 29, 2018	25R_E Dusk Flank	930 – 953
Phase 4b	Nov 29, 2018	April 16, 2019	25R_E Dayside	953 – 997
Phase 4c	April 16, 2019	June 29, 2019	29R_E Dawn Flank	997 – 1018
Phase 4d	June 29, 2019	Sept 30, 2019	29R_E Nightside	1018 – 1044
Phase 5a	Sept 30, 2019	Nov 24, 2019	29R_E Dusk Flank	1044 – 1060
Phase 5b	Nov 24, 2019	April 23, 2020	29R_E Dayside	1060 - 1103
Phase 5c	April 23, 2020	June 22, 2020	29R_E Dawn Flank	1103 – 1121
Phase 5d	June 22, 2020	Oct 6, 2020	29R_E Nightside	1121 – 1150
Phase 6a	Oct 6, 2020	Nov 24, 2020	29R_E Dusk Flank	1150 – 1165
Phase 6b	Nov 24, 2020	April 27, 2021	29R_E Dayside	1165 – 1208
Phase 6c	April 27, 2021	June 24, 2021	29R_E Dawn Flank	1208 – 1224
Phase 6d	June 24, 2021	Oct 6, 2021	29R_E Nightside	1224 – 1255
Phase 7a	Oct 6, 2021	Nov 28, 2021	29R_E Dusk Flank	1255 – 1268
Phase 7b	Nov 28, 2021	April 28, 2022	29R_E Dayside	1268 – 1313
Phase 7c	April 28, 2022	June 9, 2022	29R_E Dawn Flank	1313 – 1325
Phase 7d	June 9, 2022	Oct 17, 2022	29R_E Nightside	1325 – 1362
Phase 8a	Oct 17, 2022		29R_E Dusk Flank	1362 -

Table 1-3 MMS Mission Phases

1.5 REFERENCES

The following documents and drawings in effect on the day this specification was signed **shall** apply to the extent specified herein. In the event of conflict between this document and any referenced document, the document with latest publication date will govern.

The following is a list of applicable references and publications.

Section	Document Number	Title	Revision/Date
Many	461-PROJ-PLAN-0139	MMS Project Data Management Plan	Rev 1 / tbd FY2021

Table 1-4 MMS Project Applicable Documents

2.0 ACTIVE SPACECRAFT POTENTIAL CONTROL (ASPOC)

2.1 ASPOC OVERVIEW

The ASPOC instrument emits a beam of positive indium ions at energies of order 4 to 12 keV and currents of up to ~70 μA in order to control the electrical potential of the spacecraft. The emission of positive charges from the spacecraft balances the excess of charge accumulating on the vehicle from interactions with the environment. For the case of primary concern here, where photoemission of electrons drives the spacecraft potential positive relative to the plasma potential, it is necessary to emit positive ions.

By adjusting the positive emission current, the spacecraft potential can thus be adjusted to near zero value. Hence, the output of the instrument is an energetic ion beam with known energy and controlled current. By applying currents of several 10's of μA on the MMS spacecraft, the equilibrium potential will in any environment be driven into a regime which is independent of the ambient plasma density, and mainly be governed by the active ion beam current and the properties (mainly current and energy distribution) of the photo-electrons from the spacecraft surface, both of them are constant.

As a result, the spacecraft potential will be clamped to a value at which the current of the photoelectrons overcoming the potential barrier around the spacecraft equals the ion beam current. This equilibrium is established at potentials of a few Volts positive, as an inverse function of the ion beam current.

Two ASPOC instruments are installed on each of the four spacecraft and emit ion beams in antiparallel direction for symmetry reasons. Each instrument contains four individual emitters which are operated one at a time, for redundancy reasons and in order to ensure the required lifetime. Two individual ion emitters are contained in one ion emitter "module" and have a common high voltage supply. The indium reservoir and the capillary sitting on top are kept at high voltage. The ion sources are individually and indirectly heated from below by a resistor embedded into a ceramic insulator tube. This scheme enables the source to be heated from a grounded power supply and the tip itself still being kept at high voltage. The selection of the active emitter is made by switching high voltage to one of the emitter modules, and secondly by heating the active emitter.

A full description of the instrument design can be found in the ASPOC User Manual. First results from space, showing the spacecraft control capabilities of ASPOC can be found in the publication:

Nakamura, R., K. Torkar, M. Andriopoulou, H. Jeszenszky, C. P. Escoubet, F. Cipriani, P. A. Lindqvist, S. A. Fuselier, C. J. Pollock, B. L. Giles, Y. Khotyaintsev (2017), Initial Results From the Active Spacecraft Potential Control Onboard Magnetospheric Multiscale Mission, IEEE Transactions on Plasma Science, 45 (8), 1847-1852**.**

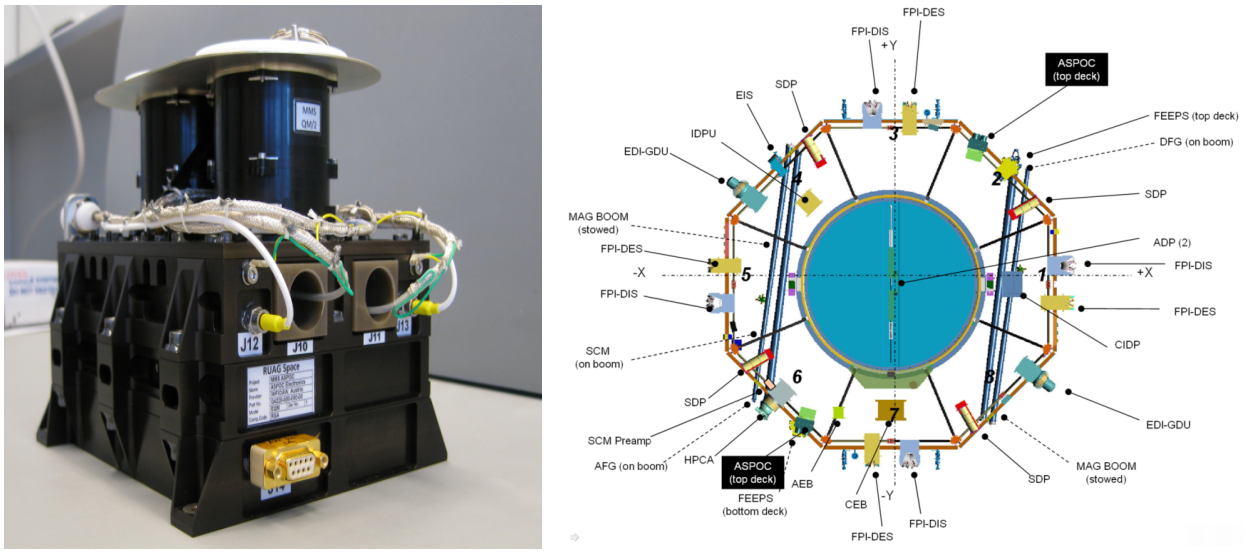

Figure 2-1 ASPOC Instrument Picture and Spacecraft Accommodation

The two ASPOC instruments are mounted at opposite sides of the instrument deck by means of brackets as shown in Figure 2-1. The ion beams of the two ASPOC instruments point in antiparallel directions such that the center axis of the ion beam is equidistant to the SDP probes. The only surfaces exposed to space shall be the top plates of the emitter modules. The rest of the instrument is inside the spacecraft envelope or covered by the Multi-Layer Insulation (MLI) of the spacecraft.

2.1.1 Status of ASPOC Instruments

The ASPOC instrument status as of September 30th, 2022 is shown in the following table:

Parameters (status as of 09/30/2022)	MMS1		MMS2		MMS3		MMS4	
	Unit A (FM9)	Unit B (FM2)	Unit A (FM3)	Unit B (FM5)	Unit A (FM7)	Unit B (FM8)	Unit A (FM4)	Unit B (FM6)
Emitter selection for phase 1-6	E2	E1	E3[1)]	E2	E3	E3	E3	E2
Filament impedance [Ohm]	204	220	209	208	220	207	212	220
Filament power [W]	0.83	0.62[2)]	0.83	0.83	0.70[*)]	0.83	0.83	0.66[2)]
Nominal operating current [µA]	10.0	10.0	10.0	10.0	10.0	10.0	10.0	10.0
Nominal beam energy [kV]	5.6	6.1	6.3	6.0	5.6	6.3	6.2	5.7
Cleaning cycles performed	4	0	0	0	0	0	0	4
Operating hours (total)	61363	61172	59331	60626	60799	60609	60691	60282
Operating hours (active)	20938	20937	19120	20617	20818	20824	20647	20648
Indium usage [%]	92.1	91.4	5.0[1)]	91.0	91.6	92.1	91.3	91.1
Rest @ 20 µA operation [h]	644	701	7740[1)]	732	687	647	708	726
Rest @ 10 µA operation [h]	1797	1956	21601[1)]	2043	1918	1807	1981	2027

[1)] Emitter changed 09/2021 [2)] Power reduced due to active filament temperature (impedance) control

Table 2-1 Status of ASPOC Instruments Table

2.2 ASPOC MEASUREMENT STANDARDS, VOLUME, AND TIMING

2.2.1 Accuracy of ASPOC Time Tags in L1b/SITL Data

ASPOC Level-1b and Scientist In The Loop (SITL) data products are containing calibrated raw data having a resolution that corresponds to the data acquisition cycle on-board. The following data products are available (given resolutions are typical values):

- Ion beam current, energy, ~ 1s resolution
- Total emitter current, ~ 1 s resolution
- Status and housekeeping, ~ 40 s resolution
- Spacecraft potential as used for control loop, ~1 s resolution
- Emitter heater current and voltage, ~ 20 s resolution
- Status flags and parameters, ~ 40 s resolution
- Secondary voltages, ~ 60 s resolution
- Internal temperatures, ~ 40 s

2.2.2 Accuracy of ASPOC Time Tags in L2 Data

ASPOC Level-2 products are daily files containing interpolated data at a resolution of 1 second (86400 records per file). For science analysis, ASPOC provides the following data:

- Ion beam current
  - individual ASPOC 1 and ASPOC 2 currents
  - and the sum
- Ion beam energies of individual ASPOCs
- Data quality information
- Individual ASPOC 1 and ASPOC 2 modes
- ASPOC ON/OFF status (ON indicates that at least one ASPOC is emitting ions)

2.2.3 Relative Telemetry Allocations and Data Volume

The nominal allocated downlink bit rate for one ASPOC unit is 150 Bits Per Second (BPS), which is composed as follows:

TELEMETRY PACKET		**SIZE**	**REGULAR ?**	**PERIOD**	**RATE**
NAME	**DESCRIPTION**	**[BYTES]**	**[YES/NO]**	**[SECS]**	**[BPS]**
ASxHNORM	Normal housekeeping data	96	Yes	40	19,20
ASxHEXTD	Extended housekeeping data	196	Yes	20	78,40
ASxHSTAT	Bent-pipe status message	20	Yes	4(*)	40,00
ASxHKRNL	Kernel status information	40	Yes	60	5,33
ASxHDUMP	Memory dump data	276	No	600	3,68
Total					**146,61**

Table 2-2 ASPOC Telemetry Allocation

(*) The ASPOC status message is generated once per second. During nominal operation, the Central Instrument Data Processor (CIDP) skips 3 out of 4 packets, resulting in a data period of 4 seconds.

Without memory dump packets, which are just downlinked on demand, the typical downlink data volume for one ASPOC unit is 1.51 Mbytes per day.

2.3 ASPOC CALIBRATION AND VALIDATION

2.3.1 Pre-Flight / On-Ground Calibration

The ASPOC instruments were switched ON, starting from March 28, 2015, during the commissioning phase. The commissioning activities consisted of different types of tests: low-voltage checkout, high-voltage checkout and single-emitter verification, simultaneous operation of two emitters, test of feedback loop using spacecraft potential information obtained from the spin-plane double probe (SDP) measurements, validation of effects on spacecraft potential control when the electron drift instrument (EDI) is emitting electron beams, long-term stability test, and interference test with other instruments.

It has already been shown in the early commissioning phase that ASPOC successfully controlled the spacecraft potential to be kept at values below 4 V, fulfilling the science requirement of MMS. As an example of commissioning-phase operations, Figure 2-2 shows the results from the extended dual-beam test of MMS4 performed on July 19, 2015. The spacecraft potential data transferred onboard ASPOC from SDP, ion currents emitted from ASPOC 1 and ASPOC 2, and the sum of the two emitters' currents are shown in Figure 2-2.

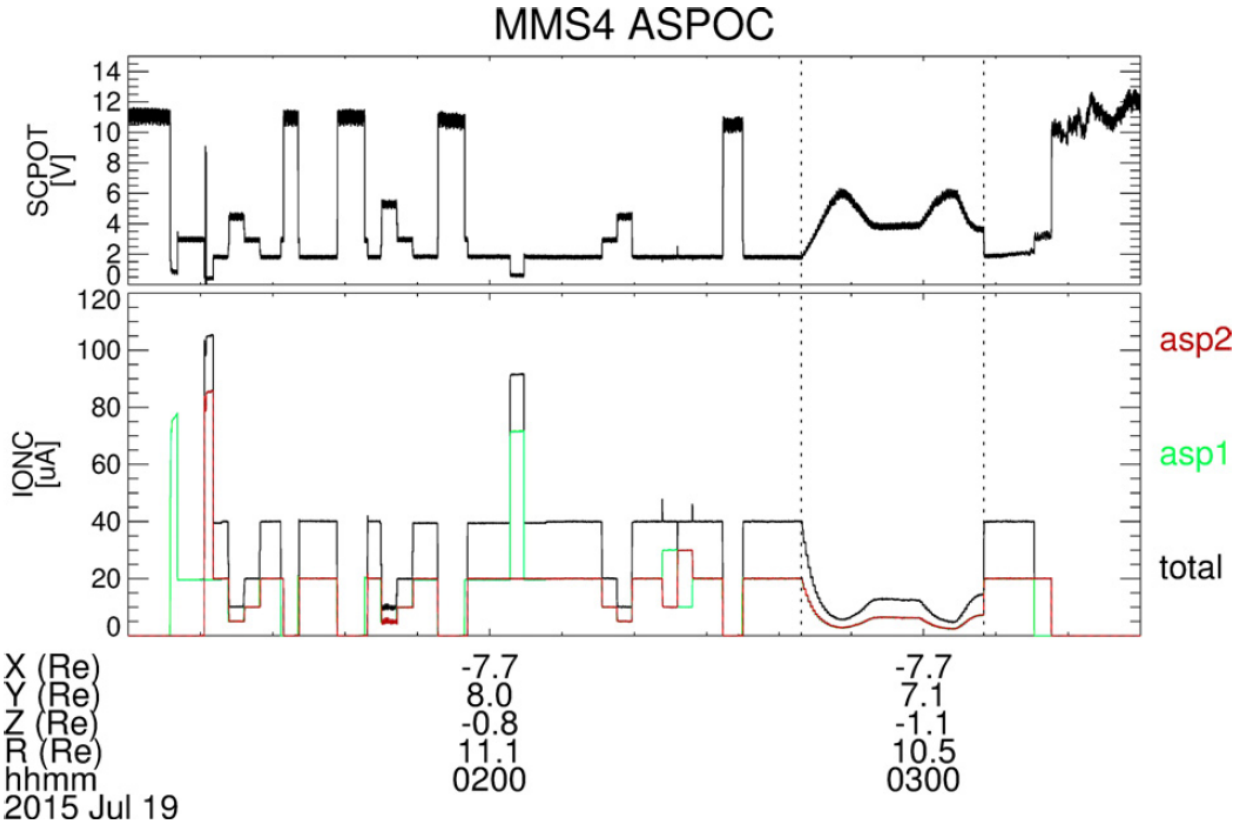

Figure 2-2 ASPOC Results from the Extended Dual-Beam Test on MMS4

During the extended tests, different current levels and different operation modes were tested. The nominal operation of ASPOC is to emit the ion beams by setting a constant current level for each of the ASPOC units. ASPOC, however, can also be operated in a way that a target spacecraft potential level is set and the ASPOC current level is automatically modified by referring to the spacecraft potential level onboard. This mode is called the feedback mode and was successfully tested during the time interval shown in Figure 2-2 (between the times indicated by the two vertical dotted lines). This mode also requires master–slave mode of two ASPOCs, for which the slave ASPOC duplicates the beam current of the master. The feedback mode not only allows keeping the spacecraft potential level close to the target value, but also enables avoiding unnecessary indium consumptions by emitting very strong ASPOC current. During this interval, the target spacecraft potential value was set to 4 V.

At the beginning of this test, the spacecraft potential was below 2 V and hence the total current level decreased. After a temporary overshoot to 6 V, the potential eventually settled at a correct constant level of 4 V after about 10 min. This procedure was repeated with a different master–slave configuration. By varying control loop parameters and the average time interval of SDP data, it is possible to tune the response time in order to minimize the overshoot level.

ASPOC started routine operations in a pseudo nominal configuration at the end of July 2015 after the completion of all the planned tests and the selection of the optimal emitter pairs for the operational phase. The nominal operation mode during the science phase is the constant current mode where a constant beam current level of 10 μA is set for both emitters. ASPOC has always been operating in this nominal mode during the following science phases. All the ASPOC level 2 science data products are publicly available from the Science Data Center (SDC) (https://lasp.colorado.edu/mms/sdc/public/).

First results from space showing the spacecraft control capabilities of ASPOC and calibration considerations, in particular

- Effects of ASPOC on Plasma Measurements,
- Plasma Density Derivation using ASPOC current and spacecraft potential, and Effects of ASPOC on Electric Field Measurements

A full description of ASPOC and its calibration results relative to this section can be found in the publication:

Nakamura, R., K. Torkar, M. Andriopoulou, H. Jeszenszky, C. P. Escoubet, F. Cipriani, P. A. Lindqvist, S. A. Fuselier, C. J. Pollock, B. L. Giles, Y. Khotyaintsev (2017), Initial Results From the Active Spacecraft Potential Control Onboard Magnetospheric Multiscale Mission, IEEE Transactions on Plasma Science, 45 (8), 1847-1852**.**

2.3.2 In-Flight Calibration

Given the nature and the comparatively easy design of the ASPOC instrument, no dedicated in-flight calibration activities are necessary.

Nevertheless, in order to characterize the relationship between the ion emission current and the Spacecraft (S/C) potential measured by the Spin-Plane Double Probe Instrument (SDP), ASPOC performs beam current sweeps on a regular basis. The sweeps cover a current range between 5 μA and 50 μA with steps of 5 μA.

Typically, but not always, the current sweeps will be scheduled in co-ordination with the overall planning at the entry into or at the exit from the region of interest, in intervals of one or more orbits.

2.3.3 Validation

Data validation and quality control includes visual inspection of plots produced from all data products and spot-checks of the data products proper. There is software in place to visualize the data products in combined displays, which facilitates the detection of inconsistencies and anomalies.

The consistency between data products will be checked in many aspects, including:

- Correlation between ion current and spacecraft potential,
- Correlation between ion current and total current flowing into the emitter,
- Correlation between currents in the emitter system and the derived quality flag,
- Correlation between ion current data products at different time resolutions,
- Correlation between instrument status and ion emission. This includes several checks, such as ion emission cannot occur with cold heater, in some instrument modes, without voltage applied to emitter.

Some of these checks can be carried out by the production software and raise warning messages. The other checks will be carried out manually/visually.

If an anomaly is found, which is related to the processing software, the production will be stopped, and new versions of data products will be generated after correction. If an identified anomaly can be attributed to the instrument performance or status, a new entry into the caveats file will be generated.

The dedicated display software also supports manual entries into the caveats file. In order to check the quality of the data products, not only the dedicated software will be used, but also the Common Data Format (CDF) validation tools will be used to check the syntax of the products.

2.4 MEASUREMENT ALGORITHM DESCRIPTIONS

2.4.1 Theoretical Basis (Operating Modes)

There are several state machines in the flight software (FSW) with a small number of operational modes in each.

In standby mode (STDB) both the emitters and their heaters are turned off. The standby mode is also the safe mode of the instrument, to which it returns autonomously under certain error conditions. The transition into standby mode also clears all error flags and the emitter selection, and disables high voltage and the heaters.

Start-up (STUP) is a state of the instrument at the beginning of an active mode when the emitter is being warmed up and ion emission has not yet started. Depending on ambient temperature and emitter condition it takes about 30 to 35 minutes to reach a temperature inside the emitters which is sufficient to ignite the ion beam. The start-up mode duration is commandable and shall exceed the actual warm-up time; the nominal value is 35 minutes. Within this period the "instrument mode" reported in telemetry will be already the commanded target mode, although there is no ion emission yet.

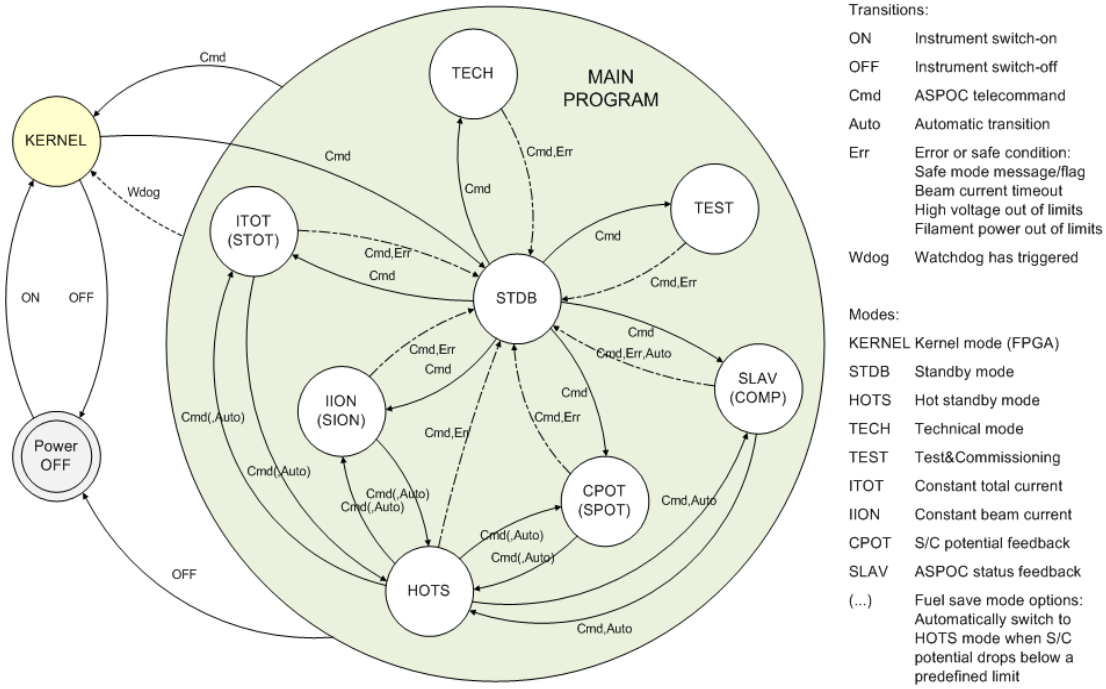

Figure 2-3 ASPOC Operating Modes

In order to reduce the time before emission starts, a “hot standby” mode (HOTS) keeps the indium in a liquid state. This mode can be used to interrupt the ion emission by command, without change of modes or emitters before and after the break. The re-ignition time is reduced to the time required to sweep the high voltage (less than a minute).

The most widely used active mode of the instrument will be the "constant total current mode" (ITOT). It sets a constant output current of the high voltage unit, which includes any losses inside the lens system. Experience has shown that the resulting emission of an almost constant ion current fulfils all requirements for spacecraft potential control in the magnetosphere and the solar wind even without on-board feedback from measurements of the spacecraft potential. When the fuel save mode option (STOT) is activated, the instrument also listens to the S/C potential message. If the beam is on, and the potential remains below the off-trigger value for more than the trigger delay time, then the instrument switches into hot standby mode. If the beam is off, and the potential remains above the on-trigger value for more than the trigger delay time, then the instrument performs in the same way as in the standard total current mode.

In "constant ion current mode" (IION) the processor of the instrument reads the monitor of the outgoing beam current and adjusts the output current of the high voltage supply to compensate for any losses in the system. When the fuel save mode option (SION) is activated, the instrument also listens to the S/C potential message. If the beam is on, and the potential remains below the off-trigger value for more than the trigger delay time, then the instrument switches into hot standby mode. If the beam is off, and the potential remains above the on-trigger value for more than the trigger delay time, then the instrument performs in the same way as in the standard ion current mode.

In the so-called feedback mode (CPOT), a measurement of the spacecraft potential is supplied to ASPOC by the SDP Instrument and this information is then used to adjust the beam current in order to maintain a constant value of the potential in a closed-loop scheme. The measurements of the spacecraft potential are updated once every second and sent to ASPOC via dedicated messages (CIDP Bent-Pipe Telemetry).

When the fuel save mode option (SPOT) is activated, the beam is on, and the potential remains below the off-trigger value for more than the trigger delay time, then the instrument switches into hot standby mode. If the beam is off, and the potential remains above the on-trigger value for more than the trigger delay time, then the instrument performs in the same way as in the standard feedback mode.

In slave mode (SLAV), the instrument performs a startup as in constant ion current mode. As soon as normal operational status is reached (startup completed), the instrument listens to the beam current and mode information received through the ASPOC status message from the other (master) unit (CIDP Bent-Pipe Telemetry) and follows the master. When the compensating mode option (COMP) is activated and the beam current of the master is non-zero, the instrument uses a set value for its own control loop twice the set value of the beam current minus the beam current of the master. In this way the sum of both ion beam currents stays at 2 times the value of the beam current commanded to the compensating slave.

The “test and commissioning” mode (TEST) will be used occasionally for low level software and interface tests and to measure the effective filament temperature when the instrument is active. Finally, a technical mode (TECH) is available for low-level commanding during commissioning and re-commissioning of emitters and to adjust operational parameters.

2.4.2 Conversion of Instrument Signals

The transformation of analogue parameters from raw values (R) into physical values (P) can be performed by means of a linear relation:

$$P = C0 + C1 * R + C2 * R^2$$

Table 2-3 lists values of C0, C1 and C2, and the values of P for different raw data values R.

#	C0	C1	C2	R	P(R)	UNIT	DESCRIPTION
1	-273.0	0.1221	0.0	0 4095	-273.0 227.0	°C	Temperature sensors
2	0.0	0.001221	0.0	0 4095	0.00 5.00	V	+3.3 V voltage monitor
3	0.0	0.001589	0.0	0 4095	0.00 6.51	V	+5 V voltage monitor
4	0.0	0.003391	0.0	0 4095	0.00 13.89	V	+12 V voltage montor
5	0.0	-0.004223	0.0	0 4095	0.00 -17.29	V	-12 V voltage monitor
6	0.0	0.030525	0.0	0 4095	0.0 125.0	µA	Emitter currents
7	0.0	0.0030525	0.0	0 4095	0.00 12.50	kV	High voltage values
8	0.0	0.004884	0.0	0 4095	0.00 20.00	V	Filament voltage monitor
9	0.0	0.030525	0.0	0 4095	0.0 125.0	mA	Filament current monitor

10	0.0	0.001221	0.0	0 4095	0.00 5.00	V	Filament and HV converter output
11	0.0	0.004	0.0	0 4095	0.00 16.38	V	Spacecraft potential
12	0.0	0.0006105	0.0	0 4095	0.00 2.50	W	Filament power
13	0.0	0.078144	0.0	0 4095	0.0 320.0	Ohm	Filament impedance
14	-241.549	0.17775586	8.004346e-6	236 1280 4095	-199.0 -0.9 620.6	°C	Filament temperature(*)

Table 2-3 ASPOC Calibration Table

(*) The calibration curve for the filament temperature is an approximation (maximum deviation is +/- 1 °C for the given range).

2.4.3 Error Analysis and Known Features in the Dataset

This chapter identifies known issues in the ASPOC data products, whereby data quality aspects as described in section 2.4.4 were taken into account. The information is provided in tabular format, containing the spacecraft, the affected time range, the number of records with an emission quality less than 2 (moderate to poor), and a severity rating (0=low, 1=high) for each anomaly.

S/C	Start Date	End Date	#Records	Severity
MMS1	2015-07-07T18:46:47Z	2015-07-07T19:02:34Z	948	1.000
MMS1	2015-07-10T18:11:40Z	2015-07-10T18:12:18Z	39	1.000
MMS1	2015-07-15T15:35:07Z	2015-07-15T15:35:43Z	37	1.000
MMS1	2015-07-18T17:58:23Z	2015-07-18T17:59:00Z	38	1.000
MMS1	2015-08-04T21:15:00Z	2015-08-04T21:50:39Z	46	0.021
MMS1	2015-08-11T13:44:26Z	2015-08-11T23:59:46Z	1632	0.044
MMS1	2015-08-12T00:00:14Z	2015-08-12T17:44:52Z	659	0.010
MMS1	2015-08-13T16:02:32Z	2015-08-13T23:59:43Z	6371	0.223
MMS1	2015-08-14T00:00:11Z	2015-08-14T23:59:58Z	23506	0.272
MMS1	2015-08-15T00:00:00Z	2015-08-15T23:59:58Z	16012	0.185
MMS1	2015-08-16T00:00:00Z	2015-08-16T23:59:58Z	35343	0.409
MMS1	2015-08-17T00:00:00Z	2015-08-17T15:30:44Z	12769	0.229
MMS1	2015-09-16T17:53:19Z	2015-09-16T19:00:17Z	1476	0.367
MMS1	2015-10-06T07:30:45Z	2015-10-06T08:16:25Z	40	0.015
MMS1	2015-11-07T13:25:46Z	2015-11-07T14:27:03Z	124	0.034
MMS1	2016-01-12T08:46:09Z	2016-01-12T09:26:14Z	1546	0.643
MMS1	2016-01-13T06:04:20Z	2016-01-13T06:27:28Z	364	0.262
MMS1	2016-04-24T00:35:17Z	2016-04-24T00:37:06Z	37	0.336
MMS1	2016-05-02T21:33:39Z	2016-05-02T23:35:34Z	248	0.034
MMS1	2016-11-14T19:51:19Z	2016-11-14T20:54:48Z	2509	0.659
MMS1	2017-02-22T21:19:53Z	2017-02-22T22:42:16Z	169	0.034
MMS1	2017-02-24T03:25:56Z	2017-02-24T06:35:54Z	393	0.034
MMS1	2017-02-25T11:36:22Z	2017-02-25T14:28:34Z	1987	0.192
MMS1	2017-02-26T19:17:33Z	2017-02-26T22:32:14Z	6265	0.536
MMS1	2017-02-28T03:13:56Z	2017-02-28T06:28:37Z	8950	0.766
MMS1	2017-03-01T11:09:48Z	2017-03-01T14:24:29Z	6975	0.597

S/C	Start Date	End Date	#Records	Severity
MMS1	2017-03-02T20:47:02Z	2017-03-02T23:59:58Z	11562	0.999
MMS1	2017-03-03T00:00:00Z	2017-03-03T00:01:45Z	106	1.000
MMS1	2017-03-04T08:05:47Z	2017-03-04T10:51:23Z	5895	0.593
MMS1	2017-03-07T06:48:59Z	2017-03-07T06:49:59Z	61	1.000
MMS1	2017-03-17T05:52:40Z	2017-03-17T05:53:44Z	65	1.000
MMS1	2017-08-15T00:58:47Z	2017-08-15T19:20:37Z	1678	0.025
MMS1	2017-12-15T02:05:01Z	2017-12-15T05:29:07Z	288	0.024
MMS1	2017-12-17T06:26:22Z	2017-12-17T09:02:26Z	3879	0.414
MMS1	2018-06-04T07:52:35Z	2018-06-04T11:56:00Z	1480	0.101
MMS1	2018-06-23T04:47:22Z	2018-06-23T05:26:36Z	2350	0.998
MMS1	2018-07-12T16:39:57Z	2018-07-12T23:59:58Z	561	0.021
MMS1	2018-07-13T00:00:00Z	2018-07-13T00:01:48Z	33	0.303
MMS1	2018-07-18T13:52:10Z	2018-07-18T13:56:30Z	38	0.146
MMS1	2018-08-10T21:53:40Z	2018-08-10T21:59:48Z	250	0.678
MMS1	2018-08-14T23:22:08Z	2018-08-14T23:30:12Z	187	0.386
MMS1	2018-09-06T21:29:53Z	2018-09-06T21:31:27Z	71	0.747
MMS1	2018-09-07T00:55:08Z	2018-09-07T01:34:47Z	49	0.021
MMS1	2018-11-05T11:07:57Z	2018-11-05T11:09:56Z	43	0.358
MMS1	2018-11-06T07:02:07Z	2018-11-06T07:07:10Z	24	0.079
MMS1	2018-12-22T07:17:40Z	2018-12-22T07:18:21Z	25	0.595
MMS1	2018-12-25T18:02:09Z	2018-12-25T23:13:13Z	395	0.021
MMS1	2018-12-30T18:54:32Z	2018-12-30T20:17:25Z	167	0.034
MMS1	2019-01-03T00:01:59Z	2019-01-03T00:04:25Z	57	0.388
MMS1	2019-01-09T10:03:49Z	2019-01-09T23:54:22Z	534	0.011
MMS1	2019-01-10T04:13:47Z	2019-01-10T04:49:01Z	40	0.019
MMS1	2019-01-11T04:21:45Z	2019-01-11T09:10:18Z	13522	0.781
MMS1	2019-02-17T18:44:35Z	2019-02-17T18:45:57Z	83	1.000
MMS1	2019-02-20T19:34:34Z	2019-02-20T19:41:15Z	210	0.522
MMS1	2019-09-16T15:51:11Z	2019-09-16T15:52:21Z	23	0.324
MMS1	2019-12-24T17:39:21Z	2019-12-24T20:10:44Z	98	0.011
MMS1	2019-12-27T15:14:57Z	2019-12-27T15:16:29Z	57	0.613
MMS1	2020-08-28T11:01:49Z	2020-08-28T11:03:14Z	58	0.674
MMS1	2020-08-30T20:45:31Z	2020-08-30T20:46:31Z	45	0.738
MMS1	2020-09-25T00:58:32Z	2020-09-25T01:00:51Z	37	0.264
MMS1	2020-11-03T18:04:46Z	2020-11-03T18:08:11Z	45	0.218
MMS1	2020-11-14T09:13:32Z	2020-11-14T09:41:26Z	1675	1.000
MMS1	2020-11-16T20:24:42Z	2020-11-16T20:37:39Z	778	1.000
MMS1	2020-11-28T06:52:41Z	2020-11-28T07:21:25Z	284	0.165
MMS1	2020-12-01T00:52:30Z	2020-12-01T01:02:54Z	187	0.299
MMS1	2021-09-17T00:44:49Z	2021-09-17T04:04:08Z	5663	0.473
MMS1	2021-10-04T16:45:44Z	2021-10-04T16:56:49Z	412	0.619
MMS1	2021-10-11T21:35:57Z	2021-10-11T21:52:19Z	111	0.113
MMS1	2021-12-25T14:50:21Z	2021-12-25T18:59:24Z	5894	0.394
MMS1	2021-12-26T03:24:22Z	2021-12-26T06:59:35Z	3813	0.295
MMS1	2021-12-29T16:17:46Z	2021-12-29T16:19:55Z	23	0.177
MMS1	2022-01-05T08:36:04Z	2022-01-05T21:36:58Z	664	0.014
MMS1	2022-01-08T17:14:59Z	2022-01-08T22:14:05Z	1404	0.078
MMS1	2022-01-12T18:17:52Z	2022-01-12T18:19:04Z	71	0.973
MMS1	2022-01-15T18:29:04Z	2022-01-15T18:30:04Z	61	1.000
MMS1	2022-01-19T09:43:08Z	2022-01-19T20:57:53Z	1605	0.040
MMS1	2022-01-22T19:52:51Z	2022-01-22T22:44:34Z	622	0.060
MMS1	2022-01-23T00:23:12Z	2022-01-23T12:18:29Z	8098	0.189

S/C	Start Date	End Date	#Records	Severity
MMS1	2022-01-26T08:34:23Z	2022-01-26T23:44:03Z	1779	0.033
MMS1	2022-01-29T20:59:25Z	2022-01-29T23:52:11Z	472	0.046
MMS1	2022-01-30T00:02:58Z	2022-01-30T09:50:17Z	561	0.016
MMS1	2022-02-05T23:16:25Z	2022-02-05T23:44:31Z	44	0.026
MMS1	2022-02-06T00:36:49Z	2022-02-06T10:04:28Z	769	0.023
MMS1	2022-02-09T11:52:01Z	2022-02-09T13:32:11Z	1722	0.286
MMS1	2022-02-12T23:16:55Z	2022-02-12T23:48:10Z	385	0.205
MMS1	2022-02-13T00:10:30Z	2022-02-13T10:58:27Z	1254	0.032
MMS1	2022-02-16T15:00:44Z	2022-02-16T15:03:50Z	179	0.957
MMS1	2022-02-20T00:20:38Z	2022-02-20T16:17:41Z	2058	0.036
MMS1	2022-03-02T14:37:26Z	2022-03-02T15:12:50Z	270	0.127
MMS1	2022-03-03T01:41:26Z	2022-03-03T03:42:54Z	111	0.015
MMS1	2022-03-06T05:55:12Z	2022-03-06T19:16:07Z	4919	0.102
MMS1	2022-03-09T14:54:29Z	2022-03-09T18:25:20Z	428	0.034
MMS1	2022-03-10T06:30:32Z	2022-03-10T07:19:04Z	31	0.011
MMS1	2022-03-13T03:19:30Z	2022-03-13T06:16:35Z	5947	0.560
MMS1	2022-03-17T04:25:03Z	2022-03-17T09:00:42Z	978	0.059
MMS1	2022-03-20T04:20:11Z	2022-03-20T20:32:51Z	6916	0.119
MMS1	2022-03-23T16:39:29Z	2022-03-23T21:17:19Z	6706	0.402
MMS1	2022-03-27T05:04:28Z	2022-03-27T19:36:15Z	11948	0.228
MMS1	2022-03-30T18:03:35Z	2022-03-30T22:54:10Z	751	0.043
MMS1	2022-03-31T06:16:43Z	2022-03-31T08:18:10Z	1328	0.182
MMS1	2022-04-03T06:14:17Z	2022-04-03T23:54:49Z	736	0.012
MMS1	2022-04-06T21:34:55Z	2022-04-06T22:26:26Z	62	0.020
MMS1	2022-04-10T07:07:07Z	2022-04-10T11:06:19Z	1103	0.077
MMS1	2022-04-13T19:35:41Z	2022-04-13T23:59:58Z	10749	0.678
MMS1	2022-04-14T00:00:00Z	2022-04-14T13:56:13Z	9541	0.190
MMS1	2022-04-17T07:59:17Z	2022-04-17T23:55:28Z	7439	0.130
MMS1	2022-04-18T00:05:54Z	2022-04-18T02:36:51Z	223	0.025
MMS1	2022-04-20T20:23:19Z	2022-04-20T21:09:03Z	87	0.032
MMS1	2022-04-24T08:51:15Z	2022-04-24T23:53:43Z	1523	0.028
MMS1	2022-04-25T00:01:08Z	2022-04-25T04:16:45Z	771	0.050
MMS1	2022-04-27T21:25:58Z	2022-04-27T22:30:16Z	156	0.040
MMS1	2022-04-28T01:57:30Z	2022-04-28T16:26:45Z	5628	0.108
MMS1	2022-05-01T11:09:04Z	2022-05-01T11:59:28Z	1201	0.397
MMS1	2022-05-05T01:27:11Z	2022-05-05T18:56:46Z	1973	0.031
MMS1	2022-05-22T11:55:10Z	2022-05-22T12:08:44Z	815	1.000
MMS1	2022-05-23T06:53:56Z	2022-05-23T11:35:43Z	1783	0.105
MMS1	2022-05-29T14:00:02Z	2022-05-29T14:03:17Z	196	1.000
MMS1	2022-06-02T04:03:33Z	2022-06-02T19:05:08Z	863	0.016
MMS1	2022-06-05T13:53:53Z	2022-06-05T16:10:53Z	160	0.019
MMS1	2022-06-06T02:16:04Z	2022-06-06T06:58:59Z	3283	0.193
MMS1	2022-06-17T06:45:25Z	2022-06-17T06:56:42Z	319	0.471
MMS1	2022-06-20T20:11:03Z	2022-06-20T23:37:01Z	2361	0.191
MMS1	2022-06-23T01:18:54Z	2022-06-23T03:22:52Z	832	0.112
MMS1	2022-06-24T07:57:12Z	2022-06-24T11:02:32Z	936	0.084
MMS1	2022-06-26T14:23:06Z	2022-06-26T17:56:22Z	318	0.025
MMS1	2022-06-29T21:33:41Z	2022-06-29T21:57:36Z	288	0.201
MMS1	2022-06-30T00:28:45Z	2022-06-30T00:29:20Z	36	1.000
MMS1	2022-07-01T04:06:19Z	2022-07-01T04:08:36Z	47	0.341
MMS1	2022-07-03T06:24:01Z	2022-07-03T06:25:35Z	62	0.653
MMS1	2022-07-06T17:47:46Z	2022-07-06T18:29:27Z	325	0.130

S/C	Start Date	End Date	#Records	Severity
MMS1	2022-07-07T01:41:02Z	2022-07-07T19:07:48Z	853	0.014
MMS1	2022-07-15T04:33:10Z	2022-07-15T04:39:42Z	338	0.860
MMS1	2022-07-16T07:38:39Z	2022-07-16T11:48:49Z	1187	0.079
MMS1	2022-07-23T03:37:56Z	2022-07-23T12:36:57Z	721	0.022
MMS1	2022-07-24T07:00:56Z	2022-07-24T20:59:02Z	1489	0.030
MMS1	2022-07-25T07:21:19Z	2022-07-25T19:53:25Z	568	0.013
MMS1	2022-08-12T16:05:33Z	2022-08-12T23:59:58Z	9668	0.340
MMS1	2022-08-13T00:00:00Z	2022-08-13T23:59:58Z	37407	0.433
MMS1	2022-08-14T00:00:00Z	2022-08-14T23:59:56Z	63803	0.738
MMS1	2022-08-15T00:04:44Z	2022-08-15T00:41:14Z	1018	0.465
MMS1	2022-08-16T16:19:34Z	2022-08-16T17:04:25Z	387	0.144
MMS1	2022-08-24T03:09:57Z	2022-08-24T23:42:09Z	1507	0.020
MMS1	2022-08-25T00:00:36Z	2022-08-25T02:41:33Z	1275	0.132
MMS1	2022-09-01T10:03:17Z	2022-09-01T12:03:59Z	500	0.069
MMS1	2022-09-05T16:21:09Z	2022-09-05T22:15:03Z	4996	0.235
MMS1	2022-09-09T20:43:35Z	2022-09-09T23:40:04Z	1588	0.150
MMS1	2022-09-16T14:16:27Z	2022-09-16T15:02:54Z	46	0.016
MMS1	2022-09-21T04:20:07Z	2022-09-21T21:16:55Z	52044	0.853
MMS2	2015-07-01T02:08:37Z	2015-07-01T04:03:03Z	82	0.012
MMS2	2015-07-20T15:20:27Z	2015-07-20T15:22:07Z	101	1.000
MMS2	2015-07-23T01:08:08Z	2015-07-23T01:09:03Z	56	1.000
MMS2	2015-08-20T22:22:52Z	2015-08-20T23:59:12Z	74	0.013
MMS2	2015-08-30T10:00:11Z	2015-08-30T22:10:55Z	1233	0.028
MMS2	2015-09-21T06:11:32Z	2015-09-21T14:00:50Z	685	0.024
MMS2	2015-12-31T09:37:54Z	2015-12-31T10:17:10Z	161	0.068
MMS2	2017-02-17T23:17:56Z	2017-02-17T23:19:56Z	114	0.942
MMS2	2017-03-07T06:38:32Z	2017-03-07T06:39:31Z	60	1.000
MMS2	2017-03-17T05:43:26Z	2017-03-17T05:44:30Z	64	0.985
MMS2	2017-08-12T03:34:36Z	2017-08-12T03:35:07Z	30	0.938
MMS2	2017-08-13T02:15:47Z	2017-08-13T02:17:28Z	87	0.853
MMS2	2017-08-27T00:42:06Z	2017-08-27T00:42:31Z	25	0.962
MMS2	2017-09-19T23:20:43Z	2017-09-19T23:21:15Z	30	0.909
MMS2	2017-09-20T13:48:24Z	2017-09-20T13:49:27Z	56	0.875
MMS2	2017-09-23T05:59:40Z	2017-09-23T06:00:34Z	53	0.964
MMS2	2017-10-12T15:49:08Z	2017-10-12T15:49:55Z	42	0.875
MMS2	2017-11-06T23:11:06Z	2017-11-06T23:24:04Z	302	0.388
MMS2	2017-11-08T01:38:57Z	2017-11-08T13:31:58Z	567	0.013
MMS2	2017-11-09T15:52:20Z	2017-11-09T23:33:41Z	1595	0.058
MMS2	2017-11-10T03:20:13Z	2017-11-10T17:39:37Z	1243	0.024
MMS2	2017-11-13T02:31:27Z	2017-11-13T18:46:47Z	8148	0.139
MMS2	2018-01-03T16:59:58Z	2018-01-03T17:00:22Z	22	0.880
MMS2	2018-02-09T00:06:05Z	2018-02-09T11:24:32Z	2448	0.060
MMS2	2018-04-29T04:28:37Z	2018-04-29T04:29:52Z	70	0.921
MMS2	2018-05-04T13:42:14Z	2018-05-04T13:42:45Z	28	0.875
MMS2	2018-05-21T13:23:57Z	2018-05-21T13:24:33Z	35	0.946
MMS2	2018-05-26T13:52:54Z	2018-05-26T13:53:23Z	28	0.933
MMS2	2018-05-27T11:22:41Z	2018-05-27T11:23:11Z	30	0.968
MMS2	2018-06-06T05:38:04Z	2018-06-06T05:38:48Z	44	0.978
MMS2	2018-06-15T22:55:00Z	2018-06-15T22:55:25Z	25	0.962
MMS2	2018-06-27T00:33:52Z	2018-06-27T00:34:35Z	37	0.841
MMS2	2018-07-01T02:34:06Z	2018-07-01T02:34:57Z	48	0.923
MMS2	2018-07-04T07:03:42Z	2018-07-04T07:04:24Z	42	0.977

S/C	Start Date	End Date	#Records	Severity
MMS2	2018-07-08T10:01:42Z	2018-07-08T10:02:05Z	24	1.000
MMS2	2018-07-22T02:20:09Z	2018-07-22T11:23:32Z	759	0.023
MMS2	2018-07-26T18:22:27Z	2018-07-26T18:23:28Z	54	0.871
MMS2	2018-08-16T11:06:25Z	2018-08-16T11:06:50Z	25	0.962
MMS2	2018-08-19T19:40:07Z	2018-08-19T19:50:33Z	61	0.097
MMS2	2018-08-27T14:57:58Z	2018-08-27T14:58:33Z	33	0.917
MMS2	2018-09-07T11:27:25Z	2018-09-07T11:27:51Z	25	0.926
MMS2	2018-09-10T01:56:43Z	2018-09-10T01:57:13Z	28	0.903
MMS2	2018-09-11T09:23:22Z	2018-09-11T09:24:03Z	37	0.881
MMS2	2018-09-22T01:39:38Z	2018-09-22T01:40:03Z	24	0.923
MMS2	2018-09-29T11:53:27Z	2018-09-29T11:53:53Z	24	0.889
MMS2	2018-10-17T11:50:35Z	2018-10-17T11:51:11Z	37	1.000
MMS2	2018-10-26T08:58:08Z	2018-10-26T08:58:29Z	21	0.955
MMS2	2018-11-14T15:53:55Z	2018-11-14T23:52:31Z	363	0.013
MMS2	2018-11-15T00:20:55Z	2018-11-15T23:56:57Z	1220	0.014
MMS2	2018-11-16T00:04:02Z	2018-11-16T23:38:26Z	6303	0.074
MMS2	2018-11-17T01:47:02Z	2018-11-17T22:51:10Z	1432	0.019
MMS2	2018-11-18T12:49:28Z	2018-11-18T22:35:57Z	1409	0.040
MMS2	2019-02-21T10:44:55Z	2019-02-21T18:33:59Z	1976	0.070
MMS2	2019-02-22T00:24:33Z	2019-02-22T16:00:32Z	1009	0.018
MMS2	2019-09-13T21:36:53Z	2019-09-13T21:37:23Z	31	1.000
MMS2	2019-09-17T18:13:49Z	2019-09-17T23:16:47Z	914	0.050
MMS2	2019-09-23T06:49:53Z	2019-09-23T06:50:16Z	22	0.917
MMS2	2019-09-28T11:19:17Z	2019-09-28T11:19:39Z	22	0.957
MMS2	2019-10-03T15:47:06Z	2019-10-03T15:47:29Z	23	0.958
MMS2	2019-10-05T23:39:08Z	2019-10-05T23:39:43Z	34	0.944
MMS2	2020-07-07T21:49:47Z	2020-07-07T22:50:06Z	90	0.025
MMS2	2020-10-31T03:42:22Z	2020-10-31T06:41:30Z	957	0.089
MMS2	2020-12-01T00:52:00Z	2020-12-01T02:04:48Z	1390	0.318
MMS2	2020-12-12T09:06:53Z	2020-12-12T09:31:21Z	1386	0.943
MMS2	2020-12-15T01:34:26Z	2020-12-15T20:57:31Z	8031	0.115
MMS2	2021-09-06T12:54:04Z	2021-09-06T16:25:57Z	191	0.015
MMS2	2021-09-07T00:11:49Z	2021-09-07T02:51:37Z	2868	0.299
MMS2	2021-09-16T20:33:05Z	2021-09-16T20:35:16Z	132	1.000
MMS2	2021-09-23T13:21:37Z	2021-09-23T14:28:34Z	266	0.066
MMS2	2021-11-02T16:29:53Z	2021-11-02T20:27:30Z	1268	0.089
MMS2	2022-02-13T00:48:14Z	2022-02-13T00:49:26Z	73	1.000
MMS2	2022-03-17T05:25:39Z	2022-03-17T08:35:41Z	232	0.020
MMS2	2022-07-07T20:07:21Z	2022-07-07T22:37:16Z	4686	0.521
MMS3	2015-07-15T22:16:31Z	2015-07-15T22:49:35Z	162	0.082
MMS3	2015-07-18T15:34:28Z	2015-07-18T15:35:41Z	74	1.000
MMS3	2015-07-19T17:59:37Z	2015-07-19T18:00:25Z	49	1.000
MMS3	2017-01-04T14:48:46Z	2017-01-04T15:04:35Z	25	0.026
MMS3	2017-01-19T11:56:06Z	2017-01-19T13:57:51Z	244	0.033
MMS3	2017-03-17T13:40:44Z	2017-03-17T13:41:48Z	65	1.000
MMS3	2017-11-22T14:11:54Z	2017-11-22T14:50:17Z	257	0.112
MMS3	2018-01-12T01:51:12Z	2018-01-12T01:52:10Z	56	0.949
MMS3	2018-01-26T07:40:21Z	2018-01-26T08:03:43Z	71	0.051
MMS3	2018-04-23T18:35:05Z	2018-04-23T19:04:13Z	1120	0.640
MMS3	2018-07-12T15:15:46Z	2018-07-12T20:57:03Z	5177	0.253
MMS3	2018-08-06T06:46:05Z	2018-08-06T08:08:36Z	131	0.026
MMS3	2018-08-12T06:08:03Z	2018-08-12T06:11:29Z	39	0.188

S/C	Start Date	End Date	#Records	Severity
MMS3	2018-09-20T10:35:57Z	2018-09-20T11:37:44Z	45	0.012
MMS3	2018-10-20T11:17:39Z	2018-10-20T11:39:36Z	257	0.195
MMS3	2018-10-27T17:17:49Z	2018-10-27T19:03:30Z	117	0.018
MMS3	2018-11-04T12:44:50Z	2018-11-04T14:04:44Z	55	0.011
MMS3	2018-11-10T13:42:43Z	2018-11-10T17:18:16Z	10671	0.825
MMS3	2018-11-16T03:40:40Z	2018-11-16T03:57:44Z	56	0.055
MMS3	2018-12-15T23:31:59Z	2018-12-15T23:34:25Z	147	1.000
MMS3	2018-12-17T18:21:42Z	2018-12-17T18:22:08Z	21	0.778
MMS3	2018-12-31T05:59:49Z	2018-12-31T06:00:16Z	25	0.893
MMS3	2019-01-01T04:27:48Z	2019-01-01T06:01:02Z	312	0.056
MMS3	2019-01-05T08:33:39Z	2019-01-05T20:43:44Z	1082	0.025
MMS3	2019-01-06T15:16:09Z	2019-01-06T23:13:25Z	1354	0.047
MMS3	2019-01-17T22:39:40Z	2019-01-17T23:04:44Z	43	0.029
MMS3	2019-01-31T05:48:16Z	2019-01-31T05:49:29Z	74	1.000
MMS3	2019-02-13T05:16:52Z	2019-02-13T23:15:18Z	1431	0.022
MMS3	2019-02-14T04:56:13Z	2019-02-14T23:59:04Z	2900	0.042
MMS3	2019-02-15T00:00:29Z	2019-02-15T23:59:58Z	34052	0.394
MMS3	2019-02-16T00:00:00Z	2019-02-16T23:59:58Z	38793	0.449
MMS3	2019-02-17T00:00:00Z	2019-02-17T23:57:38Z	30267	0.351
MMS3	2019-02-18T00:02:23Z	2019-02-18T18:25:02Z	38738	0.586
MMS3	2019-02-19T01:42:26Z	2019-02-19T23:58:42Z	41753	0.521
MMS3	2019-02-20T00:01:23Z	2019-02-20T23:59:58Z	78460	0.909
MMS3	2019-02-21T00:00:00Z	2019-02-21T23:58:16Z	28922	0.335
MMS3	2019-02-22T00:00:58Z	2019-02-22T16:54:17Z	21643	0.356
MMS3	2019-02-23T00:18:03Z	2019-02-23T21:55:49Z	4281	0.055
MMS3	2019-02-24T00:59:36Z	2019-02-24T23:12:32Z	5232	0.065
MMS3	2019-04-05T13:27:19Z	2019-04-05T13:44:49Z	634	0.603
MMS3	2019-04-16T15:24:59Z	2019-04-16T15:26:59Z	21	0.174
MMS3	2019-06-07T11:02:02Z	2019-06-07T11:57:33Z	87	0.026
MMS3	2019-08-07T08:46:34Z	2019-08-07T08:47:16Z	35	0.814
MMS3	2019-09-09T04:50:38Z	2019-09-09T21:29:39Z	1163	0.019
MMS3	2019-09-13T03:01:36Z	2019-09-13T03:15:51Z	575	0.672
MMS3	2019-09-26T03:02:21Z	2019-09-26T16:15:54Z	533	0.011
MMS3	2019-12-27T17:05:04Z	2019-12-27T17:29:23Z	23	0.016
MMS3	2020-07-22T07:47:19Z	2020-07-22T11:15:30Z	150	0.012
MMS3	2020-07-26T00:43:42Z	2020-07-26T01:46:15Z	2532	0.674
MMS3	2020-07-27T14:44:47Z	2020-07-27T14:47:11Z	115	0.793
MMS3	2020-07-29T19:04:45Z	2020-07-29T23:54:39Z	800	0.046
MMS3	2020-08-01T06:57:06Z	2020-08-01T10:21:25Z	2092	0.171
MMS3	2020-08-02T00:19:42Z	2020-08-02T21:42:13Z	33317	0.433
MMS3	2020-08-03T01:18:22Z	2020-08-03T15:40:15Z	6925	0.134
MMS3	2020-08-04T22:20:18Z	2020-08-04T22:21:20Z	63	1.000
MMS3	2020-08-05T00:44:15Z	2020-08-05T05:36:58Z	2047	0.117
MMS3	2020-08-26T13:31:23Z	2020-08-26T18:12:52Z	7530	0.446
MMS3	2020-08-27T02:21:47Z	2020-08-27T14:49:58Z	1590	0.035
MMS3	2020-08-31T10:59:48Z	2020-08-31T22:25:41Z	2285	0.056
MMS3	2020-09-02T01:30:05Z	2020-09-02T21:13:36Z	3209	0.045
MMS3	2020-09-03T00:10:59Z	2020-09-03T10:25:57Z	1431	0.039
MMS3	2020-09-04T11:02:57Z	2020-09-04T11:07:53Z	249	0.838
MMS3	2020-09-05T12:27:26Z	2020-09-05T22:12:09Z	411	0.012
MMS3	2020-09-12T08:22:16Z	2020-09-12T17:57:43Z	2911	0.084
MMS3	2020-09-14T04:42:26Z	2020-09-14T04:51:42Z	37	0.066

S/C	Start Date	End Date	#Records	Severity
MMS3	2020-09-15T21:21:23Z	2020-09-15T23:53:20Z	492	0.054
MMS3	2020-09-16T14:32:45Z	2020-09-16T17:09:14Z	161	0.017
MMS3	2020-09-17T23:37:30Z	2020-09-17T23:53:53Z	870	0.884
MMS3	2020-09-18T00:13:47Z	2020-09-18T14:34:18Z	44765	0.867
MMS3	2020-09-19T07:41:45Z	2020-09-19T23:59:58Z	58694	1.000
MMS3	2020-09-20T00:00:00Z	2020-09-20T23:59:58Z	86399	1.000
MMS3	2020-09-21T00:00:00Z	2020-09-21T23:59:58Z	86371	1.000
MMS3	2020-09-22T00:00:00Z	2020-09-22T23:59:58Z	29433	0.341
MMS3	2020-09-23T00:00:00Z	2020-09-23T23:59:58Z	84898	0.983
MMS3	2020-09-24T00:00:00Z	2020-09-24T15:30:24Z	54942	0.984
MMS3	2020-10-03T12:30:45Z	2020-10-03T12:34:27Z	134	0.601
MMS3	2020-10-10T07:48:19Z	2020-10-10T08:18:38Z	170	0.093
MMS3	2020-10-13T02:34:27Z	2020-10-13T05:29:16Z	4210	0.401
MMS3	2020-10-23T05:17:23Z	2020-10-23T07:10:22Z	420	0.062
MMS3	2020-10-26T21:55:44Z	2020-10-26T23:27:51Z	683	0.124
MMS3	2020-10-30T11:12:51Z	2020-10-30T12:49:40Z	118	0.020
MMS3	2020-11-03T02:19:03Z	2020-11-03T02:19:47Z	21	0.467
MMS3	2020-11-13T10:01:28Z	2020-11-13T13:05:54Z	304	0.027
MMS3	2020-11-14T05:38:51Z	2020-11-14T09:37:16Z	10023	0.701
MMS3	2020-11-16T20:24:30Z	2020-11-16T21:17:17Z	141	0.045
MMS3	2020-11-21T04:15:41Z	2020-11-21T04:19:15Z	79	0.367
MMS3	2020-11-24T00:53:20Z	2020-11-24T17:01:23Z	872	0.015
MMS3	2020-11-27T10:49:29Z	2020-11-27T12:58:17Z	313	0.040
MMS3	2020-11-28T04:11:34Z	2020-11-28T09:10:07Z	336	0.019
MMS3	2020-12-12T05:40:46Z	2020-12-12T05:44:13Z	158	0.760
MMS3	2020-12-18T14:42:48Z	2020-12-18T17:41:41Z	753	0.070
MMS3	2020-12-19T05:39:32Z	2020-12-19T09:25:01Z	1210	0.089
MMS3	2020-12-22T04:40:58Z	2020-12-22T21:35:43Z	7241	0.119
MMS3	2020-12-29T05:40:59Z	2020-12-29T21:06:20Z	668	0.012
MMS3	2021-01-05T19:07:25Z	2021-01-05T19:49:56Z	159	0.062
MMS3	2021-01-16T06:46:43Z	2021-01-16T07:35:36Z	144	0.049
MMS3	2021-01-19T06:53:06Z	2021-01-19T07:00:35Z	292	0.649
MMS3	2021-01-22T18:28:42Z	2021-01-22T20:06:03Z	1201	0.206
MMS3	2021-01-26T20:56:27Z	2021-01-26T20:58:38Z	132	1.000
MMS3	2021-01-29T18:42:22Z	2021-01-29T19:04:46Z	652	0.485
MMS3	2021-01-30T09:45:50Z	2021-01-30T10:42:10Z	42	0.012
MMS3	2021-02-06T06:31:07Z	2021-02-06T11:30:45Z	10979	0.611
MMS3	2021-05-18T13:32:08Z	2021-05-18T13:35:57Z	120	0.522
MMS3	2021-10-12T23:02:01Z	2021-10-12T23:08:10Z	84	0.227
MMS3	2022-07-04T05:33:07Z	2022-07-04T05:33:29Z	23	1.000
MMS3	2022-07-08T01:08:18Z	2022-07-08T23:51:01Z	5641	0.069
MMS4	2015-07-19T01:20:32Z	2015-07-19T02:35:03Z	190	0.042
MMS4	2015-07-22T15:22:54Z	2015-07-22T15:23:56Z	61	0.968
MMS4	2015-07-28T16:09:46Z	2015-07-28T16:11:09Z	84	1.000
MMS4	2015-08-05T03:37:33Z	2015-08-05T12:50:51Z	900	0.027
MMS4	2015-08-06T12:43:59Z	2015-08-06T23:04:48Z	511	0.014
MMS4	2015-08-14T11:49:59Z	2015-08-14T17:12:46Z	455	0.023
MMS4	2015-08-17T11:29:10Z	2015-08-17T13:29:38Z	179	0.025
MMS4	2015-12-13T10:05:36Z	2015-12-13T12:10:30Z	158	0.021
MMS4	2016-02-28T02:42:54Z	2016-02-28T02:43:21Z	28	1.000
MMS4	2016-08-12T08:02:14Z	2016-08-12T08:59:58Z	1240	0.358
MMS4	2016-08-13T07:55:48Z	2016-08-13T08:54:59Z	3409	0.960

S/C	Start Date	End Date	#Records	Severity
MMS4	2016-08-14T07:51:01Z	2016-08-14T08:49:58Z	3495	0.988
MMS4	2016-08-15T07:40:20Z	2016-08-15T08:39:58Z	3528	0.986
MMS4	2016-08-16T07:00:47Z	2016-08-16T07:15:22Z	66	0.075
MMS4	2016-08-17T07:58:05Z	2016-08-17T07:59:10Z	66	1.000
MMS4	2017-02-05T08:58:26Z	2017-02-05T10:10:04Z	128	0.030
MMS4	2017-02-07T10:39:11Z	2017-02-07T10:53:48Z	145	0.165
MMS4	2017-02-13T08:03:45Z	2017-02-13T11:18:07Z	11521	0.988
MMS4	2017-02-14T10:22:18Z	2017-02-14T13:27:00Z	10622	0.958
MMS4	2017-02-15T13:58:50Z	2017-02-15T17:01:49Z	728	0.066
MMS4	2017-02-16T18:54:54Z	2017-02-16T20:01:35Z	88	0.022
MMS4	2017-02-21T14:22:58Z	2017-02-21T16:50:16Z	4383	0.496
MMS4	2017-02-22T22:19:08Z	2017-02-22T23:50:30Z	195	0.036
MMS4	2017-03-04T07:34:26Z	2017-03-04T07:40:28Z	26	0.072
MMS4	2017-03-17T08:03:10Z	2017-03-17T08:04:15Z	66	1.000
MMS4	2017-05-06T10:32:37Z	2017-05-06T13:23:31Z	899	0.088
MMS4	2017-06-23T00:37:26Z	2017-06-23T03:38:10Z	805	0.074
MMS4	2017-07-04T01:19:11Z	2017-07-04T01:23:21Z	28	0.112
MMS4	2017-07-06T21:05:32Z	2017-07-06T21:26:04Z	77	0.062
MMS4	2017-07-13T05:55:08Z	2017-07-13T08:07:25Z	532	0.067
MMS4	2017-07-19T00:04:15Z	2017-07-19T00:08:44Z	32	0.119
MMS4	2017-07-20T01:41:48Z	2017-07-20T13:09:01Z	1122	0.027
MMS4	2017-08-06T10:58:00Z	2017-08-06T13:56:28Z	1073	0.100
MMS4	2017-08-08T21:18:21Z	2017-08-08T21:21:58Z	148	0.679
MMS4	2017-08-09T01:58:48Z	2017-08-09T18:34:37Z	3655	0.061
MMS4	2017-09-01T06:31:04Z	2017-09-01T18:55:38Z	523	0.012
MMS4	2017-10-18T00:02:54Z	2017-10-18T00:03:28Z	35	1.000
MMS4	2017-11-14T00:16:04Z	2017-11-14T02:16:16Z	435	0.060
MMS4	2017-11-25T09:30:34Z	2017-11-25T09:32:04Z	26	0.286
MMS4	2018-02-06T01:12:48Z	2018-02-06T03:50:50Z	455	0.048
MMS4	2018-02-11T16:20:20Z	2018-02-11T23:22:19Z	541	0.021
MMS4	2018-02-12T00:00:03Z	2018-02-12T00:01:14Z	72	1.000
MMS4	2018-03-01T05:58:37Z	2018-03-01T07:00:53Z	129	0.035
MMS4	2018-03-12T09:09:17Z	2018-03-12T13:16:04Z	2785	0.188
MMS4	2018-03-17T11:49:04Z	2018-03-17T21:10:20Z	1286	0.038
MMS4	2018-03-21T00:14:34Z	2018-03-21T00:15:15Z	42	1.000
MMS4	2018-03-23T00:28:56Z	2018-03-23T15:46:33Z	1359	0.025
MMS4	2018-03-26T02:43:06Z	2018-03-26T16:01:59Z	13561	0.283
MMS4	2018-03-31T11:56:45Z	2018-03-31T23:58:29Z	1273	0.029
MMS4	2018-04-01T02:41:23Z	2018-04-01T07:10:37Z	14625	0.905
MMS4	2018-04-03T06:46:21Z	2018-04-03T06:47:20Z	60	1.000
MMS4	2018-04-06T02:23:55Z	2018-04-06T20:52:23Z	11071	0.166
MMS4	2018-04-08T21:59:12Z	2018-04-08T22:28:06Z	102	0.059
MMS4	2018-04-09T04:58:52Z	2018-04-09T17:47:53Z	2589	0.056
MMS4	2018-04-11T17:33:09Z	2018-04-11T22:32:41Z	3947	0.220
MMS4	2018-04-12T01:03:54Z	2018-04-12T13:32:24Z	4854	0.108
MMS4	2018-04-14T13:03:17Z	2018-04-14T23:59:58Z	39391	1.000
MMS4	2018-04-15T00:00:00Z	2018-04-15T07:36:41Z	24306	0.887
MMS4	2018-04-20T08:47:35Z	2018-04-20T23:24:52Z	8386	0.159
MMS4	2018-04-22T23:48:05Z	2018-04-22T23:58:28Z	351	0.562
MMS4	2018-04-23T00:01:05Z	2018-04-23T16:16:57Z	14235	0.243
MMS4	2018-04-25T21:34:42Z	2018-04-25T22:54:34Z	546	0.114
MMS4	2018-04-26T01:16:33Z	2018-04-26T09:33:55Z	5773	0.193

S/C	Start Date	End Date	#Records	Severity
MMS4	2018-04-28T14:58:32Z	2018-04-28T23:59:57Z	9740	0.300
MMS4	2018-04-29T00:00:01Z	2018-04-29T10:13:59Z	10440	0.283
MMS4	2018-05-01T10:26:03Z	2018-05-01T14:58:03Z	1885	0.115
MMS4	2018-05-02T02:29:08Z	2018-05-02T03:58:27Z	1005	0.187
MMS4	2018-05-04T06:53:11Z	2018-05-04T22:14:10Z	1530	0.028
MMS4	2018-05-07T01:43:37Z	2018-05-07T18:06:02Z	37522	0.637
MMS4	2018-05-09T21:25:43Z	2018-05-09T22:36:06Z	407	0.096
MMS4	2018-05-10T08:19:13Z	2018-05-10T08:42:37Z	609	0.433
MMS4	2018-05-12T21:33:54Z	2018-05-12T21:34:21Z	28	1.000
MMS4	2018-05-15T15:16:31Z	2018-05-15T15:34:48Z	480	0.437
MMS4	2018-05-18T08:14:03Z	2018-05-18T23:25:39Z	1639	0.030
MMS4	2018-05-25T06:47:40Z	2018-05-25T07:56:39Z	52	0.013
MMS4	2018-05-28T03:04:51Z	2018-05-28T19:47:00Z	2536	0.042
MMS4	2018-06-06T11:37:42Z	2018-06-06T12:22:32Z	264	0.098
MMS4	2018-06-07T02:36:03Z	2018-06-07T02:56:22Z	55	0.045
MMS4	2018-06-09T13:00:38Z	2018-06-09T13:02:00Z	26	0.313
MMS4	2018-06-11T04:27:23Z	2018-06-11T05:38:18Z	2704	0.635
MMS4	2018-06-12T01:29:37Z	2018-06-12T23:45:46Z	8791	0.110
MMS4	2018-06-15T04:54:29Z	2018-06-15T10:12:22Z	511	0.027
MMS4	2018-06-19T00:02:00Z	2018-06-19T20:57:56Z	2087	0.028
MMS4	2018-06-22T12:15:17Z	2018-06-22T22:37:50Z	1080	0.029
MMS4	2018-06-23T00:13:48Z	2018-06-23T22:34:31Z	6525	0.081
MMS4	2018-06-24T08:05:28Z	2018-06-24T08:44:36Z	1575	0.670
MMS4	2018-07-03T18:07:48Z	2018-07-03T19:19:48Z	68	0.016
MMS4	2018-07-12T03:54:56Z	2018-07-12T23:02:40Z	3411	0.050
MMS4	2018-07-13T01:26:18Z	2018-07-13T22:20:59Z	2524	0.034
MMS4	2018-07-14T23:52:08Z	2018-07-14T23:59:01Z	25	0.060
MMS4	2018-07-15T00:00:28Z	2018-07-15T00:01:06Z	30	0.769
MMS4	2018-07-16T17:32:12Z	2018-07-16T17:33:08Z	34	0.596
MMS4	2018-07-23T12:48:29Z	2018-07-23T14:30:18Z	511	0.084
MMS4	2018-07-28T10:55:10Z	2018-07-28T10:58:51Z	202	0.910
MMS4	2018-07-30T01:13:06Z	2018-07-30T23:00:15Z	21825	0.278
MMS4	2018-07-31T22:07:38Z	2018-07-31T22:14:45Z	125	0.292
MMS4	2018-08-01T04:41:08Z	2018-08-01T21:20:23Z	2713	0.045
MMS4	2018-08-03T04:50:48Z	2018-08-03T18:18:50Z	519	0.011
MMS4	2018-08-04T00:58:22Z	2018-08-04T15:41:21Z	1071	0.020
MMS4	2018-08-07T21:42:36Z	2018-08-07T23:14:30Z	2967	0.538
MMS4	2018-08-08T02:33:11Z	2018-08-08T03:08:24Z	1489	0.704
MMS4	2018-08-09T02:40:38Z	2018-08-09T21:42:25Z	1774	0.026
MMS4	2018-08-11T05:45:21Z	2018-08-11T07:45:31Z	4727	0.656
MMS4	2018-08-12T03:38:01Z	2018-08-12T23:57:50Z	19666	0.269
MMS4	2018-08-13T00:01:00Z	2018-08-13T03:08:50Z	8166	0.725
MMS4	2018-08-16T08:59:35Z	2018-08-16T09:01:11Z	97	1.000
MMS4	2018-08-25T11:48:52Z	2018-08-25T12:01:50Z	639	0.820
MMS4	2018-08-26T03:03:55Z	2018-08-26T03:07:29Z	181	0.842
MMS4	2018-08-30T14:42:58Z	2018-08-30T14:56:09Z	24	0.030
MMS4	2018-09-02T05:06:39Z	2018-09-02T05:07:34Z	55	0.982
MMS4	2018-09-14T05:12:42Z	2018-09-14T05:15:30Z	168	0.994
MMS4	2018-09-20T21:48:11Z	2018-09-20T23:38:23Z	217	0.033
MMS4	2018-09-23T14:58:02Z	2018-09-23T15:11:40Z	628	0.767
MMS4	2018-09-28T21:04:15Z	2018-09-28T21:15:25Z	32	0.048
MMS4	2018-10-05T07:35:13Z	2018-10-05T08:54:37Z	100	0.021

S/C	Start Date	End Date	#Records	Severity
MMS4	2018-10-12T07:28:53Z	2018-10-12T07:35:30Z	84	0.211
MMS4	2018-10-29T00:22:56Z	2018-10-29T00:28:35Z	340	1.000
MMS4	2018-11-08T08:57:21Z	2018-11-08T08:58:08Z	48	1.000
MMS4	2018-11-14T20:14:42Z	2018-11-14T20:18:32Z	231	1.000
MMS4	2018-11-25T08:40:10Z	2018-11-25T08:52:30Z	284	0.383
MMS4	2018-12-05T23:26:54Z	2018-12-05T23:59:58Z	565	0.285
MMS4	2018-12-06T00:00:00Z	2018-12-06T00:04:34Z	239	0.869
MMS4	2018-12-19T15:59:49Z	2018-12-19T16:26:27Z	30	0.019
MMS4	2018-12-20T12:02:51Z	2018-12-20T12:09:46Z	94	0.226
MMS4	2018-12-26T22:03:00Z	2018-12-26T23:00:28Z	74	0.021
MMS4	2018-12-27T00:21:54Z	2018-12-27T01:27:26Z	336	0.085
MMS4	2019-01-01T02:45:05Z	2019-01-01T04:30:09Z	83	0.013
MMS4	2019-01-16T04:58:42Z	2019-01-16T06:39:26Z	445	0.074
MMS4	2019-01-23T08:43:37Z	2019-01-23T10:43:37Z	89	0.012
MMS4	2019-01-28T06:23:46Z	2019-01-28T16:09:53Z	390	0.011
MMS4	2019-02-08T13:24:51Z	2019-02-08T13:29:08Z	22	0.085
MMS4	2019-02-16T01:44:53Z	2019-02-16T02:23:06Z	39	0.017
MMS4	2019-02-22T06:04:35Z	2019-02-22T07:57:03Z	1901	0.282
MMS4	2019-02-23T17:53:13Z	2019-02-23T19:37:41Z	317	0.051
MMS4	2019-04-02T05:46:54Z	2019-04-02T16:04:35Z	423	0.011
MMS4	2019-04-23T19:51:27Z	2019-04-23T20:36:33Z	81	0.030
MMS4	2019-06-08T03:37:57Z	2019-06-08T03:40:44Z	124	0.738
MMS4	2019-06-28T12:40:13Z	2019-06-28T12:42:55Z	43	0.264
MMS4	2019-07-02T04:07:24Z	2019-07-02T12:33:59Z	956	0.031
MMS4	2019-07-05T12:32:24Z	2019-07-05T13:39:48Z	3357	0.830
MMS4	2019-07-06T00:00:51Z	2019-07-06T02:35:36Z	156	0.017
MMS4	2019-07-09T00:36:02Z	2019-07-09T01:18:06Z	174	0.069
MMS4	2019-07-12T12:38:46Z	2019-07-12T16:32:20Z	2213	0.158
MMS4	2019-07-19T13:01:18Z	2019-07-19T16:16:18Z	290	0.025
MMS4	2019-07-20T00:20:41Z	2019-07-20T04:20:49Z	4644	0.322
MMS4	2019-07-23T02:27:18Z	2019-07-23T02:45:05Z	1048	0.981
MMS4	2019-08-16T01:07:09Z	2019-08-16T13:45:54Z	1107	0.024
MMS4	2019-09-08T10:21:52Z	2019-09-08T15:52:22Z	224	0.011
MMS4	2019-10-04T10:28:28Z	2019-10-04T11:18:53Z	2386	0.788
MMS4	2019-10-12T09:54:04Z	2019-10-12T09:55:28Z	75	0.882
MMS4	2019-10-14T03:30:08Z	2019-10-14T03:31:28Z	32	0.395
MMS4	2019-12-03T17:48:25Z	2019-12-03T20:36:39Z	377	0.037
MMS4	2019-12-07T04:19:38Z	2019-12-07T09:16:02Z	1045	0.059
MMS4	2019-12-17T04:18:59Z	2019-12-17T06:19:48Z	135	0.019
MMS4	2020-01-04T05:11:47Z	2020-01-04T05:25:59Z	84	0.098
MMS4	2020-01-21T04:54:25Z	2020-01-21T17:51:55Z	696	0.015
MMS4	2020-01-28T09:14:36Z	2020-01-28T09:48:43Z	194	0.095
MMS4	2020-02-11T10:29:19Z	2020-02-11T10:38:11Z	60	0.113
MMS4	2020-02-15T09:07:43Z	2020-02-15T11:16:30Z	222	0.029
MMS4	2020-02-18T07:53:01Z	2020-02-18T12:14:06Z	438	0.028
MMS4	2020-02-22T08:42:25Z	2020-02-22T12:51:54Z	280	0.019
MMS4	2020-02-28T20:10:46Z	2020-02-28T21:54:46Z	299	0.048
MMS4	2020-02-29T08:48:06Z	2020-02-29T09:50:30Z	3142	0.839
MMS4	2020-03-06T22:09:06Z	2020-03-06T23:52:19Z	313	0.051
MMS4	2020-03-10T09:31:57Z	2020-03-10T12:52:08Z	3602	0.300
MMS4	2020-03-24T09:28:39Z	2020-03-24T13:48:20Z	3198	0.205
MMS4	2020-03-31T09:09:41Z	2020-03-31T13:54:13Z	7077	0.415

S/C	Start Date	End Date	#Records	Severity
MMS4	2020-04-03T21:20:41Z	2020-04-03T23:59:47Z	1312	0.137
MMS4	2020-04-04T00:01:22Z	2020-04-04T09:58:17Z	655	0.018
MMS4	2020-04-21T10:56:25Z	2020-04-21T14:22:52Z	222	0.018
MMS4	2020-05-05T10:07:17Z	2020-05-05T13:24:39Z	254	0.021
MMS4	2020-05-15T23:12:19Z	2020-05-15T23:54:34Z	514	0.203
MMS4	2020-05-16T17:44:53Z	2020-05-16T20:36:42Z	1943	0.188
MMS4	2020-06-29T03:49:47Z	2020-06-29T03:50:33Z	47	1.000
MMS4	2020-07-24T09:01:11Z	2020-07-24T09:40:20Z	65	0.028
MMS4	2020-08-06T20:13:06Z	2020-08-06T20:15:44Z	29	0.182
MMS4	2020-09-19T20:07:14Z	2020-09-19T20:09:03Z	27	0.245
MMS4	2020-09-22T02:27:57Z	2020-09-22T02:49:49Z	1129	0.860
MMS4	2020-10-27T15:45:00Z	2020-10-27T15:58:48Z	55	0.066
MMS4	2021-01-22T20:43:35Z	2021-01-22T20:45:57Z	35	0.245
MMS4	2021-02-09T09:46:04Z	2021-02-09T09:50:28Z	54	0.204
MMS4	2021-03-19T21:58:39Z	2021-03-19T22:01:53Z	27	0.138
MMS4	2021-03-30T12:21:23Z	2021-03-30T12:24:50Z	34	0.163
MMS4	2021-04-06T10:56:46Z	2021-04-06T10:59:43Z	22	0.124
MMS4	2021-04-23T23:12:33Z	2021-04-23T23:15:55Z	176	0.867
MMS4	2021-05-22T18:31:35Z	2021-05-22T18:35:26Z	29	0.125
MMS4	2021-05-25T14:57:14Z	2021-05-25T14:59:39Z	26	0.178
MMS4	2021-05-26T03:31:24Z	2021-05-26T03:35:28Z	50	0.204
MMS4	2021-06-05T21:25:07Z	2021-06-05T21:33:35Z	38	0.075
MMS4	2021-06-08T13:21:22Z	2021-06-08T13:26:55Z	33	0.099
MMS4	2021-06-22T06:45:20Z	2021-06-22T06:49:30Z	37	0.147
MMS4	2021-06-25T11:21:29Z	2021-06-25T11:47:58Z	213	0.134
MMS4	2021-07-08T13:29:07Z	2021-07-08T13:33:13Z	68	0.275
MMS4	2021-07-13T14:41:34Z	2021-07-13T14:46:56Z	59	0.183
MMS4	2021-08-21T14:31:32Z	2021-08-21T14:59:13Z	481	0.289
MMS4	2021-09-03T05:48:06Z	2021-09-03T05:53:32Z	32	0.098
MMS4	2021-09-30T11:29:00Z	2021-09-30T11:35:49Z	152	0.371
MMS4	2021-10-20T10:22:50Z	2021-10-20T10:49:53Z	121	0.075
MMS4	2021-11-27T06:33:05Z	2021-11-27T10:50:46Z	3792	0.245
MMS4	2021-11-28T00:07:13Z	2021-11-28T00:55:37Z	318	0.109
MMS4	2022-01-08T20:04:17Z	2022-01-08T20:32:23Z	99	0.059
MMS4	2022-01-15T18:29:00Z	2022-01-15T18:30:00Z	61	1.000
MMS4	2022-02-05T22:56:59Z	2022-02-05T22:57:43Z	25	0.556
MMS4	2022-08-27T14:27:19Z	2022-08-27T14:28:30Z	72	1.000

Table 2-4 ASPOC Data Product Issues as of 09/30/2022

2.4.4 ASPOC Data Quality Flags

All ASPOC science data products do contain beam current quality flags in a dedicated status byte. The ion emission quality bytes are encoded as follows:

0 no emission, both ASPOC units are off
1 emission; I_BEAM/I_TOTAL > 0.97(excellent)
2 emission; I_BEAM/I_TOTAL > 0.92 (good)
3 emission; I_BEAM/I_TOTAL > 0.75 (moderate)
4 emission; I_BEAM/I_TOTAL > 0.3 (weak)
5 emission; I_BEAM/I_TOTAL > 0.0 (poor)
6 at least one unit in cleaning mode

7	at least one unit in startup mode
255	fill value (no data)

2.5 DATA PRODUCTION ALGORITHM DESCRIPTIONS

ASPOC generates Quicklook, L1b/SITL, and L2 science data products. L1b/SITL and L2 data products are provided in CDF files, while Quicklook products are represented by data plots saved in PNG file format. The CDF files are formatted in accordance with the MMS CDF File Format Guide. The MMS file name convention is applied to all files.

2.5.1 ASPOC L1b/SITL Data Products

ASPOC Level-1b and SITL data products are containing calibrated raw data having a resolution that corresponds to the data acquisition cycle on-board. The following data products are available (given resolutions are typical values):

- Ion beam current, energy, ~ 1s resolution
- Total emitter current, ~ 1 s resolution
- Status and housekeeping, ~ 40 s resolution
- Spacecraft potential as used for control loop, ~1 s resolution
- Emitter heater current and voltage, ~ 20 s resolution
- Status flags and parameters, ~ 40 s resolution
- Secondary voltages, ~ 60 s resolution
- Internal temperatures, ~ 40 s resolution

2.5.2 ASPOC L2 Data Products

ASPOC Level-2 products are daily files containing interpolated data at a resolution of 1 second (86400 records per file). For science analysis ASPOC will provide the following data:

- Ion beam current
  - individual ASPOC 1 and ASPOC 2 currents
  - and the sum
- Ion beam energies of individual ASPOCs
- Data quality information
- Individual ASPOC 1 and ASPOC 2 modes
- ASPOC ON/OFF status (ON indicates that at least one ASPOC is emitting ions)

2.5.3 Quicklook Data Products

ASPOC Quicklook data products are PNG graphic files containing daily plots of key parameters, which reflect the status of the instrument. The following parameters are shown:

- Spacecraft potential
- Ion beam current
- Total emitter current
- Beam energy
- Filament power
- Filament impedance

The graphic on the next page shows a sample plot of ASPOC data from the MMS1 spacecraft. The bar at the bottom of the plot indicates the quality of the ion emission:

- OFF = instrument not active
- Q1-Q5 = emission quality (1=good, 5=bad)
- CLN = cleaning active
- NOE = no emission (startup active)

In addition, the background color of the plot shows if ASPOC is active and emits a significant number of ions.

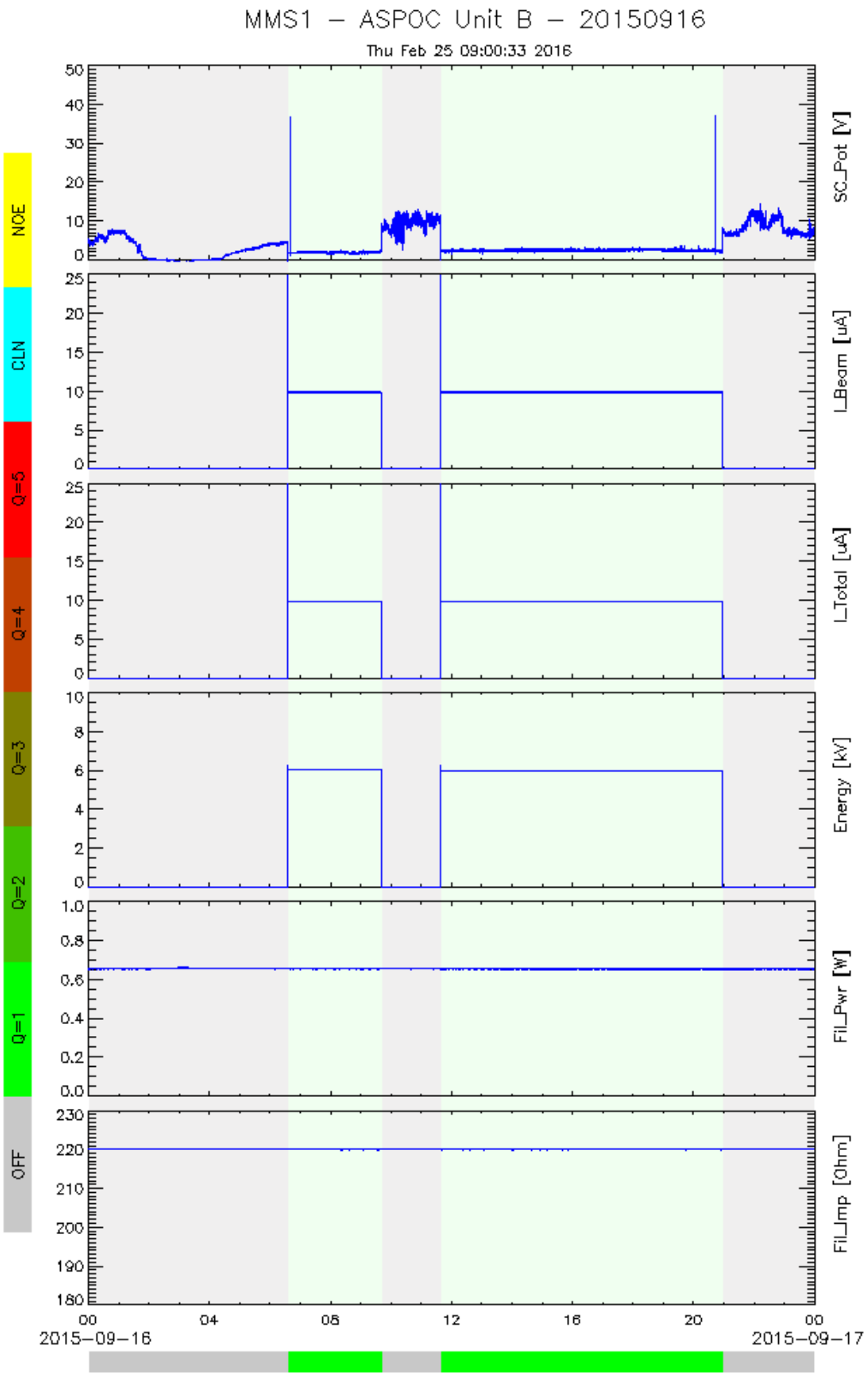

Table 2-5 ASPOC Quicklook Data Plot

2.6 APPENDIX A- ASPOC REFERENCES

The following documents and drawings in effect on the day this specification was signed **shall** apply to the extent specified herein. In the event of conflict between this document and any referenced document, the document with latest publication date will govern.

The following is a list of applicable references and publications.

Section	Document Number	Title	Revision/Date
	MMS-ASP-IWF-TN-0042	MMS ASPOC Science Data Products Guide	2.0, 02/25/2016
	MMS-ASP-IWF-UM-0001	MMS ASPOC User Manual	1.0, 09/01/2015
	http://doi.org/10.1109/TPS.2017.2694223	Nakamura, R., K. Torkar, M. Andriopoulou, H. Jeszenszky, C. P. Escoubet, F. Cipriani, P. A. Lindqvist, S. A. Fuselier, C. J. Pollock, B. L. Giles, Y. Khotyaintsev (2017), Initial Results From the Active Spacecraft Potential Control Onboard Magnetospheric Multiscale Mission, IEEE Transactions on Plasma Science, 45 (8), 1847-1852.	

Table 2-6 ASPOC Applicable Documents

3.0 MAGNETIC EPHEMERIS COORDINATES (MEC)

3.1 MEC OVERVIEW

The Magnetic Ephemeris and Coordinates (MEC) products provide information about the location and attitude, and magnetic connectivity of the four satellites comprising the Magnetospheric Multiscale (MMS) mission.

The MEC products are provided in files named after the magnetic field model used for the field-dependent quantities within the data files. These models are: T89D – the Kp-parameterized Tsyganenko 1989 model; T89Q – the Tsyganenko 1989 model with Kp=2; TS04D – the solar wind-parameterized Tsyganenko & Sitnov 2005 model. It is important to note that the key products such as position, velocity, and coordinate transformations do not depend on the magnetic field model and therefore are identical in each model product.

From a user perspective, this means that all position vectors, velocity vectors, quaternions for coordinate transformation, and attitude information can be taken from any file for the desired time period. As the T89Q product does not rely on ancillary data it will be available in final form at the lowest latency and is therefore recommended for any products not depending on the magnetic field model. For clarity, we note that the Geocentric Solar Magnetospheric (GSM) and Solar Magnetic (SM) coordinate systems (see section 3.2) are not magnetic field model dependent in this context; these coordinate systems rely on the orientation of the dipole axis and Earth's magnetic moment, both of which are derived from the International Geomagnetic Reference Field (IGRF – a representation of Earth's internal field).

3.2 COORDINATE SYSTEMS

The MEC products provide information related to the coordinate systems listed below. These can be broken down into coordinate systems based on the satellite (sections 3.2.1 and 3.2.2) and geophysical coordinate systems (section 3.2.3). To convert between these systems the MEC data products provide quaternions, see section 3.4.3 for definitions and usage details. The satellite-based coordinate systems are defined in the Alignment and Coordinate System Document listed in Table 3-6.

3.2.1 Spinning, Spacecraft-fixed Systems

- BCS – Body Coordinate System (Spinning Spacecraft Body)
- SSL – Spinning Spacecraft, Angular Momentum Vector (L) Aligned
- SMPA – Spinning Major Principal Axis (MPA)-Aligned Coordinates

3.2.2 De-spun Systems

- DBCS – De-spun Body Coordinate System (despin around BCS Z-axis).
- DSL – De-spun Spacecraft L-Vector Coordinate System (Despin around L). Non-spinning frame, in which the Z-axis is fixed in inertial space, but the transformation to DBCS is time-dependent (as well as phase-dependent).
- DMPA – De-spun Major Principal Axis (despin around Major Principal Axis). A non-spinning frame that has a fixed orientation relative to DBCS, but whose axes orientations wobble with respect to inertial space at the nutation rate.

3.2.3 Geophysical Systems

- ECI (GEI/J2000) – Earth-Centered Inertial (ECI). To fully specify the system the equinox must be defined. This system uses the mean equinox at the J2000 epoch. The z-axis is aligned with the mean celestial pole at J2000; the x-axis is aligned with the mean equinox at J2000; the y-axis

completes and lies in the plane of the celestial equator. Other Earth-Centered Inertial systems are used, as shown in Figure 3-1, the most important of which is Mean of Date (MOD).

- MOD – Mean of Date (MOD) accounts for precession of the mean equinox between the J2000 epoch and the date of interest. The definition follows that of ECI, but uses the mean equinox and mean equator of the date of interest. The coordinate system is thus time-dependent.
- GSE – Geocentric Solar Ecliptic (GSE) is not an inertial system. It is Earth-centered with the x-axis pointing towards the Sun. The y-axis lies in the mean ecliptic plane of date, pointing in the anti-orbit direction. The z-axis is parallel to the mean ecliptic pole of date.
- GSE2000 – This system is defined similarly to GSE, but uses the J2000 epoch instead of the date of interest.
- GSM – Geocentric Solar Magnetospheric (GSM) is similar to GSE, but is defined such that the centered dipole axis lies in the x-z plane. As in all of these systems, z is positive northward. The y-axis is then perpendicular to both the Sun-Earth line and the centered dipole axis. The centered dipole axis is defined for the date of interest using the first three coefficients of the IGRF. GSM is therefore a rotation about the x-axis from GSE.
- SM – Solar Magnetic (SM) is defined such that the z-axis is aligned with the dipole axis of date and the y-axis is perpendicular to both the Sun-Earth line and the dipole axis. As with GSE and GSM y is positive in the anti-orbit direction. The x-axis is therefore not aligned with the Sun vector. SM is a rotation about the y-axis from the GSM system.
- GEO – Geocentric Geographic (GEO) is an Earth-centered, Earth-fixed (ECEF) coordinate system. In this system a point on the surface of the Earth has fixed coordinates as Earth rotates. The x-axis lies in the Earth's equatorial plane (zero degrees latitude) and intersects the Prime Meridian (zero degrees longitude; the meridian of Greenwich, UK). The z-axis points to *true North*, which is roughly aligned with the instantaneous rotation axis of Earth. For low- or zero-altitude applications this system is often given in a spherical representation, however for astrophysical purposes it is usually represented as a Cartesian system (including here). This system is equivalent to the International Terrestrial Reference Frame (ITRF).

3.2.4 JPL DE421 Ephemerides

As will be detailed in section 3.2.5, one of the fundamental quantities on which coordinate system definitions and transformations are based is the Sun vector. While numerous analytic expression have been put forward to approximate this (see, e.g., [1, 2, 3]), they all have differing accuracy at different times. The LANLGeoMag software library [4, 5], in addition to two analytic expressions, allows use of the Jet Propulsion Laboratory (JPL) Development Ephemeris (DE). The MMS mission has adopted use of DE421 [6] as the standard description of orbits of solar system bodies. DE421 is intended for use between the years 1900 and 2050, encapsulating the expected span of the MMS mission, and providing sub-kilometer accuracy for the position of the Earth [6] with the solar position and velocity derived to maintain the solar system barycenter at the origin of the International Celestial Reference Frame (ICRF). For the MMS mission, and the MEC products, the Sun vector is defined as the vector from the DE421 Earth position to the DE421 Sun position, where the Earth position defines the origin of all Earth-centered coordinate systems (such as the ITRF).

3.2.5 Relationship Between Celestial and Magnetospheric Coordinate Systems

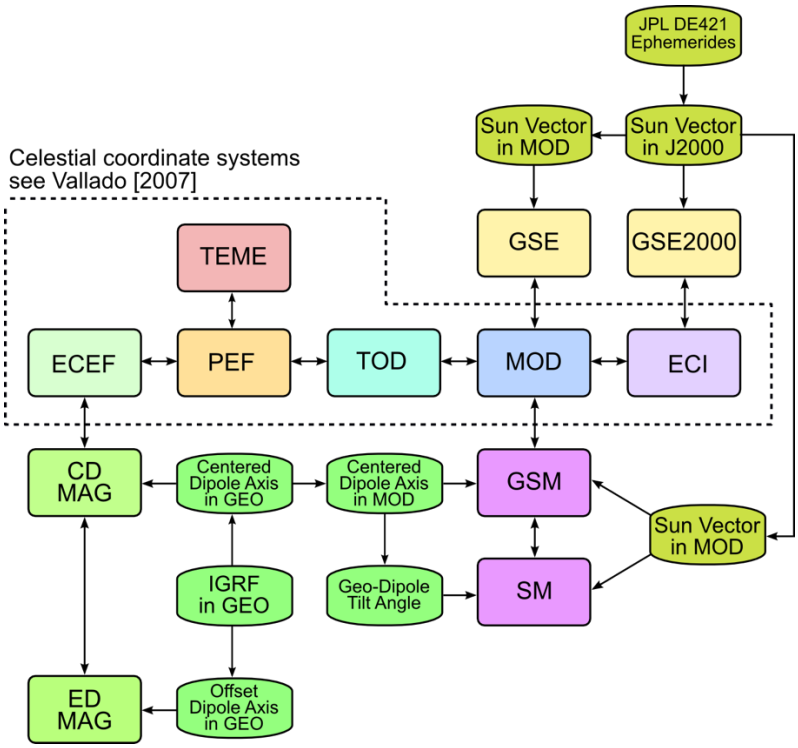

Figure 3-1 Relationship Between Astrophysical and Magnetospheric Coordinate Systems. (Coordinate systems and transformations in the dashed box are described in detail by Vallado [2007]. (Adapted from LANLGeoMag documentation.))

Figure 3-1 illustrates how the various celestial coordinate systems described by [1] (see section 3.7) are related to the magnetospheric coordinate systems described here. The coordinates systems and transformations in the dashed box are the standard celestial systems described in detail by [1]. ECEF (more commonly referred to as GEO or ITRF), ECI, and Mean-Of-Date (MOD) are described above, and the other intermediate coordinate systems are True-Of-Date (TOD), and Pseudo Earth Fixed (PEF). Transformation of ECI to MOD accounts for precession of the ecliptic, while the MOD to TOD transformations account for smaller amplitude nutation effects. The TOD to PEF transformation corrects for very small effects of *polar motion* (see section 3.7.3 of [1].) The TEME (True Equator, Mean Equinox) coordinate system is the inertial system used by the SGP4 orbit propagation code (using the so-called *Two Line Elements* or *Keplerian Elements*), and it is most closely tied to the PEF system.

The geomagnetic coordinate systems are shown in the lower left part of the figure, while the solar based GSE systems are shown in the upper right. The vertical column of boxes containing GSE, MOD, GSM, and SM are the standard system of coordinates traditionally used in magnetospheric physics [2, 3]. For comparison with other implementations used in the space physics community, see the next section.

3.3 IMPLEMENTATIONS AND SOFTWARE LIBRARIES USED

The implemented astrophysical coordinate systems and transformations are consistent with the International Astronomical Union (IAU) Fifth Fundamental Catalogue (FK5). The ICRF used by DE421 supersedes the FK5 system used here, but the ICRF celestial pole is consistent with FK5 to within the uncertainty of the FK5 celestial pole (±50 milliarcseconds), with an offset between the ICRF pole and the FK5 pole of about 23 milliarcseconds, and is considered of sufficient accuracy for MMS science. The

astrophysical and geophysical coordinate systems used by MEC all use the software implementations from the LANLGeoMag library [4, 5]. Following [1] LANLGeoMag uses the FK5 system. While some references for geophysical coordinate systems use truncated series for key calculations (e.g., [2], but see the discussion in [3] for comments on the implied error) such as Greenwich Mean Sidereal Time, LANLGeoMag uses the full series to maintain precision and accuracy. The IAU 1976 precession model and the IAU 1980 theory of nutation are used to describe the changes in the equinox and pole. Full details can be found in [1].

One consequence of the explicit integration of the geophysical systems with astrophysical systems as defined in Figure 3-1 is that all geophysical systems are explicitly derived from an inertial system with an explicit reference epoch. Earlier work [2, 7] implicitly referenced the geophysical coordinate systems to "epoch-of-date". Depending on whether only precession is accounted for, or also the effects of nutation, this would correspond to MOD or TOD. However, [3] explicitly define geophysical systems using TOD and small differences in transformations would result from changing reference inertial system. The difference between using MOD or TOD was reported by [8] as being insignificant relative to the errors in determining spacecraft position. For the purposes of this document we note that the MEC transformations follow the implementation in LANLGeoMag, as used for the earlier Van Allen Probes mission. When comparing to (or combining with) transformations from other software libraries, it is important to verify the reference inertial coordinate system, the derivation of the Sun vector, and the accuracy of the equations used to calculate the necessary astrophysical quantities; most widely used coordinate transformation routines in space physics are based on [2, 7] and do not explicitly define the inertial system as either TOD or MOD. To maintain accuracy, it is recommended to follow the coordinate system definitions given here and the Earth and Sun positions from DE 421.

3.4 IMPLEMENTATION DETAILS FOR TRANSFORMATIONS REQUIRING ATTITUDE DATA

3.4.1 FDOA Attitude Inputs

The Level-2 Ephemeris data is computed from inputs produced by the Flight Dynamics Operations Area (FDOA).

The attitude inputs provided from FDOA are:

- ISO Time,
- TAI (number of SI seconds since 1958-001T00:00:00 UTC,
- ECI-to-BCS quaternion (for frame rotation),
- the X, Y, Z rotation rate components (deg/s) (instantaneous spin axis in body frame),
- w-phase (Sun-to-body-X dihedral angle about rotation rate vector) (deg),
- right ascension (deg) and declination (deg) of body Z-axis,
- Z-phase (Sun-to-body-X dihedral angle about body Z-axis) (deg),
- right ascension (deg) and declination (deg) of angular momentum (L),
- L-phase (Sun-to-body-X dihedral angle about angular momentum vector L) (deg),
- right ascension (deg) and declination (deg) of major principal axis (P),
- P-phase (Sun-to-body-X dihedral angle about major principal axis P) (deg),
- nutation angle (deg),
- Quality flag:
  EKF=good extended Kalman filter solution with star tracker data
  CNV=filter not yet converged
  SUN=no tracker data; spin phase obtained from Sun sensor data

INT=no tracker or Sun sensor data; phase interpolated from neighboring tracker data
BAD=no tracker or Sun sensor data for a time span too large for interpolation

These quantities are computed and reported (by FDOA) at irregular intervals on a time cadence of approximately 0.5 to 1.0 s.

3.4.2 Calculation of ECI_to_DBCS and ECI-to_BCS Coordinate Systems

Conversion of coordinates between the Earth Centered Inertial J2000 (ECI) frame and the Body Centered System (BCS) frame can be accomplished by either using the FDOA-provided ECI-to-BCS quaternions or by constructing the transformation matrices and associated quaternions from the other FDOA-provided quantities. In the present implementation of the Level-2 Ephemeris products, the latter approach is used for two reasons: 1) The ECI-to-BCS quaternions in the raw FDOA attitude files are transformations of the frames rather than vectors (which are inverses of one another), and 2) the provided quaternions do not have very high numerical precision. In order to produce higher-precision ECI-to-BCS quaternions that rotate vectors instead of coordinate frames, we first compute the ECI-to-DBCS transformation matrix. For the DBCS system, Z-axis is along the Body Z axis (provided in ECI frame by FDOA), the Y-axis is normal to the plane defined by the Z-axis and the sun vector, S (where S =Sun_DE421 – Position_SC), and the X-axis completes a right-hand Cartesian system.

The DBCS-to-BCS transformation matrix is just a rotation around the Z-axis by -Z_Phase radians (also provided by FDOA). The overall transformation from ECI to BCS is then computed as the product of the two rotation matrices. The composite rotation matrix is then transformed to a unit quaternion (using routines in LANLGeoMag).

3.4.3 Attitude Interpolation

In order to provide attitude information on a regular time grid for the survey (30s cadence) and burst mode (30 ms cadence) files, the quantities provided by FDOA are interpolated in time. This is accomplished by interpolating the unit quaternions using Spherical Linear Interpolation (often referred to as SLERP) and by using linear interpolation of the other scalar quantities provided by FDOA (specifically, the Right Ascension and Declination of the Body Z-axis and the Z-phase angle). Although new (vector-rotating) ECI-to-BCS quaternions are computed from the interpolated scalar quantities, the SLERP-interpolated (frame-rotating) FDOA quaternions are used to provide a check on the calculations.

3.4.4 Quaternion Definitions and Usage

Quaternions are a number system that extends the complex numbers and are widely used in calculations of rotations. Quaternions provide a more compact and efficient representation of a rotation than a standard rotation matrix. The MEC files include a “quaternion_representation” variable that gives the order of the quaternion components. In version 2.y.z of the MEC data this is given as [qx, qy, qz, qw]. This representation means that the first three elements of the quaternion variables give the three *vector parts* of the quaternion and the last element gives the *scalar part*. All quaternions are provided as a rotation from ECI to a target system. To illustrate the use, assume we aim to transform the GSE position vector (‘mms1_mec_r_gse’) to the GSM coordinate system. For this we:

- Take the conjugate of the ECI→GSE quaternion (‘mms1_mec_quat_eci_to_gse’)
- Multiply the ECI→GSM quaternion by the GSE→ECI quaternion. Note that quaternion multiplication is not commutative.
- Use the resultant quaternion to convert GSE→GSM in a vector rotation operation.

Reference implementations for quaternion operations are given in the LANLGeoMag software [4, 5] and Python versions are provided in SpacePy [9, 10]. Other implementations are available for most popular programming languages.

In order to interpolate quaternions to a desired time, the end user should use SLERP (Spherical Linear Interpolation). If q_1 and q_2 are unit quaternion rotations (i.e. they represent transformations from one system to another) defined at times t_1 and t_2 respectively, and we wish to obtain the quaternion at time t (such that $t_1 \leq t \leq t_2$, then SLERP for quaternions can be expressed with the very simple formula;

$$q(t) = q_0(q_0^{-1}q_1)^u$$

Where $u = (t - t_1)/(t_2 - t_1)$ (i.e. $u = 0$ when $t = t_1$ and $u = 1$ when $t = t_2$). The routines to accomplish the quaternion operations can be found in LANLGeoMag and SpacePy libraries.

3.4.5 Transformations Between Spinning and De-spun Coordinate Systems

Quaternions are provided for transforming vectors from the ECI system to the following systems:

- BCS
- DBCS
- DMPA
- DSL
- GEO
- GSE
- GSE2000
- GSM
- SM
- SMPA
- SSL

For details on how these coordinate frames are defined, refer to the in “Magnetospheric Multiscale (MMS) Project Alignment and Coordinate System Document” [12].

3.5 IMPLEMENTATION DETAILS FOR TRANSFORMATIONS REQUIRING EPHEMERIS DATA

3.5.1 FDOA Ephemeris Inputs

The inputs obtained from the FDOA for ephemeris include the following quantities:

- Epoch (UTC)
- Epoch in TAI
- X, Y, Z position components in the Mean of J2000 system (units in km)
- VX, VY, VZ velocity components in the Mean of J2000 system (units in km/s)
- Mass in kg

These quantities are reported approximately every 30s.

3.5.2 Ephemeris Interpolation

In order to interpolate to a regular grid at arbitrary time resolution, we use Hermite interpolation. Hermite interpolation interpolates data points as a polynomial function of order q, and ensures that the solution matches both position and velocity points simultaneously. For the L2-ephemeris, we use the Gnu Scientific Library (GSL) routines for Hermite interpolation.

3.5.3 Transformations Between Systems

In order to transform between coordinate systems using the quaternions, the general prescription is as follows. If r_{eci} is a position vector in ECI coordinates and we wish to compute the position vector in GSM coordinates, r_{gsm}, then we would need a ECI-to-GSM quaternion, $q_{eci\_to\_gsm}$ and perform the following quaternion operation;

$$r_{gsm} = q_{eci\_to\_gsm}\ r_{eci}\ \ q^{-1}_{eci\_to\_gsm}$$

Where q^{-1} is the inverse of q. Note that as with rotation matrices, quaternions can be chained together to produce composite rotations. As with matrix multiplication, careful attention must be paid to the order of quaternion multiplication. For example, if one has a custom quaternion that transforms from "my_frame" to ECI, then,

$$r_{eci} = q_{my\_frame\_to\_eci}\ r_{my\_frame}\ \ q^{-1}_{my\_frame\_to\_eci}$$

And one can obtain a new quaternion to go from "my_frame" to GSM as follows;

$$r_{gsm} = q_{eci\_togsm}\ \{q_{my\_frame\_to\_eci}\ r_{my\_frame}\ \ q^{-1}_{my\_frame\_to\_eci}\}\ q^{-1}_{eci\_to\_gsm}$$

$$r_{gsm} = q_{eci\_to\_gsm}\ q_{my\_frame\_to\_eci}\ \ r_{my\_frame}\ \ (q_{eci\_to\_gsm}\ \ q_{my\_frame\_to\_eci}\ )^{-1}$$

where the later results because $(pq)^{-1} = q^{-1}p^{-1}$. Thus, a new quaternion to go from "my_frame" to GSM can be computed as;

$$q_{my\_frame\_to\_gsm}\ =\ q_{eci\_to\_gsm}\ q_{my\_frame\_to\_eci}$$

Also note that if one has a quaternion to go from one system to another, the quaternion for the reverse transformation is just its inverse.

3.6 LEVEL 2 ATTITUDE AND EPHERMERIS FILE CONTENTS

The variables contained within the MEC level 2 ephemeris and attitude files are consistent between the survey mode and burst mode files. The difference between these two data modes is that the survey files are provided at a 30-second cadence, while the burst mode files are provided at a resolution of 30 milliseconds.

Most variables follow the MMS variable naming convention and are of the form [*sat*]_[*instr*]_[*quant*], where *sat* represents the satellite (e.g., *mms2*), instr represents the instrument (here this is *mec*). The variable column in the tables below list [*quant*]. Where units are left blank they are either not applicable or the quantity is dimensionless. Additional metadata is provided in the data files following the mission guidelines.

3.6.1 Ancillary Data

Variable	Units	Type	Description
Epoch	ns	CDF_TIME_TT2000	Nanoseconds from J2000

dipole_tilt	degrees	CDF_DOUBLE	Dipole tilt angle
dst	nT	CDF_DOUBLE	Dst index from QinDenton files
earth_eclipse_flag		CDF_INT4	Earth eclipse flag
ext_model		CDF_CHAR	External Magnetic Field Model
gmst	degrees	CDF_DOUBLE	Greenwich Mean Sidereal Time
int_model		CDF_CHAR	Internal field model
kp		CDF_DOUBLE	Kp index from QinDenton files
l_dipole		CDF_DOUBLE	Dipole L-shell value
moon_eclipse_flag		CDF_INT4	Moon eclipse flag

Table 3-1 Ancillary Data

The eclipse flags are defined such that zero is no eclipse, one indicates penumbral eclipse, two denotes umbral eclipse.

3.6.2 Attitude

Variable	Units	Type	Description
L_phase	degrees	CDF_DOUBLE	Sun to body-X dihedral angle about angular momentum vector
L_vec	degrees	CDF_DOUBLE	Right ascension and declination of angular momentum vector
P_phase	degrees	CDF_DOUBLE	Sun to body-X dihedral angle about major principal axis
P_vec	degrees	CDF_DOUBLE	Right ascension and declination of major principal axis
Z_phase	degrees	CDF_DOUBLE	Sun to body-X dihedral angle about body Z-axis
Z_vec	degrees	CDF_DOUBLE	Right ascension and declination of body Z-axis

Table 3-2 Attitude Data

3.6.3 Coordinate Transformations

Variable	Units	Type	Description
quat_eci_to_bcs		CDF_DOUBLE	Quaternion rotation from ECI to BCS
quat_eci_to_dbcs		CDF_DOUBLE	Quaternion rotation from ECI to DBCS
quat_eci_to_dmpa		CDF_DOUBLE	Quaternion rotation from ECI to DMPA
quat_eci_to_dsl		CDF_DOUBLE	Quaternion rotation from ECI to DSL
quat_eci_to_geo		CDF_DOUBLE	Quaternion rotation from ECI to GEO
quat_eci_to_gse		CDF_DOUBLE	Quaternion rotation from ECI to GSE
quat_eci_to_gse2000		CDF_DOUBLE	Quaternion rotation from ECI to GSE2000
quat_eci_to_gsm		CDF_DOUBLE	Quaternion rotation from ECI to GSM
quat_eci_to_sm		CDF_DOUBLE	Quaternion rotation from ECI to SM
quat_eci_to_smpa		CDF_DOUBLE	Quaternion rotation from ECI to SMPA
quat_eci_to_ssl		CDF_DOUBLE	Quaternion rotation from ECI to SSL

Table 3-3 Coordinate Transformation Data

3.6.4 Position and Velocity

Variable	Units	Type	Description
r_eci	km	CDF_DOUBLE	Position vector in ECI/J2000
r_geo	km	CDF_DOUBLE	Position vector in GEO
r_gse	km	CDF_DOUBLE	Position vector in GSE
r_gse2000	km	CDF_DOUBLE	Position vector in GSE2000
r_gsm	km	CDF_DOUBLE	Position vector in GSM
r_sm	km	CDF_DOUBLE	Position vector in SM

r_moon_de421_eci	km	CDF_DOUBLE	Geocentric position vector of the Moon in ECI
r_sun_de421_eci	km	CDF_DOUBLE	Geocentric position vector of the Sun in ECI
v_eci	km/s	CDF_DOUBLE	Velocity in ECI/J2000
v_geo	km/s	CDF_DOUBLE	Velocity in GEO
v_gse	km/s	CDF_DOUBLE	Velocity in GSE
v_gse2000	km/s	CDF_DOUBLE	Velocity in GSE2000
v_gsm	km/s	CDF_DOUBLE	Velocity in GSM
v_sm	km/s	CDF_DOUBLE	Velocity in SM
geod_height	km	CDF_DOUBLE	Geodetic height
geod_lat	degrees	CDF_DOUBLE	Geodetic latitude
geod_lon	degrees	CDF_DOUBLE	Geodetic longitude
mlat	degrees	CDF_DOUBLE	Magnetic latitude
mlt	hours	CDF_DOUBLE	Magnetic local time

Table 3-4 Position and Velocity Data

3.6.5 Magnetic Field Model Dependent Quantities

Variable	Units	Type	Description
bfn_gsm	nT	CDF_DOUBLE	Magnetic field (in GSM) at northern footpoint
bfs_gsm	nT	CDF_DOUBLE	Magnetic field (in GSM) at southern footpoint
bmin_gsm	nT	CDF_DOUBLE	Magnetic field (in GSM) at minimum-B point
bsc_gsm	nT	CDF_DOUBLE	Magnetic field (in GSM) at spacecraft
pfn_geod_latlon	degrees	CDF_DOUBLE	Geodetic latitude & longitude of northern footpoint
pfn_gsm	km	CDF_DOUBLE	GSM position of northern footpoint
pfs_geod_latlon	degrees	CDF_DOUBLE	Geodetic latitude & longitude of southern footpoint
pfs_gsm	km	CDF_DOUBLE	GSM position of southern footpoint
pmin_gsm	km	CDF_DOUBLE	GSM position of minimum-B point
loss_cone_angle_n	degrees	CDF_DOUBLE	Northern loss cone angle
loss_cone_angle_s	degrees	CDF_DOUBLE	Southern loss cone angle
fieldline_type		CDF_INT4	Fieldline type

Table 3-5 Magnetic Field Mode Dependent Quantities Data

Footpoints of field lines are defined to be at 100km geodetic altitude, using the WGS84 geoid. The field line type can take the following valid values: 0 = Interplanetary magnetic field (IMF); 1 = Closed; 2 = Open Northern Lobe; 3 = Open Southern Lobe. Error values are: -1 = Inside Earth; -2 = Target Height Unreachable; -3 = Bad Trace.

3.6.6 Version Numbering

The version numbers for MEC data files use a *major.minor.micro* (x.y.z) scheme.

- Changes to the major version number indicate a change in data product contents or definitions that would break existing processing that uses the products.
- Changes to the minor version number are used to indicate the data quality for the magnetic field model. If required input data is missing, default values are used for a nominal quiet time and the minor version number is 0. If provisional input data is used (such as real-time values of the Kp index) the version number is 1. If definitive input data is used the version number is 2.
- The micro version number is incremented every time a file is reprocessed with the same major and minor version numbers. A common cause of incremented micro version numbers is a reprocessing due to an update in the raw position and attitude data received from NASA's Flight Dynamics Operations Area.

At the time of writing the major version number is 2. The major change that required an increment of the major version number was a change of definition of quaternions. In version 1.y.z the quaternions defined a frame rotation, and in version 2.y.z the quaternions define a vector rotation.

3.7 MEC APPENDIXES

3.7.1 Appendix A- References

Section	Document Number	Title	Revision/Date
tbd	461-SYS-SPEC-0115X	Alignment and Coordinate System Document	Rev X/ July 22, 2014
		Code available from github.com/drsteve/LANLGeoMag.	
		Code available from github.com/spacepy/spacepy, or via the Python Package Index (PyPI) using 'pip'.	
	https://ipnpr.jpl.nasa.gov/progress_report/42-178/178C.pdf	Folkner, W. M., Williams, J. G., & Boggs, D. H. (2009). The planetary and lunar ephemeris DE 421. IPN progress report, 42(178), 1-34.	
	https://doi.org/10.1016/S0032-0633(01)00119-2	Fränz, M., & Harper, D. (2002). Heliospheric Coordinate Systems. Planetary and Space Science, 50(2), 217-233.	
	https://doi.org/10.1007/s00585-995-0713-8	Hapgood, M. A. (1995, July). Space physics coordinate transformations: the role of precession. In Annales Geophysicae (Vol. 13, No. 7, pp. 713-716). Copernicus GmbH.	
	https://doi.org//10.5281/zenodo.1195041	Henderson, M. G., S. K. Morley, J. Niehof, and B. A. Larsen, *LANLGeoMag v1.5.16*, Zenodo	
	https://doi.org/10.5281/zenodo.4472086	Morley, S. K., J. T. Niehof, D. T. Welling, B. A. Larsen, J. Haiducek, A. Merrill, P. Killick, A. Reimer, M. Engel, A. Stricklan, A. Hendry, M. G. Henderson, SpacePy 0.2.2, Zenodo	
		Russell, C. T. (1971). Geophysical coordinate transformations. Cosmic Electrodynamics, 2(2), 184-196.	

		Vallado, D. A. and McClain, W.D., *Fundamentals of Astrodynamics and Applications*, 3rd ed., Microcosm Press, El Segundo, CA, 2007, Sec. 3.7.3 (see equation 3-78.)	

Table 3-6 MEC Applicable Documents

4.0 FAST PLASMA INVESTIGATION (FPI)

4.1 FPI OVERVIEW

The Fast Plasma Investigation (FPI) measures the differential directional flux of magnetospheric electrons and ions on the Magnetospheric Multiscale Mission (MMS) with unprecedented time resolution to resolve kinetic-scale plasma dynamics. Utilizing four dual 180-degree top hat spectrometers for electrons (DES) and four dual 180-degree top hat spectrometers for ions (DIS) around the periphery of each of the four MMS spacecraft, the spectrometers use electrostatic field-of-view deflection to provide 4pi-sr field-of-view with, at worst, 11.25-degree sample spacing. Energy/charge sampling is provided by swept electrostatic energy/charge selection over the range from a few eV/q to 30000 eV/q.

FPI performs rapid collection of electrons and positive ions in phase space densities within and near sites in the Earth's magnetosphere where reconnection (or the interconnection of magnetic field lines and astrophysical plasmas) takes place for the purpose of determining the kinetic processes occurring in the electron diffusion region that are responsible for collisionless magnetic reconnection, especially in regard to how reconnection is initiated.

A full description of the design of FPI, its ground calibration results, its in-flight calibration plan, its operational concept, and an overview of its data products can be found in the publication:

Pollock, C., Moore, T., Jacques, A., Burch, J., Gliese, U., Saito, Y., ... & Zeuch, M. (2016). Fast plasma investigation for magnetospheric multiscale. Space Science Reviews, 199(1), 331-406.

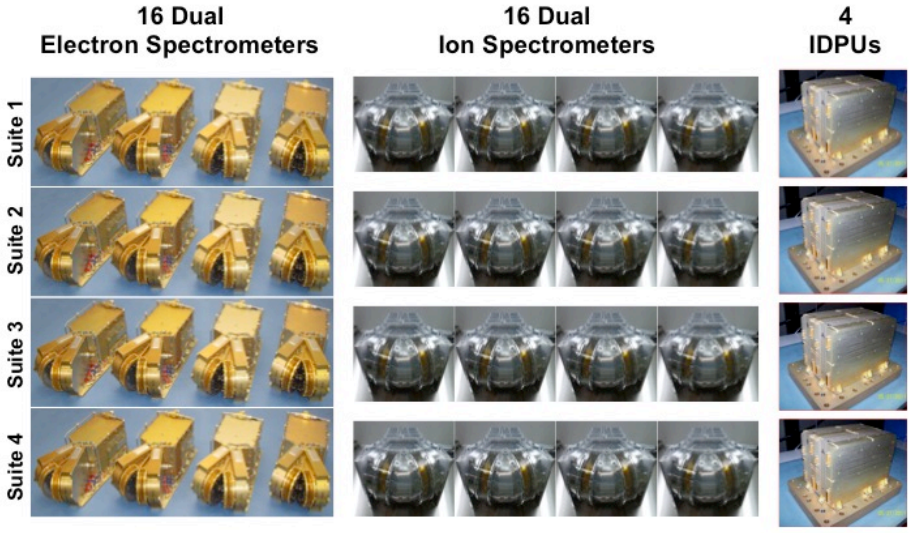

Figure 4-1 The 64 FPI Spectrometers and 4 IDPU

4.1.1 Status of FPI Spectrometers

FPI consists of eight high-speed sensors for each species, packaged in pairs as dual spectrometers, spaced around each spacecraft perimeter. This design was implemented in order to ensure that full azimuthal sampling need not depend on the spin of the spacecraft while allowing for measurement of ion and electron phase space densities at extremely high speeds. Measurements are taken at 32 different energies in 512 different directions with uniform coverage of the sky. The statistical and systematic uncertainties

of FPI data have been quantified, and Level-2 (L2) FPI data products regularly provide high-fidelity estimates of current densities using data from only a single spacecraft, enabling unprecedented studies of kinetic-scale physics. In November 2017, FPI introduced a refined energy sweep table for solar wind observations (ions: 197 eV-9222 eV; electrons: 4 eV-940 eV).

All FPI electron and ion spectrometers are functioning nominally with the exception of the following:

- MMS3 DIS008: On 6 February 2018 22:08 UTC (orbit 700), one of the two ion spectrometers in quadrant 0 began erroneously measuring anomalous counts in the highest energy ranges. Cause of the anomaly remains unknown. As a result of the anomaly, the configuration of this spectrometer pair was modified to prevent the taking of measurements above 11 keV. During sampling by other MMS3 ion spectrometer pairs above 11 keV, DIS008 repeats its highest allowed operational energy setting.
- MMS4 DES210: On 7 June 2018 12:43 UTC, the electron spectrometer pair in quadrant 1 suffered a high voltage failure and was subsequently shut down.
- MMS4 DES215: On 15 July 2018 00:47 UTC, the electron spectrometer pair in quadrant 0 suffered a high voltage failure and was subsequently shut down.

The following is a table of the anomalies that have occurred in regards to the FPI spectrometers since the start of the mission, as discussed in detail above.

Date	Time (UTC)	FPI Unit	Flight Module	Apparent Failure (Determined Via Diagnostic Testing and Analysis)
2/6/2017	22:08	DIS0	DIS008	Erroneous high counts in approx. x5 pixels at the highest energy steps
6/5/2018	12:43	DES1	DES210	HV801 on ESA high range stepper circuit
7/15/2018	00:49	DES0	DES215	HV801 on Deflector0 high range stepper circuit

Table 4-1 FPI Off-Nominal Spectrometer Status

4.1.2 Status of FPI Science Data

FPI L2 publication quality distributions and moments are generally available for all designated science regions of interest. In addition, FPI burst resolution L2 distributions and moments are generally available for all time segments selected by the SITL and successfully downlinked. The following accommodations were made in order to mitigate the FPI anomalies cited above:

- MMS3 DIS data: For MMS3 ion spectrometer energy steps higher than 11 keV from areas of the sky in which DIS008 does not contribute, an average phase space density ratio is obtained between that energy and 11 keV. DIS008 distribution data is then scaled by that ratio under the assumption that the angular structure at the highest DIS008 sampled energy is similar to any higher energy sampled by the other spectrometers. This is repeated for all energy steps that would, under nominal conditions, be above the highest DIS008 sampled energy. During data validation, any MMS3 ion measurements exhibiting high spintone counts relative to the other MMS observatories are flagged, as they are most likely an indication of differing angular structure at high energies.

- MMS4 DES data: Post-anomaly MMS4 electron Fast Survey distributions contain fill values (-1e31) to indicate look directions where DES210 and DES215 combined observations contribute greater than 75% of the time accumulation. MMS4 electron burst distributions contain fill values (-1e31) to indicate look directions corresponding to DES210 and DES215 observations. MMS4 moments files are not generated.

The FPI ground system processes all available downlinked Fast Survey and burst data, including partial segments and those that were not downlinked for all MMS observatories. That said, there are a small number of Fast Survey and burst intervals in which data is not completely available for FPI. The reasons for the incomplete record of FPI data include the following:

- No FPI data is available
  - Maneuvers: FPI is placed into safe mode (i.e., does not operate) during a window beginning thirty minutes prior to and extending to thirty minutes after the conclusion of any spacecraft maneuver.
  - Spacecraft anomalies: No FPI data collected when an observatory is in emergency safe mode.
  - Scheduled downtime: FPI did not collect science data during specific mission phases, including the majority of Phase 1X (with the exception of Bursty Bulk Flow (BBF) testing), for almost two months prior to the first tail pass, and during the long shadows of the summer of 2019.
  - Unscheduled downtime: FPI was placed in safe mode during analysis and mitigation activities of the DIS008 (MMS3) and DES210/DES215 anomalies (MMS4).
  - BDM artifacts/anomalies: There are a number of burst segments, many of them with SITL messages like "orphan burst buffer sweep," where there is no associated data.
- FPI data not publicly released
  - Tests: The FPI operations team conducts occasional tests during which no scientifically usable data is collected. This includes FPI data collected during much of Phase 1X and the FPI noise test.
  - Spacecraft anomalies: FPI data that is determined to be scientifically unusable due to spacecraft anomalies. Examples include the MMS3 timing issue in January 2017.
  - FPI anomalies: FPI data that is determined to be scientifically unusable due to an instrument anomaly, such as during sensor anomalies or faulty configuration.
- FPI distributions released, but no moments
  - FPI MMS4 DES data beginning with June 2018 due to the DES210/DES215 anomalies discussed above.
  - Data collected during moon shadows, including two short periods on 2017-11-19 and 2019-12-27.
  - Segments where there is no available magnetic field or spacecraft potential data.

4.2 FPI DATA USAGE SUMMARY CHECKLIST

When it comes to analyzing the FPI data on the MMS mission, there are important items that have been considered over the lifetime and continue to be considered as the mission continues:

FPI in the Solar Wind	4.1.1 & 4.5.6
Burst Segments	4.3.1.2 & 4.4.3.2
Instrument Thresholds vs Ambient Plasma Distribution	4.5.3

Counting Statistics and Establishing the 1-Count Level	4.5.4
Quasi-Neutrality Check	4.5.5
FPI Moment Error Calculations	4.5.7
Photoelectron Contributions	4.5.7.2
Compression Artifacts	4.5.7.3
Background Radiation	4.5.7.5
Quality Flags	4.5.8

Table 4-2 Data Usage Summary Checklist

Overall, the checklist provides a guide of the known data features and recommendations for mitigation. However, it is up to the data user to review the data and carefully consider what the measured signals indicate about the natural plasma environment versus what is indicated about any spacecraft induced plasma environment. Meanwhile, the FPI team continues to work diligently to remove as many induced effects as is possible from the FPI moment values within the data processing pipeline. Information of the components of this checklist can be found throughout the rest of the FPI section of this document as referenced above.

4.3 FPI MEASUREMENT STANDARDS AND VOLUME

4.3.1 FPI Measurement Timing

4.3.1.1 Overview

The time variable in all FPI data products mark the beginning of the data collection interval. FPI commands stepping durations within a Stepping Table on the order of 0.5 μs for 128 steps in a cycle, totaling 30 ms for DES and 150 ms for DIS. The count integration times for each species are the same for every step in the sequence: 195 μs for DES and 1000 μs for DIS. The settling times are apportioned across the sweeps based on detailed characterization of the dynamic behavior of each high voltage stepper supply. At the end of a stepping cycle, a 16-by-32 pixel resolution skymap is generated for each of 32 targeted energy levels.

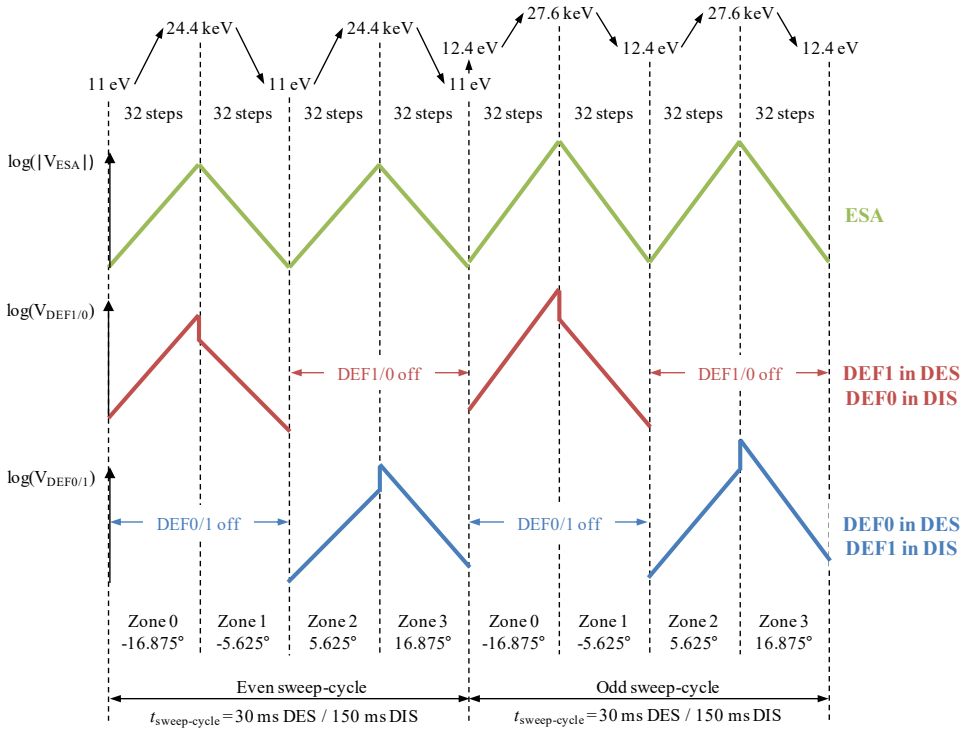

Figure 4-2 Measurements of the ESA and Deflector Plates in the DxS

4.3.1.2 Burst Data Product Timing

The Burst Data Product applies a single timestamp to all 32 skymaps generated within a stepping cycle. In this mode, complete sets of 8192 measurements are acquired every 30ms for DES and every 150 ms for DIS. As depicted in Figure 4-2, the ESA and Deflector step up and down together in a cycle. The skymap for each energy level is filled throughout the stepping cycle and is not complete until Zone 3. Therefore, the decision was made to utilize the cycle start time as the timestamp for all skymaps. A Burst Data Product may be compressed if the counts measured exceeds [limit] and is flagged within the data product.

4.3.1.2.1 Microsecond Level Precision

Each measurement in the 128-step cycle captures counts in 16 azimuth angles from both heads for each of the 4 units, totaling 128 measurements per step. While the average time allocated between stepper transitions is 234 µs (30 ms/128 steps) for DES and 1172 µs (150 ms/128 steps) for DIS, the actual time allocated per-step will differ from the average calculation up to 250 µs. To enable microsecond-level precision of FPI data products, the FPI team produces offsets for each step within a cycle for each of the 61 (and counting) unique Stepping Tables that have been utilized in operations. The correct microsecond offset table is included in every Burst Data Product for users to apply to each skymap.

4.3.1.3 Fast Survey Data Product Timing

The Fast Survey Data Product accumulates each of the 32 energy skymaps for 4.5 seconds, with a net result of 150 DES (4.5 s/30 ms) or 30 DIS (4.5 s/30 ms) Burst Data Products per accumulation cycle. This accumulation results with a “smeared” effect as the spacecraft rotates for the duration. The accumulation start time is used as the timestamp for each set of skymaps. A Fast Survey Data Product may be

compressed if the counts measured exceeds [limit] and is flagged within the data product. Additionally, the Fast Survey Mode is the nominal data collection mode for the Instrument Suite (IS), producing full Survey and Burst Data Telemetry continuously.

4.3.1.4 Slow Survey Data Product Timing

The Slow Survey Data Product accumulates each of the 32 energy skymaps for a duration of 3 spins, as provided by a Delphi pulse count. This results in a variable duration utilized per accumulation cycle. The Slow Survey mode utilizes different stepping tables than the Burst and Fast Survey Data Products. Slow Survey mode also utilizes a single quadrant (one DES and one DIS unit) while active; the selected quadrant is specified upon entering the Slow Survey mode. The accumulation start time is used as the timestamp for each set of skymaps. A Slow Survey Data Product may be compressed if the counts measured exceeds [limit] and is flagged within the data product. The Slow Survey Mode is a low data rate mode used when the Spacecraft is not in or near a targeted ROI. In this mode, a reduced set of Survey Data Telemetry is produced while Burst Data Telemetry is not.

4.3.2 Relative Telemetry Allocations and Data Volume

The FPI compression routines ensure a maximum data volume for science data products. Due to the level of compression, the Slow Survey and Fast Survey are essentially always lossy and occupy the full allocation. The burst data, by contrast, are generally compressed losslessly to a smaller volume than the maximum allocation. Because of this, the actual data usage for FPI burst data is highly variable based on environment, thus a peak and an average are both provided, along with other telemetry usage rates, in Table 4-3. FPI also collects, and downlinks, trigger data, however these data are included in the Fast Survey packet.

Slow Survey	**Fast Survey**	**Burst**	
1.28	10.24	1A	1B ->
		Peak	
		1560.00	1966.08
		Average	
		1343.00	1427.00

Table 4-3 Telemetry Use Rates for FPI (kbit/s)

The FPI burst telemetry usage was updated after MMS Phase 1A to mitigate compression related error in the DES burst data. It is also noteworthy that as two DES analyzers on MMS4 were powered off, the telemetry usage by FPI on MMS4 has lessened correspondingly. Distributions of the DES compressed image size for the four observatories are shown in Figure 4-3.

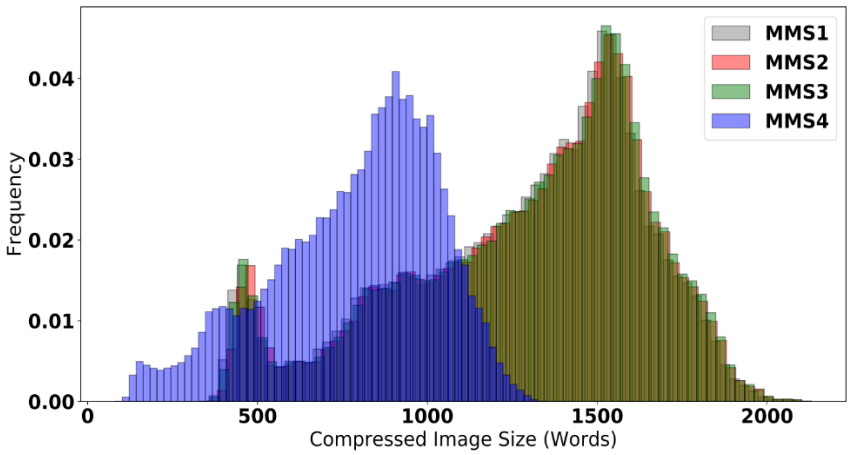

Figure 4-3 Distribution of DES Image Sizes for the Four Observatories After Two DES Were Powered Off

4.4 FPI CALIBRATION AND VALIDATION

A full description of the design of FPI and its calibration results relative to this 4.4 section can be found in the publication:

> Pollock, C., Moore, T., Jacques, A., Burch, J., Gliese, U., Saito, Y., ... & Zeuch, M. (2016). Fast plasma investigation for magnetospheric multiscale. Space Science Reviews, 199(1), 331-406.

4.4.1 Calibration Overview

Most importantly in the full calibration program, certain mathematical functions and calibration measures can only be performed on the ground, meaning on-orbit activities rely heavily on the precise framework laid out prior to flight. Within this concept, not only does calibration depend on on-ground versus in-flight, but it depends heavily on the types of particle instruments as well. The most common instrument for low-level plasmas consists of a top-hat electrostatic analyzer (ESA) geometry coupled with a microchannel-plate-based (MCP-based) detection system. Each of the four spacecraft carries eight FPI electron spectrometers (DES) and eight FPI ion spectrometers (DIS). These are packaged in pairs in back-to-back configuration, as dual spectrometers for each species: DES and DIS. Four dual spectrometers for each species are placed around the MMS instrument deck perimeter at 90◦ intervals. For each dual spectrometer, the two (undeflected) 180◦ field of view (FOV) fans are separated by 45◦ in azimuth. This FPI measurement approach means that the 3D velocity distribution functions for electrons and ions will each be assembled using eight different spectrometers, four different ESA high voltage (HV) stepping supplies, and eight different deflection HV stepping supplies. While common sets of energies and angles are targeted, the spectrometers and their HV stepping supplies all have slightly different properties that, in the case of the supplies, will evolve differently through mission life. To compensate, the effects of the voltage commands used in targeting these energy and angle sets will be monitored closely and individual HV offsets will be applied over time for each of the spectrometers. The samples in velocity space have not only absolute, but also relative uncertainties within a single 3D distribution. For this reason, separate sweep table constants are maintained for each dual spectrometer tailored to the individual HV supplies; these will be maintained and updated as necessary. The appropriate voltages are initially based on careful laboratory calibrations and have been and will continue to be updated throughout the life of the mission as determined necessary by in-flight calibration activities.

4.4.2 Pre-Flight / On-Ground Calibration

The DIS and DES flight units were calibrated in different locations in order to fulfill the timeline of this mission due to the fact that the magnitude of the FPI development and deployment required a distributed effort and the full expertise and support of numerous institutions. The timeline in this case in which the development of the instruments and spacecrafts took place occurred from 2008 to 2013, with integration and testing then having been performed from 2013 to 2014 prior to the launch and commissioning in October 2014 - January 2015. Goddard Space Flight Center (GSFC) provided development and delivery of the DES instruments and the Instrument Data Processing Units (IDPU), as well as operation and calibration procedures and associated flight software in the form of Central Instrument Data Processor (CIDP) macros. The DIS instruments were developed by the Japanese Meisei Electric Co., Ltd. under contract to Southwest Research Institute (SwRI) and with the guidance and direction both from co-Investigators at the Japanese Institute for Aeronautics and Astronautics (ISAS) and from GSFC. The Low Voltage Power Converters (LVPC) in the DES, DIS and IDPU were developed by the U.S. Space Power Electronics, Inc. The Southwest Research Institute developed the DES and DIS High Voltage Power Supplies (HVPS). GSFC procured the DES MCPs from Photonis USA and performed the preconditioning and testing for flight. The DIS MCPs were procured from Photonis France S.A.S. by the French Institut de Recherche en Astrophysique et Planetologie (IRAP). IRAP also conditioned, tested and mounted the DIS MCPs on anode boards provided by Meisei. These MCP/anodes were then re-tested by IRAP before re-delivery to Meisei for integration into the DIS sensors. The thirty-two DES and four IDPUs were functionally and environmentally tested and calibrated at GSFC. The thirty-two DIS' were environmentally tested at Meisei and ISAS (including pre- and post- environmental beam testing) and were calibrated at NASA's Marshall Space Flight Center (MSFC) Low Energy Electron and Ion Facility (LEEIF). Additional testing was performed by the GSFC FPI team after the initial deliveries, including live high voltage testing with particle sources late in the MMS observatory-level thermal vacuum sequence and an extended (1500 hours) thermal vacuum testing of all DIS and DES units designed to purge potentially thermally compromised HV801 opto-couplers. GSFC has lead responsibility for FPI Phase E mission activities in close collaboration with the development partner institutions. While all DES are nominally identical, as are all DIS, individual performance varies due to the variations in part, detectors, surface machining/finishing, and assembly; some variations in parts can change throughout the mission life. Within the specific case of FPI, the DES utilizes hemispheric geometry while the DIS incorporates toroidal geometry.

The full calibration program included determination of the operating point (MCP gain and voltage, and discriminator threshold), characterization of signal loss due to MCP gain variation, relative pixel to pixel MCP efficiency variation, cross talk, noise, coupled energy/azimuth-angle band pass locations, shapes and amplitudes and their dependence on high voltage stepper supply states, and the locations and shapes of the polar angle band passes and any dependence they have on high voltage stepper supply state. The ground calibration also characterized system dead time and the effectiveness of UV rejection. The general ground-based calibration procedure was (1) illuminate sensor with a beam sufficiently broad to fill the entrance aperture and sufficiently narrow in both energy and 2D angle to approximate an impulse stimuli; (2) execute V_{ESA} and V_{DEF} sweeps centered at voltages to pass the beam particles and wide enough to capture the V_{ESA}/V_{DEF} band pass; and (3) mechanically articulate the sensor to measure beam incidence over the complete angular range of pixel response. The zero deflection state—used in Slow Survey mode and in the case of an anomaly—was also calibrated.

4.4.3 In-Flight Calibration

To ensure the data from each set of eight spectrometers can be corrected to yield an accurate output for a given input, an extensive laboratory and in-flight calibration regimen was developed to appropriately balance operating parameters and to identify and correct for instrument variability and noise. The

extensive program of in-flight calibration is additionally executed for the purpose of maintaining a high standard of instrument calibration for all units. Quantities of interest in this calibration program include the detector systems' operating points, detection efficiencies, and HV stepping supply performance. FPI in-flight operational sequences are implemented in the form of Absolute Time Sequence (ATS) commands, which designate when planned activities are to be executed in the context of each spacecraft's activities. In this case, all activities are performed in accordance with the FPI mode-switching diagram shown in Figure 4-4. Individual commands, Relative Time Sequences (RTS) or Macros, represent individual commands that may take form in elements in the ATS. The use of these individual commands allows FPI to execute the vast array of command sequences necessary to maintain stable for orbit. An extensive program of in-flight calibration is executed for the purpose of maintaining a high standard of instrument calibration for all units. While in-flight options are limited to many instrument parameters that have been stored in up-loaded tables and/or in comment registers, they are able to be adjusted based on experience and the results of on-orbit calibration sequences.

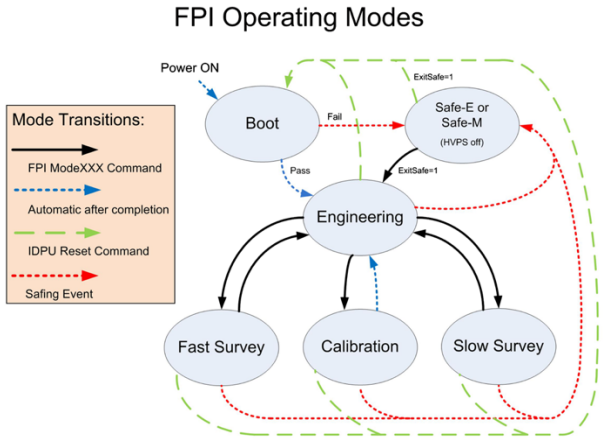

Figure 4-4 FPI IDPU State Diagram of Modes of Operations

4.4.3.1 Operating Point Calibration

The Operating Point Calibration is a method to balance the signal loss and crosstalk of the detection system, minimizing both, and ensuring that all spectrometers are at a similar operating point (crosstalk / signal loss balance). The discriminator threshold is swept through its applicable operating range at the current MCP operating voltage, and a value 50V higher. The resulting data are evaluated to determine the best MCP voltage to maintain the desired operating point. If needed, the MCP voltage is increased during periodic macro loads; the operating discriminator threshold is held constant.

The gain is nonuniform around the MCP due to the relative angle of the pore entrance to the incoming particle trajectory. Because a single MCP voltage is applied, and a single discriminator voltage is applied to all preamplifiers, a spread in operating point is typically present over the 16 pixels of a given head. As shown by the blue points (current MCP voltage) in Table 4-5, operating points are typically chosen such that the count rate crosstalk is below 10% for all DES pixels, or below 5% for all DIS pixels. Allowing the crosstalk to float up to these values will minimize the corresponding signal loss.

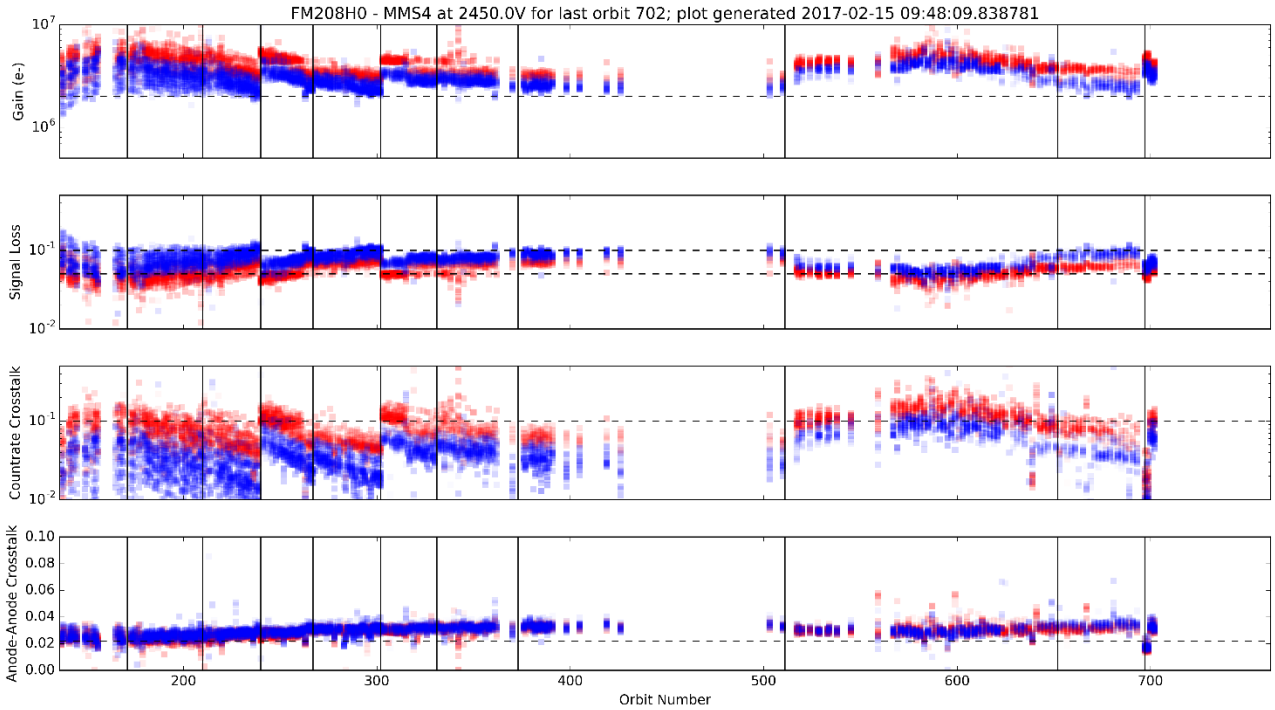

Figure 4-5 Sample Operating Point Calibration Plot (for all pixels at current voltage (blue) and an increase of 50V (red). Vertical black lines represent opportunities for a voltage increase (macro loads).

In flight, the operating point calibration is run close to L7 on both the inbound and outbound leg of the orbit, when time permits. On the ground, the DIS flight units were calibrated at the NASA MSFC Low Energy Electron and Ion Facility, and the DES were calibrated at NASA GSFC Space Plasma Instrumentation Facility.

4.4.3.2 Burst Calibration

The burst calibration process consists of the combination of algorithmic development and human oversight that is required in order to translate the low-level instrument telemetry into science-quality datasets that have been reviewed and are suitable for public release. The collection of count-values (32 azimuth-angles x 32 energies x 16 zenith-angles, characterizing all of this phase space) which results from each iteration is called “burst”, a “burst sky-map”, or a “burst-map”. There is an on-board evaluation of each burst which selects a subset of burst for ground segment processing. Burst data calibration is performed by acquiring burst resolution data for a period of up to three spins (60 s) at a selected point within the ROI of each orbit. This data is used to perform statistical analyses and flat-fielding of the FPI look directions. The errors are then corrected during ground processing. The particular data to be used are selected by the FPI team and marked for download through a similar interface to that used by the Scientist in the Loop.

Full description of the flat-fielding algorithm can be found in the publication:

Gershman, D. J., Dorelli, J. C., Avanov, L. A., Gliese, U., Barrie, A., Schiff, C., et al. (2019). Systematic uncertainties in plasma parameters reported by the fast plasma

investigation on NASA's magnetospheric multiscale mission. Journal of Geophysical Research: Space Physics, 124, 10345– 10359. https://doi.org/10.1029/2019JA026980.

Beyond burst data calibration, burst voltage calibration used may be used in conjunction with ensemble calibration to provide relative calibration of the stepper voltages. Several spins of burst data are collected and the relative position of sharp gradients and features are compared from spectrometer to spectrometer in velocity space. These measurements are then compared to pull out corrective voltages to the high voltage steppers.

Full description of the high-voltage offsets can be found in the publication:

Barrie, A. C., Schiff, C., Gershman, D. J., Giles, B. L., & Rand, D. (2021). Calibrating electrostatic deflection of charged particle sensors using ambient plasma measurements. Journal of Geophysical Research: Space Physics, 126, e2021JA029149. https://doi.org/10.1029/2021JA029149

4.4.4 Compression Pipeline

The spectrometers on the MMS spacecraft are dual half top analyzers that measure the 3-D plasma environment, and the IDPU processes the data, including performing data compression. FPI produces a full-sky count image (sky map) every 30 ms for electrons (DES) and every 150 ms for ions (DIS). The compression routine is evaluated by determining how small can a sky map be compressed while maintaining lossless compression as well as when truncation of DWT coefficients becomes necessary in lossy compression mode and what are the characteristics of the introduced compression error. Methods of compression can further be broken down into data modes- Fast Survey (FS) and Slow Survey (SS), each with their own parameters and effects.

FPI DES and DIS data are compressed within the instrument data processor using an algorithm designed for image compression.

(1) 3D data are arranged into 2D arrays
(2) A wavelet transform acts as a low pass/high pass filter
(3) Low pass/high pass component arrays are created
(4) Bit-plane encoding is applied to the arrays
(5) Starting with the high-frequency components, bits of lesser significance are discarded until size is reduced to a pre-set limit
(6) An inverse process on the ground reconstructs the data array (image)

FPI captures data over 100 times faster than previous plasma instruments, such as the CLUSTER (Geach et al., 2005) mission, requiring a higher compression ratio to fit within the telemetry allocation. These faster time resolution measurements enable scientists to observe phenomena that are spatially narrow or short in time duration, such as the electron diffusion region of a reconnecting magnetic field (Burch, Torbert, et al., 2016). This increased data rate, however, leads to proportionally increasing data volumes that must be addressed by more advanced data compression algorithms. FPI uses a Discrete Wavelet Transform and Bit Plane Encoder (DWT/BPE) (Winterrowd et al., 2010) for data compression. This is the first plasma instrument to use this method of compression, and thus serves as a benchmark for future plasma spectrometers. The DWT/BPE wavelet compression is able to compress > 99% of the FPI burst data in a lossless manner, with a compression ratio of about 5:1. The remaining 1% of data have some amount of compression error introduced, but this is considered negligible from a science perspective (Barrie et al., 2017, 2018). When the wavelet-transform data exceed the pre-set buffer limit compression

loss occurs. The compression error typically has a small effect on plasma moments. Fast Survey data is compressed more, at a rate of near 17:1. These data suffer from a greater induced error, however new efforts by the FPI team are underway to correct for these compression artifacts (da Silva et al., 2020). When applied to images, the process progressively degrades fine-scale features, but typically produces reconstructed images that are recognizable. When applied to plasma measurements, the process has the potential to alter features in a way that could affect interpretation of the data.

The majority of DIS burst sky maps are compressed in a lossless fashion, with no error introduced during compression. While approximately half of DES maps had some level of loss, it was found that there is little effect on the plasma moments and that errors present in individual sky maps are typically minor. However, this still is not to say that any compression loss cannot or will not affect the accuracy of plasma parameters. Despite the suggested tweaks, it was found that wavelet-based compression, and a DWT/BPE algorithm in particular, is highly suitable to data compression for plasma measurement instruments and can be recommended for future missions.

Full description of compression pipeline data can be found in the publication:

> Barrie, A. C., Smith, S. E., Dorelli, J. C., Gershman, D. J., Yeh, P., Schiff, C., and Avanov, L. A. (2017), **Performance of a space-based wavelet compressor for plasma count data on the MMS Fast Plasma Investigation**, *J. Geophys. Res. Space Physics*, 122, 765– 779, doi:10.1002/2016JA022645.

4.4.5 Science Data Validation

Over the mission lifespan, validation has been applied over each segment in their own relevant parameters. Prior to launch, validation took place through the hundreds of tests on the instruments and their purposes. Through the launched-mission's lifecycle, validation has transformed into ongoing reviews of the data as well as corrections to the instruments as needed as the data continues to progress.

The FPI team manages the operating point of each spectrometer by capturing a small amount of calibration data each orbit. This data is then processed and trended to create a picture of the balance between gain, signal loss, and cross talk for each of the 64 individual sensor heads. The FPI team assesses this data weekly for short term trends or behaviors and over the longer term for the trends evident in the data. The trends in the data inform if and when each sensor head may need a small adjustment to the applied MCP voltage. Using this approach throughout the mission the FPI team has been able to manage the spectrometer operating points to maintain a consistently optimal balance and performance of each sensor.

To validate FPI science data, each corrected FPI fast survey file is examined to ensure that:

(1) Spintone amplitudes are less than 50km/s in the magnetosheath
(2) Density counts are in agreement across all four observatories in a variety of environments
(3) Any systematic offsets in the bulk velocity's z-component do not exceed a few km/s in the magnetosheath

Full description of the spin tones and offsets in FPI data can be found in the publication:

> Gershman, D. J., Dorelli, J. C., Avanov, L. A., Gliese, U., Barrie, A., Schiff, C., et al. (2019). Systematic uncertainties in plasma parameters reported by the fast plasma

investigation on NASA's magnetospheric multiscale mission. Journal of Geophysical Research: Space Physics, 124, 10345– 10359. https://doi.org/10.1029/2019JA026980.

Because FPI burst and fast survey science data use the same underlying correction tables, the quality of the data between the two modes is equivalent. Therefore, validation of the fast survey data is sufficient to ensure the validity of the burst data.

In addition, the FPI team confirms that any missing science data correlates with expected routine or anomalous outages.

4.5 MEASUREMENT ALGORITHM DESCRIPTIONS

4.5.1 Theoretical Basis

The "spacecraft coordinate system" ('S/C' designation) for a given platform rotates and translates with that spacecraft, and defines the original frame for portraying the FPI data. The several different data sets produced on the ground share common elements of methodology. The fundamental scientific data product is the velocity distribution function, (x,v,t), which is directly related to the measured skymaps. It is a probability density or phase space density such that $(\mathbf{x},\mathbf{v},t)d\mathbf{x}d\mathbf{v}$ is the number of particles in phase space volume element $d\mathbf{x}d\mathbf{v}$ at time t.

4.5.2 Conversion of Instrument Signals to Phase Space Density

The FPI is dedicated to the rapid measurement of the phase space densities of electrons and positive ions within and near sites in Earth's magnetosphere where reconnection occurs. The basic scientific quantities are the phase space densities and the plasma moments. This high temporal resolution in 3D phase space measurements is unprecedented in the history of scientific space flight and by far the single biggest driver on the design and implementation of the experiment. The deployment strategy allows measurement of the 3D ion and electron phase space densities at speeds limited primarily by the stepper speeds of the high voltage power supplies and the counting statistics possible within the very short accumulation intervals imposed. The fundamental scientific data product is the velocity distribution function, f(**x**,**v**,t), which is directly related to the measured skymaps. It is a probability density or phase space density such that f(**x**,**v**,t)d**x**d**v** is the number of particles in phase space volume element d**x**d**v** at time t.

In deriving the relationship between the velocity distribution function and the skymaps, it is assumed that all of the entrance apertures of a DxS analyzer are illuminated by particles drawn from the same velocity distribution. Phase-space is sampled repeatedly and seamlessly (no "gaps" in time) with a rapid (species-dependent) cadence. The velocity distribution function contains considerable information regarding the physical state of the plasma. Plasma fluid parameters are computed as moments of the particle velocity distributions. The technique integrates f(**v**), weighted by powers of **v**, over the 3-dimensional velocity space. For the FPI data products, the integrals are evaluated numerically. This method has the advantage that it does not depend on a-priori assumptions about the form of the distribution functions. Corrections to the energies, and hence the velocities, due to a non-zero spacecraft surface potential are made prior to the integration.

More specific phase space density equations can be found in the publication:

Pollock, C., Moore, T., Jacques, A., Burch, J., Gliese, U., Saito, Y., ... & Zeuch, M. (2016). Fast plasma investigation for magnetospheric multiscale. Space Science Reviews, 199(1), 331-406.

The unprecedented spatiotemporal resolution and exceptional data quality of the phase space densities provided by the FPI spectrometers from all four spacecraft have enabled the successful determination of phase space density gradient measurements. One immediate scientific application of this capability is the direct measurement of the velocity-space structure of terms in the Vlasov equation [*Shuster et al.*, 2021]. For DES, temporal derivatives $\partial f_e/\partial t$ computed in the frame of an individual spacecraft can be determined at a cadence of 30 ms. The vector spatial gradient term ∇f_e can be approximated using four spacecraft data and making use of the usual linear gradient assumption, which in turn can be used to determine the full $v\cdot\nabla f_e$ term [*Shuster et al.*, 2019]. The resolution of these spatial derivatives is limited by the inter-spacecraft separation, which at the dayside region of interest is commonly on the order of 10 km. In principle, the velocity-space gradient term $\nabla_v f_e$ can also be measured on each spacecraft and is limited by the energy spacing, which for a typical thermal electron is on the order of 10 eV.

More detailed discussion and presentation of the science applications and techniques implemented to obtain phase space density gradient measurements using DES data may be found in the publications:

> Shuster, J., Gershman, D., L.-J. Chen, et al. (2019), MMS Measurements of the Vlasov Equation: Probing the Electron Pressure Divergence Within Thin Current Sheets, Geophys. Res. Lett., 46, https://doi.org/10.1029/2019GL083549.
>
> Shuster, J., Gershman, D., Dorelli, J., Giles, B., et al. (2021), Structures in Terms of the Vlasov Equation Observed at Earth's Magnetopause, Nature Physics, https://doi.org/10.1038/s41567-021-01280-6.

4.5.3 Instrument Thresholds vs Ambient Plasma Distribution

The FPI L2 data products reflect the full range of plasma populations in proximity to the spectrometers. This includes the ambient plasma environment within that energy range and – on occasion – spurious plasma populations induced in the vicinity of the spacecraft. All the while, the FPI team tags its data with a variety of quality flags to indicate intervals that need warrant consideration -- and perhaps correction -- when using the data for event analysis. Within this, the FPI quality flag definitions are identical for Quicklook and L2 data products.

4.5.4 Counting Statistics and Establishing the 1-Count Level

In knowing and using the statistical error information provided in the CDF files, the error associated with the inherent spectrometer counting statistics is provided in those CDF files for both the moments and for the distributions while the actual counts can still be recovered.

More specific descriptions of how statistical errors are calculated for FPI moments can be found in the publication:

> Gershman, D. J., Dorelli, J. C., F.-Viñas, A., and Pollock, C. J. (2015), The calculation of moment uncertainties from velocity distribution functions with random errors, *J. Geophys. Res. Space Physics*, 120, 6633– 6645. https://doi.org/10.1002/2014JA020775.

4.5.5 Quasi-Neutrality Check

For L2 data, FPI densities were initially scaled by an overall factor to match those of plasma waves. The overall sensitivity of DES and DIS can be subject to change with each FPI macro load in which the voltages applied to the MCP detector stack for each sensor are adjusted. In Phase 1a, the relative

sensitivity of DIS across spacecraft has not been observed to change. The sensitivity of DES with respect to DIS has changed by ~10-20% over the course of commissioning and Phase 1a. A correction factor for DES densities is derived from observations of DES and DIS in the magnetosheath. The minimum time-scale for which a correction factor can be applied is an entire orbit, though in practice the same correction factor is typically used for all orbits in a given correction cycle (~30 days). Periods where changes in DES and DIS densities are correlated and have the same ratio as in adjacent quiet magnetosheath intervals suggest that the entire relevant ion and electron distribution functions are being sampled.

4.5.6 FPI in the Solar Wind

Onboard summing of burst counts to form Fast Survey data products leads to increased numbers of counts/bin in Fast Survey skymaps. In the solar wind, the maximum number of allowable counts in each bin is exceeded leading to clipping and resulting in a distortion of the plasma moments. FPI's field-of-view is binned with 11.25x11.25 deg resolution. In the polar angle direction (+Z to -Z for each sensor), angular space is continually sampled. However, the angular response in the azimuthal direction (X-Y plane) is <10deg. Therefore, as deflection states sweep out the azimuthal plane, there are gaps in the angular sampling of ambient plasma. Sharp angular structure in both DIS and DES can lead to apparent 'spikes' in the plasma moments that are spin-phase dependent. Such a phenomenon occurs often in high Mach number plasmas, such as the solar wind.

A detailed study of FPI's response in the solar wind can be found in the publication:

> Roberts, O. W., Nakamura, R., Coffey, V. N., Gershman, D. J., Volwerk, M., Varsani, A., et al. (2021). A study of the solar wind ion and electron measurements from the magnetospheric multiscale mission's fast plasma investigation. Journal of Geophysical Research: Space Physics, 126, e2021JA029784. https://doi.org/10.1029/2021JA029784

4.5.7 Error Analysis and Known Features in the Dataset

The goal of error analysis is to specify what uncertainties attend the azimuth, energy, zenith-angle, count, and phase-space density measurements reported in the data products. The FPI L2 data products reflect the full range of ~few eV to ~30 keV plasma populations in proximity to the spectrometers. This includes the ambient plasma environment within that energy range and – on occasion – spurious plasma populations induced in the vicinity of the spacecraft. For example, when the MMS EDI instrument is emitting 500 eV electrons, one or more FPI spectrometers often registers the signal in DES energy bin 16.

The FPI team has attempted to remove as many induced effects as is possible from the moment values (des-moms and dis-moms files) within the data processing pipeline. That said, the FPI full plasma distributions (des-dist and dis-dist files) are provided without correction so that analysis work can be performed appropriate to the specific hypothesis under study.

4.5.7.1 Correction for Spacecraft Potential

The sampled energies (E, units eV) reported in the FPI L2 CDFs must be corrected for spacecraft charging effects (see Gershman et al. [2017]). Adjusted energies are calculated as:

$$E' = E \pm \Phi avg \quad (2)$$

where the '+' and '-' apply for ions and electrons, respectively, and Φavg is the average L2 spacecraft potential over each measurement interval. The specific file used for a particular L2 FPI moments CDF is listed in the meta data under global attribute 'Spacecraft_potential_filenames.'

For electrons, measurements from energies below Φmax, the peak spacecraft potential over a measurement interval, are excluded from the moments integrations to ensure no contribution from spacecraft photoelectrons.

In addition to an adjustment of energy, the directional component of particle velocity is also affected by spacecraft charging because the plasma sheath is not a perfect sphere. While not performed routinely, in areas of particular interest, a calculation can be performed to reassign particles based on traces of their path through the spacecraft plasma sheath.

More information can be found in the publications:

Barrie, A. C., et al. "Characterizing spacecraft potential effects on measured particle trajectories." *Physics of Plasmas* 26.10 (2019): 103504.

Gershman, D. J., Avanov, L. A., Boardsen, S. A., Dorelli, J. C., Gliese, U., Barrie, A. C., … Pollock, C. J. (2017). Spacecraft and instrument photoelectrons measured by the dual electron spectrometers on MMS. Journal of Geophysical Research: Space Physics, 122, 11,548– 11,558. https://doi.org/10.1002/2017JA024518

4.5.7.2 Correction for DES Photoelectrons

Burst data obtained during commissioning in the hot plasma sheet in the absence of a significant field-aligned electron population were used to characterize the internally generated photoelectrons as a function of energy, deflection state, polar angle, and spinphase. This model is available as a CDF for users interested in estimating the impact of internally generated photoelectrons on their analyses. Photoelectron skymaps [32x16x32] in units of phase space density, denoted as fphoto, are provided as a function of energy table and spacecraft spin phase. There are subtle changes in the photoelectron fluxes as a function of spacecraft spinphase because the EUV from the Sun has different incident angles to each analyzer. All observatories exhibit similar behavior such that the same angular structure of the photoelectron model is used for all spacecraft. There is a single tuning factor for each that controls the effective density of the photoelectrons. This tuning factor varies both with time and with spacecraft. The tuning factor was selected for each observatory as a function of time to give Vi,x ~ Ve,x inside the magnetosphere. The tuning factors range from ~0.5-1 and are likely accurate to ±0. 1. These factors are included as global attributes in DES moment CDF files as ‘photo_scale_factor.’

Internally generated photoelectrons, unaffected by the spacecraft potential in the sun direction produce an effective cold electron component with density ~0.5-1 cm-3 and bulk velocity ~750 km/second the anti-sunward direction. This component varies with spacecraft spin phase. A model for this signal has been developed and the signal removed for the moment calculations as of software release v2.0. It is important to note, that, these photoelectrons (internal and spacecraft) are not removed from the skymap data product as users need to be aware of this signal for their specific data interval and how its removal might affect analysis and interpretations.

CDFs that contain the unscaled DES instrument photoelectron model are available on the MMS SDC at /mms/sdc/public/data/models/fpi. Different model CDFs are needed for burst (brst) and fast survey (fast) modes and for each FPI energy-stepper table (‘pX-Y’). The relevant photoelectron model is included as a global attribute in the meta data for each FPI moms CDF as field ‘*Photoelectron_model_filenames*’.

To obtain the relevant instrument photoelectron model distribution for a given record:

1. Determine the value of *startdelphi_count_fast* or *startdelphi_count_brst* for the skymap of interest (record varying). This will be a number between 0 and 5759 and is a measure of spacecraft spin-phase (1/16^o bins).
2. Find the index I in the *startdelphi_counts_brst* or *startdelphi_counts_fast* array [360 possibilities] whose corresponding value is closest to the measured *startdelphi_count_brst* or *startdelphi_count_fast* for the skymap of interest.
3. The closest index can be approximated by I = floor(*startdelphi_count_brst*/16) or I = floor(*startdelphi_count_fast*/16)
4. For burst mode data, determine the value of *steptable_parity* for the skymap of interest (record varying). This will be either 0 or 1.

In the appropriate photoelectron model CDF:

(1) For burst data, take f_{photo} = *bgdist_p0_brst* or f_{photo} = *bgdist_p1_brst* entry with index I for parity 0 and parity 1 data respectively.
(2) For fast survey data, take f_{photo} = *bgdist_fast* with index I.

f_{photo} can now be scaled by n_{photo} in order to obtain the estimated contribution of photoelectrons to a given skymap. These phase space densities are independent of spacecraft potential. Corrected phase space densities are calculated as:

$$f = f_{L2} - n_{photo} f_{photo.} \qquad (1)$$

Negative phase space densities are permitted in the numerical integration. There is uncertainty in n_{photo} and in the model itself. Adjustment of n_{photo} to achieve $V_{ix} \sim V_{ex}$ can result in improved performance.

More information about internally generated photoelectrons can be found in the publication:

> Gershman, D. J., Avanov, L. A., Boardsen, S. A., Dorelli, J. C., Gliese, U., Barrie, A. C., … Pollock, C. J. (2017). Spacecraft and instrument photoelectrons measured by the dual electron spectrometers on MMS. Journal of Geophysical Research: Space Physics, 122, 11,548– 11,558. https://doi.org/10.1002/2017JA024518

4.5.7.3 Correction for Compression Artifacts

In Phase 1A of the mission, the DES compression was set to a level which, for high density/temperature plasmas, occasionally produced artifacts in the data. While not routinely performed, a neural network based correction can be used to remove these artifacts in areas of particular scientific interest.

With regard to spin-periodicities / velocity offsets, compression artifacts can be different for Survey and Burst data products. Imperfect spectrometer response correction tables (e.g., for signals dominating the very lowest or very highest energy channels; for data intervals very near a FPI macro change; and for data intervals for which sufficient burst calibration data was not readily available). Some of these can be addressed with time. Imperfect spacecraft potential or photoelectron signal correction. For some data intervals, data users will necessarily need to apply custom corrections. In some cases, even when the in-flight calibration tables have reduced the spin-period electron bulk velocity signal amplitude to below 50 km/s, there may appear more significant 20 s oscillations in the current density n*e*(Vi-Ve) (comparable to real current densities at the magnetopause). This is a known issue and is currently beyond the scope of our current L2 processing. If such current density oscillations are noticed, please contact the FPI team,

and we will address these on a case-by-case basis until we are able to incorporate a correction into our routine L2 processing.

More information can be found in the publication:

> da Silva, D., Barrie, A., Gershman, D., Elkington, S., Dorelli, J., Giles, B., & Paterson, W. (2020). Neural network repair of Lossy compression Artifacts in the September 2015 to March 2016 duration of the MMS/FPI data set. Journal of Geophysical Research: Space Physics, 125, e2019JA027181. https://doi.org/10.1029/2019JA027181

4.5.7.4 Correction for Pointing Error

The cross wiring of the FPI power supplies (see Pollock [2016]) leads to an inherent look direction bias, which is of opposite polarity between the two sensor heads. This leads to an average pointing error of ~ 1 degree. This pointing error also drifts with time as the system ages. A trending analysis is used to monitor this pointing error over time to confirm that the pointing offset error is small relative to the angular resolution. While not performed routinely, if desired for a case of particular scientific interest, customized moments can be calculated using corrected pointing unit vectors.

More information can be found in the publications:

> Barrie, A. C., Schiff, C., Gershman, D. J., Giles, B. L., & Rand, D. (2021). Calibrating electrostatic deflection of charged particle sensors using ambient plasma measurements. Journal of Geophysical Research: Space Physics, 126, e2021JA029149. https://doi.org/10.1029/2021JA029149

> Pollock, C., Moore, T., Jacques, A., Burch, J., Gliese, U., Saito, Y., ... & Zeuch, M. (2016). Fast plasma investigation for magnetospheric multiscale. Space Science Reviews, 199(1), 331-406.

4.5.7.5 Correction for Penetrating Radiation

Penetrating radiation can result in an apparent stationary, isotropic population of plasma in MMS/FPI data [see Gershman et al. 2019]. Penetrating radiation can affect both DES and DIS, but tends to impact DIS data more so in the magnetotail, where ambient count rates are low.

The DIS moments CDF provides fields ‘numberdensity_bg’, ‘pres_bg’, and ‘spectr_bg’, which represent the estimated number density, scalar pressure, and differential energy flux associated with penetrating radiation.

These quantities are calculated as follows:

1. The 5 lowest values (not energies) of the omni-directional spectrogram are averaged to provide ‘spectr_bg’
2. Spectr_bg is used to generate an isotropic phase space density distribution using f_bg = spectr_bg * 2 / v^4.
3. F_bg is integrated through an identical moments calculation (extrapolation, energy range, etc.…) as the corresponding L2 moments record.

4. Numberdensity_bg is the density from f_bg
5. Pres_bg is the sclar pressure from f_bg, i.e., (Pres_xx +Pres_yy+Pres_zz)/3.

Assuming that off-diagonal components of the pressure tensor and bulk velocity components of the background population are zero, n_bg and p_bg can be used to correct L2 moments for the effects of penetrating radiation (see Gershman et al. 2019)

$$n^* = n_{FPI} - n_b\,,$$
$$V_i{}^* = \frac{n_{FPI}V_{FPI,i}}{n^*},$$
$$P_{ij}{}^* = \left(P_{FPI,ij} + mn_{FPI}V_{FPI,i}V_{FPI,j}\right) - P_{b,ij} - mn^*V_i{}^*V_j{}^*,$$

and

$$T_{ij}{}^* \equiv \frac{P_{ij}{}^*}{n^*k_B}.$$

Note that n_bg and pres_bg will scale proportionally to spectr_bg, so a more careful estimate of background can be obtained and used to scale all three numbers simultaneously.

More information about correcting for penetrating radiation can be found in the publication:

> Gershman, D. J., Dorelli, J. C., Avanov, L. A., Gliese, U., Barrie, A., Schiff, C., et al. (2019). Systematic uncertainties in plasma parameters reported by the fast plasma investigation on NASA's magnetospheric multiscale mission. Journal of Geophysical Research: Space Physics, 124, 10345– 10359. https://doi.org/10.1029/2019JA026980.

4.5.7.6 Correction for Spintones

Imperfect flat-fielding (~1% residual errors) can result in significant (>10 km/s) spin-tones in DES bulk velocities [Gershman et al. 2019]. Because these systematic uncertainties are superimposed on the true velocity, an estimated spin-tone can in many cases be directly subtracted from DES data. Spin-tones are calculated in DBCS for Vxe and Vye only, though this technique can be extended to any quantify of interest (e.g., heat flux).

To calculate spin tone amplitudes, we apply a Butterworth IIR bandpass filter with coefficients:

Order	Numerator	Denominator
0	5.97957804e-05	1.0
1	0	-1.42301183
2	-2.98978902e-04	4.79664124
3	0	-4.79501766
4	5.97957804e-04	8.43180163
5	0	-5.93211177
6	-5.97957804e-04	6.88161394
7	0	-3.18997794
8	2.98978902e-04	2.60446833
9	0	-0.62795853
10	-5.97957804e-05	0.35992825

Table 4-4 Spintone Amplitudes

To obtain spin-tone estimates,

1. Load record-varying fast survey data from a 1D data product of interest (e.g., Vxe_dbcs, Vye_dbcs), a science region of interest is loaded
2. Apply Butterworth filter to data (using sample number instead of time)
3. Reverse filtered dataset
4. Apply Butterworth filter to reverse filtered dataset
5. Reverse newly filtered dataset

The forward-reverse filtering above is done to obtain zero phase distortion of the data. Spin-tones are then interpolated to burst cadence to provide high-resolution spin-tone estimates, and converted to GSE. Note that any real signal frequency content within the filter's bandpass will contribute to the spin-tone amplitude. The spin-tone field therefore provides an upper bound estimate to the systematic uncertainty associated with imperfect flat-fielding.

4.5.8 DES/DIS Quality Flags

FPI tags its data with a variety of quality flags to indicate intervals that need warrant consideration -- and perhaps correction -- when using the data for event analysis. It is important to check these and address any noted features.

4.5.8.1 Distribution File Flags

Bit	Description
0	Manually flagged interval
1	Overcounting/saturation effects likely present in skymap
2	Compression pipeline error

4.5.8.2 Moments File Flags

Bit	Description
0	Manually flagged interval
1	Overcounting/saturation effects likely present in skymap
2	Reported spacecraft potential above 20V
3	Invalid/unavailable spacecraft potential
4	Significant (>25%) cold plasma (<10eV) component
5	Significant (>25%) hot plasma (>30keV) component
6	High sonic Mach number (v/vth > 2.5)c
7	Low calculated density (n < 0.05 cm^-3)
8	BentPipe magnetic field used instead of brst l2pre magnetic field
9	Survey l2pre magnetic field used instead of brst l2pre magnetic field (burst only)
10	No internally generated photoelectron correction applied (DES only)
11	Compression pipeline error

12 spintone calculation error (DBCS only)
13 significant (>=20%) penetrating radiation (DIS only)

Note that in MMS3 DIS moments files, the Bit 0 flag is set for data that has unusually large spintone due to the DIS008 anomaly, as discussed in section 4.1.2.

4.6 DATA PRODUCTION ALGORITHM DESCRIPTIONS

4.6.1 File Structure L2 3D DES/DIS Distributions (skymaps)

Variable	Units	Type	Dim	Description
Epoch	ns	CDF_TIME_TT2000	1	Observation start time derived from packet time
errorflags	32-bit error flags	CDF_UINT4	1	Vector of data-quality indicators at epoch
compressionloss	0, 1	CDF_UINT1	1	Compression lossless/lossy indicator at epoch
steptable_parity	0, 1	CDF_UINT1	1	Step table parity
startdelphi_count	del-phi counts	CDF_UINT2	1	Del-Phi (obs spin-phase) count at epoch
startdelphi_angle	deg	CDF_REAL4	1	Del-Phi (obs spin-phase) angle at epoch
phi	deg	CDF_REAL4	32	Sky-map instrument azimuthal angles
dist	s^3/cm^6	CDF_REAL4	32 x 16 x 32	Sky-map instrument distribution
disterr	s^3/cm^6	CDF_REAL4	32 x 16 x 32	Sky-map instrument distribution 1-sigma error
avgf1counts	s^3/cm^6	CDF_REAL4	32	Avg f1-count level as a function of energy
steptimeoffsets	us	CDF_REAL4	32 x 16 x 32	Sky-map microsecond offsets from epoch
sector_despinp	00-32	CDF_UINT1	1	Sector de-Spin P value
energy	eV	CDF_REAL4	32	Sky-map energy bin centers
energy_delta	eV	CDF_REAL4	32	Sky-map delta energies

Table 4-5 L2 3D DES/DIS Skymaps

4.6.2 File Structure L2 DES Distribution Aux

Variable	Units	Type	Dim	Description
Epoch	ns	CDF_TIME_TT2000	1	Observation start time derived from packet time
errorflags	32-bit error flags	CDF_UINT4	1	Vector of data-quality indicators at epoch
disterr_photo	s^3/cm^6	CDF_REAL4	32 x 16 x 32	DES modeled photoelectron distribution
energy	eV	CDF_REAL4	32	Sky-map energy bin centers
energy_delta	eV	CDF_REAL4	32	Sky-map delta energies

Table 4-6 L2 DES Distribution Aux

4.6.3 File Structure L2 DES/DIS Moments

Variable	Units	Type	Dim	Description
Epoch	ns	CDF_TIME_TT2000	1	Observation start time derived from packet time

errorflags	32-bit error flags	CDF_UINT4	1	Vector of data-quality indicators at epoch
compressionloss	0, 1	CDF_UINT1	1	Compression lossless/lossy indicator at epoch
steptable_parity (burst only)	0, 1	CDF_UINT1	1	Step table parity
startdelphi_count	del-phi counts	CDF_UINT2	1	Del-Phi (obs spin-phase) count at epoch
startdelphi_angle (burst only)	deg	CDF_REAL4	1	Del-Phi (obs spin-phase) angle at epoch
sector_despinp (burst only)	00-32	CDF_UINT1	1	Sector de-Spin P value
pitchangdist_lowen (DES only)	keV/(cm^2 s sr keV)	CDF_REAL4	30	Electron pitch-angle distribution for "low" energies
pitchangdist_miden (DES only)	keV/(cm^2 s sr keV)	CDF_REAL4	30	Electron pitch-angle distribution for "mid" energies
pitchangdist_highen (DES only)	keV/(cm^2 s sr keV)	CDF_REAL4	30	Electron pitch-angle distribution for "high" energies
energyspectr_px	keV/(cm^2 s sr keV)	CDF_REAL4	32	Electron/Ion energy spectrum "near" +X in DBCS
energyspectr_mx	keV/(cm^2 s sr keV)	CDF_REAL4	32	Electron/Ion energy spectrum "near" -X in DBCS
energyspectr_py	keV/(cm^2 s sr keV)	CDF_REAL4	32	Electron/Ion energy spectrum "near" +Y in DBCS
energyspectr_my	keV/(cm^2 s sr keV)	CDF_REAL4	32	Electron/Ion energy spectrum "near" -Y in DBCS
energyspectr_pz	keV/(cm^2 s sr keV)	CDF_REAL4	32	Electron/Ion energy spectrum "near" +Z in DBCS
energyspectr_mz	keV/(cm^2 s sr keV)	CDF_REAL4	32	Electron/Ion energy spectrum "near" -Z in DBCS
energyspectr_par (DES only)	keV/(cm^2 s sr keV)	CDF_REAL4	32	Electron energy parallel to the magnetic field direction
energyspectr_anti (DES only)	keV/(cm^2 s sr keV)	CDF_REAL4	32	Electron energy anti-parallel to the magnetic field direction
energyspectr_perp (DES only)	keV/(cm^2 s sr keV)	CDF_REAL4	32	Electron energy perpendicular to the magnetic field direction
energyspectr_omni	keV/(cm^2 s sr keV)	CDF_REAL4	32	Omni-directional electron/ion energy spectrum
numberdensity	cm^-3	CDF_REAL4	1	Number density
numberdensity_err	cm^-3	CDF_REAL4	1	Number density error
densityextrapolation_low	cm^-3	CDF_REAL4	1	Estimated (via extrapolation to 0) contribution to density integral below 10eV
densityextrapolation_high	cm^-3	CDF_REAL4	1	Estimated (via extrapolation to infinity) contribution to density integral above 30keV
bulkv_dbcs	km/s	CDF_REAL4	3	Bulk-velocity vector in DBCS

bulkv_spin_dbcs (fast/burst only)	km/s	CDF_REAL4	3	Bulk-velocity spintone vector in DBCS
bulkv_gse	km/s	CDF_REAL4	3	Bulk-velocity vector in GSE
bulkv_spin_gse (fast/burst only)	km/s	CDF_REAL4	3	Bulk-velocity spintone vector in GSE
bulkv_err	km/s	CDF_REAL4	3	Bulk-velocity error vector
prestensor_dbcs	nPa	CDF_REAL4	3 x 3	Pressure tensor in DBCS
prestensor_gse	nPa	CDF_REAL4	3 x 3	Pressure tensor in GSE
prestensor_err	nPa	CDF_REAL4	3 x 3	Pressure tensor error
temptensor_dbcs	eV	CDF_REAL4	3 x 3	Temperature tensor in DBCS
temptensor_gse	eV	CDF_REAL4	3 x 3	Temperature tensor in GSE
temptensor_err	eV	CDF_REAL4	3 x 3	Temperature tensor error
heatq_dbcs	mW/m^2	CDF_REAL4	3	Heat-flux vector in DBCS
heatq_gse	mW/m^2	CDF_REAL4	3	Heat-flux vector in GSE
heatq_err	mW/m^2	CDF_REAL4	3	Heat-flux error vector
temppara	eV	CDF_REAL4	1	Parallel temperature
tempperp	eV	CDF_REAL4	1	Perpendicular temperature
energy	eV	CDF_REAL4	32	Sky-map energy bin centers
energy_delta	eV	CDF_REAL4	32	Sky-map delta energies

Table 4-7 L2 DES/DIS Moments

4.6.4 File Structure L2 DES/DIS Moments Aux

Variable	Units	Type	Dim	Description
Epoch	ns	CDF_TIME_TT2000	1	Observation start time derived from packet time
errorflags	32-bit error flags	CDF_UINT4	1	Vector of data-quality indicators at epoch
compressionloss	0, 1	CDF_UINT1	1	Compression lossless/lossy indicator at epoch
steptable_parity (burst only)	0, 1	CDF_UINT1	1	Step table parity
startdelphi_count	del-phi counts	CDF_UINT2	1	Del-Phi (obs spin-phase) count at epoch
startdelphi_angle (burst only)	deg	CDF_REAL4	1	Del-Phi (obs spin-phase) angle at epoch
sector_despinp (burst only)	00-32	CDF_UINT1	1	Sector de-Spin P value
pitchangdist_lowen (DES only)	keV/(cm^2 s sr keV)	CDF_REAL4	30	Electron pitch-angle distribution for "low" energies
pitchangdist_miden (DES only)	keV/(cm^2 s sr keV)	CDF_REAL4	30	Electron pitch-angle distribution for "mid" energies
pitchangdist_highen (DES only)	keV/(cm^2 s sr keV)	CDF_REAL4	30	Electron pitch-angle distribution for "high" energies
energyspectr_px	keV/(cm^2 s sr keV)	CDF_REAL4	32	Electron/Ion energy spectrum "near" +X in DBCS
energyspectr_mx	keV/(cm^2 s sr keV)	CDF_REAL4	32	Electron/Ion energy spectrum "near" -X in DBCS

energyspectr_py	keV/(cm^2 s sr keV)	CDF_REAL4	32	Electron/Ion energy spectrum "near" +Y in DBCS
energyspectr_my	keV/(cm^2 s sr keV)	CDF_REAL4	32	Electron/Ion energy spectrum "near" -Y in DBCS
energyspectr_pz	keV/(cm^2 s sr keV)	CDF_REAL4	32	Electron/Ion energy spectrum "near" +Z in DBCS
energyspectr_mz	keV/(cm^2 s sr keV)	CDF_REAL4	32	Electron/Ion energy spectrum "near" -Z in DBCS
energyspectr_par (DES only)	keV/(cm^2 s sr keV)	CDF_REAL4	32	Electron energy parallel to the magnetic field direction
energyspectr_anti (DES only)	keV/(cm^2 s sr keV)	CDF_REAL4	32	Electron energy anti-parallel to the magnetic field direction
energyspectr_perp (DES only)	keV/(cm^2 s sr keV)	CDF_REAL4	32	Electron energy perpendicular to the magnetic field direction
energyspectr_omni	keV/(cm^2 s sr keV)	CDF_REAL4	32	Omni-directional electron/ion energy spectrum
numberdensity	cm^-3	CDF_REAL4	1	Number density
numberdensity_err	cm^-3	CDF_REAL4	1	Number density error
densityextrapolation_low	cm^-3	CDF_REAL4	1	Estimated (via extrapolation to 0) contribution to density integral below 10eV
densityextrapolation_high	cm^-3	CDF_REAL4	1	Estimated (via extrapolation to infinity) contribution to density integral above 30keV
bulkv_dbcs	km/s	CDF_REAL4	3	Bulk-velocity vector in DBCS
bulkv_spin_dbcs (fast/burst only)	km/s	CDF_REAL4	3	Bulk-velocity spintone vector in DBCS
bulkv_gse	km/s	CDF_REAL4	3	Bulk-velocity vector in GSE
bulkv_spin_gse (fast/burst only)	km/s	CDF_REAL4	3	Bulk-velocity spintone vector in GSE
bulkv_err	km/s	CDF_REAL4	3	Bulk-velocity error vector
prestensor_dbcs	nPa	CDF_REAL4	3 x 3	Pressure tensor in DBCS
prestensor_gse	nPa	CDF_REAL4	3 x 3	Pressure tensor in GSE
prestensor_err	nPa	CDF_REAL4	3 x 3	Pressure tensor error
temptensor_dbcs	eV	CDF_REAL4	3 x 3	Temperature tensor in DBCS
temptensor_gse	eV	CDF_REAL4	3 x 3	Temperature tensor in GSE
temptensor_err	eV	CDF_REAL4	3 x 3	Temperature tensor error
heatq_dbcs	mW/m^2	CDF_REAL4	3	Heat-flux vector in DBCS
heatq_gse	mW/m^2	CDF_REAL4	3	Heat-flux vector in GSE
heatq_err	mW/m^2	CDF_REAL4	3	Heat-flux error vector
temppara	eV	CDF_REAL4	1	Parallel temperature
tempperp	eV	CDF_REAL4	1	Perpendicular temperature
energy	eV	CDF_REAL4	32	Sky-map energy bin centers
energy_delta	eV	CDF_REAL4	32	Sky-map delta energies

numberdensity_part	cm^-3	CDF_REAL4	32	Number density for each starting energy
bulkv_part_dbcs	km/s	CDF_REAL4	32 x (3 x 1)	Bulk-velocity vector in DBCS for each starting energy
bulkv_part_gse	km/s	CDF_REAL4	32 x (3 x 1)	Bulk-velocity vector in GSE for each starting energy
prestensor_part_dbcs	nPa	CDF_REAL4	32 x (3 x 3)	Pressure tensor in DBCS for each starting energy
prestensor_part_gse	nPa	CDF_REAL4	32 x (3 x 3)	Pressure tensor in GSE for each starting energy
temptensor_part_dbcs	eV	CDF_REAL4	32 x (3 x 3)	Temperature tensor in DBCS for each starting energy
temptensor_part_gse	eV	CDF_REAL4	32 x (3 x 3)	Temperature tensor in GSE for each starting energy
temppara_part	eV	CDF_REAL4	32	Parallel temperature for each starting energy
tempperp_part	eV	CDF_REAL4	32	Perpendicular temperature for each starting energy
part_index	0-31	CDF_UINT2	1	Recommended energy index for this epoch
scpmean	V	CDF_REAL4	1	Mean spacecraft potential derived from MMS Electric field Double Probe
bhat_dbcs	nT	CDF_REAL8	3	Unit vector magnetic field direction derived from MMS Fluxgate Magnetometers
gse_xform	N/A	CDF_REAL4	3 x 3	Matrix used to transform dbcs to gse

Table 4-8 L2 DES/DIS Moments Aux

4.6.5 Calculation of L2 DES/DIS Plasma Moments

FPI uses the typically defined set of plasma moments (e.g., *Paschmann et al.* [1998]). Moments calculations are carried out the DBCS coordinate system using Level 2 phase space density distributions and their associated energy-angle bins as described below.

Plasma Parameter	Moment Calculation	Units
Number Density	$n \equiv \iiint d^3\boldsymbol{v}\, f(v,\theta,\varphi)$	cm^{-3}
Bulk Velocity	$\boldsymbol{V} \equiv \frac{\iiint d^3\boldsymbol{v}\, \boldsymbol{v} f(v,\theta,\varphi)}{n}$	km/s
Temperature Tensor	$\overline{\overline{\boldsymbol{T}}} \equiv \frac{m \iiint d^3\boldsymbol{v}\, (\boldsymbol{v}-\boldsymbol{V})(\boldsymbol{v}-\boldsymbol{V}) f(v,\theta,\varphi)}{n k_B}$	eV
Pressure Tensor	$\overline{\overline{\boldsymbol{P}}} \equiv n k_B \overline{\overline{\boldsymbol{T}}}$	nPa

Heat Flux Vector	$\boldsymbol{q} \equiv \frac{m \iiint d^3\boldsymbol{v}\, v^2 f(v,\theta,\varphi)}{2} - \frac{nmV^2\boldsymbol{V}}{2} - \left(\left(\frac{Tr\overline{\overline{\boldsymbol{P}}}}{2}\right)\overline{\overline{\boldsymbol{I}}} + \overline{\overline{\boldsymbol{P}}}\right)\cdot \boldsymbol{V}$	mW/m^2

Table 4-9 Definition and Units of MMS/FPI Plasma Moments

The following constants are adopted to ensure proper unit conversion:

Symbol	Description	Value
m_i	Mass of ion (assuming H^+)	1.6726 x 10^{-24} g
m_e	Mass of electron	9.1094 x 10^{-28} g
E_{1eV}	Energy of 1eV particle	1.6022 x 10^{-12} erg
T_{1eV}	Temperature of 1eV plasma	11604 K
k_B	Boltzmann's Constant	1.3807 x 10^{-16} erg/K

Table 4-10 Constants Used in the Calculation in MMS/FPI Plasma Moments

Distribution Function Pre-Conditioning:

Specific energy and angle targets for a particular skymap are included as record varying entries in FPI distribution function CDFs (DBCS coordinates). FPI uses a trapezoidal triple integration scheme for its calculation of plasma moments, i.e., implicitly linearly interpolates between adjacent phase space values. Before being sent to the integration routine, skymaps are preprocessed as described below.
Because FPI has a finite energy range, we remap calculated energies using the relation:

$$U \equiv \frac{E\prime}{E_0 + E\prime} \qquad (3)$$

Here, E_0 is a constant (nominally 100 eV) that is used to remap energies from $E' \rightarrow (0,\infty)$ to $U \rightarrow (0,1)$. The final integral is not a strong function of E_0. The default E_0 = 100 eV was chosen as typical plasmas sampled by MMS have significant phase space density at that energy. The value of E_0 (units eV) used in this remapping are found in the meta data of a given L2 FPI moments CDF as global attribute '*Energy_e0'*

The low energy bound and upper energy bounds starting for the integration is listed in the CDF meta data as global attributes '*Lower_energy_integration_limit*' and '*Upper_energy_integration_limit'*, respectively. Nominally the lower limit is 10eV (even when lower energies are sampled) and the highest available energy. Exceptions to this is interval used for the *Torbert et al.* [2018] interval where the Level-2 integration was started at 100eV, and in the solar wind stepping table for DES where all energies are included.

Boundary points $f(U,\theta, \varphi=\varphi_{min}+360^o) = f(U,\theta, \varphi=\varphi_{min})$ are added to ensure that the periodic boundary condition is incorporated into the azimuthal integration.

Boundary points $f(U, \theta=0^o,\varphi) = 0$ and $f(U, \theta=180^o,\varphi) = 0$ are added to ensure that the polar integration ranges from 0 to 180. The sin(theta) dependence of the polar integration force the integrand at theta = 0 and 180 to zero regardless of the value of the phase space density.

Boundary points $f(U=0, \theta,\varphi) = 0$ and $f(U=1, \theta,\varphi) = 0$ are added to ensure the integration goes from $E' = 0$ to ∞. The scaling of the integrand by v^2 forces it to zero regardless of the ambient phase space density, and there is the assumption that at $E' \rightarrow \infty$, the phase space density of thermal plasmas approaches zero.

Low-Energy and High-Energy Extrapolation:

Low-energy and high-energy extrapolation of moments integrals are achieved by default through the inclusion of the U = 0 and U = 1 data points in the numerical integration. The use of extrapolation for a given interval is listed in CDF meta data as fields '*Low_energy_extrapolation*' and '*High_energy_extrapolation'*. If disabled, the corresponding $U = 0$ or $U = 1$ points are excluded from the integration. By default, in Level-2 data, DES has both low-energy and high-energy extrapolation enabled, since there is often finite phase space density near $U = 0$. DIS has only high-energy extrapolation enabled since there is often no significant ambient phase space density near $U = 0$.

The contribution of the low-energy and high-energy extrapolations to the number density (i.e., the first and last terms in the trapezoidal integration) are included as record varying fields *densityextrapolation_low* and *densityextrapolation_high*, respectively.

FPI Moments Integrals:

After remapping and applying extrapolations, FPI moments are then computed using the following integrals (assuming phase space densities in units s^3cm^{-6}).

Number Density:

$$n \equiv \frac{\sqrt{2}}{m^{\frac{3}{2}}}(E_0 E_{1eV})^{\frac{3}{2}} \int_0^1 dU \frac{\sqrt{U}}{(1-U)^{\frac{5}{2}}} \int_0^{\pi} d\theta \ \sin\theta \int_0^{2\pi} d\varphi \, f(U,\theta,\varphi) \qquad (4)$$

Bulk Velocity:

$$V_x \equiv -\frac{2\times10^{-5}}{nm^2}(E_0 E_{1eV})^2 \int_0^1 dU \frac{U}{(1-U)^3} \int_0^{\pi} d\theta \sin^2\theta \int_0^{2\pi} d\varphi \cos\varphi \, f(U,\theta,\varphi) \qquad (5)$$

$$V_y \equiv -\frac{2\times10^{-5}}{nm^2}(E_0 E_{1eV})^2 \int_0^1 dU \frac{U}{(1-U)^3} \int_0^{\pi} d\theta \sin^2\theta \int_0^{2\pi} d\varphi \sin\varphi \, f(U,\theta,\varphi) \qquad (6)$$

$$V_z \equiv -\frac{2\times10^{-5}}{nm^2}(E_0 E_{1eV})^2 \int_0^1 dU \frac{U}{(1-U)^3} \int_0^{\pi} d\theta \sin\theta\cos\theta \int_0^{2\pi} d\varphi \, f(U,\theta,\varphi) \qquad (7)$$

Here, the minus sign transforms the calculation in the look-direction frame into the flow-frame.

Temperature Tensor:

$$T_{xx} \equiv \left(\frac{2\times10^{-5}}{m^{\frac{3}{2}}(n\, k_B T_{1eV})}(E_0 E_{1eV})^{\frac{5}{2}} \int_0^1 dU \frac{U^{\frac{3}{2}}}{(1-U)^{\frac{7}{2}}} \int_0^{\pi} d\theta \sin^3\theta \int_0^{2\pi} d\varphi \cos^2\varphi \, f(U,\theta,\varphi) \right) - \frac{10^{10} m}{k_B T_{1eV}} V_x^2 \qquad (8)$$

$$T_{yy} \equiv \left(\frac{2\times10^{-5}}{m^{\frac{3}{2}}(n\, k_B T_{1eV})}(E_0 E_{1eV})^{\frac{5}{2}} \int_0^1 dU \frac{U^{\frac{3}{2}}}{(1-U)^{\frac{7}{2}}} \int_0^{\pi} d\theta \sin^3\theta \int_0^{2\pi} d\varphi \sin^2\varphi \, f(U,\theta,\varphi) \right) - \frac{10^{10} m}{k_B T_{1eV}} V_y^2 \qquad (9)$$

$$T_{zz} \equiv \left(\frac{2\times10^{-5}}{m^{\frac{3}{2}}(n\,k_B T_{1eV})} (E_0 E_{1eV})^{\frac{5}{2}} \int_0^1 dU \frac{U^{\frac{3}{2}}}{(1-U)^{\frac{7}{2}}} \int_0^{\pi} d\theta \sin\theta \cos^2\theta \int_0^{2\pi} d\varphi\, f(U,\theta,\varphi) \right) - \frac{10^{10} m}{k_B T_{1eV}} V_z^2 \quad (10)$$

$$T_{xy} \equiv \left(\frac{2\times10^{-5}}{m^{\frac{3}{2}}(n\,k_B T_{1eV})} (E_0 E_{1eV})^{\frac{5}{2}} \int_0^1 dU \frac{U^{\frac{3}{2}}}{(1-U)^{\frac{7}{2}}} \int_0^{\pi} d\theta \sin^3\theta \int_0^{2\pi} d\varphi \sin\varphi \cos\varphi\, f(U,\theta,\varphi) \right) - \frac{10^{10} m}{k_B T_{1eV}} V_x V_y \quad (11)$$

$$T_{xz} \equiv \left(\frac{2\times10^{-5}}{m^{\frac{3}{2}}(n\,k_B T_{1eV})} (E_0 E_{1eV})^{\frac{5}{2}} \int_0^1 dU \frac{U^{\frac{3}{2}}}{(1-U)^{\frac{7}{2}}} \int_0^{\pi} d\theta \sin^2\theta \cos\theta \int_0^{2\pi} d\varphi \cos\varphi\, f(U,\theta,\varphi) \right) - \frac{10^{10} m}{k_B T_{1eV}} V_x V_z \quad (12)$$

$$T_{yz} \equiv \left(\frac{2\times10^{-5}}{m^{\frac{3}{2}}(n\,k_B T_{1eV})} (E_0 E_{1eV})^{\frac{5}{2}} \int_0^1 dU \frac{U^{\frac{3}{2}}}{(1-U)^{\frac{7}{2}}} \int_0^{\pi} d\theta \sin^2\theta \cos\theta \int_0^{2\pi} d\varphi \sin\varphi\, f(U,\theta,\varphi) \right) - \frac{10^{10} m}{k_B T_{1eV}} V_y V_z \quad (13)$$

The temperature tensor is defined to be symmetric such that $T_{ij} = T_{ji.}$

Pressure Tensor:

$$P_{ij} \equiv 10^8 (n\,k_B T_{1eV}) T_{ij} \quad (14)$$

As with the temperature tensor, the pressure tensor is defined to be symmetric such that $P_{ij} = P_{ji.}$

Heat Flux Vector:

$$q_x \equiv \left(-\frac{2}{m^2} (E_0 E_{1eV})^3 \int_0^1 dU \frac{U^2}{(1-U)^4} \int_0^{\pi} d\theta \sin^2\theta \int_0^{2\pi} d\varphi \cos\varphi\, f(U,\theta,\varphi) \right) - 10^{-3}\left(P_{xx}V_x + P_{xy}V_y + P_{xz}V_z\right) - 10^5 V_x \left(\frac{10^{-8}\left(P_{xx}+P_{yy}+P_{zz}\right) + 10^{10} nm\left(V_x^2+V_x^2+V_z^2\right)}{2} \right) \quad (15)$$

$$q_y \equiv \left(-\frac{2}{m^2} (E_0 E_{1eV})^3 \int_0^1 dU \frac{U^2}{(1-U)^4} \int_0^{\pi} d\theta \sin^2\theta \int_0^{2\pi} d\varphi \sin\varphi\, f(U,\theta,\varphi) \right) - 10^{-3}\left(P_{xy}V_x + P_{yy}V_y + P_{yz}V_z\right) - 10^5 V_y \left(\frac{10^{-8}\left(P_{xx}+P_{yy}+P_{zz}\right) + 10^{10} nm\left(V_x^2+V_x^2+V_z^2\right)}{2} \right) \quad (16)$$

$$q_z \equiv \left(-\frac{2}{m^2} (E_0 E_{1eV})^3 \int_0^1 dU \frac{U^2}{(1-U)^4} \int_0^{\pi} d\theta \sin\theta \cos\theta \int_0^{2\pi} d\varphi\, f(U,\theta,\varphi) \right) - 10^{-3}\left(P_{xz}V_x + P_{yz}V_y + P_{zz}V_z\right) - 10^5 V_z \left(\frac{10^{-8}\left(P_{xx}+P_{yy}+P_{zz}\right) + 10^{10} nm\left(V_x^2+V_x^2+V_z^2\right)}{2} \right) \quad (17)$$

As with the bulk velocity, the minus sign in front of the integral denotes the transformation from the look-direction frame into the flow frame.

Magnetic Field Direction Calculation:

The magnetic field unit vector (**b**) is obtained by averaging each component of the magnetic field in DBCS coordinates over the relevant FPI measurement interval and calculating the direction. The particular magnetic field file used is found in the Level-2 FPI moms CDF meta data as global attribute '*Magnetic_field_filenames*.' This unit vector is used for calculation of parallel and perpendicular temperatures and well as pitch-angle spectrograms.

Temperatures parallel to and perpendicular to the magnetic field direction (unit vector **b**) are calculated from the temperature tensor using:

$$T_{\parallel} \equiv \boldsymbol{b}^T \overline{\overline{\boldsymbol{T}}} \boldsymbol{b} \qquad (18)$$

$$T_{\perp} \equiv \frac{(Tr\overline{\overline{\boldsymbol{T}}} - T_{\parallel})}{2} \qquad (19)$$

Note that because the average value is used, f the **b** varies significantly over the record time, there may be corresponding errors in the reported $T_{\parallel}$ and $T_{\perp}$ moments.

Energy-Angle Spectrograms:

In addition to plasma moments, FPI provides a set of energy-angle spectrograms in its Level-2 moments CDFs. Similar to distribution functions, Level-2 spectrograms provided in FPI CDFs do not include any corrections for instrument photoelectrons or spacecraft potential.

To obtain spectrograms, first sampled energies (E in eV) are converted to velocities (v in cm/s) using,

$$v = \sqrt{\frac{2EE_{1eV}}{m}} \qquad (20)$$

Phase space density (f in s^3/cm^6) is converted to differential energy flux (dJ/dE in $cm^{-2}\ s^{-1}$ eV/eV sr^{-1}) as,

$$\frac{dJ(E)}{dE} = \frac{v^4}{2}\frac{\sum_i f(E,\theta_i,\varphi_i)\sin\theta_i}{\sum_i \sin\theta_i} \qquad (21)$$

Here, subscripts *i* represent the set of angular bins at a given energy that meet a specified criteria for a desired data product. The contribution of each bin is weighted by its solid angle in spherical coordinates (i.e., sin θ). The angular bins used here correspond to those distribution function CDFs), i.e., are in look-direction rather than flow-direction coordinates.

Table 4-11 describes the criteria used to form each **average** (not summed) spectrogram. $\hat{\boldsymbol{v}}$ and $\hat{\boldsymbol{b}}$ describe the units vectors of look-direction and magnetic field direction (DBCS), respectively.

Data Product	Description	Relevant Angular Bins
energyspectr_omni	Omni-directional electron/ion energy spectrum	All
energyspectr_px	Electron/Ion energy spectrum "near" +X in DBCS	θ_i between 45º and 135º φ_i between 135º and 225º
energyspectr_mx	Electron/Ion energy spectrum "near" -X in DBCS	θ_i between 45º and 135º φ_i between 315º and 45º
energyspectr_py	Electron/Ion energy spectrum "near" +Y in DBCS	θ_i between 45º and 135º φ_i between 225º and 315º
energyspectr_my	Electron/Ion energy spectrum "near" -Y in DBCS	θ_i between 45º and 135º φ_i between 45º and 135º
energyspectr_pz	Electron/Ion energy spectrum "near" +Z in DBCS	θ_i between 135º and 180º All φ_i
energyspectr_mz	Electron/Ion energy spectrum "near" -Z in DBCS	θ_i between 0º and 45º All φ_i
pitchangdist_lowen (DES only)	Electron pitch-angle distribution for "low" energies	Energy indices 0 to 10 $\cos^{-1}\left(-\hat{\boldsymbol{v}}\cdot\hat{\boldsymbol{b}}\right)$ in 5º bins
pitchangdist_miden (DES only)	Electron pitch-angle distribution for "mid" energies	Energy indices 11 to 20 $\cos^{-1}\left(-\hat{\boldsymbol{v}}\cdot\hat{\boldsymbol{b}}\right)$ in 5º bins

pitchangdist_highen (DES only)	Electron pitch-angle distribution for "high" energies	Energy indices 21 to 31 $\cos^{-1}\left(-\hat{\boldsymbol{v}}\cdot\hat{\boldsymbol{b}}\right)$ in 5° bins
energyspectr_par (DES only)	Electron energy parallel to the magnetic field direction	$\cos^{-1}\left(-\hat{\boldsymbol{v}}\cdot\hat{\boldsymbol{b}}\right) \leq 30°$
energyspectr_anti (DES only)	Electron energy anti-parallel to the magnetic field direction	$\cos^{-1}\left(-\hat{\boldsymbol{v}}\cdot\hat{\boldsymbol{b}}\right) \geq 150°$
energyspectr_perp (DES only)	Electron energy perpendicular to the magnetic field direction	$60° < \cos^{-1}\left(-\hat{\boldsymbol{v}}\cdot\hat{\boldsymbol{b}}\right) < 120°$

Table 4-11 Pitchangdist Spectrograms

For the pitchangdist_* spectrograms, the energies whose differential energy fluxes are averaged together can be obtained through examination of the '*energy'* variable for the record of interest.

Spectrograms that use magnetic pitch-angle in their calculation are provided for DES only, because the electron flow frame is approximately equal to the spacecraft observation frame. In cases where the electron flow velocity approaches the sound speed, these spectrograms may be less meaningful. Ion pitch-angle distributions require a shift by the ion bulk velocity in order to be scientifically meaningful.

Partial Moments:

Partial moment CDF files contain 32-independent values for each plasma moment. Here, each value represents the numerical integration of the distribution function (methods described above) with a varying low energy bound.

The record-varying field *energy* contains a mapping of which index corresponds to which energy. The same index can be used for all elements. For example, if the 10th element of the energy array (e.g., *energy[9]*) in a given record were equal to 100 eV, then the 10th element of each corresponding moment would correspond to integrals where measurements below 100 eV were ignored (e.g., *numberdensity_part[9], temppara_part[9], bulkv_part_gse[9,0]*).

Note that low-energy extrapolation is disabled for all partial moments, leading to some differences between a partial moment starting at ~10eV and nominal Level-2 DES moments. Use of partial moments is most effective in the magnetotail when there is no significant cold electron or ion population.

Statistical Errors:

Statistical uncertainties are provided for number density, bulk velocity, temperature tensor, pressure tensor, and heat flux vector quantities in DBCS coordinates following *Gershman et al.* [2015]. These uncertainties are intended to serve as the equivalent of the standard deviation obtained from repeated Monte Carlo resampling of the dist fields in the distribution functions according to the disterr fields. For computational efficiency, Riemann sums rather than trapezoidal integration are used, and no additional boundary points or extrapolation methods are implemented.

Paschmann, G., A. N. Fazakerley, and S. J. Schwartz (1998), Moments of plasma velocity distributions, in Analysis Methods for Multi-Spacecraft Data, pp. 125–158, ISSI SA Publications Division, Noordwijk, Netherlands.

Torbert, R. B., Burch, J. L., Phan, T. D., Hesse, M., Argall, M., Shuster, R. J., et al. (2018). Electron-scale dynamics of the diffusion region during symmetric magnetic reconnection in space. Science. https://doi.org/10.1126/science.aat2998

More information about statistical errors can be found in the publication:

Gershman, D. J., Dorelli, J. C., F.-Viñas, A., and Pollock, C. J. (2015), The calculation of moment uncertainties from velocity distribution functions with random errors, J. Geophys. Res. Space Physics, 120, 6633– 6645, doi:10.1002/2014JA020775.

4.6.6 Calculation of L3 DES/DIS Pseudo Moments

FPI produces a selection of pseudo-moments, at the full burst resolution, based on the onboard trigger quantities (*See MMS/FPI-BDEP*). The dynamic range of the environment is preserved by tuning the limited range of the system to an appropriate interval using a scaling system. These simplified data undergo a robust, neural network based correction process on the ground leading to physically meaningful quantities that are accurate to within several percent of the raw high resolution science data. Because these simplified onboard data integrals are significantly smaller in data volume, all of them can be downlinked leading to a dramatic increase in available scientific data from the mission.

The available pseudo-moments include:

Electrons: Density, Pressure, Temperature, Mag Parallel Flux
Ions: Density, XY (Spin Plane) Flux, Z (Spin Axis) Flux

A full description of the design of FPI and its pre-flight and ground calibration results can be found in the publication:

Barrie, A. C., et al, Physically Accurate Large Dynamic Range Pseudo Moments for the MMS Fast Plasma Investigation (2018), https://doi.org/10.1029/2018EA000407.

4.7 FPI APPENDIXES

4.7.1 Appendix A- Voltages Over Time / Voltage Operations

The following tables represent the MMS voltage operations over time from mission launch in 2015, as demonstrated through the V14 Setting, to the current V43 Setting, as of September 30, 2022.

MMS 1

Unit	V14 Setting	V18 (124)	V20 (170)	V21 (210)	V23 (239)	V24 (267)	V25 (301)	V26 (335)
FM002H0	-2350	-50	-50	0	0	0	-25	0
FM002H1	-2400	-50	0	0	0	0	0	0
FM005H0	-2350	0	0	0	0	0	0	0
FM005H1	-2350	0	0	0	0	0	0	0
FM006H0	-2400	-50	0	0	0	0	0	0
FM006H1	-2350	-75	0	0	0	0	-25	0
FM013H0	-2300	-50	-25	0	0	0	0	0

FM013H1	-2250	-50	0	0	-25	0	0	0
FM207H0	2100	50	0	50	100	0	75	0
FM207H1	2040	50	0	25	100	25	50	0
FM209H0	2100	50	0	25	100	25	75	0
FM209H1	2070	25	0	50	75	25	75	25
FM211H0	2130	25	0	25	75	25	75	0
FM211H1	2010	50	0	50	75	25	50	0
FM212H0	2010	25	0	50	100	0	75	0
FM212H1	1980	25	0	50	75	0	100	0

Table 4-12 MMS 1 Voltage Operations (Settings V14 – V26)

Unit	V27 (373)	V28 (511)	V29 (652)	V30 (697)	V31 (743)	V32 (768)	V33 (801)	V34 (819)
FM002H0	0	0	0	-50	-75	75	0	-25
FM002H1	-25	0	0	-25	-75	25	0	0
FM005H0	0	0	0	-25	-75	25	0	0
FM005H1	0	0	0	-25	-75	25	0	0
FM006H0	0	0	0	-25	-75	50	0	-25
FM006H1	0	0	0	0	-75	0	0	0
FM013H0	0	0	0	-25	-25	25	0	-25
FM013H1	0	0	0	-25	-75	25	0	0
FM207H0	0	25	0	25	25	-25	0	0
FM207H1	0	25	0	25	50	-25	0	25
FM209H0	25	0	0	50	75	-50	0	0
FM209H1	25	0	25	50	50	-50	0	25
FM211H0	0	50	0	25	25	-25	0	25
FM211H1	0	50	0	25	25	-25	0	25
FM212H0	0	25	0	25	25	-25	0	0
FM212H1	0	25	0	25	50	-25	0	0

Table 4-13 MMS 1 Voltage Operations (Settings V27 – V34)

Unit	V35 (851)	V37 (931)	V38 (1003)	V39 (1055)	V41 (1177)	V43 (1269)	V43 Setting
FM002H0	-25	-25	-25	0	0	0	-2625
FM002H1	0	-25	-25	0	0	0	-2600
FM005H0	-25	0	-25	0	0	0	-2475
FM005H1	0	-25	-25	0	0	0	-2475
FM006H0	0	-25	-25	0	0	0	-2575
FM006H1	0	0	-25	0	0	0	-2550

FM013H0	0	-50	-25	0	0	0	-2500
FM013H1	0	0	-25	0	0	0	-2425
FM207H0	50	25	25	25	25	50	2625
FM207H1	50	50	25	25	50	50	2640
FM209H0	50	50	25	25	50	50	2725
FM209H1	50	50	25	25	50	50	2720
FM211H0	25	50	25	25	50	50	2680
FM211H1	25	50	25	25	50	50	2585
FM212H0	50	50	25	25	50	50	2560
FM212H1	50	50	25	25	50	50	2555

Table 4-14 MMS 1 Voltage Operations (Settings V35 – V43)

MMS 2

Unit	V14 Setting	V18 (124)	V20 (170)	V21 (210)	V23 (239)	V24 (267)	V25 (301)	V26 (335)
FM001H0	-2436	0	0	50	0	0	0	0
FM001H1	-2388	0	0	50	0	0	0	0
FM009H0	-2350	-100	-25	0	0	0	0	0
FM009H1	-2300	-25	-25	0	0	0	0	0
FM012H0	-2200	-50	0	0	0	0	0	0
FM012H1	-2300	-125	-50	0	0	0	0	0
FM014H0	-2275	-25	0	0	0	0	-25	0
FM014H1	-2250	0	0	0	0	0	0	0
FM201H0	2130	0	0	25	75	25	100	25
FM201H1	2100	-30	0	50	100	25	100	25
FM202H0	2100	0	0	50	100	0	100	25
FM202H1	2070	50	0	50	125	25	100	25
FM203H0	2130	0	0	25	75	25	75	25
FM203H1	2070	-50	0	50	125	25	75	25
FM204H0	2010	0	0	25	100	25	100	0
FM204H1	2100	50	0	50	100	25	75	25

Table 4-15 MMS 2 Voltage Operations (Settings V14 – V26)

Unit	V27 (373)	V28 (511)	V29 (652)	V30 (697)	V31 (743)	V32 (768)	V33 (801)	V34 (819)
FM001H0	0	0	0	0	-75	0	0	0
FM001H1	0	0	0	0	-75	0	0	0
FM009H0	0	0	0	0	-75	0	0	0

FM009H1	0	0	0	-25	-100	25	0	0
FM012H0	0	0	0	-25	-75	25	0	-25
FM012H1	0	0	0	-50	-50	50	0	0
FM014H0	0	0	0	0	-75	0	0	0
FM014H1	0	0	0	-25	-75	25	0	-25
FM201H0	0	50	0	50	75	-50	0	25
FM201H1	0	25	0	25	75	-25	0	0
FM202H0	25	25	25	50	100	-50	0	0
FM202H1	0	25	25	50	75	-50	0	0
FM203H0	0	25	0	25	50	-25	0	25
FM203H1	25	50	25	50	100	-50	0	0
FM204H0	25	0	0	50	75	-50	0	0
FM204H1	0	50	0	75	100	-75	0	0

Table 4-16 MMS 2 Voltage Operations (Settings V27 – V34)

Unit	V35 (851)	V37 (931)	V38 (1003)	V39 (1055)	V41 (1177)	V43 (1269)	V43 Setting
FM001H0	0	0	-25	0	0	0	-2486
FM001H1	0	-25	-25	0	0	0	-2463
FM009H0	0	-25	-25	0	0	0	-2600
FM009H1	0	0	0	0	0	0	-2450
FM012H0	0	-25	-25	0	0	0	-2400
FM012H1	-25	-50	0	0	0	0	-2600
FM014H0	0	-25	-25	0	0	0	-2450
FM014H1	0	-25	-25	0	0	0	-2400
FM201H0	50	50	25	25	50	50	2780
FM201H1	50	25	25	25	25	50	2670
FM202H0	50	50	25	25	50	50	2800
FM202H1	50	50	25	25	50	50	2820
FM203H0	50	50	25	25	50	50	2705
FM203H1	50	50	25	0	50	50	2745
FM204H0	50	50	25	25	50	50	2610
FM204H1	50	50	25	25	50	50	2825

Table 4-17 MMS 2 Voltage Operations (Settings V35 – V43)

MMS 3

Unit	V14 Setting	V18 (124)	V20 (170)	V21 (210)	V23 (239)	V24 (267)	V25 (301)	V26 (335)

FM007H0	-2350	0	0	25	0	0	0	0
FM007H1	-2350	0	0	50	0	0	0	0
FM008H0	-2250	-50	0	0	0	0	0	0
FM008H1	-2350	-125	-25	0	0	0	0	0
FM015H0	-2200	-50	0	0	0	0	0	0
FM015H1	-2325	-25	0	0	0	0	-25	0
FM016H0	-2275	0	-25	0	0	0	-25	0
FM016H1	-2350	-100	0	0	0	0	-25	0
FM206H0	2160	0	0	50	100	0	100	0
FM206H1	2130	0	0	25	75	25	75	0
FM213H0	2100	0	0	50	100	0	75	0
FM213H1	2190	0	0	50	100	0	75	25
FM214H0	2100	0	0	50	100	0	100	0
FM214H1	2130	0	-25	50	75	0	75	25
FM216H0	2130	25	0	25	100	25	75	25
FM216H1	2070	0	0	50	100	25	75	25

Table 4-18 MMS 3 Voltage Operations (Settings V14 – V26)

Unit	**V27 (373)**	**V28 (511)**	**V29 (652)**	**V30 (697)**	**V31 (743)**	**V32 (768)**	**V33 (801)**	**V34 (819)**
FM007H0	0	0	0	-25	-75	25	0	0
FM007H1	0	0	0	0	-75	0	0	0
FM008H0	0	0	0	-25	-75	25	0	0
FM008H1	0	0	0	0	-50	0	0	0
FM015H0	0	0	0	-50	-75	50	0	-25
FM015H1	0	0	0	-25	-50	25	0	0
FM016H0	0	0	0	-25	-75	25	0	0
FM016H1	0	0	0	-25	-75	25	0	0
FM206H0	25	0	0	25	25	-25	0	0
FM206H1	0	50	0	25	25	-25	0	25
FM213H0	0	75	0	25	50	-25	0	25
FM213H1	0	25	0	25	50	-25	0	0
FM214H0	0	50	0	25	50	-25	0	0
FM214H1	0	25	25	25	50	-25	0	0
FM216H0	25	0	0	25	75	-25	0	0
FM216H1	0	25	0	50	50	-50	0	25

Table 4-19 MMS 3 Voltage Operations (Settings V27 – V34)

Unit	V35 (851)	V37 (931)	V38 (1003)	V39 (1055)	V41 (1177)	V43 (1269)	V43 Setting
FM007H0	0	-25	-25	0	0	0	-2450
FM007H1	0	0	-25	0	0	0	-2400
FM008H0	0	-50	-25	0	0	0	-2450
FM008H1	-25	-25	-25	0	0	0	-2625
FM015H0	0	0	-50	0	0	0	-2400
FM015H1	0	-25	-25	0	0	0	-2475
FM016H0	0	-25	-25	0	0	0	-2450
FM016H1	0	-25	-25	0	0	0	-2600
FM206H0	25	50	25	25	50	50	2685
FM206H1	25	50	25	25	50	50	2655
FM213H0	25	50	25	25	25	50	2675
FM213H1	50	50	25	25	50	50	2765
FM214H0	50	50	25	0	50	50	2675
FM214H1	50	25	25	0	50	25	2605
FM216H0	50	50	25	25	25	50	2730
FM216H1	50	50	25	25	50	50	2695

Table 4-20 MMS 3 Voltage Operations (Settings V35 – V43)

MMS 4

Unit	V14 Setting	V18 (124)	V20 (170)	V21 (210)	V23 (239)	V24 (267)	V25 (301)	V26 (335)
FM003H0	-2300	-50	0	25	0	0	0	0
FM003H1	-2300	0	0	25	0	0	0	0
FM004H0	-2350	-75	-50	0	-50	0	0	0
FM004H1	-2400	-100	-50	0	0	0	-25	0
FM010H0	-2250	0	0	0	0	0	0	0
FM010H1	-2250	-25	-25	0	-25	0	0	0
FM011H0	-2350	-75	0	0	0	0	-25	0
FM011H1	-2275	-25	0	0	0	0	0	0
FM205H0	2100	25	0	50	75	50	75	0
FM205H1	1950	50	0	50	125	0	75	25
FM208H0	2100	50	0	25	75	25	75	25
FM208H1	2040	50	0	50	75	25	100	0
FM210H0	2100	25	0	50	125	0	100	0
FM210H1	2100	50	0	25	75	25	50	0
FM215H0	2160	25	0	50	100	0	75	0
FM215H1	2040	25	0	25	50	25	50	0

Table 4-21 MMS 4 Voltage Operations (Settings V14 – V26)

Unit	V27 (373)	V28 (511)	V29 (652)	V30 (697)	V31 (743)	V32 (768)	V33 (801)	V34 (819)
FM003H0	0	0	0	-25	-75	25	0	0
FM003H1	0	0	0	0	-75	0	0	-25
FM004H0	0	0	0	-25	-75	25	0	0
FM004H1	0	0	0	0	-75	25	0	-25
FM010H0	0	0	0	-25	-75	50	0	-50
FM010H1	0	0	0	-25	-75	25	0	0
FM011H0	0	0	0	-25	-75	25	0	0
FM011H1	0	0	0	0	-50	0	0	0
FM205H0	25	25	0	25	75	-25	0	0
FM205H1	0	25	25	25	75	-25	0	0
FM208H0	0	25	0	50	50	-50	0	25
FM208H1	0	25	0	50	50	-50	0	25
FM210H0	0	50	0	50	75	-50	0	0
FM210H1	25	25	0	50	50	-50	0	25
FM215H0	25	25	0	50	50	-50	0	25
FM215H1	-25	75	0	0	25	0	0	25

Table 4-22 MMS 4 Voltage Operations (Settings V27 – V34)

Unit	V35 (851)	V37 (931)	V38 (1003)	V39 (1055)	V41 (1177)	V43 (1269)	V43 Setting
FM003H0	0	-25	-25	0	0	0	-2450
FM003H1	0	-25	-25	0	0	0	-2425
FM004H0	0	-25	-25	0	0	0	-2650
FM004H1	0	-25	-25	0	0	0	-2700
FM010H0	0	-25	-25	0	0	0	-2400
FM010H1	0	-25	-25	0	0	0	-2450
FM011H0	0	-25	-25	0	0	0	-2575
FM011H1	0	-25	-25	0	0	0	-2400
FM205H0	50	50	25	25	50	50	2750
FM205H1	50	25	25	25	50	25	2600
FM208H0	50	50	25	25	50	50	2725
FM208H1	50	50	0	25	50	25	2640
FM210H0	50	0	0	0	0	0	Unit Off
FM210H1	50	0	0	0	0	0	Unit Off
FM215H0	25	0	0	0	0	0	Unit Off

FM215H1	25	0	0	0	0	0	Unit Off

Table 4-23 MMS 4 Voltage Operations (Settings V35 – V43)

4.7.2 Appendix B- Stepping Tables Over Time

The following is a list of energy stepping tables used by FPI for science operations by mission phase, date, and table designation. The start date in each row indicates when a change was made to stepping tables. A given table version would be utilized for all operations following a change and before the next change.

Start Date	Mission Phase	Table Designator	Notes
9/1/2015	1A	v04	Utilized through to Phase 1B
9/26/2016	1B	v05 & v06	Both tables identical for science purposes.
5/7/2017	2B	v07 & v08	Tables are identical for science, except for minor changes for MMS3 DIS0 only in v08.
11/14/2017	3B	v08 & v09	First use of 3 SROIs per orbit. Tables identical except for max energy range changes for DIS.

Table 4-24 List of Energy Stepping Tables Used by FPI for Science Operations by Mission Phase, Date, and Table Designation

The tables below correspond to the four rows listed above and contain details for DES and DIS stepper tables that include energy step and center energy for each step.

	Start Date: 9/1/2015 Table Designator: v04		Start Date: 9/26/2016 Table Designator: v05&06	
Species:	**DES (electrons)**	**DIS (ions)**	**DES (electrons)**	**DIS (ions)**
Step #	**Center Energy (eV)**	**Center Energy (eV)**	**Center Energy (eV)**	**Center Energy (eV)**
1	6.5	2.2	6.0	1.7
2	8.5	3.9	7.9	3.4
3	11.2	7.1	10.3	6.7
4	14.6	10.9	13.6	10.9
5	19.1	14.5	17.8	14.5
6	25.1	19.2	23.4	19.1
7	32.8	25.4	30.7	25.3
8	43.0	33.6	40.3	33.4
9	56.2	44.5	52.8	44.2
10	73.6	58.9	69.4	58.5
11	96.3	78.0	91.0	77.4
12	126.1	103.2	119.5	102.4
13	165.1	136.7	156.8	135.4
14	216.1	181.0	205.8	179.1
15	282.9	239.6	270.1	236.9
16	370.3	317.3	354.6	313.3
17	484.7	420.1	465.4	414.4
18	634.5	556.2	610.8	548.1
19	830.6	736.4	801.7	725.0
20	1087.3	975.1	1052.2	959.0
21	1423.3	1291.0	1381.0	1268.4
22	1863.2	1709.4	1812.6	1677.8
23	2438.9	2263.3	2379.1	2219.2
24	3192.6	2996.6	3122.6	2935.3

25	4179.2	3967.6	4098.4	3882.5
26	5470.7	5253.2	5379.2	5135.4
27	7161.3	6955.5	7060.2	6792.6
28	9374.3	9209.2	9266.6	8984.5
29	12271.1	12193.3	12162.6	11883.7
30	16063.2	16144.3	15963.5	15718.6
31	21027.1	21375.6	20952.2	20790.9
32	27525.0	28301.9	27500.0	27500.0

Table 4-25 Phase 1A & Phase 1B DES & DIS Stepper Table

	Start Date: 5/7/2017 Table Designator: v07&08	
Species:	**DES (electrons)**	**DIS (ions)**
Step #	**Center Energy (eV)**	**Center Energy (eV)**
1	6.5	2.2
2	8.5	3.9
3	11.2	7.1
4	14.6	10.9
5	19.1	14.5
6	25.1	19.2
7	32.8	25.4
8	43.0	33.6
9	56.2	44.5
10	73.6	58.9
11	96.3	78.0
12	126.1	103.2
13	165.1	136.7
14	216.1	181.0
15	282.9	239.6
16	370.3	317.3
17	484.7	420.1
18	634.5	556.2
19	830.6	736.5
20	1087.3	975.1
21	1423.3	1291.0
22	1863.2	1709.4
23	2438.9	2263.3
24	3192.6	2996.6
25	4179.2	3967.6
26	5470.7	5253.2
27	7161.3	6955.5
28	9374.3	9209.2
29	12271.1	12193.3
30	16063.2	16144.3
31	21027.1	21375.6
32	27525.0	28301.9

Table 4-26 Phase 2B DES & DIS Stepper Table

	Start Date: 11/14/2017 Table Designator: v08&09

EEPROM/ Table ID	EEPROM1 Tail		EEPROM2 Sheath		EEPROM4 Solar Wind	
Species:	DES (electrons)	DIS (ions)	DES (electrons)	DIS (ions)	DES (electrons)	DIS (ions)
Step #	Center Energy (eV)	Center Energy (eV)	Center Energy (eV)	Center Energy (eV)	Center Energy (eV)	Center Energy (eV)
1	6.5	2.2	6.5	2.16	4.4	210.0
2	8.5	3.9	8.5	3.91	5.2	236.8
3	11.2	7.1	11.2	7.07	6.2	267.0
4	14.6	10.9	14.6	10.93	7.3	301.1
5	19.1	14.5	19.1	14.24	8.7	339.6
6	25.1	19.2	25.1	18.54	10.3	382.9
7	32.8	25.4	32.8	24.14	12.2	431.8
8	43.0	33.6	43.0	31.44	14.5	486.9
9	56.2	44.5	56.2	40.94	17.1	549.0
10	73.6	58.9	73.6	53.32	20.3	619.1
11	96.3	78.0	96.3	69.44	24.1	698.1
12	126.1	103.2	126.1	90.43	28.6	787.2
13	165.1	136.7	165.1	117.77	33.9	887.7
14	216.1	181.0	216.1	153.36	40.2	1001.0
15	282.9	239.6	282.9	199.72	47.7	1128.8
16	370.3	317.3	370.3	260.10	56.6	1272.9
17	484.7	420.1	484.7	338.72	67.1	1435.3
18	634.5	556.2	634.5	441.11	79.6	1618.6
19	830.6	736.5	830.6	574.45	94.4	1825.1
20	1087.3	975.1	1087.3	748.10	112.0	2058.1
21	1423.3	1291.0	1423.3	974.23	132.8	2320.8
22	1863.2	1709.4	1863.2	1268.72	157.5	2617.0
23	2438.9	2263.3	2438.9	1652.24	186.9	2951.1
24	3192.6	2996.6	3192.6	2151.68	221.6	3327.8
25	4179.2	3967.6	4179.2	2802.10	262.9	3752.5
26	5470.7	5253.2	5470.7	3649.12	311.8	4231.5
27	7161.3	6955.5	7161.3	4752.19	369.8	4771.6
28	9374.3	9209.2	9374.3	6188.69	438.6	5380.7
29	12271.1	12193.3	12271.1	8059.43	520.2	6067.5
30	16063.2	16144.3	16063.2	10495.65	617.0	6841.9
31	21027.1	21375.6	21027.1	13668.31	731.8	7715.2
32	27525.0	28301.9	27525.0	17800.00	868.0	8700.0

Table 4-27 Phase 3B DES & DIS Stepper Table

4.7.3 Appendix C- Energy Profiles by Mission Phase

FPI science data collection energy configurations are dependent on mission phase. Energy steps used in a particular data file are provided in the *energy* variable. Energy profiles used since the start of the mission are listed in the following table.

Mission Phase	Orbit Range	FPI Energy Profile	Comments
Commissioning	1-172	P1	Not consistently operational
Phase 1A	173-362	P1	
Phase 1X	363-516, 531-551	N/A	Not operational

	517-534	Various	Burst Bulk Flow testing
Phase 1B	552-565	N/A	Not operational
	566-693	P2	
Phase 2A	694-696	N/A	Not operational
	697-702	P2	
	703-747	N/A	Not operational
Phase 2B	748-791	P2	
Phase 3A	792-817	P2	
Phase 3B	818-843	P2, SW	
	844-859	P3, SW	
Phase 3C	860-873	P3, SW	
	874-885	P3	
Phase 3D	886-918	P2	
	919-930	P3	
Phase 4A	931-952	P3	
Phase 4B	953-996	P3, SW	
Phase 4C	997-1010	P3, SW	
	1011-1016	P3	
	1017	P2	
Phase 4D	1018-1044	P2	
Phase 5A	1045-1048	P2	
	1049-1058	P3	
	1059	P3, SW	
Phase 5B	1060-1102	P3, SW	
Phase 5C	1103-1108	P3, SW	
	1109-1118	P3	
	1119-1120	P2	
Phase 5D	1121-1150	P2	
Phase 6A	1151-1160	P2	
	1161-1162	P3	
	1163-1164	P3, SW	
Phase 6B	1165-1208	P3, SW	
Phase 6C	1209-1216	P3, SW	
	1217-1222	P3	
	1223-1224	P2	
Phase 6D	1225-1254	P2	
Phase 7A	1255-1266	P2	
	1267-1271	P3	
	1272-1278	P3, SW	
Phase 7B	1279-1312	P3, SW	
Phase 7C	1313-1318	P3, SW	
	1319-1324	P2	
Phase 7D	1324-1356	P2	

Table 4-28 FPI Energy Profiles Since Mission Start

The following table lists the energy collection profiles that FPI has employed since launch. Note that the profile of MMS3 DIS was modified to prevent the taking of measurements above 11 keV starting with orbit 748, as discussed above.

Profile	DES	DIS
P1	10 eV - 30 keV in 32 energy steps and 4 deflection states yielding 11.25 deg angular bins	10 eV - 30 keV in 32 energy steps and 4 deflection states yielding 11.25 deg angular

	in elevation and azimuth dimensions; energy is interleaved across 2 parities	bins in elevation and azimuth dimensions; energy is interleaved across 2 parities
P2	6 eV - 30 keV in 32 energy steps and 4 deflection states yielding 11.25 deg angular bins in elevation and azimuth dimensions. Energy is identical across 2 parities	2 eV - 30 keV in 32 energy steps and 4 deflection states yielding 11.25 deg angular bins in elevation and azimuth dimensions. Energy is identical across 2 parities
P3	Identical to P2	2 eV - 18 keV in 32 energy steps and 4 deflection states yielding 11.25 deg angular bins in elevation and azimuth dimensions. Energy is identical across 2 parities
SW (solar wind)	4 eV - 940 eV in 32 energy steps and 4 deflection states yielding 11.25 deg angular bins in elevation and azimuth dimensions. Energy is identical across 2 parities	197 eV - 9222 eV in 32 energy steps and 4 effective deflection states yielding 11.25 deg effective angular bins in elevation and azimuth dimensions. Energy is identical across 2 parities. Deflection states are interleaved across 2 parities, but, due to convolution with spacecraft spin, do not provide increased angular resolution

Table 4-29 FPI Energy Collection Profiles

4.7.4 Appendix D- FPI References

The following is a list of applicable references and publications.

Section	Document Number	Title	Revision/ Date
	https://doi.org/10.1029/2021JA029149	Barrie, A. C., Schiff, C., Gershman, D. J., Giles, B. L., & Rand, D. (2021). Calibrating electrostatic deflection of charged particle sensors using ambient plasma measurements. Journal of Geophysical Research: Space Physics, 126, e2021JA029149.	
	https://doi.org/10.1002/2016JA022645	Barrie, A. C., S. E. Smith, J. C. Dorelli, D. J. Gershman, P. Yeh, C. Schiff, and L. A. Avanov (2017), Performance of a space-based wavelet compressor for plasma count data on the MMS Fast Plasma Investigation, J. Geophys. Res. Space Physics, 122, 765–779.	
	https://doi.org/10.1029/2018EA000407	Barrie, A. C., et al. “Physically Accurate Large Dynamic Range Pseudo Moments for the MMS Fast Plasma Investigation.” *Earth and Space Science* 5.9 (2018): 503-515.	
	https://doi.org/10.1063/1.5119344	Barrie, A. C., et al. "Characterizing spacecraft potential effects on measured particle trajectories." *Physics of Plasmas* 26.10 (2019): 103504.	
	https://doi.org/10.1029/2019JA027181	da Silva, D., Barrie, A., Gershman, D., Elkington, S., Dorelli, J., Giles, B., & Paterson, W. (2020). Neural network repair of Lossy compression Artifacts in the September 2015 to March 2016 duration of the MMS/FPI data set. Journal of Geophysical Research: Space Physics, 125, e2019JA027181.	

	https://doi.org/10.1002/2017JA024518	Gershman, D. J., Avanov, L. A., Boardsen,S. A., Dorelli, J. C., Gliese, U., Barrie, A. C.,...Pollock, C. J. (2017). Spacecraft and instrument photoelectrons measured by the dual electron spectrometers on MMS. Journal of Geophysical Research: Space Physics,122, 11,548–11,558.	
	https://doi.org/10.1029/2019JA026980	Gershman, D. J., Dorelli, J. C., Avanov, L. A., Gliese, U., Barrie, A., Schiff, C., et al. (2019). Systematic uncertainties in plasma parameters reported by the fast plasma investigation on NASA's magnetospheric multiscale mission. Journal of Geophysical Research: Space Physics, 124, 10345– 10359.	
	https://doi.org/10.1007/s11214-016-0245-4	Pollock, C., Moore, T., Jacques, A., Burch, J., Gliese, U., Saito, Y., ... & Zeuch, M. (2016). Fast plasma investigation for magnetospheric multiscale. Space Science Reviews, 199(1), 331-406.	
	https://doi.org/10.1002/2017GL076260	Rager, A. C., Dorelli, J. C., Gershman, D. J., Uritsky, V., Avanov, L. A., Torbert, R. B.,...Saito, Y.(2018). Electron crescent distributions as a manifestation of diamagnetic drift in an electron-scale current sheet: Magnetospheric Multiscale observations using new 7.5 ms Fast Plasma Investigation moments. Geophysical Research Letters, 45, 578–584.	
	https://doi.org/10.1029/2021JA029784	Roberts, O. W., Nakamura, R., Coffey, V. N., Gershman, D. J., Volwerk, M., Varsani, A., et al. (2021). A study of the solar wind ion and electron measurements from the magnetospheric multiscale mission's fast plasma investigation. Journal of Geophysical Research: Space Physics, 126, e2021JA029784.	
	https://doi.org/10.1029/2019GL083549	Shuster, J. R., D. J. Gershman, L. Chen, S. Wang, N. Bessho, J. C. Dorelli, D. E. Silva, B. L. Giles, W. R. Paterson, R. E. Denton, S. J. Schwartz, C. Norgren, F. D. Wilder, P. A. Cassak, M. Swisdak, V. Uritsky, C. Schiff, A. C. Rager, S. Smith, L. A. Avanov, and A. F. Viñas (2019), MMS Measurements of the Vlasov Equation: Probing the Electron Pressure Divergence Within Thin Current Sheets, Geophysical Research Letters, 46(14), 7862-7872, https://agupubs.onlinelibrary.wiley.com/doi/full/10.1029/2019GL083549	
	https://doi.org/10.1038/s41567-021-01280-6.	Shuster, J. R., D. J. Gershman, J. C. Dorelli, B. L. Giles, S. Wang, N. Bessho, L.-J. Chen, P. Cassak, S. Schwartz, R. Denton, V. Uritsky, W. R. Paterson, C. Schiff, A. Vinas, J. Ng, L. A. Avanov, D. da Silva, and R. Torbert (2021), Structures in the terms of the Vlasov equation observed at Earth's magnetopause, Nature Physics, https://www.nature.com/articles/s41567-021-01280-6	

	https://doi.org/10.1126/science.aat2998	Torbert, R. B., Burch, J. L., Phan, T. D., Hesse, M., Argall, M., Shuster, R. J., et al. (2018). Electron-scale dynamics of the diffusion region during symmetric magnetic reconnection in space. Science.	

Table 4-30 FPI Applicable Documents

5.0 HOT PLASMA COMPOSITION ANALYZER (HPCA)

5.1 HPCA OVERVIEW

The Hot Plasma Composition Analyzer (HPCA) investigation supports the Magnetospheric Multiscale mission (MMS) by determining the ways in which key marker species found in the solar wind and Earth's magnetosphere (H+, He++, He+ and O+) contribute to reconnection phenomena. The instrument is a time-of-flight (TOF) mass spectrometer designed to measure the velocity distributions of the four ion species (H+, He++, He+ and O+) known to be important in the reconnection process. The measurement technique is based on a combination of electrostatic energy-angle analysis with time-of-flight velocity analysis. The result is an accurate determination of the velocity distributions of the individual ion species. The HPCA instrument incorporates three new technologies. The first extends counting rate dynamic range by employing a novel radio frequency mass filter that allows minor species such as He++ and O+ to be measured accurately in the presence of intense proton fluxes found in the dayside magnetopause. The second ensures that TOF processing rates are high enough to overlap with the low end of the RF dynamic range, while the third enhances ion mass resolution.

A full description of the design of HPCA, its ground calibration setup and results, and its operational concept can be found in the publication:

Young, D.T., Burch, J.L., Gomez, R.G. et al, **Hot Plasma Composition Analyzer for the Magnetospheric Multiscale Mission**, Space Sci Rev 199, 407–470 (2016). https://doi.org/10.1007/s11214-014-0119-6

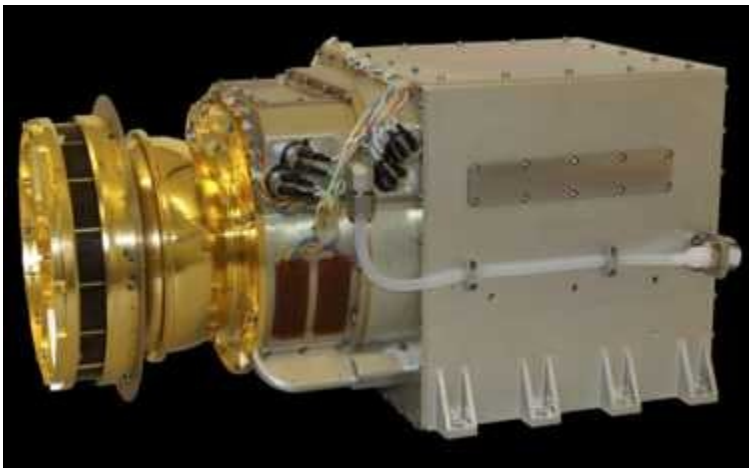

Figure 5-1 Completed HPCA Flight Model 1

For the purpose of the CMAD, a limited description is included here in order to provide the discussion for algorithm development.

5.1.1 Status of the HPCA Instruments

One HPCA instrument is mounted on each MMS spacecraft. All the HPCA instruments are functioning nominally. Over the course of the mission there have been several anomalies that have affected the production of data, and have resulted in the instrument being rebooted to clear the error. Additionally, the instruments have been rebooted after uploading new parameter tables to make changes to the instrument

configuration. These changes should be transparent to the user of the L2 files, as these configuration changes have been accounted for within the data processing pipeline.

The HPCA ground system processes all available downlinked Fast Survey and burst data, including partial segments and those that were not downloaded for all MMS observations. However, there may still be time periods when there are incomplete records, missing data, zeroes in the data, or data that is not optimal for science.

- HPCA data with non-optimal voltage settings (degraded or harder to use science). Note that the voltage setting can be found in the Moments CDF file (see section 5.6.9), while nominal voltage settings are noted in Table 5-12.
    - Maneuvers: HPCA is placed into Maneuver mode which reduces the voltages.
    - On-Orbit Gain Tests: Voltages vary over a 45 minute time period and are scheduled roughly every 6 months.
    - Radiation Belt (RB) Mode: The MCP supply is raised to keep from oversaturating the microchannel plates. Nominally this occurs when the L-shell is 5 or less. This setting has changed over the course of the mission. HPCA also operated in RB mode between science regions of interest for a while.
    - Times when the instrument has been powered on, but the ATS command sequence has not placed the instrument into a science mode.
    - Parameter Loads: HPCA occasionally loads a new set of configuration parameters to the instrument, which requires a power-down, table load, and reboot cycle.
- No HPCA data is available
    - Spacecraft anomalies: No HPCA data is collected when an observatory is in emergency safe mode.
    - Scheduled downtime: HPCA does not collect data during the yearly long shadow periods.
    - Time periods where no magnetic field data is available.

5.2 HPCA MEASURMENT STANDARDS, VOLUME, TIMING, AND COORDINATES

5.2.1 Accuracy of HPCA Time Tags in L2 Data

The time variable in all HPCA data products mark the beginning of the data collection interval. TOF measurements over 512 bins are taken at 64 different energy steps every 11.25 degrees of spacecraft rotation. Note that the 360-degree FOV is divided into 16 polar segments that correspond to the 16 simultaneously acquired histograms that are reported by the TOF hardware for each acquisition period.

- The 11.25 degrees of spacecraft rotation are the azimuth (AZ) steps
- The 64 voltage steps in each 11.25 degrees are the Energy (E/Q) steps
- The same Power Supply/RF Frequency profile is repeated for each 11.25 degree set (azimuth)
- There are 1,024 TOF data sets created every 10-second half-spin of the spacecraft (full sky view), calculated as (16 AZ) * (64 Energy) = 1024 TOF data sets

5.3 RELATIVE TELEMETRY ALLOCATIONS AND DATA VOLUME

During the nominal mission, HPCA was assigned allocation rates for slow and fast survey, as well as burst. Due to the fact that we run with both lossy and lossless compression, the size of our data can vary, based on how well the data compresses. After analyzing the rates during early mission, HPCA was able to back off on the decimation of some data products to allow for less decimated data to be downlinked.

Mode	% of Time Operated	% of HPCA Data Transmitted	Daily Allocation Rate	Daily Allocation
Slow Survey	~50%	7.4%	0.8 kbit/s	~34 Mbit
Fast Survey	~50%	51.3%	5.6 kbit/s	~236 Mbit
Fast Survey (Burst)	1.25%	41.3%	180 kbit/s	~190 Mbit
TOTAL	100%	100%	N/A	~460 Mbit

Table 5-1 HPCA Nominal Modes and Volume

5.3.1 Basic Instrument Information for Algorithm Development

MMS-HPCA measures the energy and composition of magnetospheric plasmas with an electrostatic energy analyzer (ESA) which is optically coupled to a carbon-foil based time-of-flight (TOF) section. The following sections address the operational principles of both ion-optical components.

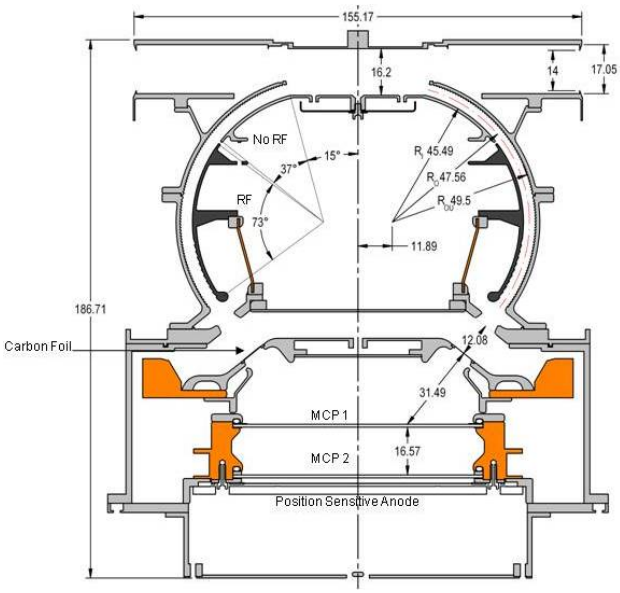

Figure 5-2 HPCA Dimensions

5.3.1.1 ESA

HPCA scans plasmas in the energy range 1 eV - 40 keV using an ESA with inner and outer conducting electrode radii of R_1 = 45.5 mm and R_2 = 49.5 mm. These conducting electrodes are more commonly called ESA plates. The ESA bending angle of $\gamma = 125.0°$ insures that UV photons from the sun do not have a direct path to the particle sensitive microchannel plates (MCPs), which can cause excessive background during data acquisition. ESAs deflect the paths of charged particles in a specified energy range set by the plate spacing ($\Delta R = R_2 - R_1$), the average plate radius, $R_0 = (R2 + R1)/2$, and the voltage

difference between the plates, $\Delta V = V_2 - V_1$; where $V_{1/2}$ is the voltage applied to the inner/outer plate. The analyzer geometry determines the energy and angular resolutions as well as the ESA's analyzer constant, *k*; a constant of proportionality between the ESA plate voltage difference and central energy of the acceptance passband. This energy is set according to (5-1):

$$E = k\Delta V \quad \textbf{(5-1)}$$

The analyzer constants of all four HPCA flight models were determined from calibration results at eight energies; 98 eV, 312 eV, 512 eV, 995 eV, 3159 eV, 10059 eV, 19525 eV, and 32040 eV. Their *k*'s are shown in the next table.

HPCA Flight Model	Analyzer Constant - *k*[eV/V]	Uncertainty (+/-) [eV/V]
1	5.42	0.01
2	5.42	0.01
3	5.39	0.04
4	5.39	0.02

Table 5-2 HPCA Flight Model Analyzer Constants

During operation, voltage is applied to the inner ESA plate of HPCA; the outer plate is held at spacecraft ground, so ΔV is just the voltage on the inner plate; $\Delta V = V_1$.

5.3.1.2 TOF

Particles that are permitted through the ESA plates, exit and are post-accelerated by a 15 kV potential on their way to one of sixteen thin carbon foils placed at the entrance to the TOF section. Ion impacts cause secondary electron emission from both foil surfaces. In the vast majority of interactions, ions assume a neutral charge state through charge exchange with the foil. Electrons emitted from the bottom surface facing the TOF section are accelerated, and focused with steering electrodes to MCP1 (see Figure 5-2), where their signals are amplified by over 6 orders of magnitude. These amplified signals then impact one of the sixteen elevation-start (β) pads shown in Figure 5-3.

Electron transit times within the TOF region are short (< 5.0 ns). By comparison, the transit time for a proton at 45 keV (60 keV with the 15 kV post acceleration), the highest energy scanned by HPCA, is > 9.0 ns. Because of this time difference, electron signals at the pads are used to signal the start of a time-of-flight measurement (TOF).

Ion signals impact MCP1 above the concentric array of sixteen anode rings (Figure 5-3). The rings are used to correct for the change in the particle flight path due to angular scattering within the foil. The ion signals are the stop signals for a TOF measurement. The ion time of flight (TOF) in this region has the analytical form (5-1):

$$TOF = \frac{d}{\sqrt{\frac{2E}{m}}} \quad \textbf{(5-1)}$$

where *d* is the length of the nominal flight path (3.15 cm), *E* the ion energy in eV, and *m* the ion mass-to-charge ratios provided in Table 5-3. HPCA measures ion TOF from 0 ns to 256 ns in 0.5 ns resolution (512 TOF channels).

Ion Species	Mass-to-Charge Ratio (M/q) [AMU/e]	Mass-to-Charge Ratio [eV/c^2 e]
H^+	1	0.939494061e9
He^{++} (alpha particle)	2	1.87898812e9
He^+	4	3.75797624e9
O^{++} (Doubly Charged Oxygen)	8	7.51595249e9
O^+	16	15.031905e9

Table 5-3 HPCA Species Mass-to-Charge Ratios

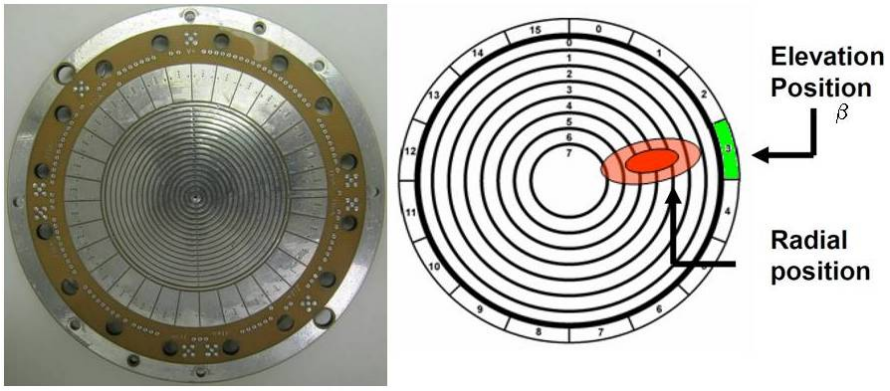

Figure 5-3 HPCA Position Sensitive Anode [At left, the anode with 16 elevation-start pads and 16 concentric stop rings. At right, the operation of the anode with respect to elevation detection, and flight distance correction]

HPCA's dual delay line, and the uncertainty in the energy loss from foil straggling makes an analytical fit with (5-1) very difficult. Instead, energy dependent TOF measurements made during calibration are used to assign channels of the TOF spectrum to specific ions as shown in Figure 5-4.

Also shown in Figure 5-4, ions of a given mass (e.g. H^+, 1 AMU) will populate a specific range of TOF channels, at a given post foil energy. The measured responses at eight energies are used to interpolate, and extrapolate the responses at other energies. Note that O^{2+} bins are not shown in Figure 5-4. This is because getting these counts requires special treatment of the background ion count product. This treatment will be discussed shortly. In addition to energy and composition, the HPCA's construction allows surveys of the plasma phase space with high resolution in solid angle. These resolutions will be discussed in later sections; but first we will discuss the technique used to get O^{2+} counts from the background ion count product.

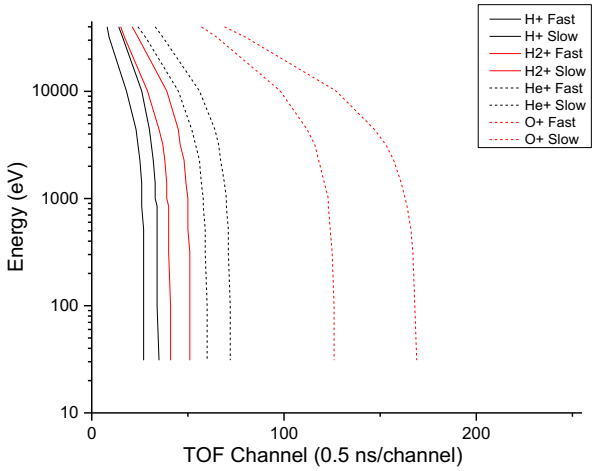

Figure 5-4 HPCA TOF Channel Assignment from Calibration

5.3.1.3 Determining Doubly Charged Oxygen Counts

The basic HPCA data product is an array of counts for 5 ion species, at 63 energies, for each elevation anode (16). Sixteen basic products, also called azimuths, are acquired every 10 seconds; half a spacecraft spin period nominally has 16 azimuths. The five ion species are protons (H^+), alpha particles (He^{2+}), helium ions (He^+), singly charged Oxygen (O^+), and background counts. The background counts are acquired in the TOF bin range between the slowest helium, and fastest singly charged oxygen ion at each energy (see Figure 5-4). These bin ranges contain ranges where the TOFs of doubly charged oxygen ions (O^{2+}) can be counted as well. To get these counts out of the background counts requires manipulation of the background product.

To start, we perform the following operation on the background ion counts:

$$\left[\frac{noise}{bin}\right]_\beta = \sum_{E=0}^{63} N_{E,\beta,Background} \Big/ \sum_{E=0}^{63} \left[N(bins)_{background}\right]_E \qquad \textbf{(5-2)}$$

which is based on the following assumptions:

1. The background is independent of energy
2. Background can be influenced by the gain of individual detector pixels
3. Ion species that can populate the background bins are in low concentration in most plasmas
4. HPCA, with its double coincidence detection scheme, greatly reduces spurious noise

In (5-2) the variable $[N(bins)_{background}]$ is the number of bins, at respective energies, over which the background counts are accumulated. Note that the sum is carried out over energy only, which addresses assumptions 1 and 2 in the list. [Noise/Bin] is then a 16 element array. Once computed, it is used to determine the corrected ion flux.

The ion flux at energy E in counts cm^{-2} sr^{-1} eV^{-1} is determined from:

$$J_{E,\beta,s} = \frac{C_{E,\beta,s}}{G(E)\left(\frac{E}{q}\right)_s} \quad \textbf{(5-3)}$$

Where G(E) is the energy specific geometric factor of the instrument at E. However, before computing $J_{E,\beta,s}$ the corrected ion counts must be calculated by subtracting the $[\text{noise/bin}]_\beta$ value as shown:

$$C_{E,\beta,s} = \left(N_{E,\beta,s} - N(bins)_{s,E} \times \left[\frac{noise}{bin}\right]_\beta\right)\Big/_{\Delta\tau} \quad \textbf{(5-4)}$$

Where $N(\text{bins})_s$ is the number of bins, at energy E, for which ion species *s* counts are accumulated. The doubly charged oxygen product comes from this when the background counter is operated upon as shown here:

$$C_{E,\beta,O++} = \left(N_{E,\beta,background} - N(bins)_{background,E} \times \left[\frac{noise}{bin}\right]_\beta\right)\Big/_{\Delta\tau} \quad \textbf{(5-5)}$$

Then the O++ flux is computed from:

$$J_{E,\beta,O++} = \frac{C_{E,\beta,O++}}{G(E)\left(\frac{E}{q}\right)_s} \quad \textbf{(5-6)}$$

5.3.2 Coordinates / Phase Space Scanning Dimensions

HPCA bins the phase-space of a plasma under observation into one dimension of energy, two of angles, and five ion masses as shown in the following table. Also included in the table are the HPCA parameters which control the dimensions, the dimensional symbols, the indices of these parameters and their ranges.

Dimension	Mediating Parameter	Symbol	Index	Index Values
Energy	ESA Voltage	*E*	*i*	0-62 (63 is flyback)
Elevation	Start Anode	β	*j*	0-15
Azimuth	Spin-Energy Sweep	α	*k*	0-15
Ion Species	Time-of-Flight Binning	*m*	*s*	0-4 : 0 = H^+; 1 = He^{2+}; 2 = He^+; 3 = O^+, 4 = background

Table 5-4 HPCA Parameters Controlling Dimensions, Symbols, and Indicies

Each of these dimensions, and how they are sampled, are included below.

5.3.2.1 ESA Voltages – Energy

During normal operation, the energy range (1 eV - 40 keV) is scanned by using a table of logarithmically spaced ESA voltages. Regardless of the instrument sampling mode (slow survey, fast survey, or burst - these modes will be discussed shortly), HPCA scans this energy range in 625 ms, including ramp and sample times. The sample time at each energy is 8.950 ms. There are 63 energy sample steps in the HPCA table; the 64th is a flyback step which sets the inner plate voltage to spacecraft ground, making $\Delta V = 0$ V.

The energy at each step is determined using (5-1). The voltages are set according to the voltage sweep tables supplied to each instrument.

5.3.2.2 Start Anodes – Elevation

At each voltage step, V_i, HPCA captures 16 individual TOF measurements; one for each elevation anode. Because of the clocking of the microchannel plates and the bias angle of their channels, there is signal gain variation between adjacent anodes which requires specific corrections. This effect is plainly evident in an elevation scan about the instrument aperture (shown in Figure 5-5).

In addition, as shown in Figure 5-2, HPCA's top-hat ESA configuration means that ions are accepted across the instrument's symmetry plane and their signals are registered on the anode that sits opposite the location of ion entry in the instrument aperture. The anode, and flight model specific, gain corrections are included in Figure 5-5.

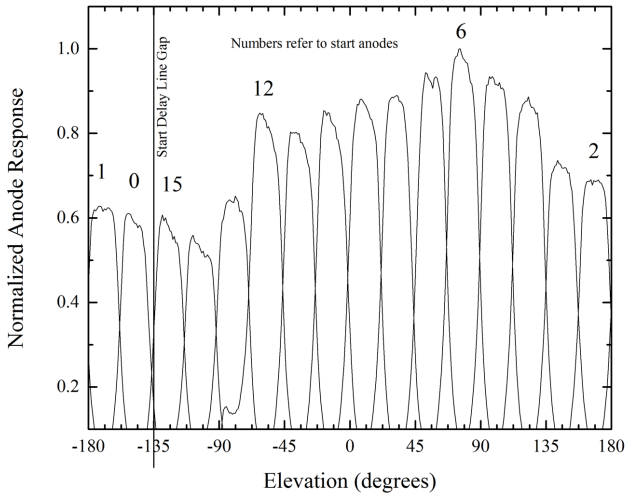

Figure 5-5 HPCA Flight Model 4 (FM4 on MMS3) Elevation and Anode Gain Response

Anode	FM1	FM2	FM3 (MMS4)	FM4 (MMS3)
0	1.69	1.96	1.58	1.63
1	1.30	1.58	1.35	1.47
2	1.39	1.52	1.42	1.42
3	1.30	1.36	1.30	1.31
4	1.20	1.16	1.23	1.11
5	1.09	1.21	1.07	1.04
6	1.05	1.14	1.00	1.00
7	1.02	1.00	1.09	1.09
8	1.04	1.02	1.05	1.14
9	1.00	1.04	1.06	1.06
10	1.06	1.09	1.13	1.13
11	1.10	1.12	1.07	1.16
12	1.07	1.14	1.04	1.05
13	1.29	1.23	1.28	1.33

14	1.65	1.41	1.38	1.65
15	1.70	1.67	1.64	1.68

Table 5-5 Anode Specific Gain Correction Factors for HPCA Flight Models 1-4

The elevation anode locations (yellow numbers on pads) and their look directions (black numbers within outer dotted circle in the figure) are shown in Figure 5-5.

The nominal centers of ion arrival directions for the instrument mounted on the spacecraft, are supplied in Table 5-6. The top-hat ESA configuration allows eight anodes to view one azimuthal direction, while the other eight view azimuthal space that is angularly displaced by 180°. The centers of the 16 anodes trace out circles of constant elevation as the spacecraft spins. As shown in Figure 5-6 and as indicated in Table 5-6, the anodes sample elevation space in its entirety; $0° \leq \beta \leq 180°$.

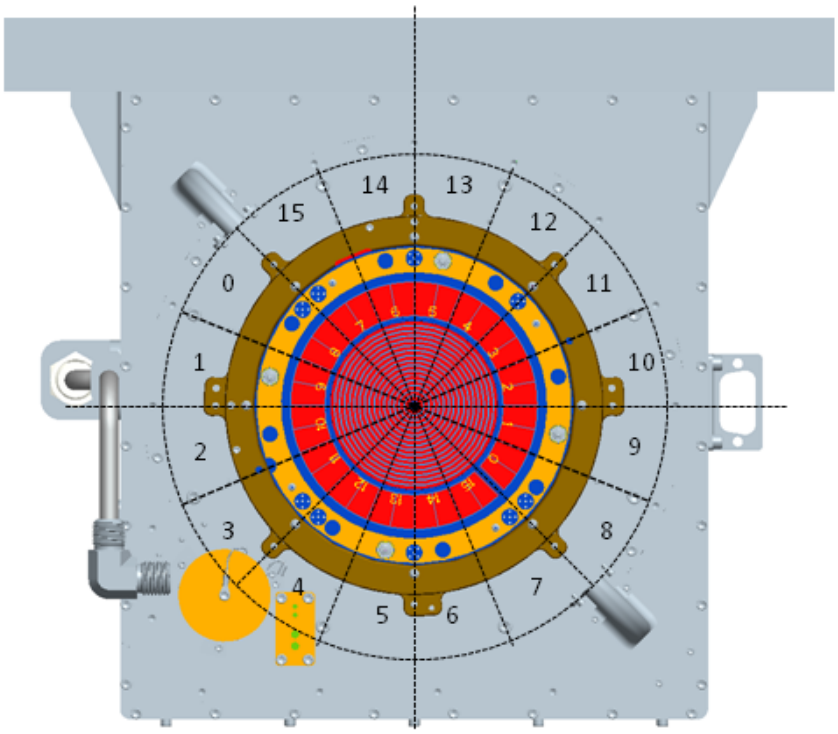

Figure 5-6 HPCA Start Anode Arrangement and Field-of-View (FOV) Sectors for Instrument Mounted on MMS Spacecraft

Anode	Centroid β View (°) - Elevation
0	123.75
1	101.25
2	78.75
3	56.25
4	33.75
5	11.25
6	11.25
7	33.75
8	56.25

9	78.75
10	101.25
11	123.75
12	146.25
13	168.75
14	168.75
15	146.25

Table 5-6 HPCA Start Nominal Anode Look Directions

The FWHM field of view (FOV) is averaged over 16 anodes and 63 energies. This value, which is unique to each flight model, is provided in Table 5-7 along with the measured uncertainty in this parameter. The values in Table 5-6 and Table 5-7 are important for determining the moments of the plasma distribution function, f(**v**). Computing these moments is a subject of later sections.

Flight Model	Δβ FWHM [°]	Δβ FWHM-Error [°]
1	24.0	0.7
2	24.8	0.7
3	24.1	0.7
4	23.8	0.7

Table 5-7 HPCA Anode-Elevation Response

In addition to gain, a correction for sky coverage is required in the calculations. Each HPCA anode covers approximately 24° or 0.419 radians (Table 5-7) in elevation. Anode centers are separated by 22.5° as shown in Table 5-6 (or 1.07 steradians). Per full energy sweep at a spin rate of 3 Hz, 11.25° of azimuthal angle space is covered. However, as shown in Figure 5-7, there is an excess of 7° (0.122 radians) in this field-of-view. Thus each anode sees 0.133 steradians of solid angle space at this spin rate. This gives an overestimation in particle flux for a given phase-space parcel, which leads to errors in f(**v**) and moment calculations. The following table (Table 5-8) provides the correction factors to prevent this error.

Anode	Solid Angle Space Correction
0	2.09
1	1.78
2	1.78
3	2.09
4	3.13
5	8.93
6	8.93
7	3.13
8	2.09
9	1.78
10	1.78
11	2.09
12	3.13
13	8.93
14	8.93
15	3.13

Table 5-8 HPCA Solid Angle Space Correction Factors

The next section addresses how the azimuth components of the plasma distribution are acquired.

5.3.2.3 Spacecraft Rotation – Azimuth

MMS has a nominal a spin period of 20 seconds. HPCA has a 90° azimuthal offset, relative to the DSS sun pulse detector, for elevation anodes 14, 15, 0, 1, 2, 3, 4, and 5, and 270° for the remaining anodes. Because of HPCA's elevation FOV and top-hat construction it sees 4π steradians (full sky view) in half a spacecraft spin. In 10 seconds, HPCA will sweep the entire energy range of 1eV - 40 keV 16 times. While the uniform sample time at each energy step was already discussed in section 5.3.2.1, the dwell times were not. These time steps are not uniform, and increase with increasing voltage magnitude. Because of these steps the azimuthal look directions vary between adjacent steps. HPCA also has an inherent FWHM azimuthal resolution of 7.0°. This is plotted in Figure 5-6.

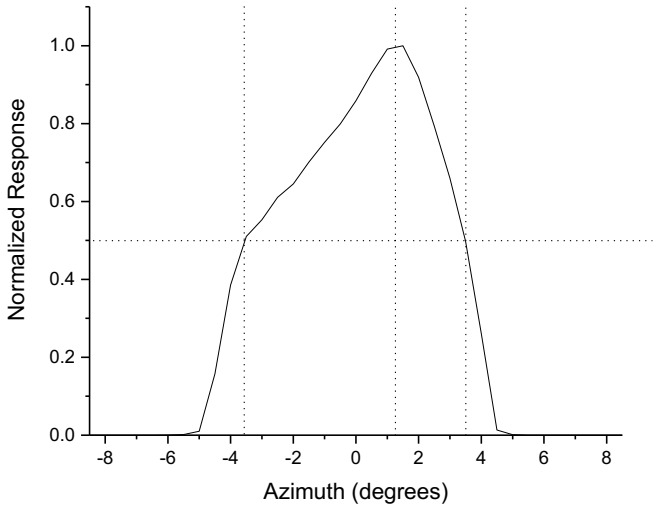

Figure 5-7 HPCA Azimuth (α) Response

The horizontal line in Figure 5-7 indicates the half-maximum response. The vertical lines, from left to right are the negative half-maximum limit, the center response, and the positive half-maximum limit. As seen here, HPCAs FWHM response is for all intents symmetric. However, the center response is offset by +1°.

This angular response is swept through 11.25° in one energy sweep. In the graphs shown below (Figure 5-8), the sequence of energies and α angles are shown as a function time, assuming at HPCA starts at Sweep Time = 0 on the x-axis. The first α-look direction is 0.275° at an energy of 1.34 eV ($V_{i=0}$ = -0.2477 V), and the last acquisition at $V_{i=62}$ = 6936 V (37454.4 eV) occurs when the α-look is 10.940°. At the end of the sweep 625 ms later α = 11.25°, and $V_{i=63}$ = 0 V.

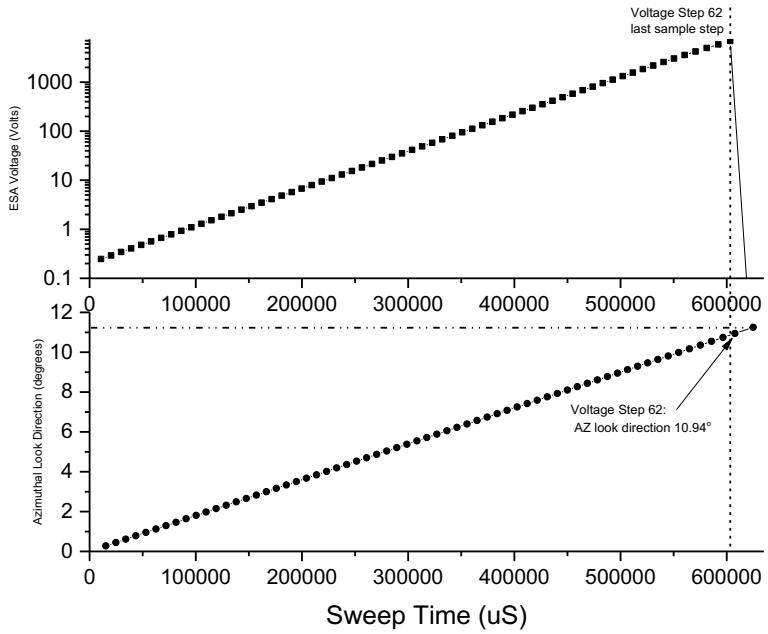

Figure 5-8 HPCA Energy Sweeping and Azimuth Look Direction

The α-look directions, calculated at the center of each energy acquisition step, are in Table 5-9.

Energy Step	α-look (°) Anodes 14, 15, 0-5	α-look (°) Anodes 6-13
0	0	180
1	0.17	180.17
2	0.341	180.341
3	0.511	180.511
4	0.681	180.681
5	0.851	180.851
6	1.021	181.021
7	1.191	181.191
8	1.361	181.361
9	1.531	181.531
10	1.701	181.701
11	1.871	181.871
12	2.042	182.042
13	2.212	182.212
14	2.382	182.382
15	2.552	182.552
16	2.722	182.722
17	2.892	182.892
18	3.062	183.062

19	3.232	183.232
20	3.402	183.402
21	3.572	183.572
22	3.743	183.743
23	3.913	183.913
24	4.083	184.083
25	4.253	184.253
26	4.423	184.423
27	4.593	184.593
28	4.763	184.763
29	4.933	184.933
30	5.103	185.103
31	5.273	185.273
32	5.444	185.444
33	5.614	185.614
34	5.784	185.784
35	5.954	185.954
36	6.124	186.124
37	6.294	186.294
38	6.464	186.464
39	6.634	186.634
40	6.804	186.804
41	6.974	186.974
42	7.145	187.145
43	7.315	187.315
44	7.485	187.485
45	7.655	187.655
46	7.825	187.825
47	7.995	187.995
48	8.165	188.165
49	8.335	188.335
50	8.505	188.505
51	8.675	188.675
52	8.846	188.846
53	9.016	189.016
54	9.187	189.187
55	9.36	189.36
56	9.535	189.535
57	9.713	189.713
58	9.894	189.894
59	10.079	190.079

60	10.269	190.269
61	10.464	190.464
62	10.666	190.666
63	10.975	190.975

Table 5-9 HPCA Azimuthal Arrival Directions in 1 Energy Sweep

Note: The values in this table are provided for diagnostic purposes. Whether they will be used to compute moments is still under consideration.

The values shown in Table 5-9 were calculated using a spacecraft spin period of 20 seconds. If this is not the case then the general expression for the HPCA azimuthal look direction is:

$$\alpha_{HPCA} = \frac{121° \pi}{180°} + \frac{2\pi}{\tau_{sc}} \left(\Delta t + \frac{\tau_{acq}}{2} + k \times \tau_{acq}\right) \quad \textbf{(5-7)}$$

where in (5-7) τ_{sc} is the spacecraft spin period, or the time between two sequential sun pulses. Δt is the time that has passed since the most recent sun pulse. τ_{acq} is the acquisition time for a full energy sweep (0.625 s). Recall that (5-7) applies to elevation anodes 14, 15, and 0-5; for anodes 6-13 add π radians, up to a maximum of 2π.

5.3.3 Geometric Factor

The convolved differential field-of-views (FOVs) in energy and solid angle space for a single HPCA elevation pixel is called its geometric factor; denoted G. G depends on energy (i) and on a pixel dependent gain factor (already discussed in Table 5-5). In this case G becomes $G_{i,j}$ and it is expressed as (5-8).

$$G_{i,j} = A_{eff}\left(E_i, \beta_j, \alpha_k\right) \left\langle \frac{\Delta E}{E} \Delta\alpha \right\rangle \Delta\beta \quad \textbf{(5-8)}$$

where A_{eff}, is an area external to the instrument which corresponds to the j^{th} start pixel's flux sensitivity; this also includes detector efficiencies. Also included are the integrated energy-azimuth response, $<\Delta E/E \, \Delta\alpha>$, which is a differential quantity that is unique to the instrument and is energy independent. $\Delta\beta$ is the FWHM elevation response of the HPCA flight model given in Table 5-7. We will first discuss A_{eff}.

5.3.3.1 Effective Area

The A_{eff} of an elevation anode, as shown in (5-9), is a sensitive external area, A_0, divided by the gain factor of the respective anode, g_j (Table 5-5).

$$A_{eff} = \frac{A_0(E_i)}{g_j} \quad \textbf{(5-9)}$$

The anode with the largest response is assigned a g_j value of 1. A_0 is computed with the calibration data from this anode. The A_0 values of all four FMs, which are energy dependent, are provided in Table 5-10.

Voltage Step (i)	A_0 FM 1 (cm^2)	A_0 FM 2 (cm^2)	A_0 FM 3 (cm^2) (on mms4)	A_0 FM 4 (cm^2) (on mms3)
0	0.025	0.021	0.023	0.024
1	0.025	0.021	0.023	0.024

2	0.026	0.022	0.024	0.025
3	0.026	0.022	0.024	0.025
4	0.026	0.022	0.024	0.025
5	0.027	0.023	0.025	0.026
6	0.027	0.023	0.025	0.026
7	0.028	0.024	0.025	0.027
8	0.028	0.024	0.025	0.027
9	0.029	0.024	0.026	0.028
10	0.029	0.024	0.026	0.028
11	0.03	0.025	0.027	0.029
12	0.03	0.025	0.027	0.029
13	0.031	0.026	0.028	0.029
14	0.031	0.026	0.028	0.029
15	0.032	0.027	0.029	0.030
16	0.032	0.027	0.029	0.030
17	0.033	0.028	0.030	0.031
18	0.033	0.028	0.030	0.031
19	0.034	0.029	0.031	0.032
20	0.035	0.029	0.032	0.033
21	0.035	0.029	0.032	0.033
22	0.036	0.030	0.033	0.034
23	0.036	0.030	0.033	0.034
24	0.037	0.031	0.034	0.035
25	0.037	0.031	0.034	0.035
26	0.038	0.032	0.035	0.036
27	0.039	0.033	0.035	0.037
28	0.039	0.033	0.035	0.037
29	0.04	0.034	0.036	0.038
30	0.041	0.035	0.037	0.039
31	0.041	0.035	0.037	0.039
32	0.042	0.035	0.038	0.040
33	0.043	0.036	0.039	0.041
34	0.043	0.036	0.039	0.041
35	0.044	0.037	0.040	0.042
36	0.045	0.038	0.041	0.043
37	0.046	0.039	0.042	0.044
38	0.046	0.039	0.042	0.044
39	0.047	0.040	0.043	0.045
40	0.048	0.040	0.044	0.046
41	0.049	0.041	0.045	0.047
42	0.05	0.042	0.046	0.048
43	0.05	0.042	0.046	0.048
44	0.051	0.043	0.046	0.048
45	0.052	0.044	0.047	0.049
46	0.053	0.045	0.048	0.050
47	0.054	0.045	0.049	0.051
48	0.055	0.046	0.050	0.052
49	0.056	0.047	0.051	0.053
50	0.057	0.048	0.052	0.054
51	0.058	0.049	0.053	0.055
52	0.059	0.050	0.054	0.056
53	0.06	0.051	0.055	0.057
54	0.06	0.051	0.055	0.057

55	0.062	0.052	0.056	0.059
56	0.063	0.053	0.057	0.060
57	0.064	0.054	0.058	0.061
58	0.068	0.057	0.062	0.065
59	0.066	0.056	0.060	0.063
60	0.063	0.053	0.057	0.060
61	0.061	0.051	0.056	0.058
62	0.057	0.048	0.052	0.054
63	0	0.000	0.000	0.000

Table 5-10 A_0's (updated per discussion in section 5.4.1)

With the values of A_0 and anode specific gain g_j discussed, we now turn to the integrated response, $<\Delta E/E\ \Delta\alpha>$.

5.3.3.2 Integrated Energy-Azimuth Response, <ΔE/E Δα>

The integrated response describes the instantaneous phase space view of HPCA, when it is tuned to center passband energy E_i, as described in (5-1) and in section 5.3.4.1. This response is a consequence of the ESA geometry; it is unique, and independent of energy. The values for FMs 1-4 are provided in Table 5-11.

Flight Model	<ΔE/E Δα> [eV/eV rads]
FM1	9.68E-03
FM2	8.27E-03
FM3 (on mms4)	7.63E-03
FM4 (on mms3)	7.46E-03

Table 5-11 <ΔE/E Δα> for HPCA FMs 1-4

These values are determined from the average instrument responses at all eight calibration energies.

5.3.3.3 Geometric Factor for HPCA

With the values included in the tables, the expression for geometric factor is now (5-10):

$$G_{i,j} = \frac{A_0(E_i)}{g_j}\left\langle\frac{\Delta E}{E}\Delta\alpha\right\rangle\ \Delta\beta\frac{\pi}{180^\circ} \qquad \textbf{(5-10)}$$

where the appropriate values have now been inserted for A_0, g_j and $\Delta\beta$. The $\pi/180°$ conversion is necessary because $\Delta\beta$ is provided in degrees in Table 5-7. With these values, it is now possible to compute particle flux, the velocity distribution function, f(**v**), and other data products. These will be covered in the later section 5.6.

5.4 HPCA CALIBRATION AND VALIDATION

5.4.1 Pre-Flight / On-Ground Calibration

The HPCA instruments were calibration on the ground, prior to delivery. As noted earlier in section 5.3.2 and in Table 5-4, the analyzer constants of all four HPCA flight models were determined from calibration results. Additionally, the A_0 values were also acquired via calibration.

In August 2015, discrepancies in moment calculations (particularly number density) were discovered. These discrepancies were traced to errors in beam current measurement during calibration. Once this was realized, the research team began inspecting magnetosheath data at the highest resolution (fast survey) to determine the inter-instrument correction factors, assuming MMS1-HPCA is accurate. The distance between the spacecraft was negligible over the time space for this data, so the flux seen by each instrument is essentially the same. The data for each instrument was averaged over the time interval into count arrays of 64 energies by 16 elevation anodes. The expression for flux (5-12) was used, with G expanded into the form shown in (5-10). With equal fluxes, and the other values accounted for, the correction values were found by solving $A_{0(FMk)} = C_k A_{0(FM1)}$, where k = 2, 3, or 4. The table determined from this analysis is reported in Table 5-10.

5.4.2 In-Flight Calibration

HPCA performs in-flight MCP "calibrations" on a half-yearly basis. The goal of the MCP gain test is to look for degradation of signal in the counting statistics, and to determine if voltages need to be adjusted to increase the signal.

After analysis of the data on the ground, the science team decides whether it is necessary to increase the MCP value on the flight unit in order to maintain optimal counting per sensor in Table 5-12.

Spacecraft	Launch (2015)	Aug 8, 2017	Dec 6, 2017	Aug 17, 2021
MMS1	-800V	-850V	-850V	-900V
MMS2	-800V	-850V	-850V	-850V
MMS3	-700V	-800V	-800V	-800V
MMS4	-650V	-750V	-800V	-800V

Table 5-12 Microchannel Plate (MCP) Voltage Settings

5.4.3 Compression Pipeline and Lossy Compression

Science processing on board consists of three distinct parts. Part 1 is the high-speed pipeline which controls the TOF data collection, reads the raw data from the TOF board into the FPGA, performs primary data decimation in the FPGA, reads the partially decimated data into the Sparc memory, and performs the secondary decimation in FSW. Part 2 consists of a sequence of operations performed on each data product as the product becomes available, rather than a pipeline, and generates each science data message sent to CIDP. The rate at which this data is processed is determined by the decimation factors. At the highest rate, Part 2 processing may occur more frequently than once per azimuth. Once a set of decimated data is available to the software, the Part 1 pipeline is directed to a second data buffer in the Sparc memory, and the first memory is processed (Part 2 processing). This processing consists of performing lossy compression and recomposing the data for subsequent operations. Part 3 is lossless compression, which ends with the data ready for inclusion in the CCSDS packet. The CCSDS packet is then composed (including adding header information such as the size [which is variable as a result of the lossless compression] and the checksum). The completed packet is handed back to the FPGA for transmission to the CIDP.

5.4.4 Validation

HPCA validates by internal science use, and use by the external community. In addition, cross-comparison with other MMS instruments have also been done. Discrepancies found generate an internal review and assessment. This has led to several adjustments being made to processing, effective area, and RF correction factors. Additionally, any anomalies during the processing of the data (found be operations

personnel or by the science community), have led to reprocessing of the entire data set to correct the errors. The current version of data is v4.2.

5.5 MEASUREMENT ALGORITHM DESCRIPTIONS

5.5.1 Theoretical Basis

The information contained in this section can also be found in the HPCA instrument paper, though an effort has been made to summarize. The sections for the detailed discussion will be noted.

In order to meet science requirements the HPCA must be capable of determining the following parameters under all conditions and in all regions where reconnection occurs:

1. Ion energy from 10 eV to 30 keV with a resolution of 20%
2. Ion arrival directions over 4π sr resolved into ~20° × 20° pixels
3. Ion energy flux from ~10^4 to ~3×10^9 keV/cm sr keV
4. Ion velocity distributions resolved into H^+, He^{++}, He^+ and O^+
5. Complete this suite of measurements within 10 s (1/2 spacecraft spin period)

[HPCA instrument paper; section 2 and 3]

From the above list of measurement requirements, corresponding performance requirements determined the detailed design of the instrument. The four ion species of interest have mass/charge (M_i/q) ratios of i = 1, 2, 4 and 16 which requires relatively low mass resolution $M/\Delta M = 4$ for separation. Because the HPCA is a time-of-flight instrument we need TOF resolution $T/\Delta T = 2M/\Delta M = 8$. The table below summarizes the HPCA performance requirements.

Parameter	Variable	Required Value
Sensitivity	Energy-dependent geometric factor Maximum potential counting rate	3 x 10^{-3} cm^2 sr keV/keV (total) 20 MHz
Mass/charge	Range Resolution (M/ΔM)	1 to 16 amu/e 4 at FWHM
Energy/charge	Range Resolution (ΔE/E) Energy range scan rate	10 eV to 40 keV ≤0.2 FWFM 64 log-spaced samples per 0.625 s
Angle	Field-of-regard Field-of-view resolution Number of pixels over 4π sr	11.25° x 360° 11.25° azimuth x 22.5° elevation FWFM 32 azimuth x 16 elevations
Dynamic range	Maximum detectable energy flux Minimum detectable energy flux Dynamin range	~3 x 10^9 keV/cm^2 sr s keV of H^+ ~3 x 10^4 keV/cm^2 sr s keV of H^+ ≥10^5
Timing	3-D velocity distribution 2-D energy-elevation scan Single sample all elevations	½ spacecraft spin (10 s) 625 ms 8.95 ms

Table 5-13 HPCA Performance Requirements

The instrument paper (section 4) discusses how some of the choices were made. The CMAD discussion in sections 5.3 and 5.4 walks through a high level instrument overview and how to apply the parameters that were chosen. For the in-depth details regarding the instrument design, including details regarding the Electrostatic Analyzer' (ESA) ion optics and electronics, see the instrument paper (section 6.1). For in-depth details about the Time of Flight Analyzer's (TOF) ion optics as well as the measurement and position coding, see section 6.2 of the instrument paper.

In section 6.4 of the instrument paper, the dynamic range choices are discussed in detail. The section addresses the problems that intense proton fluxes can produce high counting rates that could cause saturation which would swamp the signal, as well as a potential that the TOF electronics would not be able to keep up. These two problems are addressed in depth in this section, and how we chose to use the RF (radio frequency) system to reduce proton fluxes. Discussion in section 5.6.5 below show how corrections for RF are applied as needed.

5.5.2 Error Analysis and Known Features

One of the known features of the data is in regards to the volume of counts in the survey data vs the burst data. The lossy compression scheme was designed to throw away the least significant bit. The assumption was that single counts were just noise. Whereas this might normally be a good assumption, the problem is that HPCA was designed and built as a triple coincident system, such that single counts are truly counts, and not just noise. This problem was discovered in late 2018, when comparing burst data with survey data. Because of the higher levels of decimation in survey mode, the "single" counts were being added with other single counts and as such, they were making it through the lossy compression. In the case of the burst data, those same counts were removed, as if they were noise.

Testing was performed in late 2018, and an updated lossy table was loaded to the instruments on April 16, 2019. Unfortunately, the updated lossy compression table requires reloading after the instrument is powered off, which happened on August 17, 2019. This mistake was not caught until April 2021. The lossy compression table was loaded to all instruments on May 24, 2021. Additionally, all power-cycling procedures were updated to include the new lossy compression table. Lossy compression that does not remove single counts will be active from May 24, 2021 forward.

5.6 DATA PRODUCTION ALGORITHM DESCRIPTIONS

5.6.1 Level 0 - Counts

The counts acquired in a single energy sweep gives 63 values of the single acquisition product. At each (E,β,α) combination, the count rate of ion species s is (5-11):

$$C_{i,j,k,s} = \frac{N_s(E_i, \beta_j, \alpha_k)}{\Delta\tau} \qquad \textbf{(5-11)}$$

where N_s is the number of ions counted at energy i, on anode j, in azimuth k, in the acquisition period Δτ. This data product requires no processing; it is a raw count measurement.

5.6.2 Level 1a - Flux

The next data product to compute is the ion flux of species s. This is the first derived data product. The raw counts are converted to flux in units of (e eV^{-1} sr cm^{-2} s^{-1}). The conversion from count rate to flux is (5-12):

$$J_{i,j,k,s} = \frac{C_{i,j,k,s}}{G_j(E_i)\left(\frac{E_i}{q}\right)_s} \qquad \textbf{(5-12)}$$

In this equation, the term in the numerator $(E_i/q)_s$ is the mass-to-charge ratio for the ion species s: For singly charged ion species (H^+, He^+, O^+), this is equal to $(E_i/e)_s$ where e is the elementary charge ($e=1.602\times10^{-19}$ coulombs); it is $(E_i/2e)_s$ for doubly charged ions (He^{2+}, O^{2+}).

5.6.3 Level 1b - $f_s(v)$

The next data product to determine is the velocity distribution function of the ion species s. This product depends on the acquisition mode of the instrument which determines data decimation and timing. There are three HPCA survey modes: slow survey, fast survey, and burst. The nominal decimations and timing are shown in Table 5-14.

Mode	α	β	Energies E	Full Sampling Period	f(v) dimensions
Slow Survey	8	8	16	3.5 Spins (70 seconds)	5 species x 16α x 16β x 64E
Fast Survey	8	8	16	1/2 Spin (10 seconds)	5 species x 16α x 16β x 64E
Burst	16	16	64	1/2 Spin (10 Seconds)	5 species x 16α x 16β x 64E

Table 5-14 Nominal Decimations and Timing

As shown in Table 5-14, the only acquisition mode that has data in full resolution is Burst mode. Slow and Fast Survey modes have the same decimation, but are sampled at different cadences. However, moment calculations will always be carried out with an array having the burst dimensions. Because of this computing the velocity distribution function is not straightforward and it requires some discussion. In fast and slow survey the 4 steps are co-added in energy, which means that the value is the sum of 4 smaller steps. To get this to a proper count rate this value should be divided by 4 times the acquisition time, $\Delta\tau$. For decimation in elevation the new values for each are divided by two, since they are summed over two elevation bins. This process is shown in Figure 5-9.

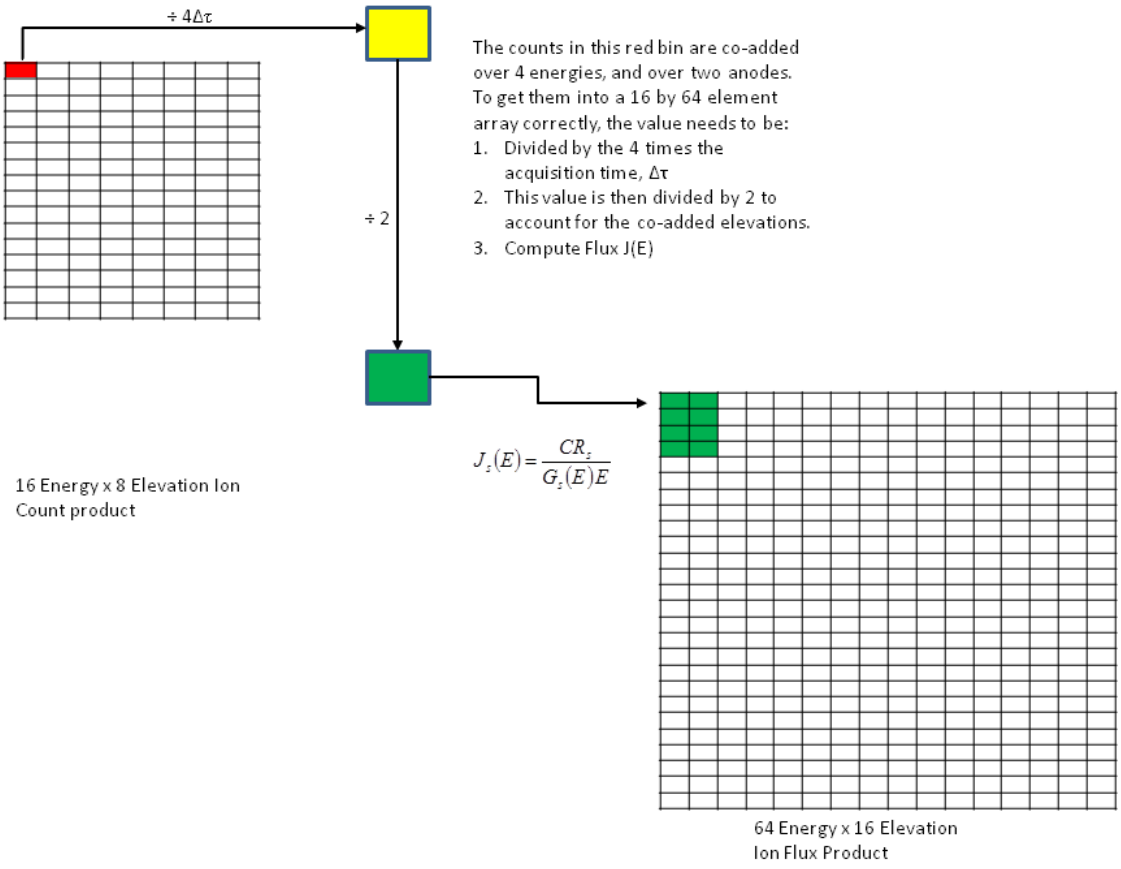

Figure 5-9 Correcting Counts for Decimation Before Converting to Flux

Up to this point, the flux is corrected for energy, and elevation decimations. It still needs to be corrected for the decimation in azimuth. This calculation only affects $f_s(v)$. Slow and fast survey azimuths are co-added, resulting in 8 azimuths per full sky view. Each of the 8 flux measurements need to be divided by 2 and made into 16 flux measurements. Once done, $f_s(v)$ can be determined as shown in (5-13):

$$f_{i,j,k,s} = \frac{J_{i,j,k,s}}{2E_i} m_s^2 \qquad \textbf{(5-13)}$$

where $f_{i,j,k}$ is the velocity distribution function for each ion species s, in $cm^{-6}\ s^3$. The value m_s is actually the mass of the ion species s in AMU multiplied by $1.0453453 \times 10^{-12}$ eV s^2 /AMU cm^2. The methods used to compute the moments from this distribution will be discussed in the following sections.

5.6.4 Plasma Distribution Moments

In the following sections computation of the distribution moments will be discussed.

5.6.4.1 Ion Number Density (n_s)

The number density of ion species s is determined by performing the following operation on the plasma distribution array $f_{i,j,k,s}$:

$$n_s = \sum_{k=0}^{15} \Delta\alpha \sum_{i=0}^{62} \frac{v_{i+1}^3 - v_i^3}{3} \sum_{j=0}^{15} 2\sin(\bar{\beta}_j)\, sin\left(\frac{\Delta\beta}{2}\right) f_{i,j,k,s} \qquad \textbf{(5-14)}$$

where $\Delta\alpha$ is the azimuthal angle coverage in an acquisition period (18.25° = 0.318 radians). The velocity values v_i, v_{i+1} are determined from the energy centroids, FWHM energy passbands of the instrument, and the mass of the respective ions, m_s. $\Delta\beta$ is the measured average FWHM elevation response of the anodes, $\Delta\beta$ = 22.44° = 0.39 radians. β_j is the look direction of the j^{th} anode from Table 5-6. The velocity bin size for each ion species s, at energy step i will be supplied in flight model specific spreadsheets.

With these simplifications, (5-14) can now be expressed in form (5-15):

$$n_s = 2\Delta\alpha \sin\left(\frac{\Delta\beta}{2}\right)\left[\sum_{j=0\cdots5,14,15} \frac{1}{\Lambda_j}\sin(\bar{\beta}_j) \sum_{k=0}^{15}\sum_{i=0}^{62} \frac{v_{i+1}^3 - v_i^3}{3} f_{i,(j=0\cdots5,14,15),k,s} + \sum_{j=6\cdots13} \frac{1}{\Lambda_j}\sin(\bar{\beta}_j) \sum_{i=0}^{15}\sum_{i=0}^{62} \frac{v_{i+1}^3 - v_i^3}{3} f_{i,(j=6\cdots13),k,s}\right] \qquad \textbf{(5-15)}$$

+

where n_s is in units of cm^{-3}. The j subscripts show that the sum is carried out over two parts j = 0-5,14,15 and j = 6-13. This is because HPCA has two sets of anodes that view azimuth spaces that are displaced 180 degrees from each other, simultaneously. Also note the inclusion of the anode coverage correction factors, Λ_j, from Table 5-8 included in the j summation. These will be included in all moment calculations.

5.6.4.2 Ion Bulk Velocity (u_s)

The three components of the bulk velocity of ion species s are computed from the following:

$$u_{x,s} = \frac{2}{n_s}\sin\left(\frac{\Delta\alpha}{2}\right) \times \left[\sum_{j=0\cdots5,14,15} \frac{1}{\Lambda_j}\left[\frac{1}{2}\Delta\beta - \frac{1}{2}\sin(\Delta\beta)\cos(2\bar{\beta}_j)\right]\sum_{k=0}^{15}\cos(\alpha_k)\sum_{i=0}^{62}\frac{v_{i+1}^4 - v_i^4}{4} f_{i,(j=0\cdots5,14,15),k,s} + \sum_{j=6\cdots13} \frac{1}{\Lambda_j}\left[\frac{1}{2}\Delta\beta - \frac{1}{2}\sin(\Delta\beta)\cos(2\bar{\beta}_j)\right]\sum_{k=0}^{15}\cos(\alpha_k)\sum_{i=0}^{62}\frac{v_{i+1}^4 - v_i^4}{4} f_{i,(j=6\cdots13),k,s}\right] \qquad \textbf{(5-16)}$$

$$u_{y,s} = \frac{2}{n_s}\sin\left(\frac{\Delta\alpha}{2}\right) \times$$

$$\left[\sum_{j=0\cdots5,14,15}\frac{1}{\Lambda_j}\left[\frac{1}{2}\Delta\beta-\frac{1}{2}\sin(\Delta\beta)\cos\left(2\bar{\beta}_j\right)\right]\sum_{k=0}^{15}\sin(\alpha_k)\sum_{i=0}^{62}\frac{v_{i+1}^4-v_i^4}{4}f_{i,(j=0\cdots5,14,15),k,s}+\right.$$
$$\left.\sum_{j=6\cdots13}\frac{1}{\Lambda_j}\left[\frac{1}{2}\Delta\beta-\frac{1}{2}\sin(\Delta\beta)\cos\left(2\bar{\beta}_j\right)\right]\sum_{k=0}^{15}\sin(\alpha_k)\sum_{i=0}^{62}\frac{v_{i+1}^4-v_i^4}{4}f_{i,(j=6\cdots13),k,s}\right]$$

$$u_{z,s}=\frac{1}{2n_s}\Delta\alpha\sin(\Delta\beta)\times\left[\sum_{j=0\cdots5,14,15}\frac{1}{\Lambda_j}\sin\left(2\bar{\beta}_j\right)\sum_{k=0}^{15}\sum_{i=0}^{62}\frac{v_{i+1}^4-v_i^4}{4}f_{i,(j=0\cdots5,14,15),k,s}+\sum_{j=6\cdots13}\frac{1}{\Lambda_j}\sin\left(2\bar{\beta}_j\right)\sum_{k=0}^{15}\sum_{i=0}^{62}\frac{v_{i+1}^4-v_i^4}{4}f_{i,(j=6\cdots13),k,s}\right]$$

The vector u_s is now expressed component wise as:

$$u_s=u_{x,s}\hat{\imath}+u_{y,s}\hat{\jmath}+u_{z,s}\hat{k}$$

where $\Delta\beta$, and $\Delta\alpha$ have already been discussed. These equations result in velocity components in units of cm s^{-1}. However, they need to be reported in units of km s^{-1}. To make this conversion multiply the components by the conversion factor 1 km / 10^5 cm.

5.6.4.3 Scalar Ion Temperature

The scalar ion temperature is determined with the following formula:

$$T_s=\left[2\Delta\alpha\frac{m_s}{3n_s}\sin\left(\frac{\Delta\beta}{2}\right)\sum_{j=0\cdots5,14,15}^{15}\frac{1}{\Lambda_j}\sin\left(\bar{\beta}_j\right)\sum_{k=0}^{15}\sum_{i=0}^{62}\frac{v_{i+1}^5-v_i^5}{5}f_{i,0\cdots5,14,15,k,s}\right]+\left[2\Delta\alpha\frac{m_s}{3n_s}\sin\left(\frac{\Delta\beta}{2}\right)\sum_{j=6\cdots13}^{15}\frac{1}{\Lambda_j}\sin\left(\bar{\beta}_j\right)\sum_{k=0}^{15}\sum_{i=0}^{62}\frac{v_{i+1}^5-v_i^5}{5}f_{i,j=6\cdots13,k,s}\right]-\frac{u_s^2m_s}{3} \quad \textbf{(5-17)}$$

where the value of m_s is given in the following table, in units of eV s^2/cm^2. At the end of the calculation, the species specific scalar temperature is reported in eV.

Ion Species	Mass-to-Charge Ratio (M/q) [AMU/e]	m_s [eV s^2/cm^2]
H^+	1	1.04535E-12
He^{++} (alpha particle)	2	4.18138E-12
He^+	4	4.18138E-12
O^{++} (Doubly Charged Oxygen)	8	1.67255E-11
O^+	16	1.67255E-11

Table 5-15 m_s values for Temperature Calculation

Note that the bulk velocity, u_s, is used in (5-17) is of form (5-18):

$$\|u_s\| = \sqrt{u_{x,s}^2 + u_{y,s}^2 + u_{z,s}^2} \quad \textbf{(5-18)}$$

5.6.4.4 Ion Temperature Tensor

The ion temperature tensor is computed from the pressure tensor, P_{ij}. The nine components of the tensor are computed from:
First the diagonal terms:

$$P_{xx,s} = m_s \sum_{k=0}^{15} \alpha_{k+1} - \alpha_k + \sin(\alpha_{k+1}) - \sin(\alpha_k) \sum_{i=0}^{62} \frac{v_{i+1}^5 - v_i^5}{5} - 2u_s \frac{v_{i+1}^4 - v_i^4}{4} + u_s^2 \frac{v_{i+1}^3 - v_i^3}{3} \sum\nolimits_{j=0}^{15} \frac{1}{12} \left[\cos(3\beta_{j+1}) - \cos(3\beta_j) + 9\left(\cos(\beta_{j+1}) - \cos(\beta_j)\right)\right] f_{i,j,k,s}$$

To remove confusion from the subscripts, we first take note that:

$$\alpha_{k+1} - \alpha_k = \Delta\alpha$$

which is the 18.25 degrees (based on a 20 second spin period) used in previous calculations.

We can also use:

$$\sin(\alpha_{k+1}) - \sin(\alpha_k) = 2\cos\left(\frac{\alpha_{k+1}+\alpha_k}{2}\right)\sin\left(\frac{\alpha_{k+1}-\alpha_k}{2}\right) \quad \textbf{(5-19)}$$

Then:

$$\frac{\alpha_{k+1} + \alpha_k}{2} = \alpha_k$$

which is the midpoint of the azimuth FOV during a single energy sweep. With these substitutions $P_{xx,s}$ becomes:

$$P_{xx,s} = m_s \sum_{k=0}^{15} \frac{\Delta\alpha}{2} + \frac{1}{2}\cos(\alpha_k)\sin(\Delta\alpha) \sum_{i=0}^{62} \frac{v_{i+1}^5 - v_i^5}{5} + \sum\nolimits_{j=0}^{15} \left[\frac{3}{2}\sin(\beta_j)\sin\left(\frac{\Delta\beta}{2}\right) - \frac{1}{6}\sin(3\beta_j)\sin\left(3\frac{\Delta\beta}{2}\right)\right] f_{i,j,k,s} - m_s n_s u_{x,s}^2$$

Which is difficult to work with because of the sum over *k*. This can be re-expressed as:

$$p_{xx,s} = m_s \left[\sum_{j=0\cdots5,14,15}^{15} \frac{1}{\Lambda_j} \left[\frac{3}{2} \sin(\beta_j) \sin\left(\frac{\Delta\beta}{2}\right) - \frac{1}{6} \sin(3\beta_j) \sin\left(3\frac{\Delta\beta}{2}\right) \right] \sum_{k=0}^{15} \frac{\Delta\alpha}{2} \right.$$
$$+ \frac{1}{2} \cos(2\alpha_k) \sin(\Delta\alpha) \sum_{i=0}^{62} \frac{v_{i+1}^5 - v_i^5}{5} f_{i,(j=0\cdots5,14,15),k,s}$$
$$+ \sum_{j=6\cdots13}^{15} \frac{1}{\Lambda_j} \left[\frac{3}{2} \sin(\beta_j) \sin\left(\frac{\Delta\beta}{2}\right) \right.$$
$$\left. - \frac{1}{6} \sin(3\beta_j) \sin\left(3\frac{\Delta\beta}{2}\right) \right] \sum_{k=0}^{15} \frac{\Delta\alpha}{2}$$
$$\left. + \frac{1}{2} \cos(2\alpha_k) \sin(\Delta\alpha) \sum_{i=0}^{62} \frac{v_{i+1}^5 - v_i^5}{5} f_{i,(j=6\cdots13),k,s} \right] - m_s n_s u_{x,s}^2$$

The remaining terms are much simpler to handle. Starting with $P_{yy,s}$

$$P_{yy,s} = m_s \left[\sum_{j=0\cdots5,14,15}^{15} \frac{1}{\Lambda_j} \left[\frac{3}{2} \sin(\beta_j) \sin\left(\frac{\Delta\beta}{2}\right) - \frac{1}{6} \sin(3\beta_j) \sin\left(3\frac{\Delta\beta}{2}\right) \right] \sum_{k=0}^{15} \frac{\Delta\alpha}{2} \right.$$
$$- \frac{1}{2} \cos(2\alpha_k) \sin(\Delta\alpha) \sum_{i=0}^{62} \frac{v_{i+1}^5 - v_i^5}{5} f_{i,(j=0\cdots5,14,15),k,s}$$
$$+ \sum_{j=6\cdots13}^{15} \frac{1}{\Lambda_j} \left[\frac{3}{2} \sin(\beta_j) \sin\left(\frac{\Delta\beta}{2}\right) - \frac{1}{6} \sin(3\beta_j) \sin\left(3\frac{\Delta\beta}{2}\right) \right] \sum_{k=0}^{15} \frac{\Delta\alpha}{2}$$
$$\left. - \frac{1}{2} \cos(2\alpha_k) \sin(\Delta\alpha) \sum_{i=0}^{62} \frac{v_{i+1}^5 - v_i^5}{5} f_{i,(j=6\cdots13),k,s} \right] - m_s n_s u_{y,s}^2$$

$$P_{zz,s} = m_s \Delta\alpha \left[\sum_{j=0\cdots5,14,15}^{15} \frac{1}{\Lambda_j} \left[\frac{1}{6} \sin(3\beta_j) \sin\left(3\frac{\Delta\beta}{2}\right) \right.\right.$$
$$\left. + \frac{1}{2} \sin(\beta_j) \sin\left(\frac{\Delta\beta}{2}\right) \right] \sum_{k=0}^{15} \sum_{i=0}^{62} \frac{v_{i+1}^5 - v_i^5}{5} f_{i,(j=0\cdots5,14,15),k,s}$$
$$+ \sum_{j=6\cdots13}^{15} \frac{1}{\Lambda_j} \left[\frac{1}{6} \sin(3\beta_j) \sin\left(3\frac{\Delta\beta}{2}\right) \right.$$
$$\left.\left. + \frac{1}{2} \sin(\beta_j) \sin\left(\frac{\Delta\beta}{2}\right) \right] \sum_{k=0}^{15} \sum_{i=0}^{62} \frac{v_{i+1}^5 - v_i^5}{5} f_{i,(j=6\cdots13),k,s} \right] - m_s n_s u_{z,s}^2$$

Now the off diagonal terms with some degeneracy:

$$P_{xy,s} = m_s \left[\sum_{j=0\cdots5,14,15}^{15} \frac{1}{\Lambda_j} \left[\frac{3}{2} \sin(\beta_j) \sin\left(\frac{\Delta\beta}{2}\right) \right.\right.$$
$$\left. - \frac{1}{6} \sin(3\beta_j) \sin\left(3\frac{\Delta\beta}{2}\right) \right] \sum_{k=0}^{15} \left[\frac{1}{2} \sin(2\alpha_k) \sin(\Delta\alpha) \right] \sum_{i=0}^{62} \frac{v_{i+1}^5 - v_i^5}{5} f_{i,(j=0\cdots5,14,15),k,s}$$
$$+ \sum_{j=6\cdots13}^{15} \frac{1}{\Lambda_j} \left[\frac{3}{2} \sin(\beta_j) \sin\left(\frac{\Delta\beta}{2}\right) \right.$$
$$\left.\left. - \frac{1}{6} \sin(3\beta_j) \sin\left(3\frac{\Delta\beta}{2}\right) \right] \sum_{k=0}^{15} \left[\frac{1}{2} \sin(2\alpha_k) \sin(\Delta\alpha) \right] \sum_{i=0}^{62} \frac{v_{i+1}^5 - v_i^5}{5} f_{i,(j=6\cdots13),k,s} \right]$$
$$- m_s n_s u_{x,s} u_{y,s}$$

$$P_{yx,s} = P_{xy,s}$$

$$P_{xz,s} = m_s \left[\sum_{j=0\cdots5,14,15}^{15} \frac{1}{\Lambda_j} \left[\frac{1}{2} \cos(\beta_j) \sin\left(\frac{\Delta\beta}{2}\right) \right.\right.$$
$$\left. - \frac{1}{6} \cos(3\beta_j) \sin\left(3\frac{\Delta\beta}{2}\right) \right] \sum_{k=0}^{15} \left[2\cos(\alpha_k) \sin\left(\frac{\Delta\alpha}{2}\right) \right] \sum_{i=0}^{62} \frac{v_{i+1}^5 - v_i^5}{5} f_{i,(j=0\cdots5,14,15),k,s}$$
$$+ \sum_{j=6\cdots13}^{15} \frac{1}{\Lambda_j} \left[\frac{3}{2} \sin(\beta_j) \sin\left(\frac{\Delta\beta}{2}\right) \right.$$
$$\left.\left. - \frac{1}{6} \sin(3\beta_j) \sin\left(3\frac{\Delta\beta}{2}\right) \right] \sum_{k=0}^{15} \left[2\cos(\alpha_k) \sin\left(\frac{\Delta\alpha}{2}\right) \right] \sum_{i=0}^{62} \frac{v_{i+1}^5 - v_i^5}{5} f_{i,(j=6\cdots13),k,s} \right]$$
$$- m_s n_s u_{x,s} u_{z,s}$$

$$P_{zx,s} = P_{xz,s}$$

$$P_{yz,s}$$
$$= m_s \left[\sum_{j=0\cdots5,14,15}^{15} \frac{1}{\Lambda_j} \left[\frac{1}{2} \cos(\beta_j) \sin\left(\frac{\Delta\beta}{2}\right) \right.\right.$$
$$\left. - \frac{1}{6} \cos(3\beta_j) \sin\left(\frac{3\Delta\beta}{2}\right) \right] \sum_{k=0}^{15} \left[2\sin(\alpha_k) \sin\left(\frac{\Delta\alpha}{2}\right) \right] \sum_{i=0}^{62} \frac{v_{i+1}^5 - v_i^5}{5} f_{i,(j=0\cdots5,14,15),k,s}$$
$$+ \sum_{j=6\cdots13}^{15} \frac{1}{\Lambda_j} \left[\frac{1}{2} \cos(\beta_j) \sin\left(\frac{\Delta\beta}{2}\right) \right.$$
$$\left.\left. - \frac{1}{6} \cos(3\beta_j) \sin\left(\frac{3\Delta\beta}{2}\right) \right] \sum_{k=0}^{15} \left[2\sin(\alpha_k) \sin\left(\frac{\Delta\alpha}{2}\right) \right] \sum_{i=0}^{62} \frac{v_{i+1}^5 - v_i^5}{5} f_{i,(j=6\cdots13),k,s} \right]$$
$$- m_s n_s u_{y,s} u_{z,s}$$

$$P_{zy,s} = P_{yz,s}$$

With the Pressure Tensor expressed as:

$$P_s = \begin{bmatrix} P_{xx,s} & P_{yx,s} & P_{zx,s} \\ P_{xy,s} & P_{yy,s} & P_{zy,s} \\ P_{xz,s} & P_{yz,s} & P_{zz,s} \end{bmatrix}$$

where the units of pressure are eV/cm3; 1 eV/cm3 = 1.602e-4 nanopascals.

To diagonalize the tensor we use the algorithm devised by Joachim Kopp [2008].
When diagonalized, P has the form:

$$P_s = \begin{bmatrix} P'_{xx,s} & 0 & 0 \\ 0 & P'_{yy,s} & 0 \\ 0 & 0 & P'_{zz,s} \end{bmatrix}$$

where ' indicates the component following diagonalization.

From the diagonalized form of the pressure tensor, we then determine T_s from:

$$T_s = \frac{P'_s}{n_s}$$

Where n_s is the number density of ion species s determined previously.

5.6.5 Data Products with RF

When computing flux with RF, multiply the counts for ion species s by the values specific to the energy step and ion species. This needs to be done for energy steps 36 - 49 (14 steps in all). Three RF tables are built: one which attenuates proton flux by 50%, one that attenuates 90%, and one more that decreases proton flux by a 99%. The computation for the flux is then:

$$J_{i,j,k,s} = \frac{C_{i,j,k,s}\varepsilon_i}{G_j(E_i)\,E_i} \qquad \textbf{(5-20)}$$

where ε_i is the attenuation correction from one of the 3 tables. Calculations of f(v) and moments follow directly from these values.

5.6.6 Level 2 Data Products: In the Magnetic Field Reference Frame

HPCA data products and moments are computed in the spacecraft reference frame using the magnetic field data acquired with the magnetometer probes on each of the spacecraft. Scalar moments, such as the number density and scalar temperature require no transformation. The remainder of this section will focus on the values which do; bulk velocity, and the pressure/temperature tensor.

5.6.6.1 Bulk Velocity in the Magnetic Field Frame

Transforming the bulk velocity into the magnetic field frame requires that we first determine a magnetic field unit vector:

$$\hat{\mathrm{b}} = \frac{\vec{B}}{\|B\|} = \frac{B_x\hat{\imath} + B_y\hat{\jmath} + B_z\hat{k}}{\sqrt{B_x^2 + B_y^2 + B_z^2}} \quad \textbf{(5-21)}$$

Once b is determined, the magnitude of the bulk velocity of species s in the direction of the magnetic field is:

$$V_{\|,s} = \vec{u}_s \cdot \hat{b} = u_{x,s}b_x + u_{y,s}y + u_{z,s}b_z \quad \textbf{(5-22)}$$

and the velocity vector of the ion species, parallel to the magnetic field (v-parallel) is then:

$$\vec{V}_{\|,s} = V_{\|,s}\hat{b} = V_{\|,s}b_x\hat{\imath} + V_{\|,s}y\,\hat{\jmath} + V_{\|,s}b_z\hat{k} \quad \textbf{(5-23)}$$

Once found, we can then use the parallel velocity vector to find the velocity vector perpendicular to the magnetic field (v-perpendicular):

$$\vec{V}_{\perp,s} = \vec{u}_s - \vec{V}_{\|,s} = \left(u_{x,s} - V_{\|x,s}\right)\hat{\imath} + \left(u_{y,s} - V_{\|y,s}\right)\hat{\jmath} + \left(u_{z,s} - V_{\|z,s}\right)\hat{k} \quad \textbf{(5-24)}$$

5.6.6.2 F(v) in Field Aligned Coordinates

Expressing the velocity distribution function in the magnetic field frame involves a translation in velocity, and a rotation. For each bin f_{ijk} in the discretized distribution function (remember that 16 adjacent azimuths/full energy sweeps constitute a full-sky observation) there will be three vector components associated with that bin, that represent the velocity relative to a component system in which the magnetic field is directed in the positive z direction. The vector components in translated into the magnetic field frame (the primed coordinate system) are determined from the base system (unprimed system) with the following:

$$\begin{aligned}\vec{v}'_{ijk,s} = \vec{v}_{ijks} - \vec{V}_{\perp,H^+} \\ = \left(v_{x,ijk,s} - V_{\perp x,H^+}\right)\hat{\imath} + \left(v_{y,ijk,s} - V_{\perp y,H^+}\right)\hat{\jmath} \\ + \left(v_{z,ijk,s} - V_{\perp z,H^+}\right)\hat{k}\end{aligned} \quad \textbf{(5-25)}$$

where $v_{x,ijk,s}$ is:

$$v_{x,ijk,s} = \sqrt{\frac{2E_i}{m_s}}\sin(\beta_j)\cos(\alpha_k) \quad \textbf{(5-26)}$$

$v_{y,ijk,s}$ is:

$$v_{y,ijk,s} = \sqrt{\frac{2E_i}{m_s}}\sin(\beta_j)\sin(\alpha_k) \quad \textbf{(5-27)}$$

and:

$$v_{z,ijk,s} = \sqrt{\frac{2E_i}{m_s}}\cos(\beta_j) \quad \textbf{(5-28)}$$

Each primed velocity value is computed on a bin-by-bin basis. The energies E_i are instrument specific and based on the voltage at each step with the analyzer constants from Table 5-2. The ms values are found in Table 5-15. For instance, f_{000,H^+} will be accompanied by values of:

$$v'_{x,000,H^+} = \sqrt{\frac{2E_0}{m_s}}\sin(123.75°)\cos(180°) - \left(u_{x,H^+} - V_{\|x,H^+}\right) \quad \textbf{(5-29)}$$

$$v'_{y,000,H^+} = \sqrt{\frac{2E_0}{m_s}}\sin(123.75°)\sin(180°) - \left(u_{y,H^+} - V_{\|y,H^+}\right) \quad \textbf{(5-30)}$$

$$v'_{z,000,H^+} = \sqrt{\frac{2E_0}{m_s}}\cos(123.75°) - \left(u_{z,H^+} - V_{\|z,H^+}\right) \quad \textbf{(5-31)}$$

and so on, until all 64 velocities, 16 elevation, and 16 azimuths are accounted for.

In addition to the velocity translation, the coordinate system must be rotated such that the magnetic field is in the direction of the +Z axis. The unit vectors of this coordinate system are:

$$\hat{X}_s = \frac{\left(\hat{b} \times \vec{u}_s\right) \times \hat{b}}{\|\vec{u}_s\|} = \frac{\begin{array}{l}\left[-(b_x u_z - u_x b_z)b_z - \left(b_x u_y - u_x b_y\right)b_y\right]\hat{\imath} \\ +\left[\left(b_y u_z - u_y b_z\right)b_z - \left(b_x u_y - u_x b_y\right)b_x\right]\hat{\jmath} \\ +\left[\left(b_y u_z - u_y b_z\right)b_y - (b_x u_z - u_x b_z)b_x\right]\hat{k}\end{array}}{\|\vec{u}_s\|} \quad \textbf{(5-32)}$$

$$\hat{Y}_s = \frac{\left(\hat{b} \times \vec{u}_s\right)}{\|\vec{u}_s\|} = \frac{\left(b_y u_{z,s} - b_z u_{y,s}\right)\hat{\imath} - \left(b_x u_{z,s} - b_z u_{x,s}\right)\hat{\jmath} + \left(b_x u_{y,s} - b_y u_{x,s}\right)\hat{k}}{\|\vec{u}_s\|} \quad \textbf{(5-33)}$$

$$\hat{Z}_s = \hat{\mathrm{b}} = \frac{B_x\hat{\imath} + B_y\hat{\jmath} + B_z\hat{k}}{\sqrt{B_x^2 + B_y^2 + B_z^2}} = b_x\hat{\imath} + b\hat{\jmath} + z_z\hat{k} \quad \textbf{(5-34)}$$

With the vector so determined, rotation matrix is:

$$T = \begin{bmatrix} \frac{[-(b_x u_z - u_x b_z)b_z - (b_x u_y - u_x b_y)b_y]}{\|\vec{u}_s\|} & \frac{[(b_y u_z - u_y b_z)b_z - (b_x u_y - u_x b_y)b_x]}{\|\vec{u}_s\|} & \frac{[(b_y u_z - u_y b_z)b_z - (b_x u_y - u_x b_y)b_x]}{\|\vec{u}_s\|} \\ \frac{(b_y u_{z,s} - b_z u_{y,s})}{\|\vec{u}_s\|} & \frac{(b_x u_{z,s} - b_z u_{x,s})}{\|\vec{u}_s\|} & \frac{(b_x u_{y,s} - b_y u_{x,s})}{\|\vec{u}_s\|} / \|\vec{u}_s\| \\ b_x & b_y & b_z \end{bmatrix} \quad \textbf{(5-35)}$$

And the matrix used to rotate the velocity components in the field aligned coordinate system is the transpose of this matrix

$$T^t = \begin{bmatrix} \frac{[-(b_x u_z - u_x b_z)b_z - (b_x u_y - u_x b_y)b_y]}{\|\vec{u}_s\|} & \frac{(b_y u_{z,s} - b_z u_{y,s})}{\|\vec{u}_s\|} & b_x \\ \frac{[(b_y u_z - u_y b_z)b_z - (b_x u_y - u_x b_y)b_x]}{\|\vec{u}_s\|} & \frac{(b_x u_{z,s} - b_z u_{x,s})}{\|\vec{u}_s\|} & b_y \\ \frac{[(b_y u_z - u_y b_z)b_y - (b_x u_z - u_x b_z)b_x]}{\|\vec{u}_s\|} & \frac{(b_x u_{y,s} - b_y u_{x,s})}{\|\vec{u}_s\|} & b_z \end{bmatrix} \quad \textbf{(5-37)}$$

With the operation:

$$\overrightarrow{v''}_s = T^t \overrightarrow{v'}_s \quad \textbf{(5-38)}$$

From the primed coordinates in equation 6.

5.6.7 HPCA Quality Flags

Quality flags are described at the top of each CDF files and is defined as follows:

Quality Flag Value	Meaning
0	Bad
1	Good
2	Good, RF on, Background on
3	Good, RF on, Background on
4	Good, RF on, Background on
5	Good, RF on, Background on
6	Good, non-sweeping data

Table 5-16 HPCA Quality Flags Definition

These quality flags are used throughout the different files and many of the different science fields have their own quality indicators based on this description.

5.6.8 File Structure L2 Ion CDF File

Most variables in the ion files are preceded by mmsX_hpca_ (with X being 1, 2, 3 or 4 depending upon the spacecraft on which the instrument is located). Names have been shorted here to allow for more space. The exception to the preceded name is the Epoch_ variables.

Variable	Units	Type	Dim	Description
Epoch	Ns	CDF_TT2000	1	Start time for the record
Epoch_MINUS	Ms	CDF_UINT2	1	Delta start time for the record from the central time
Epoch_PLUS	Ms	CDF_UINT2	1	Delta stop time for the record from the central time
polar_anode_number	n/a	CDF_UINT2	16	Polar Anode Index Value
azimuth_decimation_factor	n/a	CDF_UINT2	1	Azimuth decimation factor
polar_decimation_factor	n/a	CDF_UINT2	1	Polar Anode decimation factor
energy_decimation_factor	n/a	CDF_UINT2	1	Energy decimation factor
sweep_table_number	n/a	CDF_UINT1	1	Sweep Table index as defined in the HPCA science algorithm document
start_azimuth	n/a	CDF_UINT1	1	Start azimuth
science_mode	n/a	CDF_UINT1	1	Science mode value as defined in the HPCA science algorithm document
ion_energy	eV/q	CDF_REAL4	63	Electron voltage associated with the ion couts
hplus_flux	1/(cm^2 s sr eV)	CDF_REAL8	16 x 63	Hydrogen+ Flux for all elevation anodes across all energies
hplus_phase_space_density	cm^-6 s^3	CDF_REAL8	16 x 63	Hydrogen+ Phase Space Density for all Elevation Anodes across all energies
hplus_data_quality	n/a	CDF_UINT2	1	Per sweep status for H+, see Data_Quality_Key global attribute
heplus_flux	1/(cm^2 s sr eV)	CDF_REAL8	16 x 63	Helium+ Flux for all elevation anodes across all energies
heplus_phase_space_density	cm^-6 s^3	CDF_REAL8	16 x 63	Helium+ Phase Space Density for all Elevation Anodes across all energies
heplus_data_quality	n/a	CDF_UINT2	1	Per sweep status for He+, see Data_Quality_Key global attribute
heplusplus_flux	1/(cm^2 s sr eV)	CDF_REAL8	16 x 63	Helium++ Flux for all elevation anodes across all energies
heplusplus_phase_space_density	cm^-6 s^3	CDF_REAL8	16 x 63	Helium++ Phase Space Density for all Elevation Anodes across all energies

heplusplus_data_quality	n/a	CDF_UINT2	1	Per sweep status for He++, see Data_Quality_Key global attribute
oplus_flux	1/(cm^2 s sr eV)	CDF_REAL8	16 x 63	Oxygen+ Flux for all elevation anodes across all energies
oplus_phase_space_density	cm^-6 s^3	CDF_REAL8	16 x 63	Oxygen+ Phase Space Density for all Elevation Anodes across all energies
oplus_data_quality	n/a	CDF_UINT2	1	Per sweep status for O+, see Data_Quality_Key global attribute
B_GSE_sweep_avg	nT	CDF_REAL4	4	Magnetic field vector in DMPA plus Btotal (8 or 16 S/s), Despun MPA-aligned cartesian coordinates (from afg_srvy_l2pre_dmpa)
B_GSM_sweep_avg	nT	CDF_REAL4	4	Magnetic field vector in GSM plus Btotal (8 or 16 S/s), Geocentric Solar Magnetospheric (GSM) cartesian coordinates (see aft_srvy_l2pre_gsm)
Epoch_Angles	ns	CDF_TT2000	1	Start time for the Azimuth Angles Associated with each 1/2 spin
Epoch_MINUS_Angles	ms	CDF_UINT4	1	Delta start time for the record from the central time
Epoch_PLUS_Angles	ms	CDF_UINT4	1	Delta stop time for the record from the central time
azimuth_angles_degrees	degree	CDF_REAL8	16 x 16	Azimuth Angles in degrees for each anode for each HPCA half-spin
azimuth_angles_per_ev_degrees	degree	CDF_REAL8	16x16x 63	Azimuth Angles per eV in degrees for each anode for each HPCA half-spin
centroid_elevation_angle	degree	CDF_DOUBLE	16	Center Elevation Angles of each of the Anodes
azimuth_index	n/a	CDF_UINT2	16	Azimuth index value
energy_step_number	n/a	CDF_UINT2	63	Energy step index value

Table 5-17 L2 Ion CDF File

5.6.9 File Structure L2 Moments CDF File

Most variables in the moments files are preceded by mmsX_hpca_ (with X being 1, 2, 3 or 4 depending upon the spacecraft on which the instrument is located). Names have been shorted here to allow for more space.

Variable	Units	Type	Dim	Description
Epoch	ns	CDF_TT2000	1	Start time for the record
Epoch_MINUS	ms	CDF_UINT2	1	Delta start time for the record from the central time
Epoch_PLUS	ms	CDF_UINT2	1	Delta stop time for the record from the central time
spin_number	n/a	CDF_UINT4	1	Spin Number for each HPCA half-spin
ion_energy	eV/q	CDF_REAL4	63	Electron Voltage associated with the ion counts
sweep_table_number	n/a	CDF_UINT1	1	Sweep Table Index as defined in the HPCA Science Algorithm Document
science_mode	n/a	CDF_UINT1	1	Science Mode Value as defined in the HPCA Science Algorithm Document
hplus_number_density	cm^-3	CDF_REAL8	1	Number Density Hydrogen+ for each HPCA half-spin
hplus_ion_bulk_velocity	km/s	CDF_REAL8	3	Ion Bulk Velocity Hydrogen+ for each HPCA half-spin (x, y, z)
hplus_scalar_temperature	eV	CDF_REAL8	1	Scalar Temperature Hydrogen+ for each HPCA half-spin
hplus_ion_pressure	nPa	CDF_REAL8	3 x 3	Ion Pressure Tensor Hydrogen+ for each HPCA half-spin (xx,yx,zx,xy,yy,zy,xz,yz,zz)
hplus_temperature_tensor	eV	CDF_REAL8	3 x 3	Ion Temp. Tensor Hydrogen+ for each HPCA half-spin (xx,yx,zx,xy,yy,zy,xz,yz,zz)
heplus_number_density	cm^-3	CDF_REAL8	1	Number Density Helium+ for each HPCA half-spin
heplus_ion_bulk_velocity	km/s	CDF_REAL8	3	Ion Bulk Velocity Helium+ for each HPCA half-spin (x, y, z)
heplus_scalar_temperature	eV	CDF_REAL8	1	Scalar Temperature Helium+ for each HPCA half-spin
heplus_ion_pressure	nPa	CDF_REAL8	3 x 3	Ion Pressure Tensor Helium+ for each HPCA half-spin (xx,yx,zx,xy,yy,zy,xz,yz,zz)
heplus_temperature_tensor	eV	CDF_REAL8	3 x 3	Ion Temp. Tensor Helium+ for each HPCA half-spin (xx,yx,zx,xy,yy,zy,xz,yz,zz)
heplusplus_number_density	cm^-3	CDF_REAL8	1	Number Density Helium++ for each HPCA half-spin
heplusplus_ion_bulk_velocity	km/s	CDF_REAL8	3	Ion Bulk Velocity Helium++ for each HPCA half-spin (x, y, z)
heplusplus_scalar_temperature	eV	CDF_REAL8	1	Scalar Temperature Helium++ for each HPCA half-spin
heplusplus_ion_pressure	nPa	CDF_REAL8	3 x 3	Ion Pressure Tensor Helium++ for each HPCA half-spin (xx,yx,zx,xy,yy,zy,xz,yz,zz)
heplusplus_temperature_tensor	eV	CDF_REAL8	3 x 3	Ion Temp. Tensor Helium++ for each HPCA half-spin (xx,yx,zx,xy,yy,zy,xz,yz,zz)

oplus_number_density	cm^-3	CDF_REAL8	1	Number Density Oxygen+ for each HPCA half-spin
oplus_ion_bulk_velocity	km/s	CDF_REAL8	3	Ion Bulk Velocity Oxygen+ for each HPCA half-spin (x, y, z)
oplus_scalar_temperature	eV	CDF_REAL8	1	Scalar Temperature Oxygen+ for each HPCA half-spin
oplus_ion_pressure	nPa	CDF_REAL8	3 x 3	Ion Pressure Tensor Oxygen+ for each HPCA half-spin (xx,yx,zx,xy,yy,zy,xz,yz,zz)
oplus_temperature_tensor	eV	CDF_REAL8	3 x 3	Ion Temp. Tensor Oxygen+ for each HPCA half-spin (xx,yx,zx,xy,yy,zy,xz,yz,zz)
B_GSE_spin_avg	nT	CDF_REAL4	4	Magnetic field vector in DMPA plus Btotal (8 or 16 S/s) for each HPCA half-spin (x, y, z, total) [see afg_srvy_l2pre_dmpa]
B_GSM_spin_avg	nT	CDF_REAL4	4	Magnetic field vector in GSM plus Btotal (8 or 16 S/s) for each HPCA half-spin (x, y, z, total) [see afg_srvy_l2pre_gsm]
hplus_ion_bulk_velocity_GSM	km/s	CDF_REAL8	3	Bulk Velocity in GSM for H+ for each HPCA half-spin (x, y, z)
hplus_tperp	eV	CDF_REAL8	1	Tperp H+ for each HPCA half-spin
hplus_tparallel	eV	CDF_REAL8	1	Tparallel H+ for each HPCA half-spin
hplus_vperp	km/s	CDF_REAL8	4	Vperp vector plus Magnitude for H+ for each HPCA half-spin (x, y, z, total)
hplus_vparallel	km/s	CDF_REAL8	4	Vparallel vector plus Magnitude for H+ for each HPCA half-spin (x, y, z, total)
hplus_vperp_GSM	km/s	CDF_REAL8	4	Vperp vector plus Magnitude in GSM for H+ for each HPCA half-spin (x, y, z, total)
hplus_vparallel_GSM	km/s	CDF_REAL8	4	Vparallel vector plus Magnitude in GSM for H+ for each HPCA half-spin (x, y, z, total)
heplus_ion_bulk_velocity_GSM	km/s	CDF_REAL8	3	Bulk Velocity in GSM for He+ for each HPCA half-spin (x, y, z)
heplus_tperp	eV	CDF_REAL8	1	Tperp He+ for each HPCA half-spin
heplus_tparallel	eV	CDF_REAL8	1	Tparallel He+ for each HPCA half-spin
heplus_vperp	km/s	CDF_REAL8	4	Vperp vector plus Magnitude for He+ for each HPCA half-spin (x, y, z, total)
heplus_vparallel	km/s	CDF_REAL8	4	Vparallel vector plus Magnitude for He+ for each HPCA half-spin (x, y, z, total)
heplus_vperp_GSM	km/s	CDF_REAL8	4	Vperp vector plus Magnitude in GSM for He+ for each HPCA half-spin (x, y, z, total)
heplus_vparallel_GSM	km/s	CDF_REAL8	4	Vparallel vector plus Magnitude in GSM for He+ for each HPCA half-spin (x, y, z, total)
heplusplus_ion_bulk_velocity_GSM	km/s	CDF_REAL8	3	Bulk Velocity in GSM for He++ for each HPCA half-spin (x, y, z)
heplusplus_tperp	eV	CDF_REAL8	1	Tperp He++ for each HPCA half-spin
heplusplus_tparallel	eV	CDF_REAL8	1	Tparallel He++ for each HPCA half-spin

heplusplus_vperp	km/s	CDF_REAL8	4	Vperp vector plus Magnitude for He++ for each HPCA half-spin (x, y, z, total)
heplusplus_vparallel	km/s	CDF_REAL8	4	Vparallel vector plus Magnitude for He++ for each HPCA half-spin (x, y, z, total)
heplusplus_vperp_GSM	km/s	CDF_REAL8	4	Vperp vector plus Magnitude in GSM for He++ for each HPCA half-spin (x, y, z, total)
heplusplus_vparallel_GSM	km/s	CDF_REAL8	4	Vparallel vector plus Magnitude in GSM for He++ for each HPCA half-spin (x, y, z, total)
oplus_ion_bulk_velocity_GSM	km/s	CDF_REAL8	3	Bulk Velocity in GSM for O+ for each HPCA half-spin (x, y, z)
oplus_tperp	eV	CDF_REAL8	1	Tperp O+ for each HPCA half-spin
oplus_tparallel	eV	CDF_REAL8	1	Tparallel O+ for each HPCA half-spin
oplus_vperp	km/s	CDF_REAL8	4	Vperp vector plus Magnitude for O+ for each HPCA half-spin (x, y, z, total)
oplus_vparallel	km/s	CDF_REAL8	4	Vparallel vector plus Magnitude for O+ for each HPCA half-spin (x, y, z, total)
oplus_vperp_GSM	km/s	CDF_REAL8	4	Vperp vector plus Magnitude in GSM for O+ for each HPCA half-spin (x, y, z, total)
oplus_vparallel_GSM	km/s	CDF_REAL8	4	Vparallel vector plus Magnitude in GSM for O+ for each HPCA half-spin (x, y, z, total)
MCP_VMON_MIN_converted	V	CDF_DOUBLE	1	Minimum Microchannel plate (MCP) voltage
TOF_VMON_MIN_converted	V	CDF_DOUBLE	1	Minimum Time of Flight (TOF) voltage

Table 5-18 L2 Moments CDF File

5.6.10 File Structure L2 TOF Counts CDF File

Variable	Units	Type	Dim	Description
Epoch	ns	CDF_TT2000	1	Start time for the record
Epoch_MINUS	ms	CDF_UINT2	1	Delta start time for the record from the central time
Epoch_PLUS	ms	CDF_UINT2	1	Delta stop time for the record from the central time
tof_energy	eV/q	CDF_FLOAT	8	Electron Voltage associated with the tof counts
tof_energy_delta_minus	eV	CDF_FLOAT	8	Delta eV for the record from the central TOF voltage
tof_energy_delta_plus	eV	CDF_FLOAT	8	Delta eV for the record from the central TOF voltage
tof_bin_index	n/a	CDF_UINT1	128	TOF binning index
tof_counts	counts	CDF_UINT2	8 x 128	TOF Counts for all angles, across all energies

Table 5-19 L2 TOF Counts CDF File

5.7 APPENDIX A- HCPA REFERENCES

The following is a list of applicable references and publications.

Section	Document Number	Title	Revision/Date
All	10160.13-HPCA_CONOPS	Hot Plasma Composition Analyzer Concept of Operations for the MMS mission	2010
All	10160.13-MMS-HPCA_IUM-01	HPCA Instrument User Manual (IUM)	2013
5.6.4.4	https://doi.org/10.1142/S0129183108012303	J. Kopp, "Efficient Numerical Diagonalization of Hermitian 3 × 3 Matricies," *International Journal of Modern Physics C*, vol. 19, no. 03.	March 2008
All	10160.13-MMS-HPCA_SCI_ALG_UM	MMS HPCA Science Algorithms and User Manual	20160310
5	670-Proj-Plan-CMAD	MMS Project Calibration & Measurement Algorithms Document (CMAD)	2020
All	https://doi.org/10.1007/s11214-014-0119-6	Young, D., J. L. Burch, R. G. Gomez, A. De Los Santos, G. P. Miller, P. Wilson IV, N. Paschalidis, S. A. Fuselier, K. Pickens, E. Hertzberg, C. J. Pollock, J. Scherrer, P. B. Wood, E. T. Donald, D. Aaron, J. Furman, D. George, R. S. Gurnee, R. S. Hourani, A. Jacques, T. Johnson, T. Orr, K. S. Pan, S. Persyn, S. Pope, J. Roberts, M. R. Stokes, K. J. Trattner, J. M. Webster (2016), Hot Plasma Composition Analyzer for the Magnetospheric Multiscale Mission, Space Science Reviews, 199(1-4), 407-470.	2016

Table 5-20 HCPA Applicable Documents

6.0 ENERGETIC PARTICLE DETECTOR (EPD)

6.1 EPD OVERVIEW

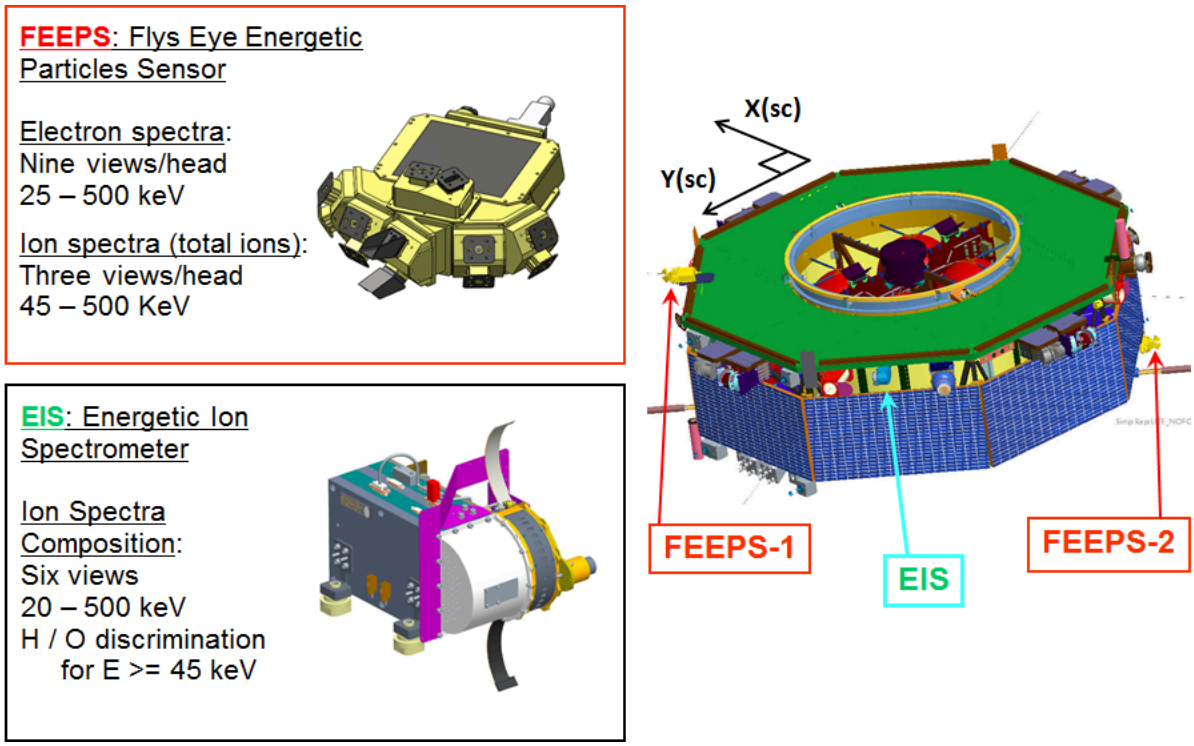

Figure 6-1 Summary of the Capabilities and Spacecraft Mounting of the EPD Instruments: EIS and FEEPS. [Note that the energy ranges of measurements have varied somewhat over the course of the mission] (from Mauk et al., 2016)

The science objectives and an overview of the Energetic Particle Detector (EPD) investigation are provided in Mauk et al. (2016). EPD comprises two different instrument types: the Energetic Ion Spectrometer (EIS; with a detailed description provided by Mauk et al., 2016) and the Fly's Eye Energetic Particle Spectrometer (FEEPS; Blake et al., 2016). There are two FEEPS instruments and one EIS instrument on each spacecraft (Figure 6-1). They are intended to yield an instantaneous all-sky view for electrons (Figure 6-2) and fast all-sky sampling for ions. This set of sensors (two FEEPS instruments plus one EIS instrument) is identical on each of the four MMS spacecraft. To obtain true "allsky" electron sampling from the FEEPS sensors, it was necessary to mount one of the instruments on the instrument deck and the other onto the spacecraft subsystem deck (Figure 6-1). The two instruments are identical to each other, and they are designed such that when one of them is turned upside down with respect to the other, the fields of view complement each other (Figure 6-2). Also, the orientation of the ion sensors provides two fan-shaped fields of spaced 120° apart, with EIS providing the 3rd fan, resulting in EPD ion 3 sensors each located 120° apart (Figure 6-2).

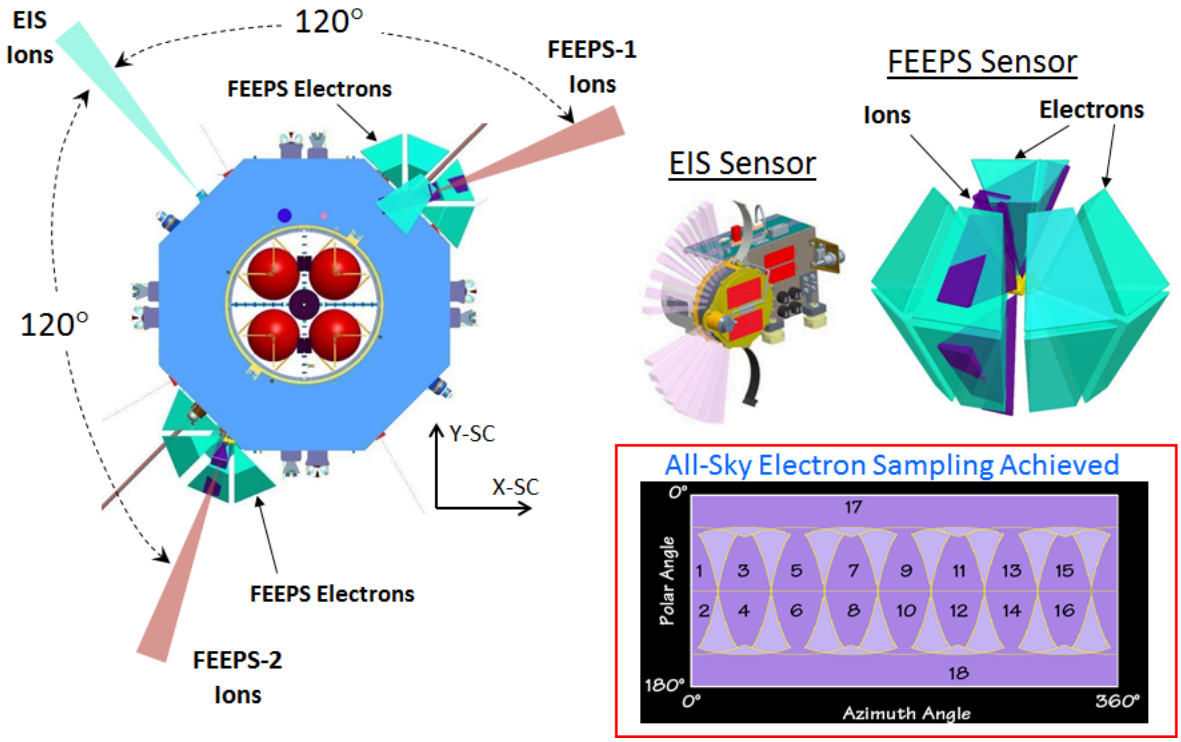

Figure 6-2 The EPD fields-of-view are Configured to Provide Maximum Sky Coverage of Energetic Particles. [The two FEEPS sensors provide nearly simultaneous full-sky electron coverage, whereas the two FEEPS sensors complement the EIS fan-shaped FOV to provide ion coverage in approximately 1/3 of a spin.] (from Mauk et al. [2016])

The Energetic Particle Detector suite of sensors supports the study of the fundamental physics of magnetic reconnection by:

1. Remotely sensing the positions and speeds of boundaries and other structures near reconnection sites using energetic ions.
2. Sensing the magnetic topology of near reconnection sites using energetic electrons.
3. Remotely sensing reconnection acceleration sites using both electrons and ions.
4. Determining the cause of energization of energetic electrons and ions by reconnection.

6.1.1 Energetic Ion Spectrometer (EIS)

Each EIS instrument (Figure 6-1) combines multi-directional viewing into a single compact sensor head using: 1) a time-of-flight (TOF) system that uses a microchannel plate (MCP) detector and thin foils that generate secondary electrons, to measure particle TOF and pulse height (PH); and 2) six solid-state detectors (SSDs) that measure particle energy (E). The MCP has start and stop anodes. Measuring the time difference between start and stop signals determines the particle's TOF. The anodes are divided into six angular segments; these provide a measure of the particle's direction of travel. EIS measures ion energy, directional, and compositional distributions using "Energy by Time-of-Flight" (ExTOF) for the higher-energy ions and "MCP-Pulse- Height by Time-of-Flight" (PHxTOF) for the lower-energy ions. EIS also measures electron energy and directional distributions using collimated SSD energy measurements (from designated "electron SSDs" that have 2 μm of aluminum flashing deposited on them to keep out protons with energies less than about 250 keV).

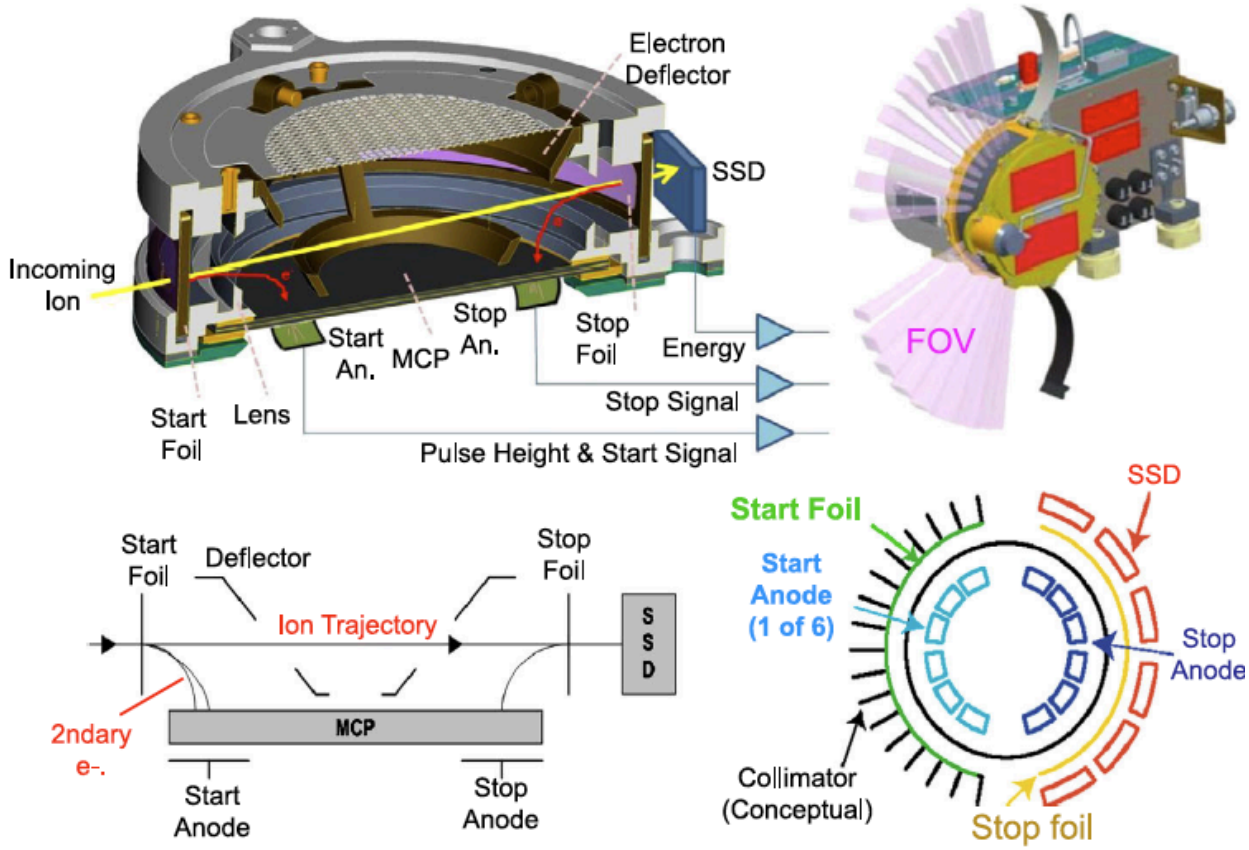

Figure 6-3 Schematics Detailing How the EIS Sensor Works

6.1.2 Fly's Eye Energetic Particle Sensor (FEEPS)

The second EPD instrument, is the Fly's Eye Energetic Particle Spectrometer (FEEPS). These sensors (Figure 6-2) measure:

1) the energy-angle distribution and composition of ions (20-500 keV, with a goal of 10-1000 keV) at a time resolution of <30 seconds;
2) the energy-angle distribution of total ions (45-500 keV, with a goal of 40-1000 keV) at a time resolution of <10 seconds; and
3) the coarse and fine energy-angle distribution of energetic electrons (25-500 keV, with a goal of 20-1000 keV) at time resolutions of <0.5 and <10 seconds, respectively.

FEEPS provides an instantaneous all-sky view of electrons (with coarse angular resolution), then turns coarse into more refined angular resolution by means of rotation. The two FEEPS ion "fans", in conjunction with the one EIS ion fan, provide all-sky total-ion coverage every ⅓ of a spin. Each of the two FEEPS instruments on each spacecraft comprises 12 individual fields of view; 9 electron views (Figure 6-4a) and 3 ion views (Figure 6-4b). Eight of the nine electron views are grouped into pairs resulting in four "heads" comprising two "eyes" each. Each electron eye comprises a shaped pinhole, a 1.8-micron aluminum foil that blocks protons with energy >200, and a shaped, 1-mm SSD measures the energy of the incoming electron. The combination of the pinhole and of the SSD shapes yield a trapezoidal shape for the field of view for each eye (Figure 6-4a).

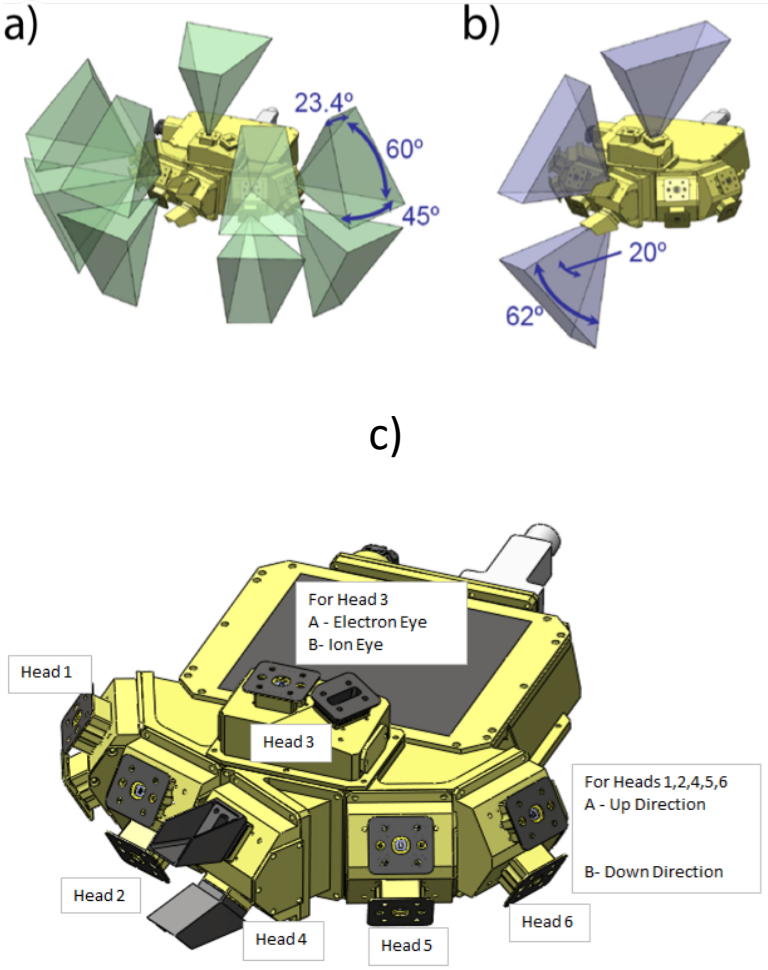

Figure 6-4 The FOVs of the FEEPS (a) Electron and (b) Ion Sensors, or "Eyes", while (c) Each Pair of Eyes is Combined into One of Twelve "Heads" on Each FEEPS Sensor (from Blake et al. [2016])

Two of the ion sensors (i.e., "eyes") on each FEEPS instrument are combined into a single "head" (Figure 6-4c). Each ion eye comprises a slot-shaped pinhole followed by a rectangular-shaped, 9-micron thick SSD which measures the energy of the ions. The response of these detectors to electrons is minimized by the thinness of the SSD's; electrons tend to pass right through leaving a signal below the detection threshold, and ions are stopped, resulting in the detection of above-threshold energies. There will be residual electron contamination in the ion responses that needs to be managed. The two "equatorial" ion sensors each have a sunshade (Figure 6-4c) to keep the sun from illuminating the entrance slot (the ion sensors are very sensitive to the sun, whereas nominally, the electron sensors are not because of the thin foils placed over the telescope apertures). The slot shape of the pinhole and the rectangular shape of the SSD together yield a fan-like field-of-view of about 20° x 60° (Figure 6-4a-b).

A final set of electron and ion views is held by a 3rd type of head, the Electron-Ion Head (e.g., Head 3 in Figure 6-4c). This head contains one electron eye and one ion eye. Ideally, the field-of-view of the third ion head should be carefully aligned with the views of the other two ion heads to effectively yield a broad, 280° fan-shaped field of view. However, to keep the third ion sensor from viewing the axial electric field sensors, the third view had to be tilted somewhat away from the ideal configuration (Figure 6-4b).

6.1.3 Status of EPD Sensors

On MMS1, the solid-state detector (SSD) utilized in telescope T4 (for both ExTOF ion and electron data), is responding anomalously, and should not be used at this point in time. It acts like it is under-biased, but the true cause is unknown.

For the MMS1 spacecraft, the HV system experienced micro-discharge anomalies that caused the HV to be shut down by the onboard software on 30 January 2016, with some anomalous behavior seen for the first time on 21 January 2016, about 6 months after HV turn on. Because only 3 EIS units were required, the HV on EIS1 was disabled for the rest of the prime mission. Beginning on 18 April 2016, EIS1 was put into high-resolution electron mode with "electronenergy" burst data enabled. On 31 January 2018, HV (and ion species data) on MMS1 was re-enabled and no further anomalies have been reported to-date. EIS1 data prior to 21 January 2016 are assumed to be unaffected by these anomalies.

The efficiency of ion detection for making ExTOF and PHxTOF ion measurements evolves over time because of variations of the gain of the microchannel plate in each of the EIS units. To-date a nominal efficiency multiplier is utilized with the Level 2 data, but slow evolutions of those efficiencies have not been folded into the data processing. The multiplicative error is up to about ±30%.

Many of the FEEPS eyes suffer from light contamination, likely due to direct sunlight and glint coming through foils that were damaged during launch. This and other issues have been substantially, though not completely, corrected via a series of CIDP updates implemented between October 2016 and August 2017.

The first energy channels (i.e., lowest energy channel, with index 0) from FEEPS ion and electron sensors have their threshold set very near to or within the noise threshold. These channels from most (but not all) eyes are often measuring noise and should not be used for scientific data analysis. See section 6.4.3 for additional details.

6.2 EPD MEASUREMENTS STANDARDS, VOLUME, AND TIMING

6.2.1 EIS Viewing

	TOF x PH				TOF x E and Ions				Electrons			
	Degrees	Unit-X	Unit- Y	Unit-Z	Degrees	Unit-X	Unit- Y	Unit-Z	Degrees	Unit-X	Unit- Y	Unit-Z
T0	72.18	0.306	-0.952	0.000	72.18	0.306	-0.952	0.000	61.12	0.483	-0.876	0.000
T1	45.56	0.700	-0.714	0.000	45.56	0.700	-0.714	0.000	34.5	0.824	-0.566	0.000
T2	20	0.940	-0.342	0.000	20	0.940	-0.342	0.000	9	0.988	-0.156	0.000
T3	-9	0.988	0.156	0.000	-9	0.988	0.156	0.000	-20	0.940	0.342	0.000
T4	-34.5	0.824	0.566	0.000	-34.5	0.824	0.566	0.000	-45.56	0.700	0.714	0.000
T5	-61.12	0.483	0.876	0.000	-61.12	0.483	0.876	0.000	-72.18	0.306	0.952	0.000

Figure 6-5 The Unit Vectors of the Look Directions of the EIS Telescopes. [Care should be exercised when considering the telescopes highlighted in the differently-shaded rows as these look directions are substantially blocked.] (from Mauk et al. [2016])

The quantitative centroids of the view directions for all six look directions, within the EIS coordinate system, for each of the EIS data products, are shown in Figure 6-5. The central directions of the center of each PHxTOF, ExTOF, Ion-SSD (the same as ExTOF), and Electron-SSD pixel are given as the angle from the X-axis within the XY-plane, with positive angles towards the –Y-axis (also toward the direction that has been designated the "T0" direction; we realize that it is unusual to have positive angles towards

the –Y-axis rather than the +Y-axis). To the right of each angle in Figure 6-5 is the unit vector of the view direction in the instrument coordinate system. Views T2 for electrons and T3 for ions have substantial obstruction from the shielding needed to keep the sun out (see Figure 10 in Mauk et al. [2016]). The off-color rows are the views that are substantially obstructed. Nonetheless these views corrected to the best of our ability and are represented in our data products. Care should be exercised for these particular views.

The transformation matrix that transforms a vector (e.g., a unit view direction such as those provided in Figure 6-5) into the MMS Spacecraft Frame is provided here. $v_{sc} = T_{EIS} \cdot V_{EIS}$, where V_{EIS} is the vector in the EIS frame of reference, T_{EIS} is the 3 x 3 transformation matrix, and $v_{sc} = T_{EIS}$ is the vector in the spacecraft frame. For this expression:

$$T_{EIS} = \begin{pmatrix} \frac{-1}{\sqrt{2}} & 0 & \frac{1}{\sqrt{2}} \\ \frac{1}{\sqrt{2}} & 0 & \frac{1}{\sqrt{2}} \\ 0 & 1 & 0 \end{pmatrix}$$

NOTE: The version of this transformation matrix reported in Mauk et al. (2016) is incorrect and this one should be used instead.

ID#	Head	Orientation	Species	Azimuth	Elevation	Weighted Elevation	Unit-X	Unit- Y	Unit-Z
1	1	Up	Electons	-67.5	30	25	0.347	-0.837	0.423
2	1	Down	Electons	-67.5	-30	-25	0.347	-0.837	-0.423
3	2	Up	Electons	-22.5	30	25	0.837	-0.347	0.423
4	2	Down	Electons	-22.5	-30	-25	0.837	-0.347	-0.423
5	3	Top	Electons	0	90	95	-0.087	0.000	0.996
6	3	Top	Ions	60	78	78	0.104	0.180	0.978
7	4	Up	Ions	-30	41	41	0.654	-0.377	0.656
8	4	Down	Ions	-30	-41	-41	0.654	-0.377	-0.656
9	5	Up	Electrons	22.5	30	25	0.837	0.347	0.423
10	5	Down	Electrons	22.5	-30	-25	0.837	0.347	-0.423
11	6	Up	Electrons	67.5	30	25	0.347	0.837	0.423
12	6	Down	Electrons	67.5	-30	-25	0.347	0.837	-0.423

Figure 6-6 The Look Direction Unit Vector (v) of Each FFEPS Eye in the FEEPS Coordinate System (FCS) (from Mauk et al. [2016])

6.2.2 FEEPS Viewing

Figure 6-6 shows the unit vectors for each of the 12 FEEPS eyes in the FEEPS Coordinate System (FCS). The "elevation" angle is the angle made by unit vectors out of the *XY*-plane. The "weighted elevation" adjusts the elevation to account for the non-symmetric shape of the electron fields of view with respect to their centers. Note that the transformation of vectors (v) from the $FEEPS_1$ (FEEPS-payload-deck or the "up" direction) or FEEPS-2 (FEEPS-bottom-deck) to the spacecraft coordinate system (BCS) is achieved using $\mathrm{v}_{FEEPS} = \mathrm{T1,2}_{FEEPS_{1,2}} \cdot \mathrm{v}_{FEEPS}$, where

$$\mathrm{T1}_{FEEPS_1} = \begin{pmatrix} \frac{1}{\sqrt{2}} & \frac{-1}{\sqrt{2}} & 0 \\ \frac{1}{\sqrt{2}} & \frac{1}{\sqrt{2}} & 0 \\ 0 & 0 & 1 \end{pmatrix} \quad \text{and} \quad \mathrm{T2}_{FEEPS_2} = \begin{pmatrix} \frac{-1}{\sqrt{2}} & \frac{-1}{\sqrt{2}} & 0 \\ \frac{-1}{\sqrt{2}} & \frac{1}{\sqrt{2}} & 0 \\ 0 & 0 & -1 \end{pmatrix}.$$

These are rotation matrices which convert the FEEPS telescope look direction vectors (v_{FEEPS}), from the FEEPS coordinate frame (FCS) to BCS. These vectors are defined looking out to space along the center

line for each telescope's field-of-view and are the same for both the top and bottom units. v_{FEEPS} in FCS is given in Figure 6-6 for each sensor.

6.2.3 EPD Ephemeris and Magnetic Field Information Requirements

Because EPD is spin-based and the spin phase relative to the Sun is known onboard, the EPD team will estimate the L1B transformation matrix between the SC coordinate system and GSE by assuming that the following is roughly true: SC_{z_GSE} = (sin 2.5° , 0, cos 2.5°). While this estimate suffices for Level 1b where ephemeris data is not available on the correct timescale, it **IS NOT SUFFICIENT** for Level 2. In the estimated transformation matrix, there is a ±30° uncertainty in the angle that the SC_z axis makes with respect to the XZ_{GSE}-plane. This is due to the substantial variability in that angle which is allowed by mission standards.

The following are the data provided in FEEPS data products which are essential to data analysis:

• For Each Detector Look Direction (within each spin sector)
1. Pitch Angle (using available magnetic field vector in SC coordinates)
2. Unit Vector in GSE of Look Directions.

These data are included for convenience:

• One set for each spin sector
3. BX, BY, BZ in SC coordinates*
4. SC position (X, Y, Z) in GSE*
5. SC latitude and longitude in GSM*
6. Moon position in GSE*
7. SC to GSE Transformation Matrix* (9 numbers)
8. GSE to GSM Transformation Matrix* (9 numbers)
9. Spin Rate*

**These required parameters are provided for users in the L1b and L2 EIS or FEEPS data files.*

The possibility of earthshine contamination of the FEEPS ion detectors can be computed using the negative of the SC position in GSE (#4 above) and the detector look direction in SC coordinates. In addition, the possibility of sunshine contamination is derived using the detector look direction in GSE with respect to the X_{GSE}-axis. At Level 1B, earthshine estimations will have an uncertainty of ±30°, while sunshine contamination will be fairly accurate because the primary uncertainty in the spacecraft orientation resides in the roll angle about the spacecraft-Sun line.

6.2.4 EIS File Versioning

To optimize scientific return, the instrument team may infrequently alter the onboard lookup tables (LUT), which define the spectral "channels" (see instrument description below) in a given EIS data product over the course of the mission. Each such change defines a new "LUT period" with each LUT period containing its own unique set of spectral channels. This means that over the course of the mission, a given data variable may change in structure (i.e., number or species specification of energy channels). To highlight and record these changes, the LUT period of a given spectral variable is indicated by a "_P<n>_" in the names of affected variables. Additionally, regular changes in the "Calibration Matrices" used for ground-based data processing, which do not require the introduction of a new LUT, such as adjusting high voltage states to address MCP gain levels or data optimization (i.e., changing decimation factors). These changes will affect the nature of the data within data files, but not the variable names.

Changes to both the onboard LUTs and ground-based "Cal Matrices" define specific data "regimes", which are indicated using a unique EIS file versioning paradigm where the version indices *"*_x.y.z.cdf"* correspond to:

- x: the LUT period and associated "P<n>" in CDF variable names
- y: the specific iteration of the Cal Matrix used for data processing
- z: processing iteration of specific file
-

Each "vX.Y" combination corresponds to a given data "regime", summarized in Table 6-1 below.

Regime (New 2021)	**Regime (Old)**	**Period Start**	**Period End**	**Changes**
v1.0	v1.0	3/12/2015 (Launch)	2015-07-29/00:00:00	Initial LUT & processing state
v2.0	v2.0	2015-07-29/00:00:00	2015-08-29/00:00:00	Changes to extof & electronenergy channels
v2.1	v2.1	2015-08-29/00:00:00	2015-09-24/00:00:00	phxtof decimation changed
v3.0	v3.0	2015-09-24/00:00:00	2015-11-20/00:00:00	Changes to phxtof channelization
v3.1	v3.1	2015-11-20/00:00:00	2016-01-30/00:00:00	Changes to post-processing calibration factors
v3.2	v3.1	2016-01-30/00:00:00	2016-08-04/00:00:00	HV raised to improve MCP gain on MMS4
v3.3	v3.2	2016-08-04/00:00:00	2016-08-06/00:00:00	phxtof decimation changed
v3.4	v3.3	2016-08-06/00:00:00	2016-09-26/00:00:00	HV raised to improve MCP gain on MMS3
v4.0	v4.0	2016-09-26/00:00:00	2016-11-01/00:00:00	Changes to extof, phxtof, & electronenergy channels
v4.1	v4.1	2016-11-01/00:00:00	2017-04-30/00:00:00	Changes to post-processing calibration factors
v4.2	v4.1	2017-04-30/00:00:00	2017-11-17/00:00:00	Changes to post-processing calibration factors
v4.3	v4.2	2017-11-17/00:00:00	2018-04-30/00:00:00	Changes to phxtof and extof efficiencies/spectra, etc.
v4.4	v4.2	2018-04-30/00:00:00	2018-11-30/00:00:00	Changes to post-processing calibration factors
v4.5	v4.2	2018-11-30/00:00:00	2019-05-01/00:00:00	Changes to post-processing calibration factors
v4.6	v4.2	2019-05-01/00:00:00	2019-12-05/00:00:00	Changes to post-processing calibration factors

V5.0	V5.0	2019-12-05/00:00:00	Present	Changes to electronenergy channels on MMS4

Table 6-1 Summary of the EIS Versioning Scheme

6.3 EPD CALIBRATION AND VALIDATION

6.3.1 EIS Pre-Flight / On-Ground Calibration

A full description of the design of EIS and its pre-flight and ground calibration results can be found in the following publication:

> Mauk B.H. et al, **The Energetic Particle Detector (EPD) Investigation and the Energetic Ion Spectrometer (EIS) for the Magnetospheric Multiscale (MMS) Mission**, Space Sci Rev 199, 471-514 (2016). https://doi.org/10.1007/s11214-014-0055-5

As explained in Mauk et al. (2016), the full range of parameters (azimuth angle, elevation angle, particle input position, energy, species) **could** not be exercised within calibration facilities. Instead, a combination of theory, empirical expressions, and spot validation were used to construction the calibration matrix. Initial estimates of the particle energies throughout the sensor, scattering efficiencies, and detection efficiencies was developed with a Mathematica routine that utilized various available empirical relationships (energy losses in materials, scattering characterizations, efficiency of secondary electron generation, solid-state-detector pulse-height-defect, etc., etc.). That routine created numerous 6-order polynomials for the functional relationships between the various parameters. Those polynomials were then tweaked according to beams calibration runs, cross-checks with similar instruments that had gone through cross-calibration activities (RBSPICE on Van Allen Probes), and then, flight cross-calibration on MMS as described in the section 6.3.2.

Understanding of the EIS instrument response is based on a coordinated array of approaches, specifically: (i) bench testing of channel gains and other characteristics based on calibrated pulse inputs, (ii) calibrations using particle accelerator beams, (iii) calibrations using radiation sources, (iv) simulations of particle interactions with matter using such tools as GEANT4, and (v) geometric calculations. Two particle accelerators were used for calibrating EIS: (1) the APL ion particle accelerator that generates narrow ion beams of H, He, O (N often used as proxy), Ar, and other ions species from energies as low as about 12 keV up to 170 keV; and (2) the GSFC Van de Graff, accelerator that generates electron and ion species beams from ~100 keV to > 1MeV. Two different radiation sources were used: a Ba133 source and a degraded Am241 radiation source (the source is degraded by placing a thin mylar foil between the source and the sensor, which yields a very broad spectrum of alpha particle energies). To perform the calibrations, sources were procured in a configuration to completely fill the instrument field-of-view and thus calibrate all six (6) look directions simultaneously.

Details of the EIS calibration matrices are provided in section 6.4.4. The EIS calibration matrix carries parameters that correct for different responses of the six different telescopes within each unit. Flat-fielding has been carried out by examining the relative responses of the six different telescopes in each EIS unit to environments that are roughly isotropic.

6.3.2 EIS In-Flight Calibration

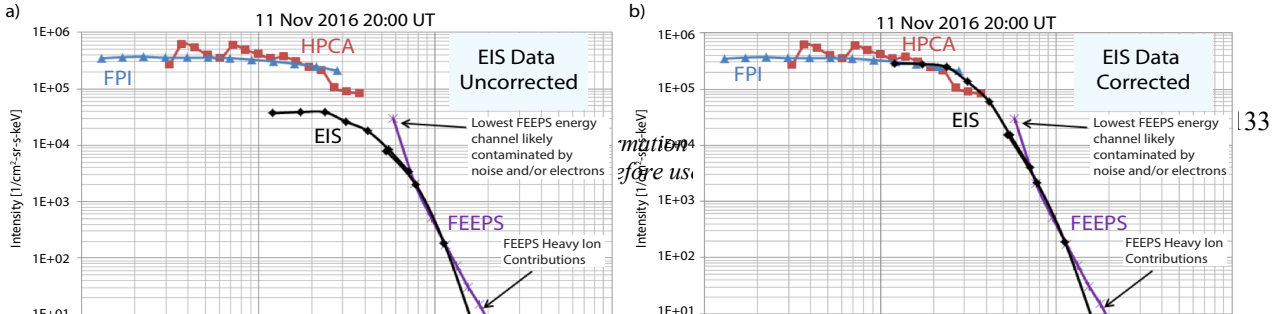

Figure 6-7 Example of the Comparison of Omni-directional Proton Spectra from the EIS, FEEPS, HPCA, and FPI/DIS Sensors on MMS 3 (a) before and (b) after the EIS Data was Corrected [L2 data was used for all sensors except HPCA (L1b), which did not have L2 data available at the time that the cross-calibration efforts were made]

Considerable efforts were made in Spring/Summer 2017 regarding the cross-calibration of ion (specifically proton) measurements amongst the MMS instruments: EIS, FEEPS, FPI/DIS, and HPCA. The basic gain state of the EIS sensor for measuring protons, which is variable because of changing microchannel plate efficiencies, is established by comparing the EIS and FEEPS ion measurements at ~80 keV. That energy is low enough to where we have become confident that protons dominate over heavy ions, and it is high enough to avoid energy-dependent efficiency problems that occur at lower energies. Additional cross-calibration efforts revealed that the EIS PHxTOF data, which bridges the energy gap between the upper energy limits of FPI/DIS (30 keV) and HPCA (40 keV) and the lower energy limit of the ExTOF (~50 keV) and FEEPS (~60 keV) data, was underestimating the flux by approximately a factor of 5. Based on the strong agreement between the plasma sensors (FPI/DIS and HPCA) and the high confidence in the relatively "pure" ion measurement by FEEPS (due to their very thin SSDs), the decision was made to adjust the EIS PHxTOF data by applying an energy-dependent numerical correction of the form:

$$E_{\mathrm{PHxTOF}} = \frac{1}{\frac{1}{2}*\left[1+\alpha_{\mathrm{PH}}\left(\tanh\left(\frac{E-\beta_{\mathrm{PH}}}{\gamma_{\mathrm{PH}}}\right)+1\right)\right]},$$

where E is energy and α_{PH}, β_{PH}, γ_{PH} are coefficients equal to 0.3, 45, and 1, respectively.

Figure 6-7 shows an example comparing the proton spectra from the various instruments (a) before and (b) after the EIS data was corrected. Minor adjustments were also made to the lowest energy EIS ExTOF data to correct for foil efficiencies. This correction is of the form:

$$E_{\mathrm{ExTOF}} = \frac{1}{\frac{1}{2}*\left[1+\alpha_{\mathrm{E}}\left(1-\tanh\left(\frac{E-\beta_{\mathrm{E}}}{\gamma_{\mathrm{E}}}\right)+1\right)\right]},$$

where E is energy and α_{E}, β_{E}, γ_{E} are coefficients equal to 0.3, 45, and 1, respectively.

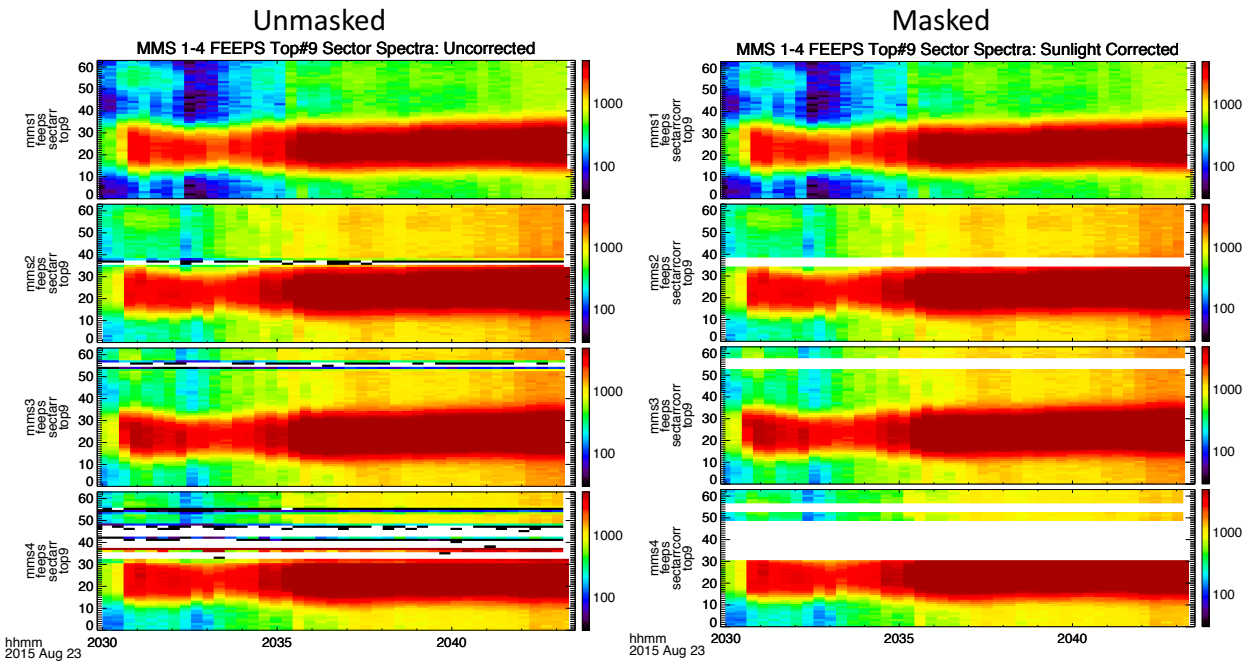

Figure 6-8 An Example of the Effects of Sunlight Contamination in the FEEPS Burst Data [This data shows intensity for time versus spin sector for each spacecraft (MMS1-4 from top to bottom) for 23 August 2015. The white and black splotched horizontal lines permeating the MMS2-4 data on the left shows the effect of sunlight contamination on certain sectors. The panels on the right show the same data with the affected sectors appropriately masked]

Cross calibration has also taken place for electrons between EIS and FEEPS. Pre-launch characterization for EIS has been found to be adequate (see section 6.3.3). Efficiencies for EIS electrons were obtained from cross-calibration activities that took place with EIS's sister instrument, RBSPICE, on the Van Allen Probes mission.

Further details and results of the EIS in-flight calibration can be found in the publication:

> Cohen, I. J., et al., **Dominance of high-energy (>150 keV) heavy ion intensities in Earth's middle to outer magnetosphere**, J. Geophys. Res. Space Physics (2017) https://doi.org/10.1002/2017JA024351

6.3.3 FEEPS Pre-Flight / On-Ground Calibration

Pre-flight calibration is covered in the FEEPS instrument paper (Blake, et al., 2016). As summarized in section 6.1.3, many of the FEEPS eyes suffer from light contamination, likely due to sunlight and glint coming through foils (on electron eyes) that were perforated during launch. An example of the light contamination is shown in Figure 6-8, which plots FEEPS burst data from electron eye #9 of the bottom deck. The Y-axis is the spin sector, the X-axis is time, and intensities are plotted in color. The horizontal lines containing discontinuities contained in the second through fourth plots in the left column show sectors affected by sunlight contamination, whereas the top left plot for MMS1, lacking these rows, indicates an uncontaminated sensor. The plots in the right column, marked "Masked", show how those sunlight contaminated sectors can be effectively removed.

Using such FEEPS burst data sector maps, one can identify the affected sectors during any period of the mission on all eyes of the FEEPS instruments. For example, Figure 6-9 shows the sector masks that were produced after a survey of contamination conducted during August-September 2015. These masks flag all sectors that were affected by contamination during the period examined. These plots show the contaminated sectors (X-axis) from each eye (Y-axis) for each of the spacecraft during this period. Yellow blocks identify affected eyes/sectors, while blue blocks are good, unaffected eyes/sectors.

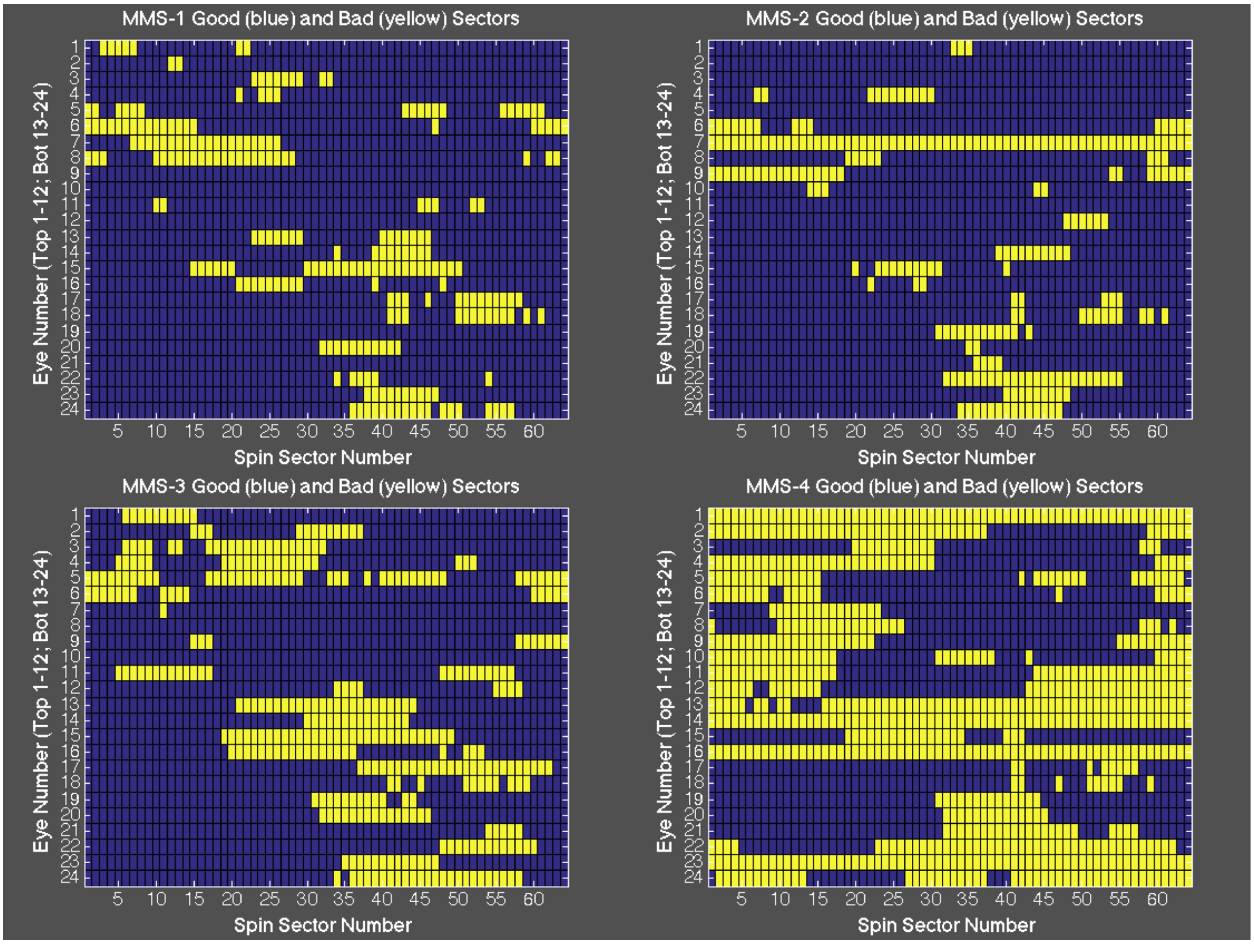

Figure 6-9 Mapping of those Sectors from Each Eye Affected (yellow) and Unaffected (blue) by Sunlight Contamination on Each Spacecraft during August-September 2015

6.3.3.1 FEEPS Lowest-Energy Channels

As previously mentioned, the first energy channels (i.e., lowest energy channel, with index 0) from FEEPS ion and electron instruments have their threshold set very near to or within the noise threshold. These channels from most (but not all) eyes are thus measuring noise and should not be used for scientific data analysis. Additionally, on several of the FEEPS eyes, the second and/or third energy channels require threshold adjustment as of 04 April 2016. An example of the effects from this are shown in the energy distributions in Figure 6-10. Here, energy distributions (in count rates) from a relatively isotropic angular distribution with high-count-rates from 02 August 2015 are shown from each of the electron eyes on MMS1. Different colors show the different eyes, as labeled, with eyes from the top deck instrument (e.g., T10) shown with stars and those from the bottom deck instrument (e.g., B10) shown with diamonds.

These distributions show how the first few channels on several eyes are counting lower than the other eyes. These affected eyes should not be included for science analysis.

6.3.3.2 FEEPS Flat Field

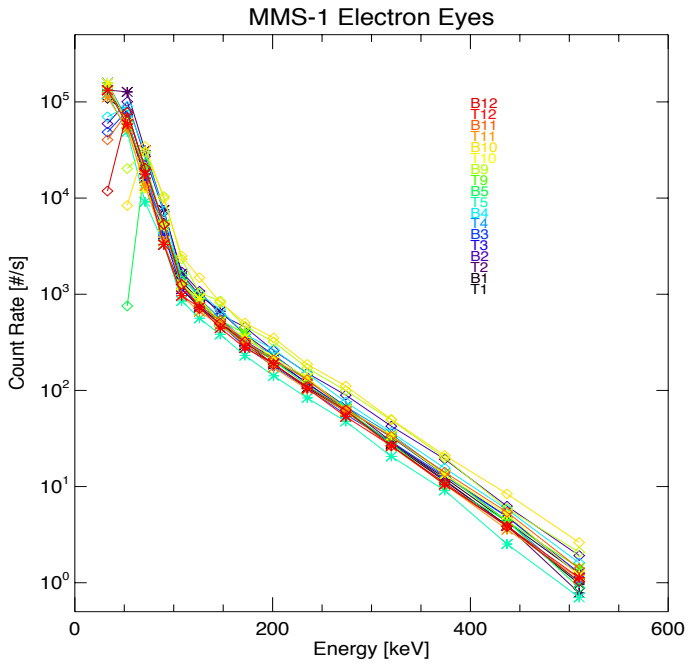

Figure 6-10 Energy Spectra of the 24 Individual FEEPS Eyes (3 ion and 9 electrons per sensor, top and bottom) on MMS1 [The reduced count rates observed in the lowest energy channel for multiple eyes is contributed to thresholds set near or at the sensor's noise threshold]

A flat-fielding effort has been made to ensure that FEEPS data from all of the FEEPS telescopes are consistent. For the electron data, the correction involves a linear shift in the energy channels. For these, a constant energy is added or subtracted to each eye's energy channels' limits. That method was deemed necessary due to the nature of the disagreement from eye to eye, which showed a stronger disagreement at lower energies. Also, the effectiveness of this correction was clear during injection events, in which energy dispersed enhancements of electrons were observed by the spacecraft. To determine these energy offset corrections, we examined a number of periods (>10) during 2016 that exhibited steady local plasma conditions and high FEEPS count rates. During these periods, we compared the 1-spin averaged omnidirectional distributions from all of the eyes on each spacecraft and calculated the correction offsets that brought each closest to the mean distribution from all eyes. That method assumes that the correction factors are all spread around the true distribution, which is confirmed by comparisons to the EIS average distributions from the same times. The same method was applied for the ion eyes, though (interestingly) the corrections for the ion eyes were best when applied using a gain (i.e., multiplicative) factor. These correction factors have been organized into tables containing adjustments for each FEEPS channel and eye over all instruments and spacecraft.

6.3.4 FEEPS In-Flight Calibration

Figure 6-11 presents an example of the effect of the light contamination in survey data. From top to bottom it shows: electron omnidirectional averaged energy spectra from survey data, ion omnidirectional

averaged energy spectra from fast survey data, and the spin sector number from a period 02 August 2015. Note that the spin-tone signatures in the electron and ion data are the result of sunlight contamination in the survey data product. This is masked onboard via masking tables loaded onto the spacecraft periodically since August 2016. Figure 6-3 records the onboard masking tables used to-date to mask sunlight-contaminated raw spin sectors in the onboard production of FEEPS fast and slow survey data. For data products prior to these changes, please refer to the data quality flags when using any FEEPS survey data for science. Sunlight contamination is removable from burst data products using masks identified from sector masks as described previously in section 6.3.3.

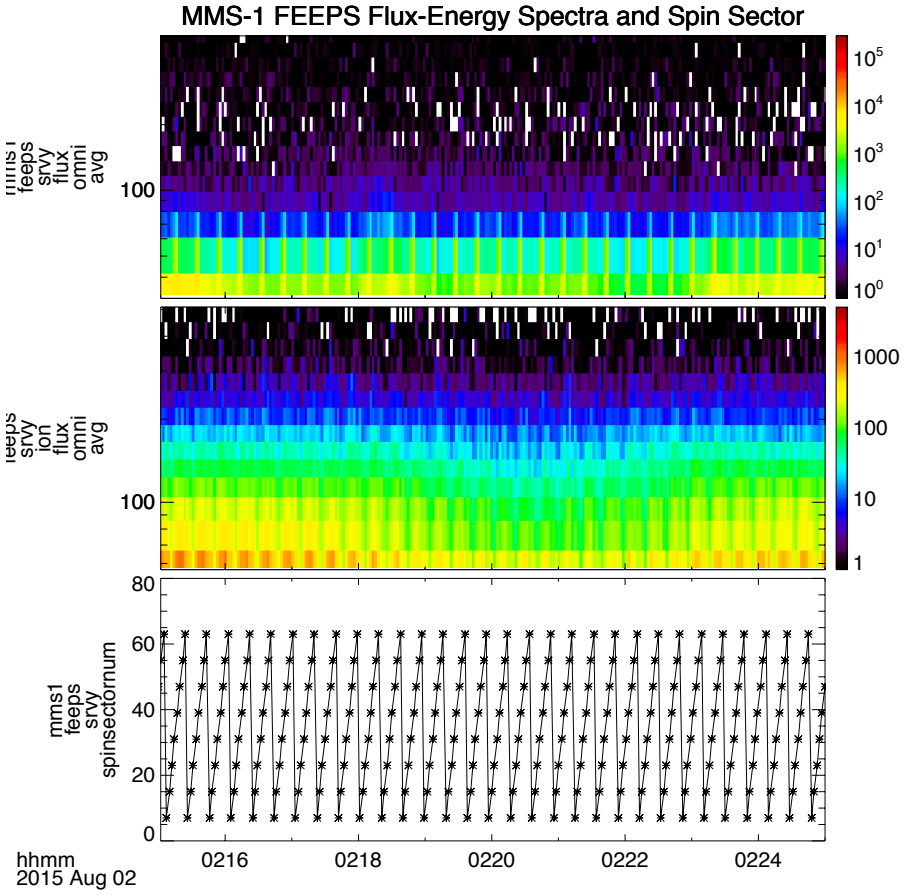

Figure 6-11 Example of the Effect of Sunlight Contamination on FEEPS Survey Data [Omni-directionally-averaged energy spectra for electrons and ions are shown in the top and middle panels, respectively. The bottom panel shows the spin sector]

Upload/Change	MMS1 Execution	MMS2 Execution	MMS3 Execution	MMS4 Execution
1st onboard table[1]	2016-08-05/20:05:00	2016-08-05/21:17:40	2016-08-06/02:04:13	2016-08-06/03:46:46
Fix to 1st onboard table[2]	2016-09-14/16:15:00	2016-09-14/17:30:00	2016-09-14/18:44:51	2016-09-14/19:59:46
Fix to 1st onboard table[3]	2017-02-16/19:30:05	2017-02-14/23:29:54	2017-02-17/14:20:14	2017-02-17/15:50:07
2nd onboard table (top)	2017-08-16/19:40:06	2017-08-16/21:45:38	2017-08-16/23:41:07	2017-08-17/13:34:12
2nd onboard table (bottom)	2017-08-16/19:44:03	2017-08-16/21:48:55	2017-08-16/23:44:24	2017-08-17/13:31:15
3rd onboard table	2018-01-24/01:43:31	2018-01-24/22:08:27	2018-01-18/16:11:39	2018-01-18/17:54:34

[1]*incorrectly applied masking table for top units to the count observations on both top and bottom units, failed to mask live-time correction (LTC), & applied the masking tables to all burst count observations;*
[2]*removed masking of survey & burst count observations in the bottom units - no changes to top units;*
[3]*implemented correct unit specific onboard masking to survey counts and LTC along with removing masking of burst count observations;*

Table 6-2 History of Sunlight Contaminating Masking Tables Implemented to-date Onboard MMS Spacecraft

6.3.5 Data Processing Pipeline

Figure 6-12 shows the plan for processing the EPD (FEEPS and EIS) data. Algorithms for generating Levels 1a and 1b data are generated by the EPD Team at LASP (FEEPS) and APL (EIS), and are transferred to the MMS SOC at LASP for execution. Level 2 data for FEEPS and EIS are generated by the EPD Team at LASP (with certification by Aerospace) and APL, respectively. The Level 2 products are then delivered to the MMS SOC. Figure 6-12 shows details of the processing, including highlighting the need for the availability of magnetic field data and ephemeris data at various stages of the production. Figure 6-13 shows additional details of the more complex FEEPS data production chain.

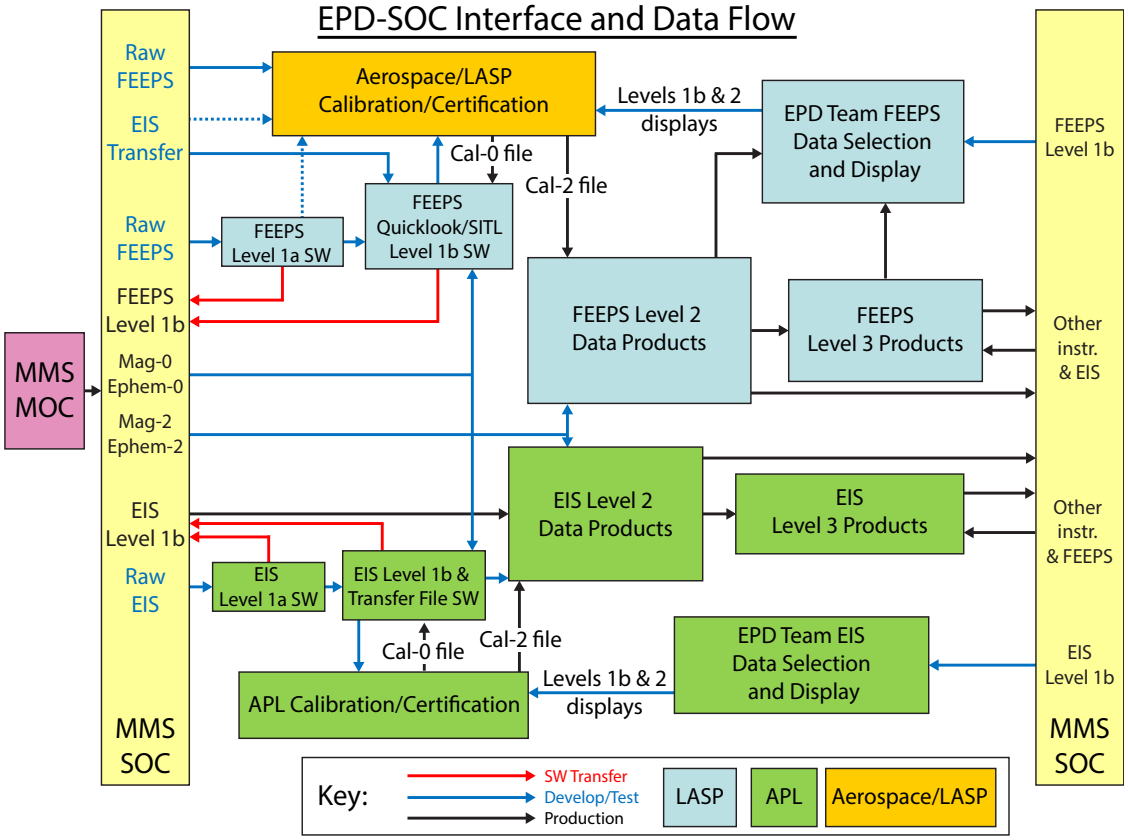

Figure 6-12 Details of the EPD-SOC Interface and Data Flow [Levels 1a and 1b are generated by the MMS SOC at LASP, while Level 2 and higher products are generated by the EPD team at LASP (FEEPS) and APL (EIS)]

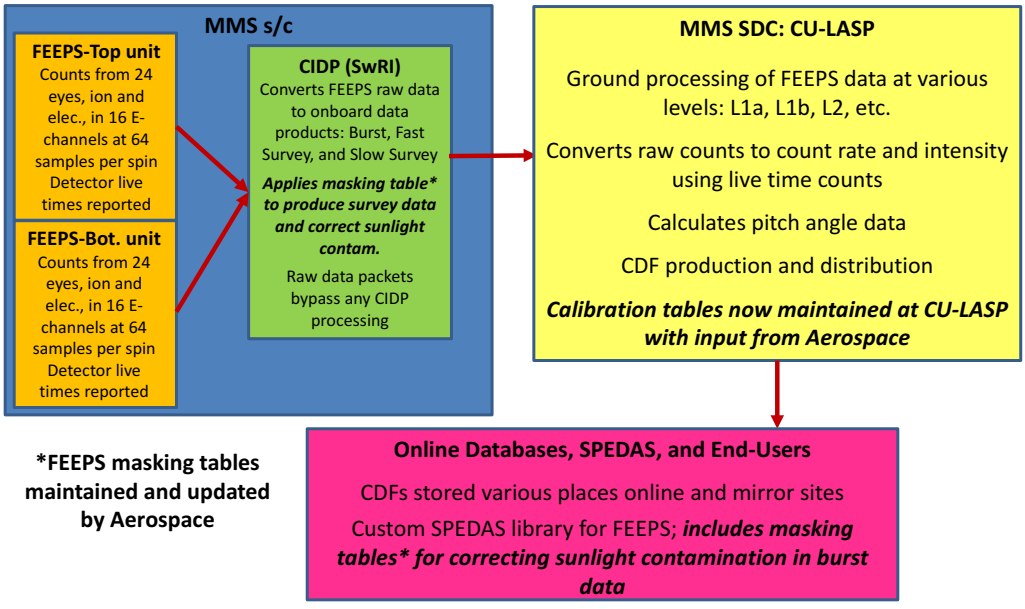

Figure 6-13 The Four Institutions Involved in Producing the Final FEEPS Data Set [SwRI (responsible for the CIDP onboard each spacecraft), LASP (responsible for calibration tables, data processing, and the POC), Aerospace (responsible for data calibration factors and updates), and APL (responsible for validation and management)]

6.3.6 Validation

Over the mission lifespan, data validation has been conducted by the EPD Investigation Team, broader MMS Science Working Team, and the general user community. Prior to launch, validation was conducted through a rigorous suite of testing and verification processes summarized in Mauk et al. (2016). Since launch, validation has continued via regular ongoing reviews of the data as well as corrections to the instruments as needed as the data continues to progress. As detailed in section 6.3.2, cross-comparison with other MMS instruments has been conducted. Resulting discrepancies generated an internal review and assessment that led to several adjustments being made to efficiencies and other parameters included in the EIS calibration matrices. Additionally, any anomalies during the processing of the data (found be operations personnel or by the science community), have led to reprocessing of the entire data set to correct the errors. The EPD team confirms that any missing science data correlates with expected routine or anomalous outages.

6.4 EPD ALGORITHM DESCRIPTIONS

6.4.1 Conversion from Counts/sec to Flux (L1->L2)

The data that comes down from both EIS and FEEPS is mostly in the form of counts per accumulation period (i.e., spin sector) per sensor. A "sensor" is a small portion of measurement parameter space, where the parameters correspond to "look direction" (in 2 dimensions), energy, and "species" (i.e., electrons or ions; where ions are protons, helium ions, or oxygen ions). The prime challenge for ground processing is to turn each of these data values from a "counts per accumulation" (C/A) to intensity [1/(cm^2-s-sr-keV)] for the particular parameter state represented by the sensor. The algorithm for doing so is documented here.

1) Because a SSD response (output rate for a given channel) tends to be roughly linear when rates are low, but non-linear when rates are high, for high rates one must be prepared to perform a "dead-time correction" to reconstruct the true input rates. That correction is performed using a "live-time (LT) counter" (for FEEPS) or a "dead-time counter" (for EIS). Depending on how this number is generated, there is a conversion procedure to convert it into a "fractional live-time" (e.g., FLT = accumulation time / LT). For EIS there are other factors that go into the dead-time correction (e. g., processor speed) and the full algorithm is documented elsewhere.

2) Convert *C/A* to *counts per second* ($C/S \equiv R$) using:

$$R = \frac{C/A}{TA \times FLT},$$

where TA is the channel accumulation period and FLT is the aforementioned live-time correction.

3) If judged to be needed, subtract off a background, generally caused by cosmic rays:

$$RC = R - CR\_BG.$$

To-date, this correction remains unapplied in EPD data. This background is apparent in instances of low counting statistics. Note that CR_BG is energy-dependent with a peak corresponding to a minimum ionizing energy near 300 keV for FEEPS and 160 keV for EIS (with its thinner detectors).

4) Convert *R* to *Intensity* (*I*) as such:

$$I = \frac{R}{(E_2 - E_1) \times eG},$$

where *eG* is the efficiency (*e*) times the geometric factor (*G*) and E_1 and E_2 are the lower and upper energy bounds of the channel, respectively. *Note that* eG*,* E_1*, and* E_2 *are "calibration factors" that are provided in the "Calibration Matrix" spreadsheet (see Appendix A) to the processing software. There is one complete set of numbers for each of the hundreds of channels.*

More about these factors is provided in section 5.1.

5) When plotting the data or using it for calculations, the intensity is often identified with a central energy, often estimated as the geometric mean $\left(E_{\mathrm{gm}} = \sqrt{E_1 \times E_2}\right)$, an estimate that would be exact if the spectral index (*g*) were equal to 2 in the expression $I + C \times E^{-g}$, where *C* is a constant and *E* is energy.

The result of all of this processing can be notionally thought of as filling one or more spreadsheets with the column headings for each look direction like:

- Spacecraft
- Instrument
- Direction (θ,φ)
- Pitch Angle
- Energy (E_1, E_2, E_{gm})
- Counts per Accumulation (*C/A*)
- Counts per Second (*C/S*)
- Intensity (*I*)
- Species

The pitch angle (PA) is the angle of the look direction with respect to the magnetic field ($PA = \cos^{-1}\left[\vec{d} \times \vec{b}\right]$), where $\vec{d}$ is minus the unit view direction vector in spacecraft coordinates (i.e., the look direction in GSE coordinates) and $\vec{b}$ is the unit magnetic field vector in spacecraft coordinates (BCS). This angle is needed immediately because ordering the particle data by the magnetic field is central to understanding the data.

The generation of low and high-level data products from this notional spreadsheet is all about organizing the data in different ways (e.g., choose one look direction – or average all look directions - and one species generate an energy spectrum, etc.).

6.4.2 FEEPS Conversion from Counts to Flux (L1->L2)

Level 1b: FEEPS L2 data is organized into CDF formatted data files. The variables in these files correspond to data derived from the counts variable contained in L1A, primarily count rate and intensity, as well as variables containing magnetic field pitch angle data, ephemeris data and data quality indicators. The intensity value is calculated using the following components:

Live Time (LT):

$$LT = C * LTC,$$

where C = 8E-6 and LTC is the Live Time Counts.

Count Rate (CtRt):

$$CtRt = \text{Ct / LT} - \text{CRBG} = \text{Ct / (C*LTC)} - \text{CRBG},$$

where Ct is the counts and $CRBG$ is the cosmic ray background, which is currently defined in the FEEPS calibration file as a constant ($CRBG = 0.0$).

Intensity (I):

$$I = \text{CtRt / ((E2-E1)*Eff*GF}$$

where $E1$ and $E2$ are the energy step bounds, Eff is the efficiency, and GF is the geometric factor defined in the FEEPS calibration file.

Percent Uncertainty (%σ):

$$\% \sigma = 100\% * \sqrt{\text{Ct}},$$

where the one standard deviation measurement uncertainty of the counts is defined by the standard Poisson counting error $\sigma_{,Q} = \sqrt{Ct}$

There are four types of FEEPS L1b data:

1. L2 electron burst
2. L2 ion burst
3. L2 electron survey
4. L2 ion survey

These types are represented in the data file names. Note that the top/bottom field of the L1A file names have been moved into the files as a component of the variable names:

- mms1_feeps_brst_l1b_electron_20211019023633_v6.1.1.cdf
- mms1_feeps_srvy_l1b_ion_20211019000000_v6.1.1.cdf

6.4.3 FEEPS Data Quality Flags

MMS FEEPS data quality indicators allow the scientific community access to the most comprehensive FEEPS data set without being overwhelmed by detailed characteristics of the instrument health. A simple system of quality indicators is advantageous for encouraging the correct usage of the MMS FEEPS data by scientists within and outside the MMS team. The system of data quality indicators is identical for Burst and Survey data products, although some quality indicators will be unique to Survey data and unused for Burst data. A quality indicator is assigned to each time step for each FEEPS eye (i.e., telescope).

The FEEPS data quality indicators combine knowledge of contamination features in the FEEPS observations and onboard operations. FEEPS Team members have used the high resolution FEEPS observations (burst mode) to identify sun contamination features which are dependent on the spacecraft spin, i.e., dependency on spin sector. Onboard spin sector masking has been implemented before the summation of high-resolution observations into low resolution Survey sectors to avoid the irreversible contamination of Survey data. Furthermore, the FEEPS instrument is routinely operated in an instrument calibration mode which is unsuitable for scientific research. In summary, the quality indicators are a product of the comparison between sun contamination tables, onboard masking tables, and onboard calibration times.

The highest-resolution FEEPS observations are recorded in burst mode at a rate of 64 samples per spin, which are referred to as spin sectors. In survey mode, the FEEPS observations are recorded at an eighth of

the burst-mode resolution by summing the 64 spin sectors into 8 survey sectors per spin onboard the spacecraft. Removing sunlight contamination from the survey data requires masking contaminated spin sectors onboard before summing into survey sectors and transmitting to Earth. A spin sector mask table can be updated on each of the MMS spacecraft to avoid contamination in future survey mode observations and since the burst data contains the highest available angular resolution, onboard burst masking is not necessary.

The time-dependent contamination tables and onboard masking tables share a similar structure where both tables for a single spacecraft consist of a 64×24 table, with the 64 rows representing the 64 spin sectors in a spin and each column representing a FEEPS eye/sensor (top 1 – 12 and bottom 1 – 12). In a contamination table, each individual entry consists of a "0" or "1", representing "clean" or "contaminated". In an onboard masking table, each individual entry consists of 4 digits where each digit indicates if each of the following values have been masked (=1) or not masked (=0): survey counts, survey LTC, burst counts, burst LTC. The onboard calibration time periods are marked with the binary L1a variable "…calstate". The corresponding time dependent contamination table and onboard masking table is included in the FEEPS data products for transparency in the assignment of the quality indicators. The more advanced user does have the option to pick and choose whether to accept these quality indicators, although, this more advanced option is highly discouraged without the guidance of a FEEPS team member.

An overview of the quality indicators can be found below and is followed by a detailed description of each quality indicator assignment. While the following description uses a color scheme to indicate data quality, similar to a traffic light, the quality indicators are reported as integers in the data products.

These are the data quality flags are included in Level 2 data products.

For BURST- and RAW-mode data, there are three possible quality indicators:

- Green (Quality Indicator = 0): No contaminated or masked spin sectors (best data quality);
- Red (Quality Indicator = 3): Contaminated spin sector is associated with BURST and RAW data (this data is not recommended for scientific use);
- Grey (Quality Indicator = 4): FEEPS calibration data (this data is generated by the instrument itself and is not recommended for scientific use);

For SURVEY-mode data, there are five possible quality indicators:

- Green (Quality Indicator = 0): No contaminated or masked spin sectors (best data quality);
- Yellow (Quality Indicator = 1): Among the spin sectors used to create a SURVEY aggregate spin sector, onboard masking is successfully applied to a minimum of 1 and a maximum of 7 spin sectors and there is no contamination in any of the individual spin sectors . Note that since this indicator applies only when onboard masking is applied, some sectors are not observed.
- Orange (Quality Indicator = 2): There is contamination of between 0 and 50% of the not-masked sectors. Warning: this data contains contamination;
- Red (Quality Indicator = 3): Same as orange except that there is contamination of 50% or more of the not-masked sectors. IN ADDITION, this indicator applies to the case where onboard masking is applied to all 8 spin sectors in the aggregate sector.
- Grey (Quality Indicator = 4): FEEPS calibration data (this data is generated by the instrument itself and is not recommended for scientific use);

Burst-mode observations only use the “Green”, “Red”, and Grey” quality indicators. If a burst spin sector is contaminated and/or masked in any way (counts or LTC), the spin sector is recorded with the “Red” quality indicator (1) and is not recommended for scientific use. Without contamination and masking, a burst spin sector is recorded with the “Green” quality indicator (0), representing the best available data. The “Grey” quality indicator will be described later in this document. Using the contamination table and onboard masking table to assign a quality indicator is described in “pseudo code” below. Remember, the onboard masking table entry contains four digits, with the third and fourth digit recording the burst count masking and LTC masking.

```
IF (Contamination EQ 1) OR (Onboard[3] EQ 1) OR (Onboard[4] EQ 1) THEN Quality = 1
```

All five quality indicators ("Green”, “Yellow”, “Orange”, “Red”, “Grey”) can be assigned to the survey observations. In survey mode, eight spin sectors are accumulated onboard into a single survey sector and thus, onboard masking is used to remove contamination, although, not always successfully. If a survey sector does not contain any contaminated or masked spin sectors, then the survey sector is recorded with the “Green” quality indicator (0) and represents the best available data. If a survey sector does not contain any contamination and includes a total of 1 to 7 masked spin sectors, then the survey sector is recorded with the “Yellow” quality indicator (2). The “Yellow” quality indicator shows the user that not all spin sectors have been observed within the survey sector and thus the data will not represent the full angular coverage of the survey sector. Both “Green” and “Yellow” quality indicators do not contain any contamination and are encouraged for scientific use.

Since the onboard masking began in August 2016 and the contamination identification has evolved over time, not all contamination has been masked onboard before summing into survey sectors. The “Orange” quality indicator (3) is recorded when a survey sector contains less than 50% contaminated spin sectors. The user should exercise caution when using “Orange” quality data and is encouraged to contact FEEPS team members for guidance when publishing scientific results. Lastly, data recorded with the “Red” quality indicator (1) is not recommended for scientific use. The “Red” quality indicator applies to any survey sector which contains more than 50%. The “Grey” quality indicator will be described later in this document.

As a reminder, an onboard masking table entry contains four digits, with the first and second digit recording the survey count masking and LTC masking. The onboard masking must include counts and LTC to be considered completely masked and a partially masked spin sector is considered the same as a contaminated spin sector. Partially masked spin sectors are primarily a concern during the initial implementation of onboard masking between July 2016 and February 2017. Assigning a quality indicator to a survey sector requires examining the contamination and masking status of each of the eight summed spin sectors and comparing the total masked and contaminated spin sectors with the above quality indicator criteria. Again, “pseudo code” for the survey quality indicator is below.

```
Clean = 0 ;Initialize clean spin sector counter at 0
Bad = 0 ;Initialize bad spin sector counter at 0
Masked = 0 ;Initialize masked spin sector counter at 0
FOR spinSect = 1, 8 DO BEGIN
        Onboard = the 4-digit Onboard masking table entry for current spin sector
        Contamination = the sun contamination table entry for the current spin sector
        IF (Onboard[1] NE Onboard[2]) THEN BEGIN
 Bad = Bad + 1 ; Increment bad counter bc current spin sector is not completely masked
          STOP
        ENDIF ELSE IF (Contamination EQ 1 ) AND ( Onboard[1] EQ 0 ) THEN BEGIN
```

```
 Bad = Bad + 1 ; Increment bad counter bc current contaminated spin sector isn't masked
          STOP
        ENDIF ELSE IF (Onboard[1] EQ 1 ) THEN BEGIN
          Masked = Masked + 1 ; Increment masked counter
      STOP
        ENDIF ELSE Clean = Clean + 1 ; Increment clean counter
ENDFOR
IF (Clean EQ 8 ) THEN BEGIN
        Quality = 0 ; All 8 spin sectors are clean, assign "Green" quality indicator
ENDIF ELSE IF (Masked EQ 8 ) THEN BEGIN
        Quality = 1 ; All 8 spin sectors are masked, assign "Red" quality indicator
ENDIF ELSE IF ( (Bad EQ 0) & (Masked > 0) ) THEN BEGIN
        Quality = 2 ; Masked sectors total between 1 and 7, assign "Yellow" quality indicator
ENDIF ELSE IF (Bad/(Bad+Clean) < 0.5 ) THEN BEGIN
        Quality = 3 ; Less than 50% spin sectors are bad, assign "Orange" quality indicator
ENDIF ELSE Quality = 1 ; 50% or greater spin sectors are bad, assign "Red" quality indicator
```

The final input into the assignment of data quality indicators is the timing of onboard calibration testing. The time intervals when the FEEPS instrument is in the onboard calibration mode are marked with the binary L1a variable "…calstate" and the data is not suitable for scientific research. If a burst or survey sector contains calibration testing data, the sector is assigned the "Grey" quality indicator (4).

```
IF (calstate EQ 1 ) THEN Quality = 4
```

These data quality indicators allow for quick sorting of the FEEPS data for scientific use, although the more advanced user does have the option to pick and choose whether to accept these quality indicators. This more advanced option is highly discouraged, but is provided to show transparency in the assignment of the quality indicators. The FEEPS data sets contain variables for the sun contamination tables, onboard masking tables, and calibration mode, such that the data quality indicators can be reproduced by others.

6.4.4 EIS Calibration Matrix Overview

The response of the EIS sensors is complicated, and our understanding is based on a coordinated array of approaches, specifically:

i) bench testing of channel gains and other characteristics based on calibrated pulse inputs;
ii) calibrations using particle accelerator beams;
iii) calibrations using radiation sources;
iv) simulations of particle interactions with matter using such tools as GEANT4; and
v) geometric calculations.

All of this information can be captured within an Excel Spreadsheet, with one sheet per sensor head. This spreadsheet captures various functional relationships with polynomial fits up to the 6^{th} order. We will be referencing various portions of such a spreadsheet and will often do so by specifying the cell that is in the upper left had corner of the referenced region of the spreadsheet. All the information described below, plus an additional hard-wired geometric factor and flat field function for the six electron and six ion telescopes (look directions) per sensor (not shown), is sufficient to determine the efficiency of detection of particles within an EIS sensor.

An example of such a calibration matrix is shown in Figure 6-14 and specifically captures:

1) *Rows 5-12*: The coefficients of the 6th-order polynomial fit expressing the SSD-measured energy in keV as a function of the internal sensor SSD data numbers (E-DN) for the six large
2) electron (columns B-G) and six large ion (columns I-N) SSD pixels.
3) *Rows 20-26*: The coefficients of the 6th-order polynomial fit expressing the SSD-measured
4) energy in keV as a function of the internal sensor SSD data numbers (E-DN) for the six small
5) electron (columns A-G) and six small ion (columns H-N) SSD pixels.
6) *Cells B31-37*: The coefficients of the 6th-order polynomial fit expressing the ion TOF in nanoseconds (ns) as a function of the internal TOF data number (TOF-DN).
7) *Cells D35-H41*: The coefficients of the 6th-order polynomial fit expressing the TOF in ns (TOF[ns]) as a function of the ion energy in keV coming into the sensor for different species (H, He, and O), taking into account the amount of materials in the form of foils that the ion must pass through to get the time-of-flight section.
8) *Cells J35-N41*: The inverse of the cells in 4) for each species, i.e. the coefficients of the 6^{th}-order polynomial fit expressing the ion energy coming into the sensor in keV as a function of the TOF(ns) in ns.
9) *Cells B45-F52*: The coefficients of the 6^{th}-order polynomial fit expressing the SSD deposited energy in keV as a function of the measured energy in keV, taking into account the pulse height defect associated with SSD measurements.
10) *Cells I45-M52*: The coefficients of the 6^{th}-order polynomial fit expressing the energy input to the sensor in keV as a function of the energy deposited within the sensitive volume of the SSD, accounting for all of the materials that an ion must pass through before getting to the sensitive area of the SSD, including the SSD dead-layer.
11) *Cells B57-J63*: The coefficients of the 6^{th}-order polynomial fit expressing the scattering efficiency of the sensor (efficiency between 0 and 1) as a function of the incoming energy in keV for different particle species (e-, H, He, O, and S), taking into account the scattering within the collimator foil and the start foil and considering two possible software constraints on the valid time-of-flight (designated "P-1 sec" and "P-3 sec"). For electrons, this information includes scattering within the 2 μm of Al flashing that is deposited on the front surface of the SSD to keep out energetic protons.
12) *Cells L61-O66*: The coefficients of the 6th-order polynomial fit expressing the dE/dX (electronic) in keV/μm as a function of the ion TOF in ns, based on the laboratory-validated finding that the efficiency of emission of secondary electrons from the start and stop foils scales according to the dE/dX (electronic) within the emitting surfaces of the foil. Cells L58-O59 provide the laboratory-determined number of secondary electrons emitted for a "standard candle" of ~4.5 MeV alpha particles from a slightly degraded Am241 radiation source (with dE/dX of approximately 160 keV/μm within carbon).

In Figure 6-14, the information described above is used to determine the energy and efficiency characteristics for the various channels comprising the EIS onboard data products (the channels shown are notional, not comprehensive). Four different kinds of channels are defined: 1) electron energy channels (rows 74-77); 2) ion energy channels (derived strictly from SSD measurements; rows 81-84); 3) TOFxE channels (rows 88-98); and 4) TOFxPH channels (rows 102-108). The user of this spreadsheet fills out the information in Columns A through H (which includes the data numbers for the range of energy or TOF, depending on the channel type), and the spreadsheet automatically calculates all of the other columns, including incoming energy ranges ("Ein1", "Ein2") and various contributions to the detection efficiency. The final intensity of a channel is derived by normalizing the channel count-rate by a geometric factor (not shown), a flat-fielding function (now shown), and by the "Eff-2" shown in the right-most column of each row. This energy assigned to each channel is the geometric mean of the energy range, called "mean Ein" in column O.

Note: All Energies are in keV																
Linear-Linear: SSD Measured-Energy = P6[SSD Energy-Channel]																
Large Pixel Electrons								Large Pixel Ions								
	Sec 0	Sec 1	Sec 2	Sec 3	Sec 4	Sec 5			Sec 0	Sec 1	Sec 2	Sec 3	Sec 4	Sec 5		
a0	-4.22E+00	-4.22E+00	-4.22E+00	-4.22E+00	-4.22E+00	-4.22E+00		a0	-4.2741	-4.2741	-4.2741	-4.2741	-4.2741	-4.2741		
a1	9.85E-01	9.85E-01	9.85E-01	9.85E-01	9.85E-01	9.85E-01		a1	9.73E-01	9.73E-01	9.73E-01	9.73E-01	9.73E-01	9.73E-01		
a2	-8.48E-04	-8.48E-04	-8.48E-04	-8.48E-04	-8.48E-04	-8.48E-04		a2	-8.53E-04	-8.53E-04	-8.53E-04	-8.53E-04	-8.53E-04	-8.53E-04		
a3	1.00E-06	1.00E-06	1.00E-06	1.00E-06	1.00E-06	1.00E-06		a3	1.07E-06	1.07E-06	1.07E-06	1.07E-06	1.07E-06	1.07E-06		
a4	-5.89E-10	-5.89E-10	-5.89E-10	-5.89E-10	-5.89E-10	-5.89E-10		a4	-7.02E-10	-7.02E-10	-7.02E-10	-7.02E-10	-7.02E-10	-7.02E-10		
a5	1.62E-13	1.62E-13	1.62E-13	1.62E-13	1.62E-13	1.62E-13		a5	2.35E-13	2.35E-13	2.35E-13	2.35E-13	2.35E-13	2.35E-13		
a6	-1.56E-17	-1.56E-17	-1.56E-17	-1.56E-17	-1.56E-17	-1.56E-17		a6	-3.14E-17	-3.14E-17	-3.14E-17	-3.14E-17	-3.14E-17	-3.14E-17		
								Transition	1707	1707	1707	1707	1707	1707		
								a0	-50205.45	-50205.45	-50205.45	-50205.45	-50205.45	-50205.45		
								a1	29.41155	29.41155	29.41155	29.41155	29.41155	29.41155		
								a2	0	0	0	0	0	0		
Small Pixel Electrons								Small Pixel Ions								
	Sec 0	Sec 1	Sec 2	Sec 3	Sec 4	Sec 5			Sec 0	Sec 1	Sec 2	Sec 3	Sec 4	Sec 5		
a0	-4.22E+00	-4.22E+00	-4.22E+00	-4.22E+00	-4.22E+00	-4.22E+00		a0	-4.2741	-4.2741	-4.2741	-4.2741	-4.2741	-4.2741		
a1	9.85E-01	9.85E-01	9.85E-01	9.85E-01	9.85E-01	9.85E-01		a1	9.73E-01	9.73E-01	9.73E-01	9.73E-01	9.73E-01	9.73E-01		
a2	-8.48E-04	-8.48E-04	-8.48E-04	-8.48E-04	-8.48E-04	-8.48E-04		a2	-8.53E-04	-8.53E-04	-8.53E-04	-8.53E-04	-8.53E-04	-8.53E-04		
a3	1.00E-06	1.00E-06	1.00E-06	1.00E-06	1.00E-06	1.00E-06		a3	1.07E-06	1.07E-06	1.07E-06	1.07E-06	1.07E-06	1.07E-06		
a4	-5.89E-10	-5.89E-10	-5.89E-10	-5.89E-10	-5.89E-10	-5.89E-10		a4	-7.02E-10	-7.02E-10	-7.02E-10	-7.02E-10	-7.02E-10	-7.02E-10		
a5	1.62E-13	1.62E-13	1.62E-13	1.62E-13	1.62E-13	1.62E-13		a5	2.35E-13	2.35E-13	2.35E-13	2.35E-13	2.35E-13	2.35E-13		
a6	-1.56E-17	-1.56E-17	-1.56E-17	-1.56E-17	-1.56E-17	-1.56E-17		a6	-3.14E-17	-3.14E-17	-3.14E-17	-3.14E-17	-3.14E-17	-3.14E-17		
								Transition	1707	1707	1707	1707	1707	1707		
Time of Flight: Linear-Linear								a0	-50205.4	-50205.45	-50205.45	-50205.45	-50205.45	-50205.45		
TOF(ns) = P6[TOF-channel]								a1	29.41155	29.41155	29.41155	29.41155	29.41155	29.41155		
								a2	0	0	0	0	0	0		
a0	0															
a1	0.25		Time-of-Flight							Time-of-Flight						
a2	0		Log10(TOF(ns)) = P6[Log10(Energy-into-sensor)]							Log10(Energy-into-Sensor) = P6[Log10(TOF(ns)						
a3	0			H	He	O	S			H	He	O	S			
a4	0		a0	4.07022	6.67771	30.4431	22.8091		a0	4.27224	4.85607	5.20187	5.21416			
a5	0		a1	-4.44458	-9.48197	-53.3389	-36.9054		a1	-2.00664	-1.82712	-0.27687	1.0163			
a6	0		a2	3.57637	8.05253	41.8469	27.7864		a2	0.168871	-0.502946	-4.28586	-6.45182			
			a3	-1.76968	-3.81436	-17.5368	-11.2656		a3	-0.531903	0.629342	5.45036	7.0375			
			a4	0.49005	0.996382	4.09294	2.55162		a4	0.598064	-0.338004	-3.67144	-4.08484			
			a5	-0.070962	-0.135639	-0.503966	-0.305732		a5	-0.241902	0.080924	1.24278	1.19879			
			a6	0.004173	0.007517	0.025568	0.015132		a6	0.03666	-0.002469	-0.160795	-0.136054			
Pulse-Height Defect								Given SSD energy, What are the input energies coming into the sensor								
Log10[SSD Deposited-Energy] = P6[Log10(SSD Measured-Energy)]								Log10[Input Energy] = P6[Log10(SSD Deposited Energy)]								
	e	H	He	O	S				e	H	He	O	S			
a0	0	0.11867	0.307255	0.529719	0.550292			a0	1.05307	1.25705	1.54463	1.2593	1.26368			
a1	1	0.896368	0.776169	0.920533	0.958583			a1	0.14046	0.171718	-0.34265	2.27329	2.42085			
a2	0	0.02439	0.035927	-0.080915	-0.030018			a2	-0.373825	0.087186	0.579905	-2.62401	-2.82329			
a3	0	0.000589	0.005311	-0.025027	-0.049949			a3	0.647852	-0.004526	-0.187744	1.49633	1.63798			
a4	0	-0.000518	-0.001249	0.032986	0.028446			a4	-0.274551	0.027604	0.043237	-0.404066	-0.456966			
a5	0	0	0	-0.008163	-0.00513			a5	0.049721	-0.009543	-0.005471	0.053539	0.063008			
a6	0	0	0	0.000636	0.000314			a6	-0.003351	0.000892	0.000268	-0.002806	-0.003447			
Scatter Efficiency											For Foil Efficiences					
Log10(Efficiency) = P6[Log10(incoming Energy]											Log10(dE/dX (keV/mic)) = P6[Log10(E inTOF chamber)					
	e 3-Sec	p 1-Sec	p 3-Sec	He 1-Sec	He 3-Sec	O 1-Sec	O 3-Sec	S 1-Sec	S 3-Sec		Note: E-TOF is calculated from TOF(ns) and 6 cm flight path					
a0	-21.897	-23.1498	-17.0693	-35.4583	-24.5146	-60.122	-30.9256	4.80265	2.77665		H	He	O	S		
a1	46.2624	49.6625	35.5823	69.4742	45.9133	87.6626	34.7874	-50.9711	-39.7241	Start norm	1.8	1.8	1.8	1.8		
a2	-39.7908	-43.3106	-30.1752	-55.6854	-35.0682	-49.4277	-10.1167	66.6342	53.1123	Stop norm	1.4	1.4	1.4	1.4		
a3	17.8517	19.6744	13.3435	23.3922	13.9965	13.1316	-2.23677	-36.4353	-29.3104	a0	1.498410	1.597758	1.788343	1.864166		
a4	-4.41111	-4.91613	-3.24984	-5.43708	-3.08225	-1.48922	1.84537	10.0107	8.10283	a1	0.558056	0.833696	0.154667	0.433350		
a5	0.569924	0.641564	0.413957	0.663662	0.355483	0.011999	-0.369034	-1.37094	-1.11556	a2	-0.386226	-0.962019	0.794291	0.376468		
a6	-0.030119	-0.034211	-0.021576	-0.033269	-0.016793	0.007043	0.02497	0.074683	0.061086	a3	0.544472	0.825306	-0.689586	-0.461162		
										a4	-0.331377	-0.308763	0.260376	0.208833		
										a5	0.076581	0.049080	-0.044271	-0.040284		
										a6	-0.006107	-0.002818	0.002726	0.002726		

Figure 6-14 Example of Coefficients of up to the 6th-Order Used to Define the Functional Relationship of Multiple Parameters in the EIS Calibration Matrix

6.4.5 Known Features in the Dataset (Data Caveats)

6.4.5.1 EIS

a) Telescopes (T3-ion, T2-electron) affected by sun shield: Ion telescope T3 and electron telescope T2 are substantially blocked by the instrument's sun shield. Although these telescopes obtain valid data and are supplied in the EIS data products, care should be exercised in using these telescopes if anomalies are seen.

b) EIS1 telescope (T4) SSD anomaly: On MMS1, the solid-state detector (SSD) utilized in telescope T4 (for both ExTOF ion and electron data), is responding anomalously and should not be used at this point in time. It acts like it is under-biased, but the true cause is unknown.

c) EIS1 HV micro-discharges anomalies: For the MMS1 spacecraft, the HV system experienced micro-discharge anomalies that caused the HV to be shut down by the onboard software on 30 January 2016, with some anomalous behavior seen for the first time on 21 January 2016, about 6 months after HV turn on. Because only 3 EIS units were required, the HV on EIS1 was disabled for the rest of the prime mission. EIS1 data prior to 21 January 2016 are assumed to be unaffected by these anomalies.
   i. Beginning on 18 April 2016, EIS1 was put into high-resolution electron mode with "electronenergy" burst data enabled.
   ii. ii. HV (and ion species data) on MMS1 was re-enabled beginning on 31 January 2018. No further issues have been recorded to-date.

d) HV turnoff in inner magnetosphere: From launch through 8 August 2016, the high voltage (ion data) on all EIS units was turned off inside a radial distance of 7 R_E. The disabling of the HV system does not affect the collection of electron data.
   i. Beginning on 8 August 2016, this turn on/off point was reduced to 6 R_E on MMS2; the change to 6 RE was implemented on all spacecraft beginning on 22 March 2017.
   ii. On 1 March 2018, the HV on/off flight rule was changed from 6 RE to L=6.
   iii. On 12 March 2019, the HV on/off flight rule was changed from L=6 to L=5 for MMS4; after analysis revealed little degradation this was applied to MMS1-3 on 4 June 2019.

e) HV turnoffs during long eclipse seasons and campaigns: At the following times, certain or all EIS units had the HV disabled or were entirely powered off – affecting data availability.
   i. 12-30 June 2016 – Long-eclipse season
   ii. 6-15 March 2019 – Turbulence campaign
   iii. 17-31 August 2019 – Long-eclipse season
   iv. 8-19 August 2020 – Long-eclipse season

f) EIS electron data availability: Because of data volume limitations, and because the FEEPS sensors are the primary energetic electrons sensors, electrons are only measured on certain EIS units at any given time; which units are used for electrons was switched approximately every 14 orbits (~14 days) during MMS Phases 1, and was changed to every 3 orbits (~15 days) before the beginning of Phase 2b. Prior to the EIS1 HV anomaly detailed in item c), electrons were measured either on EIS1/3 or EIS 2/4. The units that are not generating electron data are instead generating what is called "event" data for diagnosing instrument performance.
   i. After the EIS1 high-resolution electron mode was enabled, the swapping was disabled for EIS1, but remains in effect for EIS2-4.
   ii. Beginning on 15 March 2017, this swapping was changed to every 5 orbits (~15 days). Burst electron data is obtained only from EIS1 and only following the reconfiguration of EIS1 into a high-resolution electron sensor.
   iii. EIS electron data collection beyond 6 RE was discontinued for MMS2-4 on 14 November 2017; electron data ceased on MMS1 with the re-enabling of the HV on 31 January 2018 (see item c.ii above).
   iv. EIS electron data was re-enabled on MMS4 only on 5 December 2019 with new energy channels covering from ~300 keV to >1.8 MeV

g) Cosmic ray background in electron data: Penetrating cosmic rays generate a low-level band of contamination in the electron spectra (at about 1 count/s) centered between 150-200 keV. This contamination has not been subtracted from the foreground.

h) Helium charge-state: Despite being labeled as "alpha" in the ExTOF files, the charge state of the helium (and oxygen) ions is unmeasured.

i. New vX.Y.100+ files of L2 EIS data, produced and made publicly available in Summer 2021 changed the names of these "alpha" variables to "helium" to more accurately represent their content. These

corrections were not applied to L1a/b data files and older data files that include the original "alpha" variable names should not be used.

i) PHxTOF species determination: While in principle the low energy PHxTOF data products are able to discriminate between proton and oxygen, this discrimination works only when the heavy and light ion intensities are similar. Given the reality of the relative intensities, there is no automated procedure that can cleanly separate the light and heavy ion intensities for the PHxTOF lower energies, and the PHxTOF oxygen measurements are deemed unreliable and should be used with great caution. As such, several PHxTOF oxygen channels were reallocated to allow for better proton energy resolution beginning on 26 September 2016.

j) Solar proton contamination in electron measurements: Because of the technique used by EIS to measure electrons, a simple SSD with 2 μm of aluminum flashing on top, there will be periods of time (for solar proton events in particular) when the electron measurements are contaminated with >250 keV protons.

k) Cross-calibration efforts: During the first half of 2017, a considerable effort went into cross calibrating the EIS, FPI, HPCA, and FEEPS-ion sensors in their overlap regions. Based on this effort, the calibration matrices for EIS were substantially modified. As of this writing the new calibration matrices have been applied to all data following 1 November 2016. It is our intention to apply the calibration matrices on earlier data over time. The major change is in the efficiencies of protons at energies less than 50 keV, yielding intensities near 30 keV that are a factor of 5 higher than originally estimated.
    i. The results of these cross-calibration efforts were implemented in the reprocessing of the complete L2 EIS dataset (new vX.Y.100+ files) that were made publicly available in Summer 2021. These corrections were not applied to L1a/b data files.

l) Flat-fielding: An initial flat-fielding attempt has been made to adjust the EIS intensities. This initial attempt is known to be imperfect and is expected to be improved over time.

m) Efficiency effects on flux determinations: The efficiency of ion detection for making ExTOF and PHxTOF ion measurements evolves over time because of variations of the gain of the microchannel plate in each of the EIS units. To-date a nominal efficiency multiplier is utilized with the Level 2 data, but slow evolutions of those efficiencies have not been folded into the data processing. The multiplicative error is up to about ±30%.

n) EIS file versioning: The full reprocessing of the L2 EIS dataset in Summer 2021 (new vX.Y.100+ files) updated the file versioning reported in Figure 6-2.

6.4.5.2 FEEPS

a) Sunlight contamination in survey data: Many of the FEEPS eyes suffer from light contamination, likely due to direct sunlight and glint coming through foils that were damaged during launch. This light contamination is identifiable in spectra specific to an individual spin sector and, therefore, correctable in burst mode data. For survey data products, prior to the CIDP changes implemented in October 2016, this contamination has an uncorrectable effect on some of the FEEPS eyes. Since the survey data products are produced by aggregating burst resolution data onboard each spacecraft for some eyes, the sunlight-contaminated sectors are unfortunately being combined with good sectors to produce the lower resolution corrupted survey sectors. This and other issues have been corrected via a series of CIDP updates implemented between October 2016 and August 2017. However, the fix is not perfect; some sunlight contamination still manages to make its way into the data product and should always be considered first when contamination associated with rotation are clear in the "spin tones" of the data products. For all data before and after these changes, please be aware of this contamination source and account for it in your studies. With burst data, please ensure that the affected eyes/sectors have been removed for analysis, and with survey data, be aware of the presence of this contamination in the data and proceed with caution for any scientific studies with that portion of the dataset. Badly

affected telescopes can also be removed from studies using survey data. More details, including examples of the sunlight contamination and examples of maps of the affected eyes and sectors from each spacecraft are provided in section 6.3.2. NOTE: these effects change over time. Quality flags are provided in Level 2 data products to aid in the cautious use of survey data products. The MMS-specific IDL-based SPEDAS routines for FEEPS have been implemented with a hardwired filtering for eliminating the bad eyes and sectors.

b) Sunlight contamination in burst data: For data between October 2016 and August 2017, some burst data were also adversely affected; please refer to section 6.3.2 and contact members of the EPD team for guidance on any data analyses using data during this period.

c) Spin tone: Despite flat fielding efforts (see section 6.3.2.1), the spin tone is still often visible in FEEPS electron data binned by pitch angle or gyro-phase. This is because the flat fielding changes the energy channel bounds for each FEEPS eye and sunlight contamination removes sectors from some telescopes in each spin. In effect, different telescopes are measuring slightly different energies. In a future version of the Level 2 data product, the data will be interpolated onto a common energy grid, which should mostly remove the spin-tone due to flat fielding. Currently, these inconsistencies can have a noticeable effect when combined with exponentially decaying energy spectra. In addition, the maximum or minimum values in the spin distribution might be missed if they fall in a contaminated sector.

d) FEEPS unit timing: Prior to the October 2016 Central Instrument Data Processor (CIDP) changes, the FEEPS top and bottom units used independent times for the initial (i.e., 0^{th}) sector of each spin. This misalignment is being accounted for in the data products, and the onboard correction was implemented on each spacecraft with the CIDP changes in October 2016. The CIDP changes will ensure that both top and bottom instruments trigger simultaneously on the sun-pulse signal on each spacecraft and that no alignment on the ground will be necessary. Prior to this date, the science data will contain a default fill value indicating NAN for any sectors that were affected by the misalignment. This effect is mostly superficial, but is documented here for completeness.

e) Energy thresholds for lowest energy channels: The first energy channels (i.e., those with the smallest indices) from FEEPS ion and electron sensors have their threshold set very near to or within the noise threshold. These channels from most (but not all) eyes are often measuring noise and should not be used for scientific data analysis. When included in the omni-directional product, these eyes result in a discrepancy at the lowest energy channel(s). On several of the FEEPS eyes, the second energy channels also require threshold adjustment as of 04 April 2016. The effect of this is clear when comparing energy spectra from independent eyes during periods with high count rates and isotropic angular distributions. The affected eyes/energy-channels will show large (factor of 5 or more) decreases or increases in the count rates compared to the other eyes. An example of this is shown in Figure 6-10. The affected channels should **not** be included for any scientific analysis.

f) Integral channels: The last energy channels (i.e., those with the highest energy level, with index 15) for FEEPS ion and electron instruments are effectively integral channels, combining counts from all energies greater than those in index 14. Thus, these data are an independent and different dataset from the other channels and should not be included in combined spectra or energy distributions with the other channels.

g) Solar Energetic Particle (SEP) contamination in electron channels: it is expected that there will be some response in the electron sensors to SEPs, however, as of 04 April 2016), the electron measurements seem to be relatively unaffected by these events.

h) Ion measurement contamination by electrons: the ion measurements are largely unaffected by energetic electron contamination. This is due to the ultra-thin detectors used in the FEEPS ion eyes, which are less than 15 μm thick.

i) Radiation belts: As of 3 April 2020, the FEEPS data agree well with Van Allen Probes in Earth's outer radiation belt, however, some contamination of the electron data may be present due to enhanced background levels during times of very hard radiation belt spectra (i.e., high intensities of

>1 MeV electrons). Caution should be taken when using these data in the radiation belts, but they do provide a reasonably accurate measure of outer radiation belt electrons. If the opportunity arises in the future there will be an effort to monitor the >500 keV fluxes at GEO (using GOES13, 14, 15, 16 and 17) for cases of hard spectra and then use the results to generate a baseline hardness at which the contamination starts to rise. As of writing, it has been too magnetically quiet to obtain that data.

j) X-ray response: Based on tests conducted during solar X-ray flares on 04 and 09 November 2015, the FEEPS ion and electron instruments have no significant response to solar X-rays.
k) Cross-calibration efforts: Preliminary cross-calibration has been conducted between FEEPS with EIS and FPI. Those results show good agreement between the instruments; however, no formal cross-calibration factors have been applied to the dataset, so use caution when combining these data products. Combined distributions are expected to be officially produced as a Level 3 data product.
l) Quality indicators: Level 2 data products contain a data quality indicator which is described in section 6.4.2.
m) Cosmic ray background in electron data: Penetrating cosmic rays generate a low-level band of contamination in the electron spectra (at about 1 count/s) centered on about ~300-350 keV. This contamination has not been subtracted from the foreground.

6.5 DATA PRODUCTS

6.5.1 Data Products Overview

Three levels of data product available for scientific or engineering use referred to as L1A, L1B, and L2. The first level, L1A, contains sensor counts represented as numerical values (as opposed to telemetry bytes in level 0), L1B contains synthesized data such as pitch angles and intensity. L2 data contains refinements to pitch angle and ephemeris data and is the data level intended for use in scientific analysis. The dataset consists of a collection of timestamped files which are formatted in accordance with the International Solar-Terrestrial Physics/Space Physics Data Facility (ISTP/SPDF) standard Common Data Format (CDF).

Level 1b: The CDF variables in these files correspond to data derived from the counts variable contained in L1A (count rate and intensity) as well as variables containing magnetic field pitch angle data, ephemeris data and data quality indicators. The algorithm for calculating intensity is provided in section 6.4.1.

There are four types of FEEPS L1b data:

1. L1B electron burst
2. L1B ion burst
3. L1B electron survey
4. L1B ion survey

These types are represented in the data file names.

- mms1_feeps_brst_l1b_electron_20211019023633_v6.1.1.cdf
- mms1_feeps_srvy_l1b_ion_20211019000000_v6.1.1.cdf

Level 1b: These are observatory level data products; for each spacecraft, there would be one set from FEEPS (the two instruments combined) and one set from EIS. At the “Record” level there is time (UTC), a quality flag, (bad sector flag, but no quality flag in FEEPS L1b) an accumulation time for each channel,

a spin sector, perhaps a spin number, and magnetic field and ephemeris data. At the detector or look direction level there is pitch angle, GSE look direction (Solar Angle + Elevation), live-time (not in FEEPS L1b) or dead-time, and the E1 of the lowest energy channel. At the channel level, there are 4-position "vectors", specifically: {EGM, counts-per-accumulation, counts-per-second, rough-intensity}, where EGM is the geometric mean of E_1 and E_2 [$\sqrt{E_1 \times E_2}$], the energy bounds of the energy channel. The deviations of E_1 and E_2 for each channel from EGM are also reported. Here the "rough-intensity" is results from the conversion of "counts-per-second" to "intensity" using only approximate, uncertified calibration matrices, as are the energies, $E($ and $E*$. No live-time or dead-time correction is applied to the counts, the counts/second, or the rough intensity. As with the Level 1a product, for each record the UTC time (or equivalent) must be recorded and a standard for whether that time is the beginning or the middle of an accumulation time. Quicklook data displays and any needed SITL data products are generated at this level. Note that there are no EIS and FEEPS data that are joined together at this point in time. The Level 1b data products are listed here, with FEEPS in black and EIS in green (note that "top" and "bottom" FEEPS sensors are now combined):

01. L1b-FEEPS-Electron-Burst
02. L1b-FEEPS-Electron-Survey
03. L1b-FEEPS-Ion-Burst
04. L1b-FEEPS-Ion-Survey
05. L1b-EIS-PhxTOF-Ion-Burst
06. L1b-EIS-ExTOF-Ion-Burst
07. L1b-EIS-PhxTOF-Ion-Survey
08. L1b-EIS-ExTOF-Ion-Survey
09. L1b-EIS-Electron-Energy-Survey (diagnostic)*
10. L1b-EIS-Electron-Energy-Burst (diagnostic)**
11. L1b-EIS-Ion-Energy-Burst (diagnostic)
12. L1b-EIS-Ion-Energy-Survey (diagnostic)

*EIS Electron Energy Survey is only available on select spacecraft at any given time.
**EIS Electron Energy Burst became a standard data product for EIS1 in April 2016.
NOTE: EIS Level 1b data is used for Quicklook Plotting and Scientist-in-the-Loop (SITL) considerations.

Level 2: These data are identical in format and content as the Level 1b dataset. The difference is: 1) live-time or dead-time corrections are applied to the counts per second as reported in this product, and before the generation of intensity. 2) "rough-intensity" values are replaced with "refined-intensity", 3) rough values of E1 and E2 are replaced with refined values, 4) preliminary magnetic field is replaced with updated magnetic field, 5) predict ephemeris is replaced with updated ephemeris, and 6) the record-level quality flag is updated. The list of Level 2 data products is nearly identical to the Level 1b products. Note that only Level 2 products 1-8 are generally available to the scientific community, with 9 and 10 selectively available. Again, products from FEEPS are in black and those from EIS are in blue:

01. L2-FEEPS-Electron-Burst
02. L2-FEEPS-Electron-Survey
03. L2-FEEPS-Ion-Burst
04. L2-FEEPS-Ion-Survey
05. L2-EIS-PhxTOF-Ion-Burst
06. L2-EIS-ExTOF-Ion-Burst
07. L2-EIS-PhxTOF-Ion-Survey
08. L2-EIS-ExTOF-Ion-Survey

There are several types of EIS L2 data products
05. L2-EIS-PhxTOF-Ion-Burst

06. L2-EIS-ExTOF-Ion-Burst
07. L2-EIS-PhxTOF-Ion-Survey
08. L2-EIS-ExTOF-Ion-Survey
09. L2-EIS-Electron-Energy-Survey (diagnostic)*
10. L2-EIS-Electron-Energy-Burst (diagnostic)**
11. L2-EIS-Ion-Energy-Burst (diagnostic)
12. L2-EIS-Ion-Energy-Survey (diagnostic)

These types are represented in data file names such as:

- mms1_epd-eis_brst_l2_extof_20210822071603_v5.0.4.cdf

Level 3: Refer to section 6.5.7, "Level 3 EPD Data Products" for a detailed description of higher-level data products.

6.5.2 File Structure L2 FEEPS Electron

The variables contained within the FEEPS Level 2 Products generated within the MMS Science Data Center (SDC), are outlined in Table 6-3 and Table 6-4 below. All of these FEEPS variables begin with,

*<prefix> = mms**<#>**_epd_feeps_**<DATA_RATE>**_l2_,*

where **<#>** is the spacecraft number and ***<DATA_RATE>*** is the telemetry mode (srvy, brst, or raw). ***<SIDE>*** will be "top" or "bottom" to indicate which FEEPS unit the data correspond to. The **<#>** portion found in several variables represents the sensor identifier number.

Data Parameter	Description	Units
Epoch	UTC timestamp at sector center	TT2000
<prefix>_electron_spinsectnum	Spin sector in which the spacecraft was oriented during data acquisition	-----
<prefix>_electron_energy	Centroid of differential energy channels associated with each of 16 FEEPS channels	keV
<prefix>_electron_energy_lower_bound	Lower bound of differential energy channels associated with each of 16 FEEPS channels	keV
<prefix>_electron_energy_upper_bound	Upper bound of differential energy channels associated with each of 16 FEEPS channels	keV
<prefix>_<SIDE>_electron_count_rate_sensorid_<#>	Count rate	counts/s
<prefix>_<SIDE>_electron_intensity_sensorid_<#>	Unidirectional differential flux per spin sector	1/(cm^2-s-sr-keV)
<prefix>_<SIDE>_electron_sector_mask_sensorid_<#>	Array of bad sector flags for a packet	-----
<prefix>_electron_spin	The number of spacecraft rotations	Seconds
<prefix>_electron_spin_duration	Period of the spin	-----
<prefix>_electron_integration_sectors	Integration sectors	-----
<prefix>_electron_bfield	Magnetic field vector	nT
<prefix>_electron_pitch_angle	Pitch angle with respect to local magnetic field	Degrees

<prefix>_electron_scpos_ec_gse	Spacecraft position in Earth-centered geocentric solar ecliptic coordinates	Km
<prefix>_electron_scz_vec_gse	Spacecraft Unit Vector Z-Axis in Earth-centered Geophysical Coordinates	-----
<prefix>_electron_scy_vec_gse	Spacecraft Unit Vector Y-Axis in Earth-centered Geophysical Coordinates	-----
<prefix>_electron_scx_vec_gse	Spacecraft Unit Vector X-Axis in Earth-centered Geophysical Coordinates	-----
<prefix>_electron_moon_pos_gse	Position of the moon in Earth-centered Geophysical Coordinates	Km
<prefix>_electron_radius	Radial distance in Earth radii	R_E (Earth radii)
<prefix>_electron_lat_gse	Latitude in Earth-centered Geophysical Coordinates	Degrees
<prefix>_electron_lon_gse	Longitude in Earth-centered Geophysical Coordinates	Degrees
<prefix>_electron_l_shell	Dipole L shell in Earth radii determined using Solar Magnetospheric latitude	R_E (Earth radii)
<prefix>_electron_lat_gsm	Latitude in Solar Magnetospheric Coordinates	Degrees
<prefix>_electron_lon_gsm	Longitude in Solar Magnetospheric Coordinates	Degrees

Table 6-3 List of the Burst Variable Included in the FEEPS Electron Data Product

Data Parameter	Description	Units
epoch	UTC timestamp at sector center	TT2000
<prefix>_electron_spinsectnum	spin sector in which the spacecraft was oriented during data acquisition	-----
<prefix>_electron_energy	Centroid of differential energy channels associated with each of 16 FEEPS channels	keV
<prefix>_electron_energy_lower_bound	Lower bound of differential energy channels associated with each of 16 FEEPS channels	keV
<prefix>_electron_energy_upper_bound	Upper bound of differential energy channels associated with each of 16 FEEPS channels	keV
<prefix>_<SIDE>_electron_count_rate_sensorid_<#>	Count rate	counts/s
<prefix>_<SIDE>_electron_intensity_sensorid_<#>	Unidirectional differential flux per spin sector	$1/(cm^2$-s-sr-keV)
<prefix>_<SIDE>_electron_sector_mask_sensorid_<#>	array of bad sector flags for a packet	-----
<prefix>_electron_spin	The number of spacecraft rotations	-----
<prefix>_electron_spin_duration	period of the spin	Seconds
<prefix>_electron_integration_sectors	integration sectors	-----
<prefix>_electron_bfield	magnetic field vector	nT
<prefix>_electron_pitch_angle	Pitch angle wrt local magnetic field	Degrees
<prefix>_electron_scpos_ec_gse	Spacecraft position in Earth-centered geocentric solar ecliptic coordinates	Km

<prefix>_electron_scz_vec_gse	Spacecraft Unit Vector Z-Axis in Earth-centered Geophysical Coordinates	-----
<prefix>_electron_scy_vec_gse	Spacecraft Unit Vector Y-Axis in Earth-centered Geophysical Coordinates	-----
<prefix>_electron_scx_vec_gse	Spacecraft Unit Vector X-Axis in Earth-centered Geophysical Coordinates	-----
<prefix>_electron_moon_pos_gse	the position of the moon in Earth-centered Geophysical Coordinates	Km
<prefix>_electron_radius	radial distance in Earth radii	R_E (Earth radii)
<prefix>_electron_lat_gse	latitude in Earth-centered Geophysical Coordinates	Degrees
<prefix>_electron_lon_gse	longitude in Earth-centered Geophysical Coordinates	Degrees
<prefix>_electron_l_shell	Dipole L shell in Earth radii determined using Solar Magnetospheric latitude	R_E (Earth radii)
<prefix>_electron_lat_gsm	latitude in Solar Magnetospheric Coordinates	Degrees
<prefix>_electron_lon_gsm	longitude in Solar Magnetospheric Coordinates	Degrees

Table 6-4 List of the Survey Variable Included in the FEEPS Electron Data Product

6.5.3 File Structure L2 FEEPS Ion

The variables contained within the FEEPS Level 2 Products generated within the MMS Science Data Center (SDC), are outlined in Table 6-5 and Table 6-6 below. All of these FEEPS variables begin with,

*<prefix> = mms**<#>**_epd_feeps_**<DATA_RATE>**_l2_,*

where **<#>** is the spacecraft number and ***<DATA_RATE>*** is the telemetry mode (srvy, brst, or raw). ***<SIDE>*** will be "top" or "bottom" to indicate which FEEPS unit the data correspond to. The **<#>** portion found in several variables represents the sensor identifier number.

Data Parameter	Description	Units
Epoch	UTC timestamp at sector center	TT2000
<prefix>_ion_spinsectnum	Spin sector in which the spacecraft was oriented during data acquisition	-----
<prefix>_ion_energy	Centroid of differential energy channels associated with each of 16 FEEPS channels	keV
<prefix>_ion_energy_lower_bound	Lower bound of differential energy channels associated with each of 16 FEEPS channels	keV
<prefix>_ion_energy_upper_bound	Upper bound of differential energy channels associated with each of 16 FEEPS channels	keV
<prefix>_<SIDE>_ion_count_rate_sensorid_<#>	Count rate	counts/s
<prefix>_<SIDE >_ion_intensity_sensorid_<#>	Unidirectional differential flux per spin sector	1/(cm^2-s-sr-keV)
<prefix>_<SIDE>_ion_sector_mask_sensorid_<#>	Array of bad sector flags for a packet	-----
<prefix>_ion_spin	The number of spacecraft rotations	-----

<prefix>_ion_spin_duration	Period of the spin	Seconds
<prefix>_ion_integration_sectors	Integration sectors	-----
<prefix>_ion_bfield	Magnetic field vector	nT
<prefix>_ion_pitch_angle	Pitch angle with respect to local magnetic field	Degrees
<prefix>_ion_scpos_ec_gse	Spacecraft position in Earth-centered geocentric solar ecliptic coordinates	Km
<prefix>_ion_scz_vec_gse	Spacecraft Unit Vector Z-Axis in Earth-centered Geophysical Coordinates	-----
<prefix>_ion_scy_vec_gse	Spacecraft Unit Vector Y-Axis in Earth-centered Geophysical Coordinates	-----
<prefix>_ion_scx_vec_gse	Spacecraft Unit Vector X-Axis in Earth-centered Geophysical Coordinates	-----
<prefix>_ion_moon_pos_gse	Position of the moon in Earth-centered Geophysical Coordinates	Km
<prefix>_ion_radius	Radial distance in Earth radii	R_E (Earth radii)
<prefix>_ion_lat_gse	Latitude in Earth-centered Geophysical Coordinates	Degrees
<prefix>_ion_lon_gse	Longitude in Earth-centered Geophysical Coordinates	Degrees
<prefix>_ion_l_shell	Dipole L shell in Earth radii determined using Solar Magnetospheric latitude	R_E (Earth radii)
<prefix>_ion_lat_gsm	Latitude in Solar Magnetospheric Coordinates	Degrees
<prefix>_ion_lon_gsm	Longitude in Solar Magnetospheric Coordinates	Degrees

Table 6-5 List of the Burst Variables Included in the FEEPS Ion Data Product

Data Parameter	Description	Units
Epoch	UTC timestamp at sector center	TT2000
<prefix>_ion_spinsectnum	Spin sector in which the spacecraft was oriented during data acquisition	-----
<prefix>_ion_energy	Centroid of differential energy channels associated with each of 16 FEEPS channels	keV
<prefix>_ion_energy_lower_bound	Lower bound of differential energy channels associated with each of 16 FEEPS channels	keV
<prefix>_ion_energy_upper_bound	Upper bound of differential energy channels associated with each of 16 FEEPS channels	keV
<prefix>_<side>_ion_count_rate_sensorid_<#>	Count rate	counts/s
<prefix>_<side>_ion_intensity_sensorid_<#>	Unidirectional differential flux per spin sector	$1/(cm^2\text{-}s\text{-}sr\text{-}keV)$
<prefix>_<side>_ion_sector_mask_sensorid_<#>	Array of bad sector flags for a packet	-----
<prefix>_ion_spin	The number of spacecraft rotations	-----
<prefix>_ion_spin_duration	Period of the spin	seconds
<prefix>_ion_integration_sectors	Integration sectors	-----

<prefix>_ion_bfield	Magnetic field vector	nT
<prefix>_ion_pitch_angle	Pitch angle with respect to local magnetic field	Degrees
<prefix>_ion_scpos_ec_gse	Spacecraft position in Earth-centered geocentric solar ecliptic coordinates	Km
<prefix>_ion_scz_vec_gse	Spacecraft Unit Vector Z-Axis in Earth-centered Geophysical Coordinates	-----
<prefix>_ion_scy_vec_gse	Spacecraft Unit Vector Y-Axis in Earth-centered Geophysical Coordinates	-----
<prefix>_ion_scx_vec_gse	Spacecraft Unit Vector X-Axis in Earth-centered Geophysical Coordinates	-----
<prefix>_ion_moon_pos_gse	Position of the moon in Earth-centered Geophysical Coordinates	Km
<prefix>_ion_radius	Radial distance in Earth radii	R_E (Earth radii)
<prefix>_ion_lat_gse	Latitude in Earth-centered Geophysical Coordinates	degrees
<prefix>_ion_lon_gse	Longitude in Earth-centered Geophysical Coordinates	degrees
<prefix>_ion_l_shell	Dipole L shell in Earth radii determined using Solar Magnetospheric latitude	R_E (Earth radii)
<prefix>_ion_lat_gsm	Latitude in Solar Magnetospheric Coordinates	Degrees
<prefix>_ion_lon_gsm	Longitude in Solar Magnetospheric Coordinates	degrees

Table 6-6 List of the Survey Variables Included in the FEEPS Ion Data Product

6.5.4 File Structure EIS Electronenergy

These data are identical in format and content as the Level 1b dataset. The difference is: 1) live-time or dead-time corrections are applied to the counts per second as reported in this product, and before the generation of intensity. 2) “rough-intensity” values are replaced with “refined-intensity”, 3) rough values of E1 and E2 are replaced with refined values, 4) preliminary magnetic field is replaced with updated magnetic field, 5) predict ephemeris is replaced with updated ephemeris, and 6) the record-level quality flag is updated. The list of Level 2 data products is nearly identical to the Level 1b products. Note that only Level 2 products 1-8 are generally available to the scientific community, with 9 and 10 selectively.

6.5.5 File Structure L2 EIS ExTOF and PHxTOF

Level 1B (L1B) files are exactly the same format as Level 2 (L2) files, they have merely been produced with less reliable data including some or all of the following: predicted ephemeris an attitude information (as opposed to definitive information), lower-level FGM data, preliminary calibration tables.

The files are International Solar-Terrestrial Physics/Space Physics Data Facility (ISTP/SPDF) standard Common Data Format (CDF) files. There are three L2 files, one for each data type.

1. electronenergy: (note that electron data may be contaminated with (>250 keV protons).
2. extof: High-energy (ExTOF) ion spectra organized by particle species.
3. phxtof: Low-energy (PHxTOF) ion spectra organized by particle species.

All the principal variables in each file have the same “time axis” (DEPEND_0 attribute), so the file can be thought of as a simple rectangular “table” with each time value of the Epoch variable defining a “row”

and each non-constant CDF variable as a "column". The Epoch is the midpoint of the accumulation interval. Time_Minus and Time_Plus (DELTA_PLUS and DELTA_MINUS attributes) give the start and stop edges of the time bin as specified by the ISTP CDF standard.

There is one spectral variable for each "species": electron, proton, alpha, oxygen, or "dump" (where "dump" captures every event that was not classified as one of the defined species). Each spectral variable has a DEPEND_1 attribute that points to a (constant) variable which gives the centers of the energy bins and that variable, in turn, has DELTA_PLUS and DELTA_MINUSattributes that point to variables giving the bin edges (as described in the ISTP CDF standard). Each spectrum is given in three data units (or using three "calibrations"):

1. counts: The raw number of counts collected during the current accumulation interval (see discussion of the "Timing and Geometry Block" below). This value is uncorrected in any way and may be used to calculate the relative uncertainty of all three "calibrations" using standard Poisson statistics.
2. cps: The count rate [counts/s] in each energy bin. This quantity may be corrected for instrument saturation effects (this procedure is still in development).
3. flux: The calibrated differential intensity [1/cm2-sr-s-keV] of charged particles in each energy bin.

There are 6 spectral variables for each calibration (numbered 0-5) corresponding to the 6 look directions (or "telescopes") of the instrument.

The variables in each spectral file can be grouped into four conceptual "blocks":

1. Timing and Geometry: Describes the time period over which the measurement was taken and low-level attitude and instrument configuration data needed to calibrate the raw counting rates in these files.
2. Spectral: One CDF variable for each species and calibration.
3. Ephemeris, Attitude, and Pitch Angle: Spacecraft position, look direction, pitch angle, and magnetic field.
4. Basic Rates: Raw total counting rates in various instrument subsystems. These give a quick overview of the measured environment and state of the instrument.

Apart from the Epoch variables, which follow the general ISTP standard, the EIS variables all begin with a "prefix" following the standard MMS naming scheme:

<eis_prefix> = mms<#>_epd_eis_<DATA_RATE>_<LEVEL>_<DATA_TYPE>_,
indicated in the variables below by "*".

1) The Timing and Geometry block consists of the following variables:
   - *epoch, time minus, time plus* – Standard CDF time specifications for the measurement window.
   - **starttai, *midtai, *endtai* – The beginning, middle, and end of the measurement window in International Atomic Time (TAI) expressed as seconds since 1958 (standard MMS spacecraft time).
   - **spin* – A 16-bit spin counter (0-65535). This is retained in L2 data for instrument team use in file validation.
   - **sector* – The first sector (0-31) of the measurement that may include multiple sectors. A full revolution of the spacecraft is divided into 32 evenly spaced sectors. Several sectors are combined for measurements in most data products so that only 8 or 16 measurements, for example, are made in a revolution. Data products may be collected only every nth spin. This is

retained in L2 data primarily for instrument team use in validation, but it may prove useful to other investigators as a simple way of performing rough attitude filtering or grouping.

- **quality* – bit flags indicating reliability of the data, these values are still under development.

2) The Spectral block variables are named with the form:

<SPECIES> P<LUT PERIOD> <DATA UNITS> T<#>

3) The Ephemeris, Attitude, and Pitch Angle block consists of the following variables:
   - **pitch_angle_t<#>* - The angle between the particle flow vector and the magnetic field for each of the 6 "telescopes". The particle flow vector is the negative of the telescope look direction.
   - **look_t<#>* – The look direction of the telescope in the standard GSE coordinate frame.
   - **b* – The magnetic field used to derive the pitch angle.
   - **position_gse* – The spacecraft position with respect to the Earth in the GSE frame
   - **position_gse* – The spacecraft position with respect to the Earth in the GSM frame
   - **moon_gse* – The spacecraft position with respect to the Moon in the GSE frame
   - **sc_to_gse* – Transformation matrix for rotating a vector from the spacecraft frame (BCS) to the GSE frame [entries are by row: row1 = row1, row2 = 4-6, row3 = 7-9]
   - **gse_to_gsm* – Transformation matrix for rotating a vector from the GSE frame to the GSM frame [entries are by row: row1 = row1, row2 = 4-6, row3 = 7-9]
   - **r* – Spacecraft distance from Earth in kilometers
   - **l* – Spacecraft position L-shell for a dipole magnetic field
   - **gse_lat, *gse_lon, *gsm_lat, *gsm_lon, *sm_lat, *sm_lon* – Spacecraft position latitude and longitude in GSE, GSM, or SM frame.
   - **orbit_num* – MMS mission orbit number

4) The Basic Rates block consists of the following variables:

   For all data types:
   - **ssd<#>* – Number of pulses detected on the solid-state energy detector for telescope number 0-5
   - **vep* – Valid Events Processed – Number of events actually processed by the flight software

   For electron data:
   - **vee* – Valid Energy Events – Total number of events in all SSD (Energy) detectors.

   For ion data types:
   - **start0anode, *stop0anode* – Number of pulses on the end of the Start or Stop anode nearest to look direction 0
   - **pulseheight* – Number of events above TOF pulse height threshold
   - **vtofxee* – Number of valid ExTOF events counted.
   - **vtofxphe* – Number of valid PHxTOF events counted.

As of Summer 2021 (see §0.h.i), the EIS data variables listed in Exhibits 19-24 all include the following <eis_prefix> = mms<#>_epd_eis_<DATA_RATE>_l2, where <#> is the spacecraft number and <DATA_RATE> is the sampling mode ("srvy" or "brst").

6.5.6 File Structure L2 EIS PHxTOF

Data Parameter	Description	Units
Time_Minus	<support data> Delta from measurement window start to midpoint	s
Time_Plus	<support data> Delta from midpoint to measurement window end	s
<eis_prefix>_phxtof_duration	<support data> Total exposure time for accumulation	s
<eis_prefix>_phxtof_deadtime	<support data> Instrument deadtime	s

<eis_prefix>_phxtof_largepixel	<support data> Instrument large pixel in use (yes/no)	-----
<eis_prefix>_phxtof_starttai	<support data> Begin measurement window, TAI since 1958	s
<eis_prefix>_phxtof_midtai	<support data> Nominal measurement time, TAI since 1958	s
<eis_prefix>_phxtof_endtai	<support data> End measurement window, TAI since 1958	s
<eis_prefix>_phxtof_spin	<support data> Spacecraft spin number	-----
<eis_prefix>_phxtof_sector	<support data> Spacecraft spin sector	-----
<eis_prefix>_phxtof_quality	<support data> Quality word	-----
<eis_prefix>_phxtof_proton_P<X>_counts_t<#>	Individual telescope (look direction) proton counts for each energy channel	counts
<eis_prefix>_phxtof_proton_P<X>_cps_t<#>	Individual telescope (look direction) proton counts per second for each energy channel	1/s
<eis_prefix>_phxtof_proton_P<X>_flux_t<#>	Individual telescope (look direction) proton intensity (flux) for each energy channel	1/(cm^2-s-sr-keV)
<eis_prefix>_phxtof_oxygen_P<X>_counts_t<#>	Individual telescope (look direction) oxygen (charge state unmeasured) counts for each energy channel	counts
<eis_prefix>_phxtof_oxygen_P<X>_cps_t<#>	Individual telescope (look direction) oxygen (charge state unmeasured) counts per second for each energy channel	1/s
<eis_prefix>_phxtof_oxygen_P<X>_flux_t<#>	Individual telescope (look direction) oxygen (charge state unmeasured) intensity (flux) for each energy channel	1/(cm^2-s-sr-keV)
<eis_prefix>_phxtof_dump_counts_t<#>	Individual telescope (look direction) ion counts dump bin for each energy channel	counts
<eis_prefix>_phxtof_dump_cps_t<#>	Individual telescope (look direction) ion counts per second dump bin for each energy channel	1/s
<eis_prefix>_phxtof_dump_flux_t<#>	Individual telescope (look direction) ion intensity (flux) dump bin for each energy channel	-----
<eis_prefix>_phxtof_pitch_angle_t<#>	Pitch angle for individual telescope (look direction)	degrees
<eis_prefix>_phxtof_look_t<#>	Look direction vector in GSE for individual telescope	-----
<eis_prefix>_phxtof_b	Magnetic field in BCS coordinates	nT
<eis_prefix>_phxtof_position_gse	Spacecraft position vector in GSE	km
<eis_prefix>_phxtof_position_gsm	Spacecraft position vector in GSM	km
<eis_prefix>_phxtof_moon_gse	Spacecraft-to-moon vector in GSE	km
<eis_prefix>_phxtof_sc_to_gse	Transformation matrix from SC to GSE coordinates	-----
<eis_prefix>_phxtof_gse_to_gsm	Transformation matrix from GSE to GSM coordinates	-----
<eis_prefix>_phxtof_r	Magnitude of radial distance	km
<eis_prefix>_phxtof_l	L-shell value (dipole approximation)	-----
<eis_prefix>_phxtof_gse_lat	Latitude in GSE frame	degrees

<eis_prefix>_phxtof_gse_lon	Longitude in GSE frame	degrees
<eis_prefix>_phxtof_gsm_lat	Latitude in GSM frame	degrees
<eis_prefix>_phxtof_gsm_lon	Longitude in GSM frame	degrees
<eis_prefix>_phxtof_sm_lat	Latitude in SM frame	degrees
<eis_prefix>_phxtof_sm_lon	Longitude in SM frame	degrees
<eis_prefix>_phxtof_orbit_num	Orbit number	degrees
<eis_prefix>_phxtof_ssd<#>	Raw count rate from individual SSD	1/s
<eis_prefix>_phxtof_vep	Number of electron events processed and binned by onboard processor per second	1/s
<eis_prefix>_phxtof_start0anode	Count rate from all start anode regions	1/s
<eis_prefix>_phxtof_stop0anode	Count rate from all stop anode regions	1/s
<eis_prefix>_phxtof_pulseheight	Count rate from all start anode regions that satisfy a minimum MCP pulse height	1/s
<eis_prefix>_phxtof_vtofxee	Number of valid energy by time-of-flight (ExTOF) events per second	1/s
<eis_prefix>_phxtof_vtofxphe	Number of valid pulse height by time-of-flight (PHxTOF) events per second	1/s

Table 6-7 List of the Variables Included in the L2 EIS phxtof Burst Data Product

Data Parameter	Description	Units
Time_Minus	<support data> Delta from measurement window start to midpoint	s
Time_Plus	<support data> Delta from midpoint to measurement window end	s
<eis_prefix>_phxtof_duration	<support data> Total exposure time for accumulation	s
<eis_prefix>_phxtof_deadtime	<support data> Instrument deadtime	s
<eis_prefix>_phxtof_largepixel	<support data> Instrument large pixel in use (yes/no)	-----
<eis_prefix>_phxtof_starttai	<support data> Begin measurement window, TAI since 1958	s
<eis_prefix>_phxtof_midtai	<support data> Nominal measurement time, TAI since 1958	s
<eis_prefix>_phxtof_endtai	<support data> End measurement window, TAI since 1958	s
<eis_prefix>_phxtof_spin	<support data> Spacecraft spin number	-----
<eis_prefix>_phxtof_sector	<support data> Spacecraft spin sector	-----
<eis_prefix>_phxtof_quality	<support data> Quality word	-----
<eis_prefix>_phxtof_proton_P<X>_counts_t<#>	Individual telescope (look direction) proton counts for each energy channel	counts
<eis_prefix>_phxtof_proton_P<X>_cps_t<#>	Individual telescope (look direction) proton counts per second for each energy channel	1/s
<eis_prefix>_phxtof_proton_P<X>_flux_t<#>	Individual telescope (look direction) proton intensity (flux) for each energy channel	1/(cm2-s-sr-keV)

<eis_prefix>_phxtof_oxygen_P<X>_counts_t<#>	Individual telescope (look direction) oxygen (charge state unmeasured) counts for each energy channel	counts
<eis_prefix>_phxtof_oxygen_P<X>_cps_t<#>	Individual telescope (look direction) oxygen (charge state unmeasured) counts per second for each energy channel	1/s
<eis_prefix>_phxtof_oxygen_P<X>_flux_t<#>	Individual telescope (look direction) oxygen (charge state unmeasured) intensity (flux) for each energy channel	1/(cm2-s-sr-keV)
<eis_prefix>_phxtof_dump_counts_t<#>	Individual telescope (look direction) ion counts dump bin for each energy channel	counts
<eis_prefix>_phxtof_dump_cps_t<#>	Individual telescope (look direction) ion counts per second dump bin for each energy channel	1/s
<eis_prefix>_phxtof_dump_flux_t<#>	Individual telescope (look direction) ion intensity (flux) dump bin for each energy channel	-----
<eis_prefix>_phxtof_pitch_angle_t<#>	Pitch angle for individual telescope (look direction)	degrees
<eis_prefix>_phxtof_look_t<#>	Look direction vector in GSE for individual telescope	-----
<eis_prefix>_phxtof_b	Magnetic field in BCS coordinates	nT
<eis_prefix>_phxtof_position_gse	Spacecraft position vector in GSE	km
<eis_prefix>_phxtof_position_gsm	Spacecraft position vector in GSM	km
<eis_prefix>_phxtof_moon_gse	Spacecraft-to-moon vector in GSE	km
<eis_prefix>_phxtof_sc_to_gse	Transformation matrix from SC to GSE coordinates	-----
<eis_prefix>_phxtof_gse_to_gsm	Transformation matrix from GSE to GSM coordinates	-----
<eis_prefix>_phxtof_r	Magnitude of radial distance	km
<eis_prefix>_phxtof_l	L-shell value (dipole approximation)	-----
<eis_prefix>_phxtof_gse_lat	Latitude in GSE frame	degrees
<eis_prefix>_phxtof_gse_lon	Longitude in GSE frame	degrees
<eis_prefix>_phxtof_gsm_lat	Latitude in GSM frame	degrees
<eis_prefix>_phxtof_gsm_lon	Longitude in GSM frame	degrees
<eis_prefix>_phxtof_sm_lat	Latitude in SM frame	degrees
<eis_prefix>_phxtof_sm_lon	Longitude in SM frame	degrees
<eis_prefix>_phxtof_orbit_num	Orbit number	degrees
<eis_prefix>_phxtof_ssd<#>	Raw count rate from individual SSD	1/s
<eis_prefix>_phxtof_vep	Number of electron events processed and binned by onboard processor per second	1/s
<eis_prefix>_phxtof_start0anode	Count rate from all start anode regions	1/s
<eis_prefix>_phxtof_stop0anode	Count rate from all stop anode regions	1/s
<eis_prefix>_phxtof_pulseheight	Count rate from all start anode regions that satisfy a minimum MCP pulse height	1/s

<eis_prefix>_phxtof_vtofxee	Number of valid energy by time-of-flight (ExTOF) events per second	1/s
<eis_prefix>_phxtof_vtofxphe	Number of valid pulse height by time-of-flight (PHxTOF) events per second	1/s

Table 6-8 List of the Variables Included in the EIS phxtof Survey Data Product

6.5.7 Level 3 EPD Products

The variables contained within the EPD Level-3 products available from the MMS Science Data Center (SDC), are outlined in Exhibits 37-38 below. All of these variables begin with either,

<feeps_l3_prefix> = mms<#>_epd_feeps_<DATA_RATE>_l3_ OR
<eis_l3_prefix> = mms<#>_epd_eis_<DATA_RATE>_l3_,

where <#> is the spacecraft number and <DATA_RATE> is the telemetry mode ("srvy" or "brst"). The data files from each MMS spacecraft will include the variables below from both that spacecraft as well as combined across all available spacecraft ("mmsx").

Data Parameter	Description	Units
<feeps_prefix>_electron_intensity_omni	Omni-directional (averaged over all eyes/sensors) intensity (flux) from FEEPS	1/(cm2-s-sr-keV)
<feeps_prefix>_electron_intensity_omni_###-###keV_pad	3-sample smoothed omni-directional pitch angle distribution for specified FEEPS energy channel(s)	1/(cm2-s-sr-keV)
<feeps_prefix>_electron_intensity_omni_integral_gt##kev_pad	3-sample smoothed omni-directional pitch angle distribution for all FEEPS energies above specified value	1/(cm2-s-sr-keV)
<feeps_prefix>_electron_SCincluded	Binary indicator of which S/C FEEPS data are included in the MMS-X products	-----
<eis_prefix> electron_flux_omni	Omni-directional (averaged over all telescopes) intensity (flux) from EIS	1/(cm2-s-sr-keV)
<eis_prefix>_electron_flux_omni_###-###keV_pad	Omni-directional pitch angle distribution for specified EIS energy channel(s)	1/(cm2-s-sr-keV)
<eis_prefix>_electron_SCincluded	Binary indicator of which S/C EIS data are included in the MMS-X products	-----

Table 6-9 List of the Variables in the L3 EPD Electron Survey and Burst Data Products [the only differences in the variables is the <DATA_RATE> in the prefix]

Data Parameter	Description	Units
<feeps_prefix>_ion_intensity_omni	Omni-directional (averaged over all eyes/sensors) intensity (flux) from FEEPS	1/(cm2-s-sr-keV)

<feeps_prefix>_ion_intensity_omni_###-###keV_pad	3-sample smoothed omni-directional pitch angle distribution for energy channel(s) specified by range from FEEPS	1/(cm2-s-sr-keV)
<feeps_prefix>_ion_intensity_omni_integral_gt##kev_pad	3-sample smoothed omni-directional pitch angle distribution for all energies above specified value from FEEPS	1/(cm2-s-sr-keV)
<feeps_prefix>_ion_Scincluded	Binary indicator of which S/C FEEPS data are included in the MMS-X products	-----
<eis_prefix>_extof_proton_flux_omni	Omni-directional (averaged over all telescopes) intensity (flux) from EIS	1/(cm2-s-sr-keV)
<eis_prefix>_extof_helium_flux_omni	Omni-directional (averaged over all telescopes) intensity (flux) from EIS	1/(cm2-s-sr-keV)
<eis_prefix>_extof_oxygen_flux_omni	Omni-directional (averaged over all telescopes) intensity (flux) from EIS	1/(cm2-s-sr-keV)
<eis_prefix>_extof_###-###keV_proton_flux_omni_pad	Omni-directional pitch angle distribution for energy channel(s) specified by range from EIS	1/(cm2-s-sr-keV)
<eis_prefix>_extof_###-###keV_helium_flux_omni_pad		
<eis_prefix>_extof_###-###keV_oxygen_flux_omni_pad		
<eis_prefix>_phxtof_proton_flux_omni	Omni-directional (averaged over all telescopes) intensity (flux) from EIS	1/(cm2-s-sr-keV)
<eis_prefix>_phxtof_###-###keV_proton_flux_omni_pad	Omni-directional pitch angle distribution for energy channel(s) specified by range from EIS	1/(cm2-s-sr-keV)
<eis_prefix>_combined_proton_flux_omni	Omni-directional (averaged over all telescopes) intensity (flux) from EIS	1/(cm2-s-sr-keV)
<eis_prefix>_combined_###-###keV_proton_flux_omni_pad	Omni-directional pitch angle distribution for energy channel(s) specified by range from EIS	1/(cm2-s-sr-keV)
<eis_prefix>_ion_SCincluded	Binary indicator of which S/C EIS data are included in the MMS-X products	-----

Table 6-10 List of the Variables Included in the L3 EPD Ion Survey Data Product

Data Parameter	Description	Units
<feeps_prefix>_ion_intensity_omni	Omni-directional (averaged over all eyes/sensors) intensity (flux) from FEEPS	1/(cm2-s-sr-keV)
<feeps_prefix>_ion_intensity_omni_###-###keV_pad	3-sample smoothed omni-directional pitch angle distribution for energy channel(s) specified by range from FEEPS	1/(cm2-s-sr-keV)

<feeps_prefix>_ion_intensity_omni_integral_gt##kev_pad	3-sample smoothed omni-directional pitch angle distribution for all energies above specified value from FEEPS	1/(cm2-s-sr-keV)
<feeps_prefix>_ion_SCincluded	Binary indicator of which S/C FEEPS data are included in the MMS-X products	-----
<eis_prefix>_extof_proton_flux_omni	Omni-directional (averaged over all telescopes) proton energy-by-TOF intensity (flux) from EIS	1/(cm2-s-sr-keV)
<eis_prefix>_extof_helium_flux_omni	Omni-directional (averaged over all telescopes) helium energy-by-TOF intensity (flux) from EIS	1/(cm2-s-sr-keV)
<eis_prefix>_extof_oxygen_flux_omni	Omni-directional (averaged over all telescopes) oxygen energy-by-TOF intensity (flux) from EIS	1/(cm2-s-sr-keV)
<eis_prefix>_extof_###-###keV_proton_flux_omni_pad	Omni-directional proton energy-by-TOF pitch angle distribution for energy channel(s) specified by range from EIS	1/(cm2-s-sr-keV)
<eis_prefix>_extof_###-###keV_helium_flux_omni_pad	Omni-directional helium energy-by-TOF pitch angle distribution for energy channel(s) specified by range from EIS	
<eis_prefix>_extof_###-###keV_oxygen_flux_omni_pad	Omni-directional oxygen energy-by-TOF pitch angle distribution for energy channel(s) specified by range from EIS	
<eis_prefix>_phxtof_proton_flux_omni	Omni-directional (averaged over all telescopes) proton pulse height-by-TOF intensity (flux) from EIS	1/(cm2-s-sr-keV)
<eis_prefix>_phxtof_###-###keV_proton_flux_omni_pad	Omni-directional proton pulse height-by- TOF pitch angle distribution for energy channel(s) specified by range from EIS	1/(cm2-s-sr-keV)
<eis_prefix>_combined_proton_flux_omni	Omni-directional (averaged over all telescopes) proton combined pulse height-by-TOF and energy-by-TOF intensity (flux) from EIS	1/(cm2-s-sr-keV)
<eis_prefix>_combined_###-###keV_proton_flux_omni_pad	Omni-directional proton combined pulse height-by-TOF and energy-by-TOF pitch angle distribution for energy channel(s) specified by range from EIS	1/(cm2-s-sr-keV)
<eis_prefix>_ion_Scincluded	Binary indicator of which S/C EIS data are included in the MMS-X products	-----
mms<#>_epd_brst_fast_ion_flux_omni	Omni-directional total ion intensity (flux) combined from EIS (protons only) and FEEPS	1/(cm2-s-sr-keV)
mms<#>_epd_brst_fast_ion_###-###keV_pad	Omni-directional total ion pitch angle distribution for energy channel(s) specified by range combined from EIS (protons only) and FEEPS	1/(cm2-s-sr-keV)

Table 6-11 List of the Variables in the L3 EPD Ion Burst Data Product

6.6 APPENDIX A- EIS REFERENCES

The following documents and drawings in effect on the day this specification was signed **shall** apply to the extent specified herein. In the event of conflict between this document and any referenced document, the document with latest publication date will govern.

The following is a list of applicable references and publications.

Section	Document Number	Title	Revision/Date
	https://doi.org/10.1002/2017JA024351	Cohen, I. J., Mitchell, D. G., Kistler, L. M., Mauk, B. H., Anderson, B. J., Westlake, J. H., Ohtani, S., Hamilton, D. C., Turner, D. L., Blake, J. B., Fennell, J. F., Jaynes, A. N., Leonard, T. W., Gerrard, A. J., Lanzerotti, L. J., Allen, R. C., Burch, J. L. (2017), Dominance of high-energy (>150 keV) heavy ion intensities in Earth's middle to outer magnetosphere, J. Geophys. Res. SpacePhysics, 122, 9282–9293.	
tbd	461-XXX-XXXX-0###	EPD Data Products Guide	Rev / date
	https://doi.org/10.1007/s11214-014-0055-5	Mauk, B., J. B. Blake, D. N. Baker, J. H. Clemmons, G. D. Reeves, H. E. Spence, S. E. Jaskulek, C. E. Schlemm, L. E. Brown, S. A. Cooper, J. V. Craft, J. F. Fennell, R. S. Gurnee, C. M. Hammock, J. R. Hayes, P. A. Hill, G. C. Ho, J. C. Hutcheson, A. D. Jacques, S. Kerem, D. G. Mitchell, K. S. Nelson, N. P. Paschalidis, E. Rossano, M. R. Stokes, J. H. Westlake (2016a), The Energetic Particle Detector (EPD) Investigation and the Energetic Ion Spectrometer (EIS) for the Magnetospheric Multiscale (MMS) Mission, Space Science Reviews, 199(1-4), 471-514.	

Table 6-12 EIS Applicable Documents

6.7 APPENDIX A- FEEPS REFERENCES

Section	Document Number	Title	Revision/Date

	https://doi.org/10.1007/s11214-015-0163-x	Blake, J., B. H. Mauk, D. N. Baker, P. Carranza, J. H. Clemmons, J. Craft, W. R. Crain Jr., A. Crew, Y. Dotan, J. F. Fennell, R. H. Friedel, L. M. Friesen, F. Fuentes, R. Galvan, C. Ibscher, A. Jaynes, N. Katz, M. Lalic, A. Y. Lin, D. M. Mabry, T. Nguyen, C. Pancratz, M. Redding, G. D. Reeves, S. Smith, H. E. Spence, J. Westlake (2016), The Fly's Eye Energetic Particle Spectrometer (FEEPS) Sensors for the Magnetospheric Multiscale (MMS) Mission, Space Science Reviews, 199(1-4), 309-329.	
tbd	461-XXX-XXXX-0###	EPD Data Products Guide	Rev / date
		EDP Item Name	3.0 / date
	https://doi.org/10.1007/s11214-014-0055-5	Mauk, B., J. B. Blake, D. N. Baker, J. H. Clemmons, G. D. Reeves, H. E. Spence, S. E. Jaskulek, C. E. Schlemm, L. E. Brown, S. A. Cooper, J. V. Craft, J. F. Fennell, R. S. Gurnee, C. M. Hammock, J. R. Hayes, P. A. Hill, G. C. Ho, J. C. Hutcheson, A. D. Jacques, S. Kerem, D. G. Mitchell, K. S. Nelson, N. P. Paschalidis, E. Rossano, M. R. Stokes, J. H. Westlake (2016a), The Energetic Particle Detector (EPD) Investigation and the Energetic Ion Spectrometer (EIS) for the Magnetospheric Multiscale (MMS) Mission, Space Science Reviews, 199(1-4), 471-514.	

Table 6-13 FEEPS Applicable Documents

7.0 FIELDS

7.1 OVERVIEW

The FIELDS instrument suite consists of the Flux Gate Magnetometer (FGM), Search Coil Magnetometer (SCM), Electron Drift Instrument (EDI) and Electric Double Probes (EDP). Command and data handling for all FIELDS instrument are controlled by the FIELDS Command and Data Processing Unit (CDPU), ensuring that the precise time timing between measurements necessary for instrument operations and science data analysis are precisely measured and controlled. This section describes details of the FIELDS timing which are common to each of the FIELDS instruments. During the FIELDS Integration and Timing Test performed on each flight model, all analog and digital timing delays were measured and understood. This information is applied to all FIELDS telemetry processed from Level 0 to Level 1A on computers at the Science Data Center at LASP. Further processing is then performed at FIELDS member institutions, as described in section 8.0 (FGM), section 9.0 (SCM), section 10.0 (EDI) and section 11.0 (EDP).

7.2 FIELDS TIMING

The FIELDS CDPU receives a TAI time code and a Pulse Per Second (PPS) tone from the CIDP. The FIELDS CDPU latches the TAI time code and sets the coarse time to this whole second value at the arrival of the Time at the Tone Signal (PPS). The FIELDS CDPU has a free running clock that is used to define the fine time between the PPS tones. FIELDS data packets times are assigned with a combination of TAI (whole second) and FIELDS (fractional second) values.

The TAI and FIELDS clocks rates are different. A clock rate scaling factor (CRSF) between the TAI PPS and FIELDS clock is needed to accurately assign times to the data samples within each data packet. The clock rate scaling factor is approximated using the most frequent, routinely produced FIELDS packet is APID 0x105 packet, which is generated every 4 FIELDS clock seconds, as follows:

Let T1 be the time tag of an APID 0x105 packet. T1 consists of C1 (the latched TAI whole second) and F1 (the fractional second from the FIELDS clock). The actual TAI time corresponding to the T1 time tag can be calculated as

$$T1[TAI] = C1 + f * F1$$

where f is the CRSF between the TAI and FIELDS clocks.

Let T2 be the time tag of the subsequent packet consisting of C2 and F2 portions. The TAI time corresponding to the T2 time tag is

$$T2[TAI] = C2 + f * F2$$

These consecutive packets are 4 FIELDS seconds apart, or 4×f in terms of the TAI clock. Subtracting the TAI times associated with these two packets we get:

$$4f = C2-C1 + f * (F2-F1)$$

Solving for the CRSF produces

$$f = (C2-C1)/(4-(F2-F1)) \text{ or } DeltaC/(4-DeltaF)$$

The CDPU retrieval of the CIDP time code could be delayed by up to 35 microseconds due to the encoding of the PPS, Sun Crossing, and Delphi pulses by the CIDP on a single interface (CIDP_FIELDS_ICD). Also the oscillator frequency on the FIELDS CDPU clock is temperature dependent which can cause the rate to vary by 35 ppm over the temperature range. The rate scaling factor calculation above provides a first order correction for both of these artifacts. The scaling factor applied in FIELDS CDF files is averaged over 10 minutes.

Aside from temperature variation, FIELDS sample spacing should be constant. Therefore, the sample spacing is defined as the last packet time minus the first packet time in an interval divided by the number of samples. Sample times are adjusted by known digital timing delays, as confirmed in the FIELDS FIT test, are used to determine sample time:

sample_time[i] = reference_time + sample[i] * sample_interval - delay

Reference_time is the time tag of the first packet of an interval without mode change or data gap. If there is a gap in packet sequence count, reference time becomes the time tag of the first packet after the sequence count gap for subsequent samples.

7.3 APPENDIX A- FIELDS REFERENCES

Section	Document Number	Title	Revision/Date
	UNH-MMS-CDPUFSWUM-01	FIELDS CDPU Flight Software User Manual	Rev-1.0 / 24 October 2011
	https://lasp.colorado.edu/mms/sdc/public/datasets/fields/FIELDS_MMS_Data_Products_v0.1.pdf	FIELDS MMS Data Products Guide	*0.1*
	https://doi.org/10.1007/s11214-014-0109-8	Torbert, R.B., Russell, C.T., Magnes, W. et al. (2016). The FIELDS Instrument Suite on MMS: Scientific Objectives, Measurements, and Data Products. Space Sci Rev 199, 105–135.	

Table 7-1 FIELDS Applicable Documents

8.0 FLUX GATE MAGNETOMETER (FGM)

8.1 FGM OVERVIEW

The Flux Gate Magnetometer (FGM) measures magnetic field components on three orthogonal axes, by periodically saturating the ferromagnetic ring cores which in turn induce currents in the sense wires that are modulated by the strength of the ambient field. The MMS Flux Gate Magnetometer instrument on each observatory consists of an Analog Fluxgate Magnetometer (AFG) and a Digital Fluxgate Magnetometer (DFG), mounted on the end of two five-meter booms on either side of each observatory. Both AFG and DFG contain the same sensor design (c.f. Figure 8-1), but different electronics units. Electronic units for DFG are provided by the Space Research Institute of the Austrian Academy of Sciences (IWF), and for AFG are provided by the University of California, Los Angeles (UCLA). The instruments form a synchronized, redundant, cross- and inter-spacecraft calibrated pair of magnetometers on each observatory. The details of the instrument design are described in Russell et al. [2016].

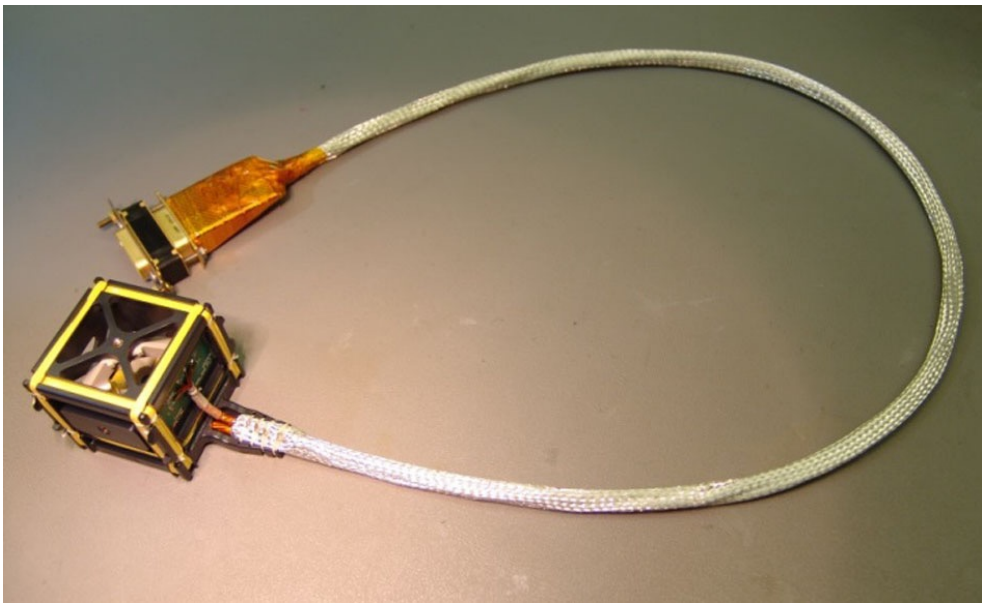

Figure 8-1 Photograph of the Fluxgate Sensor with Pigtail Harness

AFG and DFG represent a redundant system of magnetometers which enable cross-calibration to archive better data accuracy. AFG and DFG measure magnetic fields in two dynamic ranges, low-field and high field, as shown in Table 8-1.

	Low Range	**High Range**
AFG	+/- 510 nT	+/- 8200 nT
DFG	+/-650 nT	+/- 10500 nT

Table 8-1 AFG and DFG Dynamic Ranges

The ranges are commanded by the FIELDS Central Data Processing Unit (CDPU) using an algorithm with hysteresis based on the data from the magnetometer controllers.

- AFG: range change occurs at 450 nT for increasing field and at 400 nT for decreasing field. Two consecutive spins must meet this criterion.

- DFG: range change occurs at 550 nT for increasing field and at 500 nT for decreasing field. Four consecutive spins must meet this criterion.

Both AFG and DFG operate continuously, outputting data at 128 S/s for storage by the spacecraft in a burst memory buffer for later downlink. Meanwhile, FIELDS CDPU decimates this data for continuous survey downlink, but also provides the 128 S/s data in real time to the EDI instrument to enable electron beam steering. DFG employs digital filters to produce the 128 S/s data, which have an inherent real-time delay. In order to ensure meeting the time latency requirements for EDI, DFG was designed to produce data in one of two digital filter length modes: DEC 32, which sacrifices noise performance to achieve shorter delay; and DEC 64, which employs a longer filter length to optimize noise performance.

For AFG, the noise level in high range is ~10 pT/ Hz at 1 Hz, and the noise level in low range is ~5 pT/ Hz at 1 Hz.

For DFG, the noise level in high range is ~100 pT/ Hz at 1 Hz, and the noise level in low range is ~8 pT/ Hz at 1 Hz (DEC 32 mode) or ~5 pT/ Hz at 1 Hz (DEC 64 mode).

8.1.1 Status of FGM Magnetometers

All FGM units continue to operate nominally as of 2021-08-30.

Burst Mode Operations

At the beginning of the science phase, DEC 32 and DEC 64 modes were used on alternate orbits, to ensure that there were no adverse effects on EDI performance when using the DEC 64 mode, which is preferable for science. In March 2016, it was determined that DEC 64 was adequate for EDI operations, and that DFG should remain permanently in that mode. The history of these experimental operations is as follows:

2015-08-31	to 2015-12-13	Alternate orbits in DEC 32/DEC 64
2015-12-13	to 2016-01-18 15:00	Continuously in DEC 64
2016-01-18 15:00	to 2016-03-10 07:00	Alternate orbits in DEC 32/DEC 64
2016-03-10 07:00	to present	Continuously in DEC 64

Note that during periods when alternating from one orbit to the next, MMS4 operates on a schedule opposite to MMS1-3: i.e. MMS4 operates in DEC 32 mode on orbits when the others are in DEC 64, and vice versa.

Survey Mode Operations

In early 2020, the slow survey rate is increased, so that data is gathered continuously at 16 S/s. This mode of operation was first run experimentally on orbits 1059-1061 (2019/11/20-2019/11/27), and then implemented permanently as of orbit 1073 (2020/01/08). This is implemented by re-enabling fast survey mode immediately after the transition to Slow survey mode after each ROI. While this process generally works smoothly, there are occasional short (~10 second) gaps in fast survey data at the end of the ROI. [see section 8.5.2 for survey mode data processing and section 8.4.4 for a known issue with data overlap removal in v5 data products after this change in operations].

Level 2 Data Operations

The Level 2 FGM data product selects the best data suited for general science from AFG and DFG data to produce a single data product.

Currently, this is accomplished by using AFG for all FGM survey data, and DFG is used for all FGM burst data because of DFG's linear phase response.

Data Availability

FGM operates continuously for the full mission, except for times during extended eclipse when all MMS science instruments are powered off.

There have been occasional, brief instrument resets.

Anomalies and gaps in FGM data production are listed in Table 8-2.

Date	Anomaly	Observatory Affected
2015/12/11-12 Orbit 275	FIELDS reboot 23:15:00 - 00:35:00	MMS4
2015/12/12 Orbit 275	FIELDS reboot 00:50:00 - 01:50:00	MMS1
2015/12/12 Orbit 275	FIELDS reboot 02:05:00 - 03:05:00	MMS2
2015/12/12 Orbit 275	FIELDS reboot 03:20:00 - 04:20:00	MMS3
2016/7/12 Orbit 489	FIELDS reboot 21:16:00 – 22:07:00	MMS1
2016/7/19-20 Orbit 496-497	FIELDS reboot 19:41:00 - 05:24:00	MMS4
2016/7/22 Orbit 500	FIELDS reboot 18:23:00 - 19:11:00	MMS2
2016/7/22 Orbit 500	FIELDS reboot 19:56:30 - 22:44:00	MMS3
2017/01/01-04	MMS3 Timing anomaly caused undue errors in attitude/ephemeris. No L2 data available	MMS3
2017/06/08-09 Orbit 761	CDIP anomaly 03:46:16 – 16:20:00	MMS4
2017/06/30 – 2017/07/04 Orbit 769-770	CIDP reset 2017/06/30 03:38:22 – 2017/07/04 03:10:00	MMS4
2018-01-26 14:48:41 – 2018-01-27 19:48:16	0.26 s Navigation Timing anomaly: a slow drift then a reset, resulting in a slight error in spacecraft position.	MMS3
2019/01/13 – 2019/01/15 Orbit 969	S/C Processor Reset Anomaly 2019/01/13 16:35:37 – 2019/01/15 21:12:00	MMS4
2019/06/04 – 2019/06/06 Orbit 1011	S/C Processor Reset Anomaly 2019/06/04 09:16:55 2019/06/06 04:40:00	MMS3
2019/08/17 – 2019/08/28 Orbit 1032-1035	Extended eclipse: Instrument Suite Power Down	all MMS observatories and instruments
2020/04/16 – 2020/04/20	DFG latch-up: no L2 burst data	MMS2

Orbit 1101-1102	2020/04/16 19:21:20 – 2020/04/20 22:20:00	
2020/08/17 – 2020/08/28 Orbit 1132-1135	Extended eclipse: Instrument Suite Power Down	all MMS observatories and instruments
2021/08/01 – 2021/08/13 Orbit 1236-1239	Extended eclipse: Instrument Suite Power Down	all MMS observatories and instruments
2022/07/25 to 2022-08-09 1338-1342	Extended eclipse: Instrument Suite Power Down	all MMS observatories and instruments

Table 8-2 FGM Data Anomalies

8.2 FGM MEASUREMENT STANDARDS, VOLUME, AND TIMING

8.2.1 FGM Requirements

The requirement for the FIELDS Investigation is to measure the 3 axis DC Magnetic Field Vector to an accuracy of 0.1nT. This is achieved by FGM through cross-calibration with EDI. On its own, the FGM shall measure the 3 axis DC magnetic field vector in low range to an accuracy of better than or equal to 0.5 nT, with an accuracy goal of 0.1 nT in low range. The requirement for sensitivity is 0.01 nT/√Hz. The Level 2 data products should be available to the public within 30 days of downlink of the telemetry.

FGM is required to provide preliminary (L2pre) data products for use in the production of EDI, E-field, and particles Level 2 data products. The L2pre AFG and DFG data products provide the magnetic field vector with an accuracy of 1 degree and field magnitude with 1 % accuracy. In small fields where the magnetic field is less than 50 nT, the goal is to achieve 0.5 nT accuracy.

The requirements on the MMS observatory that affect the magnetometer measurement include:

1) at the location of AFG/DFG sensors, the spacecraft magnetic field shall be stable to +/-0.1nT over 4000 seconds.
2) the magnetometer boom stability shall be ±0.1° about each axis during science operations, exclusive of disturbances caused by entry into/exit from umbra,
3) the observatory shall provide sufficient attitude sensor data to enable the ground to calculate spin axis orientation of the observatory relative to ecliptic normal to within ±0.1° (3 sigma) both in sunlight and eclipse, and
4) the observatory shall provide sufficient attitude sensor data to enable the ground to calculate spin phase of the observatory to within ±0.1° (3 sigma).

8.2.2 FGM Coordinate Systems

L2 data is provided in 4 coordinate systems:

- GSE – Geocentric Solar Ecliptic
- GSM – Geocentric Solar Magnetospheric
- BCS – The MMS Body Coordinate System
- DMPA – Despun Major Principal Axis, a spacecraft-specific approximation of the GSE coordinate system. Its X-axis is in the spin plane and nominally points towards the Sun, and the Z-axis is aligned with the Major Principal Axis (MPA), which is typically inclined 3-4° towards the Sun from the ecliptic normal.

Refer to section 3.2 for a general description of MMS coordinate systems and transformation methods. Figure 8-2 shows the relationship of the FGM instrument coordinates relative to spacecraft BCS coordinates.

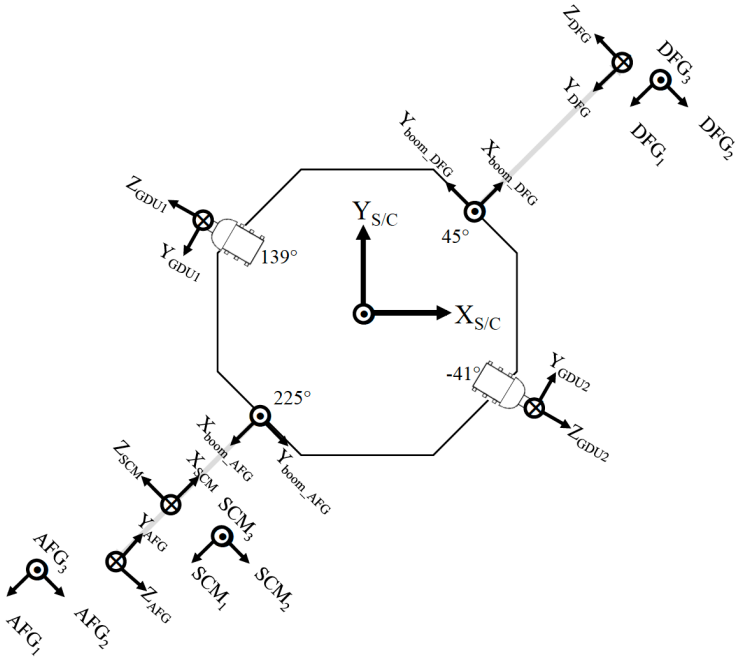

Figure 8-2 The Relationship of AFG and DFG Instrument Coordinates Relative to the MMS S/C (or BCS) Coordinates and Other Magnetic Instrument Coordinates

8.2.3 Accuracy of FGM Time Tags in L2 Data

The time tags of AFG and DFG on the same observatory are obtained from the same synchronous time base defined by the FIELDS independent clock. The FIELDS data packets times are assigned with a combination of TAI at whole second and FIELDS values at fractional second, in the following steps:

1) FIELDS CDPU receives a TAI time code and a Pulse Per Second (PPS) tone from the CIDP;
2) FIELDS CDPU latches the TAI time code and sets the coarse time to this whole second value at the arrival of the time at the PPS tone signal;
3) FIELDS CDPU has a free running clock that is used to define the fine time between the PPS tones. See section 7.0 FIELDS for more details.

In all FGM data products, time tags are center times for the sampling intervals. One time tag is provided for each 3-axis vector measurement. The effective sample times for AFG and DFG are not simultaneous. Timing accuracy relative to other FIELDS instruments is <0.1 millisecond for the spin axis component of each vector.

For DFG, the 3 vector components are sampled simultaneously to better than 100 micro-second, and the frequency response of all channels is identical, as the filters are implemented digitally. The frequency response for DEC 32 and DEC 64 modes are shown in Figure 8-3 and Figure 8-4, respectively. A DEC64/DEC32 flag is available as the mms?_dfg_pfmode (where '?' matches the observatory number, 1, 2, 3, or 4) data quantity in L1A data, but this is not passed on to the L2 data files, as of v5. The planned upcoming v6 L2 FGM data files will include these flags.

For AFG, the 3 channels on each unit are simultaneous to better than 1 millisecond. Differences are due to difference in the frequency response of each channel, as shown in Figure 8-5. The frequency response of each unit, as well as each of the two redundant ADCs have similar, but not identical frequency response, which is well characterized by the Fields Integrated Timing (FIT) tests. The frequency response of the AFG analog filter is comparable to DFG DEC 64 mode. The time tags in the L2 data files are adjusted to correspond to the timing of the Instrument X-axis, which is nominally aligned with the spacecraft spin axis (denoted Z in the MMS coordinate systems). No signal processing is applied to correct the relative the delays between the spin plane channels and the spin axis channel, as this would alter the frequency response of the spin plane components. Further details of FGM timing and frequency response are discussed in Torbert [2014].

Frequency response of both AFG and DFG dominated by a recursive filter implemented in the FIELDS CDPU that is applied to all FGM data, regardless of instrument source (AFG or DFG), instrument mode (low range/high range), or instrument-dependent filtering (DEC32/DEC64 for DFG, ADCA/ADCB for AFG). Timing corrections appropriate to each instrument and each mode of operation are fully characterized by the FIT tests. Each AFG/DFG L0 telemetry data packet contains housekeeping data indicating the instrument mode. UNH L1A processing software applies timing corrections accordingly for each mode.

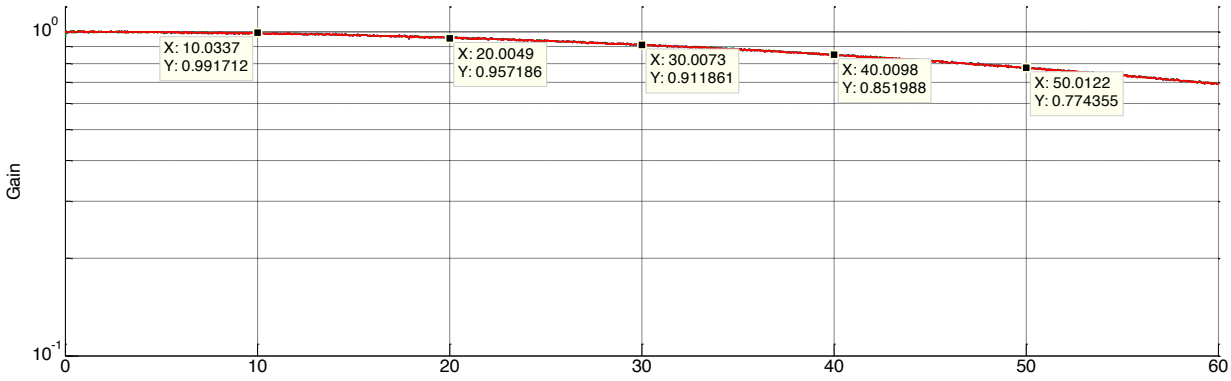

Figure 8-3 Frequency Response for DEC 32 Mode of DFG in Low Range

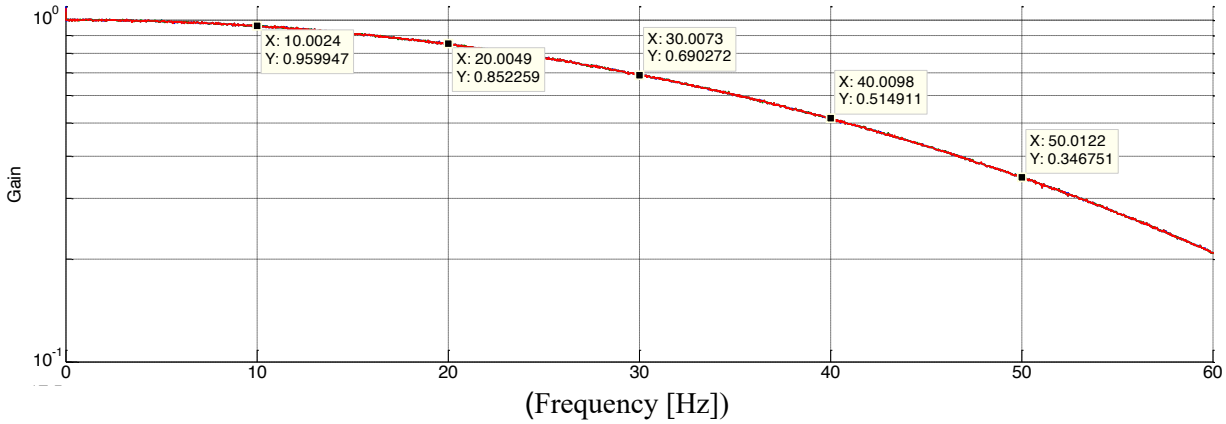

Figure 8-4 Frequency Response for DEC 64 Mode of DFG in Low Range

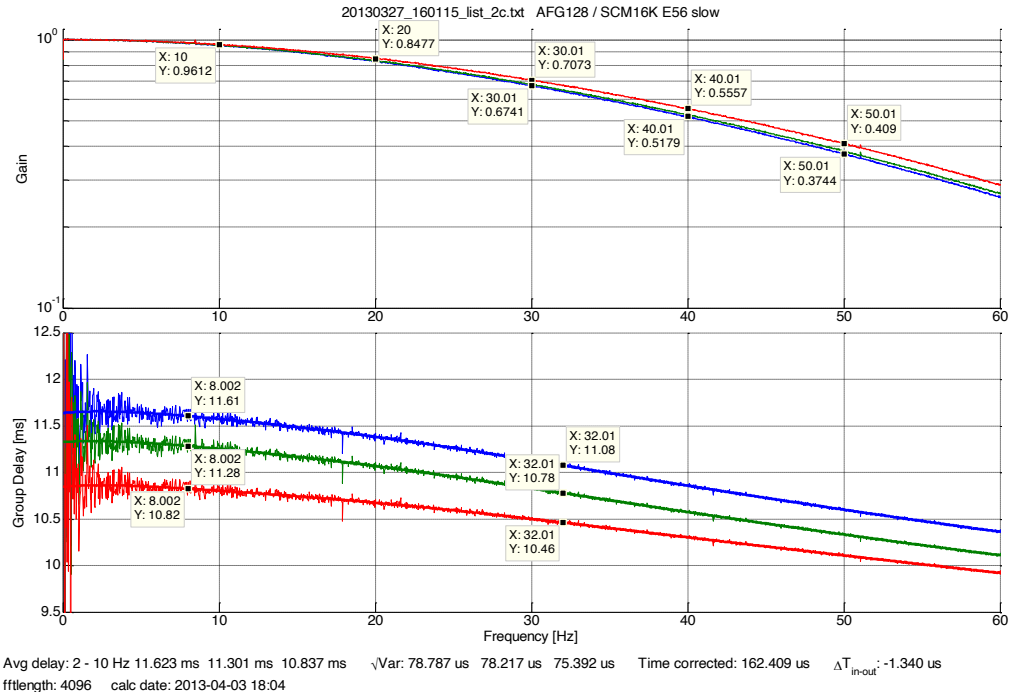

Figure 8-5 AFG FM4 128 S/s Frequency Response for X (Blue), Y (Green), and Z (Red) Instrument Axes

Each FGM unit provides data to the FIELDS CDPU at a fixed rate of 128 samples/sec. These data are stored in burst memory for downlink by command. In addition, the FIELDS CDPU reduces the sample rate to implement fast and slow survey modes for continuous transmission to the ground. Data rates are shown in Table 8-3.

Mode	Sample Rate
Burst	128/sec
Fast Survey	16/sec
Slow Survey	8/sec

Table 8-3 FGM Data Rate Modes

The sampling on different observatories is not synchronized. For calculations using multi-spacecraft data, such as curlometer, the users are recommended to first interpolate the data to the same time stamp.

8.2.4 Data Volume

	Survey		Burst
	SLOW	FAST	
Raw data rate (bit/sec)	60	120	960
Orbit averaged rate (bit/sec)	90* (currently 120)		11.4**

Table 8-4 Raw and Orbit-Averaged Telemetry Downlink Rates for AFG and DFG [*Assuming 50% Duty Cycle for ROI Per Orbit (Current ROI duty cycle is less; however, Fast Survey currently runs at 100% duty cycle). **Assuming 17 Minutes of Burst Downlink/day]

Telemetry is compressed by a factor of 2, and is uncompressed and converted to floating point values in L1A data processing. Data volume for L2 is higher, as it is provided in multiple coordinate systems.

Average data volume per daily L2 survey file: 68 MB

Data volume per L2 burst file:

For first 6 months of science phase, average burst file size was about 1 MB, with an average of 27 burst files per day.

8.3 MAGNETOMETER MEASUREMENT ALGORITHM AND UNCERTAINTY ESTIMATION

8.3.1 Measurement Algorithm

Three components of the magnetic field are measured in the spinning spacecraft frame and are converted into a true vector measurement that can be transformed into geophysical coordinates with the aid of spacecraft attitude measurements. The magnetometer measurements from the three sensor axes need to be corrected by the offsets and gains for each axis, and then by a series of angular corrections illustrated in Figure 8-6. The three sensor axes (marked as $\mathbf{e}_1$, $\mathbf{e}_2$, and $\mathbf{e}_3$) are not exactly orthogonal, thus the first step is to convert the sensor coordinates into an orthogonalized sensor system, with θ_1 being the angle between Z_{Ortho} and $\mathbf{e}_1$, θ_2 being the angle between $\mathbf{e}_2$ and $\mathbf{e}_3$, and ϕ_{12} being the angle between X_{Ortho} and the projection of $\mathbf{e}_2$ in the X-Y_{Ortho} plane. A differential gain factor g_{SP} accounts for the difference in gain between the measurements along the $\mathbf{e}_1$ and $\mathbf{e}_2$ vectors. Step 2 is to align $\mathbf{z}_{\text{Ortho}}$ to the Spin Axis (SA) frame – more properly called the major principal axis (MPA) frame – with s_x and s_y being the projections of $\mathbf{z}_{\text{Ortho}}$ along $\mathbf{x}_{SA}$ and $\mathbf{y}_{SA}$, and θ being the angle between $\mathbf{z}_{SA}$ and $\mathbf{z}_{\text{Ortho}}$. In step 3, the absolute determination of the azimuth, denoted ϕ_{abs}, of $\mathbf{x}_{SA}$ relative to the nominal radial direction of the AFG boom in the spin plane yields the rotation to a boom direction principal axis frame, denoted Orthogonalized Magnetometer Boom (OMB). The gain factors g_{SA_abs} and g_{SP_abs} are applied to the spin axis and spin data, respectively. In step 4, the measurements are transformed into the spinning MMS spacecraft major principal axis (SMPA) frame, by rotating by -225° with respect to the spin axis. Note that the SMPA frame is a close approximation to the BCS frame.* The $\mathbf{B}_{SMPA}$ data is despun to the $\mathbf{B}_{DMPA}$ frame (which is a close approximation to GSE coordinates) using spin phase data provided by the Flight Dynamics and Orbital Analysis (FDOA) branch of GSFC. Finally, the $\mathbf{B}_{DMPA}$ data are transformed into GSE and GSM geophysical coordinates under the assumption that the MPA is aligned with the angular momentum vector provided by the definitive attitude data products.

Full details of this process are discussed in Anderson et al. [2022].

* SMPA differs from BCS only by a $\lesssim 1°$ misalignment of the MPA from the BCS Z-axis. The MPA vector in BCS coordinates is used to transform $\mathbf{B}_{SMPA}$ to the $\mathbf{B}_{BCS}$ data product that is provided in the L2 data files. The most up-to-date measurement of the MPA vector relative to the BCS is found in the INERTIA TENSOR CALIBRATION REPORT (INERTIACAL) generated by the FDOA after each spacecraft maneuver.

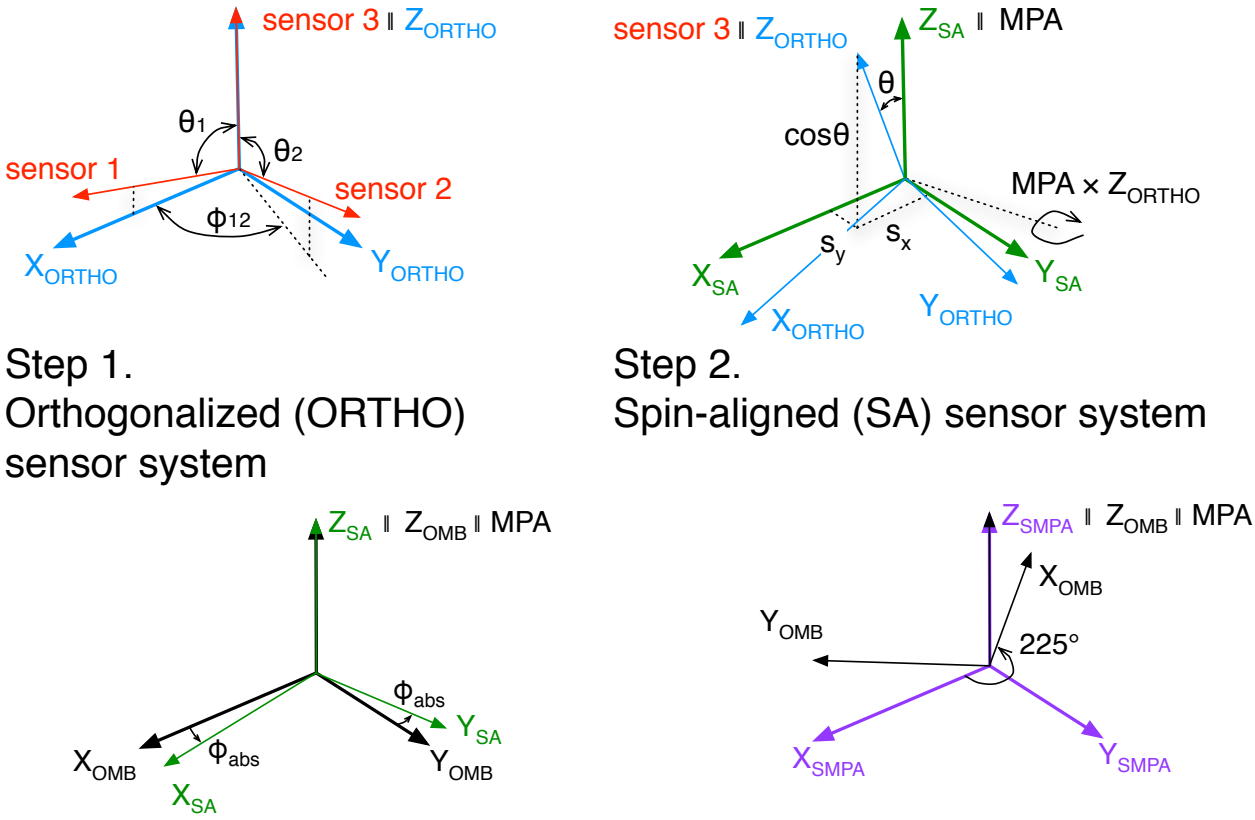

Figure 8-6 Diagram of the Coordinates and Axes Used in the Calibration Process

In the above figure, angles and parameters derived for the calibrations are also shown. Top left panel shows the coordinate system 1-2-3 described by the unit vectors $\hat{e}_1$, $\hat{e}_2$, and $\hat{e}_3$, (cf. Figure 2.1-1 and 2.1-2 of Anderson et al. [2021]). Top right panel shows the spin aligned sensor system, X_{SA}, Y_{SA}, Z_{SA}, and the angle between $\hat{e}_3$ and the spin axis (defined as Z_{SA}) together with the projections of $\hat{e}_3$ in the X_{SA} and Y_{SA} directions. Left bottom panel shows the orthogonal magnetometer boom (OMB) system and its relationship to the SA system consisting of a rotation of ϕ_{abs} about the spin axis, Z_{SA}. The lower right panel shows the definition of the SMPA frame, which is closely aligned with the Body Coordinate System (BCS) of the MMS spacecraft. Rotation from OMB to SMPA consists of a rotation about the spin axis from boom coordinates into spacecraft coordinates

8.3.2 Net Uncertainty Estimation

The sources of uncertainty in the FGM measurements come from the uncertainties in the sensor offsets, gains, and angular parameters. A complete discussion of uncertainty estimation and mathematical equations can be found in Anderson et al. [2023].

The uncertainty due to gains comes from the g_{abs} uncertainty times the background field. The pre-flight gain calibrations are accurate to 0.01% or better [Russell et al., 2016]. Refinements in the gain are typically smaller than this, so while important for resolving offsets, the gains are not major contributors to

the total uncertainty [Plaschke et al., 2019]. In flight, the absolute gain calibrations exhibit apparently random variability between spacecraft of about 0.01%. In the ROI, the magnetic field is ~100 nT so the uncertainty due to gains is on the order of ~10 pT.

The uncertainty due to orientation is also proportional to the background field. The star camera accuracy is 0.01° or better [Tooley et al., 2016] and corrections to the axes orthogonality and sensor orientation relative to pre-flight calibration are typically less than 0.05° their variability, indicative of errors between spacecraft, is less than 0.01°. Hence, in the ROI where the magnetic field is ~ 100 nT, the angular error in the vector orientation is of order 0.01° (10^{-4} radians), so the orientation error is of order 10 pT.

As discussed in detail in section 4 of Anderson et al. [2023], the offsets typically vary by 0.1 to 0.3 nT over an orbit, but variations of up to 1 nT do occur during eclipse epochs when the sensor temperature varies substantially. These variations are determined to somewhat better than ~100 pT. Note the offset error dominates the contributions of the net relative calibration uncertainty and the primary focus of minimizing errors in the inter-spacecraft calibration is on the offsets. Efforts to optimize the gain and orientation calibrations are motivated because of their effects on the offset estimation rather than for their direct influence on the uncertainties.

8.4 FGM CALIBRATION AND VALIDATION

Ground and in-flight calibrations determine the twelve calibration parameters defined in section 8.3.1, which include the six angular parameters defined in Figure 8-6, the offsets on each sensor axes (o_1, o_2 and o_3), the relative and absolute gains in spin plane (g_{SA_abs}, g_{SP}) and the absolute gain along spin axis (g_{SP_abs}).

The methods of pre-flight calibration are discussed in Russell et al. [2016]. The application of these pre-flight calibrations to the data, and the methods of in-flight calibration are discussed in Anderson et al. [2023].

8.4.1 Pre-Flight Calibration / On-Ground Calibration

To assure intra-sensor timing knowledge, an extensive suite of calibrations was conducted as part of the FIELDS Interference and Timing (FIT) campaign [Torbert et al., 2014]. The phase and gain curves versus frequency, and the relative timing delay as compared to other FIELDS instruments were measured with 10 microsecond accuracy for each of the of the AFG and DFG sensor channels. These calibration data show that both the AFG and DFG have the capability to measure the DC and low frequency component of the vector magnetic field over the full range of each magnetometer with a timing accuracy of better than 0.1 ms. Timing corrections were determined for each flight unit, for each data rate (Burst, Fast/Slow Survey), digital filter length (for DFG only) and magnetic field range (High/Low). These timing calibrations are applied in L1A data, as described in section 8.5.2.

An extensive magnetic cleanliness program for the MMS satellite system was supervised and validated by the magnetometer team, as described in Russell et al. [2016]. Pre-flight measurements of spacecraft-generated magnetic fields at the sensor locations were compared with in-flight observations of the instrument offsets [Anderson et al., 2023].

As described in Russell et al. [2016], extensive calibration and cross-calibration of the magnetometers was undertaken by Technical University Braunschweig, Germany, at the magnetic coil facility MAGNETSRODE, as well as at the μ-metal chamber at UCLA. Gain (sensitivity) versus sensor temperature and electronic temperature, non-linearity of the gain, as well as alignment as a function of

sensor temperature is determined. These measurements are determined for high range and low range on each unit, as cross-talk characteristics may differ between ranges.

8.4.2 In-Flight Calibration

The FGM in-flight calibration methods are described in Russell et al. [2016]. Details of implementation have changed, as described or referenced in this document. Anderson et al. [2023] provides a consolidated presentation of the current in-flight calibration process.

In-flight calibrations adjust the 12 parameters of gain, offset and alignment summarized in Table 8-5. These parameters are determined after the pre-flight characterization of gain (as a function of sensor and electronics temperature) and non-linearity (section 8.4.1) have been applied. The 12 calibration parameters must be determined for each field range. On a spin-stabilized spacecraft, 8 of these calibration parameters can be determined independently in 4 pairs: o_1, o_2; s_x, s_y; θ_1, θ_2 and φ_{12}, g_{SP} [Plaschke, Auster et al., 2019]. Bromund et al. [2015] describes how this process is adapted to MMS FGM and performed independently on each magnetic field range. The spin axis offset, o_3, is determined in low range by the EDI method [Plaschke, Nakamura et al., 2014] or Solar Wind Alfven method [Plaschke, 2019] . This offset can be extrapolated to high range, while low range spin axis gain can be extrapolated from high range, where it is determined by comparison with the Earth magnetic field T02 model, along with the absolute spin phase alignment. The in-flight calibration effort is coordinated among three institutions: Goddard Space Flight Center (GSFC), IWF, and UCLA. On a weekly basis, the full magnetometer team (FGM, SCM, EDI) reviews the combined calibration product in a magnetometer conference (or "MagCon") led by UCLA [Bromund et al., 2015].

Orthogonalization and Spin Plane Offsets

As discussed in section 8.3.2, the primary sources of error are the instrument offsets, and these parameters have the largest variability. The spin plane offsets can be evaluated accurately on 15-mintute time windows generally for > 50% of each orbit, while the spin axis offsets can be evaluated accurately on an on an orbit-by-orbit basis. Figure 8-7 gives a sense of the relative magnitude of short- and long-term trends on the offsets in the low range.

		Calibration Parameters	Parameter Names and Time Window		Physical Methods Used	Owner
			Low field range	High Field Range		
CALIBRATION PROCESS	"ORTHOGONALIZATION"	spin plane offsets	o_1, o_2 ~15 min	o_1, o_2 ~2 hour	Minimize spectral power at ωspin in the spin plane.	GSFC
		spin plane gain differential and non-orthogonality	g_{SP}, φ_{12} ~1 day	g_{SP}, φ_{12} ~2 hour	Minimize spectral power at 2ωspin in the spin plane.	
		orthogonality of spin plane sensors relative to spin axis sensor	θ_1, θ_2 >7days	θ_1, θ_2 ~2 hour	Minimize linear regression factor between spin-plane sensor offset (determined by sine fit to each spin) and the spin-axis field.	
		sensor alignment relative to spin axis	s_x, s_y ~1 day	s_x, s_y ~2 hour	Minimize spectral power at ωspin on the spin axis.	
	EDI	spin axis offset	o_3 ~1 day		Electron time of flight method: Electron Drift Instrument (EDI) provides |B| Solar Wind method: optimize o_3 to minimize $\|B_{measured}\|$	IWF
	EARTH FIELD	high range: absolute gains, absolute phase		$g_{SP\ abs}$, g_{SA_abs}, φ_{abs} 1 month	Fit to Data to Earth Field Model using weighted linear regression.	UCLA
	RANGE JOINING and INTERSPACECRAFT	spin axis: low range gain, high range offset	$g_{SA\ abs}$ ~1 month	o_3 ~1 month	Propagate high range gains to low range, cross-calibrating AFG, DFG, 4 observatories. Propagate low range offset to high range.	
		low range spin plane: absolute gain, absolute phase	g_{SP_abs}, φ_{abs} ~1 month		Match gain and phase of low range data to high range data, cross-calibrating AFG, DFG, and the 4 observatories while AFG is in high range and DFG is in low range.	

Table 8-5 In-flight Calibration Methods Listed in the Order of Evaluation [The calibration quantities determined by each method in each gain range are listed, together with the approximate time window required to calculate updates in the calibration files. The calibration effort is divided between three institutions, with each institution taking ownership of a subset of the calibration methods, as shown]

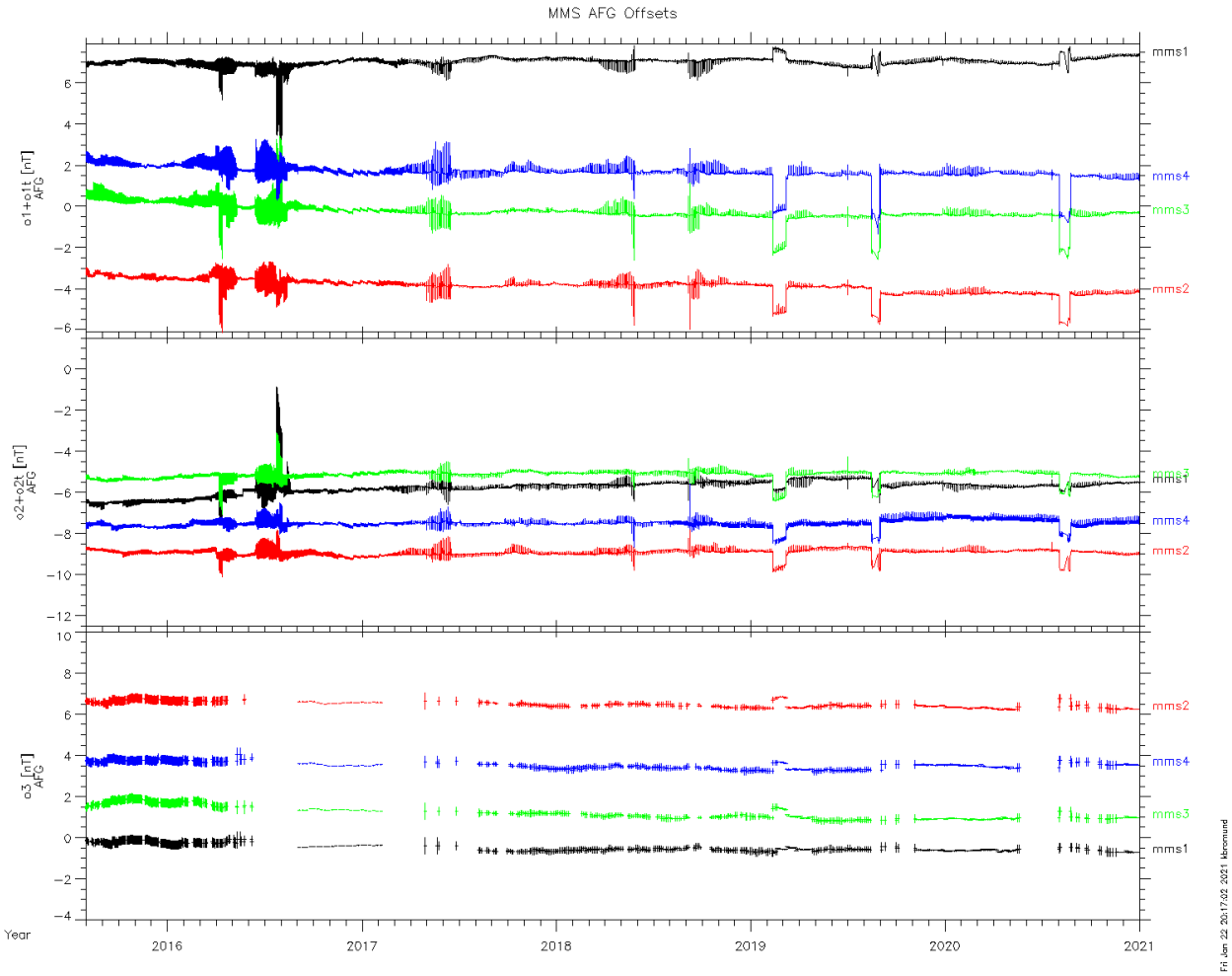

Figure 8-7 Mission Trend of AFG Offsets [DFG shows similar short-term variations and trends. Spin axis offsets (o1+o1t and o2+o2t) show measured (and corrected) short-term offset changes. Error on spin plane offset measurements are <0.05 nT. Error bars are shown on spin axis data to estimate probable level of orbit-scale variations. Note that large changes in spin axis offsets during maneuvers are not always reflected in the o3 measurements due to insufficient data]

As will be documented in Anderson et al. [2023], the quality of the calibration process has improved over the course of the mission primarily because of improved dynamic models for the variations in the offset parameters o_1, o_2 in low range, as well as the dynamic models of the alignment angles $\theta 1$, $\theta 2$. Each of these refinements are cumulative and can be summarized as follows.

1) The dynamic model for o_1, o_2 is a constant value that is updated once each orbit at perigee, and the dynamic model for $\theta 1$, $\theta 2$ is a constant value that is updated once each week. Updates for each interval are based solely on data available during each interval.
2) The model for o_1, o_2 has an additional component that is a function of sensor temperature that is determined empirically in-flight. This accounting for variations as large as 0.5 nT in low range (excluding the larger variations during eclipse), as described in Bromund, et al. [2016].

3) The model for o_1, o_2 has an additional component that is a linear function of electronics temperature (consistent with pre-flight calibrations), accounting for errors as large as 0.2 nT, often during the ROI.
4) The constant component of o_1, o_2 may be updated at times of maneuvers, in addition to each perigee update.
5) Dynamic changes in the $\theta 1$, $\theta 2$ parameters are derived from measured sensor temperature using second order polynomial functions, whose linear and quadratic factors were determined from pre-flight alignment calibrations. Empirical constants added to the polynomial fits and are updated only as necessary to account for variations with time scale > 1 month, as observed in mission trends. This eliminates reliance on data within each 7-day evaluation window, which by late 2016 were found to exhibit bias > 0.02 deg. for periods > 1 month, causing errors >0.2 nT in ~400 nT fields.
6) The constant component of o_1, o_2 may be updated at arbitrary times within an orbit, as required to fit observed dynamic changes on time scales ranging from 1 minute to ~1 day, with magnitudes ranging from 0.05 nT to ~0.3 nT. Such changes become more common later in the mission, but also existed earlier and were not systematically corrected.
7) The model for o_1, o_2 has two additional components that depend on the thermal loading from the Sun and Earth, respectively, on the spin-axis oriented faces of the sensor, as described in Bromund, et al. [2021].
    a. Thermal loading on the sunward-tilted face is related to the sun angle (the angle of the spin axis direction, $\hat{\mathbf{L}}$, relative to the spacecraft-sun direction, $\hat{\mathbf{r}}_S$). The sun angle drifts seasonally with the orbit and is adjusted by ~1 deg. on routine maneuvers to maintain the nominal ~3° sun angle. In addition, spin axis tilt maneuvers increase the sun angle to ~15° during sun tilt maneuvers for extended eclipses (2019 and later). This contributes a component to the offset that is proportional to $\hat{\mathbf{r}}_S \cdot \hat{\mathbf{L}}$. The constants of proportionality are determined empirically.
    b. Thermal loading from Outgoing Longwave Radiation (OLR) from the Earth onto the sensor face that is normal or anti-normal to the spin axis (i.e. the 'top' or 'bottom' of the sensor, respectively). This contributes a component to the offset that is proportional to $(\hat{\mathbf{r}}_E \cdot \hat{\mathbf{L}})/\boldsymbol{r}_E^2$ ie, it is a function of the angle of the spin axis of the spacecraft relative to the direction towards the Earth, $\hat{\mathbf{r}}_E$, and the inverse square of the distance from the Earth, $\boldsymbol{r}_E$. Constants of proportionality are determined empirically for the separate cases of OLR incident on the top or bottom of the sensor.

Spin Axis Offset Calibration

When the EDI instrument operates in Field-mode, the spin axis offset can be determined from the EDI time-of-flight (TOF) method. The TOF is measured from emitting and receiving of time-coded sequences of electron beams perpendicular to the ambient magnetic field, which provides independent measurements of the magnetic field modulus [Plaschke, Nakamura et al., 2014]. When the spacecraft trajectory is in the solar wind, the spin axis offset can also be determined from the Alfven technique, as described in Plaschke [2019]. The Alfven technique uses the intervals when the solar wind perturbations are predominately transverse to the magnetic field (i.e. Alfvenic disturbances), so the spin axis offset can be estimated by minimizing the variability of the field magnitude (i.e. compressional power). The offsets estimated from the TOF method started to become less reliable in Feb 2019, so a combination of TOF method and Alfven method has been implemented. During intervals when neither method is available (e.g. in the tail season), the relative offsets are adjusted to minimize AFG-DFG and inter-spacecraft differences, and absolute offsets are corrected only after a reliable calibration results from either the EDI or Solar Wind method.

Calibration for Absolute Accuracy and Inter-Calibration

The Earth field comparison / range joining process that is described in Russell, et al. [2016] process was updated in the second year of the science operations to improve the inter-calibration of the 4 observatories, and the current process is described as follows.

Earth Field Model Comparison for High Range Data

The measurement near perigee are used to inter-calibrate the magnetometers to the same external field, using the Tsyganenko T02 model with IGRF2015 Earth main field model. The spin axial component and spin component need to be greater than 2000 nT to perform the comparison because earth field model being more accurate in the high field region. And both components need to be less than 8000 nT to avoid the influence of instrument saturation (c.f. Table 8-1). For each instrument, the high range g_{SP_abs}, g_{SA_abs}, φ_{abs} are obtained for each orbit and then averaged over a four-week window to minimize the influence of orbit-to-orbit variations, but keeping the long-term variations. Because all instruments deviate from the reference model by very similar amounts, while the relative difference between each instruments are over an order of magnitude less than the averaged difference between all instruments and the model, the magnetometer team decided to only correct the relative difference between instruments and attribute the averaged difference between all eight instruments and the model to the error in the model rather than the error in the instruments.

Range Joining and Inter-Spacecraft Calibration

In the region where the AFG and DFG magnetometers change from low range to high range the median of the four AFG magnetometers and the four DFG magnetometers are cross-calibrated. In the inbound orbits the AFG magnetometers switch from low range to high range first, and the high range median AFG data are adjusted to match the low range median DFG data by specifying a delta for the median high range AFG offset. The median DFG high range data are then adjusted to match the high range median AFG data. Finally, these changes are propagated back to low range to adjust the median gains and offsets for low range. The individual magnetometers are then adjusted to match the new medians. As a result, for the spin axis data new high range offsets and low range gains and offsets are determined. These methods are performed in GSE coordinates, in order enable inter-spacecraft calibration. The spin plane data are monitored as part of the process, with the primary effect being a misalignment in terms of relative pointing between the different instruments, but this is generally below the 0.1% level, not significant for portions of the orbit where MMS is acquiring fast mode data, and thus the spin plane calibration parameters are not routinely adjusted.

8.4.3 Science Data Assessment (Validation)

There are plasma environments encountered by MMS providing natural conditions suitable to test the accuracy of the calibrated data. The magnetotail lobe has low plasma density and nearly uniform magnetic field, thus the differences in the measurements between MMS spacecraft are dominated by uncertainty in the calibrated data. Another region for testing is in the quiet solar wind, when the field magnitude is low, less than about 5 nT, any residual errors in the calibrated data are more readily identified owing to the small natural magnetic field and its variations.

Figure 8-8 shows an example of an MMS magnetotail pass, and the vertical dashed lines and arrow indicate the northern magnetotail lobe encounter lasting roughly four hours on 14 July 2019. Panel (g) and (h) shows the current density (derived from $\nabla\times\mathbf{B}$), and $\nabla\cdot\mathbf{B}$, and panel (i) shows the magnetic field error estimates, εB_J and εB_{Div}, calculated as the product of spacecraft separation s and the deduced current

density or the divergence of **B**. The εB_{Div} are unambiguously error estimates, but the εB_J are dominated by real currents except in the lobe. Thus in the lobe, the εB_J are considered as an error upper limit since the current density should be very small, but is not identically zero. In this example, εB_J is generally below 60 pT and εB_{Div} is no larger than 30 pT, which indicate the accuracies being better than the 100 pT objective.

Within this figure below, panel (a) shows FGM1 magnetic field data in GSE coordinates from MMS1 and panel (b) shows the field magnitude. Panels c through e are show data from HPCA on MMS1 showing the proton flux versus energy (c), proton density (d), and proton temperature (e). Panel (f) shows the tetrahedron quality factor in black (left axis) and the average MMS separation in red (right axis). Panel (g) shows the current density, J, derived from ∇×B, and panel (h) shows ∇·B both calculated using finite difference derivatives from all four MMS observatories. Bottom panel (i) shows estimates of the magnetic field error estimates, εB_J and εB_{Div}.

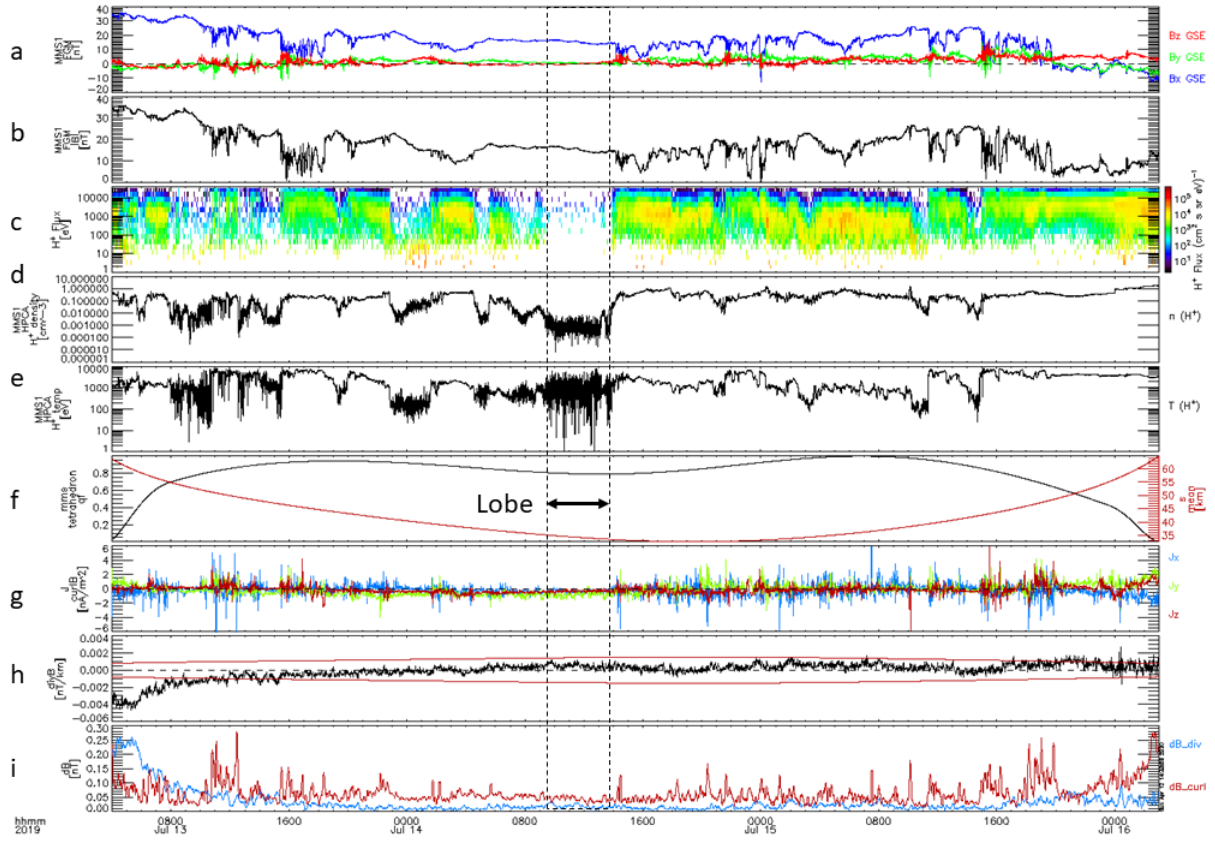

Figure 8-8 Overview of MMS Magnetotail Pass on 13 to 16 July 2019

Similar analysis is performed for the solar wind interval on May 1 to 3, 2019. During close spacecraft separation of 15 to 25 km, εB_J and εB_{Div}, are in the range of 0.1 to 0.2 nT throughout the solar wind interval on 1 and 2 May, indicating that the gradient scale lengths in the solar wind may be sufficiently short to introduce errors in the finite difference gradient calculations. Thus, the curl and divergence error estimates in the solar wind are not useful measures of the data uncertainty. Instead, we use pairwise differences between MMS spacecraft to identify systematic errors. Figure 8-9 shows pairwise differences in the magnetic field for the interval from 08:50 to 09:00 UT on 2 May 2019, which has a steady and weak solar wind magnetic field. The X-GSE and Y-GSE differences have small baseline shifts and a dominant spin tone signal with amplitudes anywhere from below 20 pT to above 50 pT, but below 100

pT. This indicates that errors in the calibrated data in the spin plane, nearly coincident with the GSE X-Y plane, are below 100 pT. The Z-GSE differences indicate consistent offsets between observatories between 0.1 and 0.2 nT for the 1-3 and 3-4 pairs, approaching 0.1 nT for the 1-2, 2-3, and 2-4 pairs, and well below 0.1 nT only for the 1-4 pair. The results for this solar wind interval indicate that on some occasions the calibration process does not achieve the goal of 0.1 nT accuracy.

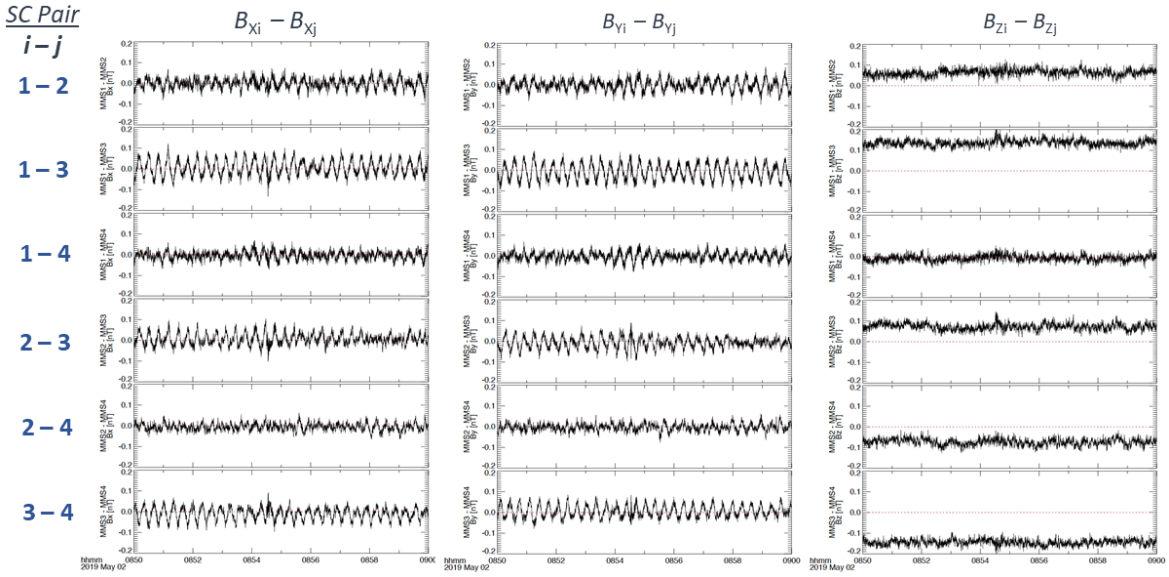

Figure 8-9 Expanded View of the Pairwise Differences in the Magnetic Field for the 08:50 to 09:00 UT Interval on 2 May 2019 Showing Differences in the Magnetic Field for All Three Magnetic Field Components in GSE Coordinates

In general, the FGM L2 data accuracy should meet the 100pT requirement, but there could be intervals having higher data errors. More examples of uncertainty analysis and statistical estimates can be found in section 6 of Anderson et al. [2023]. The next section will discuss the possible causes that limit measurement accuracy.

8.4.4 Known Issues

The known issues with data accuracy fall into the following categories:

Issues requiring improvements to the data processing software that is run at the MMS SDC

The version of the data processing algorithm is recorded in the X-version of the L2 files (c.f. section 8.5.3.4). The version release notes are listed in Table 8-6. The improvements that affect science data are primarily the implementation of new data flags, data overlap issues, and improvements to attitude data processing.

- Data overlap issues after the implementation of continuous 16 S/s survey mode operations (c.f. section 8.1.1) are corrected in v6, but can be corrected by users of v5 data files by inspecting the mms?_fgm_mode_srvy_l2 housekeeping value (c.f. Table 8-10), and removing all data points where mms?_fgm_mode_srvy_l2 is less than 15 S/s.

- Data discontinuities at L2 survey data file boundaries (00:00 UTC). These are due using the average L-vector for 24-hour time period in each data file. As the L-vector typically changes by ~0.05° degree with each perigee pass, jumps of ~0.1 nT can be introduced into data within the ROI. This issue is fixed in v5.
- A 7-minute wobble with amplitude ~0.05° in the effective spin axis, attributed to oscillation of the SDP wire booms after maneuvers. The oscillation decays with a time scale on the order of ~10 hours, when it can result in errors of ~0.1 nT in the measured difference of the magnetic field between separate spacecraft, which can result in errors in current density as calculated by curlometer techniques. This issue is also fixed in v5.
- An 18-second nutation in the spacecraft spin axis, which decays over a period of hours after a maneuver. And has a similar effect as the 7-minute wobble. This is not currently planned to be corrected, but can be anticipated after perigee and times of maneuver.

X-Version	Notes	First Epoch Available as of 2021-11-20	Last Epoch When Used for Production
4	• First version used for public release of L2. • Renamed variables to conform with new MMS variable name guidelines (obs_instr_paramName[_coordSys]_mode_level) o Mag field parameters include 'b' for paramName. o Use 'r' instead of 'pos' for S/C position paramName. o Eliminated 'rate', replaced with 'bdeltahalf'. Added 'rdeltahalf'. o l1a_mode is now just 'mode' • Variable names are not backwards compatible with v3 data files available to MMS instrument teams during commissioning!	2015-09-01	2017-05-05
5	• Y-version number comes from cal file entries. • Ensures there are 2 ephemeris points before/after data to enable proper spline. • Fix to depend_0 of rdeltahalf: fixes bug when reading position data. • L-vector for DMPA2GSE transformation is smoothed with a gaussian filter, instead of using a single average value for the day. This short-term filter avoids introducing artificial jumps at 00:00 UTC and removes 7-minute 'wobble' after maneuvers in the GSE and GSM results. • Fixes error with DEFATT file selection found when choosing the daily DEFATT files to be used in Phase 2. • Fixed bug where reference Etemp was used for high range gain. Now uses measured Etemp.	2016-09-01	TBD
6	• Able to read flag files that are delivered to the SDC together with updated calibration files. New flags implemented by v6 are: MNVR, SHAD, NOISE, OFFST, O3WARN and STWARN. • Add DFG PFMODE flag as support data to indicate DEC 32 mode	TBD	

	• Fix data overlap issues (simultaneous 8 S/s and 16 S/s data) at 'fast/slow' survey mode changes. • Use CDF_REAL8 (double precision) CDF data type for ephemeris data, instead of CDF_REAL4 (single precision float). • Apply temperature dependent gain when converting offsets specified as nT into pseudo-nT before applying calibrations.		

Table 8-6 Data File X-Version Release Notes [See FGM Version Release Notes at the SDC web site Datasets section for latest updates (https://lasp.colorado.edu/mms/sdc/public/datasets/fields/fgm_vrn.txt)]

Issues corrected by improvements to the calibration algorithms:

Calibration methods that help to achieve the FGM accuracy goal of 0.100 nT are incorporated into L2 production as soon as practical. However, reprocessing and validating previous data requires additional effort, and thus these issues may still be present in data versions currently available for earlier epochs. The Y-version number of the L2 files may be used to determine if these processes have been applied to the data in any given file. For a full discussion of the FGM versioning conventions, see section 8.5.3.4. The primary improvements to the calibration process are discussed in section 8.4.2. Table 8-7 lists each of the significant improvements, the Y-version and Epoch when they were first incorporated into L2 processing and the Epoch when they are first available in re-processed data.

Modification to Calibration Process	**Y-version first available in L2**	**Epoch when routinely introduced; (first epoch of data re-processed with this method, if applicable, as of 2022-10-20)**
New data selection criteria avoid periods of rapid temperature change when evaluating θ angles	31 or earlier	2016-05-05 ~00:30
Remove spintone related to changes in Sensor Temperature during each orbit.	43	2016-07-01 18:07:46
Current method for Earth Field Comparison first applied	53	2016-09-01
Remove spintone due to changes in offset baseline when necessary, particularly at maneuvers. (v10)	61	2016-11-18 01:52:28 (2016-09-01)
Manual changes allowed to update the values of s_x and s_y immediately after a maneuver (rather than on the next orbit after the maneuver). Reduces spin tone on the Z-axis on some orbits with maneuvers.	77	2017-03-14
Use mission averages of alignment angles (Theta1, Theta2), replacing weekly evaluations. This can improve the evaluation of the temperature dependence of the offsets, potentially reducing spin tone within the ROI by ~0.05-0.10 nT	86	2017-05-21 16:47:49 (2016-09-01)
Remove spintone related to changes in Electronics Temperature in MMS1 Survey data (AFG).	86	2017-05-21 16:47:49 (2016-09-01)
Range Joining: Spin Axis Gains: evaluated on the interval 2016-08-31 11:05 to 2017-02-10 16:07; Weekly updates of low range spin axis offsets throughout that same interval.	87	2017-06-14 (2016-09-01)

Remove spintone related to changes in Electronics Temperature in Survey data (AFG) for all spacecraft.	138	2018-05-16 11:04:27
Remove spintone due to magnetic offset baseline shifts at arbitrary times, as identified in AFG-DFG differences. This method identifies baseline shifts as small as 0.05 nT, with timing accuracy <60s. even when obscured by variations in the ambient field.	141	2018-05-28 15:38:00
0.14 nT 'Glitches' began to occur randomly in MMS4 Survey (AFG) data as of 2017-09-22. Spin tone amplitude will be enhanced by 0.14 nT for an average of 45 minutes. Glitches recur at random after an average of 10 hours. Durations follow a power law distribution. Glitches that persist longer than 30 seconds are corrected by an automated process.	151	2018-07-31 12:33:06
Solar Wind method used for spin axis offsets, when possible.	181	2019-02-27
Range Joining update of low range spin axis gain, evaluated on interval 2018/11/15T12:58 to 2019/04/23T16:07	188	2019-05-19
Account for offset variations due to Thermal Loading from Earth IR. Reduces spin tone in high fields by ~0.05-0.20 nT and improves evaluation of temperature dependence of the offsets, potentially reducing spin tone within the ROI by 0.05 – 0.1 nT.	304	2021-07-06 19:40:34

Table 8-7 Lists the Y-Version and Epoch of L2 Data at which Improvements to the Calibration or Calibration Process were Introduced to the Calibration File, as well as the Earliest Epoch Reprocessed with these Improvements

Issues that cannot be corrected, but are flagged in L2 data:

Flagged data are not removed from the data files, as they may still be valid and usable for some applications. However, flagged data should not be loaded by L2 data access routines (e.g. mms_load_fgm in SPEDAS) by default. The flags parameter should always be examined to determine whether missing data can be loaded by overriding this default behavior.*

Flagged data issues fall into 3 categories:

- Issues that are flagged in all available L2 data.
- Issues that are tracked and recorded by the FGM team, to be flagged in the v6 data files planned for release in the near future.
- Issues that may persist for an indeterminant amount of time after the flagged intervals. These issues are primarily related to recovery from eclipse or maneuvers.

Currently flagged categories are listed and described in Table 8-8 and the L2 flag format may be found in Table 8-12 in section 8.5.3.6.

* Note that the data quality flag should always be loaded by default, to raise visibility. Unfortunately, the flags parameter is classified as CDF 'support data' in v5 or earlier L2 files, and thus this parameter is not loaded by default by many CDF reader utilities. This will be corrected in v6 data files.

Description of Issue	Method of Flagging	Flag Name (data version availability)
Saturation: The magnetic field exceeds the dynamic range of the instrument. In the early phases of the mission, saturation occurs in high field range at every perigee pass. Low field range saturation is not an issue, due to range change operations implemented automatically by the FIELDS CDPU For each sensor axis.	Data are automatically flagged by the L2 processing software when the raw value of the data contained in the L1A data are equal to the maximum or minimum integer value that can be expressed in the 24-bit ADC output, corresponding approximately to the values expressed in nT in Table 8.1.	B1SAT, B2SAT, B3SAT, (v3+)
Range Change data spikes. Times changes of dynamic range are not precisely flagged in raw data. Data are corrected to the extent possible, but some spikes may remain. Also, any ringing due to anti-alias filtering of the sudden change cannot be corrected.	Data intervals at the times range changes are automatically flag	RANGE (v3+)
Data spikes of ~0.1-0.2 nT that remain after correcting for sudden changes in the offset on one of the spin plane sensors.	Identified by examining differences between AFG and DFG on each spin axis sensor.	OFFST (v6+)
Periods of rapid ~0.1 nT or larger offset shifting. Appears as excess noise in the data. See example in Figure 8-10.	Identified primarily by examining the difference between the fields measured by AFG and DFG, which can be attributed to a specific instrument by comparisons of spectrograms.	NOISE (v6+)
Noise due to thruster solenoid during maneuvers. Data spikes repeating with a 10-second period.	Flagged according to the mission timeline provided by the FDOA.	MNVR (v6+)
Nutation with 18-sec period, decaying with a time constant on the order of 1 hour. Seen as a spin tone in the spin plane.	May be inferred by the presence of the MNVR flag in earlier data	MNVR (v6+)
Excess spin tone due to increased variability of offsets during eclipse.	In v6, shadow periods are automatically identified by the rapid decrease in temperature.	SHAD (v6+)
Spin tone as large as ~0.2 nT on the Z-axis (~ecliptic normal). This is due to the fact that alignment of Sensor 3 with respect to the spin axis is sensitive to temperature. The calibration process does not account for these angular changes, which primarily only affect data in fields larger than typical in the ROI.	In v6, shadow periods are automatically identified by the rapid decrease in temperature. Thus, the initial portion of this issue will be flagged. In all data versions, the sensor temperature parameter STEMP (c.f. Table 8-10) so the user may identify periods of rapidly decreasing temperature.	SHAD (v6+)
Offset on the spin axis significantly larger than 0.10 nT.	Inferred by AFG-DFG and inter-spacecraft comparison, in absence of good EDI or Solar Wind data.	O3WARN (v6+)

Spin tone significantly larger than 0.1 nT may be present: amplitude of spin tone is too variable to be corrected with existing methods.	Inferred by comparison of AFG-DFG, or from observed spin tone.	SPWARN (v6+)

Table 8-8 Known Issues Flagged in FGM Data

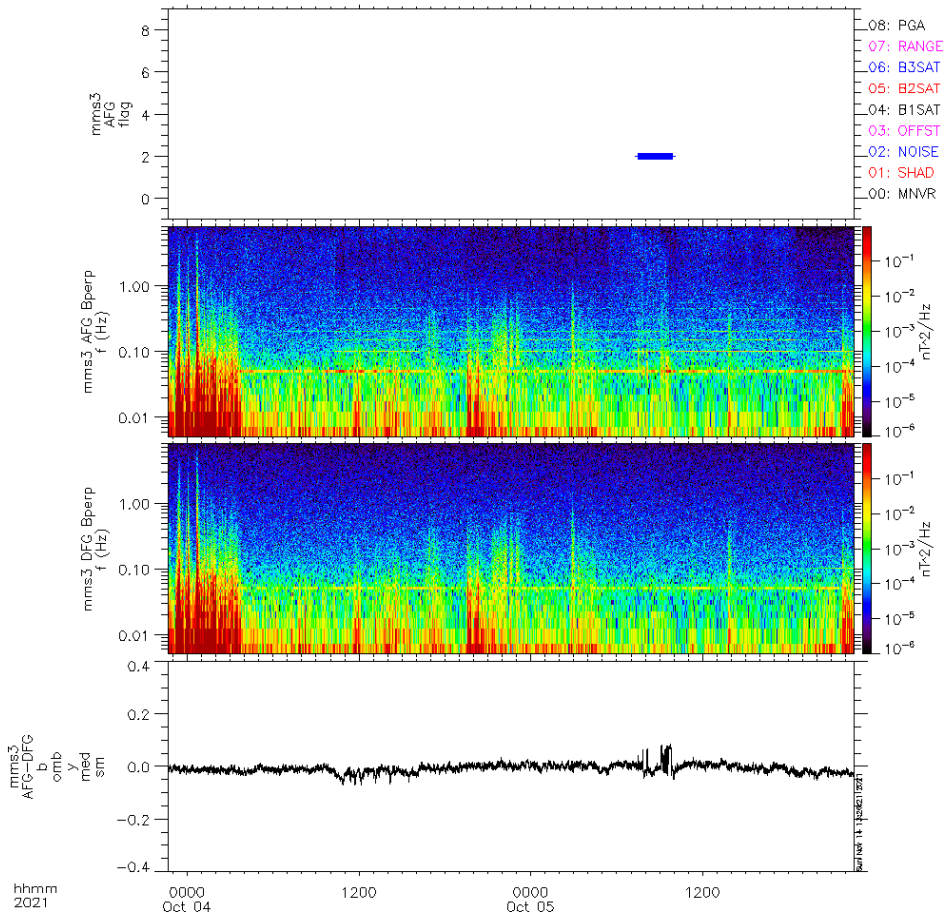

Figure 8-10 Example of an Interval that will be Flagged as NOISE

Regarding the above figure, an interval that will be flagged as NOISE is indicated by the horizontal line on the top panel corresponding to the interval of rapid ~0.1 nT changes in the offset identifiable when examining the difference between the fields measured by AFG and DFG (bottom panel). The second and third panels show the time variation of power spectral density for AFG and DFG, respectively, clearly revealing excess noise only on AFG during that time period. At the same time, there are unusually prominent higher harmonics of the spin tone, as well as distinct periods where broadband noise exceeds the typical AFG noise level of 5 nT/√Hz @ 1Hz by less than a factor of 2, and thus is not flagged. The NOISE flag is set in L2 Survey data (taken from AFG), but not in L2 Burst (taken from DFG).

8.5 FGM DATA PRODUCTION ALGORITHM DESCRIPTIONS

8.5.1 Description of Data Products

FGM Level 2 science products use the best available calibration applied that is available 26 days after receipt. However, revised L2 products will be released if significantly better calibrations become available later in the mission. The rather involved calibration procedure is described in Anderson et al. [2023]. The Level 2 files to not contain the abbreviations “AFG” or “DFG”, instead “FGM” is being used. The data files are processed with final ephemeris, attitude and spin phase information. L2 data are available from 2015, Sep. 01 onwards. Data prior to this date gathered during the MMS commissioning phase were available to the MMS team as preliminary L2 (L2pre) data files.

The FGM data product combines the DFG and AFG data into a single data product, choosing the best data suited for general science. The L2 FGM survey data is taken from the AFG due to consistent low noise (low and high range), but because of the linear phase response (constant group delay) of the DFG, L2 FGM burst data is taken from the DFG.

In addition to the magnetic field measurements, the files contain ephemeris information provided at the intrinsic FDOA product resolution (30 sec). Cubic spline interpolation may be used to interpolate the ephemeris data to the times of the magnetic field measurements for the purpose of deriving spacecraft separation vectors. Enough ephemeris data will be included to allow for proper interpolation of the ephemeris vectors to each magnetic field vector contained within the file. L2 burst and L2 survey data files will always contain at least two ephemeris data points before the start of the data and two ephemeris data points after the end of the data. For example, even if the duration of a burst is only a few seconds, the data file will contain at least 4 ephemeris data points (2 minutes of ephemeris) to allow for a proper cubic spline fit. This may lead to data overlap when concatenating consecutive bursts, but as each burst is downloaded and processed separately, in order for the ephemeris data to always be useful, each burst file must be treated as if there will be no consecutive bursts. [Note: as of 2015/4/18, only one ephemeris vector is guaranteed before and after the magnetometer data. In the worst case, there may be only 2 or 3 ephemeris data points in a short burst file.]

8.5.2 Data Production Algorithms

The algorithms for data production are as follows:

<u>Level 1A (L1A):</u>

- Decompress Level 0 telemetry (c.f. FIELDS CDPU Flight Software User’s Manual)
- Apply a single FIELDS time tag to each vector measurement
- Correct FIELDS time to TAI (c.f. section 7.0 FIELDS)
- Correct for delay of Mag measurement relative to FIELDS time determined from FIT testing
- Convert 24-bit counts are converted floating point pseudo-nT values, by dividing by the following scale factors:
    - AFG low range: -16000
    - AFG high range: 1000
    - DFG low range: 13000
    - DFG high range: 800
- Re-arrange instrument X,Y,Z axes to Sensor 1,2,3 axes. [c.f. Torbert et al. [2014] figure 13]

<u>Level 2 (L2):</u>

The Level 2 process accepts Level 1A as an input, and applies processes in the following sequence:

1. Combine Fast and Slow survey data, removing data overlap:
    - Slow and Fast survey data are separate data products produced by the CDPU, with an intentional overlap between modes to avoid data gaps.
    - The separate Level 1A data products are combined into a single Level 2 survey data product, where each sample is tagged with its source sampling rate.
2. Correct known glitches from pre-flight testing (range change glitches)
3. Post-process housekeeping sensor and electronics temperature data (smoothing filters, glitch removal)
4. Apply pre-flight calibrations for gain (including temperature dependence) and non-linearity
5. Apply In-flight calibration – adjustments to gain, alignment, and offset
6. Flag (but not remove) artifacts identified during in-flight calibration
7. Apply post-processing to definitive attitude (smoothing and interpolation) and ephemeris (Hermite spline interpolation from intrinsic (> 30 sec) resolution)
8. Rotate each vector into spacecraft and geophysical coordinates

Details of these processes are provided in Russell et al. [2016], updated as appropriate by Anderson et al. [2023].

Note that the preliminary L2 data that supports L2 data processing for other instruments are produced with these identical algorithms. The only difference is that the preliminary calibrations have not been updated by comparison with the earth's magnetic field to make (generally minor) adjustments to the instrument gain, and the magnetic offsets on the spin axis have not been updated with either the EDI or Solar Wind method.

8.5.3 L2 File Structure

FGM L2 data files that follow the MMS CDF data format guidelines for variable names and metadata content. Separate files are produced for each spacecraft, MMS1, MMS2, MMS3 and MMS4. In the filenames and variable names listed in this section, replace '#' with 1,2,3, or 4 to correspond to MMS1, MMS2, MMS3 or MMS4, respectively. Separate files are available Survey data and Burst data. The content of Burst and Survey files are the same, however, the parameter names differ in each file. This section lists the parameter names for Survey data files, for burst files, replace '_srvy' with '_brst' in Table 8-9 through Table 8-11.

All L2 data files specify the instrument name as 'fgm'. Note that the L2pre data described in section 8.5.1 is available in the same format as L2 data, except that both AFG and DFG data available in burst as well as survey mode, and the filenames and parameter names differ in that they indicate "afg" or "dfg" rather than "fgm". Note that L2pre data files that were available to the MMS team during the commissioning phase used the v3 data format for parameter names, which is not compatible with the v4 format described in this document.

Notes Regarding Preliminary L2 Commissioning data:

L2pre AFG and DFG files that were available to the MMS team for the commissioning phase used the v3 data format, which is not compatible with the v4 format described in this document, because the variable names are slightly different. These commissioning data were last re-processed on 2015-12-17 using Y-version 11 calibrations.

For significant portions of the commissioning phase, survey data was acquired at 128 samples/second. These survey data are available in L2pre srvy mode files in a decimated format, with a data rate of 16 S/s.

The full resolution 128 S/s data are available only in special ‘iwfl2pre’ CDF files that do not follow the standard filename and variable name conventions. These iwfl2pre files provide data in GSE and GSM coordinates and were processed using the same calibrations as the v3 l2pre commissioning files. They are available in the SDC hierarchy as mode ‘f128’, and level ‘iwfl2pre’.

8.5.3.1 Survey File Conventions

The survey data files combine Slow Survey and Fast Survey data into a single data product. The mms?_fgm_mode_srvy_l2 parameter identifies the whether a given data point was collected in slow survey or fast survey mode, by specifying the precise data rate of the L1A FAST or SLOW survey file from which it was obtained. This floating point parameter will be nearly, but not precisely, equal to 8.0 or 16.0 S/s for SLOW and FAST survey, respectively.

Survey files start at with the first complete packet following the even 00:00:00.000 UTC day boundary, so the file names can be uniquely specified by the Year, Month and Day (yyyyMMdd) of the file start time.

8.5.3.2 Burst File Conventions

Burst data are measured inside the region of interest at specific times and are downlinked with 128 samples per second.

There is one burst file for each burst segment, as defined by the MMS burst memory management. It may be necessary to concatenate multiple burst files to obtain all data for continuous burst intervals that span multiple segments. There is generally more than one burst file per day, so the name of the burst file specifies the start time of the burst, rounded down to the nearest second: yyyyMMddHHmmss.

8.5.3.3 File Name Conventions

File names specify the observatory (Replace ‘#’ with 1, 2, 3, or 4 for MMS1, MMS2, MMS3, or MMS4, respectively), instrument (always fgm for FGM), data mode (srvy for Survey, brst for burst, data level, yyyy for year, MM for Month, dd for day, and version numbers X, Y, Z, as described below in section 8.5.3.4.

Survey Files: mms?_fgm_srvy_l2_yyyyMMdd_vX.Y.Z.cdf

Burst Files: mms?_fgm_brst_l2_yyyyMMddHHmmss_vX.Y.Z.cdf

8.5.3.4 Version Numbering Conventions

Version numbers are specified as vX.Y.Z, following the general MMS guidelines for file versioning. The descriptions of each version level, as specifically interpreted for FGM, are as follows:

- X is the interface number. Increments in X represent a significant change to the format of the file has been made. E.g. new parameters added, or parameters re-named. X also increments upon significant change in the algorithm of the processing software.
- Y is the quality number. This number represents a change in the quality of the data in the file, which would require re-processing of previously processed data. FGM has a slightly non-standard usage of the Y quality number:

  - The Y version number of the calibration increments with each weekly Magnetometer Conference, at which a new calibration file is released. Usually, the only change to the calibration is that the tables are extended to include later epochs. However, a new calibration version Y may also revise previous epochs. These revisions are listed in Table 8-7.
  - Thus, for FGM, a change in Y version from file to the next does not necessarily indicate a better calibration method was used to data released for previous epochs with a lower Y version. This behavior differs between data files with X-version 4 and X-version 5 or higher:
    - X-version 4: Reprocessed data files for a given epoch will have a higher Y-version, even though the calibration for the epoch of the data file has not changed, if the only change to the calibration file was to extend the calibration to later epochs.
    - X-version 5 or higher: The Y-version of a data files corresponds to the sequence number of the Magnetometer Conference at which the calibration for the epochs contained withing the data file was last revised. However, it is possible that the revised calibration methods that result in an increment of the Y-version may not result in a significantly improved calibration for all epochs.
  - Y does not reset to 0 when X increments.
- Z is the revision number. Z is set to 0 the first time a given file is processed, and is incremented each time the file is re-processed for any reason. Z is reset to 0 after X or Y is incremented.

8.5.3.5 L2 File Content

The content of Burst and Survey files are the same. For the Burst parameter names and labels, replace '_srvy' with '_brst' in Table 8-9 through Table 8-11.

The parameters in each CDF file are summarized in Table 8-9, Table 8-10, and Table 8-11. Table 8-9 lists the names of the magnetic field data parameters. Table 8-10 lists the magnetic field housekeeping parameters that are designated as VAR_TYPE = 'support_data'.

The content of Burst and Survey files are the same. For the Burst parameter names and labels, replace '_srvy' with '_brst' in Table 8-9, Table 8-10, and Table 8-11.

Name	Type	Dimension	Labels [description]	Unit
Epoch	CDF_TIME_TT2000	0:[]	TT2000	Nanoseconds, epoch terrestrial time J2000
mms?_fgm_b_gse_srvy_l2	CDF_REAL4	1:[4]	Bx GSE, By GSE, Bz GSE, Bt	nT
mms?_fgm_b_gsm_srvy_l2	CDF_REAL4	1:[4]	Bx GSM, By GSM, Bz GSM, Bt	nT
mms?_fgm_b_dmpa_srvy_l2	CDF_REAL4	1:[4]	Bx DMPA, By DMPA, Bz DMPA, Bt	nT
mms?_fgm_b_bcs_srvy_l2	CDF_REAL4	1:[4]	Bx BCS, By BCS, Bz BCS, Bt	nT
mms?_fgm_flag_srvy_l2 *	CDF_UINT4	0:[]	mms?_fgm_flag_srvy_l2 *	0=good. See Table 8-12 for bit definitions

Table 8-9 L2 Magnetic Field Time Series Data Parameters [All parameters have VAR_TYPE = 'data'. For burst files, replace '_srvy' with '_brst' in the parameter names and labels]. * indicates VAR_TYPE was 'support_data' prior to v6.

Name	Type	Dimension	Labels [description]	Unit
mms?_fgm_hirange_srvy_l2	CDF_UINT1	0:[]	mms?_fgm_hirange_srvy_l2 [high/low magnetic field range]	1=high range, 0=low range
mms?_fgm_stemp_srvy_l2	CDF_FLOAT	0:[]	mms?_fgm_stemp_srvy_l2 [sensor temperature]	C
mms?_fgm_etemp_srvy_l2	CDF_FLOAT	0:[]	mms?_fgm_etemp_srvy_l2 [electronics temperature]	C
mms?_fgm_pfmode_srvy_l2 **	CDF_UINT1	0:[]	mms?_fgm_pfmode_srvy_l2 [DEC mode]	1 = DEC 32 0 = DEC 64
mms?_fgm_mode_srvy_l2	CDF_FLOAT	0:[]	mms?_fgm_mode_srvy_l2 [data rate, accounting for clock drift. Unambiguously identifies the source data mode of a given record, regardless of the output time sequence delta-t.]	Samples/s

Table 8-10 L2 Housekeeping Data Parameters Associated Record-for-Record with the Magnetic Field Data. All parameters are VAR_TYPE='support_data'. For burst files, replace '_srvy' with '_brst' in the parameter names and labels. ** indicates parameters not available prior to v6.

Name	Type	Dimension	Labels	Unit
Epoch_state	CDF_TIME_TT2000	0:[]	TT2000 [time tags for ephemeris data]	Nanoseconds, epoch terrestrial time J2000
mms?_fgm_r_gse_srvy_l2	CDF_REAL8 ***	1:[4]	X GSE, Y GSE, Z GSE, R	Km
mms?_fgm_r_gsm_srvy_l2	CDF_REAL8 ***	1:[4]	X GSM, Y GSM, Z GSM, R	Km
mms?_fgm_rdeltahalf_srvy_l2 *	CDF_FLOAT	0:[]	mms?_fgm_rdeltahalf_srvy_l2 [1/2 delta-t for ephemeris data]	s

Table 8-11 L2 CDF File Ancillary Ephemeris Parameters have VAR_TYPE = 'data', except * indicates VAR_TYPE= 'support_data'. * indicates data type was CDF_REAL4 prior to v6) [For burst files, replace '_srvy' with '_brst' in the parameter names and labels]**

8.5.3.6 Data Flag Definitions

Table 8-12 summarizes the flags that may be applied to the data, identifying the associated bit flags within the 32-bit mms?_fgm_flag_srvy_l2 data quantity. New X-version may implement new flags, so the table also shows the X-version in which each flag is first introduced. Flagged issues are discussed in detail in section 8.4.4.

MNEMONIC	Bit	Meaning	Example Figure	X-Version First implemented
MNVR	00	Maneuver	TBD	6
SHAD	01	Shadow	TBD	6
NOISE	02	Noise (rapid offset shifting).	TBD	6
OFFST	03	Abrupt Offset shift	TBD	6
B1SAT	04	B1 saturated	TBD	2
B2SAT	05	B2 saturated	TBD	2
B3SAT	06	B3 saturated	TBD	2
RANGE	07	Range-change glitch	TBD	2
O3WARN	08	Offset on axis 3 (Spin Axis)	TBD	6
STWARN	09	Spin Tone warning	TBD	6

Table 8-12 List of Types of Flags that may be Applied to the Data [identifying the associated bit flags within the 32-bit word stored in the mms#_fgm_flag_srvy_l2 parameter, and the X-version of the data file when the flag is first available. A bit value of 1 indicates that a given flag is set, so that an overall flag word value of 0 indicates good data]

Flags can be displayed in SPEDAS (Angelopoulos et al., 2019) using the 'bitplot' tplot option, e.g.:

labels = strsplit("MNEM MNVR SHAD NOISE OFFST B1SAT B2SAT B3SAT RANGE O3WARN STWARN")
options, " mms?_fgm_flag_srvy_l2", tplot_routine='bitplot', psyms=1, colors = 'lrbm', labels=labels, yrange=[-1,N_ELEMENTS(labels)]

8.5.3.7 Error Estimation Metadata in CDF Files

No specific CDF metadata are provided to give quantitative estimates of the error of each record. Each CDF file contains the global TEXT attribute that provides a description of the data set, including the current overall error estimate. Data points that may not meet these criteria are flagged, as discussed in section 8.4.4. The format of the flags is defined above in section 8.5.3.6.

8.6 APPENDIX A- FGM REFERENCES

Section	Document Number	Title	Revision/Date
	TBD	Anderson, B. J. et al. (in preparation to be submitted 2023), In-Flight Calibration and Performance of the Magnetospheric Multiscale Fluxgate Magnetometers, *Space Sci. Rev.*	
	https://doi.org/10.1007/s11214-018-0576-4	Angelopoulos, V., Cruce, P., Drozdov, A. *et al.* (2019) The Space Physics Environment Data Analysis System (SPEDAS). *Space Sci Rev* 215, 9.	

	ntrs.nasa.gov/api/citations/20170003856	Bromund, K. R., H. K. Leinweber, F. Plaschke et al., In-Flight Calibration Processes for the MMS Fluxgate Magnetometers, Abstract SM51A-2555 presented at 2015 Fall Meeting, AGU, 14-18 Dec.	
	ntrs.nasa.gov/api/citations/20160014711	Bromund, K. R., F. Plaschke, R. J. Strangeway, B. J. Anderson, B. G. Huang, et al. (2016) In-Flight Calibration Methods for Temperature-Dependent Offsets in the MMS Fluxgate Magnetometers, Abstract SM21A-2455 presented at 2016 Fall Meeting, AGU, 12-16 Dec.	
	agu2021fallmeeting-agu.ipostersessions.com/Default.aspx?s=8F-AB-99-DF-DF-34-6B-3C-29-4D-04-F6-AC-C1-C3-7D	Bromund, K. R., B. G. Huang, B. J. Anderson, et al. (2021), Crucial Role of Thermal Gradients in MMS Fluxgate In-Flight Calibration, Poster SH35D-2103 presented at 2021 Fall Meeting, AGU, 13-17 Dec	
	UNH-MMS-CDPUFSWUM-01	FIELDS CDPU Flight Software User's Manual	Rev-1.0 / 24 October 2011
	lasp.colorado.edu/mms/sdc/public/datasets/fields/FIELDS_MMS_Data_Products_v0.1.pdf	FIELDS MMS Data Products Guide	1.0 / April 20, 2016
	lasp.colorado.edu/mms/sdc/public/datasets/fields/FGM_DataProductsGuide2016Apr20.pdf (superseded by this document)	Leinweber, H. K. et al., The MMS Fluxgate Magnetometers Science Data Products Guide	
	461-SYS-SPEC-0115	MMS Alignment and Coordinate System Document	Rev C/ July 22, 2014

	https://doi.org/10.1088/0957-0233/25/10/105008	Plaschke, F., Nakamura, R., Leinweber, H. K., Chutter, M., Vaith, H., Baumjohann, W., Steller, M., and Magnes, W. (2014) Flux-gate magnetometer spin axis offset calibration using the electron drift instrument, Meas. Sci. Technol., 25, 105008.	
	https://doi.org/10.5194/gi-8-63-2019	Plaschke, F., H. U. Auster, et al. (2019) Advanced calibration of magnetometers on spin-stabilized spacecraft based on parameter decoupling, Geosci. Instrum. Method. Data Syst., 8, 63–76.	
	https://doi.org/10.5194/gi-8-285-2019	Plaschke, F. (2019) How many solar wind data are sufficient for accurate fluxgate magnetometer offset determinations?, Geosci. Instrum. Method. Data Syst., 8, 285–291.	
	https://doi.org/10.1007/s11214-014-0057-3	Russell, C., B. J. Anderson, W. Baumjohann, K. R. Bromund, D. Dearborn, D. Fischer, G. Le, H. K. Leinweber, D. Leneman, W. Magnes, J. D. Means, M. B. Moldwin, R. Nakamura, D. Pierce, F. Plaschke, K. M. Rowe, J. A. Slavin, R. J. Strangeway, R. Torbert, C. Hagen, I. Jernej, A. Valavanoglou, I. Richter (2016), The Magnetospheric Multiscale Magnetometers, Space Science Reviews, 199(1-4), 189-256.	
	https://doi.org/10.1007/s11214-015-0220-5	Tooley, C., R. Black, B. Robertson, J. Stone, S. Pope, and G. Davis (2016), The Magnetospheric Multiscale Constellation, Space Science Reviews, 199(1-4), 23-76.	

	https://doi.org/10.1007/s11214-014-0109-8	Torbert, R.B., Russell, C.T., Magnes, W. et al. (2016). The FIELDS Instrument Suite on MMS: Scientific Objectives, Measurements, and Data Products. Space Sci Rev 199, 105–135.	

Table 8-13 FGM Applicable Documents

9.0 SEARCH COIL MAGNETOMETER (SCM)

9.1 SCM OVERVIEW

The tri-axial search-coil magnetometer (SCM) with its associated preamplifier provides the three-dimensional measurement of the magnetic field fluctuations. The analog magnetic waveforms measured by the SCM are digitized and processed inside the digital signal processor (DSP) together with the electric field data provided by the spin-plane double probe (SDP) and the axial double probe (ADP). Both magnetic and electric field data are collected and stored by the central instrument data processor (CIDP) via the Fields central electronics box (CEB). Magnetic waveforms and spectra are available at different time resolution depending on the selected mode. Finally, the SCM calibration is checked at least once per orbit thanks to the onboard calibration signal provided by DSP and the SCM sensor temperature is measured by a thermistance (housekeeping data). A full description of the design of SCM, its ground calibration results, its in-flight calibration sequence, its operational concept, and an overview of its data products can be found in the publication:

Le Contel, O. et al, **The search-coil magnetometer for MMS**, *Space Sci Rev* **199,** 257–282 (2016). https://doi.org/10.1007/s11214-014-0096-9

Updated information can be found in the SCM data product guide.

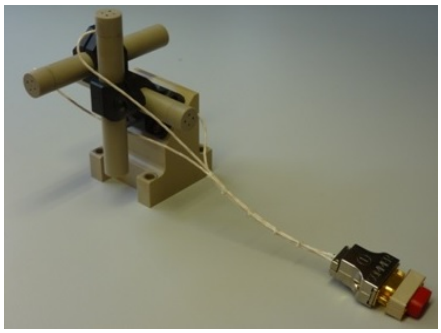

Figure 9-1 SCM Sensor

Figure 9-2 SCM Pre-Amplifier

9.2 AC MAGNETIC FIELD WAVEFORMS (ACB)

9.2.1 Overview

The SCM waveform is sampled at 32 samples per second (S/s) in the survey mode[1], 8192 S/s in the burst mode and finally 16384 S/s in the high-speed burst mode.

9.2.1.1 Heritage

Similar SCM have been previously flown by LPP (or formerly) on many earth-orbiting (GEOS-2, Cluster/STAFF, THEMIS/SCM) and interplanetary (Galileo, Cassini) missions. Multi-chip vertical technology has been already used for SCM preamplifier on THEMIS probes. MMS like search-coil have been also provided by LPP to equip the future Magnetospheric Mercury orbiter of the ESA/JAXA BepiColombo mission.

Search Coil Magnetometer	**Cluster II (ESA)**	**THEMIS (NASA)**	**MMS (NASA)**
SCM Instrument	STAFF-SC(LPP*)	SCM(LPP*)	SCM(LPP)
SCM Onboard Spectra	STAFF-SA (LESIA)	DSP(LASP)	DSP (LASP)
Language	WF: Fortran Spectra: IDL	IDL	IDL
WF Calibration method	Continuos Fourier domain	Continuous Time domain	Continuous Time domain

Table 9-1 Heritage of SCM Waveform Samples and Onboard Spectra

** CETP became LPP on Jan. 1st, 2009*

9.2.1.2 Product Description

Operation Modes	**Data Type**	**# Comp.**	**Frequency Range**	**APID/ HEX**	**Sample Rate S/s**
Slow survey (SS)	Waveform	3		16e	32

1SCM waveforms are sampled at the same sample rate (32 S/s) for both slow and fast survey modes and stored in the same survey CDF file.

Relative Allocation: 50% (1% of downlinked data)	LFB (DSP) spectra	2	0.2 Hz-6kHz (64 bins)	171	0.06 (1 sp/16 s)
Fast survey (FS) RA: 50 % (25% of downlinked data)	Waveform	3		16e	32
	LFB (DSP) spectra	3	0.2 Hz-6kHz (64 bins)	171	0.25 (1 sp/ 4s)
Burst (B) RA: 50% but only1-2% downlinked (74% of data)	Waveform	3		2a8/2c2	1024/8192
	LFB (DSP) spectra	3	0.2 Hz-6kHz (64 bins)	2b0	10

Table 9-2 Product Descriptions

9.2.2 Theoretical Description

Responsibility	Usual Convention	MMS/SCM Convention	Usual Files Content	MMS/SCM Wave Form Products
Mission Level NASA	Raw data		Telemetry packets	
Mission level NASA+SDC	Level 0	L0	De-commuted data	Binary files TM counts
Instrument suite level FIELDS/UNH	Level 1	L1A	Decompressed and time tagged data	CDF files TM counts (LONG64) Time tagged (TT2000) SCM123 instrument spinning frame
Instrument team level SCM/LPP	Level 2	L1B	Calibrated data	CDF files nT (FLOAT) □ **Converting counts to V to nT is a tricky process!** High-pass filtered SCM123 instrument spinning frame (~OMB)
SCM/LPP		L2		CDF files

				nT High-pass filtered GSE frame
Instruments and/or science teams level	Level 3	L2+	Value added data: Use of a model and/or external data (e.g. merged products, automated noise removal, polarization parameters, etc.)	Work in progress: Merged FGM(LF)/SCM(HF) data Interference cleanup (?)

Table 9-3 Theoretic Descriptions

Decompression:

- Takes care of data loss due to compression (need of a status flag/fillvalue)
- Also takes care of saturation (status flag/fillvalue)

Timing:

- Packet time, clock derivation, delay is taken care of at the Fields consortium level

Waveform: from Counts to Volts

- ADC conversion ±2.5V on 16bits with an input DSP gain of 0.403 to fit the ±6.25V output to DSP:
- [Optional] Centering of Waveform (removing DC):

Waveform: from Volts to nT

performed continuously in time domain by convolution
in(t) = out(t) *c(t) where c(t)= $FT^{-1}[1/h(f)]$ is called kernel
(nk is the size of the kernel) and h(f) is the transfer function or frequency response of the antenna, Bessel low-pass filter and digital filter.

- a large nk gives better calibration, but is time consuming

- Get kernel suitable for use by shifting by nk/2, applying Hanning window.
- Note: IDL control function assumes that the center of the kernel is at index nk/2, so no delay is introduced.

Edge behavior determined by /edge_zero, /edge_wrap, or /edge_truncate.
For MMS L1B, we added and use /edge_mirror. With no /edge keyword, set all data within nk/2 samples of the edge to zero.

Kernel Size

Lower limit depends on the frequency resolution we want.
Criteria : $\Delta f/f<1$ at F_{min} where $\Delta f/f=f_s/(nk*f)$ □ $nk_{min}>f_s/f_{min}$
Higher limit depends on the computing time and the loss of the first half and last half of the convolution window we can afford.
Our choice for L2 production:

Mode	Name	**f_s=sample rate (S/s)**	**$f_{min(L1B)}$ (Hz)**	**$f_{min(L2)}$ (Hz)**	**$f_{max}=f_{Nyquist}$ (Hz)**	**nk**
Slow Survey & Fast Survey	scsrvy	**32**	**0.03**	**0.5**	**16**	**2048**
Burst (Nightside)	scb	**8192**	**0.5**	**1**	**4096**	**32768**
High Burst	schb	**16384**	**16**	**32**	**8192**	**2048**

Table 9-4 Parameters Used by the SCM Calibration Program for Each Sampling Mode

Antenna Frequency Response

Search Coil Magnetometer response or transfer function (TF) is frequency dependent!
□Need to apply a different gain and phase correction for each considered frequency

Filters Frequency Response

Digital filter

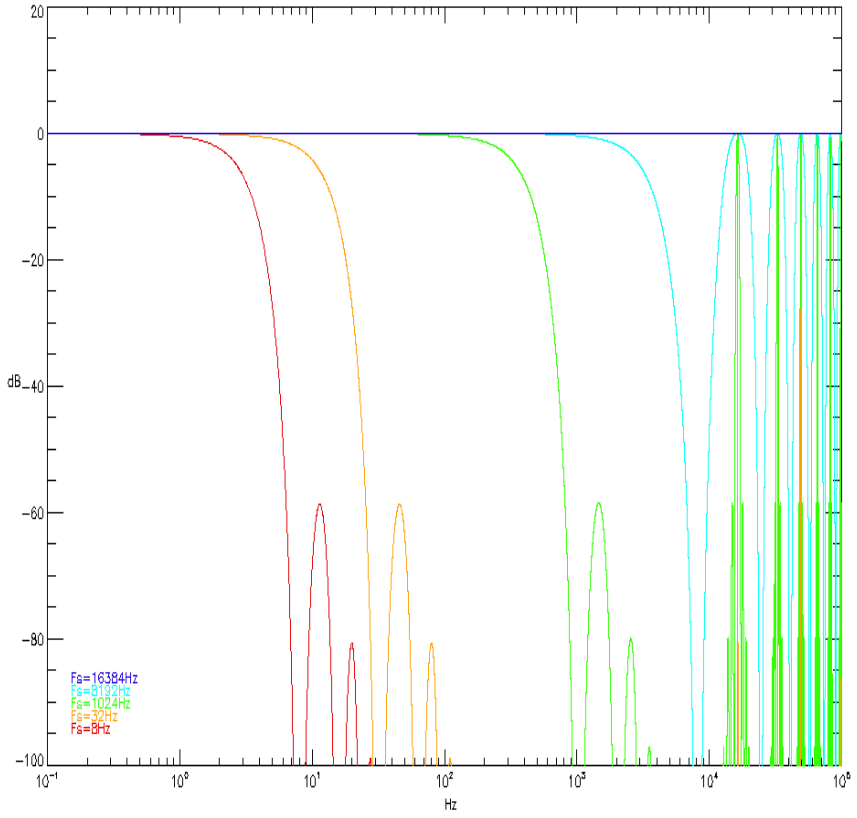

Figure 9-3 Frequency Response of Digital Filters

5-pole low pass Bessel (-3dB at 6.5*k*Hz)

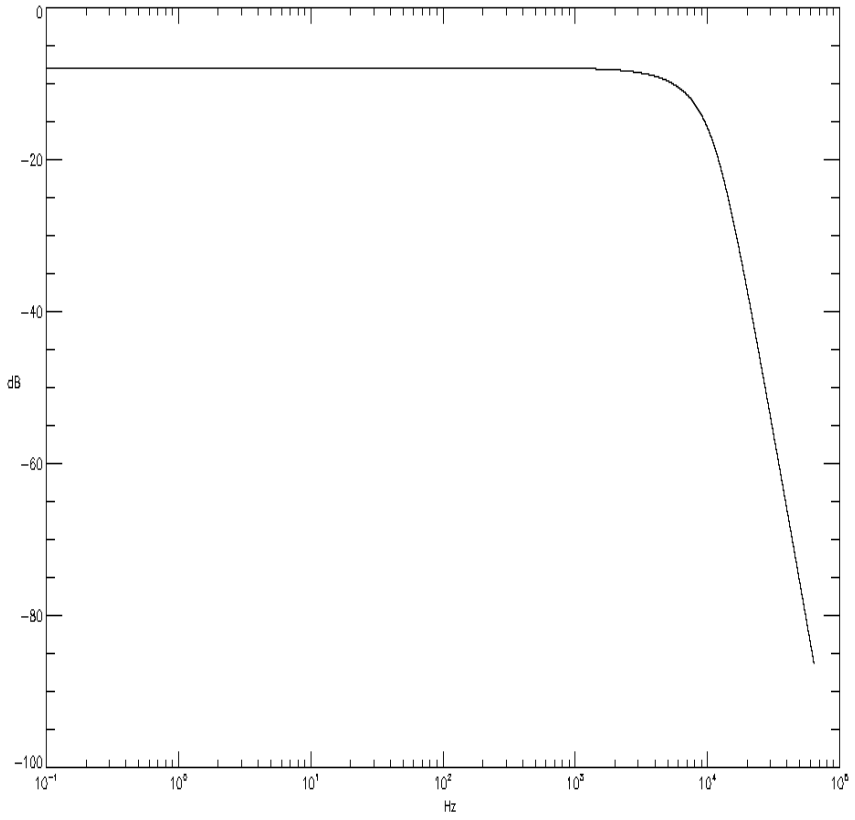

Figure 9-4 Frequency Response of 5-Pole Low Pass Bessel Filter

Their responses are taken into account:
h(f)=Antenna_resp(f)xDFB(f)xBessel_filter_resp(f) (+filter between F_{min} and F_{max})

Waveform Calibration Algorithm

- Instrument and filter responses:

  $kernel_{complex}(i_f)=h_{ant}(i_f)xh_{DFB}(i_f)xh_{HP\_Bessel}(i_f)$
  with $f(i_f)=i_f*df$, $i_f=0\ldots nk$ and $df=f_{Nyquist}/nk$
- Filter $f<f_{min}$: $kernel_{complex}(i_f<i_{fmin})=0$
- Filter $f>f_{max}$: $kernel_{complex}(i_f>i_{fmax})=0$
- Obtain kernel: $kernel_{real}(i_t)=Real(FT^{-1}[kernel_{complex}(i_f)])$ (Check that Imaginary part is 0)
- Zero time of the kernel is at index $i_t=0$, shift that to index nk/2 to get a kernel suitable for linear convolution and to allow application of the window
- Hanning windowing (As this is a continuous calibration, the window must be applied to kernel, rather than to the waveform): $kernel(i_t)=kernel_{real}(i_t)xHanning(nk)$ (Other possibilities, coscub, trapez, etc.)
- Normalize kernel: $kernel(i_t)=kernel(i_t)/nk$
- Convol signal with kernel: $in(t)=out_{+edge\_mirror}(t)*kernel((i_t))$ (Don't forget to shift back -nk/2)

- Remove average from signal.

Contiguous Burst Segments Calibration Algorithm

- L1a CDF files are reprocessed for contiguous burst periods (with precise time tag recalculations)
- Six contiguous L1a CDF files in a single run and the four inner segments are kept to produce L1b and L2 CDF files having the same time tag for CDF name as others instruments. The same operation is then repeated with a shift by four segments for the next six segments
- Note that because all burst periods are not downlinked at the same time, but depending on their Figure of Merit attributed by the SITL selection, this processing is run again one month after the downlink of the last isolated burst segment. It allows to check if a new contiguous burst period has been downlinked and if a longer merged burst period can be produced.

CDF versioning

SCM cdf files use a versioning defined as follows: x.y.z.cdf where

- x means an important change of the calibration program or cdf content
- y means an improvement of the data quality (e. g., change of the calibration file)
- z a minor bug correction or reprocessing

SCM version history can be found here: https://lasp.colorado.edu/galaxy/pages/viewpage.action?spaceKey=mms&title=SCM+Release+Notes (restricted access to MMS team members)

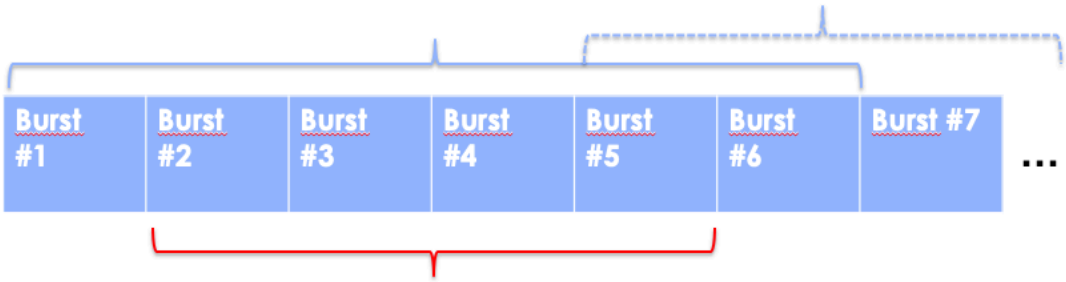

Figure 9-5 Contiguous Segments Management

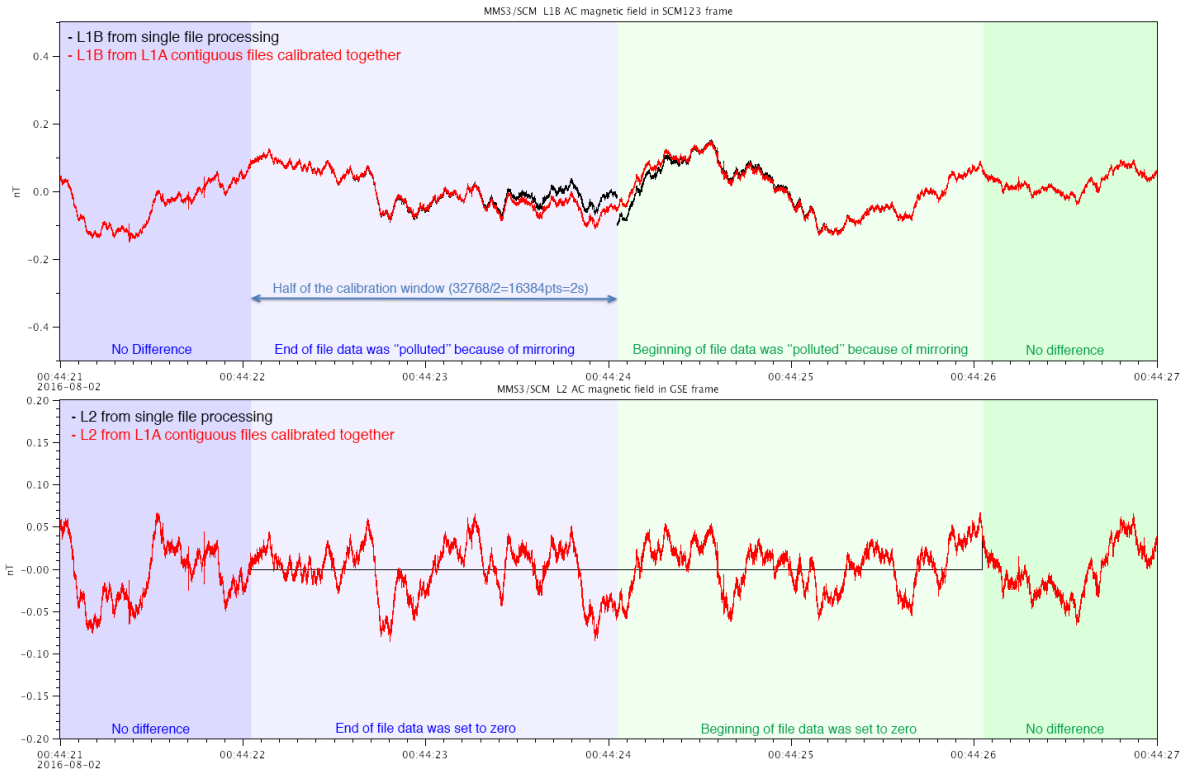

Figure 9-6 Comparison Between Non-Contiguous (Black) and Contiguous (Red) Processing

Spin Tone Removal:

Spin tone (DC magnetic field signature on spinning components X and Y) was removed for Cluster/STAFF (and THEMIS/SCM) for higher computation precision during the calibration process. Not hard to do with strong Earth DC magnetic field and 4 or 5s spin period. However, fitting MMS 20s spin period is tricky as 'constant' magnetic field may vary a lot during these 20s. Anyway, spin tone removal is not needed anymore as 'double precision' (64bits floats) allows to keep the spin tone in the X and Y components without losing precision.

Data is also high-pass filtered. Only few spin-tone remains at very strong DC magnetic fields (perigee). Notice that MMS/SCM never saturated even at high DC field.

De-spin is done when moving from SCM123(OMB) to GSE using the FDOA attitude and ephemeris files.

9.2.3 Calibration and Validation

9.2.3.1 Calibration

The initial SCM calibration consists of measuring the frequency response of transfer function (gain and phase) of the three antennas mounted onboard each spacecraft. This measurement is carried out on the ground in a facility with a very high cleanliness electromagnetic environment. The stability of each transfer function is monitored along the mission life thanks to an in-flight calibration sequence performed at least once per orbit.

9.2.3.1.1 Pre-Flight / On-Ground Calibration

Antenna complex frequency response obtained from gain and phase measurements on-ground in Chambon-la-Forêt:

SCM standalone transfer functions have been measured at the National Magnetic observatory of Chambon-la-forêt without their thermal blanket and using 2m diameter Helmholtz coils facility at ambient temperature.

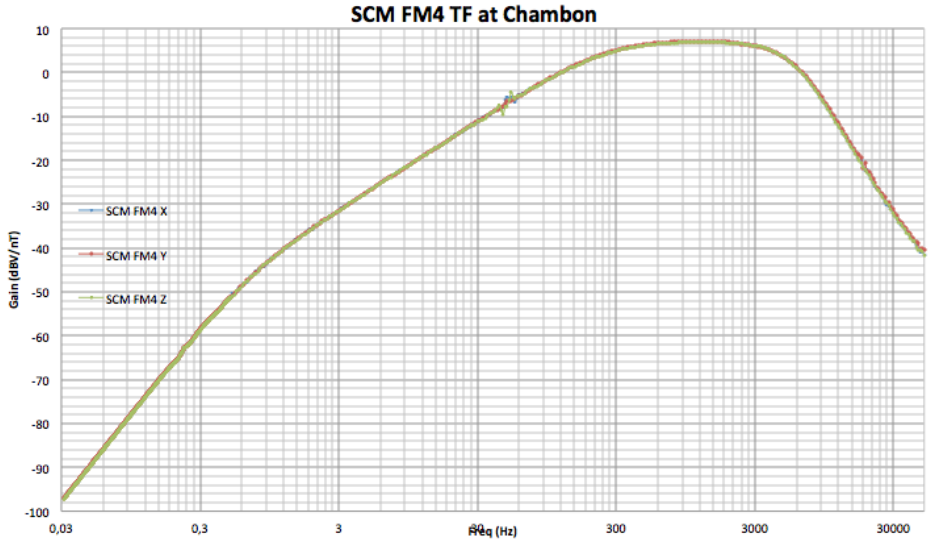

Figure 9-7 SCM FM4 TF at Chambon

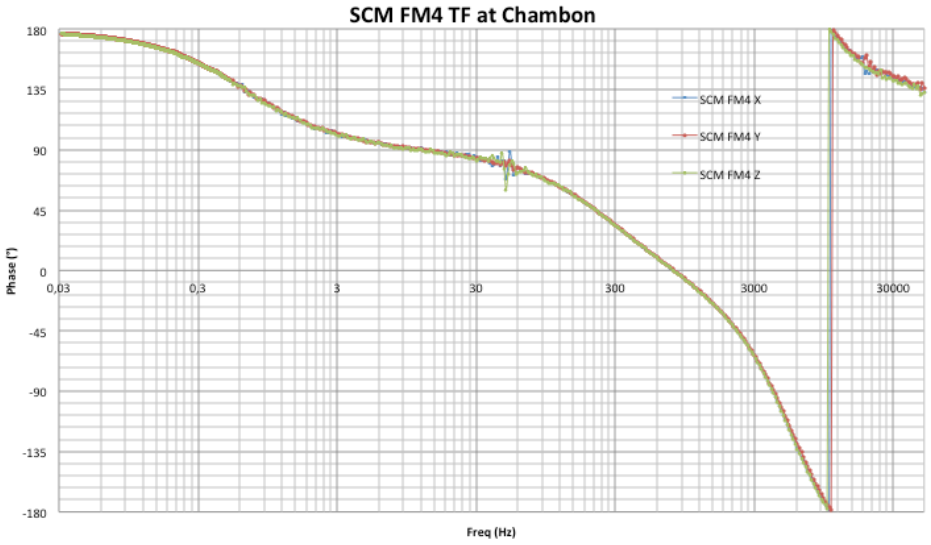

Figure 9-8 SCM FM4 TF at Chambon

9.2.3.1.2 In-Flight Calibration

The SCM calibration is executed at least once per orbit. The calibration signal sweep is broken into 4 segments with increasing sample frequencies and the whole calibration sequence lasts less than 90 sec. The frequency of the calibration signal doubles every 4 cycles from 0.125 Hz to 4096 Hz. Each segment will consist of four different frequencies as shown in the table.

Duration (Seconds)	64	4	.3125	.078125
Cal Signal Frequencies (Hz)	.125 .25 .5 1	2 4 8 16	32 64 128 256	512 1024 2048 4096
Sampling Rate (Samples/Second)	16	256	4096	16384

Table 9-5 Description of the SCM Calibration Sequence

SCM transfer function verification loop

1. estimates the output amplitude for each frequency (using 4 cycles)
2. computes the 16 ratios (from 0.125 to 4096 Hz) between input and output signals and detect possible phase delay
3. compares gain and phase with the previous calibration transfer function values (first files being transfer functions measured at laboratory)
4. updates, if needed the SCM, transfer function by generating a new SCM transfer function with corrected gain and phase for the corresponding frequency.

9.2.3.2 Confidence in Measurements

The gain (resp. phase) differences at 1 kHz between different antennas of the same tri-axis are less than 0.1 dBV/nT (resp. 1.5°) and between antennas of different tri-axis are less than 0.3 dBV/nT (resp. 1.5°). Also, it has been checked that the gain (resp. phase) differences with and without a thermal blanket are no larger than 0.1 dBV/nT in gain (resp. 1°).

9.2.3.3 Comparison of Other Measurements

- Cross-calibrations (DFG, AFG) based on spin modulation @20s, 2 components in the spin plane.

- Cross-calibrations (DFG, AFG) based on common frequency range (0.1-4Hz: slow survey, 0.1-8Hz: fast survey, burst 0.1-32 Hz), 3 components.

From in-flight AFG/DFG and SCM comparisons, SCM gains have been found to be lower than DFG/AFG gains by about 14%. This gain correction have been applied to all antennas onboard all satellites and all SCM L2 CDF have been reprocessed. .

- Tests of synchronization with electric field waveform (SDP-ADP).

9.2.3.4 Quality Control and Diagnostics

1) A quality factor is given for each data point. This is a string of 3 characters where each letter refers to one SCM physical antenna in the SCM123 order (see Figure 9-1):

- 'G' : good data. Only these data points can be used for scientific analysis

- 'Z': data that are affected (L1B) or set to zero (L2) by convolution boundary effect,
- 'S' : saturated data (equal to VALIDMIN or VALIDMAX)
- 'X' : out of range data (<VALIDMIN or > VALIDMAX)
- 'B' : fillvalue/bad data (Not a Number : NaN)

In-flight calibration sequences described above are analyzed routinely (every orbit) to check that the transfer function of each antenna (4x12) remains unchanged. Plots and statistics are produced and available on line for consultation at http://mms.lpp.upmc.fr/?page=calibration.

SCM spectra averaged over the time period corresponding to the mode (survey, burst) and dynamic spectra are produced routinely and available for consultation at http://mms.lpp.upmc.fr/?page=quicklook. They allow to detect possible anomalous behavior of antennas. Data validation is based on these two diagnostics in addition to inspection of individual periods and further investigations as required. AC Magnetic Field Power Spectral Density (BPSD).

9.3 AC MAGNETIC FIELD POWER SPECTRAL DENSITY (BPSD)

9.3.1 Overview

Onboard Fourier spectra computed by DSP are available from 0.2 Hz to 6 kHz with a time resolution of 16 s in Slow Survey, 2 s in Fast Survey.

9.3.1.1 Heritage

Similar SCM have been previously flown by LPP (or formerly CETP) on many earth-orbiting (GEOS-2, Cluster/STAFF, THEMIS/SCM) and interplanetary (Galileo, Cassini) missions. Multi-chip vertical technology has been already used for SCM preamplifier on THEMIS probes. MMS like search-coil have been also provided by LPP to equip the future Magnetospheric Mercury orbiter of the ESA/JAXA BepiColombo mission.

In particular, the analog magnetic waveforms measured by the SCM are digitized and processed inside the digital signal processor (DSP) developed by LASP (Ergun et al., 2016) based on the THEMIS heritage (Cully et al., 2008).

Cully, C.M., Ergun, R.E., Stevens, K. *et al.* The THEMIS Digital Fields Board. *Space Sci Rev* **141,** 343–355 (2008). https://doi.org/10.1007/s11214-008-9417-1

9.3.2 Product Description

Power spectral density of Magnetic field fluctuations (nT^2/Hz) computed by onboard FFTs by the Digital Signal Processor (DSP) from SCM waveforms during slow survey modes between 0 and 8192 Hz. Their nominal time resolution is 16 s for slow survey and 2 s for fast survey, and nominal number of frequency channels is 56 with logarithmic frequency scale.

This product is computed in space from individual components that are not synchronized to the 1 second pulse. Therefore, the timing between channels can be inaccurate by a fraction of a second. The samples times are interval start times taken from the x component.

- SCM1 (spin plane component, -x SCM sensor) component magnetic power spectral density.
- SCM2 (spin plane component, -z SCM sensor) component magnetic power spectral density.
- SCM3 (spin axis component, -y SCM sensor) component magnetic power spectral density.
- Omni-directional magnetic power spectral density: square root of the sum of the squares of **3 components**.

9.3.3 Theoretical Description

$nT^2/Hz=(SdC)(G_{ADC})^2(G_{DSP})^2(BWC)(HWC)(SCDRC)DSPFRC)(SCMFRC)$
where
SdC = Spectra Data deCompressed (Spec $counts^2$)
G_{ADC} = ADC Gain (Volts per count in the ADC) = (2.5V ADC / 32767counts)
G_{DSP} = DSP(EWO) Gain (Volts at DSP input / Volts at ADC) = (1./0.403V DSP Input) / (V ADC)
BWC = Bandwidth correction = (1) / (8Hz)
HWC = Hanning window correction= (1) / (0.375)
SCDRC = Spectral Compression Dynamic Range Correction = (1 Waveform $Counts^2$) / (16 Spec $Counts^2$)
DSPFRC = DSP Frequency Response Correction = 5-pole low pass Bessel, -3dB at 6.5 *f*(Hz)
No digital filter correction because sampling frequency is not downscaled (16kS/s).
SCMFRC = SCM Frequency Response Correction = SCM TF *f*(Hz)

9.3.4 Calibration and Validation

In addition of the transfer function checking and corrections that we perform for SCM Waveforms (see 9.2.3), the power spectral density obtain from the waveforms and the one coming from DSP are also compared to validate their value.

9.4 APPENDIX A- SCM REFERENCES

Section	Document Number	Title	Revision/Date
	https://doi.org/10.1007/s11214-008-9417-1	Cully, C.M., Ergun, R.E., Stevens, K. et al. (2008). The THEMIS Digital Fields Board. Space Sci Rev 141, 343–355.	
	https://doi.org/10.1007/s11214-014-0115-x	Ergun, R. E., et al., (2016). The Axial Double Probe and Fields Signal Processing for the MMS Mission. Space Sci Rev 199, 167–188.	
	https://doi.org/10.1007/s11214-008-9371-y	Le Contel, O., Roux, A., Robert, P. et al. (2008). First Results of the THEMIS Search Coil Magnetometers. Space Sci Rev 141, 509–534.	
	https://doi.org/10.1007/s11214-014-0096-9	Le Contel, O., Leroy, P., Roux, A. et al. (2016). The Search-Coil Magnetometer for MMS. Space Sci Rev 199, 257–282.	
	Science_Data_Products_Guide_vol2_SCM_v11_20160301.pdf	MMS-SMART Science Data Products Guide: SCM	
	https://doi.org/10.1007/s11214-014-0109-8	Torbert, R.B., Russell, C.T., Magnes, W. et	

		al. (2016). The FIELDS Instrument Suite on MMS: Scientific Objectives, Measurements, and Data Products. Space Sci Rev 199, 105–135.	

Table 9-6 SCM Applicable Documents

10.0 ELECTRON DRIFT INSTRUMENT (EDI)

10.1 EDI OVERVIEW

The Electron Drift Instrument on MMS measures the displacement of a weak beam of test electrons that, when emitted in certain directions in the plane perpendicular to the magnetic field, return to the spacecraft after one or more gyrations. This displacement (drift step) is related to the electric field. Two Gun-Detector Units (GDU) are mounted on opposite sides of each spacecraft and face opposite hemispheres. They are controlled via a DPU board (EDI Controller) inside the FIELDS Central Electronics Box (CEB). Two measurement techniques are used that are run in parallel and complement each other: for small drift steps, the displacement is obtained from triangulation of beam directions; for larger drift steps the difference in times-of-flight of beams that are injected in nearly anti-parallel directions is used to calculate the drift step. The time-of-flight measurements also provide the magnetic field strength, thereby enabling the determination of the offsets in the spin axis component of the AFG and DFG flux gate magnetometers. A by-product of this operating mode (Electric Field Mode) are ambient electrons at pitch angle 90 degrees within the energy window of the detectors. These are transmitted in telemetry whenever no return beam has been detected within a fixed time interval. Due to the data quality categories used on-board these are referred to as “Quality Zero” data. In a second operating mode (Ambient Mode) the EDI detectors can be used to sample ambient electrons at pitch angles 0, 90 and 180 degrees at high time resolution.

A full description of the design of EDI, its ground calibration and its operational modes can be found in the publication:

Torbert, R.B., et al, **The Electron Drift Instrument for MMS**, Space Sci Rev 199, 283–305 (2016). https://doi.org/10.1007/s11214-015-0182-7

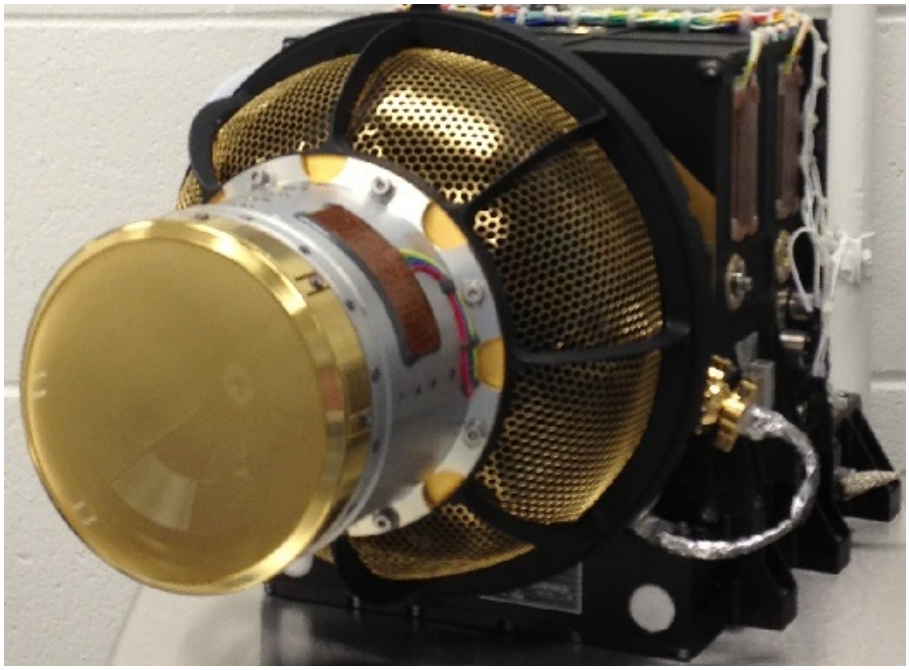

Figure 10-1 EDI Gun-Detector Unit

10.1.1 Status of EDI

Several of the opto-couplers in the high voltage amplifiers in the Gun and Gun-Detector Electronics (GDE) continue to experience trends, limiting the life of the instrument and impacting available operational choices. This was known already during integration and testing on the ground. Continual trending analysis throughout the mission aided in making operational decisions that ensured the extension of the opto-coupler life cycle. In addition, a few failures occurred due to HV discharges, and in one case the filament of the electron beam generation system in the Gun reached its end of life. Table 10-1 provides a summary of the opto-coupler trending situation and the component failures and their impact on operations, ordered by observatory.

Date	Observatory / Unit / Hardware Element	Event / Failure / Trending	Impacted Mode	Operational Change
Jan 2022	MMS1 / GDU1 / Gun Deflector1	Optocoupler Deterioration	EFIELD: Loss of beam return in azimuthal section for large deflections from symmetry axis	None; Safe Mode entry prevented by increasing out-of-limits persistence
Nov 2016	MMS2 / GDU2 / Gun Anode Amplifier	HV discharge	EFIELD: GDU2 no longer usable	Continued with single-gun EFIELD mode
Feb 2022	MMS2 / GDU1 / Gun Filament	End of life	EFIELD: GDU1 no longer usable	EFIELD: GDU1 no longer usable
Jun 2022	MMS2 / GDU1 / Optics Lower Injector	Optocoupler Deterioration	AMBIENT: future loss of geometric factor for large polar look directions	Minimize continuing deterioration by avoiding perpendicular and alternating pitch angle sampling
May 2017	MMS3 / GDU1 / Gun Cathode	Optocoupler Deterioration	EFIELD: GDU1 no longer usable	Continued with single-gun EFIELD mode
Sep 2019	MMS3 / GDU2 / Gun Deflection System	Sudden deterioration after HV discharge	EFIELD: Beam pointing accuracy degradation	Stopped L2 EFIELD production; continued L1A production for Flux Gate spin axis offset calibration using EDI time-of-flight measurements
Jan 2020	MMS3 / GDU2 / Gun Deflector5	Optocoupler Deterioration	EFIELD: Loss of beam return in azimuthal section for large deflection from symmetry axis	None; Safe Mode entry prevented by increasing out-of-limits persistence

May 2021	MMS3 / GDU2 / Optics Upper Injector	Optocoupler Deterioration	AMBIENT: loss of geometric factor for poleward look directions (in field aligned and alternating pitch angle modes)	Restrict sampling to perpendicular pitch angles (least amount of stress on optocoupler)
Jan 2022	MMS3 / GDU1 / Optics Upper Deflector	Optocoupler Deterioration	EFIELD: potential loss of geometric factor and ability to detect signal return for poleward look directions	None; Safe Mode entry prevented by increasing out-of-limits persistence
Apr 2020	MMS4 / GDU2 / Optics Upper Deflector	Optocoupler Deterioration	EFIELD: potential loss of geometric factor and ability to detect signal return for poleward look directions	None; Safe Mode entry prevented by increasing out-of-limits persistence
Sep 2022	MMS4 / GDU1 / Optics Upper Injector	Optocoupler Deterioration	EFIELD: potential loss of geometric factor and ability to detect signal return for poleward look directions	Decision pending

Table 10-1 Summary of EDI Instrument Degradation and Operational Impact

10.1.2 Mode Scheduling

In the first years of the mission science operations were restricted to altitudes above 4 Re. Later in the mission this limit was reduced to 3Re in order to help with EDP calibration in the inner magnetosphere. EFIELD operations were typically scheduled on the outbound and inbound side for several hours (typically 5 hours), except in mission phase 1X where operations were reduced to conserve opto-coupler life, and phase 2A where no EFIELD operations were scheduled for the same reason.

In the remaining part of the orbit, Ambient Mode was used. Originally one sampling mode, field aligned or alternating between field aligned and perpendicular electrons, was used per orbit. Starting with phase 3B this was changed to switching between three sampling modes, where the first sampling intervals ended at the end of SROI1 and the third interval started at the beginning of SROI3. The detector energy was 500eV initially, but was later reduced to 250eV due to deteriorating opto-couplers. Table 10-2 summarizes the Ambient Mode Operations over the mission.

OBS	**Mission Phase**	**From**	**To**	**Sampling Mode**	**L2 Data Product**		
					Field Aligned	**Perpendicular**	**Alternating**
1	1A	2015-09-01	2016-01-06	FA	amb		
234	1A	2015-09-01	2016-01-04	FA	amb		
1	1A, 1X	2016-01-14	2016-06-12	FA	amb-pm2		
234	1A, 1X	2016-01-04	2016-06-12	FA	amb-pm2		

1234	1X	2016-07-29	2016-09-12	ALT			amb-alt-cc
134	1B	2016-09-12	2016-10-13	ALT			amb-alt-oc
2	1B	2016-09-12	2016-10-07	ALT			amb-alt-oc
2	1B	2016-10-09	2016-10-09	ALT			amb-alt-cc
2	1B	2016-10-10	2016-10-13	ALT			amb-alt-oc
1234	1B, 2A	2016-10-14	2017-05-05	FA	amb-pm2		
1234	2B	2017-05-05	2017-05-24	ALT			amb-alt-oob
1234	2B, 3A	2017-06-18	2017-11-14	FA	amb-pm2		
1234	3B, 3C	2017-11-14	2018-05-10	FA / ALT / FA	amb-pm2		amb-alt-oob
1234	3C, 3D, 4A	2018-05-10	2019-02-12	FA	amb-pm2		
1234	4B	2019-02-12	2019-03-05	FA / ALT / FA	amb-pm2		amb-alt-oob
1234	4B-D, 5A	2019-03-05	2019-10-31	FA / ALT / 90	amb-pm2	amb-perp-ob	amb-alt-oob
1234	5A-C	2019-10-31	2020-05-11	FA / ALT / 90	amb-pm2	amb-perp-ob	amb-alt-oob
123	5C	2020-05-11	2020-06-23	FA / ALT / 90	amb-pm2	amb-perp-ob	amb-alt-oob
1	5D, 6A	2020-06-23	2020-11-02	FA / ALT / 90	amb-pm2	amb-perp-ob	amb-alt-oob
123	6A	2020-11-02	2020-11-24	FA / ALT / 90	amb-pm2	amb-perp-ob	amb-alt-oob
123	6B	2020-11-24	2020-12-08	FA / 90 / 90	amb-pm2	amb-perp-ob	
123	6B, 6C	2020-12-08	2021-05-04	FA / Safe / 90	amb-pm2	amb-perp-ob	
1	6C-D, 7A-D	2021-05-04	current	90 / FA / 90	amb-pm2	amb-perp-ob	
3	6C-D, 7A-D	2021-05-04	current	90 / 90 / 90		amb-perp-ob	
2	7D	2022-06-16	current	Safe / Safe / FA	amb-pm2		

Table 10-2 Ambient Mode Sampling Options Summary

10.2 EDI DATA VOLUME AND TIMING

10.2.1 Electric Field Mode Time Tags

Raw (level 0) EDI electric field mode data are organized in data structures that contain electron beam firing directions and measured times-of-flight of detected return beams, along with a quality indicator,

timing information and other measurement settings such as the time-of-flight correlator code clock dividers that are needed for the ground analysis, as well as some auxiliary information. The raw data structures have the same size and content in burst and survey telemetry, although they are organized differently in the level 0 telemetry.

The time tags assigned to L2 data are not the centers of the 5 second analysis time intervals, but are calculated as the average of the times of all detected return beams that contributed to the result. For that reason the EDI L2 electric field data are not spaced regularly in time. Moreover, there are times when no adequate data are found in a given 5 second interval, resulting in data gaps.

The E-Field telemetry bit rates and volume are shown in Table 10-3.

10.2.2 Ambient Electron Mode Time Tags

Ambient Electron Mode data are sampled on a regular basis at a rate of 1024 samples per second for burst data and 32 samples per second for survey data. The sampling for burst data is contiguous. That is, there is no gap between the accumulation windows of subsequent samples. In survey the accumulation windows cover only 50% of the time between two subsequent samples.

Given the regular sampling, the raw telemetry contains only the packet coarse and fine time in each packet and the time tags for each sample are constructed on the ground during the processing of the L1A data. The time tags identify the centers of the accumulation windows. The onboard timing is controlled by the 2^{23} Hz (8,338 MHz) FIELDS Master clock. The frequency error of this clock (of the order of 10 ppm) is corrected for on the ground when constructing the sample time tags. The residual error on the time tags is 50us.

10.2.3 EDI Data Volume

Table 10-3 shows the Survey and Burst data volumes for EDI in E-Field and Ambient Mode.

Telemetry Mode	EDI Mode	Size (bytes)	Cadence (seconds)	Bit Rate (bits per second)
Survey	E-Field	794	4	1588
Survey	Ambient	786	4	1572
Burst	E-Field	5216	1	41728
Burst	Ambient	8746	1	69968

Table 10-3 EDI Data Volume in Survey and Burst for E-Field and Ambient Mode

10.3 EDI CALIBRATION AND VALIDATION

10.3.1 Pre-Flight / On-Ground Calibration

For successful operation of electric field mode precise knowledge and control of the electron beam firing direction of the gun is mandatory, requiring a dedicated ground calibration to determine the deviation of the actual deflection characteristics from a modeled behavior individually for each gun.

The EDI detector on the other hand has a fairly wide field of view in order to be able to accommodate the aberration of the return beam direction with respect to the firing direction which can be up to several degrees depending on electric and magnetic field conditions. In addition, the uniformity requirements on the detector over the azimuth angle (translating into sensor anodes) of its look direction are not too stringent since the variation of the signal is dominated by the variability of the electric and magnetic

fields as well as statistical effects in the correlator that is used for electron beam modulation, return beam detection and time-of-flight measurement. For that reason, a detector characterization on the ground was deemed sufficient.

A more elaborate characterization of the detector for the purpose of Ambient Mode data processing was performed in orbit.

A description of the design of EDI and a summary of its pre-flight and ground calibration results can be found in the publication:

> Torbert, R.B., et al, **The Electron Drift Instrument for MMS**, Space Sci Rev 199, 283–305 (2016). https://doi.org/10.1007/s11214-015-0182-7

10.3.1.1 Electron Guns

The main purpose of the gun calibration was the determination of two gun deflection voltages (called XD and YD) as a function of polar and azimuth angles of the beam firing direction on a fine angular grid. Due to the deflection characteristics two grid sizes were used, two degrees for polar angles below 70 degrees, and one degree between 70 and 96 degrees. The azimuthal grid size was one degree. In addition to the beam pointing calibration, values of the gun focus voltage and wehnelt voltage were determined, and beam profiles were recorded for a subset of the beam pointing directions. While the wehnelt voltage is fixed for a given energy and is tuned to achieve maximum output beam current, the focus voltage impacts the beam profile and is dependent on the beam pointing directions, although a coarser grid than for the beam pointing was sufficient. These calibrations were performed for two energies, 1 keV and 500eV, and for two guns also for 250 eV. Since the reference voltages for the gun are generated in the Gun-Detector electronics (GDE) a particular gun calibration is always valid for the pair of Gun and GDE that were used together in the calibration.

The calibrations were carried out at the Space Research Institute (Institut für Weltraumforschung) in Graz, Austria, using a dedicated vacuum chamber. Stepper motors were used to orient the gun with respect to a position sensitive detector. An iterative approach was used to determine the XD and YD deflection voltages that pointed the beam's center (as defined by peak emission) on the detector. The requirement for beam pointing accuracy is 1 degree, with a goal of a residual error below 0.1 degrees for the deviation of the calculated location of the beam current peak on the detector from the reference point.

Figure 10-2 shows the residual angular error at 500eV energy as a polar color map for Gun SN 4 in GDU SN 9 which is installed as GDU2 on MMS4 500eV energy. Figure 10-3 shows the residual error at 1 keV for the same Gun. Except for isolated small regions near the center (symmetry axis) the goal of 0.1 degrees residual error is met for both energies.

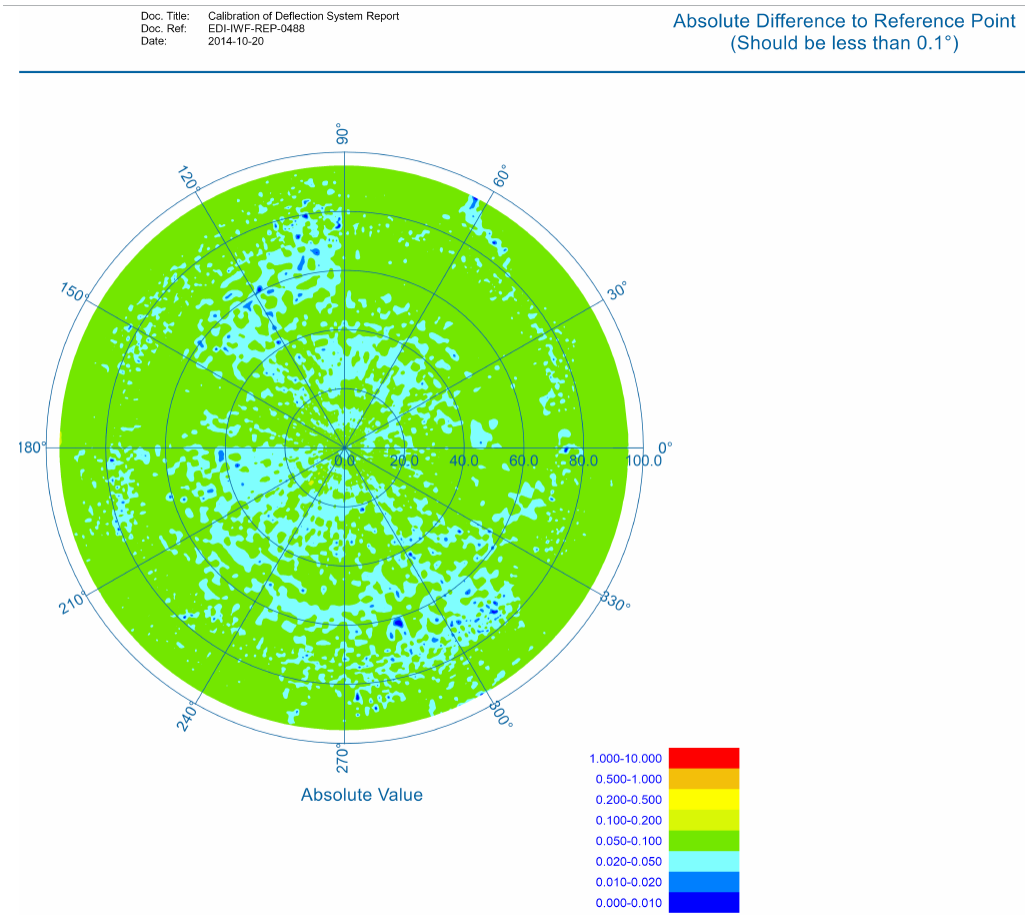

Figure 10-2 Gun SN 4 Residual Beam Pointing Error at 500 eV

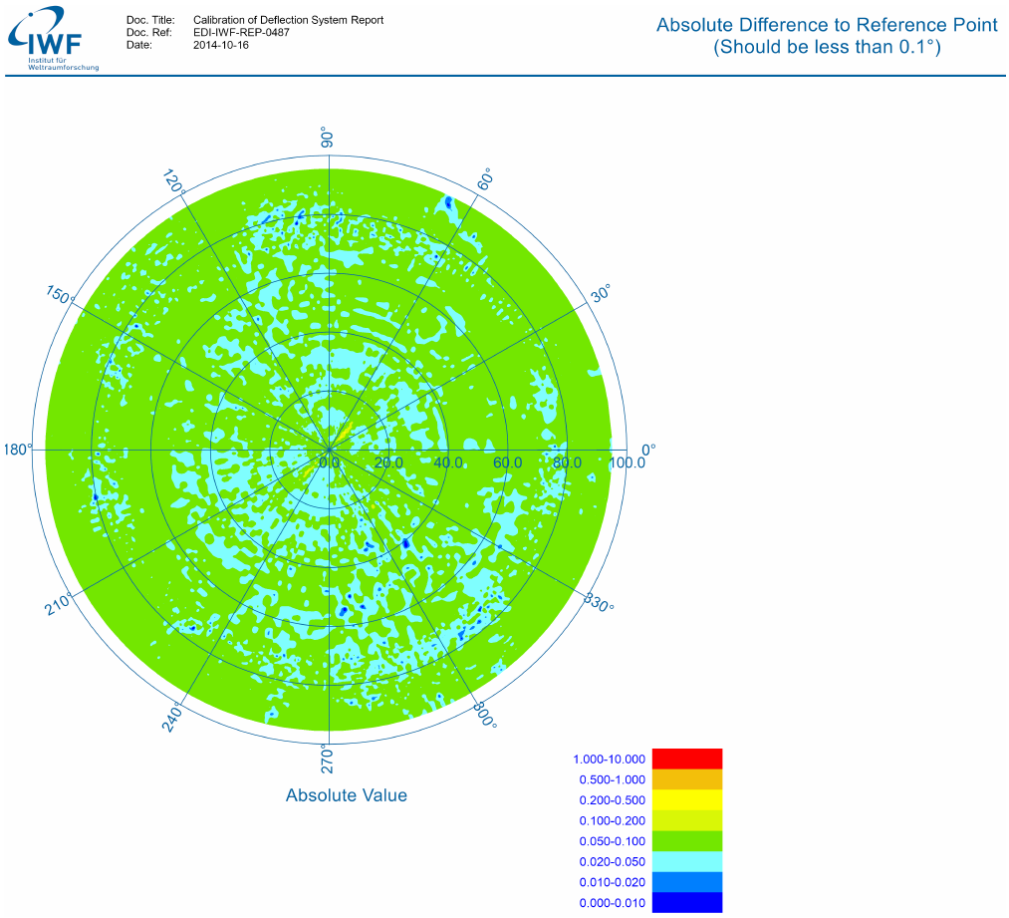

Figure 10-3 Gun SN 4 Residual Beam Pointing Error at 1 keV

10.3.1.2 Detectors

10.3.1.2.1 Sensor Tests

The sensor subunit of each GDU with its micro-channel plates (MCP), HV supply, custom pre-amplifiers and subsequent processing electronics went through a standalone testing sequence that was tightly interwoven with the sensor assembly. The test steps consisted of preamplifier threshold trimming, pre-amplifier delay variation measurement, a thermal test and electrical tests prior to and after board coating and a final vacuum test where MCP gain uniformity as well as aliveness of the signal path for each of the 32 azimuthal channels were demonstrated by rotating the sensor slowly by 360 degrees around its symmetry axis while illuminating the MCP input face with a fine pencil electron beam, and the MCP operating voltage was determined

The subsequent figures are from Sensor SN 8 which is integrated in GDU SN9 on MMS4.

Figure 10-4 shows the measured preamplifier signal delay variation as a function of input pulse height. The test was performed using test pulses and only for only two of the 32 amplifiers, channels 7 and 27. Channel 27 is special in that there is a calibration spoke near its anode which leads to increased capacitance for this channel, resulting in a slightly larger signal delay through the pre-amplifier. The minimum delay (for large input pulse height) was approximately 20 ns. The largest delay at 1.2 x

threshold was 60 ns for channel 27, leading to a variation of 40 ns which is well below the 60 ns specified in the sensor requirements.

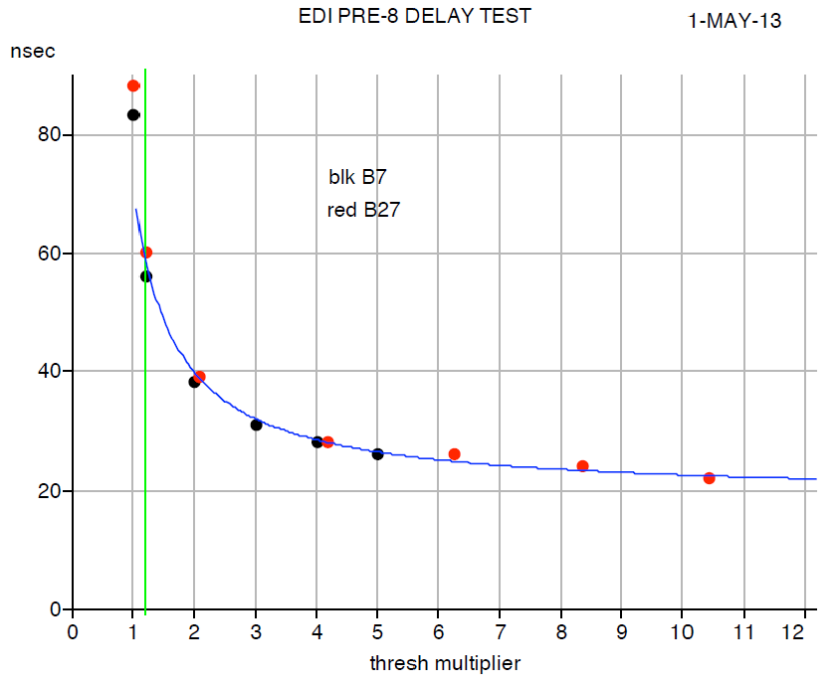

Figure 10-4 EDI Sensor SN8 Preamplifier Delay Measurements

Figure 10-5 shows the result of the roll test of Sensor SN8. Due to the fine electron beam used and the fine grained azimuthal steps of the 360 degree roll the gaps between anodes were resolved, as indicated by the periodic dips of the count rate. The worst-case change in count rate over all channels was approximately 10%, well below the required 25%, for the operational MCP high voltage of 2400 volts.

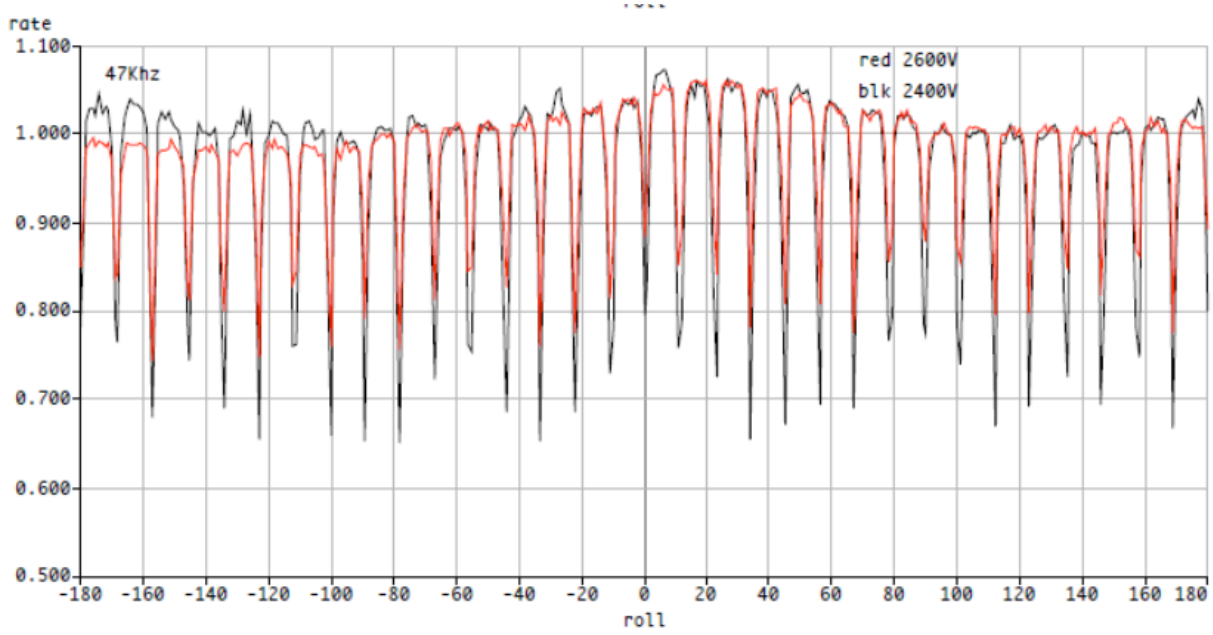

Figure 10-5 EDI Sensor SN8 Roll Test Results at 2400V and 2600V

10.3.1.2.2 Optics Modeling

The large number of electrodes in the electrostatic optics of the detector section of the EDI GDUs results in a large parameter space for the operation of the detector. The commercial "Lorentz" software suite was used to perform extensive simulations of the optics in order to determine appropriate sets of voltages to achieve the desired response to the incoming electron beam. Driving factors were finding suitable tradeoffs between signal-to-noise ratio and angular acceptance window width.

The Lorentz software provided both the electric field solution as well as the calculation of electron trajectories taking the physical structure of the optics into account. For any given look direction thousands of trajectories were calculated and the positions of those which would hit the micro-channel plates were recorded. The input trajectories were varied over input angle and location so that all possible successful trajectories over the full range of angles and source locations were bounded by the simulation. With the simulation results maps of input angle versus Sensor anode number were built for a given look direction.

Figure 10-6 shows a comparison of between simulated and measured response for three optics look directions (polar angle) of 30, 60 and 90 degrees. There is good agreement regarding the shape and extent of the response. The agreement provided verification that the simulation is accurate and could be used with confidence for developing lookup tables for the electrode voltages of the optics.

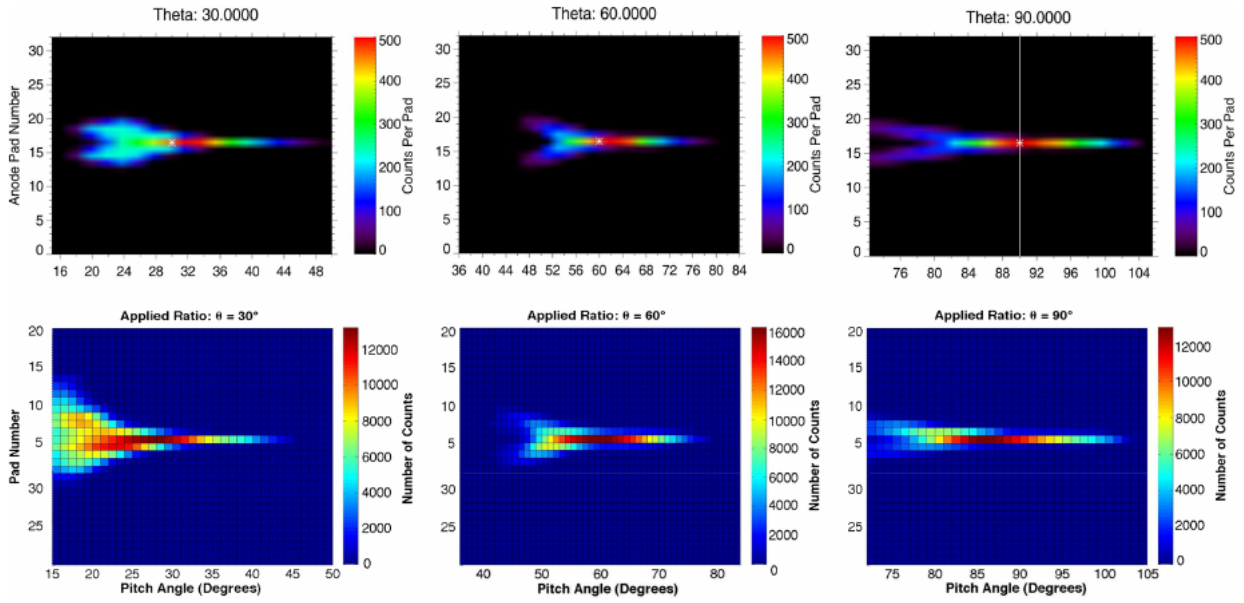

Figure 10-6 Comparison of Simulated Response (top row) and Measured Response (bottom row) of the EDI Optics for Three Look Directions [The vertical axis shows the anode pad number of the counts received by that pad and the horizontal axis shows the angular range relative to the symmetry axis of the GDU]

10.3.1.2.3 Detector Characterization

Characterizations of the detectors were performed on all flight GDUs during component level testing. The electron source for these characterizations was a broad beam generated using a UV backlit thin plate with chrome coating. The plate was biased negatively at the desired voltage (energy) and photoelectrons emanating from the plate were accelerated towards a grid at ground potential between the plate and the GDU. The GDU was mounted on a manipulation table that allowed the rotation of the GDU 360 degrees

around its symmetry axis and pitching the GDU towards/away from the beam so that incident angles between 0 and 110 degrees relative to the symmetry axis could be achieved. Figure 10-7 illustrates the test setup.

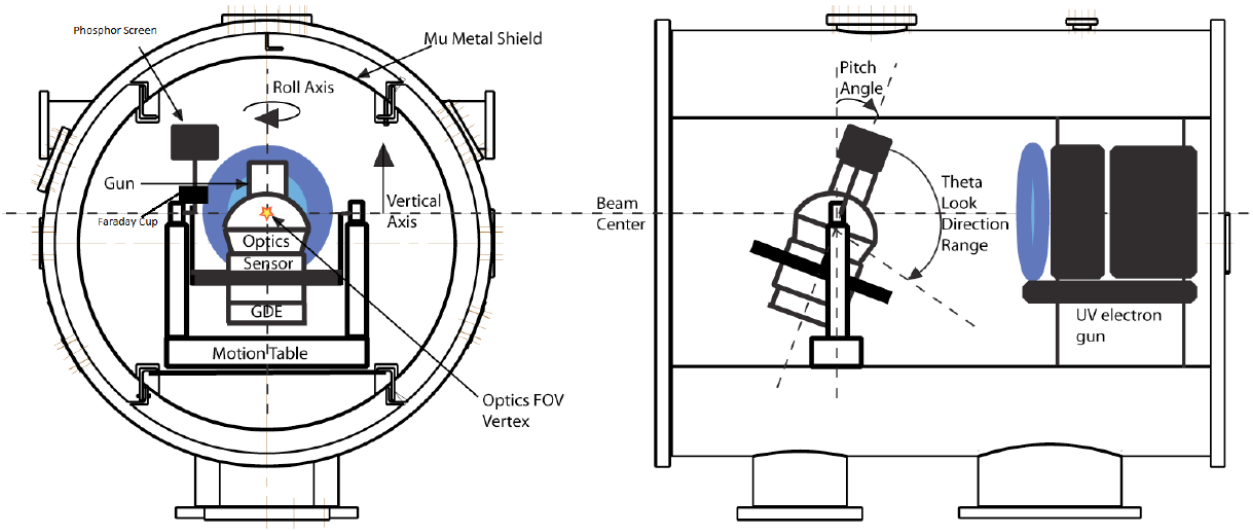

Figure 10-7 EDI GDU Detector Characterization Test Setup

The characterization performed consisted of roll tests around the symmetry axis for selected combinations of optics look-angles and associated pitch angles. These tests demonstrated the desired degree of uniformity of the integrated detector system and established the dependency of the effective beam area on polar angle for monodirectional and monoenergetic beams. Another set of tests was run to demonstrate and characterize the polar acceptance. In these tests the GDU was pitched for a number of look directions, from 0 to 110 degrees at fixed roll angle and fixed optics look direction (that is, fixed optics electrode voltages). In addition to these tests, adequate rejection of UV light was demonstrated. All tests were performed at 500 eV and 1 keV beam energy and included variations of the beam energy by 10% relative to the energy setting of the detector.

Figure 10-8 illustrates the result of a roll test at 500eV energy for pitch angle zero and a optics look direction of 90 degrees. This combination of instrument pitch angle and optics look angle results in the beam entering the optics along the center of polar acceptance window for the configured look direction. The beam is focused onto a narrow azimuthal range and the variation in count rates for roll angles that map the peak response to a single anode is well below the desired goal of 50%.

Figure 10-9 shows the result of a UV sensitivity test that demonstrates excellent UV rejection. The optics energy was 500 eV and the look angle was 90 degrees. At most one count was seen in any pitch angle / sensor anode bin within in the accumulation time window of 125 ms.

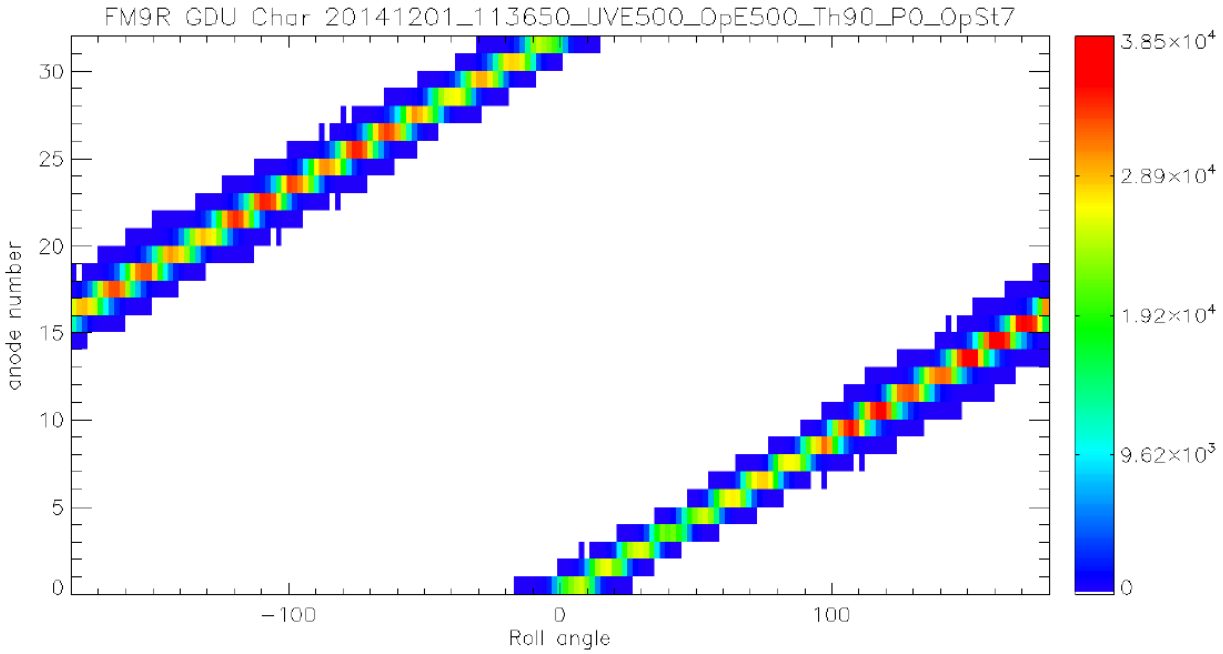

Figure 10-8 GDU SN9 Roll Test at 500 eV for Pitch Angle 0 (GDU Symmetry Axis Vertically, Perpendicular to the Beam) and Optics Look Direction 90 Degrees

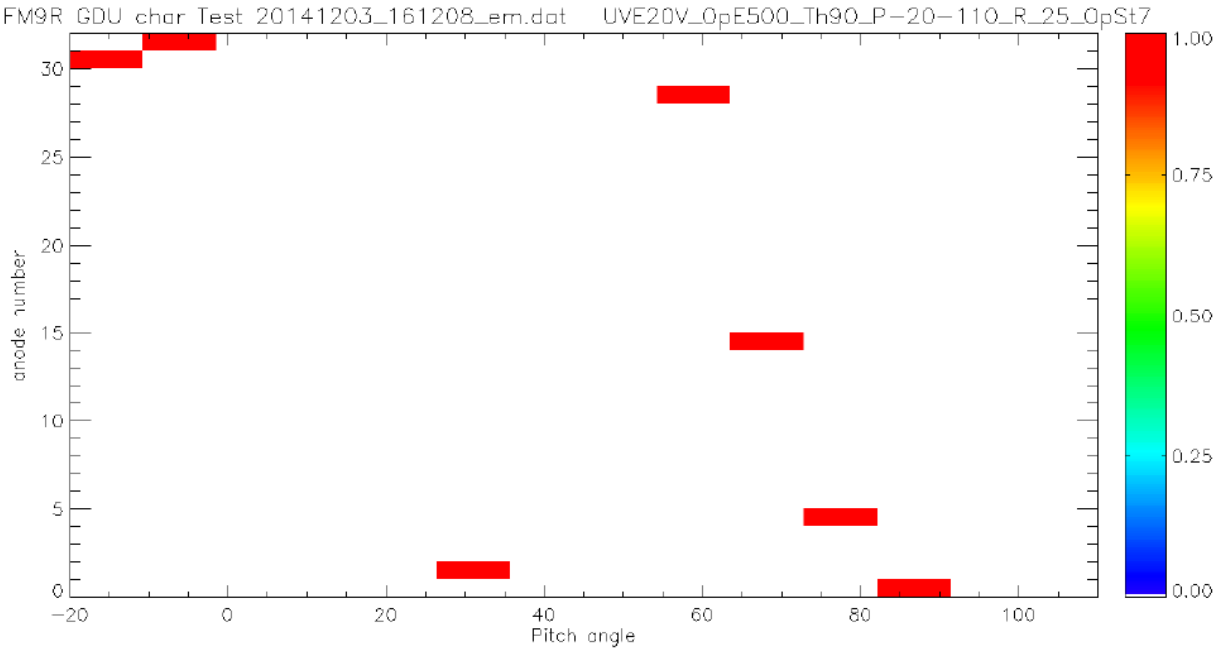

Figure 10-9 GDU SN9 UV Sensitivity Test at 500 eV [Counts per 125 ms as a function of pitch angle and anode number for a fixed roll angle of 25 degrees and an optics look direction of 90 degrees]

10.3.2 In-Flight Calibration

10.3.2.1 Electric Field Mode

For Electric Field Mode the crucial calibration is that of beam firing direction vs deflection voltages, as it impacts both the ability to fire the beam accurately in the plane perpendicular to B and the ability to perform triangulation in the ground analysis. On the engineering model GDU it was demonstrated that the calibration remains valid after subjection the gun to a vibration test. In-orbit calibration of the gun was therefore not needed. The rate of return beams seen by each GDU during the commissioning phase was considered adequate to perform successful ground analysis. Also, in-orbit calibration would have required excessive amounts of run time in a diagnostic version of electric field mode where small voltage offsets are added on top of the calibrated values to determine if this results in a better rate of beam return detections. As several of the EDI high voltage opto-couplers were known to be limiting the useful life of the instrument it was decided not to pursue this diagnostic mode.

10.3.2.2 Ambient Electron Mode

Ambient Mode calibration consists of three steps: flat-fielding the detector response, relative adjustment between the two GDUs on each observatory and conversion to fluxes.

For the purpose of determining the instrument correction function that flat-fields the detectors' response as a function of look direction, a special diagnostic "Detector Characterization" has been run at the beginning of the outbound operations (4Re) every other orbit between September 2016 and April 2017, and then once every 7 orbits until November 2020. Each detector characterization steps the optics look direction from 0 (along the symmetry axis) to 101 degrees. Near the pole more fine grained stepping is used as the instrument's response function exhibits a higher change per degree in that region. For each look direction setting a special Sensor test mode is run. This mode samples counts from all 32 anodes in eight steps of four contiguous and simultaneously sampled anodes and sends the counts down in a special telemetry packet. The sampling time is set slightly below 125 ms so that a complete sampling of all 32 anodes is completed in slightly under one second. The mode is run repeatedly for each optics look angle setting. The total duration of one complete detector characterization is approximately 12 minutes. In the analysis the obtained data are filtered to eliminate effects of natural time variation and pitch angle dependency of fluxes. The result of a detector characterization is a map of anode-to-anode variations in count rates that are due to the instrument's response. Results from several detector characterizations have been combined to get a good average and remove uncertainties from residuals in undesired effects (e.g. pitch angle dependency of fluxes). Figure 10-10 shows the derived azimuthal correction factors for GDU1 (SN 3) on MMS1 from the seven executions of the detector characterization that have been merged to arrive at a single averaged azimuthal correction map.

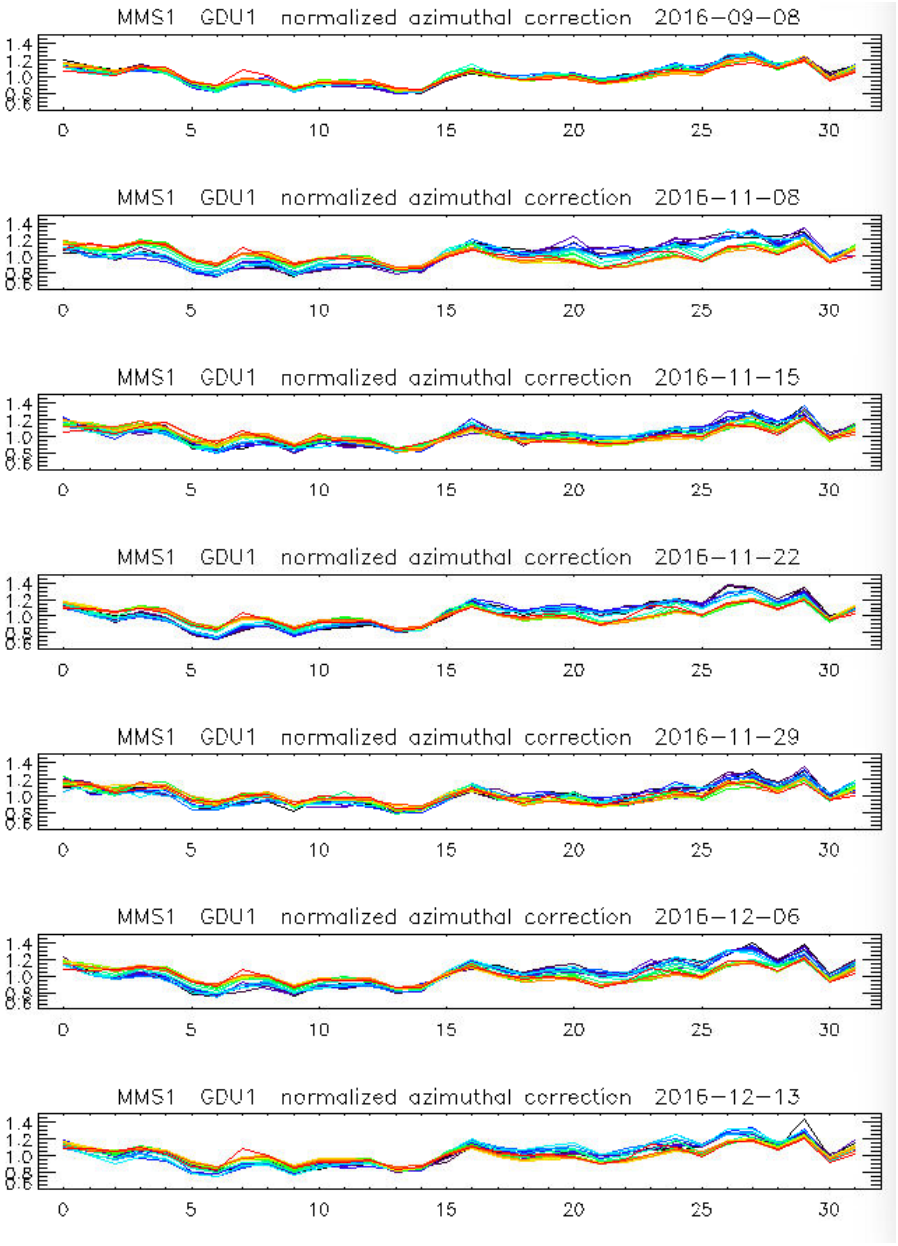

Figure 10-10 Azimuthal Correction Factors for MMS1 GDU1 (SN3) for the Seven Detector Characterizations that were Used to Arrive at an Average Azimuthal Correction Map [The colors in each panel separate data from different optics looks angles]

The second part of the flat-fielding concerns the polar correction (dependency on optics look direction). This correction has been initially derived from short time intervals of Ambient Mode data during the commissioning phase. Improvements to the map have been made by using the data from the above detector characterizations as well as comparisons with L2 DES fluxes. Figure 10-11 shows the resulting polar flat-fielding function which is generic and is applied to all GDUs.

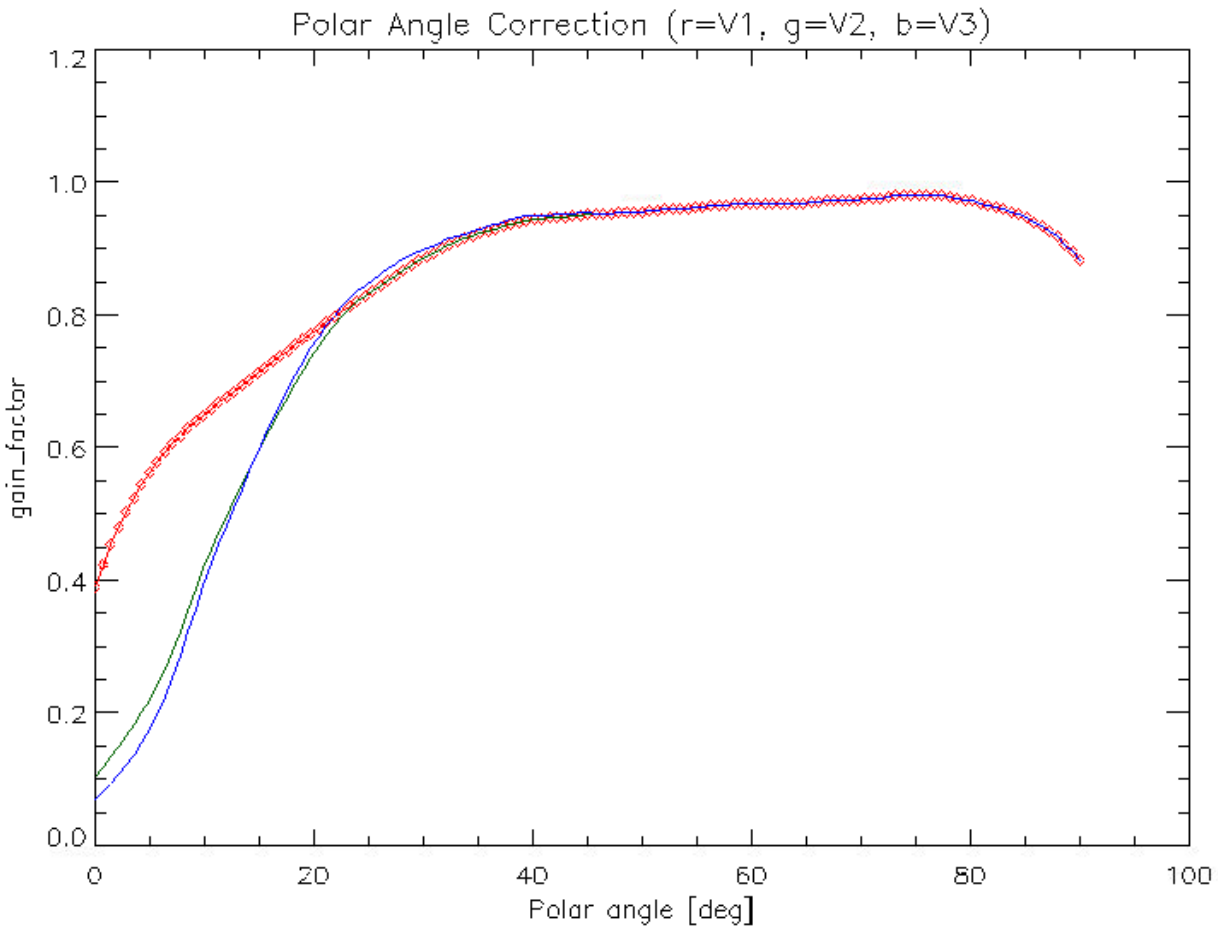

Figure 10-11 Polar Correction for EDI Ambient Mode Data [The red trace shows the original version (V1) derived from EDI burst data during a quiet interval during the commissioning phase. The green trace is the improved correction derived from in-flight detector characterization data. The blue trace (V3) is a slight correction for small polar angle values derived by comparing EDI data with L2 DES fluxes]

Relative counts levels of the two GDUs are determined from daily Ambient Mode data separately for field-aligned and perpendicular samples and by removing data from times of high variability of the count rates.

The absolute calibration factors for the conversion to fluxes are determined from comparison with FPI DES L2 data.

10.3.3 Validation

EDI Electric field data are validated by their usage in the cross-calibration of the EDP electric field data. They serve as a baseline to establish and remove offsets in the EDP data.

EDI Ambient Mode data are validated by their cross-calibration with DES fluxes using DES energy bins closest to the EDI Detector energy setting.

10.4 EDI ELECTRIC FIELD MEASUREMENT ALGORITHM DESCRIPTIONS

10.4.1 Theoretical Basis

The basic concept of determining the displacement ("drift step") of a test beam of electrons after one or more gyrations in the ambient magnetic field from triangulation of firing directions and from time-of-flight differences is described in section 3 of

> Torbert, R.B., et al, **The Electron Drift Instrument for MMS**, Space Sci Rev 199, 283–305 (2016). https://doi.org/10.1007/s11214-015-0182-7

To find the beam directions that will hit the detector, EDI sweeps each beam in the plane perpendicular to B at a fixed angular rate of 0.22°/ms until a signal has been acquired by the detector. Once signal has been acquired, the beams are swept back and forth to stay on target. Beam detection is not determined from the changes in the count-rates directly, but from the square of the beam counts divided by the background counts from ambient electrons, i.e., from the square of the instantaneous signal-to-noise-ratio, SNR2. This quantity is computed from data provided by the correlator in the Gun-Detector Electronics that also generates the coding pattern imposed on the outgoing beams. If the squared signal-to-noise ratio exceeds a threshold, this is taken as evidence that the beam is returning to the detector. The thresholds for SNR2 are chosen dependent on background fluxes. They represent a compromise between getting false hits (induced by strong variations in background electron fluxes) and missing true beam hits. The basic software loop that controls EDI operations is executed every 2 ms. As the times when the beams hit their detectors are neither synchronized with the telemetry nor equidistant, EDI data have no fixed time-resolution. Data are reported in telemetry slots. In Survey, using the standard packing mode 0, there are eight telemetry slots per second and GDU. The last beam detected during the previous slot will be reported in the current slot. If no beam has been detected the data quality will be set to zero. In Burst telemetry there are 128 slots per second and GDU. The data in each slot consists of information regarding the beam firing directions (stored in the form of analytic gun deflection voltages), times-of-flight (if successfully measured), quality indicators, time stamps of the beam hits, and some auxiliary correlator-related information.

10.4.2 Error Analysis and Known Features in the Dataset

Triangulation errors are determined from the radial and azimuthal extent of the 95% confidence level iso-contour of the 2-dimensional cost function, and are propagated from the 2-dimensional drift step in the gyro-plane to the 3-dimensional drift velocity and electric field vectors in the target coordinate systems.

Time-of-flight method errors on the drift step magnitude are computed using the student's t-test which measures the significance of a difference of means. The errors are reported at the 95% confidence level. The azimuthal error is determined from the spread of the firing directions. Propagation of the errors to the 3-dimensional drift velocity and electric field vectors is done in the same way as for the triangulation analysis.

10.4.3 EDI Quality Flags

There are no quality flags in the L2 E-Field data products. For data derived from triangulation analysis the reduced χ^2 value is available in the L2 data set in case filtering of the data is desired.

10.5 EDI AMBIENT ELECTRON MEASUREMENT ALGORITHM DESCRIPTIONS

10.5.1 Theoretical Basis

EDI Ambient Electron Mode has the capability to sample at either 90 degrees pitch angle or at 0/180 degrees (field aligned), or to alternate between 90 degrees and field aligned with selectable dwell times. The choices for energy are 250eV, 500eV and 1keV. The two EDI Gun-Detector Units are mounted on opposite sides of the spacecraft and their detectors are facing opposite hemispheres. At any given time their look directions are set to look strictly into opposite directions. So, when sampling field aligned data, while one detector is looking along **B** the other is looking anti-parallel to **B** (corresponding to pitch angles of 180 and 0 degrees, respectively). The detectors switch roles approximately every half spin of the spacecraft as the tip of the magnetic field vector spins outside the field of view of one detector and into the field of view of the other detector.

The look direction of the detector is defined by a polar angle with respect to the symmetry axis of the detector, and an azimuth angle. The polar angle is set by applying the correct voltages to the electrodes in the upper section of the EDI optics. The azimuth angle impacts the selection of four contiguous (out of 32) anodes of the sensor. There is a variety of configuration options regarding the detailed anode selection with regard to the nominal pitch angle. To make the choice apparent to the L2 end user in an easy way, the chosen option together with the sampled pitch angles impacts the name of the L2 data product. This is outlined in detail in the following subsections.

10.5.1.1 Ambient Mode Raw Telemetry

10.5.1.1.1 Survey Telemetry

Survey telemetry reports a single channel per GDU. Sampled data are from non-contiguous time intervals. There are 32 samples per second, so samples are spaced by 31.25 ms. Each sample is accumulated over half of the sample spacing, or 15.625 ms. The associated time tags identify the center of each sampling interval.

The single channel per GDU can be either a combination (sum) of two adjacent anodes, or a data from one anode. This is controlled independently for field aligned and perpendicular sampling. The details are given in a table further below.

Look directions are reported at the same rate as the count rate channels. The azimuth angle reported in L1A telemetry (mms*X*_edi_amb_phi) can be turned into the respective anode numbers for GDU1 and GDU2 for the purpose of applying a relative calibration, as outlined in a table further below. Note, however, that as a function of spacecraft rotation and magnetic field orientation, the anode used for the sampling may have actually changed during the sampling interval.

10.5.1.1.2 Burst Telemetry

Burst telemetry reports four channels (numbered 1 through 4) per GDU from four contiguous anodes with one ms time resolution (1024 samples per second), using continuous sampling. The counts in the reported channels are compressed in the L0 data, using a lossy compression (errors in the reconstruction of the uncompressed counts are below one sigma). The L1A data stores the de-compressed counts data.

Look directions are reported at one eighth of the count channels rate (one set of look directions every 7.8125 ms). For the determination of anode numbers the azimuth of the look direction (mms*X*_edi_amb_phi) must be expanded to match the time resolution of the counts channels. A cross-

reference between reported azimuth and the anode number for each counts channel as a function of the mode configuration is given in a table further below.

10.5.1.1.3 Flip Flags

The flight software maintains the detector look directions in its basic processing cycle every 2ms such that the polar angle of the optics and the sensor anode numbers best match the selected pitch angles in accordance with the mode configuration options. Owing to spacecraft rotation and directional magnetic field variation, the direction to be maintained can slide out of the field of view of the detector. This happens typically every half spin, and the two detectors swap their roles. As this occurs when the polar angle reaches 90 degrees ("horizon"), this kind of swap impacts only the azimuth angle (and thus the sensor anode selection), while the polar angle remains close to 90 degrees for each detector.

When Ambient Mode is configured to alternate between field aligned and perpendicular sampling, there is, in addition, a rapid switch of look directions each time the dwell time for the current pitch angle expires. This change in look direction impacts the polar angle and thus causes a slew of high voltages on some of the electrodes in the upper section of the optics. The response time of the HV amplifiers is of the order of 2 ms. Each time this kind of switch takes place, there is therefore a transitional period during which the sampled counts represent neither perpendicular nor field aligned data.

Both the horizon flips and the field aligned/perpendicular flips are indicated via flip flags (L1A variable mms*X*_edi_flip) in L1A telemetry. The flip flags should be used to eliminate transitional burst data in alternating mode. Details are given further below.

The dwell times in alternating modes are restricted to values that ensure that the look direction switches between field aligned and perpendicular sampling fall into the non-data taking periods of the non-contiguous sampling of the survey data.

10.5.1.1.4 Anode Selection / Placemat

Two options exist for the selection of sensor anodes. They are referred to as *centered* and *one-sided* placement. These options can be selected separately for field aligned and perpendicular data.
In the case of centered placement, the number of the four contiguous anodes are chosen such that their combined center (the gap between the inner two anodes) is the best match for the current pitch angle.
In the case of one-sided placement, the anode numbers are chosen such that the center of the lowest numbered of the four anodes is the best match for the current pitch angle.

For one-sided perpendicular sampling there is an additional option that impacts only the burst telemetry channels 2, 3, and 4:

- either place the other three anodes (burst channels 2,3,4) such that they sample towards lower pitch angles in both GDUs
- or let the anodes in GDU1 sample towards lower pitch angles (90º and lower) and the anodes in GDU2 sample towards higher pitch angles (90º and higher)

10.5.1.2 L1A Variable Relation to L2 Data Product Names

This section describes the L1A variables that impact the L2 data product names.

mms*X*_edi_amb_pitchmode -- This L1A variable indicates which pitch angles have been sampled.

- 0: Field aligned sampling only (pitch angles 0º/180º)

- 1 or 3: Alternating between field aligned (pitch angles 0º/180º) and perpendicular (pitch angle 90º) sampling. In this case the L1A variable "mms*N*_edi_amb_dwell" indicates the amount of time spent sampling data in between switches between field aligned and perpendicular directions. The number is given in units of 1/512 seconds.

- 2: Perpendicular sampling only (pitch angle 90º only)

mms*X*_edi_amb_pacmo -- This L1A variable impacts, for field aligned sampling:
- the anode selection (centered vs one-sided)
- the number of anodes that are summed in the channel reported in survey telemetry:
  - two anodes for centered
  - one anode in the case of one-sided anode placement

mms*X*_edi_amb_perp_onesided -- This L1A variable impacts, for perpendicular sampling:
- the anode selection (centered vs one-sided)
- the number of anodes that are summed in the channel reported in survey telemetry:
  - two anodes for centered
  - one anode in the case of one-sided anode placement

mms*X*_edi_amb_perp_bidirectional -- This L1A variable impacts only burst data for perpendicular sampling. It indicates whether both GDUs sample pitch angle 90º and lower ("mono-directional"), or whether GDU1 and GDU2, respectively, sample pitch angle 90º and lower / higher ("bidirectional").

Table 10-4 summarizes how the discussed L1A variables are related to the L2 data product names.

L2 Data Product Name	**L1A Variable** mms*X*_edi_amb_...				**Sampled Pitch Angles**
	...pitchmode	...pacmo	...perp_onesided	...perp_bidirectional	
amb	0	1	N/A	N/A	0 / 180
amb-pm2	0	2	N/A	N/A	0 / 180
amb-alt-oc	1 o 3	2	0	N/A	0 / 180 and 90
amb-alt-cc	1 or 3	1	0	N/A	0 / 180 and 90
amb-alt-oom	1 or 3	2	1	0	0 / 180 and 90
amb-alt-oob	1 or 3	2	1	1	0 / 180 and 90
amb-perp-ob	2	2	1	1	90

Table 10-4 EDI Ambient Mode L2 Data Product Names

Table 10-5 below summarizes the anode placement and pitch angle 90º sampling direction for each L2 data product.

L2 Data Product Name	**Anode Placement for PA 0º/180º**	**Anode Placement for PA 90º**	**Pitch angle 90º sampling direction**

amb	centered	N/A	N/A
amb-pm2	one-sided	N/A	N/A
amb-alt-oc	one-sided	centered	N/A
amb-alt-cc	centered	centered	N/A
amb-alt-oom	one-sided	one-sided	mono-directional
amb-alt-oob	one-sided	one-sided	bi-directional
amb-perp-ob	N/A	one-sided	bi-directional

Table 10-5 Sensor Anode Placement for EDI L2 Ambient Mode Data Products

10.5.1.3 Anode Placement Details

For the purpose of identifying the anodes used for each survey and burst data channel, it is best to turn the L1A azimuth angle `mmsX_edi_amb_phi` into a reference anode number N that serves as a basis for identifying the per-channel anode numbers dependent on the mode configuration details:

$$N = \text{round}(\texttt{mms}X\texttt{\_edi\_amb\_phi} / 11.25)$$

The table below shows how the per-channel anode numbers can be derived from the reference anode number N for each L2 data product. The per-channel anode numbers can be used as indices into the 2D relative calibration tables for each GDU.

L2 Data Product	Pitch Angle	Anode Placement	Survey		Burst							
			GDU1	GDU2	GDU1				GDU2			
					ch1	ch2	ch3	ch4	ch1	ch2	ch3	ch4
amb amb-alt-cc amb-alt-oc	0/180 0/180/90 90	centered	N – 1, N	15 – N, 16 - N	N - 2	N - 1	N	N + 1	14 - N	15 - N	16 - N	17 - N
amb-pm2 amb-alt-oc amb-alt-oom	0/180 0/180 0/180/90	one-sided	N	15 - N	N	N + 1	N + 2	N + 3	15 - N	16 - N	17 - N	18 - N
amb-alt-oob	0/180/90	one-sided	N	15 - N	N	N + 1	N + 2	N + 3	15 - N	14 - N	13 - N	12 - N
amb-perp-ob	90	one-sided	N	15 - N	N	N + 1	N + 2	N + 3	15 - N	14 - N	13 - N	12 - N

Table 10-6 Sensor Anode Numbers per Channel for Each EDI L2 Ambient Mode Data Product

10.5.1.4 Calculation of Azimuth Angles for Data Channels

For the calculation of particle trajectories in the L2 data, the per-channel anode numbers from the above table need to be turned into azimuth angles. Table 10-7 provides the necessary formulas. Note that GDU2 angles are given in GDU2 coordinates.

N = reference anode number, derived from L1A telemetry variable mms*X*_edi_amb_phi
A = per-channel anode number, as given in Table 10-7

Telemetry	Anode Placement	GDU1	GDU2
Burst	any	$\varphi = (A + 0.5) * 11.25°$	$\varphi = (A + 0.5) * 11.25°$

Survey	centered	$\varphi = N * 11.25°$	$\varphi = (16 - N) * 11.25°$
Survey	one-sided	$\varphi = (N + 0.5) * 11.25°$	$\varphi = (15.5 - N) * 11.25°$

Table 10-7 Relation of Sensor Anode Numbers to Azimuth Angles of EDI Detector Look Direction

10.5.1.5 Flip Flag Summary

Table 10-8 summarizes how flip flags are handled, depending on L2 data product and telemetry.

L2 Data Product Name	Survey	Burst
amb	ignored	ignored
amb-pm2	ignored	ignored
amb-alt-oc	ignored	insert fill data for the pair of flagged data points (fluxes) and the data point immediately following
amb-alt-cc	ignored	insert fill data for the pair of flagged data points (fluxes) and the data point immediately following
amb-alt-oom	ignored	insert fill data for the pair of flagged data points (fluxes) and the data point immediately following
amb-alt-oob	ignored	insert fill data for the pair of flagged data points (fluxes) and the data point immediately following
amb-perp-ob	ignored	ignore

Table 10-8 EDI Ambient Mode Flip Flag Handling

10.5.2 Error Analysis and Known features in the Dataset

The error analysis of the EDI ambient electron data takes into account the statistical variation of the raw counts, properly propagated through the sensor deadtime correction as well as uncertainties from the three calibration steps.

10.5.2.1 Dead Time Correction

The dead time correction is given by

$$C = R \cdot t_A \; / \; (\; t_A - R \cdot t_D)$$

with the following abbreviations:

C	dead time corrected counts
R	raw counts
t_A	the accumulation time (1/1024 sec for burst, 1/64 sec for survey)
t_D	the sensor dead time (200ns)

The error propagation from raw to dead time corrected counts is

$$err_C = err_R \cdot [\, t_A \; / \; (\; t_A - R \cdot t_D) \,]^{\,2}$$

where the one-sigma error *sqrt(R)* is used for err_R.

10.5.2.2 Calculation of Ambient Electron Flux Errors

The calculation of absolute fluxes is given by the formula

$$F = C \cdot R \cdot A$$

where

- F is the absolute flux
- C is the dead time corrected counts
- R is the relative calibration (a function of detector look angles)
- A is the absolute calibration factor

The error in the absolute flux is calculated according to

$$err_F = F \cdot SQRT [(err_C / C)^2 + (err_R / R)^2 + (err_A / A)^2]$$

The error err_C for the dead time corrected counts is given in section 3.4.1. The second term err_R/R is ignored at the moment, as the information on the relative calibration is still being improved, especially for small polar look angles where the relative calibration R factor is largest. For the third term err_A/A, we assume a factor of 0.2 (20% error), based on the general level of agreement in comparisons between DES burst Quicklook data and EDI ambient burst data.

10.5.3 EDI Quality Flags

Currently there are no quality flags in the L2 Ambient Electron data sets. It is planned to add a flip flag that indicates times during which the detectors were in a transitional state due to rapid changes of look directions.

10.6 EDI DATA PRODUCTION ALGORITHM DESCRIPTIONS

The following Level 2 EDI data products are being generated.

Electric Field Data -- This is the primary data product generated from data collected in electric field mode. The science data generated are drift velocity and electric field data in various coordinate systems. They are derived from triangulation and/or time-of-flight analysis. Where both methods are applicable, their results will be combined using a weighting approach based on their relative errors.

Quality-Zero Data -- These data are a by-product generated from data collected in electric field mode. Whenever no return beam is found in a particular time slot by the flight software, the data to be reported will be flagged with the lowest quality level (quality zero). The ground processing generates a separate data product from these counts data.

Ambient Electron Data -- The raw counts data collected in ambient mode are going through a three step calibration for conversion to fluxes. The first step performs a dead time correction of the raw counts and applies a flat-fielding calibration that removes the instrument response dependency on look direction (optics polar angle and sensor anode pad number). The second step brings the flat-fielded counts from the GDUs to the same level. The third step is a multiplication with a factor to convert from relative, dead time corrected counts to fluxes.

10.6.1 E-Field Data Processing

Generation of L2 Electric Field Mode data is a three step process as illustrated in Figure 10-12. In the first step L1A files are generated from L0 raw telemetry. Aside from extraction of data this involves a conversion of the analytic voltages that represent the gun firing direction in the L0 data to the azimuth and polar angles of a spherical coordinate system that has its Z axis along the GDU symmetry axis pointing outward in the spacecraft spin plane and the X axis along the negative spacecraft body Z axis. In addition, since the return beam hits are asynchronous in nature to any onboard clock, separate time tags in TT2000 format are calculated for every individual beam based on the timing information in the L0 files. Raw times-of-flight in digital units are converted to micro-seconds.

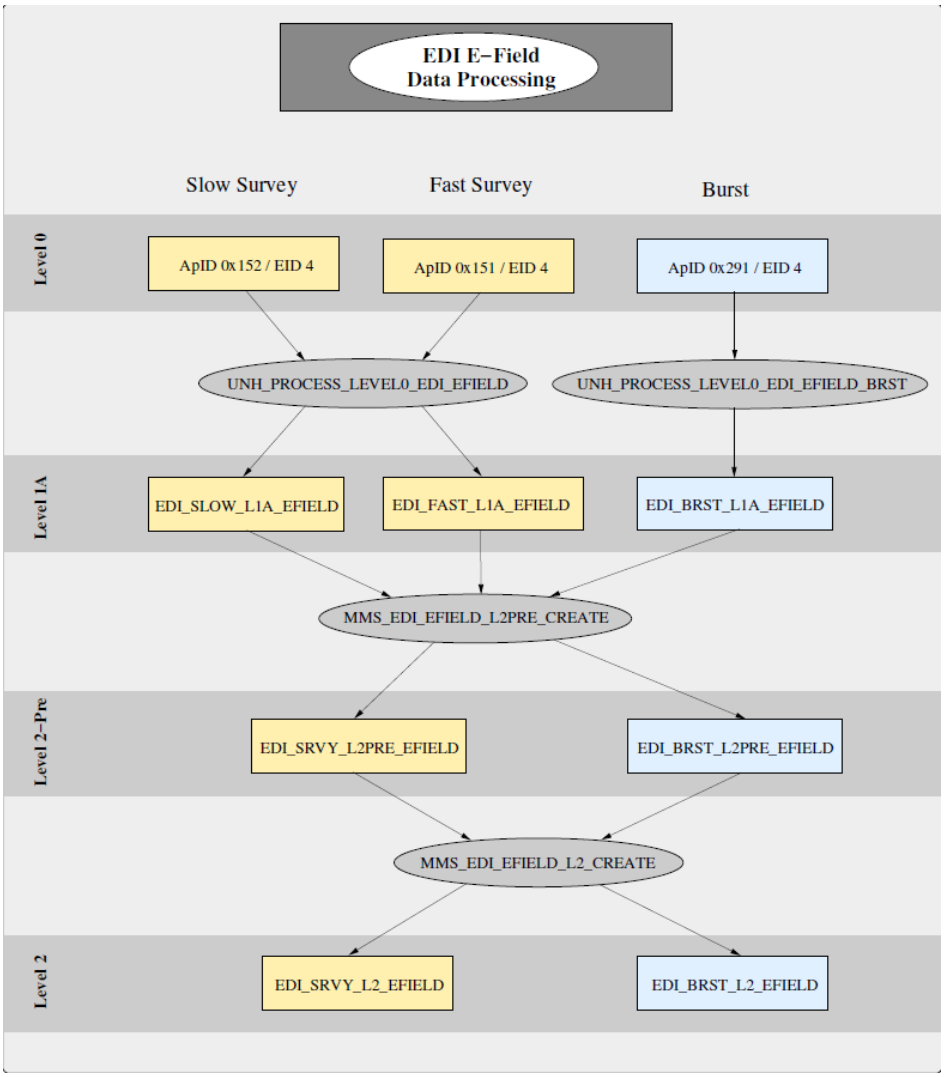

Figure 10-12 EDI Electric Field Mode Data Processing Flow

In the second step the L1A data are processed to level L2-Pre. Data are preselected by quality and are sent through a process that attempts to determine the number of gyrations for each beam based on its time-of-flight and the gyro time derived from DFG L2Pre magnetic field data. The resulting data set is analyzed with both the triangulation and time of flight method as outlined further below. For the purpose of the analysis the data are grouped into five-second time intervals. For each analysis interval an average magnetic field vector is calculated for the definition of a gyro plane, that is, the plane perpendicular to the

magnetic field. Beam firing directions are then represented as clock angles in that plane with respect to a reference direction which is chosen to be closest to the line towards the sun.

10.6.1.1 Triangulation Analysis

The triangulation analysis procedure determines the drift step by searching for the target-point that minimizes an appropriate 'cost-function'. The cost-function is constructed, for each grid-point in the plane, by adding up the (squared) angle-deviations of all beams in a chosen time interval from the direction to that grid-point. Each beam contribution to the cost-function is normalized by the (squared) error in the firing directions, which is a function of beam pointing direction and varies between 1° and 4°, using an analytic model for the beam profile as a function of the polar angle of the gun firing direction. The grid-point with the smallest value of the cost-function is taken as the target. If a beam has been identified as a multi-runner of order *N* by the preceding runner order analysis, it is associated with a grid-point at *N* times the radial distance. When identification of the order from the runner order analysis is ambiguous, the respective beams are treated as single-runners. This assumption works well in most cases, as, compared the EDI implementation on ESA's Cluster project, the design of the correlator and the choice of code frequencies makes the occurrence of multi-runners much less likely. To speed up the search, the procedure uses a coarse grid to identify a restricted range in which the final search is performed with a much finer grid. The electron trajectories are approximated by circles whose radius is based on the magnetic field strength.

The analysis fails if the drift step and/or the magnetic field significantly vary within the chosen time interval (5 seconds). Such cases can be identified by the variance in the magnetic field, by the quality of the fit (as measured by its reduced χ^2), and by the errors in the computed drift step.

Using the DFG L2pre magnetic field data, the drift steps can be converted to drift velocities and electric field data.

Errors are determined from the radial and azimuthal extent of the 95% confidence level iso-contour of the 2-dimensional cost function and are propagated from the 2-dimensional drift step in the gyro-plane to the 3-dimensional drift velocity and electric field vectors in the target coordinate systems.

In addition to the drift step, drift velocity and electric field vectors and their respective errors, various processing parameters such as the number of beams involved in the analysis and the reduced χ^2 are stored in the resulting L2pre data files for the purpose of reducing the L2pre data set to L2 data as described in section 3.2.3.

10.6.1.2 Time-of-Flight Analysis

Deduction of the drift step (and the drift velocity) from analysis of the difference in the times-of-flight of the two beams is, in principle, straightforward. If the drift step is large enough such that the firing directions become nearly parallel, the beams in the analysis interval can be grouped into two nearly oppositely directed sets. The set with the larger times-of-flight then must contain the beams directed towards the target, the other set those directed away from the target. This assignment settles the drift direction, and the drift magnitude is then computed from the magnitude of the difference in the times-of-flight.

This simple scheme would require stable conditions (i.e., non-varying gyro time and times-of-flight) over the analysis interval. Since this is not always the case, especially in the magnetosheath, the analysis makes use of the gyro time determined from the DFG L2pre data and interpolated to the times of the EDI

beam hits. The differences between the measured times-of-flight and the interpolated gyro times are calculated separately for the two sets of beams. For each set the average difference from the gyro time is calculated and the two averages are then combined. This way any fixed magnitude offset in the gyro-time that might result from a residual error in the magnetic field calibration will cancel out. The set with the larger average identifies the direction towards the target. Multiplication of half the time-of-flight difference (the combination of the two averages as described above) with the electron velocity yields the drift step magnitude.

Calculation of drift velocities and electric fields is done in the same fashion as for the triangulation analysis.

The error on the drift step magnitude is computed using the student's t-test which measures the significance of a difference of means. The error is reported at the 95% confidence level. The azimuthal error is determined from the spread of the firing directions. Propagation of the errors to the 3-dimensional drift velocity and electric field vectors is done in the same way as for the triangulation analysis.

10.6.1.3 Filtering of L2 Pre Data

In the final step the L2Pre data are filtered using various quantities stored in the L2pre files. For triangulation, the filter criteria are:

(1) Reduced χ^2 below 10000
(2) At least three beams in the analysis interval
(3) Beam spread is greater than 15 degrees
(4) Drift step magnitude is less than 3 times the triangulation baseline
(5) Product of triangulation baseline [m], number of beams and B magnitude [nT] is greater than 5000
(6) Electric Field error is less than 1 mV/m
(7) Electric Field error is larger than 0.1 mV/m
(8) The relative error of the electric field magnitude less than 1 (100%)

Filter (5) was not present originally. It was added in October 2016 to remove bad data in variable fields.

For the time-of-flight analysis the filter criteria are:

(1) Drift step magnitude greater than 1 meter
(2) Electric field error less than 1 mV/m
(3) Relative error of electric field magnitude less than 1 (100%)

10.6.1.4 File Structure L2 EFIELD Data

For the L2 electric field data product, survey and burst files contain the same quantities with only the telemetry identifier (<tlm>) being different (<tlm> = srvy or <tlm> = brst).
Filenames:

mms<N>_edi_srvy_l2_efield_<yyyymmdd>_v<x.y.z>.cdf
mms<N>_edi_brst_l2_efield_<yyyymmddhhmmss>_v<x.y.z>.cdf

Important note: The drift velocities and electric field quantities in the L2 EDI electric field data files are not corrected for spacecraft velocities. They are given in the moving spacecraft frame of reference. That is, "gse" and "gsm" in the variable names refer only to coordinate systems, not frames of reference.

Name	Description	Type	Units
mms<N>_edi_vdrift_dsl_<tlm>_l2	Drift velocity vector in DSL coordinates	FLOAT	km/s
mms<N>_edi_vdrift_gse_<tlm>_l2	Drift velocity vector in GSE coordinates	FLOAT	km/s
mms<N>_edi_vdrift_gsm_<tlm>_l2	Drift velocity vector in GSM coordinates	FLOAT	km/s
mms<N>_edi_e_dsl_<tlm>_l2	Electric field vector in DSL coordinates	FLOAT	mV/m
mms<N>_edi_e_gse_<tlm>_l2	Electric field vector in GSE coordinates	FLOAT	mV/m
mms<N>_edi_e_gsm_<tlm>_l2	Electric field vector in GSM coordinates	FLOAT	mV/m
mms<N>_edi_tri_weight_<tlm>_l2	Weight of triangulation method when merging results from triangulation and time-of-flight analyses	INT2	percent
Support Data			
Epoch	Time tags	TT2000	ns
mms<N>_edi_t_delta_minus_<tlm>_l2	Time between start of analysis interval and time tag	FLOAT	ns
mms<N>_edi_t_delta_plus_<tlm>_l2	Time between time tag and end of analysis interval	FLOAT	ns
mms<N>_edi_tri_rchisq_<tlm>_l2	Reduced Chi-Squared from triangulation analysis	FLOAT	none
mms<N>_edi_v_dsl_delta_minus_<tlm>_l2	Drift velocity negative error	FLOAT	km/s
mms<N>_edi_v_dsl_delta_plus_<tlm>_l2	Drift velocity positive error	FLOAT	km/s
mms<N>_edi_v_gse_delta_minus_<tlm>_l2	Drift velocity negative error	FLOAT	km/s
mms<N>_edi_v_gse_delta_plus_<tlm>_l2	Drift velocity positive error	FLOAT	km/s
mms<N>_edi_v_gsm_delta_minus_<tlm>_l2	Drift velocity negative error	FLOAT	km/s
mms<N>_edi_v_gsm_delta_plus_<tlm>_l2	Drift velocity positive error	FLOAT	km/s
mms<N>_edi_e_dsl_delta_minus_<tlm>_l2	E-field negative error	FLOAT	mV/m
mms<N>_edi_e_dsl_delta_plus_<tlm>_l2	E-field positive error	FLOAT	mV/m
mms<N>_edi_e_gse_delta_minus_<tlm>_l2	E-field negative error	FLOAT	mV/m
mms<N>_edi_e_gse_delta_plus_<tlm>_l2	E-field positive error	FLOAT	mV/m
mms<N>_edi_e_gsm_delta_minus_<tlm>_l2	E-field negative error	FLOAT	mV/m
mms<N>_edi_e_gsm_delta_plus_<tlm>_l2	E-field positive error	FLOAT	mV/m

Table 10-9 L2 E-FIELD Data

10.6.2 Quality-Zero Data

The lowest quality level in the raw (and in the L1A) electric field data (quality zero) signals that no return beam was detected during a given time slot. Counts accumulated in these time slot are considered a proxy for the ambient electron flux at the energy of the detector. In regions with high variability of the magnetic/electric fields, very low magnetic fields, or high ambient electron fluxes at the energy of the detector, EDI will have difficulty identifying the return beams (if there are any). Consequently, in those regions there will be a higher rate of quality-zero data. Care must be taken in general when interpreting these data. First, they are uncalibrated raw counts. Second, even though they did not pass the detection

threshold for the squared signal-to-noise ratio, some of the counts samples can represent a mix of beam and background electrons. The data can be useful as boundary markers, or for detecting anisotropies in the 90 degree pitch angle data.

The processing extracts the counts data (one ms accumulation time base) and the gun firing directions. From the latter the associated detector look directions are deduced and the particle motion directions are calculated. Particle motion directions are specified in the form of azimuth and polar angle in the respective coordinate system (GSE, GSM) using the following convention:

- Polar angle = acos(z / magnitude)
- Azimuth angle = atan(y / x)

Since the counts are unmodified raw counts, no error is specified as it is straightforward for the user to calculate the one-sigma error (square root of the counts). The uncertainty in the particle motion direction is given as a single constant angular error number that is derived from the characteristic FWHM of the optics' polar acceptance and the half width of the sensor's azimuthal field of view.

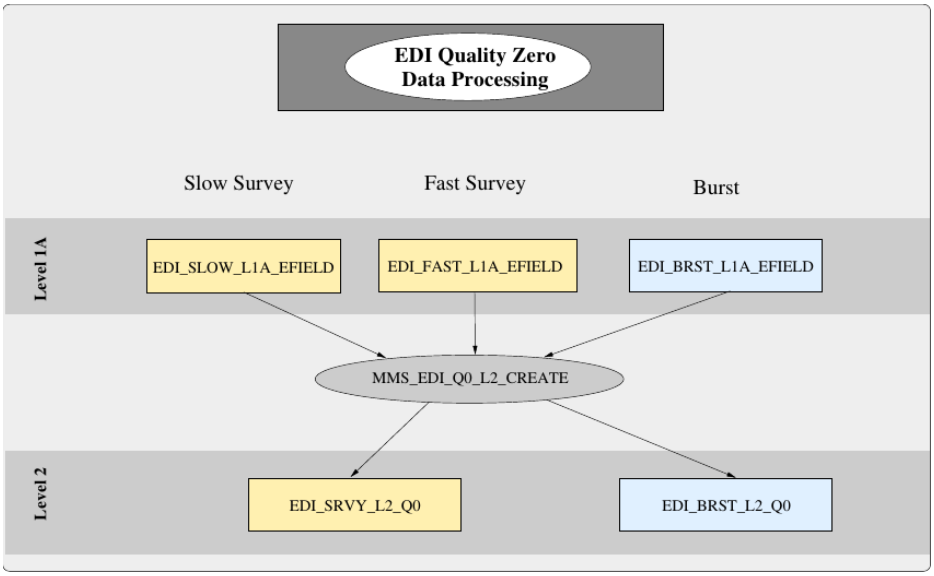

Figure 10-13 EDI Quality-Zero Data Processing

10.6.2.1 File Structure L2 Quality-Zero Data

For the L2 quality zero data product, survey and burst files contain the same quantities with only the telemetry identifier being different (<tlm> = srvy or <tlm> = brst)

File Names:

mms<N>_edi_srvy_q0_l2_<yyyymmdd>_v<x.y.z>.cdf
mms<N>_ edi_brst_q0_l2_<yyyymddhhmmss>_v<x.y.z>.cdf

Name	Description	Type	Units
mms<N>_edi_counts_gdu1_<tlm>_l2	Raw counts measured by the detector in GDU1; accumulation time is 1/1024 seconds	UINT2	counts

mms<N>_edi_counts_gdu2_<tlm>_l2	Raw counts measured by the detector in GDU2; accumulation time is 1/1024 seconds	UINT2	counts
mms<N>_edi_traj_gse_gdu1_<tlm>_l2	Direction of particle motion for GDU1 electrons in GSE	FLOAT	degrees
mms<N>_edi_traj_gse_gdu2_<tlm>_l2	Direction of particle motion for GDU2 electrons in GSE	FLOAT	degrees
mms<N>_edi_traj_gsm_gdu1_<tlm>_l2	Direction of particle motion for GDU1 electrons in GSM	FLOAT	degrees
mms<N>_edi_traj_gsm_gdu2_<tlm>_l2	Direction of particle motion for GDU2 electrons in GSM	FLOAT	degrees
Support Data			
epoch_gdu1	Time tags for GDU1 counts, trajectories and detector energy	TT2000	ns
epoch_gdu2	Time tags for GDU2 counts, trajectories and detector energy	TT2000	ns
epoch_timetag	Time tags for optics state variable	TT2000	ns
mms<N>_edi_optics_state_<tlm>_l2	Optics State	UINT2	none
mms<N>_edi_energy_gdu1_<tlm>_l2	GDU1 detector energy	UINT2	eV
mms<N>_edi_energy_gdu2_<tlm>_l2	GDU2 detector energy	UINT2	eV

Table 10-10 L2 Quality-Zero Data

10.6.3 Ambient Mode Data

Ambient Mode data processing of Level 2 data and Quicklook (QL) data is illustrated in Figure 10-14. The initial common step is the generation of L1A data from the raw L0 data. In this step data are extracted, time tags in TT2000 format are added to each record, and for burst data the compressed counts data are decompressed.

For the QuickLook Data, the counts data are corrected for dead time effects, the instrument response function that removes the geometric factor dependency on the look direction is applied (flat-fielding) and the counts from the GDUs are brought to the same level (relative calibration).

For the L2 ambient data, the absolute calibration factor is applied in addition, and an error for the resulting fluxes is calculated that takes into account various error terms as outlined in section 10.5.2.2. Particle motion directions are calculated and given in GSE and DBCS coordinates. As in the case of the quality zero data the uncertainty in these directions is specified as a single angle.

The order of steps for the calculation of fluxes in the ambient data processing is:

1. Dead time correction – for survey data where the telemetry channels contain the summed counts of two adjacent anodes (data products amb, amb-alt-cc and the perpendicular data of amb-alt-oc)

the assumption is made that both anodes contribute evenly. The raw counts must be divided by two, then the deadtime correction is performed, and the result is then multiplied by a factor of 2

2. Relative calibration (flat-fielding)
3. Application of Inter-GDU adjustment factor
4. Conversion to fluxes – the absolute calibration factors stored in the L2 calibration files are for burst data. That is, they are valid for accumulation times of 1 ms and single anodes. For survey data the following adjustments are made:
    a. One-sided anode placement (single anode): division of the absolute calibration factor by 16 to account for the longer accumulation time of survey data, This applies to data products amb-pm2, amb-alt-oom, amb-alt-oob, amb-perp-ob and the field aligned data in amb-alt-oc
    b. Centered anode placement: division of the absolute calibration factor by 32 to account for the longer accumulation time of survey data and the fact that data from two anodes have been combined. This applies to data products amb, amb-alt-cc and the perpendicular data of amb-alt-oc

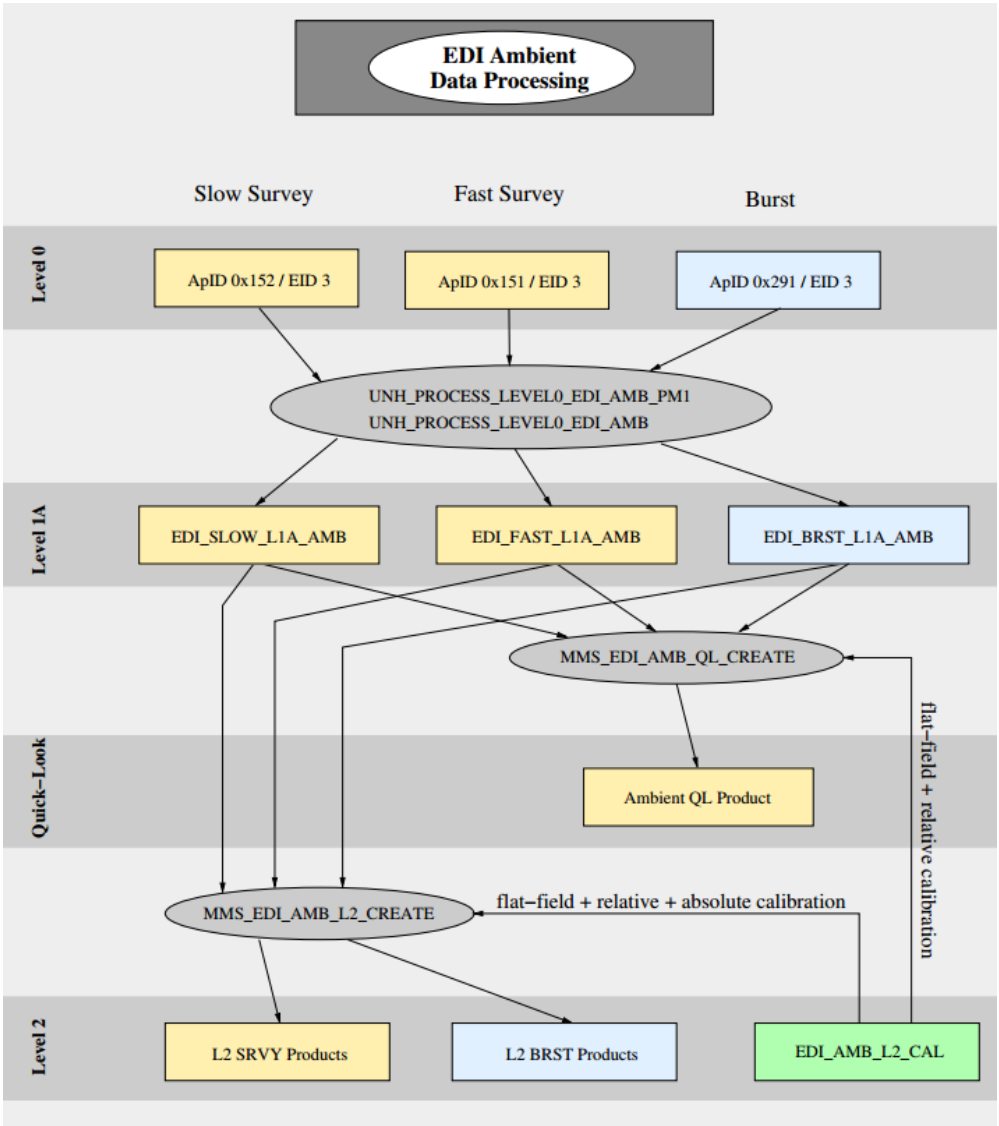

Figure 10-14 EDI Ambient Mode Data Processing Flow

10.6.3.1 File Structure L2 AMBIENT Field Aligned Mode Data

10.6.3.1.1 Survey

File Names:

mms<N>_edi_srvy_l2_amb_<yyyymmdd>_v<x.y.z>.cdf
mms<N>_edi_srvy_l2_amb-pm2_<yyyymmdd>_v<x.y.z>.cdf

Name	Description	Type	Units
mms<N>_edi_flux1_0_srvy_l2	Electron flux along pitch angle 0	FLOAT	$cm^{-2}\ s^{-1}sr^{-1}$
mms<N>_edi_flux1_180_srvy_l2	Electron flux along pitch angle 180	FLOAT	$cm^{-2}\ s^{-1}sr^{-1}$
mms<N>_edi_traj1_dbcs_0_srvy_l2	Direction of particle motion for pitch angle 0 electrons in DBCS, given as in spherical coordinates. First component: azimuth (in DBCS xy plane), second component: polar angle (with respect to DBCS z)	FLOAT	degrees
mms<N>_edi_traj1_dbcs_180_srvy_l2	Direction of particle motion for pitch angle 180 electrons in DBCS	FLOAT	degrees
mms<N>_edi_traj1_gse_0_srvy_l2	Direction of particle motion for pitch angle 0 electrons in GSE	FLOAT	degrees
mms<N>_edi_traj1_gse_180_srvy_l2	Direction of particle motion for pitch angle 180 electrons in GSE	FLOAT	Degrees
Support data			
Epoch	Time tags for fluxes, trajectories, GDU numbers, flux errors and flip indicator	TT_2000	ns
epoch_timetag	Time tags for optics state and GDU energies	TT_2000	ns
mms<N>_edi_flip_0_180_srvy_l2	Indicator for rapid detector look direction changes	UINT1	none
mms<N>_edi_optics_state_srvy_l2	EDI detector optics state	UINT1	none
mms<N>_edi_energy_gdu1_srvy_l2	EDI GDU1 energy	UINT2	eV
mms<N>_edi_energy_gdu2_srvy_l2	EDI GDU2 energy	UINT2	eV
mms<N>_edi_gdu_0_srvy_l2	GDU number for pitch angle 0 data	UINT1	none
mms<N>_edi_gdu_180_srvy_l2	GDU number for pitch angle 180 data	UINT1	none
mms<N>_edi_flux1_0_delta_srvy_l2	Error for pitch angle 0 flux	FLOAT	$cm^{-2}\ s^{-1}sr^{-1}$

mms<N>_edi_flux1_180_delta_srvy_l2	Error for pitch angle 180 flux	FLOAT	$cm^{-2}\ s^{-1}sr^{-1}$

Table 10-11 L2 Ambient Field Aligned Mode Survey Data

10.6.3.1.2 Burst

File Names:

mms<N>_edi_brst_l2_amb_<yyyymmddhhmmss>_v<x.y.z>.cdf
mms<N>_edi_brst_l2_amb-pm2_<yyyymmddhhmmss>_v<x.y.z>.cdf

Name	Description	Type	Units
mms<N>_edi_flux1_0_brst_l2 mms<N>_edi_flux2_0_brst_l2 mms<N>_edi_flux3_0_brst_l2 mms<N>_edi_flux4_0_brst_l2	Electron flux in four separate directional channels close to pitch angle 0	FLOAT	$cm^{-2}\ s^{-1}sr^{-1}$
mms<N>_edi_flux1_180_brst_l2 mms<N>_edi_flux2_180_brst_l2 mms<N>_edi_flux3_180_brst_l2 mms<N>_edi_flux4_180_brst_l2	Electron flux in four separate directional channels close to pitch angle 180	FLOAT	$cm^{-2}\ s^{-1}sr^{-1}$
mms<N>_edi_traj1_dbcs_0_brst_l2 mms<N>_edi_traj2_dbcs_0_brst_l2 mms<N>_edi_traj3_dbcs_0_brst_l2 mms<N>_edi_traj4_dbcs_0_brst_l2	Particle motion directions for the four channels close to pitch angle 0 in DBCS	FLOAT	degrees
mms<N>_edi_traj1_dbcs_180_brst_l2 mms<N>_edi_traj2_dbcs_180_brst_l2 mms<N>_edi_traj3_dbcs_180_brst_l2 mms<N>_edi_traj4_dbcs_180_brst_l2	Particle motion directions for the four channels close to pitch angle 180 in DBCS	FLOAT	degrees
mms<N>_edi_traj1_gse_0_brst_l2 mms<N>_edi_traj2_gse_0_brst_l2 mms<N>_edi_traj3_gse_0_brst_l2 mms<N>_edi_traj4_gse_0_brst_l2	Particle motion directions for the four channels close to pitch angle 0 in GSE	FLOAT	degrees
mms<N>_edi_traj1_gse_180_brst_l2 mms<N>_edi_traj2_gse_180_brst_l2 mms<N>_edi_traj3_gse_180_brst_l2 mms<N>_edi_traj4_gse_180_brst_l2	Particle motion directions for the four channels close to pitch angle 180 in GSE	FLOAT	degrees
Support data			
Epoch	Time tags for fluxes, trajectories, GDU numbers, flux errors and flip indicator	TT_2000	ns
epoch_timetag	Time tags for optics state and GDU energies	TT_2000	ns
mms<N>_edi_flip_0_180_brst_l2	Indicator for rapid detector look direction changes	UINT1	none
mms<N>_edi_optics_state_brst_l2	EDI detector optics state	UINT1	none
mms<N>_edi_energy_gdu1_brst_l2	EDI GDU1 energy	UINT2	eV
mms<N>_edi_energy_gdu2_brst_l2	EDI GDU2 energy	UINT2	eV
mms<N>_edi_gdu_0_brst_l2	GDU number for pitch angle 0 data	UINT1	none

mms<N>_edi_gdu_180_brst_l2	GDU number for pitch angle 180 data	UINT1	none
mms<N>_edi_flux1_0_delta_brst_l2 mms<N>_edi_flux2_0_delta_brst_l2 mms<N>_edi_flux3_0_delta_brst_l2 mms<N>_edi_flux4_0_delta_brst_l2	Errors for pitch angle 0 flux channels	FLOAT	$cm^{-2}\ s^{-1}sr^{-1}$
mms<N>_edi_flux1_180_delta_brst_l2 mms<N>_edi_flux2_180_delta_brst_l2 mms<N>_edi_flux3_180_delta_brst_l2 mms<N>_edi_flux4_180_delta_brst_l2	Errors for pitch angle 180 flux channels	FLOAT	$cm^{-2}\ s^{-1}sr^{-1}$

Table 10-12 L2 Ambient Field Aligned Burst Data

10.6.3.2 File Structure L2 AMBIENT Alternating Pitch Angle Mode Data

10.6.3.2.1 Survey

File Names:

mms<N>_edi_srvy_l2_amb-alt-cc_<yyyymmdd>_v<x.y.z>.cdf
mms<N>_edi_srvy_l2_amb-alt-oc_<yyyymmdd>_v<x.y.z>.cdf
mms<N>_edi_srvy_l2_amb-alt-oob_<yyyymmdd>_v<x.y.z>.cdf

Name	Description	Type	Units
mms<N>_edi_flux1_0_srvy_l2	Electron flux along pitch angle 0	FLOAT	$cm^{-2}\ s^{-1}sr^{-1}$
mms<N>_edi_flux1_90_gdu1_srvy_l2	Electron flux for pitch angle 90, measured by GDU1	FLOAT	$cm^{-2}\ s^{-1}sr^{-1}$
mms<N>_edi_flux1_90_gdu2_srvy_l2	Electron flux for pitch angle 90, measured by GDU2	FLOAT	$cm^{-2}\ s^{-1}sr^{-1}$
mms<N>_edi_flux1_180_srvy_l2	Electron flux along pitch angle 180	FLOAT	$cm^{-2}\ s^{-1}sr^{-1}$
mms<N>_edi_traj1_dbcs_0_srvy_l2	Direction of particle motion for pitch angle 0 electrons in DBCS, given as in spherical coordinates. First component: azimuth (in DBCS xy plane), second component: polar angle (with respect to DBCS z)	FLOAT	degrees
mms<N>_edi_traj1_dbcs_90_gdu1_srvy_l2	Direction of GDU1 particle motion for pitch angle 90 electrons in DBCS	FLOAT	degrees
mms<N>_edi_traj1_dbcs_90_gdu2_srvy_l2	Direction of GDU2 particle motion for pitch angle 90 electrons in DBCS	FLOAT	degrees

mms<N>_edi_traj1_dbcs_180_srvy_l2	Direction of particle motion for pitch angle 180 electrons in DBCS	FLOAT	degrees
mms<N>_edi_traj1_gse_0_srvy_l2	Direction of particle motion for pitch angle 0 electrons in GSE	FLOAT	degrees
mms<N>_edi_traj1_gse_90_gdu1_srvy_l2	Direction of GDU1 particle motion for pitch angle 90 electrons in GSE	FLOAT	degrees
mms<N>_edi_traj1_gse_90_gdu2_srvy_l2	Direction of GDU2 particle motion for pitch angle 90 electrons in GSE	FLOAT	degrees
mms<N>_edi_traj1_gse_180_srvy_l2	Direction of particle motion for pitch angle 180 electrons in GSE	FLOAT	degrees
Support Data			
Epoch_0_180	Time tags for pitch angle 0 and 180 fluxes, associated trajectories, GDU numbers, flux errors and flip indicators	TT_2000	ns
Epoch_90	Time tags for GDU1 and GDU2 pitch angle 90 fluxes, associated trajectories, flux errors and flip indicators	TT_2000	ns
epoch_timetag	Time tags for optics state, GDU energies and dwell time	TT_2000	ns
mms<N>_edi_flip_0_180_srvy_l2	Indicator for rapid detector look direction changes	UINT1	none
mms<N>_edi_flip_90_srvy_l2	Indicator for rapid detector look direction changes	UINT1	none
mms<N>_edi_optics_state_srvy_l2	EDI detector optics state	UINT1	none
mms<N>_edi_dwell_srvy_l2	Dwell time setting for sampling field aligned and perpendicular pitch angle data	FLOAT	s
mms<N>_edi_energy_gdu1_srvy_l2	EDI GDU1 energy	UINT2	eV
mms<N>_edi_energy_gdu2_srvy_l2	EDI GDU2 energy	UINT2	eV
mms<N>_edi_gdu_0_srvy_l2	GDU number for pitch angle 0 data	UINT1	none
mms<N>_edi_gdu_180_srvy_l2	GDU number for pitch angle 180 data	UINT1	none
mms<N>_edi_flux1_0_delta_srvy_l2	Error for pitch angle 0 flux	FLOAT	cm^{-2} $s^{-1}sr^{-1}$
mms<N>_edi_flux1_90_delta_gdu1_ srvy_l2	Error for GDU1 pitch angle 90 flux	FLOAT	cm^{-2} $s^{-1}sr^{-1}$

mms<N>_edi_flux1_90_delta_gdu2 _srvy_l2	Error for GDU2 pitch angle 90 flux	FLOAT	$cm^{-2}\ s^{-1}sr^{-1}$
mms<N>_edi_flux1_180_delta_srvy_l2	Error for pitch angle 180 flux	FLOAT	$cm^{-2}\ s^{-1}sr^{-1}$

Table 10-13 L2 Ambient Alternating Pitch Angle Mode Survey Data

10.6.3.2.2 Burst

File Names:

mms<N>_edi_brst_l2_amb-alt-cc_<yyyymmddhhmmss>_v<x.y.z>.cdf
mms<N>_edi_brst_l2_amb-alt-oc_<yyyymmddhhmmss>_v<x.y.z>.cdf
mms<N>_edi_brst_l2_amb-alt-oob_<yyyymmddhhmmss>_v<x.y.z>.cdf

Name	Description	Type	Units
mms<N>_edi_flux1_0_brst_l2 mms<N>_edi_flux2_0_brst_l2 mms<N>_edi_flux3_0_brst_l2 mms<N>_edi_flux4_0_brst_l2	Electron flux in four separate directional channels close to pitch angle 0	FLOAT	$cm^{-2}\ s^{-1}sr^{-1}$
mms<N>_edi_flux1_90_gdu1_brst_l2 mms<N>_edi_flux2_90_gdu1_brst_l2 mms<N>_edi_flux3_90_gdu1_brst_l2 mms<N>_edi_flux4_90_gdu1_brst_l2	Electron flux in four separate directional channels close to pitch angle 90, measured by GDU1	FLOAT	$cm^{-2}\ s^{-1}sr^{-1}$
mms<N>_edi_flux1_90_gdu2_brst_l2 mms<N>_edi_flux2_90_gdu2_brst_l2 mms<N>_edi_flux3_90_gdu2_brst_l2 mms<N>_edi_flux4_90_gdu2_brst_l2	Electron flux in four separate directional channels close to pitch angle 90, measured by GDU2	FLOAT	$cm^{-2}\ s^{-1}sr^{-1}$
mms<N>_edi_flux1_180_brst_l2 mms<N>_edi_flux2_180_brst_l2 mms<N>_edi_flux3_180_brst_l2 mms<N>_edi_flux4_180_brst_l2	Electron flux in four separate directional channels close to pitch angle 180	FLOAT	$cm^{-2}\ s^{-1}sr^{-1}$
mms<N>_edi_traj1_dbcs_0_brst_l2 mms<N>_edi_traj2_dbcs_0_brst_l2 mms<N>_edi_traj3_dbcs_0_brst_l2 mms<N>_edi_traj4_dbcs_0_brst_l2	Particle motion directions for the four channels close to pitch angle 0 in DBCS	FLOAT	degrees
mms<N>_edi_traj1_dbcs_90_gdu1_brst_l2 mms<N>_edi_traj2_dbcs_90_gdu1_brst_l2 mms<N>_edi_traj3_dbcs_90_gdu1_brst_l2 mms<N>_edi_traj4_dbcs_90_gdu1_brst_l2	Particle motion directions for the four channels close to pitch angle 90 in DBCS, measured by GDU1	FLOAT	degrees
mms<N>_edi_traj1_dbcs_90_gdu2_brst_l2 mms<N>_edi_traj2_dbcs_90_gdu2_brst_l2 mms<N>_edi_traj3_dbcs_90_gdu2_brst_l2 mms<N>_edi_traj4_dbcs_90_gdu2_brst_l2	Particle motion directions for the four channels close to pitch angle 90 in DBCS, measured by GDU2	FLOAT	degrees
mms<N>_edi_traj1_dbcs_180_brst_l2 mms<N>_edi_traj2_dbcs_180_brst_l2 mms<N>_edi_traj3_dbcs_180_brst_l2 mms<N>_edi_traj4_dbcs_180_brst_l2	Particle motion directions for the four channels close to pitch angle 180 in DBCS	FLOAT	degrees

mms<N>_edi_traj1_gse_0_brst_l2 mms<N>_edi_traj2_gse_0_brst_l2 mms<N>_edi_traj3_gse_0_brst_l2 mms<N>_edi_traj4_gse_0_brst_l2	Particle motion directions for the four channels close to pitch angle 0 in GSE	FLOAT	degrees
mms<N>_edi_traj1_gse_90_gdu1_brst_l2 mms<N>_edi_traj2_gse_90_gdu1_brst_l2 mms<N>_edi_traj3_gse_90_gdu1_brst_l2 mms<N>_edi_traj4_gse_90_gdu1_brst_l2	Particle motion directions for the four channels close to pitch angle 90 in GSE, measured by GDU1	FLOAT	degrees
mms<N>_edi_traj1_gse_90_gdu2_brst_l2 mms<N>_edi_traj2_gse_90_gdu2_brst_l2 mms<N>_edi_traj3_gse_90_gdu2_brst_l2 mms<N>_edi_traj4_gse_90_gdu2_brst_l2	Particle motion directions for the four channels close to pitch angle 90 in GSE, measured by GDU2	FLOAT	degrees
mms<N>_edi_traj1_gse_180_brst_l2 mms<N>_edi_traj2_gse_180_brst_l2 mms<N>_edi_traj3_gse_180_brst_l2 mms<N>_edi_traj4_gse_180_brst_l2	Particle motion directions for the four channels close to pitch angle 180 in GSE	FLOAT	degrees
Support Data			
Epoch_0_180	Time tags for pitch angle 0 and 180 fluxes, associated trajectories, GDU numbers, flux errors and flip indicators	TT_2000	ns
Epoch_90	Time tags for GDU1 and GDU2 pitch angle 90 fluxes, associated trajectories, flux errors and flip indicators	TT_2000	ns
epoch_timetag	Time tags for optics state, GDU energies and dwell time	TT_2000	ns
mms<N>_edi_flip_0_180_brst_l2	Indicator for rapid detector look direction changes	UINT1	none
mms<N>_edi_flip_90_brst_l2	Indicator for rapid detector look direction changes	UINT1	none
mms<N>_edi_optics_state_brst_l2	EDI detector optics state	UINT1	none
mms<N>_edi_dwell_brst_l2	Dwell time setting for sampling field aligned and perpendicular pitch angle data	FLOAT	s
mms<N>_edi_energy_gdu1_brst_l2	EDI GDU1 energy	UINT2	eV
mms<N>_edi_energy_gdu2_brst_l2	EDI GDU2 energy	UINT2	eV
mms<N>_edi_gdu_0_brst_l2	GDU number for pitch angle 0 data	UINT1	none
mms<N>_edi_gdu_180_brst_l2	GDU number for pitch angle 180 data	UINT1	none
mms<N>_edi_flux1_0_delta_brst_l2 mms<N>_edi_flux2_0_delta_brst_l2 mms<N>_edi_flux3_0_delta_brst_l2 mms<N>_edi_flux4_0_delta_brst_l2	Errors for pitch angle 0 flux channels	FLOAT	$cm^{-2}\ s^{-1}sr^{-1}$

mms<N>_edi_flux1_90_delta_gdu1_brst_l2 mms<N>_edi_flux2_90_delta_gdu1_brst_l2 mms<N>_edi_flux3_90_delta_gdu1_brst_l2 mms<N>_edi_flux4_90_delta_gdu1_brst_l2	Errors for GDU1 pitch angle 90 flux channels	FLOAT	$cm^{-2}\ s^{-1}sr^{-1}$
mms<N>_edi_flux1_90_delta_gdu2_brst_l2 mms<N>_edi_flux2_90_delta_gdu2_brst_l2 mms<N>_edi_flux3_90_delta_gdu2_brst_l2 mms<N>_edi_flux4_90_delta_gdu2_brst_l2	Errors for GDU2 pitch angle 90 flux channels	FLOAT	$cm^{-2}\ s^{-1}sr^{-1}$
mms<N>_edi_flux1_180_delta_brst_l2 mms<N>_edi_flux2_180_delta_brst_l2 mms<N>_edi_flux3_180_delta_brst_l2 mms<N>_edi_flux4_180_delta_brst_l2	Errors for pitch angle 180 flux channels	FLOAT	$cm^{-2}\ s^{-1}sr^{-1}$

Table 10-14 L2 Ambient Alternating Pitch Angle Mode Burst Data

10.6.3.3 File Structure L2 AMBIENT Perpendicular Mode Data

10.6.3.3.1 Survey

File Names:

mms<N>_edi_srvy_l2_amb-perp-ob_<yyyymmdd>_v<x.y.z>.cdf

Name	Description	Type	Units
mms<N>_edi_flux1_90_gdu1_srvy_l2	Electron flux for pitch angle 90, measured by GDU1	FLOAT	$cm^{-2}\ s^{-1}sr^{-1}$
mms<N>_edi_flux1_90_gdu2_srvy_l2	Electron flux for pitch angle 90, measured by GDU2	FLOAT	$cm^{-2}\ s^{-1}sr^{-1}$
mms<N>_edi_traj1_dbcs_90_gdu1_srvy_l2	Direction of GDU1 particle motion for pitch angle 90 electrons in DBCS	FLOAT	degrees
mms<N>_edi_traj1_dbcs_90_gdu2_srvy_l2	Direction of GDU2 particle motion for pitch angle 90 electrons in DBCS	FLOAT	degrees
mms<N>_edi_traj1_gse_90_gdu1_srvy_l2	Direction of GDU1 particle motion for pitch angle 90 electrons in GSE	FLOAT	degrees
mms<N>_edi_traj1_gse_90_gdu2_srvy_l2	Direction of GDU2 particle motion for pitch angle 90 electrons in GSE	FLOAT	degrees
Support Data			
Epoch	Time tags for fluxes, associated trajectories and flux errors	TT_2000	ns
epoch_timetag	Time tags for optics state and GDU energies	TT_2000	ns
mms<N>_edi_optics_state_srvy_l2	EDI detector optics state	UINT1	none
mms<N>_edi_energy_gdu1_srvy_l2	EDI GDU1 energy	UINT2	eV

mms<N>_edi_energy_gdu2_srvy_l2	EDI GDU2 energy	UINT2	eV
mms<N>_edi_flux1_90_delta_gdu1_ srvy_l2	Error for GDU1 pitch angle 90 flux	FLOAT	$cm^{-2}\ s^{-1}sr^{-1}$
mms<N>_edi_flux1_90_delta_gdu2 _srvy_l2	Error for GDU2 pitch angle 90 flux	FLOAT	$cm^{-2}\ s^{-1}sr^{-1}$

Table 10-15 L2 Ambient Perpendicular Mode Survey Data

10.6.3.3.2 Burst

File Names:

mms<N>_edi_brst_l2_amb-perp-ob_<yyyymmddhhmmss>_v<x.y.z>.cdf

Name	Description	Type	Units
mms<N>_edi_flux1_90_gdu1_brst_l2 mms<N>_edi_flux2_90_gdu1_brst_l2 mms<N>_edi_flux3_90_gdu1_brst_l2 mms<N>_edi_flux4_90_gdu1_brst_l2	Electron flux in four separate directional channels close to pitch angle 90, measured by GDU1	FLOAT	$cm^{-2}\ s^{-1}sr^{-1}$
mms<N>_edi_flux1_90_gdu2_brst_l2 mms<N>_edi_flux2_90_gdu2_brst_l2 mms<N>_edi_flux3_90_gdu2_brst_l2 mms<N>_edi_flux4_90_gdu2_brst_l2	Electron flux in four separate directional channels close to pitch angle 90, measured by GDU2	FLOAT	$cm^{-2}\ s^{-1}sr^{-1}$
mms<N>_edi_traj1_dbcs_90_gdu1_brst_l2 mms<N>_edi_traj2_dbcs_90_gdu1_brst_l2 mms<N>_edi_traj3_dbcs_90_gdu1_brst_l2 mms<N>_edi_traj4_dbcs_90_gdu1_brst_l2	Particle motion directions for the four channels close to pitch angle 90 in DBCS, measured by GDU1	FLOAT	degrees
mms<N>_edi_traj1_dbcs_90_gdu2_brst_l2 mms<N>_edi_traj2_dbcs_90_gdu2_brst_l2 mms<N>_edi_traj3_dbcs_90_gdu2_brst_l2 mms<N>_edi_traj4_dbcs_90_gdu2_brst_l2	Particle motion directions for the four channels close to pitch angle 90 in DBCS, measured by GDU2	FLOAT	degrees
mms<N>_edi_traj1_gse_90_gdu1_brst_l2 mms<N>_edi_traj2_gse_90_gdu1_brst_l2 mms<N>_edi_traj3_gse_90_gdu1_brst_l2 mms<N>_edi_traj4_gse_90_gdu1_brst_l2	Particle motion directions for the four channels close to pitch angle 90 in GSE, measured by GDU1	FLOAT	degrees
mms<N>_edi_traj1_gse_90_gdu2_brst_l2 mms<N>_edi_traj2_gse_90_gdu2_brst_l2 mms<N>_edi_traj3_gse_90_gdu2_brst_l2 mms<N>_edi_traj4_gse_90_gdu2_brst_l2	Particle motion directions for the four channels close to pitch angle 90 in GSE, measured by GDU2	FLOAT	degrees
Support data			
Epoch	Time tags for fluxes, associated trajectories and flux errors	TT_2000	ns
epoch_timetag	Time tags for optics state and GDU energies	TT_2000	ns
mms<N>_edi_optics_state_brst_l2	EDI detector optics state	UINT1	none
mms<N>_edi_energy_gdu1_brst_l2	EDI GDU1 energy	UINT2	eV
mms<N>_edi_energy_gdu2_brst_l2	EDI GDU2 energy	UINT2	eV
mms<N>_edi_flux1_90_delta_gdu1_brst_l2 mms<N>_edi_flux2_90_delta_gdu1_brst_l2	Errors for GDU1 pitch angle 90 flux channels	FLOAT	$cm^{-2}\ s^{-1}sr^{-1}$

mms<N>_edi_flux3_90_delta_gdu1_brst_l2 mms<N>_edi_flux4_90_delta_gdu1_brst_l2			
mms<N>_edi_flux1_90_delta_gdu2_brst_l2 mms<N>_edi_flux2_90_delta_gdu2_brst_l2 mms<N>_edi_flux3_90_delta_gdu2_brst_l2 mms<N>_edi_flux4_90_delta_gdu2_brst_l2	Errors for GDU2 pitch angle 90 flux channels	FLOAT	$cm^{-2}\ s^{-1}sr^{-1}$

Table 10-16 L2 Ambient Perpendicular Mode Burst Data

10.7 APPENDIX A- EDI REFERENCES

The following documents and drawings in effect on the day this specification was signed **shall** apply to the extent specified herein. In the event of conflict between this document and any referenced document, the document with latest publication date will govern.

The following is a list of applicable references and publications.

Section	Document Number	Title	Revision/Date
	https://doi.org/10.1007/s11214-016-0238-3	Torbert, R.B., Vaith, H., Granoff, M. et al. (2016). Erratum to: The Electron Drift Instrument for MMS. Space Sci Rev 199, 307–308.	
	https://doi.org/10.1007/s11214-015-0182-7	Torbert, R.B., Vaith, H., Granoff, M. et al. (2016). The Electron Drift Instrument for MMS. Space Sci Rev 199, 283–305.	
	https://doi.org/10.1007/s11214-014-0109-8	Torbert, R.B., Russell, C.T., Magnes, W. et al. (2016). The FIELDS Instrument Suite on MMS: Scientific Objectives, Measurements, and Data Products. Space Sci Rev 199, 105–135.	

Table 10-17 EDI Applicable Documents

11.0 ELECTRIC DOUBLE PROBES (EDP)

11.1 EDP OVERVIEW

The Spin-plane Double Probe (SDP) and the Axial Double Probe (ADP) instruments are part of the FIELDS instrument suite of the MMS. The combination of SDP and ADP is referred to as the Electric field Double Probe (EDP) instrument. EDP measures the 3-D electric field with an accuracy of 0.5mV/m over the frequency range from DC to 100kHz. SDP consists of 4 biased spherical probes extended on 60m long wire booms 90 degrees apart in the spin plane, giving a 120m baseline for each of the two spin-plane electric field components. ADP consists of 2 biased cylindrical probes extended on 12m long stiff booms along the spacecraft axis, giving a 29.2m baseline for the axial electric field component. SDP and ADP should measure the spin-plane electric field with accuracy 0.5 mV/m and the axial electric field with accuracy of 1 mV/m. Double-probe electric field experiments have been flown on a number of spacecraft including Cluster. The EFW instrument on Cluster has been operating since 2000. MMS data analysis will leverage the work done for Cluster.

The detector of the SDP instrument consists of four orthogonal spherical sensors deployed from 60m cables in the spin plane of the spacecraft, four mechanical deployment units, each containing 3 boom electronic boards (BEBs). The detector of ADP consists of two cylindrical sensors deployed on 12m long stiff booms along the spacecraft axis, each containing 2 BEBs. The analog to digital conversion of the signals is done by the DSP (Digital Signal Processor) located in the FIELDS CEB (Central Electronic Box). The potential drop between two opposing spherical or cylindrical sensors is measured to provide an electric field measurement. The average value of SDP probe to spacecraft potential provides information on the spacecraft potential. The instrument can also perform current sweeps to provide the current-voltage curve and, thus, the electron temperature and density. The potentials of each spherical and cylindrical sensor and nearby conductors are controlled in order to minimize errors associated with photoemission from the spheres and impact of plasma electrons and ions on the spheres. For more details on SDP, ADP and DSP refer to the instrument descriptions in Lindqvist et al., (2016) and Ergun et al., (2016).
The SDP has four probes configured in two orthogonal probe pairs in the spin plane on each spacecraft and ADP has two probes approximately along the spacecraft spin axis as shown in Figure 11-1. The angle between the probe pair 12 and X_{SC} is approximately 30 degrees.

The instrument sends a negative bias current to the probes. The total of the plasma and photoelectron currents must then equal the bias current, so the probe potential adjusts to the operating point shown in Figure 11-2 (assuming a bias current of 140 nA). This has the advantage of putting the instrument on the steep part of the curve (i.e. the low resistance part), even in low density environments. Small fluctuations in the currents (whether caused by actual changes in the plasma or simply stray currents) then do not significantly affect the probe voltage. The probe pairs remain stably grounded (with a small offset) to their local plasma environment. Stray currents and plasma density fluctuations do not show up as an electric potential drop between the probes.

The optimal value of the bias current is determined to large extent by the photoelectron current, which in turn depends on the solar UV flux as well as on the photo-emissive properties of the probe surfaces. Therefore, the bias current needs to be adjusted over the course of the mission to account for changing solar UV flux and probe surface characteristics.

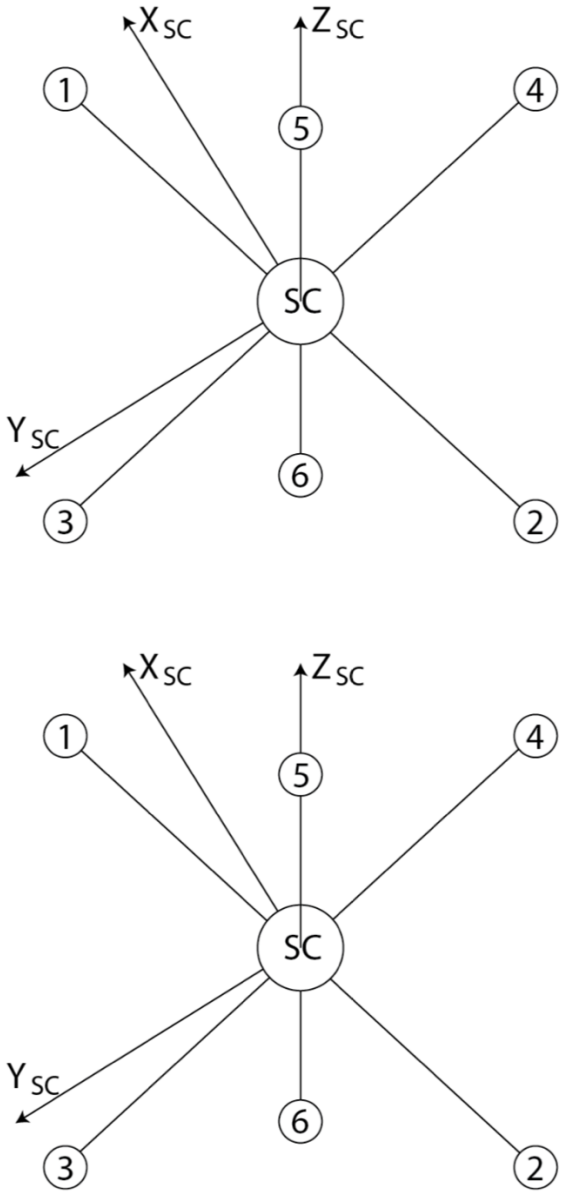

Figure 11-1 Schematic of SDP and ADP Probes

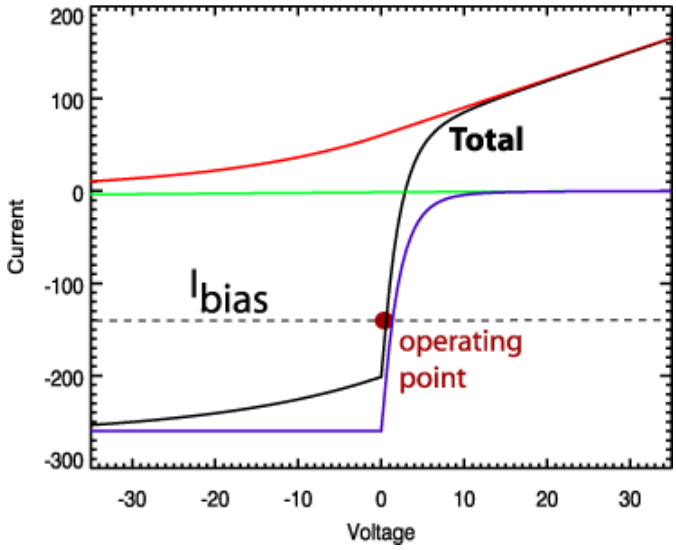

Figure 11-2 Idealized Current-Voltage Curve of a Biased Probe in a Low Density (1 cc) Plasma [The total current to the probe is sum of electron current (red), ion current (green) and photoelectron current (purple)]

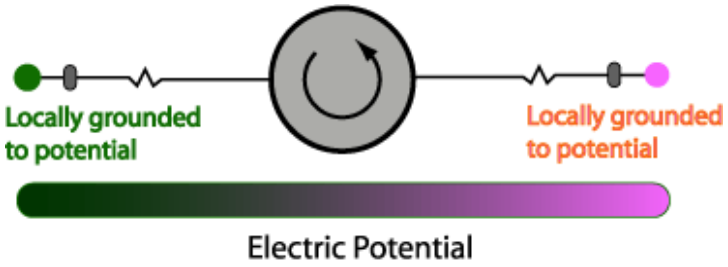

Figure 11-3 Electric Field Mode (biased probes)

Since the current biasing grounds each probe to the local plasma potential, the difference between the probe potentials divided by the length between the probes gives the electric field as shown in Figure 11-3. Normally, the full spin plane electric field is computed using the orthogonal signals P12 and P34 and axial electric field using P56 (see Figure 11-1). The average value of the probe to spacecraft potentials provides the spacecraft potential.

11.1.1 Status of EDP Probes

Probe 2 on MMS2 and Probe 4 on MMS4 are out of commission and they are no longer being used for electric field measurements. In each case, a micro-meteoroid severed a wire in the thick cable (between spacecraft and pre-amplifier). Probe 2 on MMS3 was recently hit by a micro-meteoroid and this probe is also out of commission.

Probe 4 on MMS4 can be used for AC High Frequency Electric field measurements, but has zero bias current, so it is not useable for DC measurements. The Pre-amplifier on MMS2, Probe 2, has no supply voltage on one side, so it cannot be used. MMS2, MMS3 and MMS4 are producing AC and DC fields

using 3 Spin-plane probes and the two unaffected axial probes. All probes on MMS1 are healthy and functioning.

Full 3D electric field measurements continue within specifications for all spacecraft. In June 2016, a micrometeoroid severed a single bias wire of MMS4 Probe 4 (SDP4) adversely affecting the frequency range DC-~600 Hz. For this range, the FIELDS team successfully reconfigured the electric field instrument and implemented a post-processing routine using the 3 healthy probes to determine the E-field components in the spin plane. Using comparison data from before June 2016, Figure 11-4 shows that the resulting uncertainty remains less than the 0.5 mV/m mission success requirement with only a modest increase in the noise floor. A second micrometeoroid impact occurred in Sept 2018 to Probe2 (SDP2) on MMS2 which severed its 12V power. A flight software mod in early Oct 2018 reconfigured signals from the three remaining SDP probes to continue MMS2 spacecraft potential calculations, several burst trigger quantities, and the 1% duty cycled AC E-field, keeping MMS2 within specifications. More recently, on May 8, 2022, a micrometeoroid impacted MMS3 on probe 2, resulting in loss of function of that probe. Once again, the remaining 3 probes were configured so that full L1 performance continues. Thus, all four spacecraft are still returning the full science performance requirement.

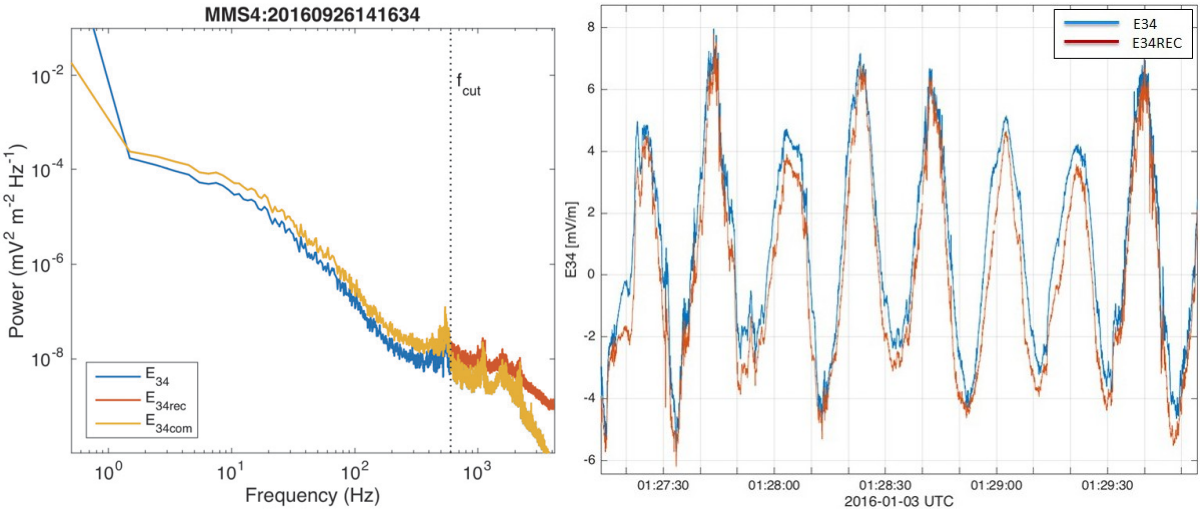

Figure 11-4 Comparison of (Left) Measured (Blue) and Reconstructed (Orange) Wave Forms Using Data Taken Prior to the Anomaly and (Right) Post-Anomaly Noise Levels of the Measured (Blue), Reconstructed (Orange), and Combined (Yellow) Products Along the SDP3-4 Axis

11.2 EDP MEASUREMENTS AND TIMING

The basic EDP sample rates are 8 samples/second in slow survey, 32 samples/seconds-1 in fast survey, and 8192 samples/seconds-1 in burst mode. During the tail season (phase 1X), 21 April - 26 July 2016, the burst mode sample rate was increased to 16384 samples/second.s-1. During the dusk season (phase 1X-1B), 5 August - 13 October 2016, the slow survey sample rate was increased to 32 samples/second.s-1.

The sampling of the DC raw data signals (individual probe potentials and probe potential differences) are done by a single analog to digital converter (ADC) running at 218 = 262144 s-1. This means that the data are not sampled simultaneously, but in the following order, with a delta time of 2-18 s or about 3.815 µs between each sample:

The data in the EDP CDF files have been time tagged to the sampling of V1, neglecting the time difference between the sampling of the different channels. For slow and fast survey data, with a time

resolution of 31.25 ms, the sample time delay of up to 34 μs can be neglected. For detailed high time resolution studies using burst data, with a time resolution of 122 μs, the sample time delay of up to 34 μs may be significant. Users wishing to do, e.g., cross spectral analysis of burst data, are advised to correct the timing themselves, using the individual probe data in the Level 2 Spacecraft potential file (brst_l2_scpot).

Sequence Number	Signal Sample	Delay with respect to first sample [μs]
0	**V1**	**0**
1	**V2(*)**	**3.815**
2	V3	**7.629**
3	V4(*)	**11.444**
4	**V5**	**15.259**
5	**V6(*)**	**19.073**
6	**-**	**22.888**
7	**E12**	**26.703**
8	**E34**	**30.518**
9	**E56**	**34.332**

Table 11-1 Sampling Sequence and Delays of EDP DC Raw Data

11.2.1 Pre-Flight / On-Ground Calibration

A description of the design of EDP and its pre-flight and ground calibration can be found in these publications. The combination of the spin plane probes and axial probes provides a 3D electric field on each spacecraft which is necessary for the science goals of the MMS mission. The details of the probe configurations and operations are explained in the EDP overview section 11.1.1 and these publications.

Ergun, R. E., et al. **The Axial Double Probe and Fields Signal Processing for the MMS Mission**. Space Sci Rev 199, (2016). https://doi.org/10.1007/s11214-014-0115-xhttps://doi.org/10.1007/s11214-014-0115-x

Lindqvist, P.-A., et al. **The Spin-Plane Double Probe Electric Field Instrument for MMS**. Space Sci Rev 199, (2016). https://doi.org/10.1007/s11214-014-0116-9

11.3 EDP CALIBRATION AND VALIDATION

There is no on-board processing performed on SDP/ADP data which will be included in the science products. Ground processing includes decommutation and calibration into physical units of raw data. Further scientific processing includes spin fitting of probe-probe difference signals, determination of offsets in the raw data, determination of DC offsets in the despun data (sunward and duskward offsets), amplitude correction, and despinning the full resolution data. The Axial Double Probe (ADP) instrument measures the DC to ~ 100kHz electric field along the spin axis of the MMS spacecraft, completing the vector electric field when combined with the SDP. We produce 2 levels of data L2pre DCE and L2. In

order to create L2pre electric field data, first we remove sweeps and maneuver time intervals where the measurements have been impacted by spacecraft thrusters. Then we remove the spacecraft spin tone from ADP and SDP and using E.B=0 iteration, we correct the ADP component and store it as L2pre DCE data. In L2pre DCE files, we restore SDP components to L2pre DCE2D. Figure 11-6 shows the algorithm for generating the L2pre data.

11.4 EDP ALGORITHM DESCRIPTIONS

11.4.1 Theoretical Basics

This section gives descriptions of the processing and calibration of SDP, ADP and EPSD raw data to obtain the final electric field data. The EDP raw probe potential data is saved in L1b level. There are six probes on each spacecraft that calculate the potential (V1 to V6). The potential data goes through the following steps as explained in this section to calculate the 3 dimensional electric field (2 components in spinning plane and one component in axial direction).

11.4.2 SDP Algorithm

As the first stage of calibration it is necessary to perform initial cleaning of the data at which we remove intervals with: bad data due to issues with electronics, probe saturations due to low plasma density in the magnetospheric lobes (when ASPOC is not operating), and saturations due to non- optimal bias current settings occurring in dense plasmas such as magnetosheath. If the spacecraft is in the solar wind we apply a correction for the wakes usually present in the raw data. All the possible problems with the data are recorded in the bitmask supplied with the data.

Spin fits. After initial cleaning of the data a spin fitting procedure is performed; the output of this procedure provides basic parameters, which are used later in the calibration procedure. In the presence of a constant ambient electric field, the raw data signal (probe potential difference) is a sine wave where the amplitude and phase give the electric field magnitude and direction. A least-squares fit to the raw data of the form

$y = A + B \cos(\omega t) + C \sin(\omega t) + D \cos(2\omega t) + E \sin(2\omega t) + ...$

is done on 20 seconds of data once every 5 seconds (the spacecraft spin period is about 20 seconds). The fit is done individually on E12 and E34 to obtain a set of terms for each of the raw data signals.
The standard deviation of the raw data from the fitted sine wave can be used as indication of high frequency variations in the data. Higher order terms, D, E, ..., may be used for diagnostics of data quality: normally the higher order terms are much smaller than B and C, and the opposite situation would indicate problems with the measurements.

Offsets. The sine and cosine terms, B and C after correction for DSL offsets provide the 5-sec resolution electric field in DSL:

$E_{x5s} = \alpha B - \Delta E_x$
$E_{y5s} = \alpha C - \Delta E_y$

where α is the amplitude correction factor due to the ambient electric field is "short-circuited" by the presence of the spacecraft and wire booms, and ΔE_x and ΔE_y are the *DSL offsets*, which are determined from cross-calibration with EDI and particle instruments, as well as from the inter- spacecraft calibration.

As the spin fitting procedure would typically yield different values for the electric field from the two different probe pairs, it is useful to introduce additional offset which describes the difference between the two measurements, $\Delta p12p34$, which we call the *Delta offset*:

Δx p12p34 = Ex5s(E12) – Ex5s(E34)
Δy p12p34 = Ey5s(E12) – Ey5s(E34)

The delta offset is expected to vary relatively slowly, on a typical time-scale of several months and is therefore determined from statistical comparison of electric fields from the two probe pairs.

The despun full resolution electric field is obtained as follows:

Ex = Re[ε12] – Δx p12p34 + Re[ε34]
Ey = Im[ε12] – Δy p12p34 + Im[ε34]

where $\varepsilon 12 = (E12 - \Delta_{raw\ 12})e^{i\varphi 12}$, $\varepsilon 34 = (E34 - \Delta_{raw\ 34})e^{i\varphi 34}$, and $\varphi 12 = \varphi 34 + \pi/2$ is the spin phase of probe 1 with respect to the sun; *Raw data DC offset*, $\Delta_{raw} = \langle A \rangle$, is based on parameter A of the fit on first equation. Ideally, the DC level of the raw data should be zero, however small differences between the probe surfaces and in the electronics create a DC offset in the raw data. If not corrected, it shows up as a signal at the spin frequency in the despun electric field. The 5s resolution values of A are smoothed using 5 adjacent points according to the formula

$\langle A \rangle = 0.1*A_{i-2} + 0.25*A_{i-1} + 0.3*A_i + 0.25*A_{i+1} + 0.1*A_{i+2}$ (8)

after which <A> is resampled to the full time resolution of the data using linear interpolation.

It may be noted that asymmetries due to the direction to the sun have the dominant contribution to the offsets, so that the following inequalities are typically satisfied:

$\Delta E_x >> \Delta E_y$
Δx p12p34 >> Δy p12p34

This SDP calibration process will provide the L2pre DCE2D data products.

11.4.3 ADP Algorithm

The L2 pre DCE2D data is used as input to generate L2 pre DCE data and L2 data. In this stage of calibration, we use data from FPI, FGM and EDI instruments. IF fast FPI and survey E-field EDI data are available, they will be used for calibrations purposes. The L2 calibration code detects the solar wind, magnetosheath, magnetopause, magnetotail and inner magnetosphere regions to set the gain values based on plasma parameters in each environment. If the spacecraft is in solar wind, FPI data is not used for calibration.

Offsets. In order to remove offsets from the data, we use four baselines when the necessary data are available:

A. E + Vi x B median-smoothed to 60 s.
B. E + Ve x B median smoothed to 10s.
C. EDI E-Field mode averaged to 10 s.
D. E.B averaged to 20 s only in magnetotail.

The E.B baseline is only used in magnetotail regions. Vi and Ve are ion and electron velocities respectively provided by FPI instrument. All the available baselines are merged together to remove the

offset from L2 data. Figure 11-5 and Figure 11-6 show the algorithm for the L2 pre and L2 DCE data. The L2pre data can be reconstructed using L2 calibration processing data following this procedure:

EL2pre.Y(*,0) = (EL2.Y(*,0) + Residue.Y(*,0)) / 1.06
EL2pre.Y(*,1) = (EL2.Y(*,1) + Residue.Y(*,1)) / 1.06
EL2pre.Y(*,2) = (EL2.Y(*,2) + Residue.Y(*,2)) / 1.12 – ResidueL2pre.Y(*,2)

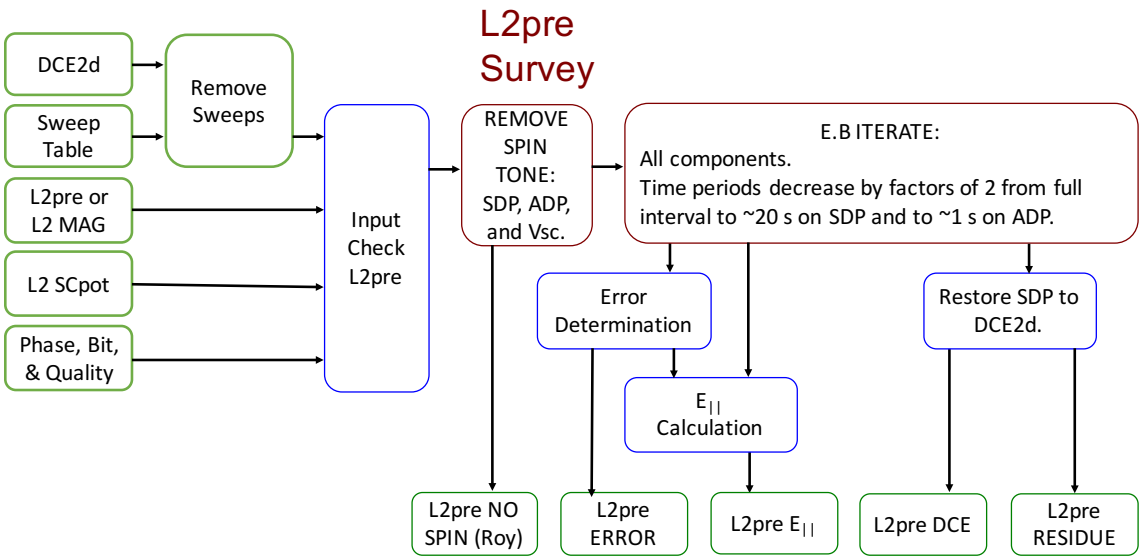

Figure 11-5 L2Pre Calibration Algorithm

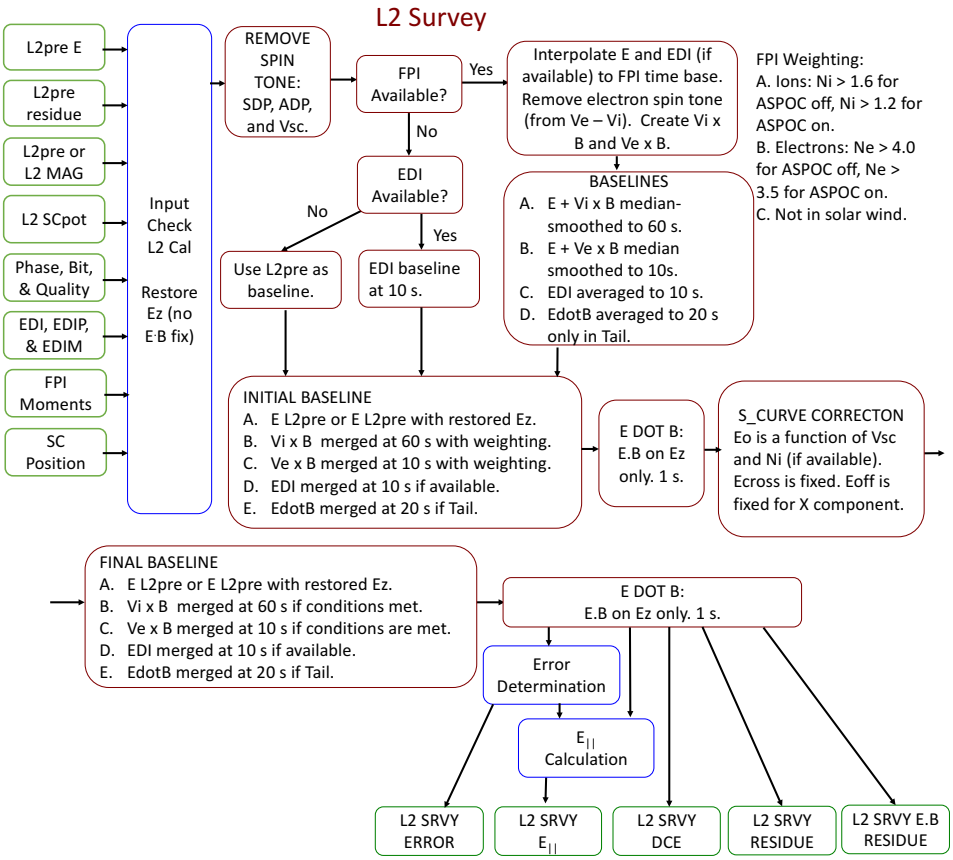

Figure 11-6 L2 Calibration Algorithm

11.4.4 EPSD Algorithm

The analog electric waveforms measured by EDP are digitalized and processed inside the digital signal processor (DSP) developed by Laboratory of Atmospheric and Space Physics (Ergun et al., 2016). This process provides the raw data for Electric field power spectral density (EPSD). The calibration code gets the processed on board data and applies corrections to hanning window and compressions performed in DSP. We also correct for DSP and Pre-amplifier gains.

The Solitary Wave Detector (SWD) is a data product created by the FIELDS Digital Signal Processor (DSP) board. The intent of the SWD is to make an approximate count of the number of kinetic electric field solitary structures (e.g. phase space holes or double layers) observed per unit time within a set of amplitude ranges. The SWD operates on 65,536 Sample/s waveform data from any of the three antenna differential pair AC-coupled signals (E12 AC, E34 AC, E56 AC). Nominally, and for most of the mission on most spacecraft, the SWD operates on E12 AC data. A window width (32, 64, 128 or 256 points) is specified, as are five threshold amplitude values. These threshold values define the upper and lower bounds on four amplitude bins. For each window, the SWD algorithm calculates a pseudo-rms value and a peak value of the input differential electric field waveform data. The pseudo-rms is calculated as follows: (i) the average of the data in each window is subtracted, (ii) the average-subtracted data within the window are summed, (ii) the summed value is divided by the number of points within the window. The ratio is then calculated of the peak amplitude (maximum absolute value of the average-subtracted data within the window) to the pseudo-rms. If this ratio exceeds 4, the algorithm adds one count to one

SWD amplitude bin. This bin is determined by the peak amplitude value and the used-defined bounds on the four amplitude bins.

The SWD is always active when FIELDS DSP is in Fast Survey, and it returns counts in each of the four defined amplitude bins at a reporting period of 0.5 * (N +1) seconds, where N can be set from 0 to 63. Internal to the SWD, counts are recorded as a 12-bit number. This number is compressed to eight bits using a lossy pseudo-log compression scheme (3 exponent, 5 mantissa bits) before being returned to the ground.

The SWD data product is successful at identifying regions where the peak/rms value of AC-coupled electric fields is often large (e.g. Hansel et al. 2021, https://doi.org/10.1029/2021JA029389).

11.5 DATA PRODUCTS

The EDP instrument runs in several modes: **Fast** survey (normally run in the scientific Region of Interest, ROI), **Slow** survey (normally used outside the ROI), and **Burst** (for selected intervals within the ROI). The EDP data products can be broadly divided in **Level 1** (raw data) and **Level 2** (science data). The following table lists the possible combinations and their corresponding folder names in the hierarchical mms data file structure:

Level	**Mode**			
	Fast	**Slow**	**Burst**	**Survey**
Level 1	L1b	L1b	L1b	L1b
Level 2	L2a, L2pre, L2	L2a, L2pre, L2	L2pre, L2	L2

Table 11-2 EDP Operating Modes and Data Levels

As seen, there is a collective name Survey, which encompasses both Fast and Slow survey. The designations l2a and l2pre are used for intermediate and preliminary Level 2 data. For each of the entries in the table above, there are a number of possible available data types:

Mode_Level	**Data_type**	**Access**	**Description**
Level 1 (raw data)			
{fast,slow,brst}_l1b	dce	EDP internal	Raw electric field, Individual probe potentials
brst_l1b	ace	EDP internal	(Only during commissioning)
brst_l1b	hmfe	EDP internal	Raw electric field, 65536 s^{-1}, 10% duty cycle (adjustable)
srvy_l1b	ace	EDP internal	AC electric field, 131072 s^{-1}, 0.1% duty cycle (16ms/16s)
srvy_l1b	dce	EDP internal	Raw electric field, Individual probe potentials (Do not use)

srvy_l1b	sweeps	EDP internal	Current-voltage sweeps
Level 2			
{fast,slow}_l2a	dce2d	EDP internal	Raw electric field, Spin fit results and offsets
{fast,slow,brst}_l2pre	dce2d	EDP internal	Despun electric field in DSL, Ez calculated using E.B=0
{fast,slow,brst}_l2pre	dce	EDP internal	Despun electric field in DSL after preliminary calibration
{fast,slow,brst}_l2	dce	Public	Despun electric field in DSL and GSE
brst_l2	hmfe	Public	Despun electric field in DSL, 65536 s^{-1}, 10% duty cycle
srvy_l2	hfesp	Public	Electric Field spectra 592 - 65536 Hz
{fast,slow,brst}_l2	scpot	Public	Spacecraft potential, Individual probe potentials
fast_l2	epsd	Public	Power spectral density by DSP
fast_l2	swd	Public	Impulsive Electric Field Structure Counts

Table 11-3 EDP Data Types and Descriptions

In the table above, the third column indicates whether the data are intended for internal or public use.

All data are stored in CDF files according to the MMS-wide data standards. For EDP data, the file naming convention is:

<observatory>_edp_<mode>_<level>_<datatype>_<datetime>_<version>.cdf where

<observatory> = {mms1, mms2, mms3, mms4}
<mode> = {fast, slow, brst, srvy}
<level> = {l1b, l2a, l2pre, l2, ql, sitl}
<datatype> = {dce, ace, hmfe, hfesp, sweeps, dce2d, scpot} <datetime> = {yyyymmdd, yyyymmddhhmmss}

<datatype> = {dce, ace, hmfe, hfesp, sweeps, dce2d, scpot}
<datetime> = {yyyymmdd, yyyymmddhhmmss}
<version> = vx.y.z

where x, y, and z are the major version, minor version, and revision.

The major version changes when updates to productions software have been made to change file format and/or contents. The minor version changes with new calibrations and/or correction of errors which do not affect the file format. The revision is incremented each time a file is re-generated using the same software, e.g., due to more data becoming available.

11.5.1 L2 Data Products

L2_dce: Final 3D DC E-field in DSL and GSE coordinates. Both spin plane and spin axis E-field have been processed through elaborate calibration procedures involving comparisons with FPI and EDI data to obtain the best possible scientific data quality. The E-field data are given in both DSL and GSE coordinates.

L2_hmfe: EDP despun AC electric field data in DSL. It contains AC-coupled vector E-field burst data. Data are not sampled continuously, but using a duty cycle.

L2_hfesp: EDP E12 electric field spectra. It contains power spectra of the E12 probe-probe potential difference. Data are not sampled continuously, but using a duty cycle.

L2_scpot: Spacecraft potential. The spacecraft potential is calculated by averaging the four SDP probe-to-spacecraft potentials and correcting for the probe-plasma potential and the short-circuiting effect of the 60 m long booms. The product also contains the probe-spacecraft potential for all 6 EDP probes.

11.5.2 Bitmasks and Quality Flags

Many of the data products include a quality indicator and a bitmask indicating specific issues with the data. The quality indicator is a value between 0 and 3, with the meaning given in Table 11-4.

Quality indicator	Meaning
0	Very bad data or no data available
1	Bad data, use with caution
2	OK data, use with some caution
3	Good data

Table 11-4 EDP Quality Indicator

The EDP bitmask is a 16-bit unsigned integer where each bit indicates a specific issue with the data, as listed in Table 11-5.

Bit position	Hex value	Decimal value	Meaning if bit is set (1)	Quality index
0	0x0001	1	Probe(-s) are disabled	0
1	0x0002	2	Probe(-s) have bad bias setting	1
2	0x0004	4	Probe(-s) are saturated	0
3	0x0008	8	Probe(-s) are saturated due to low density	1
4	0x0010	16	Probe(-s) are sweeping bias current	1
5	0x0020	32	SDP Probe(-s) are in shadow from ADP Booms	1

6	0x0040	64	ASPOC is emitting non-zero current	2
7	0x0080	128	-	-
8	0x0100	256	Asymmetric probe configuration (e.g MMS4 after 2016-06-12)	2
9	0x0200	512	Maneuver is ongoing	1

Table 11-5 EDP Bitmask Values and Corresponding Quality Indicator

11.5.3 Level 1 Data Products

L1b_dce: EDP raw data (for internal use by the EDP team). It contains the 3 probe-probe potential differences, used to calculate the vector electric field (E12, E34 and E56), and 3 of the individual probe-spacecraft potentials (V1, V3 and V5).

L1b_hmfe: EDP raw AC electric field data (for internal use by the EDP team). It contains AC-coupled burst data from the 3 probe-probe potential differences. Data are not sampled continuously, but using a duty cycle.

L1b_ace: EDP raw AC E12 data (for internal use by the EDP team). It contains AC-coupled data from the E12 probe-probe potential difference. Data are not sampled continuously, but using a duty cycle. Spectra are produced on ground.

L1b_sweeps: EDP current-voltage sweeps (for internal use by the EDP team). It contains current-voltage sweeps done on the probes for diagnostic purposes, normally at the start and at the end of each ROI.

11.5.4 Level 2 Data Products

L2a_dce2d: An intermediate E-field product (for internal use by the EDP team). It contains the electric field in the spinning frame, together with the computed spin fit coefficients, spin phase and various offsets. The L2a fast files are used as input to both the L2pre fast processing and the L2pre burst processing, ensuring consistency between the fast and burst data.

L2pre_dce2d: Preliminary 2D DC E-field in DSL coordinates (for internal use by the EDP team). The spin plane E-field (Exy) is computed from the SDP probes (E12 and E34), corrected for various offsets. The spin axis E-field (Ez) is obtained using the condition $\mathbf{E}\cdot\mathbf{B}=0$ when the magnetic field elevation above the spin plane is more than 10 degrees.

L2pre_dce: Preliminary 3D DC E-field in DSL coordinates (for internal use by the EDP team). The spin plane E-field (Exy) is unchanged from the preliminary 2D DC E-field, and the spin axis E- field (Ez) is computed from the ADP probes (E56).

L2_epsd: Electric field power spectral density. It contain the electric field waveforms measured by DSP.

All level 2 data products are listed below.

Brief description: Despun electric field in DSL	
File name: mms{1,2,3,4}_edp_{fast,slow,brst}_l2pre_dce2d_<datetime>_v<x.y.z>.cdf	
Variable name	**Description**
mms#_edp_dce_dsl_{fast,slow,brst}_l2pre	Ex, Ey, Ez: Electric field in DSL using E.B=0
mms#_edp_adp_{fast,slow,brst}_l2pre	Ez in DSL from ADP E56
mms#_edp_phase_{fast,slow,brst}_l2pre	Spacecraft spin phase
mms#_edp_adc_offset_{fast,slow,brst}_l2pre	Removed ADC offsets
mms#_edp_delta_offset_{fast,slow,brst}_l2pre	Removed delta offsets
mms#_edp_bitmask_{fast,slow,brst}_l2pre	Status bitmask
mms#_edp_quality_{fast,slow,brst}_l2pre	Quality flag

Table 11-6 Despun Electric Field in DSL

Brief description: Despun electric field in DSL after preliminary calibration	
File name: mms{1,2,3,4}_edp_{fast,slow,brst}_l2pre_dce_<datetime>_v<x.y.z>.cdf	
Variable name	**Description**
mms#_edp_dce_dsl_{fast,slow,brst}_l2pre	Ex, Ey, Ez: Electric field in DSL
mms#_edp_dce_par_epar_{fast,slow,brst}_l2pre	Eerr, Epar: Parallel E field and its error
mms#_edp_dce_dsl_res_{fast,slow,brst}_l2pre	Ex, Ey, Ez: Electric field residue
mms#_edp_dce_err_{fast,slow}_l2pre	Ex, Ey, Ez: Electric field error
mms#_edp_adc_offset_{fast,slow,brst}_l2pre	Removed ADC offsets
mms#_edp_delta_offset_{fast,slow,brst}_l2pre	Removed delta offsets
mms#_edp_bitmask_{fast,slow,brst}_l2pre	Status bitmask
mms#_edp_quality_{fast,slow,brst}_l2pre	Quality flag

Table 11-7 Despun Electric Field in DSL After Preliminary Calibration

Brief description: Despun electric field in DSL and GSE	
File name: mms{1,2,3,4}_edp_{fast,slow,brst}_l2_dce_<datetime>_v<x.y.z>.cdf	
Variable name	**Description**
mms#_edp_dce_gse_{fast,slow,brst}_l2	Ex, Ey, Ez: Electric field in GSE
mms#_edp_dce_dsl_{fast,slow,brst}_l2	Ex, Ey, Ez: Electric field in DSL
mms#_edp_dce_par_epar_{fast,slow,brst}_l2	Eerr, Epar: Parallel E field and its error
mms#_edp_dce_dsl_res_{fast,slow}_l2	Ex, Ey, Ez: Electric field residue
mms#_edp_dce_err_{fast,slow}_l2	Ex, Ey, Ez: Electric field error
mms#_edp_bitmask_{fast,slow,brst}_l2	Status bitmask
mms#_edp_quality_{fast,slow,brst}_l2	Quality flag
mms#_dsp_epsd_x	Power spectral density of Ex by DSP
mms#_dsp_epsd_y	Power spectral density of Ey by DSP
mms#_dsp_epsd_z	Power spectral density of Ez by DSP
mms#_dsp_epsd_omni	Omni-directional power spectral density
mms(1 or 4)_dsp_swd_E12_Counts	Counts of waveform data on E12
mms(2 or 3)_dsp_swd_E34_Counts	Counts of waveform data on E34 (Probe 2 disabled)

Table 11-8 Despun Electric Field in DSL and GSE

11.6 APPENDIX A- EDP REFERENCES

The following documents and drawings in effect on the day this specification was signed **shall** apply to the extent specified herein. In the event of conflict between this document and any referenced document, the document with latest publication date will govern.

The following is a list of applicable references and publications.

Section	Document Number	Title	Revision/Date
tbd	461-XXX-XXXX-0###	EDP Item Name	Rev / date
tbd	461-XXX-XXXX-0###	EDP Item Name	Rev / date
	https://doi.org/10.1007/s11214-014-0115-x	Ergun, R.E., Tucker, S., Westfall, J. et al. (2016). The Axial Double Probe and Fields Signal Processing for the MMS Mission. Space Sci Rev 199, 167–188.	
	https://doi.org/10.1007/s11214-014-0116-9	Lindqvist, P.-A., Olsson, G., Torbert, R.B., et al. (2016). The Spin-Plane Double Probe Electric Field Instrument for MMS. Space Sci Rev 199, 137-165.	

Table 11-9 EDP Applicable Documents

12.0 FLUXGATE-SEARCHCOIL-MERGED MAGNETIC FIELD (FSM)

12.1 FSM OVERVIEW

The Fluxgate-Searchcoil Merged (FSM) data product for the Magnetospheric Multiscale (MMS) mission is created by merging data from the fluxgate (FGM) and searchcoil (SCM) magnetometers into a single level-3 data product. The merging method involves pre-flight timing and noise floor analysis determining the in-flight noise floor as well as. The resulting data product has the DC component of FGM, the sampling rate and Nyquist frequency of SCM, and a reduced noise floor within the transition band of the merging filter. Here, we describe the statistical inter-calibration process as well as the merging filter. A full description of the SCM-FGM cross-calibration methodology, the merging filter, and the applications of the dataset can be found in the following two publications:

Fischer, D., Magnes, et al. (2016). Optimized merging of search coil and fluxgate data for MMS. *Geoscientific Instrumentation, Methods and Data Systems*, *5*(2), 521–530. https://doi.org/10.5194/gi-5-521-2016

Argall, M. R., Fischer, D., Le Contel, O., Mirioni, L, et al. (2018). The Fluxgate-Searchcoil Merged (FSM) Magnetic Field Data Product for MMS. *ArXiv E-Prints*. https://arxiv.org/abs/1809.07388

12.2 INPUT DATA

Input data for the FSM data product comes from the L1A FGM and L1B SCM datasets. The L2 datasets are not used because the merging process needs to occur before data from the different axes are mixed via coordinate system rotations. For FGM and SCM, the closest common coordinate system is Orthogonalized Magnetometer (OMB), which, for FGM, differs from the 123 sensor coordinate system by an orthogonalization transformation and is equivalent to the SCM 123 sensor coordinate system. Data in OMB coordinates is not available at in L2.

In addition, only burst data is merged. The fast and slow survey mode data products are not merged.

12.2.1 FGM

Two fluxgate magnetometers are used to create the FGM dataset: the analog fluxgate (AFG) and digital fluxgate (DFG) magnetometers. The sensors differ by the addition of a tuning capacitor in AFG. The electronics, however, were designed based on different operating principles (Russell et al. 2014; Magnes et al. 2008), providing robust redundancy. Data from AFG is used for the survey dataset and DFG is used for the burst dataset. As a result, the burst FSM data also uses data from the DFG instrument.

DFG data is sampled at 8192 S/s and is decimated to the burst data rate of 128 S/s by two, named DEC32 and DEC64. In DEC32 mode, the sampling rate is reduced to 256 S/s via a 32-point average, then is decimated to 128Hz. This mode produces aliasing, but reduces the group delay so that the magnetic field can be passed faster to the Electron Drift Instrument (EDI) (Torbert et al. 2015) for beam emittance angle adjustments, reducing the amount of prediction required. In DEC64 mode, the sampling rate is reduced to 128 S/s directly via 64-point averaging. Each mode has unique effects on the measured signal and so are handled separately in the production of the FSM dataset.

The DFG data in OMB coordinates is processed to L2-quality via the same algorithms that process the publicly available L2 datasets. This folds in the results of in-flight calibration, which entails 1) spin tone removal to determine orthogonalization parameters, 2) range joining to remove jumps between low- and high-range, 3) cross-calibration with the Electron Drift Instrument (EDI) (Torbert et al. 2014) and/or

application of the Davis-Smith method (Leinweber, et al. 2008) to remove spin-axis offsets, 4) earth-field comparisons to determine absolute calibration factors, and 5) inter-spacecraft comparisons to remove relative differences. Additional details of the calibration and L2 processing can be found in (Russell et al. 2014).

From here onward, DFG and AFG data are referred to as FGM data, where FGM burst data implies the use of DFG and FGM survey data implies the use of AFG. Individual instrument names will be used only when specific instrument characteristics require it.

12.2.2 SCM

The SCM L1B data is already calibrated by the SCM instrument team. This involves 1) decompression, 2) data cleaning, 3) conversion from counts to Volts, 4) application of a transfer function to convert Volts to nano-Tesla (nT), and 5) application of a high-pass filter with cutoff at 0.5 Hz for burst data. A definitive description of the SCM L1B data product can be found in the SCM section of this CMAD.

12.3 MERGING METHODOLOGY

The Finite Impulse Response (FIR) filter designed to merge the FGM and SCM datasets uses knowledge of the noise floor of each instrument observed in-flight to determine the cross-over frequency at which the two datasets are merged. The FSM data product consists primarily of FGM data below the cross-over frequency and SCM data above the cross-over frequency. The cross-over frequency is where the noise floors of the two instruments intersect.

12.3.1 In-Flight Noise Floor

The FGM and SCM instrument noise floors are determined in-flight. Figure 12-1 outlines the procedure. The top row of panels show the power spectral density (PSD) of the x-component of the magnetic field measured by DFG and SCM for an entire burst data file on 2015-09-01. Here and in the figures that follow, DFG data is presented in the left column and SCM data in the right column. The second row shows the distribution of signal as a function of frequency. At each frequency, the PSD was separated into bins of size 0.5 Log(nT^2/Hz) and accumulated over the duration of the burst file. In the last row, histograms from all burst files in September of 2015 were accumulated into a single distribution.

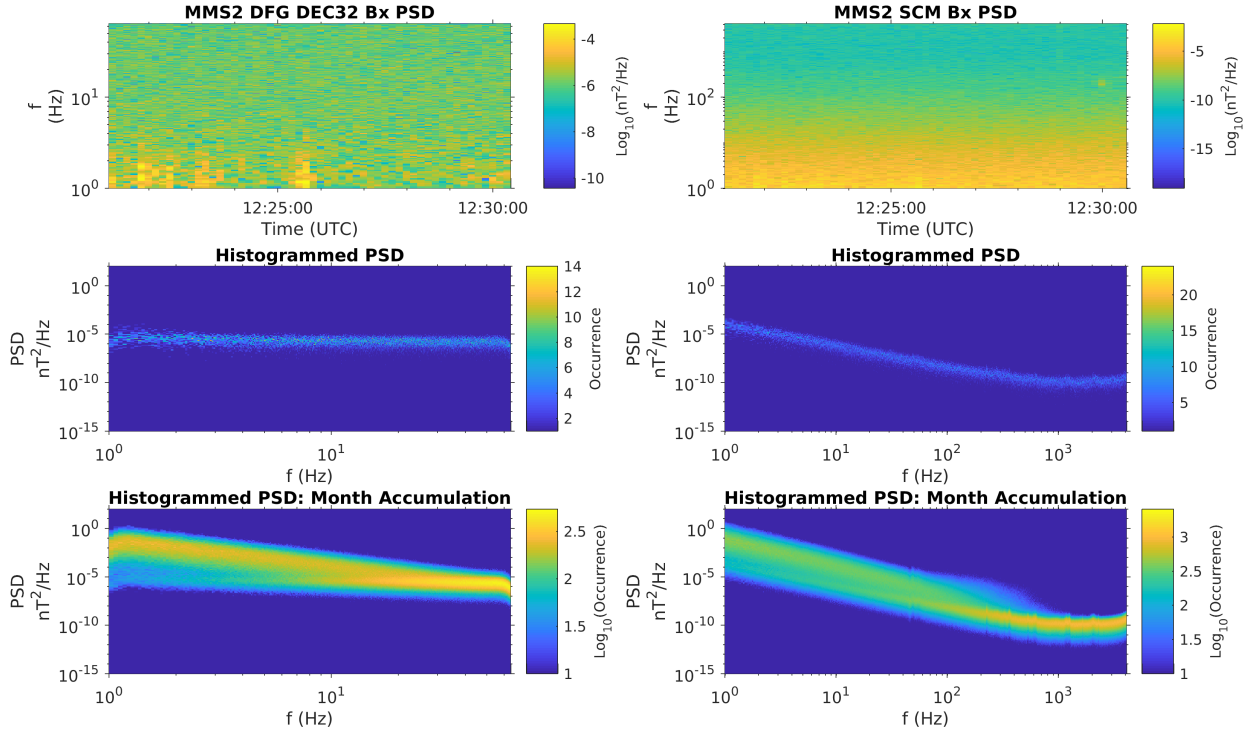

Figure 12-1 Method for Determining the In-flight Noise Floors (top). The PSD of the Time Series Waveforms is Calculated for a Burst Interval (middle). The PSD is Histogrammed at Each Time Step (bottom). The Histograms are Accumulated Across All Burst Intervals.

To compute the PSDs, FGM is first high-pass filtered with a cut-off frequency of fc = 1Hz to mimic the SCM calibration process and to prevent leaking of DC signal to higher frequencies. Next, a sinc-function and Chebyshev window taper T = 20 s data intervals which are then Fast Fourier Transformed (FFT-ed) to the frequency domain to calculate PSD. Subsequent windows contain 50% overlap. A time interval of T = 20 s was chosen for both FGM and SCM for two reasons: 1) a frequency resolution of $f = 1/T = fs/N = 0.05$Hz (where fs is the sample rate and N is the number of samples per FFT) is high enough to decipher peaks in the statistical distributions, and 2) the frequency bins and their spacing are the same for DFG and SCM up to the Nyquist frequency f_N of DFG. This allows us to make gain and phase comparisons between the two instruments, as will be shown later.

The PSD histograms have a bimodal distribution that is better seen in Figure 12-2, which shows vertical cuts through each component at 2Hz. Overplotted as a blue vertical line is the mean value of the noise floor across each component. A peak at a PSD of $\sim 10^{-6}$ nT^2/Hz for FGM and $\sim 10^{-5}$ nT^2/Hz occurs slightly below the value of the ground-measured noise floor at 2Hz. This peak is the in-situ measured noise floor.

A second, larger distribution of occurs to the right of the first. Unlike the peaks associated with the noise floor, it is observed at the same PSD value of ~10^{-2} nT^2/Hz for both FGM and SCM. Plots similar to were made for individual burst intervals containing significant wave activity and revealed peaks in the distribution coincident with this second peak (not shown). Thus, this second peak is associated with signal driven by physical phenomena.

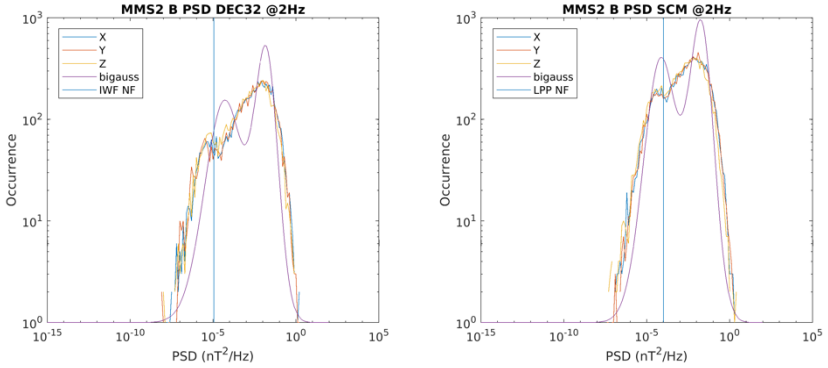

Figure 12-2 Bimodal Distribution in PSD Identifies Noise Floor and Signal Peaks (A cut through the PSD histograms at 2 Hz reveals a bimodal distribution with the left peak associated with noise and the right peak associated with signal.)

Such a procedure has been applied to all three components of the magnetic field (Figure 12-3). The peaks associated with the in-flight noise floor (green circles) and physical signal (magenta x's) were identified by eye at a select number of frequencies and fit with an exponential (solid lines of the same color). The noise floor determined on the ground for FGM and SCM is represented by the red dashed line in each panel. Note that the ground-measured noise floor overlaps with the noise floor observed in-flight.

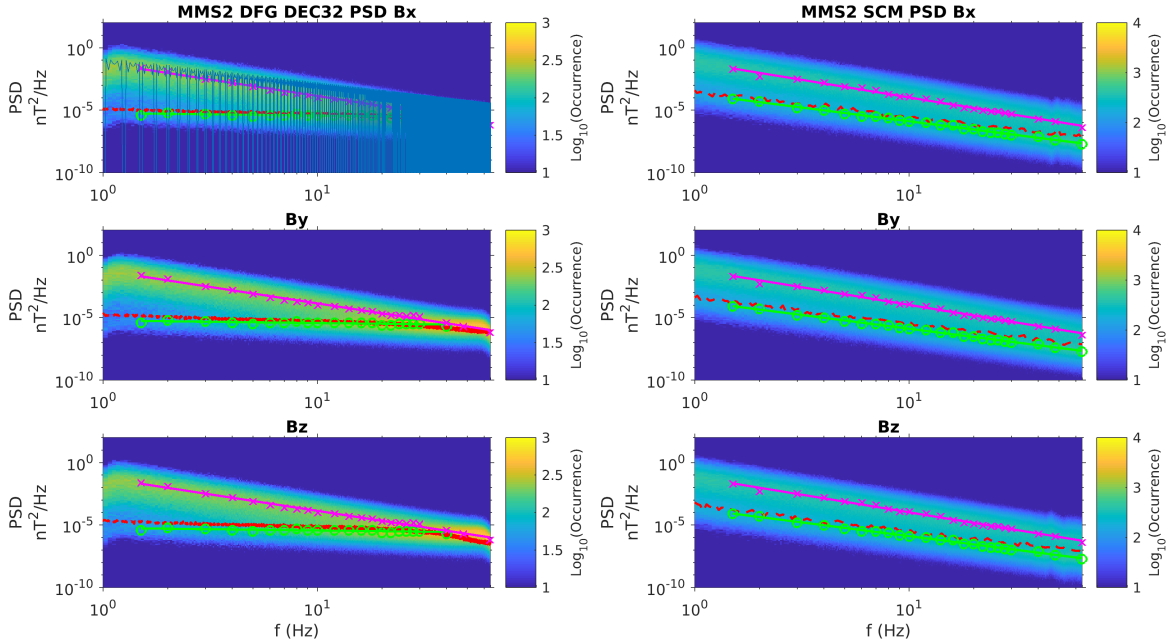

Figure 12-3 In-flight Noise Floor Coincides with Ground-Measured Noise Floor (Histogrammed PSD for FGM (left) and SCM (right), x,y, and z-components (top, middle, bottom). Noise floors are overplotted in magenta. Hand-picked peaks in PSD are in green and magenta.)

12.3.2 Cross-Over Frequency

Applying this methodology to all four spacecraft results in fits to the noise and signal distributions observed by each spacecraft. These are shown in Figure 12-4. The noise spectrum is distinct for each instrument, but the signal spectrum is the same to within the accuracy of the methodology, providing additional support for the classification.

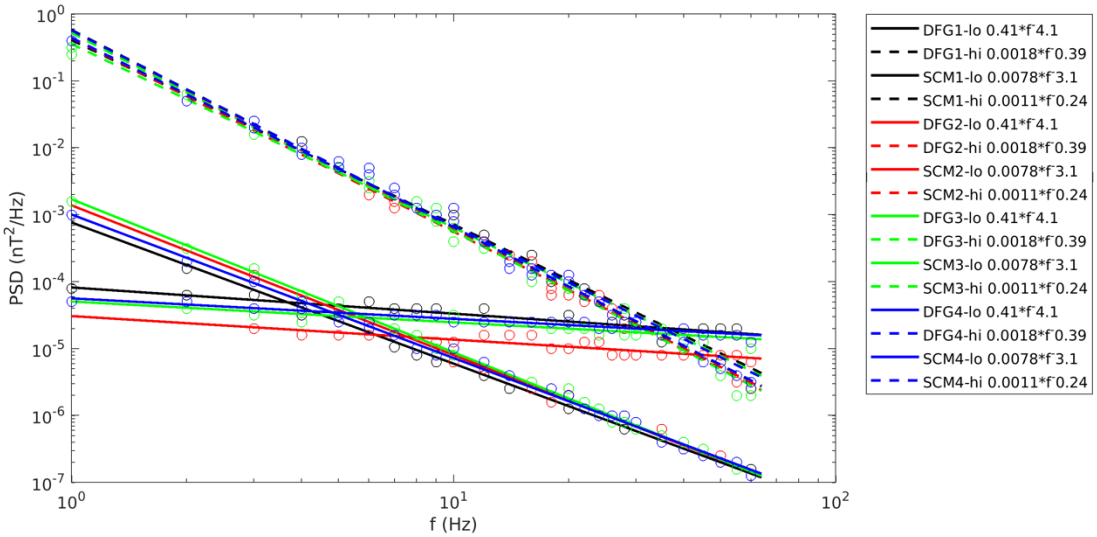

Figure 12-4 Noise and Signal Distribution for FGM and SCM, Along with Their Functional Forms ("lo" (hi) represents the noise (signal) distribution fits.)

The frequency at which the noise floor fits from FGM and SCM intersect one another (the "cross-over" frequency, 4-5 Hz) determines the cut-off frequency of the merging filter, described later.

12.3.3 Cross-Calibration

Signal gain and phase differences between FGM and SCM must be accounted for in the merging process. To calculate gain and phase delays, the noise and signal distributions must be separated. This is accomplished by selecting a frequency-dependent threshold value for PSD below which all values are considered noise and above which all values are considered signal. The threshold value is taken to be the maximum between components of the ground-measured noise floor at each frequency. This was chosen because the pre-flight noise floor is higher than the in-situ noise floor. By separating the signal from the noise distributions, we are able to compare DFG and SCM signals to determine long-term trends in gain and phase delays.

Gain for the signal distribution is shown in the left column of Figure 12-5. It is computed as $G = |R^2|$, where $R = B(f)/\delta B(f)$ and $B(f)$ and $\delta B(f)$ are the FFTs of the magnetic field measured by FGM and SCM, respectively. The gain and phase delays are then histogrammed by the same procedures as for PSD described in section 12.3.1, with bin sizes for gain and frequency of 0.5 and 0.05Hz, respectively. Signal gain $G_S = 1$ throughout the frequency range of FGM, which is a testament to the calibration and cross-calibration efforts undertaken by the magnetometer teams. The width of the distribution increases toward higher frequency, which is primarily caused by the lack of sufficiently strong signal and an inability to cleanly separate noise from signal at $f > 20\ Hz$.

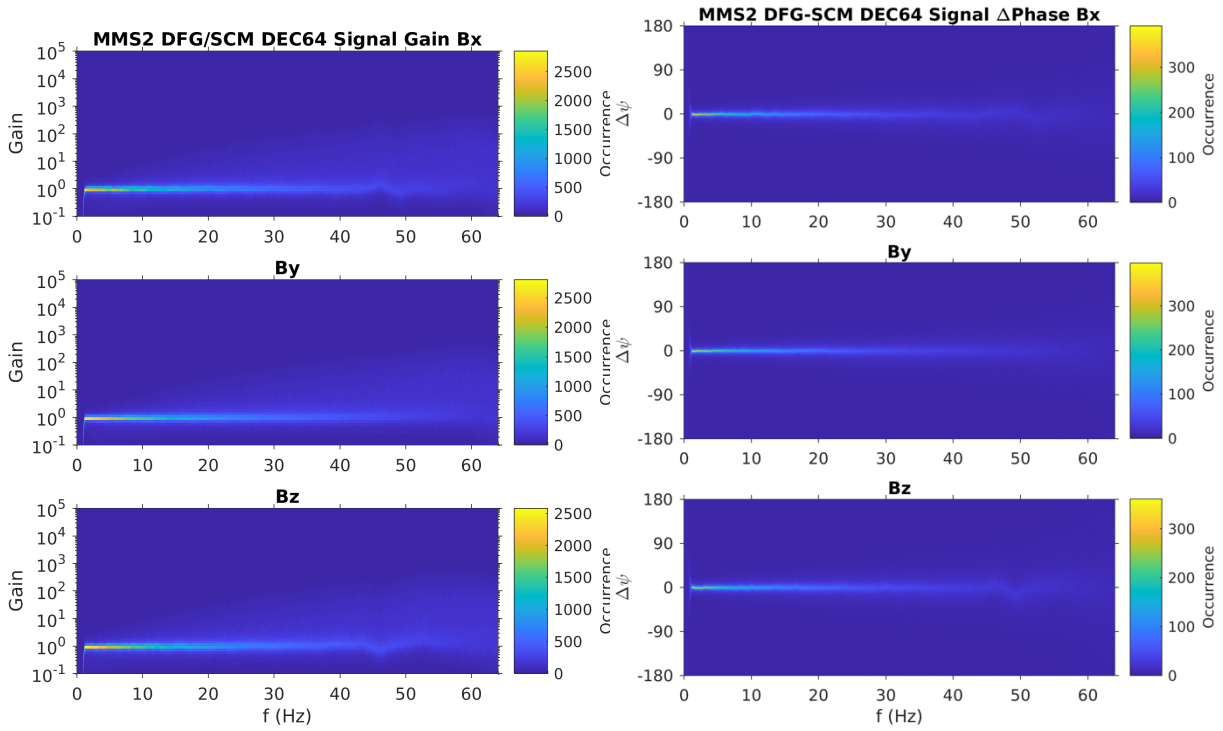

Figure 12-5 Gain Ratio and Phase Differences Between DFG and SCM Used for Cross-Calibration Purposes (The gain ratio is unity and there is zero phase difference so there is no need for correction in the FSM algorithm.)

Phase delay distributions are shown in the right half of Figure 12-5. Phase delay is computed as $\Delta\varphi = \tan^{-1}\left(\Re(R)/\Im(R)\right)$ then histogrammed in the same manner as PSD and gain. Distributions associated with signal are strongly peaked at $\Delta\varphi = 0°$, indicating the high timing accuracy between the two instruments. Again, the distribution spreads as frequency approaches f_N.

In summary, cross-calibration reveals a signal gain of $G_S = 1$ and a phase delay of $\Delta\varphi = 0°$, indicating that no further corrections are required before merging the data.

12.3.4 FIR Filters

The FIR filter for FGM consists of three separate low-pass FIR filters with cutoff frequencies f_c of 4, 7, and 32 Hz. The two filters with $f_{c1} = 4\ Hz$ and $f_{c2} = 7\ Hz$ serve to provide an interval of 50% gain surrounding the cross-over frequency f_x of each instrument pair. Both are sinc functions truncated at 16385 points (2 s duration) and tapered with a Blackman window. The third FIR filter with $f_{c3} = 32\ Hz$ acts as an anti-aliasing filter. It is a sinc function truncated at 2049 points (0.25 s duration) tapered with a Chebychev window. The total duration of the filter is 4.25 s.

An equivalent high-pass merging filter for SCM is constructed via spectral reversal of the low-pass FIR filter such that the sum of their gains is unity across all frequencies.

Figure 12-5 shows the impulse and frequency response of the low- and high-pass FIR filters. Cut-off frequencies of the three filters are depicted by green vertical lines in the frequencies response panels. Between the lower two cut-off frequencies, there is an interval of 50% gain for both filters, effectively averaging the two instruments together within the interval. The reason for this is that the noise distributions in Figure 12-2 and Figure 12-3 have a finite width, indicating that the cross-over frequency

is more of a cross-over frequency interval. This is apparent in individual spectra (shown later). Beyond 32 Hz, the antialiasing filter prevents signal above the FGM Nyquist frequency from folding back into the spectra.

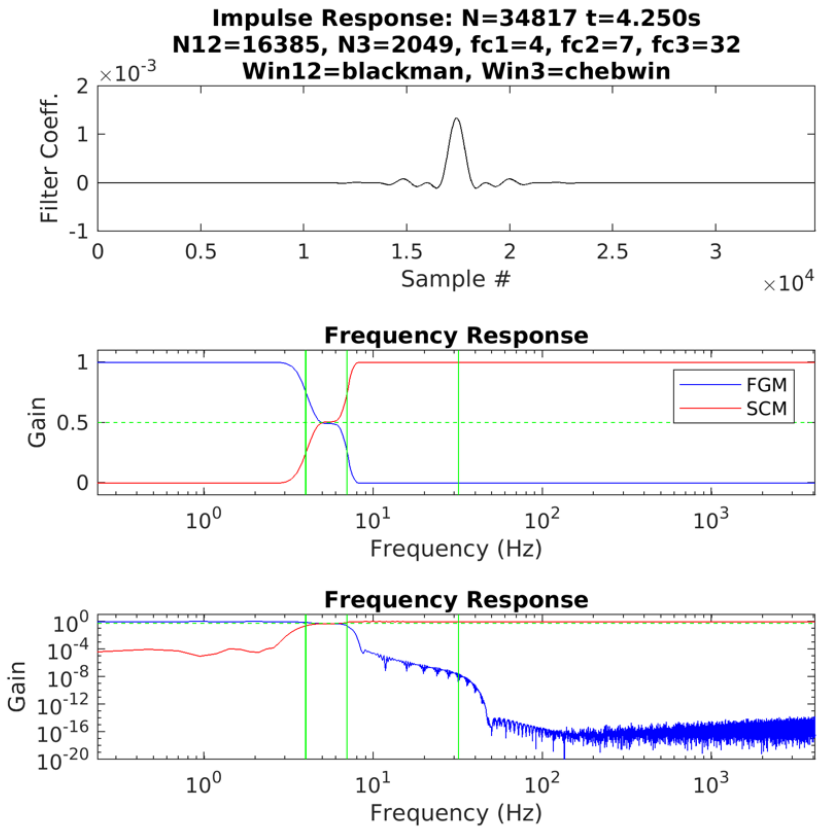

Figure 12-6 FIR Filter that Merges the FGM and SCM Datasets (The impulse response (top) and frequency response (center, bottom) of the FIR filter. Merging occurs between 3 and 6 Hz.)

12.3.5 Improved Noise Floors

One benefit of the merging filter is that the resulting FSM dataset has a reduced noise floor within the bandpass of the merging filter when compared to the FGM and SCM noise floors individually. This is apparent when the merging filter is applied to the FGM and SCM noise spectra determined in Figure 12-2 and Figure 12-3. Figure 12-6 shows the results with the FGM noise and signal spectra shown in blue, the SCM noise and signal spectra shown in green, and the resulting FSM noise and signal spectra shown in red. The cut-off frequencies of the three merging filters are shown as vertical lines. Below f_{c1}, the FSM noise floor is that of FGM while above f_{c2} the FSM noise floor is that of SCM. Within the merging region, the resulting FSM noise floor is reduced compared to the FGM and SCM noise floors.

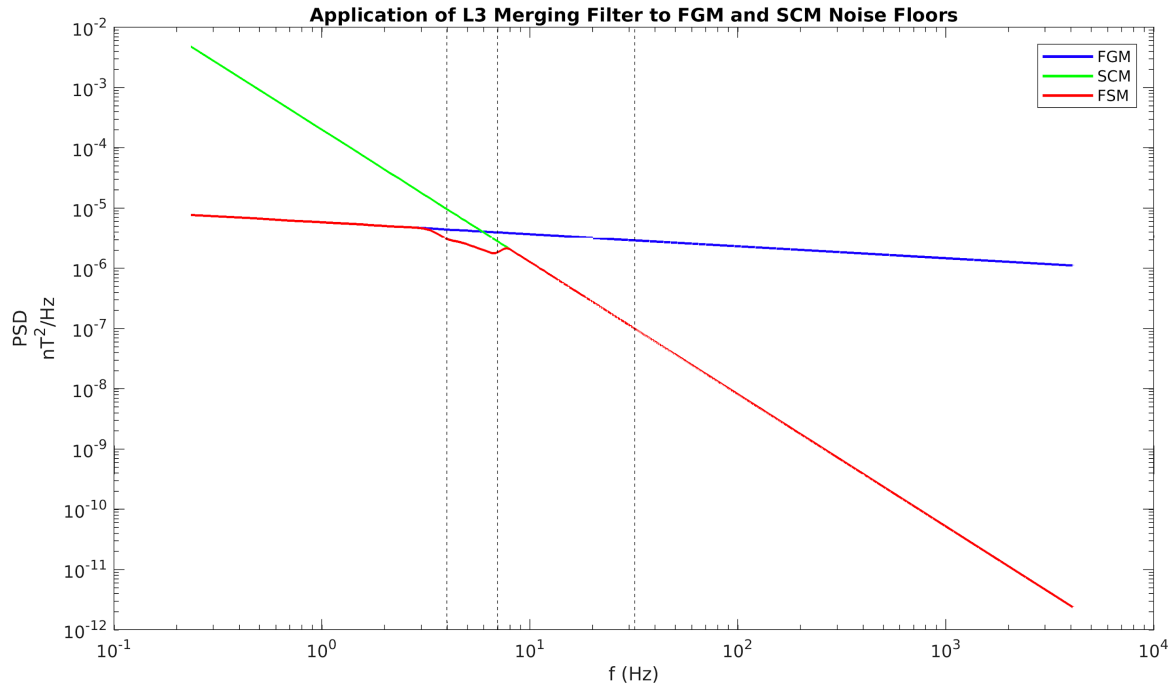

Figure 12-7 Application of the Merging Filter Results in an Improved Noise Floor for the FSM Data Product (The merging filter is applied to the observed noise and signal spectra, resulting in a lower noise floor within the 4-7 Hz bandpass).

12.3.6 Validation

To validate the merging filter, it is applied to FGM and SCM data during a quiet interval identified through spectrograms and histograms as in for events when the PSD distribution overlaps with the observed noise floor. The resulting spectra for FGM (solid blue), SCM (solid red), and FSM (solid black) are shown in Figure 12-8 for the x-, y-, and z-components. The respective ground-measured noise floor and the noise and signal distributions are plotted as dotted, dashed, and dot-dashed lines and the central frequency of the cross-over interval is represented by a vertical dashed line. The FSM spectra is invisible underneath the FGM and SCM spectra except near the cross-over frequency, where it is smaller in magnitude. Thus, the merging process successfully creates a new FSM data product that behaves like FGM at low frequencies, SCM at high frequencies, and has a lower noise floor in the merging interval.

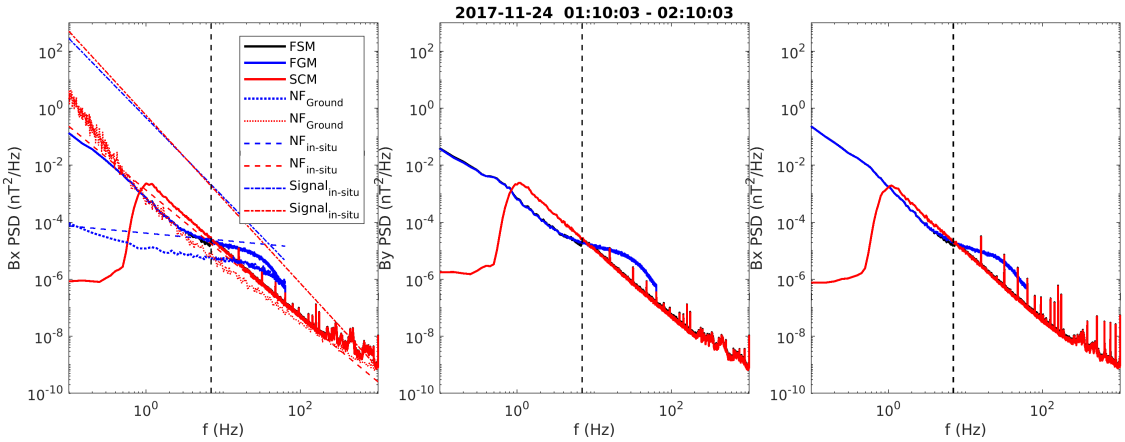

Figure 12-8 FSM Data Shown as the Merger of FGM and SCM Data with Improved Noise Floor in the Merging Interval

12.4 DATA PRODUCT ALGORITHM DESCRIPTIONS

An overview of the FSM algorithm is shown in Figure 12-9. Level 1A FGM data (upper-left green oval) in OMB coordinates is processed through the standard L2 data processing algorithm described in the FGM CMAD section. The data is then segregated by sampling rate, DEC32/DEC64, hi/lo-range, and other operating modes for individual analysis. To align the time tags with the SCM data, a 1 kHz compensation filter (Fischer, et al. 2016) is applied, the data is resampled to 8 kHz, and a fractional delay is applied. At this point, the FGM data is ready to be merged.

The L1B SCM data in OMB coordinates (lower-right green oval) is examined for mode (e.g. sampling rate) changes and data gaps produced by the low-pass filter (see the SCM CMAD section). It is then ready to be merged.

Next, the low-pass merging filter is applied to the FGM data, the high-pass merging filter is applied to the SCM data, and the resulting data is summed together to produce an FSM data product in OMB coordinates. Standard algorithms are then applied to transform the data into GSE and GSM coordinates.

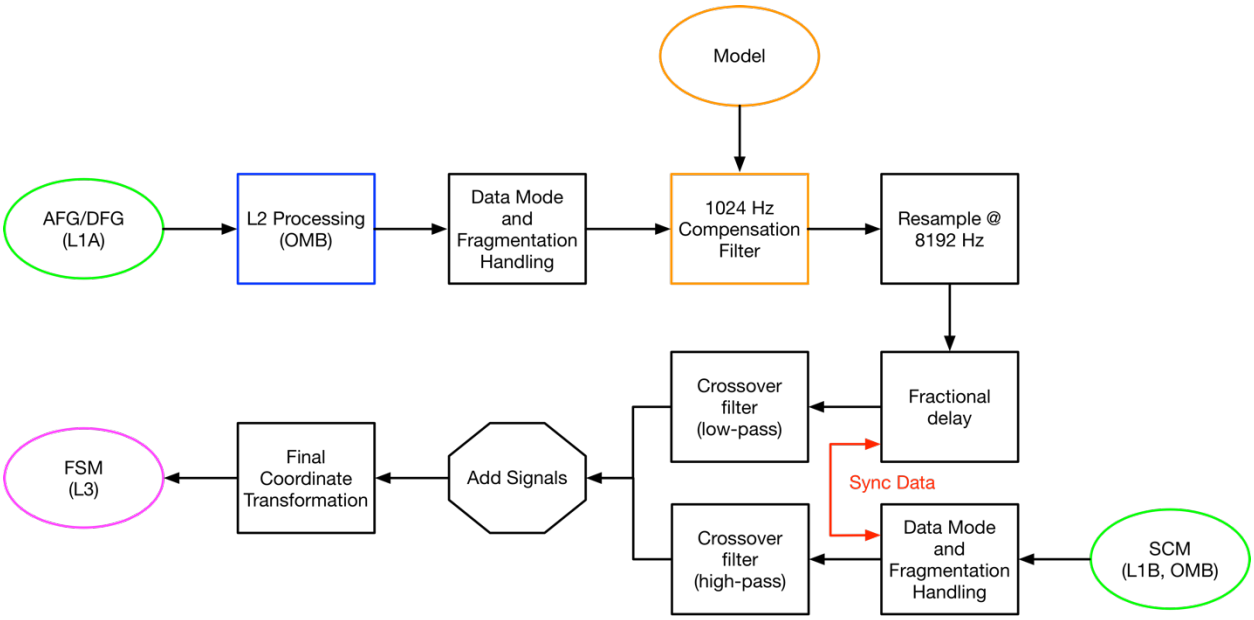

Figure 12-9 Work Flow of the FSM Merging Process

12.5 FILE STRUCTURE

12.5.1 L3 FSM 8kHz

12.5.1.1 Variables

Variable Name	Description
Epoch	Timestamps of the time series magnetic field data
[sc]_fsm_epoch_delta_brst_l3	Sample interval of the time series magnetic field data
[sc]_fsm_b_gse_labls_brst_l3	Axis labels for the magnetic field data in GSE coordinates
Epoch_state	Time stamps for the state variables

label_r_gse	Axis labels for the spacecraft position in GSE coordinates
represent_vec_tot	Components of the position variable
[sc]_fsm_b_gse_brst_l3	Vector magnetic field in GSE coordinates
[sc]_fsm_r_gse_brst_l3	Spacecraft position in GSE coordinates

Table 12-1 FSM File Structure Variables

12.5.1.2 File Versions

Version	Modifications
v1.0.0	First version
v1.1.0	Updated valid data range for B and DEPEND_0 for flags.

Table 12-2 FSM File Versions

12.6 APPENDIX A- FSM REFERENCES

The following documents and drawings in effect on the day this specification was signed **shall** apply to the extent specified herein. In the event of conflict between this document and any referenced document, the document with latest publication date will govern.

The following is a list of applicable references and publications.

Section	Document Number	Title	Revision/Date
	https://arxiv.org/abs/1809.07388 https://doi.org/10.48550/arXiv.1809.07388	Argall, M. R., et al., (2018). The Fluxgate-Searchcoil Merged (FSM) Magnetic Field Data Product for MMS. *ArXiv E-Prints*.	
	https://doi.org/10.5194/gi-5-521-2016	Fischer, D., Magnes, et al. (2016). Optimized merging of search coil and fluxgate data for MMS. Geoscientific Instrumentation, Methods and Data Systems, 5(2), 521–530.	
	https://doi.org/10.1088/0957-0233/19/5/055104	Leinweber, H. K., Russell, C. T., Torkar, K., Zhang, T. L., & Angelopoulos, V. (2008). An advanced approach to finding magnetometer zero levels in the interplanetary magnetic field. Measurement Science and Technology, 19(5), 55104.	
		Magnes, W., Oberst, M., Valavanoglou, A., Hauer, H., Hagen, C., Jernej, I., et al. (2008). Highly integrated front-end electronics for spaceborne fluxgate sensors. Measurement Science and Technology, 19(11), 115801.	

	https://doi.org/10.1007/s11214-014-0057-3	Russell, C. T., Anderson, B. J., Baumjohann, W., Bromund, K. R., Dearborn, D., Fischer, D., et al. (2014). The Magnetospheric Multiscale Magnetometers. Space Science Reviews, 199(1), 189–256.	
	https://doi.org/10.1007/s11214-014-0109-8	Torbert, R. B., Russell, C. T., Magnes, W., Ergun, R. E., Lindqvist, P.-A., Le Contel, O., et al. (2016). The FIELDS Instrument Suite on MMS: Scientific Objectives, Measurements, and Data Products. Space Science Reviews, 199(1), 105–135.	
	https://doi.org/10.1007/s11214-015-0182-7	Torbert, R. B., Vaith, H., Granoff, M., Widholm, M., Gaidos, J. A., Briggs, B. H., et al. (2016). The Electron Drift Instrument for MMS. Space Science Reviews, 199(1), 283–305.	

Table 12-3 FSM Applicable Documents

13.0 APPENDIXES

List of abbreviations, acronyms, units, and measurements are gathered below. It is important to note that these charts are reflective of this document and may not be comprehensive of all of the possibilities and meanings for each term.

13.1 ABBREVIATIONS AND ACRONYMS

Abbreviation / Acronym	Definition
ABM	Absolute Beam Monitor
AC	Alternating Current
ACB	AC Magnetic Field
ADCDES	Analog to Digital Converter Dual Electron Spectrometer
ADP	Axial Double Probe
ADPDIS	Axial Double Probes Dual Ion Spectrometer
AFG	Analog Flux Gate Magnetometer
APID	Application Process Identifier
APL	Applied Physics Laboratory
ASPOC	Active Spacecraft Potential Control Instrument
ATS	Absolute Time Sequence
AZ	Azimuth
BBF	Bursty Bulk Flow
BCS	Body Coordinate System
BDM	Burst Data Management
BEB	Boom Electronic Board
BEBFPI	Boom Electronic Board Fast Plasma Investigation
Bkgd	Background (in data quality the discussion is regarding correction for background counts)
BPS	Bits Per Second
BWC	Bandwidth Connection
CCSDS	Consultative Committee for Space Data Systems
CDF	Common Data Format
CDPU	Command and Data Processing Unit
CEB	Central Electronics Box
CETP	Centre d'etude des Environnements Terrestre et Planetaires
CIDP	Central Instrument Data Processor
CLN	Cleaning Active
CMAD	Calibration and Measurement Algorithms Document
COMP	Compensating Mode Option
CPOT	So-Called Feedback Mode
CRBG	Cosmic Ray Background
CRSF	Clock Rate Scaling Factor
Ct	Counts
CtRt	Count Rate
DBCS	De-spun Body Coordinate System
DC	Direct Current
DCC	DC Converter

DCE	3D DC E-field
DCE2D	2D DC E-field
DE	Development Ephemeris
DEF	Deflection
DES	Dual Electron Spectrometer
DFG	Digital Flux Gate Magnetometer
DIS	Dual Ion Spectrometer
DMPA	De-Spun Major Principal Axis
DPG	Data Products Guide
DPU	Data Processing Unit
DSCS	De-Spun Spin-Axis Coordinate System
DSL	Despun Spacecraft L-axis (coordinate system)
DSP	Digital Signal Processor
DSPFRC	DSP Frequency Response Range Correction
DWT	Discrete Wavelet Transform
DWT/BPE	Discrete Wavelet Transform and Bit Plane Encoder
ECEF	Earth-centered, Earth-fixed Coordinate System
ECI	Earth-Centered Inertial
EDI	Electron-Drift Instrument
EDP	Electric Double Probes
EIS	Energetic Ion Spectrometer
EPD	Energetic Particle Detector
EPSD	Electric field Power Spectral Density
E/Q	Energy Steps
ESA	Electrostatic Analyzer
EUV	Extreme Ultraviolet
FCS	FEEPS Coordinate System
FDOA	Flight Dynamics Operations Area
FEEPS	Fly's Eye Energetic Particle Spectrometer
FFT	Fast Fourier Transformed
FGM	Flux Gate Magnetometer
FIELDS	MMS Instrument Suite for the Measurement of Fields and Waves
FIR	Finite Impulse Response
FIT	FIELDS Integrated Timing/ FIELDS Interference and Timing
FK5	Fifth Fundamental Catalogue
FLT	Fractional Live Time
FM	Flight Model
FOV	Field of View
FPGA	Field Programmable Gate Arrays
FPI	Fast Plasma Investigation
FS	Fast Survey
FSM	Fluxgate-Searchcoil-merged Magnetic Field
FSW	Flight Software
FWHM	Full Width at Heigh Maximum

GDU	Gun-Detector Unit (two per Electron-Drift Instrument)
GEO	Geocentric Geographic
GEOS-2	Geostationary Scientific Satellite (European Space Agency)
GF	Geometric Factor
GSE	Geocentric Solar Ecliptic (coordinate system)
GSFC	Goddard Space Flight Center
GSL	Gnu Scientific Library
GSM	Geocentric Solar Magnetospheric
HEX	Hexadecimal
HOTS	Hot Standby Mode
HPCA	Hot Plasma Composition Analyzer
HV	High Voltage
HVPS	High Voltage Power Supplies
HWC	Hanning Window Correction
IAU	International Astronomical Union
ICRF	International Celestial Reference Frame
IDL	Interactive Data Language (coding language)
IDPU	Instrument Data Processing Units
IGRF	International Geomagnetic Reference Field
IION	Constant Ion Current Mode
IIR	Infinite Impulse Response
IMF	Interplanetary Magnetic Field
ION	Ion Data
IRAP	French Institut de Recherche en Astrophysique et Planetologie
IS	Instrument Suite
ISAS	Japanese Institute for Aeronautics and Astronautics
ISTP/SPDF	International Solar-Terrestrial Physics/Space Physics Data Facility
ITF	Instrument Team Facility
ITOT	Constant Total Current Mode
ITRF	International Terrestrial Reference Frame
IUM	Instrument User Manual
IWF	Space Research Institute of the Austrian Academy of Sciences
JAXA	Japan Aerospace Exploration Agency
JPL	Jet Propulsion Laboratory
L	Level
LASP	Laboratory for Atmospheric and Space Physics
LEEIF	Low Energy Electron and Ion Facility
LPP	Laboratoire de Physique des Plasmas
LT	Live Time
LTC	Live Time Correction
LUT	Onboard Lookup Tables
LVPC	Low Voltage Power Converters

MAGNETSRODE	Magnetic Coil Facility at the Technical University Braunschweig, Germany
MCP	Micro Channel Plate
MEC	Magnetic Ephemeris Coordinates
MLI	Multi-Layer Insulation
MMS	Magnetospheric Multiscale Mission
MOD	Mean of Date
MOM	Moments
MPA	Major Principle Axis
MSFC	Marshall Space Flight Center
NASA	National Aeronautics and Space Administration
NOE	No Emission (Startup Active)
OFF	Instrument Not Active
OLR	Outgoing Longwave Radiation
OMB	Orthogonalized Magnetometer Boom
PA	Pitch Angle
PDMP	Project Data Management Plan
PEF	Pseudo Earth Fixed
PH	Pulse Height
PPS	Pulse Per Second
PSD	Power Spectral Density
RB	Radiation Belt
RBSPICE	Radiation Belt Storm Probes Ion Composition Experiment
RF	Radio Frequency
ROI	Region of Interest
RPA	Retarding Potential Analyzer
RTS	Relative Time Sequence
SA	Spin Axis
S/C ; SC	Spacecraft Coordinate System; Signal Loss Crosstalk; Spacecraft
SCDRC	Spectral Compression Dynamic Range Correction
SCM	Search Coil Magnetometer
SCMFRC	SCM Frequency Response Correction
SdC	Spectra Data deCompressed
SDC	Science Data Center
SDP	Spin-Plan Double Probe Electric Field Instrument
SITL	Scientist In The Loop
SION	Fuel Save Mode Option
SLAV	Slave Mode
SLERP	Spherical Linear Interpolation
SM	Solar Magnetic Coordinates
SMPA	Spinning Major Principal Axis (MPA)-aligned Coordinates
SOC	Science Operations Center
SPEDAS	Space Physics Environment Data Analysis System
SPOT	Fuel Save Mode Option
SS	Slow Survey

SSD	Solid-state Detectors
SSL	Spinning Spacecraft, Angular Momentum Vector (L) Aligned
STAFF	Spatio-Temporal Analysis of Field Fluctuations experiment (ESA Cluster mission)
STDB	Standby Mode
STEMP	Sensor Temperature Parameter
STOT	Fuel Save Mode Option
STP	Solar Terrestrial Probe
STUP	Startup State
SwRI	Southwest Research Institute
TAI	International Atomic Time
TECH	Technical Mode
TEME	True Equator, Mean Equinox
TEST	Test and Commissioning Mode
TF	Search-coil Magnetometer Response
THEMIS	Time History of Events and Macroscale Interactions during Substorms (mission)
TOD	True of Date
TOF	Time of Flight
TOF-DN	Time of Flight Data Number
UCLA	University of California, Los Angeles
UNH	University of New Hampshire
UTC	Coordinated Universal Time / Universal Time Coordinated
UV	Ultraviolet
WF	Wave Form

13.2 UNITS AND MEASUREMENT

Abbreviation Unit / Measurement	Definition
b	Magnetic Field Unit Vector
B	Magnetic Field Strength
dB	Decibel
dBV/nT	Decibel Volts per NanoTesla
C/A	Counts per Accumulation
C/S	Counts per Second
deg	Degree
dxdv	Phase Space Volume Element
E	Particle Energy
e	Energy
e	Elementary Charge
Eff	Efficiency
EGM	Geometric Mean of the Energy Bounds of the Energy Channel
eV	Energy (electronvolt)
Exy	Spin Plane E-field
Ez	Spin Axis E-field
F(v)	Plasma Distribution Function / Velocity Distribution Function
Hz	Frequency (Hertz)
I	Intensity
kbit/s	Kilobit/Second
keV	Energy (kiloelectronvolts)
kHz	Frequency (kilohertz)
km/s	Distance; kilometers/second; ExB Velocity
m	Ion Species Dimension Symbol; Time of Flight Binning Mediating Parameter; Ion Mass to Charge Ratios
Mbit	Megabit
Mbytes	Megabyte
ms	Time (milliseconds)
mV/m	Electric Field
nA	Current (nanoamps)
nT	Magnetic field strength (nanoteslas)
ns	Time (nanoseconds)
ohm	Electrical Resistance
P	Physical Values
ppm	Parts Per Million
R	Raw Values
R_E	Earth Radii
S/s	Samples/Second
t	Time
TA	Channel Accumulation Period
V*DEF*	Voltage of the Deflector
V*ESA*	Voltage of the Electrostatic Analyzer

Ve,x	Electron Velocity
Vi,x	Ion Velocity
ΔE_x	DSL Offset
ΔE_y	DSL Offset
∇f_e	Vector Spatial Gradient Term
α	Amplitude Correction ; Azimuth Dimension ; Spin-energy Sweep Mediating Parameter
β	Elevation Dimension Symbol ; Start Anode Mediating Parameter
$\partial f_e/\partial t$	Temporal Derivatives
µA	Current (microamps)
µs	Time (microseconds)
ωt	Angular Frequency times Time
θ	Theta; Angle describing particle direction
φ	Angle describing particle direction
Φ	Azimuth angle

13.3 LIST OF FIGURES

13.4 LIST OF TABLES

Appendix H: MMS Inclusion, Diversity, Equity, and Accessibility (IDEA) Plan

INTRODUCTION:

The MMS team recognizes that inclusion, diversity, equity, and accessibility (IDEA) are essential to achieving the excellence for which NASA strives. We are committed to implementing a robust IDEA approach to ensure systematic and sustainable fairness, impartiality, and equity in all our business, research, and operations practices. For the period of performance covered by this Senior Review, MMS will emphasize fulfilling NASA's 2022 Strategic Plan goals toward fulfilling Presidential Executive Orders 13985 and 14041 by focusing on furthering participation by underserved communities in our mission activities. As stated by NASA Administrator Bill Nelson, "we are stronger together, and diversity is our strength."

Research has shown that diverse teams and a shared perception of inclusion leads to a high sense of belonging, high levels of trust, increased employee engagement and enhanced team innovation. (See https://www.cio.com/article/189194/5-ways-diversity-and-inclusion-help-teams-perform-better.html). Because the selection of the MMS team occurred in 2005, many elements of institutional and individual diversity are long established. The MMS team has steadily become more diverse since that time, both by the expansion of science participation as the project moved from the development stage to flight and through the internal EEO efforts of the major institutions involved. This plan, therefore, focuses on expanding and enhancing *inclusion* best practices, both to solidify that steady progression toward greater representational diversity on our own team and – perhaps more importantly – to be a visible part of the heliophysics community's activities to attract and retain a more diverse talent base.

GOALS, PRINCIPLES, AND GUIDANCE:

Because MMS is a NASA Strategic Mission, and its data use involves a large proportion of the space physics community both nationally and abroad, the MMS team proposes to align its strategy with that of the American Geophysical Union's Diversity and Inclusion Strategic Plan. Most MMS scientists and many of its engineers are members of this professional society and/or attend its gatherings. AGU's work to elevate concerns about the lack of participation by historically underrepresented communities in the geosciences is mature, is professionally managed, and its benchmarking data – when broken out for the SPA section – are directly relevant to MMS. By directly targeting inclusion within the space physics community, MMS can best impact the broader IDEA goals held by NASA and our nation.

The inclusion principles directly adapted for MMS are:

> *value the contributions of diversity to MMS and respect the individual identities of participants engaged*
>
> *proactively provide equitable access to MMS resources, collaborations, publications, recognition, and leadership positions, regardless of personal identity and background*
>
> *ensure MMS is a safe, welcoming, and supportive environment for all that wish to participate*
>
> *cultivate a culture of respect and be a model organization—and community—for inclusive practices*

We strive for this objective of inclusivity because it enhances the quality and impact of the space physics enterprise and its workforce; it directly supports the personal fulfillment, career success, and impact of MMS participants by facilitation of their contributions; and it is the morally and ethically right thing to do.

[*adapted from: AGU Diversity and Inclusion Strategic Plan 2019*]

COMPOSITION OF THE TEAM:

The MMS project is fortunate to have the support of many of our community's leading space physics institutions. All these organizations have ongoing, robust equal opportunity efforts that govern their local practices and responsibilities. Each of these MMS teams plan to leverage their local resources to support MMS's inclusion initiatives. A few of these resources are:

The NASA Office of Diversity and Equal Opportunity (ODEO) provides an overall framework for the mission with an inclusion plan at the agency level that includes a wide range of diversity, inclusion, and civil rights policies, programs, and services to promote innovation, trust, respect, and excellence within its ranks.

The Goddard Project Scientist Office and MMS Mission Operations Center leadership are able to work with the GSFC Human Resources Office and the GSFC Office of Diversity and Equal Opportunity to benchmark and track local team member demographics (e.g., gender, race, age, disability, career level, etc.) to ensure the project continues to attract a diverse talent pool and that diversity is reflected at all levels of the project. MMS will involve these professionals when developing materials/surveys for broad dissemination. In addition, the GSFC Heliophysics Division supports a dedicated IDEA team that establishes best practices and, when appropriate, pools resources for multi-mission IDEA initiatives. MMS anticipates participating in the consolidation of IDEA initiatives that are common among the several flight missions responding to this Senior Review.

In all cases, emphasis will be placed on that institutions' personnel recruitment strategies and how they might be employed to identify MMS students and postdocs originating from underrepresented communities.

BARRIERS SPECIFIC TO MMS:

Barriers to creating a diverse and inclusive working environment within MMS are the same barriers that affect our national space physics and aeronomy (SPA) community. These include:

1) *awareness within the scientific community of the benefits of diversity, and the evidence for those benefits*
2) *sustaining – over a highly extended mission lifetime – an environment in which everyone is actively engaged, empowered, and informed*
3) *ability to expand engagement in all aspects of MMS activities (e.g., collaborations, publications, meetings, leadership, recognition), particularly for those from underserved and disadvantaged communities*
4) *ability to obtain relevant demographic measures and data to inform decision-making about MMS inclusion efforts and to regularly monitor progress in achieving results*

[*adapted from: AGU Diversity and Inclusion Strategic Plan 2019*]

The significance of inclusion's impact on the recruitment and retention of participants is often overlooked, despite research demonstrating their correlation. MMS believes that actively prioritizing inclusion will result in our participants wishing to continue and share their work and so will sustain MMS's high level of scientific output.

ACTION PLAN FOR FY24-FY26:

In support of NASA's core value of Inclusion and the SMD Science Plan Strategy 5.3.7, the MMS team will take intentional and strategic steps to create and maintain a diverse, inclusive, and safe work environment and mitigate the identified barriers through the following activities:

- **MMS Weekly Science Telecons:** Since launch, MMS has held weekly science telecons for the purpose of fostering cross-team collaboration and providing tutorial-level data analysis information. The 20+ research groups associated with MMS take turns formulating the agenda and leading the discussion. Since the previous Senior Review, MMS leadership intentionally invited earlier career members of those organizations to be telecon leaders for the purpose of increasing their visibility and leadership experience. By offering a greater level of engagement across the many MMS research teams, we can bring all to the same level of expertise. The result is more opportunity for collaboration and more confidence in the scientific results before public presentation and peer review. In the coming years, we plan to encourage our more experienced researchers to be more proactive in contacting other telecon speakers, especially those with less experience, to offer advice and encouragement on their research.

- **MMS Early Career Grants:** While research funding continues, MMS plans to continue its practice of awarding Early Career Grants. Early career researchers associated with instrument teams are traditionally funded through large contracts/grants awarded to an institution's Lead Co-I. In order to increase the visibility of our early career scientists, provide training in project leadership and demonstrate their ability to win independent research, MMS awards 5-to-10 one-year NASA grants per year. Research proposals – focused on MMS science objectives – are evaluated and awarded per nominal NASA FAR processes and requirements. This activity is managed as a joint activity by members of the MMS Science Working Group. The SWG ensures there is a diverse group of potential candidates and provides mentorship through the lifecycle of the project. Measures of success are the retention of these scientists within the heliophysics community and their ability to obtain permanent research positions. We feel it is imperative to continue that program as it supports those exiting a postdoc position to establish a permanent position at the institution best suited to their development. Statistics from the inception of this initiative are shown in Table H.1:

Table H.1: Early Career Grant Statistics

Year	#Grants	% to underrepresented groups	% retained within Heliophysics community	% attained permanent positions
2019	6	33%	100%	≥67%
2020	9	67%	100%	≥44%
2021	8	88%	100%	too early to determine
2022	3	66%	100%	too early to determine

- **MMS Leadership Training:** Starting with the 2020 Senior Review, all key positions on MMS were assigned deputies for the purpose of succession planning and for training future PIs and Project Scientists. Several of these individuals have already been promoted into these positions (Table 4.x of the 2023 MMS Senior Review Proposal). MMS continues to appoint new individuals into these career development positions in anticipation of their eventually assuming leadership positions on MMS or other missions. These deputies-in-training participate as ex-officio members of the MMS Science Working Group (SWG), which is the executive decision-making body for the broader MMS Science Working Team (SWT). The MMS SWG ensures there is a diverse group of potential candidates for these positions and provides mentorship through the lifecycle of their training.

- **MMS IDEA Spotlight:** MMS proposes to include short IDEA training "posts" as part of its regular telecons and workshops. Modeled after an ongoing GSFC Heliophysics Division IDEA newsletter,

these single-slide posts are intended to provide a continuous stream of easy-to-absorb training modules on inclusion topics with suggestions for practical action and links to further information. Figure H.2 shows example posts. The goal is to provide a minimum of 12 per year with the posts linked to the weekly MMS science telecon site, included in the slide decks presented at the MOC/SOC operations status telecons, and included in project-level slide decks presented at MMS SWT and Community Science Workshops. These training slides will serve as a consistent expression of MMS's commitment to its inclusion goals and a gentle reminder to team members to pursue the actions contained in this plan. Posts for MMS will help our team (1) increase their understanding of implicit and unconscious bias, the effects and impact of privilege, and historic discrimination and misrepresentation; (2) build skillsets to promote a respectful and inclusive team environment; and (3) receive periodic reminders about utilizing their local resources for outreach to underrepresented groups. If approved, this initiative would be managed by the MMS Deputy Project Scientist.

Figure H.2: Three examples of potential IDEA Spotlight posts/presentation slides

- **MMS Meeting Code of Conduct:** MMS proposes to develop a written Code of Conduct to be disseminated when participants register for its SWT and Community Science meetings. The code would specify the team's principles, standards, and ethical expectations that team members will be held to as they engage in meeting activities. It will address how conflicts would be resolved; what steps will be taken to ensure that all voices can be heard respectfully; and what process will be implemented to promote cultural awareness. Utilizing AGU's Meetings Code of Conduct and the USRA-LPI Meetings Code of Conduct as starting points, the MMS Code will be developed in collaboration with professionals within the NASA GSFC and SwRI offices of diversity and equal opportunity. If approved, this initiative would be managed by the MMS Deputy Payload PI and MMS Deputy Project Scientist.
- **Workshop Inclusion Survey:** To understand and develop mitigations to participation barriers at its workshops, MMS proposes to develop a short, online post-workshop "satisfaction" survey. Focused on inclusion factors and indicators of psychological safety, and intended to be completed within 3-5 minutes, the survey will allow MMS to steadily improve its workshop formats and technologies over time, eventually providing the full range of inclusive practices that best support the space physics community. Our team has already adopted a standard of including virtual participants at all in-person workshops and anticipates introducing closed-captioning, better enforcement of its existing accessible plot standards, and providing additional methods to engage in real time discussions. Automatic database-driven storage and graphic display of survey results will be used to provide transparency, drive change, and, separately, report improving outcomes in this area to future Senior Review cycles. If approved, this initiative would be managed by the MMS Deputy Payload PI with implementation assistance by the MMS SOC.

- **MMS Anonymous Feedback Box:** MMS proposes to develop an online anonymous feedback box. Periodic advertisements of this feedback box within the MMS team can act as a "pulse survey" mechanism to gauge our team's climate and prevent backsliding on our goals. Automatic database-driven storage and including an ability for users to classify the feedback as a question, suggestion, comment, or concern will allow MMS to track the quantity and tone of feedback over time. If approved, this initiative would be jointly managed by the MMS Payload PI and MMS Project Scientist.

SUMMARY:

The MMS team is at its best when every member feels respected, included, and heard—when everyone can show up as themselves and do their best work every day. The MMS team is committed to creating a positive work experience for scientists and engineers of all identities and experience through activities that provide steadily increasing levels of accommodation, integration, visibility, and opportunity (Table H.2).

Table H.2: Summary of MMS Inclusion Plan Activities

Frequency	Initiation	Activity	Re Barrier #	Quantifiable Element	Impact Assessment
Weekly	FY2015	MMS Weekly Science Telecons	1, 2, 3	Sustained level of presentation and participation by the approx 24 associated intitutions.	Perceptable increases in AGU SPA and Local Institution Diversity Surveys
Yearly	FY2019	MMS Early Career Grants	2, 3	Attainment of Permanent Positions	
3 yr plan	2020 Senior Review	MMS Leadership Training Program	1, 2, 3	Promotions into Leadership, within MMS or elsewhere	
Monthly	Proposed	IDEA Spotlight	1	Sustained inclusion in presentation decks	
Semiyearly	Proposed	Mission Workshop Inclusion Survey	2, 4	Sustained use and dissemination of results at each Workshop, documentation of technology and other improvements	Improvements in Workshop Inclusion Survey scores and in the tone of anonymous feedback
Monthly	Proposed	MMS Meeting Code of Conduct	2	Sustained dissemination of link (full text) at each Telecon (Workshop) along with documentation of enforcement actions	
Ongoing	Proposed	MMS Anonymous Feedback Box	2, 4	Sustained level of feedback over time and dissemination of related Q&A	